Transactions of the ASME

HEAT TRANSFER DIVISION
Chairman, R. J. SIMONEAU
Secretary, F. A. KULACKI
Senior Technical Editor, K. T. YANG
Technical Editor, I. CATTON
Technical Editor, M. EPSTEIN
Technical Editor, G. M. FAETH
Technical Editor, R. GREIF
Technical Editor, P. J. MARTO
Technical Editor, R. H. PLETCHER
Technical Editor, R. K. SHAH
Technical Editor, R. VISKANTA

BOARD ON COMMUNICATIONS
Chairman and Vice President
MICHAEL J. RABINS

Members-at-Large
W. BEGELL
W. G. GOTTENBERG
D. KOENIG
M. KUTZ
F. LANDIS
J. LOCKE
J. ORTLOFF
C. PHILLIPS
H. C. REEDER
K. REID

President, FRANK M. SCOTT
Executive Director,
PAUL ALLMENDINGER
Treasurer,
ROBERT A. BENNETT

PUBLISHING STAFF
Mng. Dir., Publ., J. J. FREY
Dep. Mng. Dir., Pub.,
JOS. SANSONE
Managing Editor,
CORNELIA MONAHAN
Production Editor,
JACK RUMMEL

The Journal of Heat Transfer (ISSN 0022-1481) is published quarterly for $90 per year by The American Society of Mechanical Engineers, 345 East 47th Street, New York, N Y 10017. Second class postage paid at New York, NY and additional mailing offices. POSTMASTER: Send address changes to The Journal of Heat Transfer, c/o THE AMERICAN SOCIETY OF MECHANICAL ENGINEERS, P.O. Box 3199, Grand Central Station, New York, NY 10163.

CHANGES OF ADDRESS must be received at Society headquarters seven weeks before they are to be effective. Please send old label and new address.

PRICES: To members, $36.00, annually; to nonmembers, $90.00. Add $6.00 for postage to countries outside the *United States and Canada.*

INDEXED by the Engineering Index, Inc.

Journal of Heat Transfer

Published Quarterly by The American Society of Mechanical Engineers

VOLUME 106 • NUMBER 2 • MAY 1984

ANNOUNCEMENTS

TECHNICAL PAPERS

(Contents continued)

TECHNICAL NOTES

DISCUSSION

The Effect of a Wall Boundary Layer on Local Mass Transfer From a Cylinder in Crossflow

R. J. Goldstein
Fellow ASME

J. Karni

Department of Mechanical Engineering,
University of Minnesota,
Minneapolis, Minn. 55455

A naphthalene sublimation technique is used to determine the circumferential and longitudinal variations of mass transfer from a smooth circular cylinder in a crossflow of air. The effect of the three-dimensional secondary flows near the wall-attached ends of a cylinder is discussed. For a cylinder Reynolds number of 19000, local enhancement of the mass transfer over values in the center of the tunnel are observed up to a distance of 3.5 cylinder diameters from the tunnel wall. In a narrow span extending from the tunnel wall to about 0.066 cylinder diameters above it (about 0.75 of the mainstream boundary layer displacement thickness), increases of 90 to 700 percent over the two-dimensional flow mass transfer are measured on the front portion of the cylinder. Farther from the wall, local increases of up to 38 percent over the two-dimensional values are measured. In this region, increases of mass transfer in the rear portion of the cylinder, downstream of separation, are, in general, larger and cover a greater span than the increases in the front portion of the cylinder.

Introduction

Knowledge of the circumferential and longitudinal variations of heat transfer from a circular cylinder in crossflow is necessary for the successful design of heat transfer equipment and instrumentation such as boilers, heat exchangers, hot-wire anemometers, and electrical conductors. For this reason, and because of its relatively simple flow and design characteristics compared to other streamline-shaped surfaces, the circular cylinder has been subjected to many theoretical and experimental studies of which references [1–10] are only a sample.

In recent years, many experimental investigations have been directed to a better understanding of the effect of turbulence, tunnel blockage, and suface roughness on heat transfer. Examples of such studies are given in references [2, 11–16]. These studies do not include a quantitative investigation of the longitudinal as well as peripheral variations of transfer coefficients near the wall-attached end of a cylinder.

It is known that three-dimensional separated flows develop near the base of an obstacle protuding from a wall when the obstacle is exposed to a crossflow. The main qualitative feature of these flows, a horseshoe vortex system, has been studied extensively, mostly using flow visualization techniques (cf., references [17–25]). Although qualitatively understood in terms of the effect of the boundary layer in the approaching flow, a sound theoretical solution for this complex flow pattern is as yet unavailable. The data, however, suggest that the horseshoe vortex system appears throughout a large velocity range and with many different geometries. Sedney and Kitchens [20], for example, found that the vortex structure they observed in supersonic turbulent flow conditions is similar to that seen by Norman [19], who studied obstacles in low-speed laminar flows. Marchal and Sieverding [21] observed essentially the same vortex system in front of the leading edge of a turbine blade. Evidence of the existence of horseshoe vortices were also found in heat transfer pattern studies of narrowly-spaced heat exchanger fins (cf., references [26–28]).

The main objective of the present work is to develop and apply a method of measuring local transfer coefficients around and along a circular cylinder at all locations, near the tunnel wall as well as away from it. Thus, the effect of the three-dimensional secondary flows, including the horseshoe vortex system, on mass (heat) transfer characteristics of a cylinder can be determined. The naphthalene sublimation technique is used. A long cylinder, coated on the outside with naphthalene, is installed vertically in a wind tunnel such that its naphthalene-covered surface extends from below the bottom wall of the tunnel to near the top wall. Measurements are taken along the cylinder over the span $0 < y/L < 0.6$ and around its entire circumference. The variations of Sherwood number with angle and distance from the tunnel wall have been determined at Re $\simeq$ 19000 and $\delta^*/d = 0.0877$.

Experimental Apparatus and Measurement Technique

The apparatus consists of three main parts: the test cylinder, the wind tunnel, and the data acquisition system.

Test Cylinder. The cylinder is made of stainless steel tubing with a diameter of 25.4 mm and a length of 305 mm, which is equal to the height of the wind tunnel. A recess about 1-mm deep is machined into the outer surface of the stainless steel tube in the region where naphthalene cover is desired. The naphthalene layer extends over most of its outer surface. A span of 19.1 mm adjacent to each end is left uncoated.

Before each test, a new naphthalene casting is made in the following way. The cylinder is mounted inside a two-piece aluminum mold with an inside diameter that matches the outside diameter of the cylinder near its ends but not in the recessed region. Molten naphthalene is then poured into the recess. After the naphthalene solidifies and the entire apparatus is cooled to room temperature, three ring heaters and a heat gun are employed to heat the mold from the outside until its temperature reaches about 75–78°C. Meanwhile, air is blown through the center of the cylinder, keeping it near room temperature. As a result, the mold expands while the cylinder and the naphthalene layer remain relatively unchanged. This allows a separation of the mold from the cylinder without damaging the naphthalene cast.

With the aid of ring heaters and a few thermocouples, the temperature of the cylinder and the mold can be controlled before and during the casting process. Thus, all the casts are obtained in the same way and under the same thermal con-

Contributed by the Heat Transfer Division for publication in the JOURNAL OF HEAT TRANSFER. Manuscript received by the Heat Transfer Divison June 6, 1983.

ditions. The errors which could have resulted from variation of crystallization characteristics between runs are minimized. The naphthalene surface is extremely smooth everywhere, wide) corresponding to the lines where the two mold pieces join. The strips are smoothed off with a small file before each run. Then, as the cylinder is put in the wind tunnel, the strips are positioned at $\theta = 135$ deg and 315 deg. The measured mass losses, which are virtually symmetrical around the periphery, indicate that the strips have no significant effect on the outcome of the experiment.

Nine thermocouples are used for temperature measurements on the cylinder. They are installed on the stainless steel surface 1.0 mm below the outer surface of the naphthalene layer. Five thermocouples are positioned along the cylinder and the other four are located around its circumference. These thermocouples monitor the temperature during the wind tunnel runs as well as during the casting process. Four thermocouples are installed in the two mold pieces.

Wind Tunnel. The experiments are performed in a suction-type wind tunnel. The entrance section of the tunnel contains two filters, a honey-comb flow straightener and dampening screens before the 9 to 1 contraction section. This is followed by a rectangular test section measuring 61-cm wide by 30.5-cm high. The tunnel is run open cycle. The free stream velocity (U_∞) is determined from the dynamic pressure which is measured by an impact tube in conjunction with a wall static tap. The impact-static pressure difference is detected by a Baratron solid-state capacitance-type pressure meter capable of sensing 10^{-3} mm-Hg. The static pressure is determined by subtracting the room-static tap pressure difference from the room barometric pressure. The turbulence intensity of the free stream (T_u) was measured without the cylinder present. The tunnel's bottom wall boundary layer is tripped just upstream of the test section. (The tripping wire diameter is about 1.6 mm.) Measurements of the mainstream boundary layer profile were conducted while the cylinder was out of the wind tunnel. The tip of the impact tube used in the measurements was positioned about 5 mm upstream of the cylinder's stagnation line ($\theta = 0$ deg) location during mass transfer data runs. The velocity variation in the boundary layer was close to a one-seventh power profile. The displacement thickness of the mainstream boundary layer, δ^*, is such that the center of the wind tunnel ($y/L = 0.5$) corresponds to $y/\delta^* = 68.4$ and $y/d = 1.0$ corresponds to $y/\delta^* = 11.4$. Table 1 lists the operating conditions during the test runs.

The test cylinder is positioned vertically in the middle of the tunnel's cross section, about 432 mm downstream of the boundary layer trip. The naphthalene-covered portion extends from 6.4 mm below the tunnel's bottom wall to 260 mm above it (about 45 mm below the top wall). A schematic view of the cylinder as it is positioned in the wind tunnel is shown in Fig. 1. The cylinder is mounted into a 50.8-mm diameter delrin AF rod whose upper surface is aligned smoothly with the bottom wall. The rod has a round hole, 25.4 mm in diameter and 25.4-mm deep. The hole diameter equals the cylinder O.D. and assures a very tight fit between the naphthalene surface and the bottom wall. Another delrin rod with a diameter equal to that of the test cylinder is inserted through the top plate to join the top end of the cylinder. Besides holding the cylinder firmly in place, the two delrin rods also insulate the cylinder from outside thermal influences. During data runs, the tunnel temperature is monitored by means of a 0.1°F

Nomenclature

C_p = specific heat, at constant pressure, for air
d = diameter of the test cylinder
D_f = mass diffusion coefficient for naphthalene vapor in air; taking Sc = 2.5 [29], $D_f = \nu/2.5$
h = local convective heat transfer coefficient
h_m = local mass transfer coefficient
H = shape factor, δ^*/δ_2
k = thermal conductivity
L = length of test cylinder (also the height of the wind tunnel)
$\dot{m}$ = local naphthalene mass transfer rate per unit area of the cylinder surface
n = exponential power in the heat-mass transfer correlation equation, equation (4)
$\bar{p}_v$ = local vapor pressure of naphthalene at the cylinder surface averaged over the time of exposure in the wind tunnel
R_n = gas constant for naphthalene (universal gas constant divided by molecular weight of naphthalene—128.19)
$\bar{T}$ = local temperature of naphthalene surface averaged over exposure time in wind tunnel
T_u = turbulence intensity
t = thickness of naphthalene layer
U_∞ = mean velocity of main stream
W = width of the wind tunnel test section
x = direction along the tunnel test section
y = direction along the cylinder center line; $y = 0$ on the tunnel bottom wall
z = direction across the tunnel test section
α = thermal diffusivity, $k/C_p\rho$
δ = mainstream boundary layer thickness
δ^* = displacement thickness of mainstream boundary layer just upstream of the cylinder
δ_2 = momentum thickness of mainstream boundary layer just upstream of the cylinder
Δt = change in local naphthalene thickness due to sublimation during exposure in wind tunnel
$\Delta\tau$ = time of cylinder exposure in wind tunnel
θ = angle around the cylinder measured from the front stagnation point, deg
μ = dynamic viscosity of air
ν = kinematic viscosity of air, μ/ρ
ρ = density of air
ρ_s = density of solid naphthalene
$\bar{\rho}_{v,w}$ = local naphthalene vapor density on the cylinder surface averaged over exposure time in wind tunnel

Dimensionless parameters

Nu = Nusselt number, hd/k
Pr = Prandtl number, ν/α
Re = Reynolds number based on cylinder diameter, $U_\infty d/\nu$
Re_x = Reynolds number based on distance from virtual origin of wall boundary layer to the leading edge of the cylinder
Re_{δ_2} = Reynolds number based on momentum thickness of the main flow boundary layer just upstream of the cylinder's location, $U_\infty\delta_2/\nu$
Sc = Schmidt number, ν/D_f (= 2.5 for naphthalene in air [29])
Sh = Sherwood number, $h_m d/D_f$
$\overline{\mathrm{Sh}}$ = Sherwood number averaged over the circumference at a constant y
y/δ^* = dimensionless elevation
y/d = dimensionless elevation

Table 1 Operating conditions

Free Stream

Re	≃ 19,000	Re	≃ 13,700
Re_x	≃ 490,000	Re_x	≃ 350,000
U_∞	≃ 12.0 M/S	U_∞	≃ 8.6 M/S
T_u	≃ 0.43%	T_u	≃ 0.54%

$d = 25.4$ mm

blockage ratio, $d/W = 0.0417$

aspect ratio, $L/d = 12/1$

Bottom Wall Boundary Layer, Re ≃ 19,000**

$\delta^* \simeq 2.23$ mm
$\delta_2 \simeq 1.73$ mm
$H \simeq 1.29$
$Re_{\delta_2} \simeq 1294$

**Measurements at Re ≃ 13,700 are limited to the two-dimensional flow region.

ASTM-certified thermometer positioned at the center of the tunnel cross section, about 1 m downstream of the cylinder, and with a thermocouple fastened to the tunnel's bottom wall near the cylinder.

Data Acquisition System. The data acquisition system includes a modified lathe, a depth gage, a signal conditioner, and a digital voltmeter.

The lathe is equipped with a special gear wheel having 60 holes evenly spaced around its circumference. With the aid of these holes and specifically designed pin, the gear's rotational motion can be stopped and locked in place every 6 deg. A ruler with 0.01 in. spacing is mounted on the lathe bed. It is used to monitor the movement of the Compound Rest which houses the depth sensor. This sensor is a Schaevitz Linear-Variable-Differential-Transformer (LVDT) gage, type PCA-220-010; it has a linear range of .020 in. (~0.51 mm) and a resolution of about $\pm\ 5-6\times10^{-6}$ in. ($\sim 1.3-1.5\times10^{-4}$ mm). This fine resolution is two-to-three orders of magnitude smaller than the actual change in naphthalene thickness during the tests which varies from about 1.3×10^{-2} to about 1.3×10^{-1} mm. The gage is connected to a Schaevitz model CAS-025 signal conditioner that converts the a-c voltage output of the gage to a d-c voltage which is measured with a digital voltmeter.

To enable repositioning of the cylinder such that readings can be taken at the same locations on the surface as in previous (pre-tunnel exposure) measurements, a small, conic-shaped recess is indented into the stainless steel surface near the top of the cylinder. When the cylinder is put in the wind tunnel, this recess is always positioned in the same angle relative to the stagnation point. Before the sublimation depth measurements begin, the cylinder is placed on the lathe horizontally between two centers. The lathe gear is then locked into place while the tailstock is left somewhat loose, permitting manual rotation of the cylinder while the lathe shaft stays stationary. By moving the Compound Rest along the cylinder and slowly rotating it, the gage position is adjusted to the center of the small recess where the lowest possible reading on the stainless steel surface near the top of the cylinder can be obtained. The tailstock is then tightened, securing the cylinder in its place. The gage is, therefore, set at the same starting point relative to the cylinder's orientation in the tunnel before each set of measurements begins.

The measurements are conducted in the following manner. First, the cylinder is rotated by means of the lathe's shaft to a particular angle, θ; then, the locking pin is pushed into the hole corresponding to the desired angle, keeping the cylinder in a fixed position. Next, the Compound Rest is driven laterally along the cylinder, stopping at predetermined locations on the ruler and allowing the depth gage to take

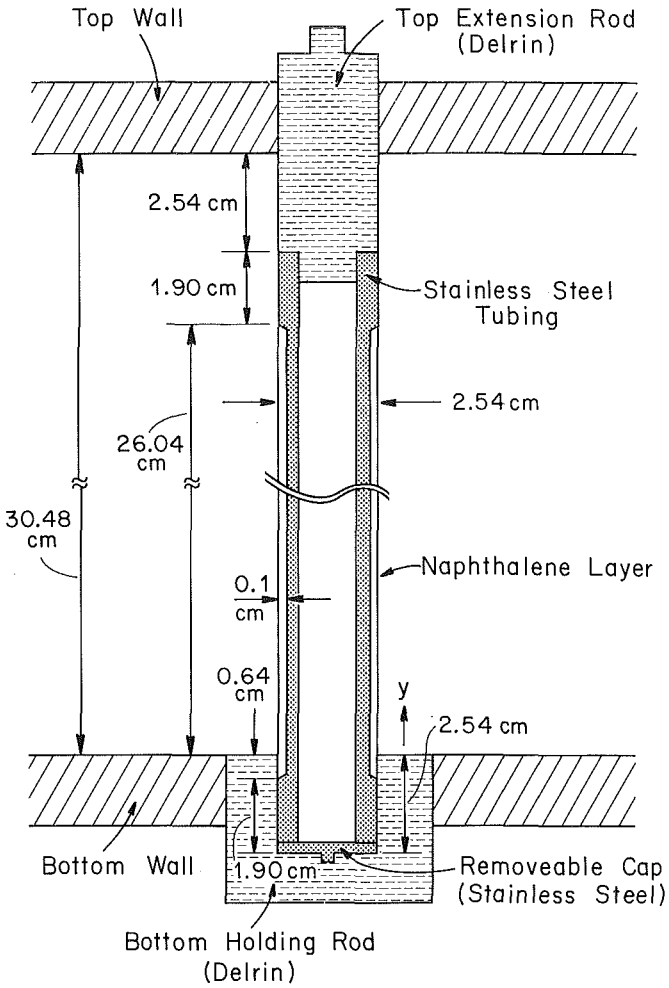

Fig. 1 A schematic view of naphthalene cylinder installed in the wind tunnel (dimensions in centimeters)

readings at the designated points on the naphthalene surface. At each angle, measurements are also taken at two points on the stainless steel surface, one near each end of the cylinder—these are reference points for the rest of the readings at that angle. A datum line between the two reference points is calculated and all the measurements on the naphthalene are taken relative to it. This procedure is repeated at all the required angles around the circumference of the cylinder.

The employment of an ultra-precision depth gage combined with a careful measuring procedure produced a high level of precision and repeatability in the measurements.

Procedure

Using the equipment described above, initial readings of the naphthalene surface contours are taken before each data run at designated locations along and around the cylinder's outer surface. Upon completion of these measurements, the cylinder is sealed in a specially made container to prevent sublimation due to natural convection. It is then taken to the wind tunnel and exposed to the air stream for a period of 50–70 min, depending upon operating conditions. Finally, a second set of readings of the surface profile is obtained at the same locations as before.

The local sublimation depth, Δt, is determined by subtracting the final local measurement from the initial one. In all the test runs, the largest values of Δt never exceed 0.5 percent of the cylinder diameter. Since the mainstream flow has no naphthalene in it, the local mass transfer coefficient is given by

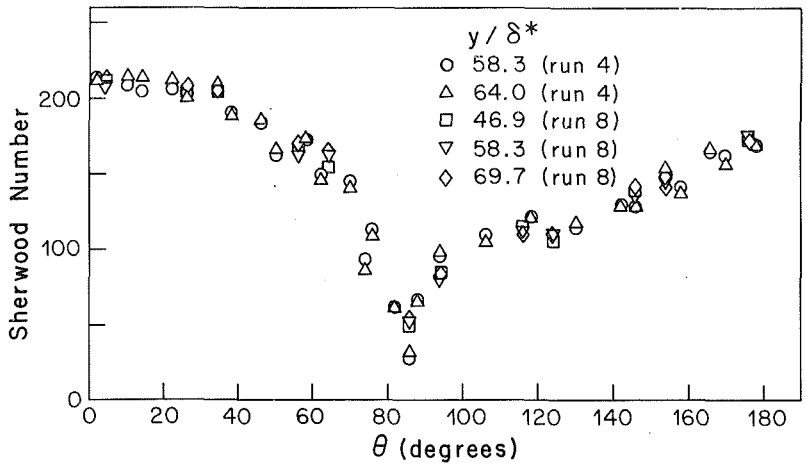

Fig. 2 Circumferential distribution of Sh at several elevations confined to the two-dimensional region; Re = 19000

$$h_m = \frac{\dot{m}}{\bar{\rho}_{v,w}} = \frac{\rho_s \Delta t / \Delta \tau}{\bar{\rho}_{v,w}} \tag{1}$$

where

$$\bar{\rho}_{v,w} = \frac{\bar{p}_v(\bar{T})}{\bar{T} R_n} \tag{2}$$

and

$$\rho_s = 1.145 \text{ gm/cm}^3 \text{ [25])}$$

$\bar{T}$ is obtained for each location from the readings of one or two thermocouples closest to it. The corresponding $\bar{p}_v$ is then determined by the Sogin vapor pressure-temperature relation [29].

The results are expressed in terms of the local Sherwood number

$$\text{Sh} = \frac{h_m d}{D_f} \tag{3}$$

Sublimation by natural convection occurs primarily during the sublimation depth measurements. It is found experimentally to take place at a rate of about 1.0×10^{-4} mm/min. A correction factor, based on this rate and the measurement time is used in the calculations to copmensate for this error. At the locations where the sublimation rate due to the tunnel's air stream is lowest (near the flow separation angle), the natural convection correction factor is about 15 percent of the total sublimation depth. Much smaller corrections (5 percent or less) are needed elsewhere on the naphthalene surface.

Results

Mass transfer measurements were taken around the whole circumference of the cylinder. The results were essentially indifferent to the side of the symmetry line on which the measurements were performed.

Near the middle of the wind tunnel the mass transfer distribution around the cylinder is not influenced by variations along the span (length) of the cylinder. The flow around the cylinder in this region is, effectively, two dimensional and the assumption of infinite cylinder length is appropriate. In Fig. 2, the measured peripheral Sh distribution is shown for several elevations above the wall, all, however, at sufficient elevation to be in the region of two-dimensional flow. The heat or mass transfer distribution pattern in the two-dimensional flow region is well known. As θ increases from zero at the stagnation point, the static pressure on the cylinder surface drops and the flow accelerates. However, the gradual increase of the cylinder boundary layer thickness with distance from stagnation causes a gradual decrease in the heat (mass) transfer. As separation is approached, the boundary layer increases in size and its velocity profile approaches a separation contour [30]. These two effects result in a sharp decrease of the local heat (mass) transfer rate. A relatively rapid increase in Sh is seen in the wake immediately downstream of the separation point. As θ increases from 100 deg to 130 deg, Sh remains nearly unchanged. It then gradually increases as θ approaches 180 deg.

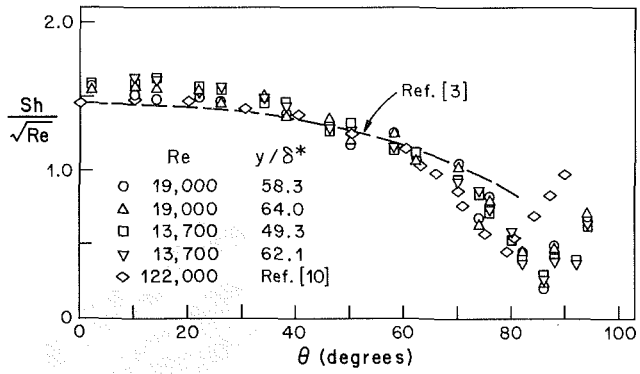

Fig. 3 The experimental and theoretical distributions of Sherwood number in the front portion of the cylinder; two-dimensional region

The measured values of Sherwood number are compared in Fig. 3 with Frossling's theoretical solution for two-dimensional laminar flow [3]. Measured values of Sh at Re = 13700 and 19000 are shown for several sufficiently high elevations to be in the two-dimensional region. Mass transfer data obtained by Sogin and Subramaniam [10] for Re = 122000, Sc = 2.5 (naphthalene) and T_u = 0.8 percent are also shown in the figure. Frossling calculated the Nusselt number distribution in the front portion of a cylinder for Pr = 0.7. His results were correlated with the mass transfer data by means of the relation

$$\text{Sh/Nu} \sim [\text{Sc/Pr}]^n \tag{4}$$

the value of the n power is taken to be 0.34, as recommended by Zukauskas [2], for the front portion of the cylinder; Sc is equal to 2.5 [29]. In the range 0 deg $< \theta <$ 40 deg, the data points are 2–7 percent above the theoretical curve which was calculated assuming no turbulence effect. In the range 40 deg $< \theta <$ 70 deg, the increasing influence of the oncoming separation on the boundary layer profile causes the real (measured) Sh to fall off. Since the theory does not account

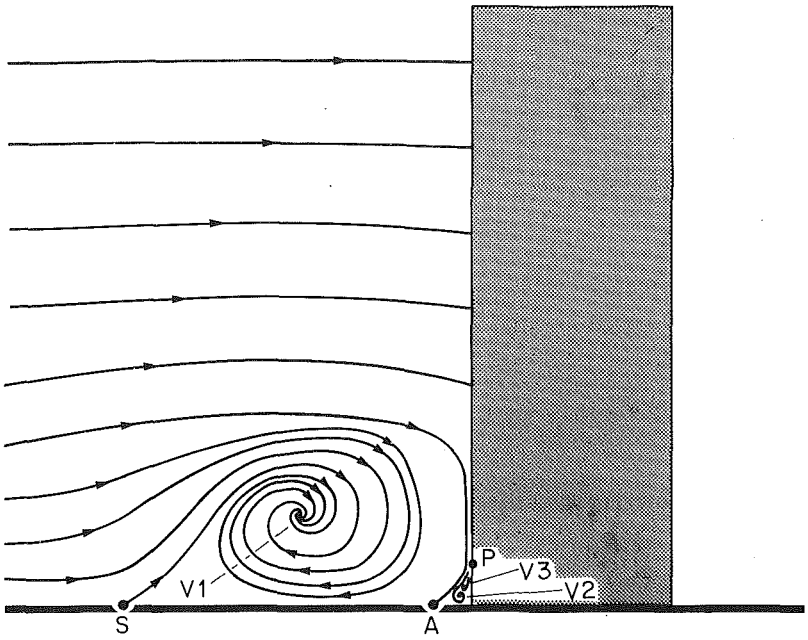

Fig. 4(*a*) Plane of symmetry representation of the horseshoe vortex system. *S* and *P* are separation points; *A* is an attachment point.

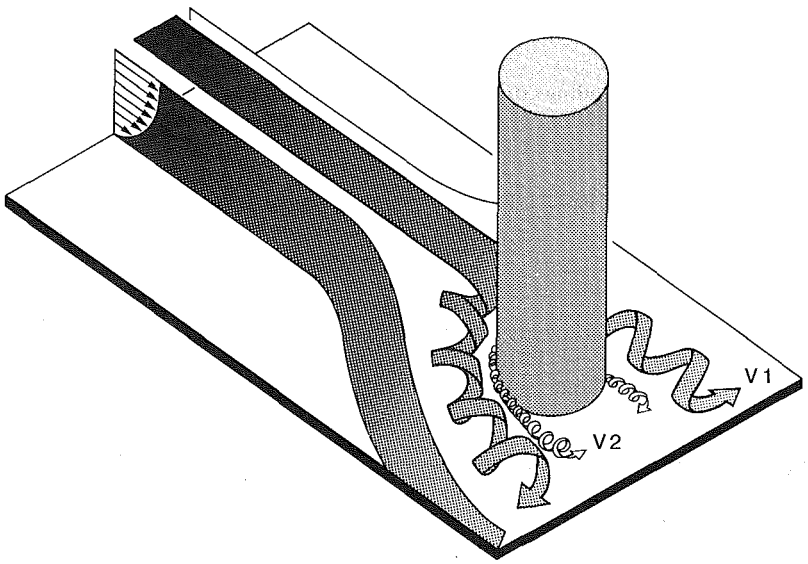

Fig. 4(*b*) Three-dimensional boundary layer separation and horseshoe vortex system in the region of interaction between mainstream boundary layer and a cylinder protruding from a wall

for separation, it diverges from the measured value when $\theta > 70$ deg, where separation effects predominate.

The circumferential average Sh ($\overline{\text{Sh}}$) values were determined from the local measurements using the summation

$$\overline{\text{Sh}} = \frac{\sum_{i=1}^{j} \text{Sh}_i \Delta\theta_i}{\sum_{i=1}^{j} \Delta\theta} = \frac{1}{360 \text{ deg}} \sum_{i=1}^{j} \text{Sh}_i \Delta\theta_i \qquad (5)$$

where j is the total number of measurements at a given y/δ^* and $\Delta\theta_i = (\theta_{i+1} - \theta_{i-1})/2$.

Discussion of circumferential average Sherwood number variation with y/δ^* is given later. In the two-dimensional flow region, the following values were obtained:

at Re = 13700, $\overline{\text{Sh}} = 128$

at Re = 19000, $\overline{\text{Sh}} = 143$

These values were compared to the heat transfer results of earlier studies. They agree within 10 percent with the correlation curves of Zukauskas [2] and Whitaker [31]. In general, the data from many different investigations show scatter of ± 25 percent around these correlation curves.

In a region extending spanwise along the cylinder from the tunnel wall to $y/\delta^* = 40$ ($y/d = 3.5$), deviations from the mass transfer pattern in the two-dimensional flow regime are detected. The tunnel wall affects the flow conditions in this region and the Sh distribution is no longer independent of y. It is appropriate, therefore, to discuss the flow mechanisms that cause the changes in mass transfer before the resutls obtained in the wall-effected region are presented.

Studies of the flow near the base of a cylinder in crossflow

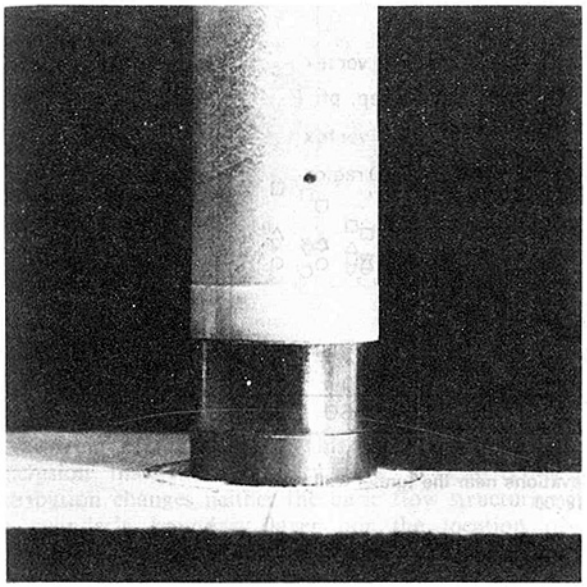

Fig. 5 The trench on the cylinder's surface. The main flow direction is from left to right; $y = 0$ is at the plane adjacent to the bottom line of the trench.

reveal a breakdown of the two-dimensional crossflow pattern. The increase in static pressure due to the deceleration of the main flow as it approaches the cylinder is larger than the slower fluid in the wall boundary layer can overcome. The result is a spanwise secondary flow toward the tunnel wall and the separation of the approaching boundary layer upstream of the cylinder. Driven by the spanwise pressure gradients, a horseshoe vortex system is formed in the region of separation (cf., references [17–25]). This system is shown in Figs. (4*a*) and 4(*b*). Figure 4(*a*) is a plane of symmetry view based on a model suggested by Norman [19] and adapted by Sedney and Kitchens [20] combined with the pattern implied by the mass transfer results of this study. Similar models were suggested by Hunt, Abell, Peterka, and Woo [23] and Baker [24]. Figure 4(*b*) is a schematic presentation of the three-dimensional flow pattern in the cylinder-boundary-layer interaction region. Despite the fact that the number of vortices formed between the primary separation at S and the attachment at A may vary from one to five or even seven [19, 20], only one vortex ($V1$) is shown there in Figs. 4(*a*) and 4(*b*). Since no measurements were taken on the tunnel wall, only the vortices which directly affected mass transfer from the cylinder are shown in the figures. The vortex $V1$ is of the same order-of-magnitude as the main-flow boundary layer thickness; it is one-order-of-magnitude larger than $V2$, which itself is so small that most invetigators were unable to observe it. The work of Sedney and Kitchens [20] and Baker [24], however, affirms the existence of $V2$. The mass transfer results of this work imply the existence of the yet smaller vortex $V3$. This last vortex, which is not shown in Fig. 4(*b*), can be traced around the front portion of the cylinder, just above $V2$.

As will be shown, the three vortices shown in Fig. 4(*a*) directly affect the mass transfer patterns on the cylinder. Especially pronounced is the influence of $V2$. This vortex is apparently so intense that it creates an observable trench in the naphthalene surface. The trench seen in Fig. 5 was created during the normal exposure time of the cylinder in the wind tunnel. The main-flow direction in Fig. 5 is from left to right. As shown in Fig. 1, the cylinder was set in the wind tunnel such that part of its naphthalene-covered surface extended under the tunnel wall and thus was unaffected by the flow. The trench was formed just above the tunnel wall, extending spanwise from $y/\delta^* \sim 0$ to about $y/\delta^* \sim 0.4$ (a distance of about 0.9 mm). Its formation could be observed during the

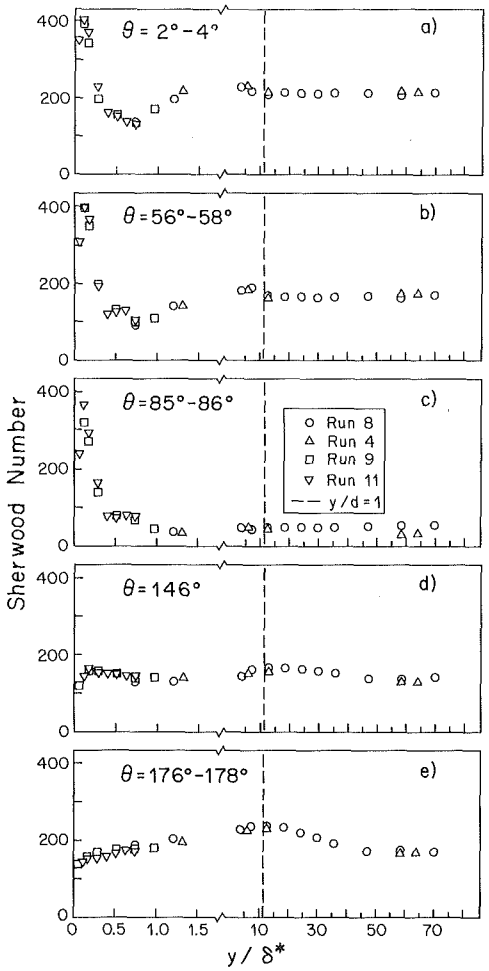

Fig. 6 Variation of Sherwood number along the cylinder at representative angles: $\delta^* = 2.23$ mm; Sc = 2.5; scale change at $y/\delta^* = 1.6$; Re ≃ 19000

Table 2 Peripheral angles corresponding to measurements shown in Fig. 6

		Exact angle of measurement				
Symbol	Run no.	Fig. *a*	Fig. *b*	Fig. *c*	Fig. *d*	Fig. *e*
○	8	4 deg	56 deg	85 deg	146 deg	176 deg
△	4	2 deg	58 deg	86 deg	146 deg	178 deg
□	9	2 deg	58 deg	86 deg	146 deg	178 deg
▽	11	2 deg	58 deg	86 deg	146 deg	178 deg

test run. As θ increases past 90 deg, the trench gradually disappears since the vortex which creates it leaves the cylinder surface and goes off in the mainstream direction. A careful inspection of the trench with the aid of a microscope reveals a "U"-shape cross section, as would be expected if indeed it was created by a small but very intense vortex. Moreover, a second depression—much smaller and almost invisible—can be detected just above the trench at y/δ^* between 0.5 and 0.7. This depression apparently is created by the $V3$ vortex shown in Fig. 4(*a*). Enchancement of mass transfer due to the large vortex $V1$ is found at elevations of $y/\delta^* \sim 3$ to $y/\delta^* \sim 8$. Because of its size, $V1$ affected a greater span of the cylinder surface than its smaller counterparts. However, the magnitude of the increase associated with $V1$ is small compared to that associated with $V2$.

Spanwise variations of Sherwood number are shown for representative angles in Fig. 6. Table 2 is given as a supplement to Fig. 6; it lists the angle θ of each data point shown in the figure. (Note the scale change of the y/δ^*-axis in this figure.) The front and the back of the cylinder show different patterns. Large values of Sh are found in the front of the

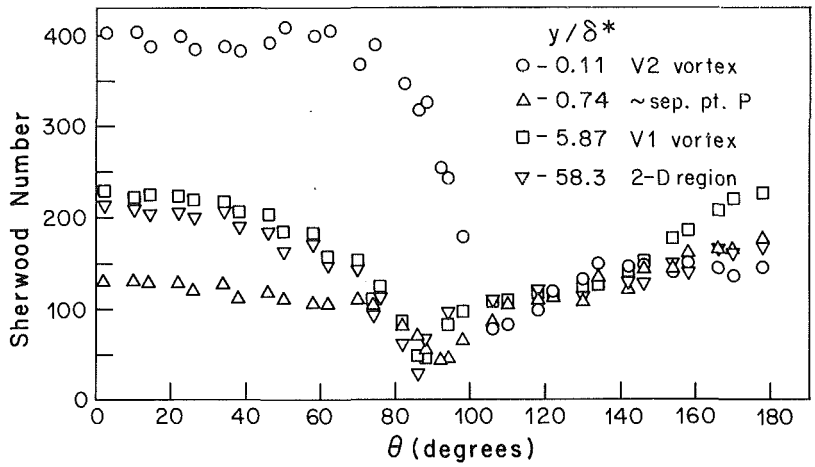

Fig. 7 Sherwood numbers at several elevations near the tunnel wall and in the two-dimensional region; Re ≃ 19000

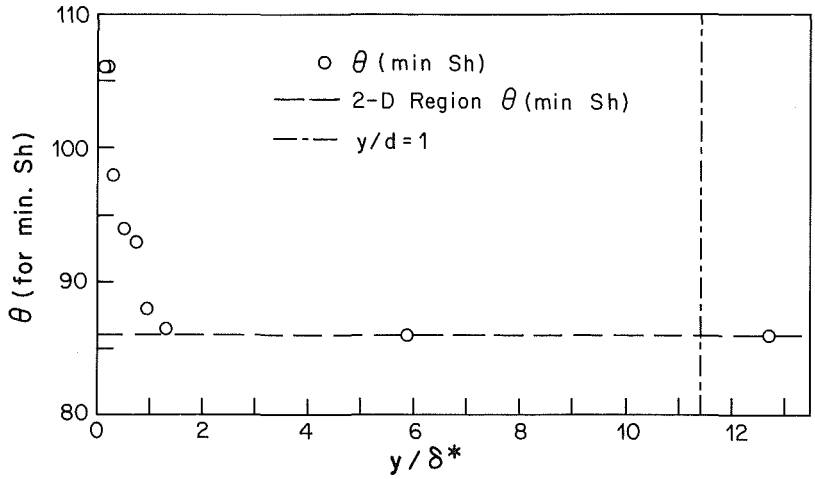

Fig. 8 Variation of the angle corresponding to minimum Sh number with y/δ^*; Re ≃ 19000

cylinder (Figs. 6*a*, *b*, *c*) for $y/\delta^* \sim 0.1$ to 0.2, apparently due to the intense vortex *V*2; no such peaks are observed in the back (Figs. 6*d* and *e*). In the wake region, increases of mass transfer are seen up to $y/\delta^* \simeq 40$ ($y/d \simeq 3.5$), while, in the front, there is little variation in Sh for $y/\delta^* > 10$ ($y/d > 0.9$). Near $\theta = 180$ deg (Fig. 6*e*), Sh has a maximum increase of about 38 percent over the two-dimensional region value at the same angle; this occurs at $y/\delta^* \simeq 6$. For $\theta < 70$ deg, increases of 7–13 percent over Sh values in the two-dimensional region are seen at $y/\delta^* \simeq 5$. The small increases in the front portion of the cylinder at $y/\delta^* \sim 3$ to 8 (Fig. 6*a* and *b*) are attributed to the vortex *V*1. The extensive increases of Sh in the back region could result from the stretching of the wake's eddies due to the additional Reynolds stresses created by the spanwise pressure gradients. In general, it is possible for very small vorticity amplifications to produce relatively large increases in wall-heat(mass)-transfer as was shown by Sutera [32] for a near stagnation point flow. Similar effects could take place in the wake of a cylinder. Very near the separation point (Fig. 6*c*), Sh is virtually unchanged for all $y/\delta^* > 1$. However, under the influence of the vortex *V*2, an increase of about 700 percent over this Sh value is seen at $y/\delta^* = 0.114$. The relative increases of Sh over the two-dimensional flow values gradually decline as θ decreases from 85 deg to 0 deg. Near $\theta = 0$ deg, the Sh peak is about 90 percent higher than its two-dimensional value.

A local minimum in Sh is observed at $y/\delta^* \simeq 0.74$ for 0 deg $< \theta <$ 60 deg and at $y/\delta^* \simeq 0.9$ to 1.2 for 60 deg $< \theta <$ 90 deg. This minimum is associated with the separation line which corresponds to point *P* of Fig. 4(*a*). Separation at this location was detected by Sedney and Kitchens [20], Hunt, Abell, Peterka, and Woo [23]; and Baker [24]. The measurements show a small peak, or a shoulder, appearing consistently at all θ between 10 deg and 90 deg at $y/\delta^* =$ 0.5–0.7 (Figs. 6*b* and *c*). This peak may be due to the vortex *V*3 postulated in Fig. 4(*a*).

A comparison of the longitudinal variation of Sh in the wake at $\theta = 146$ deg and $\theta = 178$ deg (Figs. 6*d* and *e*) reveals somewhat different characteristics at the two angles. As y/δ^* decreases from 5 to zero, a continuous decline of Sh is observed at $\theta = 178$ deg. On the other hand, a moderate increase appears at $\theta = 146$ deg as y/δ^* decreases from 1.2 to 0.2. The same pattern could be seen at all θ between 115 deg and 150 deg. This increase is much less pronounced than its counterparts in the front portion of the cylinder. Nevertheless, it is indicative of some mixing pattern which takes place in that region.

The circumferential distribution of Sh in the two-dimensional region is compared in Fig. 7 with the distributions at $y/\delta^* = 5.87$, where the maximum effect of the vortex *V*1 is detected, at $y/\delta^* = 0.114$, where the maximum effect of the vortex *V*2 is seen, and at $y/\delta^* = 0.74$, where local minimum is found in the front portion of the cylinder (separation point *P* of Fig. 4*a*). The significant enhancement due to *V*2 is evident. The distribution at $y/\delta^* =$ 5.87 is similar to the two-dimensional distribution, especially

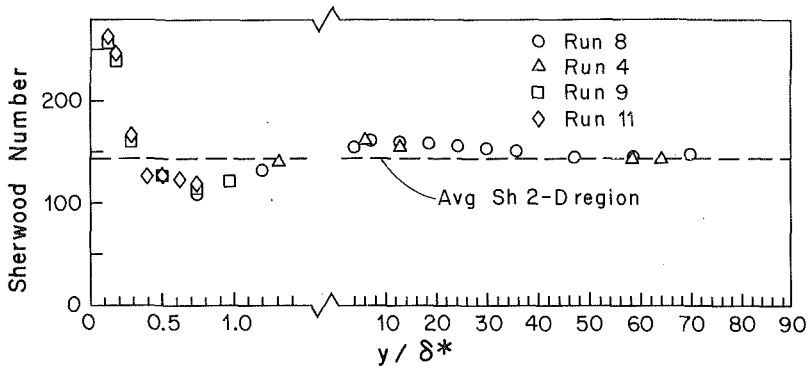

Fig. 9 Variation of average Sh with distance from the tunnel wall: δ^* = 2.23 mm; scale change at $y/\delta^* = 1.6$; Re ≃ 19000

in the front of the cylinder. This observation leads to the conclusion that the secondary flow ($V1$) affecting this distribution changes neither the basic flow structure within the cylinder's boundary layer nor the location of the separation angle where the lowest values of Sh are observed.

Figure 8 shows the variation of the angle corresponding to the minimum value of Sh with y/δ^*. For $y/\delta^* > 1.2$ (i.e., at elevations somewhat higher than the separation point P—Fig. 4*a*), no significant change in location takes place. At smaller y, the angle at which the minimum Sh occurs increases sharply as the tunnel wall is approached.

The circumferental average of Sh ($\overline{\text{Sh}}$) was determined using equation (5). The variation of $\overline{\text{Sh}}$ along the cylinder is shown in Fig. 9. The increase over the two-dimensional value is about 13 percent at $y/\delta^* = 5.87$, and 83 percent at $y/\delta^* = 0.114$. A small secondary peak due to the effect of the vortex $V3$ is seen at $y/\delta^* = 0.51$.

Final Remarks

The effect of a wall boundary layer on mass transfer from a cylinder has been described for Re = 19000 and δ^*/d = 0.0877. The measurements indicate a close association between the horeshoe vortex system and mass transfer characteristics in the front portion of the cylinder. A small but very intense vortex located near the cylinder tunnel-wall attachment line produces extremely high values of Sh over a narrow strip near the base of the cylinder and part way around its circumference. Spanwise pressure gradients, created by the interaction between the cylinder and the tunnel wall boundary layer, enhance heat transfer in the cylinder wake region up to a distance of $40\delta^*$ ($3.5d$) from the wall.

Acknowledgment

Support for this work from the Air Force Office of Scientific Research is gratefully acknowledged.

References

1 Krall, K. M., and Eckert, E. R. G., "Heat Transfer to a Transverse Circular Cylinder at Low Reynolds Numbers Including Rarefaction Effect," *Heat Transfer 1970 (Proceedings of the 4th International Heat Transfer Conference, Versailles, France)*, Paper FC 7.5, Vol. 13, Amsterdam, Elsevier Publishing, 1970.

2 Zukauskas, A., "Heat Transfer from Tubes in Crossflow," *Advances in Heat Transfer*, Vol. 8, New York, Academic Press, 1972, pp. 93-160.

3 Frossling, N., *Acta Univ.*, Lund. Vol. 2, No. 4, 1940. English trans. NACA TM 1432, 1958, p. 36.

4 Lohrisch, W., *Forshung, Geb. Ingenieur*, No. 322, 1929.

5 Kroujilin, G., "The Heat Transfer of a Circular Cylinder in a Transverse Air Flow in the Range of Re = 6000-425,000," *Tech. Phys. USSR*, Vol. 5, No. 4, 1938, pp. 289-297.

6 Schmidt, E., and Wenner, K., *Forschung, Geb. Ingwes.*, Vol. 12, No. 2, 1941, pp. 65-73.

7 Giedt, W. H., "Investigation of Variation of Point Unit Heat Transfer Coefficients Around a Cylinder Normal to an Air Stream," *Trans. ASME*, Vol. 71, 1949, pp. 375-381.

8 van Meel, D. A., "A Method for the Determination of Local Convective Heat Transfer From a Cylinder Placed Normal to an Air Stream," *Int. J. Heat Mass Transfer*, Vol. 5, 1962, pp. 715-722.

9 Achenback, E., "Total and Local Heat Transfer from a Smooth Circular Cylinder in Crossflow at High Reynolds Number," *Int. J. Heat Mass Transfer*, Vol. 18, 1975, pp. 1387-1396.

10 Sogin, H. H., and Subramanian, V. S., "Local Mass Transfer from Circular Cylinders in Cross Flow," ASME JOURNAL OF HEAT TRANSFER, Vol. 83, 1961, pp. 483-493.

11 Lowery, G. W., and Vachon, R. I., "The Effect of Turbulence on Heat Transfer from Heated Cylinders," *Int. J. Heat Mass Transfer*, Vol. 18, 1975, pp. 1229-1242.

12 Aiba, S., Ota, T., and Tsuchida, H., "Heat Transfer and Flow Around a Circular Cylinder with Tripping Wires," *Warme- und Stoffubertragung*, Vol. 12, 1979, pp. 221-231.

13 Kestin, J., and Wood, R. T., "The Influence of Turbulence on Mass Transfer from Cylinders," ASME JOURNAL OF HEAT TRANSFER, Vol. 93, 1971, pp. 321-327.

14 Achenbach, E., "The Effect of Surface Roughness on the Heat Transfer from a Circular Cylinder to the Cross Flow of Air," *Int. J. Heat Mass Transfer*, Vol. 20, 1977, pp. 359-369.

15 Zukauskas, A. A., Zyugzda, I. I., and Survila, V. Y. U., "Effect of Turbulence on Heat Transfer from Cylinders in Crossflow at Critical Reynolds Numbers," *HT-Soviet Research*, Vol. 10, 1978, pp. 1-8.

16 Zukauskas, A. A., Simanavicius, V. S., Daujotas, P. M., and Ziugzda, J. J., "Heat Transfer from Rough Cylinder in Crossflow of Water at Critical Re," *HT-Soviet Research*, Vol. 10, 1978, pp. 79-89.

17 Thwaites, B., *Incompressible Aerodynamics*, Oxford, Clarendon Press, 1960, pp. 551-554.

18 Gregory, N., and Walker, W. S., "The Effect on Transition of Isolated Surface Excrescences in the Boundary Layer," *R&M*, No. 2779, ARC, England, 1955.

19 Norman, R. S., "On Obstacle Generated Secondary Flows in Laminar Boundary Layers and Transition to Turbulence," Ph.D. thesis, Illinois Institute of Technology, Chicago, IL, 1972.

20 Sedney, R., and Kitchens, C. W., "The Structure of Three Dimensional Separated Flows in Obstacle, Boundary Layer Interactions," *AGARD Conference Proceedings No. 168*, 1975.

21 Marchal, P. H., and Sieverding, C. H., "Secondary Flows Within Turbomachinery Bladings," *AGARD Conference Proceedings* No. 214, 1977.

22 Langston, L. S., "Crossflows in a Turbine Cascade Passage," ASME *Journal of Engineering for Power*, Vol. 102, 1980, pp. 866-874.

23 Hunt, J. C. R., Abell, C. J., Peterka, J. A., and Woo, H., "Kinematical Studies of the Flow Around Free or Surface-Mounted Obstacles; Applying Topology to Flow Visualization," *Journal of Fluid Mechanics*, Vol. 86, 1978, pp. 179-200.

24 Baker, C. J., "The Turbulent Horseshoe Vortex," *J. Wind Eng. and Ind. Aerodyn.*, Vol. 6, 1980, pp. 9-23.

25 Langston, L. S., and Boyle, M. T., "A New Surface-Streamline Flow-Visualization Technique," *Journal of Fluid Mech.*, Vol. 125, 1982, pp. 53-57.

26 Jones, T. V., and Russell, C. M. B., "Heat Transfer Distribution on Annular Fins," ASME Paper No. 78-HT-30, 1978.

27 Kruckels, W. W., "Determination of Local Heat Transfer Coefficients in Forced Convection Air Flow by Aid of Photometric Measurements," *AIChE Symposium Series*, Vol. 68, No. 118, 1972, pp. 112-118.

28 Saboya, F. E. M., and Sparrow, E. M., "Local and Average Transfer Coefficients for One Row Plate Fin and Tube Heat Exchanger Configurations," ASME JOURNAL OF HEAT TRANSFER, Vol. 96, 1974, pp. 265-272.

29 Sogin, H. H., "Sublimination from Disks to Air Streams Flowing Normal to Their Surfaces," *Trans. ASME*, Vol. 80, 1958, pp. 61-71.

30 Schlichting, H., *Boundary Layer Theory*, 7th ed., New York, McGraw-Hill, 1979, p. 171.

31 Whitaker, S., "Forced Convection Heat Transfer Correlations for Flow in Pipes, Past Flat Plates, Single Cylinders, Single Spheres, and for Flow in Packed Beds and Tube Bundles," *AIChE Journal*, Vol. 18, 1972, pp. 361-371.

32 Sutera, S. P., "Vorticity Amplification in Stagnation-Point Flow and Its Effect on Heat Transfer," *Journal of Fluid Mechanics*, Vol. 21, 1965, pp. 513-534.

D. C. McCormick
Assistant Research Engineer,
United Technologies Research Center,
East Hartford, Conn. 06108

F. L. Test
Professor.
Mem. ASME

R. C. Lessmann
Professor.

Department of Mechanical Engineering
and Applied Mechanics,
University of Rhode Island,
Kingston, R.I. 02881

The Effect of Free-Stream Turbulence on Heat Transfer From a Rectangular Prism

This paper discussses the effect of free-stream turbulence on the constant temperature heat transfer rate from the surface of a two-dimensional rectangular body that is subject to a strongly favorable pressure gradient. Free-stream turbulence levels of 2 to 5 percent enhanced the heat transfer by 48 to 55 percent over predicted laminar values. Free-stream turbulence levels of 10 to 35 percent produced heat transfer results that behaved in some aspects as turbulent predictions, although considerably enhanced in magnitude over the predicted values.

Introduction

This work presents a continuation of research that is concerned with forced convective heat transfer from blunt bodies of rectangular cross section. Previous wind tunnel studies by Sam, Lessmann, and Test [1] and Test and Lessmann [2] investigated the fluid mechanics and heat transfer characteristics of a two-dimensional model having a 6/1 aspect (chord to height) ratio. One significant result reported by [2] was a 50 percent increase in the laminar heat transfer over analytical predictions. This enhancement in heat transfer was attributed to free-stream disturbances in the wind tunnel created by wake oscillations behind the model.

An outdoor study by Test, Lesmann, and Johary [3] obtained heat transfer measurements for a 6/1 aspect ratio model having 6 times the chord of the wind tunnel model. The high natural turbulence of the environment resulted in free-stream turbulence levels of 20 to 40 percent; and the laminar heat transfer was reported to be enhanced by about 300 percent. One of the main goals of this research was to determine how wind tunnel studies could be used to predict behavior in the natural environment. In the end, it indicated a need for a better understanding of the free-stream turbulence heat transfer interaction in order to achieve this goal.

Several other investigators have also examined the effect of free-stream turbulence on heat transfer. Many studies [4–7] have reported significant increases in heat transfer of 60 to 80 percent in the vicinity of the stagnation line on cylinders with free-stream turbulence intensitites under 10 percent. Due to the strong favorable pressure gradient in such stagnation regions, the flow remains laminar in this situation.

Flat-plate experiments have produced conflicting evidence concerning the influence of free-stream turbulence with and without a favorable pressure gradient in both laminar and turbulent flows. Kestin [6] and Junkhan and Serovy [4] reported no enhancement for laminar flow with zero pressure gradient and also none in turbulent flow with or without a pressure gradient. However, for laminar flow over a flat plate with a presure gradient, Junkhan and Serovy [4] reported about a 20 percent enhancement for a free-stream turbulence level of 3 percent; whereas Kestin [6] reported a smaller enhancement of 6 percent for 4.5 percent turbulence intensity. In contrast to the results of [4] and [6], Smith and Kuethe [5] and Dyban and Epik [8], when working in overlapping Reynolds number ranges, found heat transfer enhancement of 30–50 percent for laminar zero pressure gradient flow subjected to 6–9 percent free-stream turbulence.

Contributed by the Heat Transfer Division and presented at the National Heat Transfer Conference, Seattle, Washington, July 24–27, 1983. Manuscript received by the Heat Transfer Division April 11, 1983. Paper No. 83-HT-29.

Dyban and Epik [8] reported a 20 percent enhancement for turbulent flow without a pressure gradient with 9 percent free-stream turbulence. Simonich and Bradshaw [9] and Slanciauskas and associates [10, 26] also reported heat transfer increases for zero pressure gradient turbulent flows. Both found about a 30 percent enhancement for 6–8 percent free-stream turbulence intensity. Blair [24] used heat transfer to predict transition in accelerating flows but did not discuss whether the heat transfer in the laminar region or the turbulent region was enhanced by free-stream turbulence.

Many investigators have proposed an enhanced viscosity to model the effects of free-stream turbulence in a boundary layer [5, 9, 10, 11]. This idea is based on the assumption that the mechanims of the interaction is one of added mixing due to free-stream pulsations penetrating the boundary layer as opposed to the assumption of ordered secondary motions triggered by some instability mechanism. Kestin [6] propsed that the mechanism of the interaction in the vicinity of a stagnation line on a cylinder was an amplification of certain free-stream vortices. Kestin and Wood [12] then identified streamwise-directed, near-surface vortex structures in such a flow using flow visualization and hot-wire anemometry. Sutera et al. [13] also showed that such a mechanism could quantitatively explain the observed results. Test and Lessmann [2] postulated a similar vortex structure caused by the centrifugal instability of diverging streamlines near the two-dimensional stagnation line on a rectangular body. These Goertler type vortices were conceived of as being triggered and sustained by the energy contained in the free-stream turbulence.

This investigation examines the free-stream turbulence influence on the heat transfer from a rectangular body of 4/1 aspect ratio, when a two-dimensional stagnation line is located on the upper surface near the leading edge (40 degree angle of attack). For this case, a strong favorable pressure gradient exists over the surface similar to the forward facing portion of a cylinder. The increased resolution, decreased aspect ratio, and varied free-stream turbulence levels of the present study, when combined with the results of [2] and [3], provide a better understanding of heat transfer from bodies of rectangular cross section.

Experimental Apparatus and Technique

The experimental apparatus used in this study is very similar to that used in [2], with the main difference being the dimensions of the model and the resolution it affords for measuring the local heat transfer coefficient.

Experiments were carried out in a low-speed, open-circuit

wind tunnel with a 0.77-m (30.5-in.) square test section preceded by a 15 to 1 area contraction. The free-stream turbulence level of the empty tunnel is about 0.5 percent.

The model had a rectangular cross-section and dimensions of 20.32 cm (8 in.) chord by 5.08 cm (2 in.) height (4/1 aspect ratio) and extended across the entire test section perpendicular to the flow. The model was mounted to allow adjustment to any angle of attack and was constructed of plexiglass with exception of the test surface, and an aluminum back plate as shown in Fig. 1. The test surface consisted of 16 heater unis each 1.08 cm (.425 in.) chordwise and 4.75 cm (1.870 in.) spanwise separated by 1.6 mm (0.0625 in.) plexiglass strips.

The construction details of the heaters and heat loss estimates are described in [2]. The local heat transfer coefficient, repesentative of each heat unit, is calculated from

$$h = \frac{k_e\,(\Delta T_e)}{\Delta x_e\,\Delta T_t} - Q_c \qquad (1)$$

The development of equations (1) and the evaluation of Q_c are described in [14].

All measurements were taken at steady conditions. Adjustments were made with variable resistors until an isothermal surface of 11°C (20°F) ± 3 percent above ambient was obtained. Possible errors in thermocouple calibration, recorder accuracy, thermal conductivity measurements, temperature and velocity control, and heat loss evaluations lead to an uncertainty in the calculated Stanton number of ± 6 percent, based on 95 percent of the data falling within the range.

The test heater units were separated from the guard heater units by two 0.95-cm (0.375-in.)-wide plexiglass strips. One of these had 18 surface pressure taps that spanned the chord of the model. The free-stream velocity distribution over the model was determined by referencing the pressure taps to a place where the pressure and velocity were known. Pressure readings were made with a Datametric electronic manometer accurate to ± (0.4 percent of reading + 0.02 percent of scale), which in general is much smaller than the size of the observed pressure fluctuations.

Velocity profiles and turbulence measurements were taken using a Disa constant temperature hot-wire anemometer. The velocity uncertainty inherent in use of the calibration curve was typically less than ± 3 percent for 95 percent of the data. The main uncertainty in the velocity profile measurements

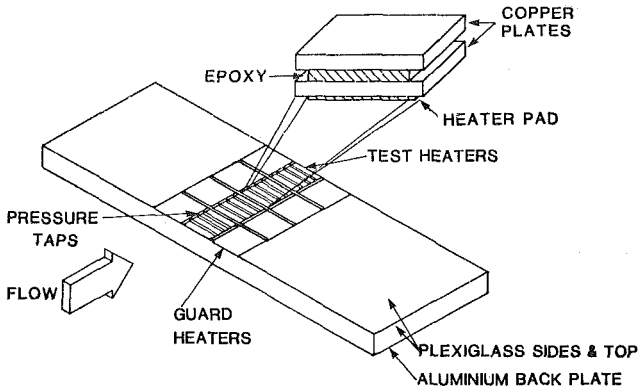

Fig. 1 Construction details of model

was due to an unavoidable position error in setting the zero. The probe was zeroed visually by touching the probe to its reflected image on the model surface. An estimate of this position error as it propagated into the velocity profile was found by replicating a profile five times and calculating the resulting standard deviation in velocity at the measuring stations.

All heat transfer experiments were performed at a 40-deg angle of attack such that a stagnation line existed near the leading edge. Smaller angles of attack would give a separation bubble on the upper surface and higher angles of attack would cause the separation line to move back from the leading edge. Morton [25] who investigated potential flow past asymmetric wedges predicted, for this geometry, that the flow would have a stagnation line at the leading edge for an angle of attack of 34 deg. An upstream velocity of 9.14 m/s (30 ft./s) was used for all experiments.

Wind Tunnel Turbulence

The free-stream turbulence in the unobstructed wind tunnel is about 0.5 percent. The presence of the model at a 40-deg angle of attack increases the free-stream turbulence to about 5.5 percent. A similar increase to 2.5 percent was reported by [2] when a 6/1 model was present at a 30 deg angle of attack. In [2], the elevated levels of free-stream turbulence were

Nomenclature

C = chord of model or constant in Falkner-Skan velocity distribution
C_p = $1 - U_\infty^2/U_0^2$
f' = nondimensional velocity U/U_∞, function of η
f'' = derivative of f' with respect to η
h = convective heat transfer coefficient
K = constant in Smith-Kuethe eddy diffusivity formulation
ke = thermal conductivity of epoxy separation in heater units
M = exponent in Falkner-Skan velocity distribution equation
P = pressure
Pr = Prandtl number
Q_c = heat loss correction
Re_x = local Reynolds number
St_x = local Stanton number
T = temperature
U = mean velocity in x-direction
U_0 = free-stream velocity well upstream of model
U_∞ = local free-stream velocity
u' = fluctuating velocity in x-directions
u^* = shear velocity
V = mean velocity in y-direction
v' = fluctuating velocity in y-direction
X = coordinate parallel to surface with origin at leading edge
y = coordinate perpendicular to surface with origin on surface

Greek

δ = boundary layer thickness
ϵ = eddy diffusivity
η = boundary layer variable $\left(y\sqrt{\frac{U_\infty}{\nu x}}\right)$
ΔT_e = temperature difference across the epoxy
ΔT_t = temperature difference between top surface and free-stream
ΔX_e = epoxy thickness
ν = kinematic viscosity
ρ = density
θ = nondimensional temperature, $(T - T_w)/(T_\infty - T_w)$
θ' = derivative of θ with respect to η

Subscripts

W = value at the wall
∞ = value in the local free-stream

Special

$(\bar{\ })$ = time average value of variable

found to be due to vortex shedding and wake oscillation behind the model which propagated upstream.

An oscillograph trace of the fluctuating velocity in the present experiment reveals a relatively low frequency oscillation of about 10 Hertz. This is in good agreement with the shedding vortex frequency behind a plate normal to a stream whose height is vertical projection of a 20.3-cm (8-in.) surface inclined at 40 deg as given in [15]. It was therefore concluded that the elevated background turbulence level here was also due to the shedding of vortices. Since this frequency is low and the disturbance nearly harmonic, it is not truly turbulent, which is characterized by more random frequencies. It would be more appropriate to refer to the phenomenon as free-stream disturbance.

In order to minimize such disturbances, a splitter plate was mounted behind the model. This splitter plate was a 89-cm (35-in.)-long plywood sheet that spanned the width of the wind tunnel and tended to stabilize the oscillating wake behind the model. It reduced the free-stream disturbance level by more than 50 percent.

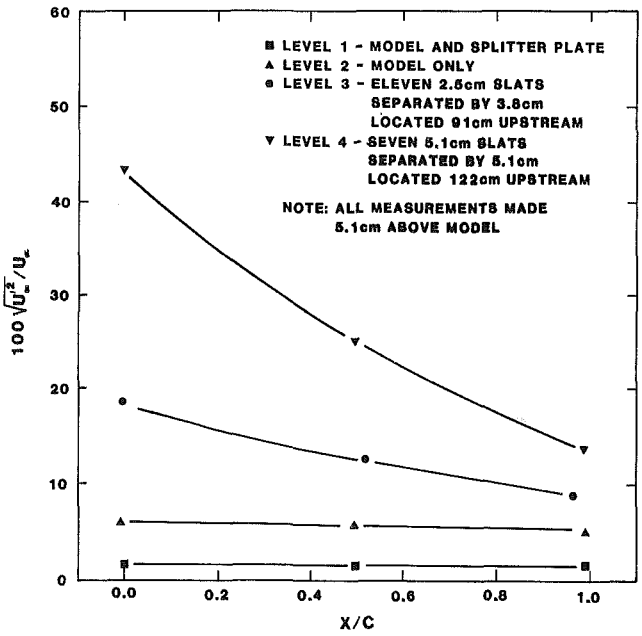

Fig. 2 Free-stream turbulence distribution

Two different levels of free-stream turbulence were then introduced by spaced horizontal slats located upstream of the model that also spanned the width of the wind tunnel. The turbulence produced by these slats contained some large-scale eddies, but this was the only way high turbulence levels (30 to 40 percent) could be produced. If a grid to produce small-scale turbulence of this magnitude was installed, the turbulence decayed too rapidly. It can be said, therefore, that turbulence of this type consists of some free-stream disturbance. All of these oscillations, including the vortex induced disturbances, show as an rms voltage during hot-wire measurements. This was recorded as $\sqrt{\overline{u_\infty'^2}}$ and will henceforth be referred to as free-stream turbulence. It is recognized, however, that the magnitude has a significant "disturbance" component. This type of turbulence is characteristic of that occurring in the natural environment, which has a significant large-scale component.

Figure 2 plots the variation of the resulting free-stream turbulence levels against position along the model's top surface at stations well outside the boundary layer. The abscissa is the normalized distance from the leading edge. Also potted are the turbulence levels created by wake oscillations when only the model and then the model and splitter plate are present in the wind tunnel. These four different cases will be referred to as turbulence levels 1–4, where 1 corresponds to the lowest turbulence intensity.

Heat Transfer Results

Figure 3 shows the heat transfer from the upper surface of the model for turbulence levels 1–4. Since free convection effects are negligible, based on a criterion reported in [16], comparison of the experimental results to analytic solutions is straightforward. The Ambrok turbulent heat transfer solution [17] and the Smith-Spalding laminar heat transfer solution [18], as reported by [19] for a typical free-stream velocity distribution over the model, are plotted with the experimental heat transfer results for comparison. Since the streamwise velocity distribution shown in Fig. 4 varies little at each turbulence level, the analytic solutions for these cases are nearly the same.

For turbulence levels 1 and 2, the experimental results parallel the laminar solution with the exception of the first data point of levels 1 and 2 and the last point of level 2. The percent difference from the laminar solution is shown in Fig. 5 for these two cases. It appears that with the exception of the first and last data points, the experimental results are very

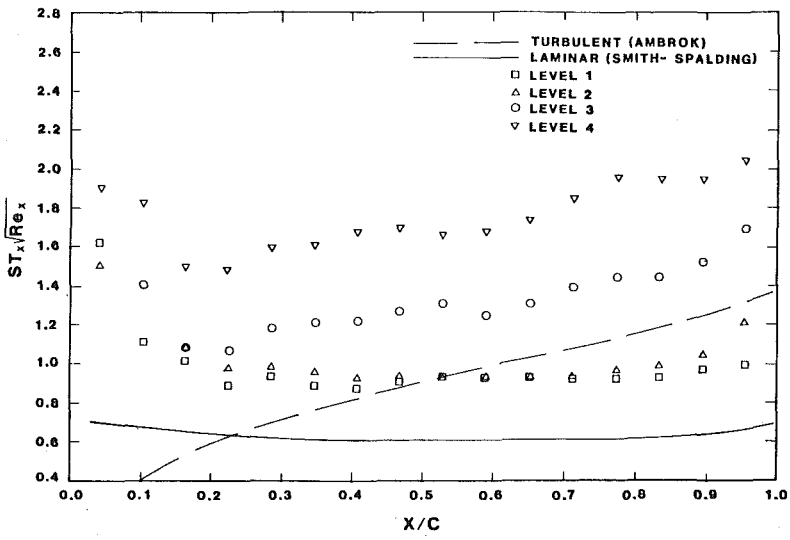

Fig. 3 Heat transfer results

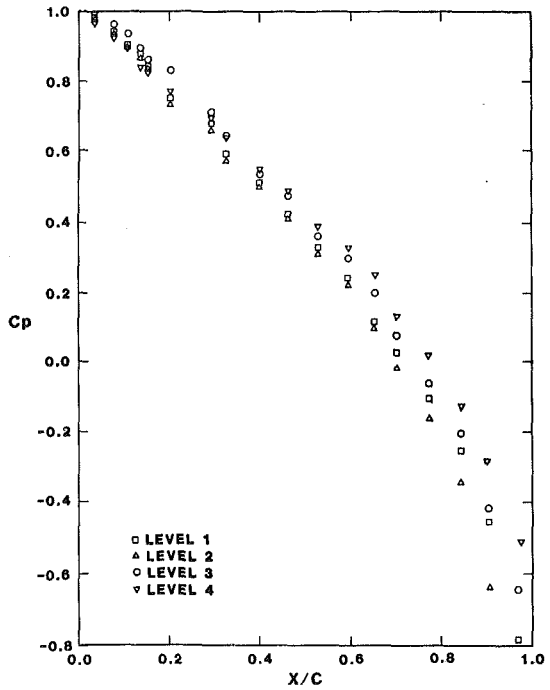

Fig. 4 Pressure coefficient distribution over model

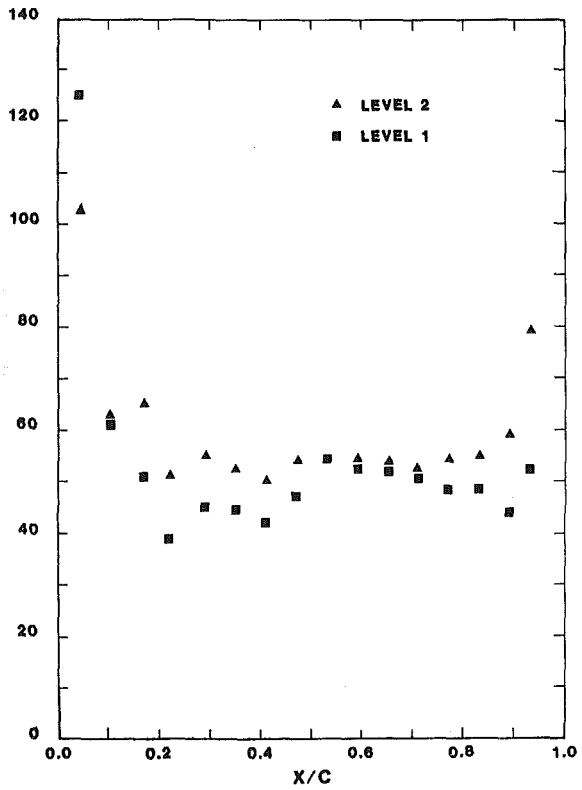

Fig. 5 Percent difference in Stanton number between experimental results and laminar solution

"laminarlike." The heat transfer is enhanced at nearly a constant value of 50 percent due to the nearly constant free-stream turbulence distribution over the model (Fig. 2).

The results in Fig. 3 for levels 1 and 2 show very little difference, even though the turbulence intensity for level 2 was double that for level 1; the 50 percent increase in heat transfer was also obtained for the 6/1 aspect ratio in [2] where the free-stream turbulence was 2.5 percent. The reason for this lack of change in the heat transfer results probably won't

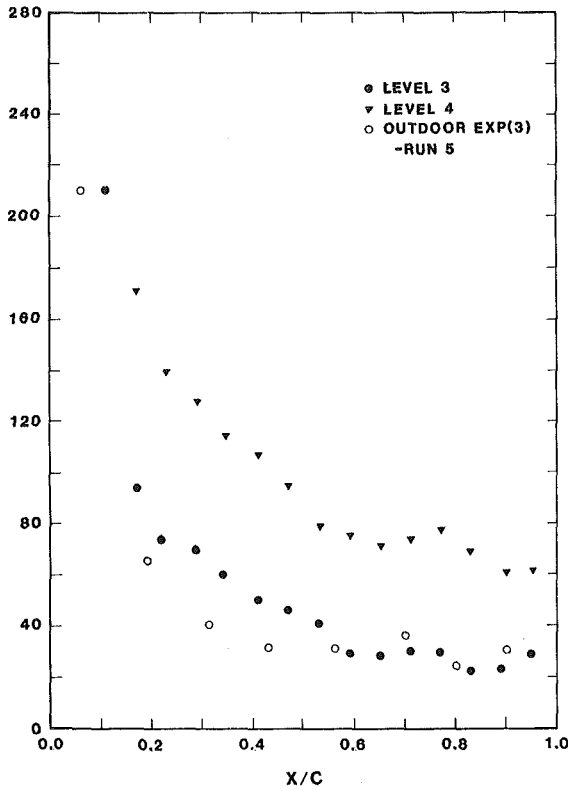

Fig. 6 Percent difference in Stanton number between experimental results and turbulent solution

be explained until the physics of heat transfer enhancement by free-stream turbulence is understood.

In the vicinity of the stagnation lines, the effect of free-stream turbulence appears to be more dramatic. The enhancement here is in line with the findings of [4–7], whose authors studied the effect of free-stream turbulence on heat transfer in the vicinity of the stagnation line of a cylidner. The data shows more than a doubling in the heat transfer for 2 to 5 percent turbulence intensity.

The deviation of the last data point of level 2 is explained by the findings of [2]. Test and Lessmann made detailed turbulence intensity measurements over a similar 6/1 aspect ratio model at an angle of attack such that a stagnation line was at the leading edge. They reported an increased turbulence and corresponding heat transfer enhancement towards the downstream portion of the model due to wake oscillation behind the model. This effect is not present for level 1, since the wake is stabilized in this case by the splitter plate.

For turbulence levels 3 and 4, the heat transfer no longer parallels the laminar solution but follows the turbulent solution. Figure 6 shows the percent difference between the experimental data and the turbulent solution for levels 3 and 4. Comparison of this figure to the free-stream turbulence distributions over the model in these cases (Fig. 2) appears to show a reasonable correlation between the decay of the free-stream turbulence level and the decay in the percent enhancement. From this, one might conclude that the high turbulence intensity triggered a turbulent boundary layer and that the free-stream turbulence enhances the turbulent heat transfer.

Enhancement of turbulent heat transfer has been reported by [9] and [10]. The results of [9], a 5 percent enhancement for each 1 percent free-stream turbulence, is in line with the present results, but as will be shown, the corresponding boundary layer velocity profiles cannot be fitted to a standard law of the wall velocity profile. Thus the flow is not "classically" turbulent where the turbulence is generated near

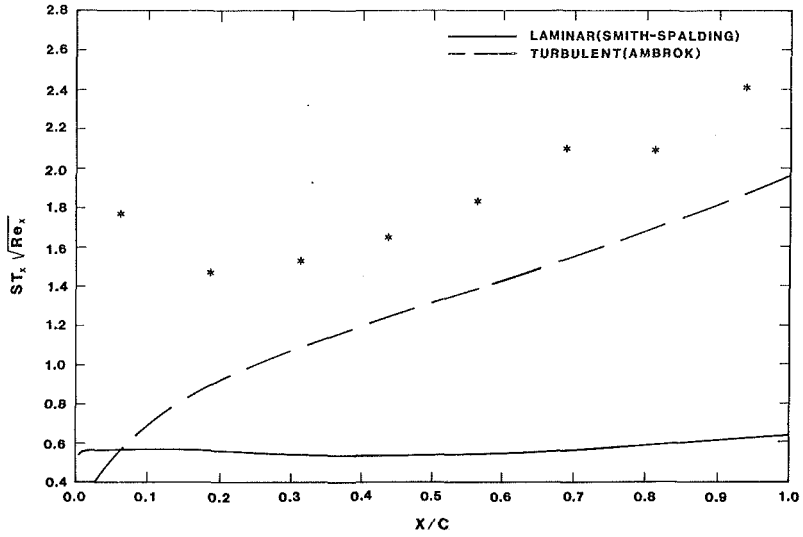

Fig. 7 Comparison of outdoor data with analytical solution

the edge of the viscous sublayer but rather the free-stream turbulence appears to be penetrating into the boundary layer, causing "turbulentlike" transport effects.

The heat transfer study in the natural environment [3] reported flow over the model to be laminar. This fact was deduced from the value of the length Reynolds number and by comparing the experimental heat transfer results to the Ambrok turbulent solution and to the Smith-Spalding laminar solution. The experimental results appeared to parallel the laminar solution. Reexamination of these data indicates that they more readily follow the turbulent solution, at an enhanced level, except near the stagnation line. This is shown in Fig. 7, which compares the corresponding analytic solutions to run 5 of [3], for which the contaminating effects of natural convection were minimal. As with the experimental results of the present study, the effect of free-stream turbulence in the vicinity of a stagnation line has a more pronounced effect. In Fig. 6, the percent difference from the turbulent solution, with the exception of the first two data points, is a nearly constant 30 percent for the outdoor data resulting from a free-stream turbulence level of 31 percent.

Heat transfer results for turbulence levels 3 and 4 have similar characteristics in that there is a strong correlation between the free-stream turbulence level and the percent difference from the turbulent solution. For the outdoor study [3], the environmental turbulence, though no detailed measurements were taken to confirm this, was probably constant over the surface of the model due to the large-scale of the turbulence. Since the increase over the turbulent solution is nearly constant (except for the first two data points), this case also shows a correlation between the turbulent heat transfer and the local free-stream turbulence level.

When comparing wind tunnel results with those in the outdoor environment, one must be aware of blockage effects in the wind tunnel and three-dimensional effects in the natural environment. It was shown in [2] that wind tunnel blockage effects do not influence the heat transfer results by more than 2 percent, and the use of side wings to eliminate three-dimensional effects in the natural environment is discussed in [3].

Figures 6 and 7 show a 30 percent increase for a 30 percent turbulence intensity for the outdoor results, while the wind tunnel results indicate approximately an 80 percent increase for the same turbulence level. This fact demonstrates the importance of more fully characterizing the type of turbulence in a flow when developing a predictive model, since environmental disturbances are different in scale and frequency content compared with wind tunnel turbulence. The outdoor data were only recorded when velocities normal to the main flow direction were usually less than 30 percent of the velocity component in the flow direction. The directional effect in the outdoor free-stream turbulence level could therefore be as much as 8 percent. This might be part of the reason why the heat transfer enhancement in the outdoors was less than in the wind tunnel for the same recorded free stream turbulence.

Heat transfer results from the lower turbulence levels (1 and 2) and the findings of [2] have the common charactertistics that the heat transfer parallels the laminar solution at an enhanced level. For these cases, the free-stream disturbances are created by wake oscillations. Two of the possibilities can be stated thus: Do relatively low turbulence levels tend to enhance the heat transfer over the laminar solution and at some point of increasing intensity cause the effect to become similar to turbulent predictions, or are the differences observed so far only due to the character of the free-stream turbulence? Previous studies that observed heat transfer enhancement from flat-plate pressure gradient flows [4, 6] reported results that parallel the laminar solution for low free-stream tubulence. Since the free-stream turbulence was most likely different in character in these studies compared with the present cases, the first possibility would appear to be true.

Boundary Layer Study

Since Kestin [6] reported that a structure of streamwise-directed vortices was the mechanism of the interaction between the free-stream turbulence and the boundary layer in the vicinity of a stagnation line on a cylinder, considerable effort was expended in this project to locate such a system of vortices utilizing hot-wire anemometry with the wire parallel to the flow. This effort failed to identify such a vortex structure. It should be pointed out, however, that the boundary layer was very thin (1.0 mm) due to the favorable pressure gradient, and it would only have been possible to detect stable vortices with diameters of the order of the boundary layer thickness.

Since the heat transfer for turbulence levels 3 and 4 parallels the Ambrok turbulent solution, an attempt was made in Fig. 8 to compare the velocity profiles in these cases to the universal turbulent profile in law-of-the-wall coordinates. The value of u^* in these coordinates was determined by a Clauser plot. Both profile data sets exhibit short regions of linearity, but these are inside the buffer layer and consequently the data plots well above Spalding's law. The data for level 3 also plots

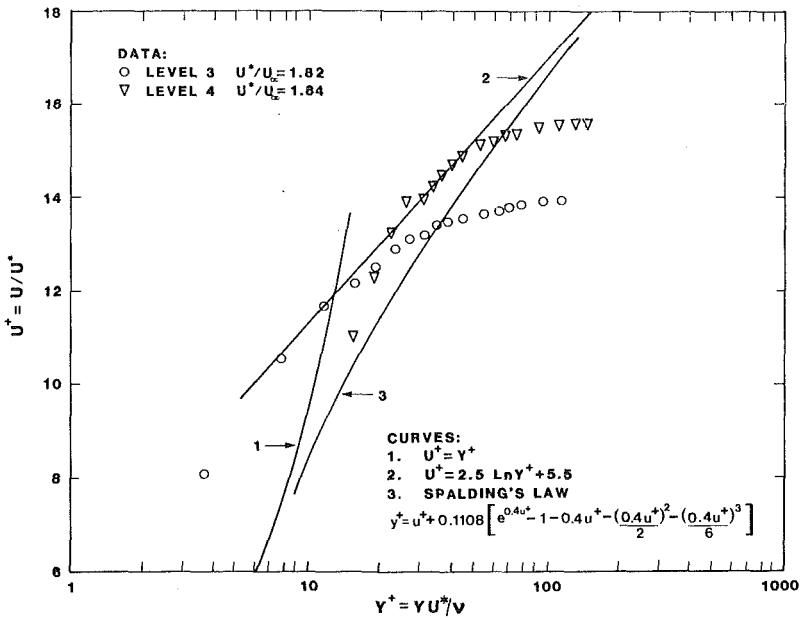

Fig. 8 Comparison of data with law of the wall

above the sublayer law, meaning that Clauser's method for determining the wall shear stress does not give a correct value for these data. Taken together, this all indicates that the classical near-wall mechanisms of turbulence generation were not active. Also from the linear stabilty theory for the Falkner-Skan profiles [21] as reported in [22], it was found that the critical Reynolds number for disturbances to amplify was an order of magnitude greater than that which was measured. Therefore, it is concluded that a turbulent boundary layer was not triggered by the high free-stream turbulence levels.

Velocity profile data for turbulence level 3 is also shown in Fig. 9. This profile was taken at cord position $x/c=0.59$, and wall proximity effects were corrected for by the method of Wills [20]. This plot shows the experimental data and a comparison to a local Falkner-Skan profile. Since the flow over the model does not exactly correspond to a wedge flow, the comparison to Falkner-Skan profiles depends on evaluating the local pressure gradient.

The theoretical free-stream velocity distribution for Falkner-Skan flow is

$$U=cx^M \tag{2}$$

Using the free-stream velocity curve fit obtained from the surface pressure taps for a particular turbulence level, M can be found locally. The Falkner-Skan momentum and energy equations [19] can then be numerically integrated provided the correct wall values are used. The deduced values of M, $f''(0)$, and $\theta'(0)$ are listed on Fig. 9.

The resulting values of $\theta'(0)$ can be used to determine the validity of this approach. It can be shown by definition that

$$\mathrm{St}_x Re_x^{1/2}=\theta'(0)/\mathrm{Pr} \tag{3}$$

If the flow over the model corresponded exactly to a wedge flow, then the Smith-Spalding laminar solution would agree with the predicted heat transfer of the local Falkner-Skan solution. The difference in the heat transfer evaluated by equation (3) was at most 6 percent when compared with the Smith-Spalding solution. Thus the application of the Falkner-Skan equation locally should provide a reasonable comparison to the experimental profile data. The Falkner-Skan profile is considered here to be the zero free-stream turbulence case. The experimental data in Fig. 9 shows a significant increase in the measured velocity gradient near the wall when compared to this profile.

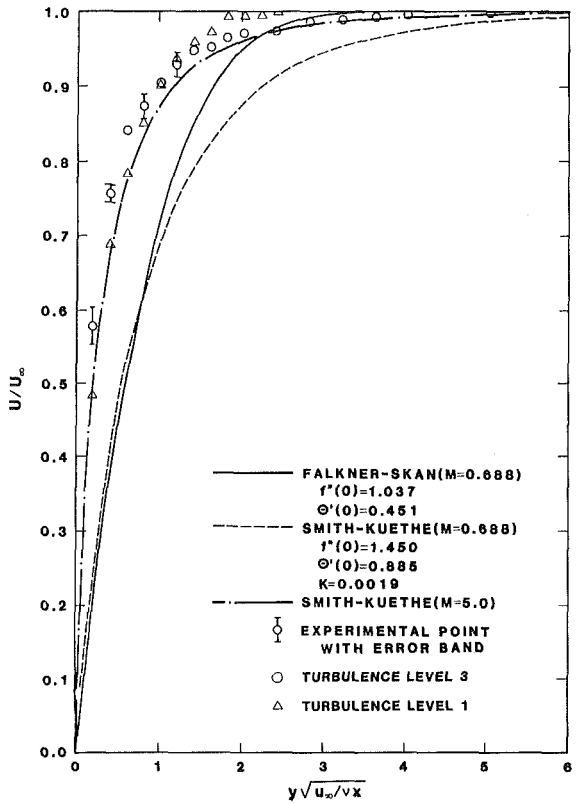

Fig. 9 Velocity profile

The data on which the curves of Fig. 9 are based give η = 2.7 when $U/U_\infty = .99$ for the Falkner-Skan (zero free-stream turbulence) case but give η = 5 for the same U/U_∞ in the experimental case of turbulence level 3. This shows that the boundary layer is thicker for the case with free-stream turbulence. The experimental data for turbulence level 3 shows a thicker boundary layer than the data for turbulence level 1.

These trends: increasing velocity gradient near the wall and increasing boundary layer thickness due to increasing levels in free-stream turbulence were also reported by Dyban et al. [23] for a flat plate zero pressure gradient flow.

Smith and Kuethe [5] proposed an eddy diffusivity model

which resulted in these same effects in the boundary layer near the stagnation line on a cylinder. Their model was based on the eddy diffusivity being equal to the product of the upstream velocity, the upstream fluctuating velocity, distance from the surface, and a constant determined from experimental fit. Their momentum and energy equations for the case of flow around a cylinder still yielded a similarity solution after the substitution of this type of eddy viscosity, since $M = 1$ in this case.

A similar approach was used here but with an eddy diffusivity based on local free-stream values for more general applicability. That is

$$\epsilon = K\sqrt{\overline{u_\infty'^2}}\, U_\infty\, y \tag{4}$$

where a turbulent Prandtl number of 1.0 is assumed so the eddy diffusivity for momentum and heat transport are the same. The addition of equation (4) to the diffusion term of the boundary layer equations, and the substitution of equation (1) and appropriate boundary conditions yields the modified "Falkner-Skan" equations

$$f''' + \frac{M+1}{2} ff'' + M(1-f'^2) + K\sqrt{\overline{u_\infty'^2}}\, \mathrm{Re}_x^{1/2}(\eta f''' + f'') = 0 \tag{5}$$

$$\theta'' + \frac{\mathrm{Pr}}{2}(M+1) f\theta' + K\,\mathrm{Pr}\sqrt{\overline{u_\infty'^2}}\, \mathrm{Re}_x^{1/2}(\eta\theta'' + \theta') = 0 \tag{6}$$

Due to the Reynolds number factor, the addition of this eddy diffusivity model does not in general yield similarity solutions but does provide ordinary differential equations which may be applied locally. The unknown constant in equation (4) was determined by numerically integrating the resulting differential equations (5) and (6), for a given turbulence level until the predicted heat transfer was equal to the experimental value. The profile resulting from this procedure is also shown on Fig. 9 together with the deduced values of K, $f''(0)$, and $\theta'(0)$.

It appears from Fig. 9 that the Smith-Kuethe model underestimates the gradient near the wall and overestimates the boundary layer thickness. Reconsideration of the momentum boundary layer equation shows that the value of M may have been underestimated. As shown in Fig. 9, an M increased to 5, in combination with the eddy diffusivity model, fits the velocity profile quite well.

If one considers that there are fluctuating components of the free-stream velocity, the turbulent X-momentum boundary-layer equation can, with the aid of the y-momentum equation, be put in the form

$$U\frac{\partial U}{\partial x} + V\frac{\partial U}{\partial y} = U_\infty \frac{dU_\infty}{dx} + \nu\frac{\partial^2 U}{\partial y^2} - \frac{\partial}{\partial y}(\overline{u'v'})$$

$$+ \frac{\partial}{\partial x}\int_y^\delta \frac{\partial}{\partial x}(\overline{u'v'})\,dy + \frac{\partial}{\partial x}(\overline{v'^2} - \overline{u'^2}) + \frac{d}{dx}(\overline{u_\infty'^2} - \overline{v_\infty'^2}) \tag{7}$$

The last two terms in equation (7) are the normal stress terms and are usually neglected in most turbulent analyses.

The "Falkner-Skan" exponent M corresponding to this form of the momentum equation is given by

$$M = \frac{x}{U_\infty^2}\left[-\frac{1}{\rho}\frac{dP_w}{dx} + \frac{d}{dx}(\overline{v_\infty'^2} - \overline{u_\infty'^2}) - \int_0^\delta \frac{\partial}{\partial x}(\overline{u'v'})\,dt\right] \tag{8}$$

Since the y-momentum equation is retained in this derivation, the usual assumption that the pressure gradient across the boundary layer is negligible doesn't necessarily hold with significant free-stream turbulence. The effect of this on the determination of M using surface pressure tap data is shown in equation (8). The additional terms due to free-stream turbulence are zero if the turbulence is homogeneous and the integrated gradient of the Reynolds stress is negligible. But turbulence generated by a set of horizontal slats or disturbances created by wake oscillation may not result in negligible values for these terms and a significant underestimation of M is possible, if these terms are neglected.

An increased value of M in combination with an eddy diffusivity shows good agreement with the velocity profile data; but the predicted heat transfer, based on the deduced value of $\theta'(0)$, in this case is nearly three times the experimental value. However, the effect of vertical gradients in the normal stress terms as shown in equation (7) were not considered in the energy equation. This illustrates a further need for a better understanding of the underlying physics of large-scale disturbances penetrating into a boundary layer. Knowledge is needed concerning the distribution of velocity fluctuations inside the layer rather than just knowing the magnitude of the free-stream disturbances.

Conclusions

A summary of the conclusions from this study are:

1 The effect of free-stream turbulence is most dramatic in the vicinity of a stagnation line where the flow is laminar. Small upstream turbulence levels (2–5 percent) double the heat transfer over the predicted values. Large upstream turbulence levels (30 percent) triple the heat transfer over the predicted value. This suggests a possible peaking effect.

2 Low free-stream turbulence levels (2–5 percent) due to wake oscillations enhance the heat transfer from a favorable pressure gradient flow by about 50 percent over the Smith-Spalding lamianr solution. For high free-stream turbulence levels (10–30 percent) generated by horizontal slats, the heat transfer follows the Ambrok turublent solution at an enhanced level of approximately 4 percent for every 1 percent free-stream turbulence over the range 10–35 percent turbulence intensity. The velocity profile data show that a classically turbulent boundary layer does not exist for these cases.

3 The average velocity profiles inside the boundary layer are distorted by free-stream turbulence. The distortion is characterized not only by an increased velocity gradient near the wall and an increased boundary layer thickness, but also by an increased fullness that is reminiscent of the effect of a higher than measured local pressure gradient.

4 A more detailed knowledge of the free-stream turbulence structure, such as, scale, frequency, and gradients of velocity fluctuations (inside and outside the boundary layer), is needed to develop a predictive model for free-stream turbulence effects.

Acknowledgment

This research was performed under the auspices of NSF Grant ENG CME-7916890.

References

1 Sam, R. G., Lessmann, R.C., and Test, F. L., "An Experimental Study of Flow over a Rectangular Body," ASME *Journal of Fluids Engineering*, Vol. 101, Dec. 1979, pp. 443–448.

2 Test, F. L., and Lessmann, R. C., "An Experimental Study of Heat Transfer During Forced Convection over a Rectangular Body," ASME JOURNAL OF HEAT TRANSFER, Vol. 102, Feb. 1980, pp. 146–151.

3 Test, F. L., Lessman, R. C., and Johary, A., "Heat Transfer During Wind Flow over Rectangular Bodies in the Natural Environment," ASME JOURNAL OF HEAT TRANSFER, Vol. 103, May 1981, pp. 262–267.

4 Junkhan, G. H., and Serovy, G. K., "Effects of Free-Stream Turbulence and Pressure Gradient on Flat-Plate Boundary-Layer Velocity Profiles and on Heat Transfer," ASME JOURNAL OF HEAT TRANSFER, Vol. 89, May 1967, pp. 169–175.

5 Smith, M. C., and Kuethe, A. M., "Effects of Turbulence on Laminar Skin Friction and Heat Transfer," *The Physics of Fluids*, Vol. 9, No. 12, Dec. 1966, pp. 2337–2344.

6 Kestin, J., "The Effect of Free-Stream Turbulence on Heat Transfer Rates," *Advances in Heat Transfer*, Vol. 3, 1966, pp. 1–32.

7 Dyban, E. P., and Epik, E. Y., "Some Heat Transfer Features in the Air Flows of Intensified Turbulence," *Proceedings of the 4th International Heat Transfer Conference*, 1970, FC 5.7.

8 Dyban, E. P., and Epik, E. Y., "Heat Transfer in a Boundary Layer in Turbulized Air Flow," *Proceedings of 6th International Heat Transfer Conference*, 1978, FC (a)-4.

9 Simonich, J. C., and Bradshaw, P., "Effect of Free-Stream Turbulence on Heat Transfer Through a Turbulent Boundary Layer," ASME JOURNAL OF HEAT TRANSFER, Vol. 100, Nov. 1978, pp. 671-677.

10 Slanciauskas, A., and Pedisius, A., "Effect of Free-Stream Turbulence on Heat Transfer in the Turbulent Boundary Layer," *Proceedings of 6th International Heat Transfer Conference*, 1978, FC (a)-4.

11 Miyazaki, H., and Sparrow, E. M., "Analysis of Effect of Free-Stream Turbulence on Heat Transfer and Skin Friction," ASME JOURNAL OF HEAT TRANSFER, Vol. 99, Nov. 1977, pp. 614-619.

12 Kestin, J., and Wood, R. T., "Enhancement of Stagnation Line Heat Transfer by Turbulence," *Progress in Heat and Mass Transfer*, Vol. 2, 1969, pp. 249-253.

13 Sutera, S. P., Maeder, P. F., and Kestin, J., "On the Sensitivity of Heat Transfer in the Stagnation Point Boundary Layer to Free-Stream Vorticity," *Journal Fluid Mechanics*, 1963, Vol. 16, pp. 497-520.

14 McCormick, D. C., "Effect of Free-Stream Turbulence and Separated Flow on Heat Transfer," M.S., thesis, Department of Mechanical Engineering, University of Rhode Island, Feb. 1983.

15 Blevins, R. D., *Flow Induced Vibrations*, Van Nostrand Reinhold, 1977.

16 Mucoglu, A., and Chen, T. S., "Mixed Forced and Free Convection on Inclined Surfaces," Paper 78-WA/HT-46, presented at ASME annual meeting San Francisco, 1978.

17 Ambrok, G. S., "Soviet Physics," *Technical Physics*, Vol. 2, 1957, pp. 1979.

18 Smith, A. G., and Spalding, D. B., *Journal Royal Aeronautical Society*, Vol. 62, 1958, pp. 60.

19 Kays, W. M., and Crawford, M. E., *Convection Heat and Mass Transfer*, 2d ed., McGraw-Hill, New York, 1980.

20 Wills, J. A. B., "The Correction of Hot-Wire Readings for Proximity to a Soild Boundary," *Journal of Fluid Mechanics*, 1962, pp. 388-396.

21 Wazzan, A. R., Okamura, T., and Smith, A. M. O., McDonnell-Douglas Co. Rep. DAC-67086, 1968.

22 White, F. M., *Viscous Fluid Flow*, McGraw-Hill, New York, 1974.

23 Dyban, E. P., Epik, E. Y., and Surpun, T. T., "Characteristics of the Laminar Layer with Increased Turbulence of the Outer Stream," *International Chemical Engineering*, July 1977, Vol. 17, No. 3, pp. 501-504.

24 Blair, M. F., "Influence of Free-Stream Turbulence on Boundary Layer Transition in Favorable Pressure Gradients," ASME *Journal of Engineering for Power*, Vol. 104, Oct. 1982, pp. 743-750.

25 Morton, W. B., "On the Discontinuous Flow of Liquid Past a Wedge," *Philosophical Magazine*, Ser. 6, 1921, pp. 801-808.

26 Pedisius, A. A., Kazimekas, P. V., and Slanciauskas, A. A., "Heat Transfer From a Plate to a High-Turbulence Air Flow," *Heat Transfer-Soviet Research*, Vol. II, No. 5, Sept.-Oct. 1979.

D. C. McCormick
Assistant Research Engineer,
United Technologies Research Center
East Hartford, Conn. 06108

R. C. Lessmann
Professor.

F. L. Test
Professor.
Mem. ASME
Department of Mechanical Engineering
and Applied Mechanics,
University of Rhode Island,
Kingston, R.I. 02881

Heat Transfer to Separated Flow Regions From a Rectangular Prism in a Cross Stream

A series of experiments have been performed to determine the constant surface temperature heat transfer and the corresponding surface pressure variation on a two-dimensional rectangular prism in crossflow whose aspect ratio (chord to height) was 4/1. Results are presented for a surface exposed to both separated and reattached flow and for a wake exposed surface, each for several different angles of attack. Universal Stanton number and pressure coefficient curves result when data are plotted against downstream distance scaled by the length of the near-constant pressure portion of the separated bubble for the reattaching case. This is varified by comparison to other studies involving different geometries. The Nusselt number at reattachment seems to be dependent only on reattachment Reynolds number for these cases. The variation of the local Stanton number across the wake facing surface was found to be a function of angle of attack.

Introduction

Several investigations have been concerned with separated and reattached flows (separation bubbles) on blunt bodies [1–11]. In general, details of the heat transfer and pressure variation in separated flows depend on the prior history of the upstream boundary layer. In the cases of interest here, potential flow influences are much more important and boundary layer effects are typically negligible. That is, separation occurs at a corner rather than because a boundary layer lacking in momentum encounters a sufficiently large adverse pressure gradient. The pressure field inside the separated flow region is then determined largely by the outer stream flow passing around the body.

Blunt bodies with rectangular cross sections (prisms) of various aspect ratios (chord to height) have been investigated. Few of these studies have simultaneously examined the pressure and heat transfer distribution inside the bubble or considered the angle of attack, angle between direction of upstream flow and the chord of the prism, as a parameter. Robertson et al. [1] reported mean and fluctuating surface pressures in the separated and reattached regions of a prism with an aspect ratio of 1. For angles of attack between 15 and 45 deg, the flow was reported to reattach. Sam et al. [2] and Test and Lessmann [3] investigated surface pressure and heat transfer characteristics of a prism having a 6/1 aspect ratio (Fig. 1(*a*)). A separation bubble was reported to exist for angles from 0 to 30 deg.

A number of experiments have been concerned with flat plates of finite thickness with various nose shapes. Roshko and Lau [4] examined pressure distributions in such flows (Fig. 1(*b*)) and proposed a scaling that correlated their pressure data inside the bubble, independent of nose shape, except for one of their cases that allowed a considerable boundary layer to develop prior to separation. Robertson et al. [1] and Sam et al. [2] also found this scaling to collapse their pressure coefficients onto the same curve as [4]. This suggests the possibility of a universal curve for the pressure distribution inside separation bubbles for which the boundary layer thickness upstream of separation is negligible.

Ota et al. [5–7] have examined the flow characteristics and heat transfer in the separated and reattached flow on a flat plate with several wedge shaped noses of differing included angle (Fig. 1(*c*)). Ota and Itasaka [5] examined the flow characteristics in the separated, reattached, and redeveloped region of a blunt flat plate for $\beta = 180$ deg. One significant conclusion from this study was that reattachment occured 4 to 5 plate thicknesses downstream of separation and was independent of Reynolds number. Sam et al. [2] reported similar results for a prism of 6 to 1 aspect ratio. Both of these experiments were in the Reynolds number range 10^4–10^5.

Ota and Kon [6] reported heat trasnfer and the corresponding temperature and velocity profiles for the geometry of [5] and found the distribution of $Nu/Re^{2/3}$ to be nearly independent of Reynolds number. However, the experimental heat transfer results of [6] were not confirmed in a later study by these same authors [7]. In [7], the heat transfer and velocity, temperature, and turbulence profiles for a flat plate with nose wedge angles of 60, 90, 120, and 180 deg, and also a round nose, were examined. An important result of this study was a reattachment Nusselt number–Reynolds number relationship that was independent of nose shape when the

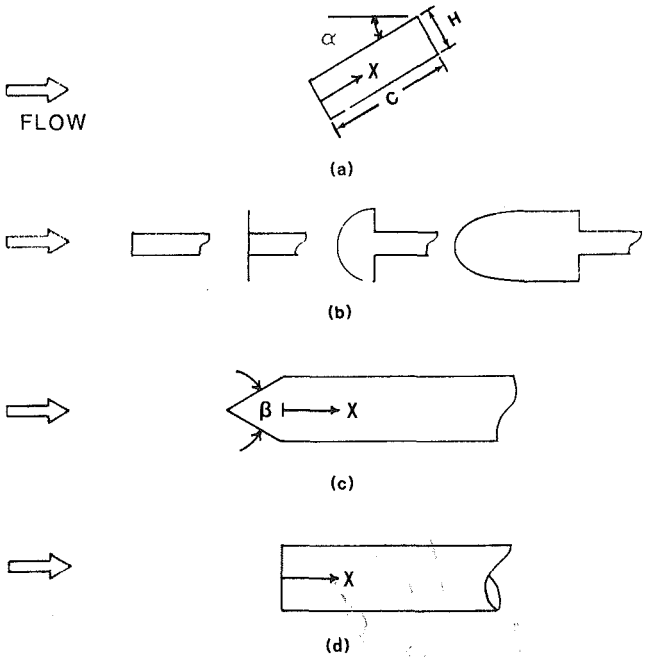

Fig. 1 Various separated flow experimental geometries

Contributed by the Heat Transfer Division and presented at the National Heat Transfer Conference, Seattle, Washington, July 24–27, 1983. Manuscript received by the Heat Transfer Division April 15, 1983. Paper No. 83-HT-28.

reattachment distance was used as the characteristic length scale.

Kottke et al. [8] reported Sherwood numbers for the same geometry as in [7]. By scaling the Sherwood number to the reattachment value and the position coordinate to the reattachment distance, a single curve, independent of nose shape, was reported.

In other investigations by Ota et al. [9, 10] the fluid mechanics and heat transfer in the separated, reattached, and redeveloped regions of a longitudinal blunt circular cylinder are reported (Fig. 1(*d*)). For this axisymmetric case, the characteristics of the flow and heat transfer were found to be very similar, qualitatively, to the blunt flat plate case. A correlation between the reattachment Nusselt and Reynolds numbers with the reattachment distance as the characteristic length was found to be very similar to those reported for the flat plate cases [6, 7]. Therefore, the reattachment distance, based on these studies, would appear to be a suitable scale for relating different geometries.

The present study experimentally determines the reattachment position, surface pressure distribution and constant surface temperature heat transfer distribution as a function of angle of attack and Reynolds number for a two-dimensional 4/1 aspect ratio prism (Fig. 1(*a*)). By scaling the pressure and heat transfer results to appropriate characteristic values and comparing the results to the aforementioned investigations, universal pressure and heat flux variations that hold for separation bubbles where the influence of the upstream boundary layer is negligible are presented. These involve the use of a new length scale, the length of the near constant pressure region at the forward end of the separation bubble. This is shown to give much more universal results inside the separated region than does use of the reattachment length. Also constant surface temperature heat transfer results for the fully separated downstream wake facing surface of the prism are reported.

Experimental Apparatus and Technique

Experiments were carried out in a low-speed, open-circuit wind tunnel with a 0.77-m (30.5-in.) square test section preceeded by a 15 to 1 area contraction. The free-stream turbulence level of the empty tunnel was about 0.5 percent. Velocities upstream were 9.14 m/s (30 ft/s) and 15.24 m/s (50 ft/s).

Two experimental models were used in this study: one for heat transfer and surface pressure measurements and the other to determine reattachment position. Both models were of rectangular cross section and had dimensions of 20.32-cm (8-in.) chord by 5.08-cm (2-in.) height (4/1 aspect ratio) and extended across the entire test section perpendicular to the flow. Adjustment to any angle of attack was possible.

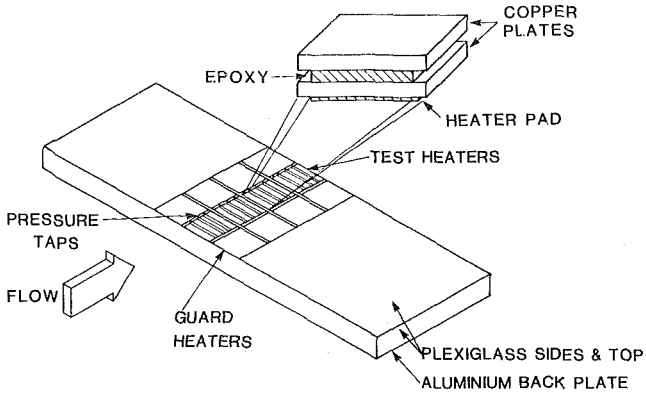

Fig. 2 Construction details of heat transfer model

The heat transfer model is very similar to that used in [3] with the main difference being in the dimensions of the model and the resolution it affords for measuring the local heat transfer coefficient. The model was constructed of plexiglass, with the exception of the test surface and an aluminum back plate as shown in Fig. 2. The test surface consisted of 16 heater units each, 1.08 cm (0.425 in.) chordwise and 4.75 cm (1.870 in.) spanwise, separated by 1.6-mm (0.0625-in.) plexiglass strips.

The construction details of the heater units and heat loss estimates are described in detail in [3]. The local heat transfer coefficient, representative of each heater unit, was calculated from

$$h = \frac{K_e(\Delta T_e)}{\Delta T_t} - Q_c \tag{1}$$

which is a steady-state heat balance that essentially equates the heat flux conducted through the heater unit to that convected from the upper surface. The temperature differences ΔT_e and ΔT_t were measured directly using copper-constantan thermocouples peened into the upper and lower copper plates above and below the epoxy core of each heater unit. These gave ΔT_e, while a reference thermocouple upstream together the upper thermocouple gave ΔT_t. Each heater unit was separately calibrated before and after the experiment to determine the epoxy conductivity K_e.

The term Q_c is complicated and is included to account for the effects of parallel heat conduction paths between the lower copper plate and the air stream through the plexiglass spacers. Typically, this term was about 8 percent of the vertical heat flux. All measurements were taken at steady state after adjustments were made with variable resistors until an

Nomenclature

C = chord length of model (see Fig. 1(*a*)) or constant pressure specific heat
C_p = pressure coefficient $(P-P_0)/1/2\,\rho U_0^2$
h = convective heat transfer coefficient
H = height of model (see Fig. 1(*a*))
k = thermal conductivity of air
K_e = thermal conductivity of epoxy separation in heater units per unit thickness
Nu = Nusselt number, hH/k
Nu_c = Nusselt number, hC/K
Nu_r = Reattachment Nusselt number, hX_r/k
Q_c = heat loss correction
Re = Reynolds number, U_0H/ν
Re_c = Reynolds number, U_0C/ν
Re_r = Reattachment Reynolds number, U_0X_r/ν
Re_D = Reynolds number for cylinder, D = diameter
St_0 = Stanton number $h/\rho CU_0$
U_0 = upstream velocity
x = distance from separation

Greek

α = angle of attack (see Fig. 1(*a*))
β = wedge angle of nose (see Fig. 1(*d*))
ΔT_e = temperature difference across the epoxy
ΔT_t = temperature difference between top surface and free-stream
ΔX_e = epoxy thickness
ν = kinematic viscosity of air
ρ = density of air

Subscripts

cp = constant pressure region value
r = reattachment value
min = minimum value
max = maximum value

isothermal surface was obtained which was 11°C ± 0.33°C (20°F ± 0.6°F) above ambient. Streamwise temperature gradients in the test heater surface were negligible, while in the larger guard heater units they were calculated to be less than 0.3°C (0.5°F). Possible lateral conduction losses, both spanwise and chordwise, due primarily to the uncertainty in setting the surface temperature, were observed to be typically less than 1.5 percent of the vertical flux.

The development of equation (1) and the evaluation of Q_c are described in [11]. When taken together, possible errors in thermocouple calibration, recorder accuracy, thermal conductivity measurements, temperature, and velocity control and heat loss evaluations lead to an estimated confidence internal for the calculated Stanton numbers of ± 6 percent (20 to 1 odds).

The test heater units were separated from the guard heater units by two 0.95-cm (0.375-in.)-wide plexiglass strips. One of these had 18 surface pressure taps that spanned the chord of the model, which were used to determine the pressure coefficient distribution. Pressure readings were made with a Datametric electronic manometer accurate to ± 0.4 percent of reading (+ 0.02 percent of scale), which in general is much smaller than the size of the observed pressure fluctuations.

The reattachment model is similar to that used in [2] with the main difference being in its dimensions. This model was constructed of plexiglass with 10 chordwise surface pressure taps to confirm correspondence with the flow over the heat transfer model. The flow over the reattachment model was assumed to be the same as that over the heat transfer model when these pressure taps showed the surface pressure distributions to be the same for a given upstream speed and angle of attack. There were 8 spanwise taps at midchord to confirm the two-dimensionality of the flow. The reattachment position was determined by a set of tufts fixed to the upper chord surface separated by 0.635 cm (0.25 in.). Therefore, the reattachment position could be determined within ± 3 percent of the chord length.

Results and Discussion

Separation Bubble. Heat transfer data for the separated and reattached flow are shown in Fig. 3 for Re = 29586 and five different angles of attack. The corresponding pressure coefficient distributions are shown in Fig. 4. The reattachment position as a function of angle of attack is correlated to a second-order, least-squares polynomial in Fig. 5, along with the results of Sam et al. [2] for a model of 6/1 aspect ratio. The reattachment position was found to be independent of Reynolds number in the range 10^4–10^5, in agreement with [2, 5, 7, 9]. The uncertainty bands of Fig. 5 are statistical, representing two standard deviations of 10 data points and five replications of each angle at two Reynolds numbers, where the set point of the apparatus was approached randomly from above and below.

Ota and Itasaka [5] and Sam et al. [2] reported reattachment at 4 to 5 times the model thicknesses for a body of rectangular cross section at 0 deg. According to this, the flow would not reattach on a prism of 4/1 aspect ratio. In fact, the flow was found to reattach at about 3.5 model thicknesses, indicating a possible reattachment dependency on aspect ratio.

The reattachment length decreases from a maximum at 0 deg to 0 at about 34 deg where a stagnation line exists at the leading edge [11]. Due to the small size of the separation bubble for angles of attack above 10 deg, the tufts influenced the separated flow significantly. At 15 deg, the reattachment length was deduced to be 16 percent of the chord, by reasoning explained later, as opposed to 22 percent as indicated directly by tuft measurement. Above 15 deg, the reattachment length was not discernible by these methods.

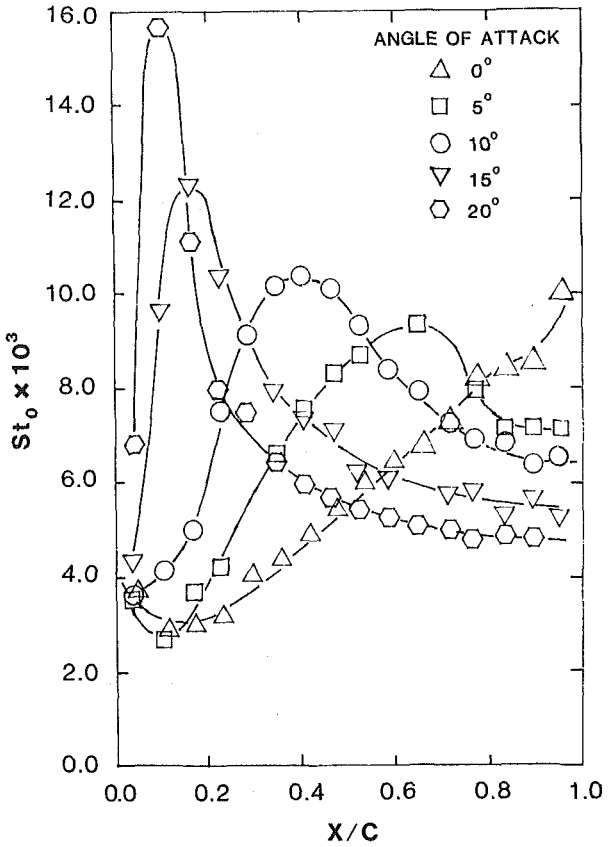

Fig. 3 Separated flow Stanton number data

The heat transfer is characterized by a peak in the vicinity of reattachment. The peak heat transfer was found to increase with increasing angle of attack or decreasing separation bubble size. A similar result of increasing peak heat transfer with decreasing bubble size was reported by Ota and Kon [7]. Their velocity and temperature profiles at reattachment showed that for the smaller separation bubbles there were larger temperature and velocity gradients at the surface. They attributed this to the thinness of the bubbles, and the relatively larger variation across the less laterally diffused separating shear layer due to a shorter reattachment length.

For 0 and 5 deg, the heat transfer near the leading edge decreases to a minimum (see Fig. 3) and then rises toward reattachment. The elevated initial values are probably due to large velocity and temperature gradients in the strong separating shear layer. This phenomenon is not observed at higher angles due to the decreased resolution inside the separation bubble. Such behavior at the leading edge has also been observed in two flat-plate investigations [6, 8].

The pressure distributions (Fig. 4) are typical of separated and reattached flows. The pressure distribution is characterized by a nearly constant pressure following the separation point at a value lower than that upstream. As reattachment is approached, the pressure rises and continues to rise to a point downstream of reattachment. After this, the pressure drops due to the favorable pressure gradient induced by the geometry of the model and wind tunnel wall. It is interesting to notice that the peak pressure coefficient increases with decreasing bubble size. This is also a characteristic of Robertson's results [1].

Ota and Kon [7] reported the reattachment heat transfer to be independent of nose shape when the length scale for the Nusselt and Reynolds numbers is the reattachment distance. The functional relationship between reattachment Nusselt number and reattachment Reynolds number was found to be a

straight line in log–log coordinates (Fig. 6). A similar relationship for the present results was found to be independent of angle of attack. This is shown on Fig. 6 for angles up to 15 deg with a least-squares curve fit. Also plotted on Fig. 6 are similar correlations reported for a blunt flat plate [6] and for a logitudinal blunt circular cylinder [10]. The results of [6, 7, 10] are all constant surface heat flux experiments. The present results indicate somewhat higher reattachment Nusselt numbers. This observation appears to be confirmed by the reported findings of [3], which are also constant surface temperature experiments. Only the 0 deg resuls of [3] are shown in Fig. 6, since in [3] the resolution was such that data were averaged over one-quarter of the chord. Data reported at higher angles are not included, since the experiment could not accurately determine reattachment Nusselt numbers for such small separation bubbles. This effect may have also influenced the 0-deg results somewhat.

Since the resulting functional relationships of Fig. 6 are very similar, especially in slope, for a variety of geometries, it appears that this is an acceptable way of correlating reattachment heat transfer – at least for flows where the boundary layer thickness upstream of the separation is negligible.

In contrast to the investigations of Ota and Kon [6, 7, 10], which reported reattachment and maximum Nusselt number

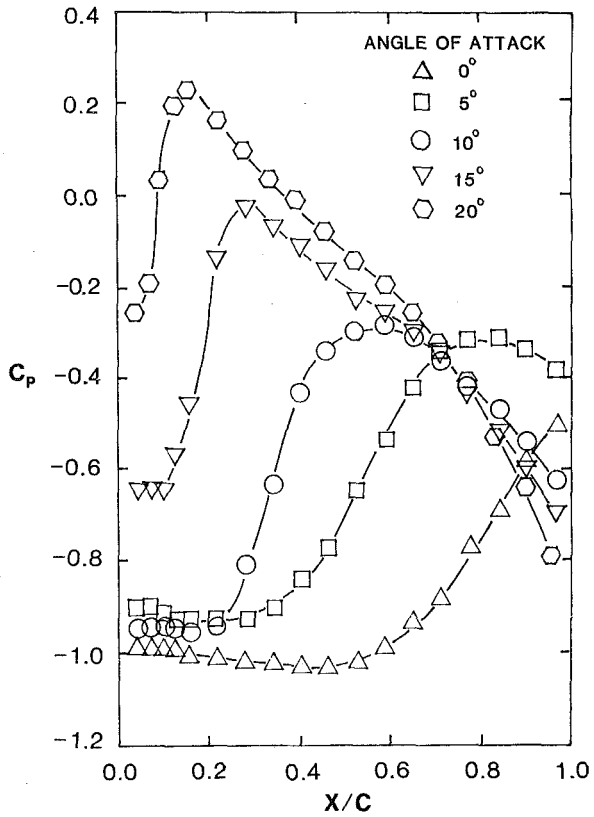

Fig. 4 Separated flow pressure coefficient data

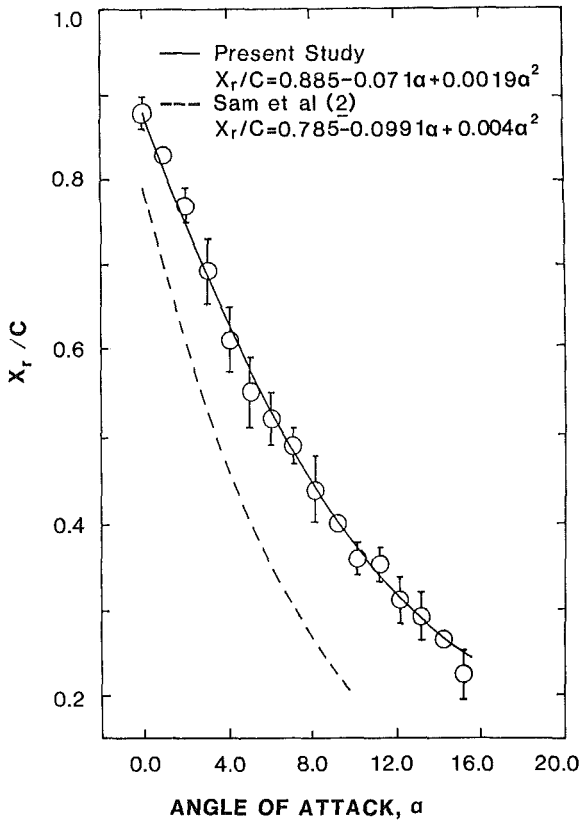

Fig. 5 Variation of reattachment distance with angle of attack

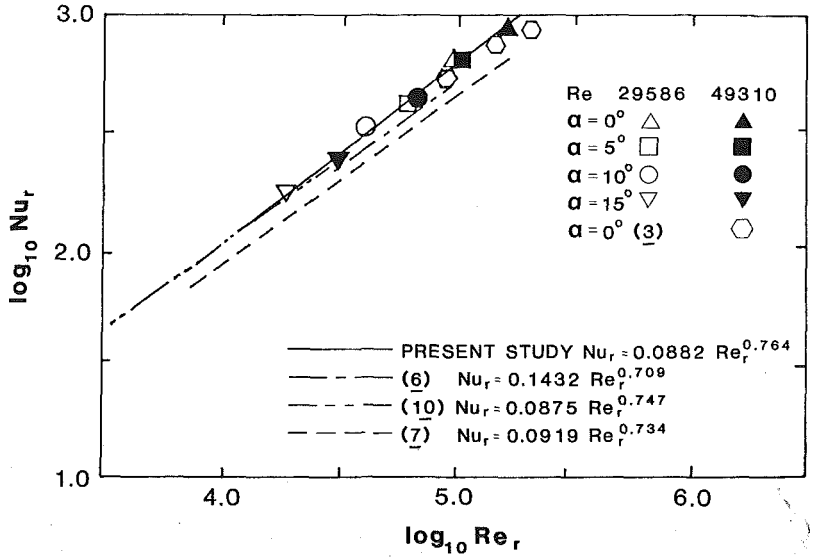

Fig. 6 Correlation between reattachment Nusselt number and Reynolds number

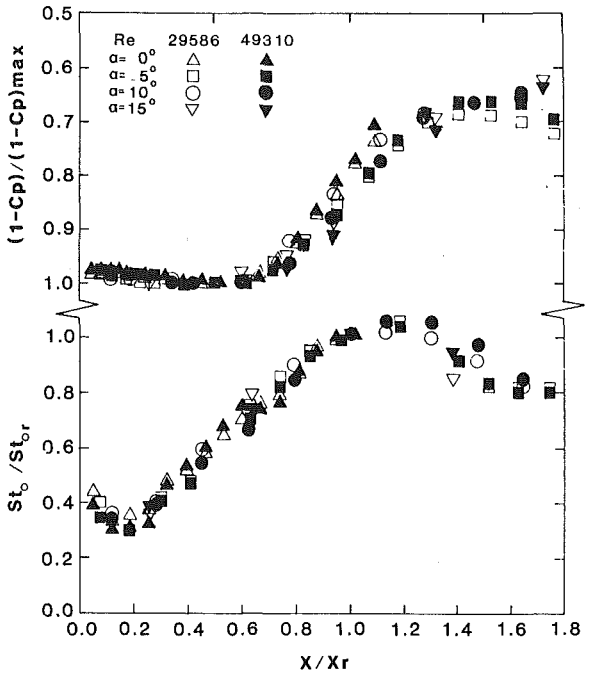

Fig. 7 Scaled data plotted against chord position normalized with the reattachment length

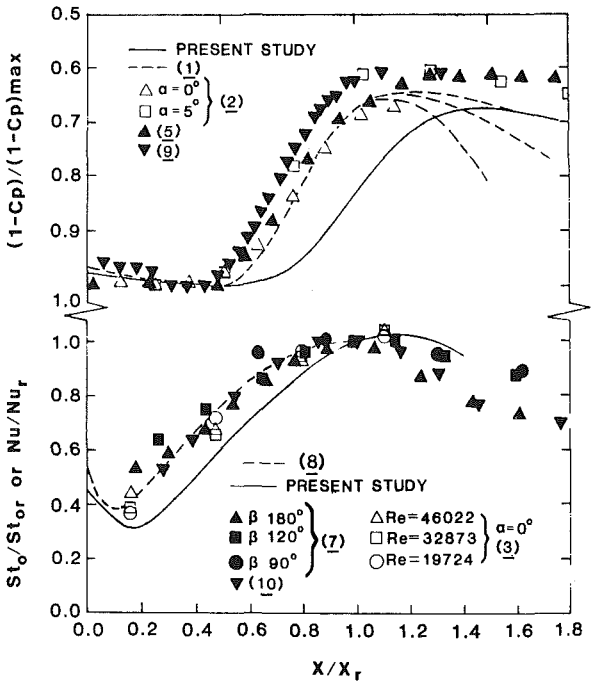

Fig. 8 Comparison of present data to other results plotted against x/x_r

to coincide, the present results indicate that reattachment precedes maximum heat transfer by 12 to 15 percent of the chord. At 15 deg, reattachment and maximum heat transfer appear to coincide. Since the resolution is only one-third the reattachment length in this case, the actual maximum value and position in heat transfer probably was not found due to the averaging tendency of the heater units. The 0-deg result shows a sharp increase in heat transfer at the back edge of the model. However, the evaluation of Q_c in equation (1) for the back heater unit was reported to be questionable [11]. Since this data point appears to deviate from the general trend, it is rejected. Therefore, the maximum heat transfer value and position for 0 deg remains undetermined.

A major emphasis of this investigation was to find suitable scales to reduce the pressure and heat transfer data onto similarity curves. Roshko and Lau [4] proposed scaling the distance coordinate to the reattachment length, and they proposed a pressure scale that was essentially the ratio of $(1 - C_p)$ to $(1 - C_p)_{max}$. The $(1 - C_p)_{max}$ factor corresponds to the nearly constant pressure region just downstream of separation, which by free-streamline theory [12], is the pressure in the bubble at the separation point. Roshko and Lau [4] chose this scale based on the assumption that the pressure distribution inside the bubble depends on the potential flow pattern approaching separation. This type of scaling is applied to the pressure coefficients in Fig. 7.

Based on the tuft measured reattachment distance, pressure data for 0, 5, and 10 deg indicate that the constant pressure region is 60 percent of the reattachment length. Using this and knowing the constant pressure region length at 15 deg, the reattachment distance for 15 deg was estimated. Recall that this length could not be accurately measured using the tuft method.

The Stanton number data, scaled to its reattachment value and plotted with the same length scaling, are shown on Fig. 7. Note that both the heat transfer and pressure data collapse onto similarity curves, and surprisingly, both curves remain reasonably similar after reattachment. Also there does not appear to be any direct geometric correlation between these two curves.

To check the universality of this scaling, these curves are compared to previously mentioned investigations. In Fig. 8, the similarity pressure curve is compared to the results of the square prism [1], the prism of 6/1 aspect ratio [2], the blunt flat plate [5], and the longitudinal blunt cylinder [9]. Also in Fig. 8, the similarity heat transfer curve is compared to the blunt flat plate with various nose shapes [7, 8], the longitudinal blunt cylinder [10], and the prism of 6/1 aspect ratio [3].

The scaled pressure data in Fig. 8 show the constant pressure region varies from 60 percent of the reattachment length for the present results to about 45 percent for the longitudinal blunt cylinder. Note that the blunt flat plate [5] and the longitudinal blunt cylinder [9] are essentially infinite aspect ratio cases at zero angle of attack. Also the 6/1 aspect ratio prism data [2] has been corrected for wind tunnel blockage. Uncorrected data from this experiment would plot lower and to the right. The trend is then one of increasing constant pressure length for decreasing aspect ratio, with the exception of the seemingly anomalous behavior of the square prism data [1]. This is most likely because reattachment on a square prism necessitates a large angle of attack. The present 4/1 aspect ratio case is about the limit where reattachment will still occur at 0 deg. Thus it seems reasonable that the relatively larger turning of the free stream in the vicinity of the separation bubble would cause larger pressure gradients and move these data up and to the left.

This all suggests the use of an alternate characteristic length, the constant pressure region length, X_{cp}. Figure 9 shows the result of using X_{cp} to scale the distance coordinate on these data. The pressure coefficients collapse onto a single curve to a distance somewhat past reattachment ($X_r/X_{cp} = 1.6$), after which the data branch, depending on the angle of attack, but independent of Reynolds number, the trend being a greater rise in pressure for increasing angle of attack.

Accordingly, with X_{cp} used as a length scale, the Stanton numbers are scaled to their value at the end of the constant pressure region (Fig. 9), which also collapses the heat transfer onto a similarity curve up to the reattachment point. After reattachment, the data diverge in branches that depend on Reynolds number (unlike the pressure data) and on angle of attack. The trend for a given angle of attack is an increasing rise in heat transfer over the value at the end of the constant

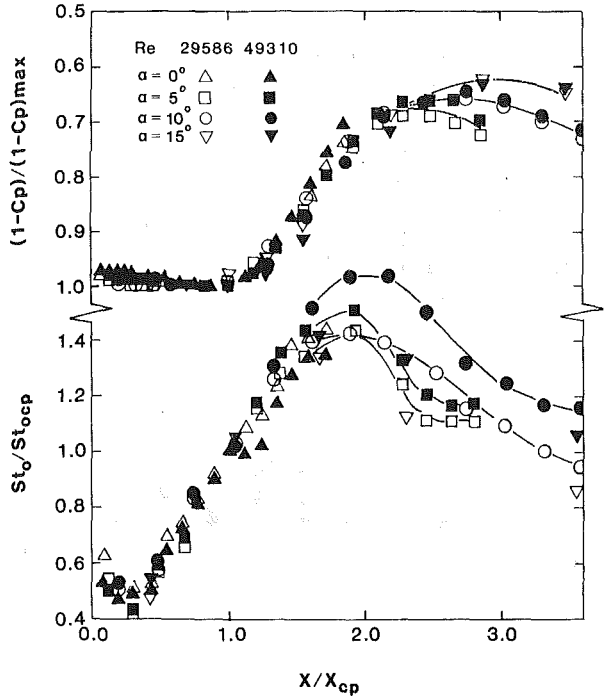

Fig. 9 Scaled data plotted against chord position normalized with the constant pressure length

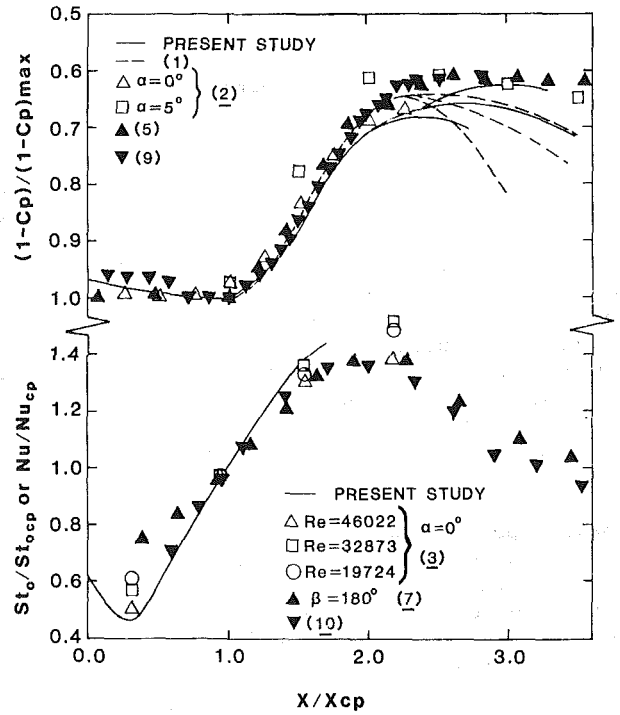

Fig. 10 Comparison of present data to other results plotted against X/X_{cp}

pressure region with increasing Reynolds number. For a given Reynolds number, the trend is an increasing rise in heat transfer with increasing angle (this is not reflected in the 15-deg results due to the averaging tendency over the heater units).

In Fig. 10, the similarity curves from Fig. 9 are compared to other investigations. The pressure coefficients from the investigations shown in Fig. 8 [1, 2, 5, 9] are replotted in Fig. 10. It is apparent that X_{cp} correlates the pressure coefficients of these several geometries onto a single universal curve.

The universal pressure curve of Fig. 10 was also compared

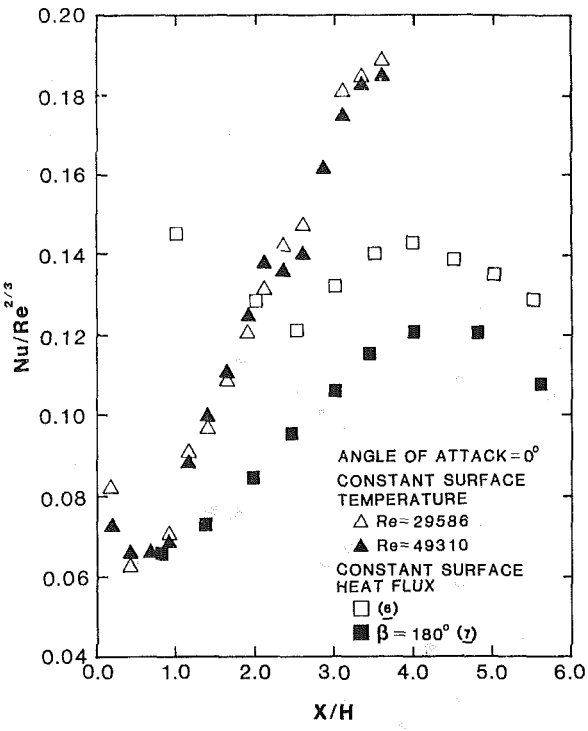

Fig. 11 Comparison of constant surface temperature and constant heat flux data for $\alpha = 0$ deg

to the results of Mueller et al. [14], who examined the separated and reattached flow downstream of a roughness element. These data were found to deviate significantly. A considerable boundary layer developed prior to separation in this situation, and this boundary layer affected the pressure distribution in the separation bubble. For such a flow, the boundary layer thickness prior to separation is not negligible and the results should not be compared to the present curve.

The heat transfer similarity curve in Fig. 10 is compared to the heat transfer result of the prism of 6/1 aspect ratio [3], the blunt flat plate [7] and the longitudinal blunt cylinder [10]. The pressure distributions from which the X_{cp}'s were determined are from [2, 5] and [10], respectively. For the other heat transfer data in Fig. 8, X_{cp} could not be determined from the literature. The 6/1 prism results agree well with the present study except near separation. This is due to the averaging tendency of the heater units discussed earlier. The longitudinal blunt cylinder result also agrees well with the present study; however, agreement is not as convincing for the flat blunt plate.

The constant-pressure length scales may be deduced empirically from the reported reattachment length data on Fig. 5 by noting that X_{cp} is nearly a constant 60 percent of reattachment for the 4/1 aspect ratio experiments and a constant 40 percent of X_r for the 6/1 case. It was attempted to analytically predict the constant pressure region length by use of the notched hodograph free-streamline theory for an inclined flat plate by Abernathy [12]. It was reported that the front portion of the separation bubble shape for a prism (6/1 aspect ratio) at 0, 5, and 10 deg was predicted by this approach based on smoke flow visualization [15]. It was, therefore, hoped that the portion of the bubble up to where the predicted free streamline became parallel to the surfae of the prism would correspond to the constant pressure region. This prediction failed at 0 deg due to the influene of the notch (the point at which the free steamline became parallel to the surface corresponds to the notch location) but gave satisfactory results between 5 and 10 deg. Over 10 deg, the

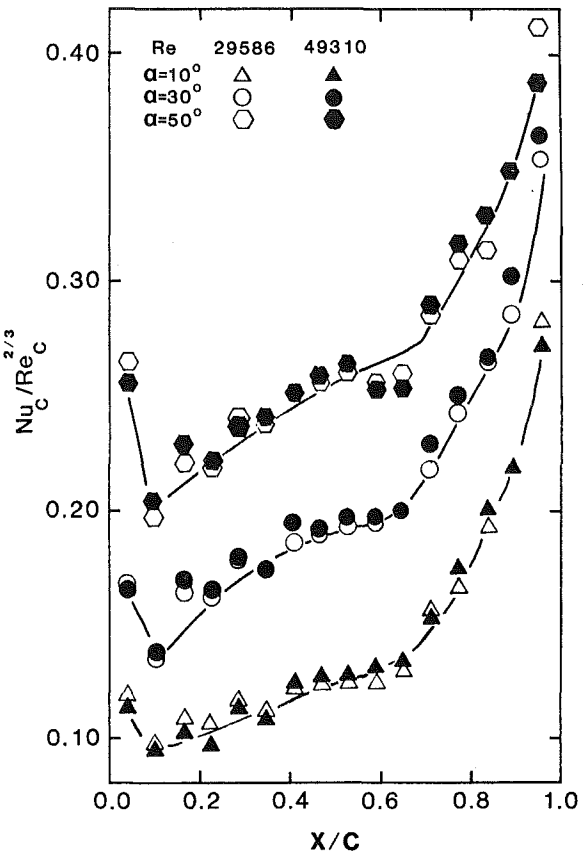

Fig. 12 Heat transfer results for wake facing surface

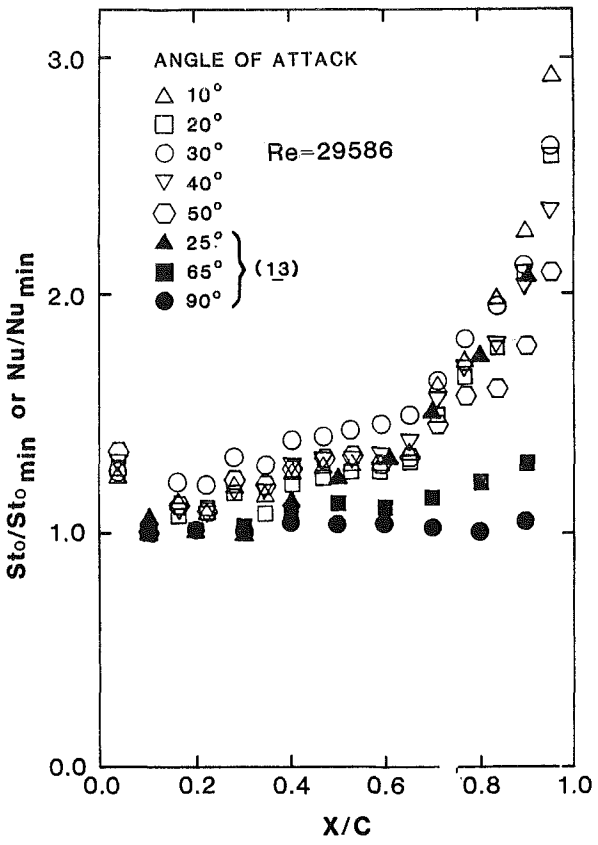

Fig. 13 Normalized wake surface heat transfer data

influence of the prism surface appears to affect the entire shape of the bubble, and thus the method failed.

In [6], for the separated and reattached flow over a blunt flat plate, $Nu/Re^{2/3}$ was reported to be independent of Reynolds number. This was also found to be true with the present results, both with the separated and reattached flow and the fully separated, wake flow (to be discussed). Therefore, this provides a means to predict the heat transfer for this geometry at any Reynolds number using the present results (constant surface temperature case). Also at 0 deg, the present heat transfer results in this coordinate were up to 50 percent higher than the constant surface heat flux blunt flat plate results of [7]. These are presented in Fig. 11.

This figure also shows the earlier results of Ota and Kon [6], which are not in agreement with their later work. Their discussion of this discrepancy is not detailed but seems to indicate that these two experiments differed in the way in which they were instrumented near the leading edge. From Fig. 11, it would appear that the first two data points from [6] are in error; however, the remaining data agrees at least in trend with the other results and is about 25 percent lower than the present case.

This is an unexpected result, since laminar solutions for unseparated zero pressure gradient flows show that a constant heat flux boundary condition results in a 35 percent greater heat transfer when compared with that caused by a constant wall temperature condition. In these cases, both the local Nusselt number and the wall shear stress monotonically decrease in the direction of flow. In the case of separated flow, our data show that the Nusselt number still basically decreases in the direction of the near wall flow (from reattachment to separation), but this is only a superficial similarity. The wall shear stress in this situation must first increase in the direction of flow and then decrease toward separation and the wall shear stress gradient influences the shape of the temperature profile. Consequently, there is no reason to expect the same qualitative dependence of heat transfer on boundary conditions in these two very different types of flow fields.

At the same time, the observed 50 percent difference in Nusselt number in Fig. 11 is characteristic of laminar unseparated flows, since the corresponding turbulent flows show an order of magnitude smaller variation with changes in the boundary condition. This may indicate that the return surface flow is near to laminar. Turbulence intensity measurements provide additional evidence for this. These show much more intense fluctuations just outside the separation bubble than any encountered within it.

Wake Exposed Surface. Figure 12 shows the heat transfer results from the downstream or wake side of the model for 10–50 deg angle of attack. It plots $Nu_C/Re_C^{2/3}$ against chord position and shows an increase in heat transfer with increasing angle of attack. The heat transfer is also greater at the trailing edge of the model.

Sogin [13] examined the heat transfer in the wake of a prism of 6.75/1 aspect ratio at 25, 65, and 90 deg and other geometries. It was reported that, in general, the heat transfer increased as the size of the wake increased. Also as the angle of attack decreased from 90 deg, the heat transfer distribution, which was initially constant, showed increased asymmetry with the greatest heat transfer at the trailing edge. This behavior was attributed to the fact that the vortex shed from the trailing edge is closer to the model than the one from the leading edge. The present results are in agreement with these observations.

For a given angle of attack [13] reported that the $Nu_C/Re_C^{2/3}$ distribution for the prism was independent of Reynolds number, except near the trailing edge. In these coordinates, the present results for the two Reynolds numbers

used (29,586 and 49,310), collapse satisfactorily to a single curve for a particular angle of attack. By interpolating linearly between 20 and 30 deg to 25 deg, the 25 deg results of [13] were found to be lower than the present results by nearly a constant 30 percent. This discrepancy is probably an aspect ratio effect. Also it is not clear whether [13] is a constant surface temperature experiment, a constant heat flux experiment, or neither.

Since the heat transfer distribution for each angle in Fig. 12 appears similar in shape, the Stanton numbers for each angle were scaled to the corresponding minimum value. These are shown in Fig. 13 together with the results of [13] in equivalent coordinates. The present data diverge at 80 percent of the chord, depending on angle of attack. The 25-deg results of [13] agree closely to the present 20-deg results. As the angle of attack increases, the rise in heat transfer over the minimum value decreases. According to the results of [13], this trend should continue until at 90 deg the distribution is flat.

Conclusions

A summary of conclusions from this study are:

1 Scaling $(1-C_p)$ to the value of the constant pressure region $(1-C_p)$max and the heat transfer to the value at the end of the constant pressure region for separation bubbles results in universal curves when the distance coordinate is scaled to the length of the constant pressure region. These universal curves apply only to situations where the boundary layer upstream of separation is thin and does not influence the value of pressure at separation.

2 The length of the constant pressure region for separated and reattached flow on prisms appears to be a constant fraction of the reattachment distance, independent of angle of attack. However, this fraction is a function of the aspect ratio of the prism.

3 The relationshp between the reattachment Nusselt number and Reynolds number is nearly independent of geometry for the cases considered when the reattachment length is used as the characteristic length.

4 For both the separated and reattached flow and the fully separated wake flow regions, the distribution of $Nu/Re^{2/3}$ was found to be independent of Reynolds number.

5 The constant surface temperature heat transfer in the separated and reattached flow regions at 0 deg was up to 50 percent higher than the equivalent constant heat flux case.

6 In all cases, the peak in both the local Stanton number curves and the scaled pressure coefficient curves occurred after reattachment. Peak heat transfer was observed to be 12–15 percent downstream of the reattachment point.

7 The observed heat transfer rates from the fully separated wake facing surface of the model indicate a near constant heat transfer coefficient across this surface for high angles of attack. Smaller angles of attack show significant variation, with the heat transfer being the highest in the vicinity of the trailing edge.

Acknowledgment

This research was performed under the auspices of NSF Grant ENG CME-7916890.

References

1 Robertson, J. M., Wedding, J. B., Peterka, J. A., and Cermak, H. E., "Wall Pressures of Separation—Reattachment Flow on a Square Prism in Uniform Flow," *Journal of Industrial Aerodynamics*, Vol. 2, 1977/1978, pp. 345–359.

2 Sam, R. G., Lessmann, R. C., and Test, F. L., "An Experimental Study of Flow Over a Rectangular Body," ASME *Journal of Fluid Engineering*, Vol. 101, Dec. 1979, pp. 443–448.

3 Test, F. L., and Lessmann, R. C., "An Experimental Study of Heat Transfer During Forced Convection Over a Rectangular Body," ASME JOURNAL OF HEAT TRANSFER, Vol. 102, Feb. 1980, pp. 146–151.

4 Roshko, A., and Lau, J. C., "Some Observations on Transition and Reattachment of a Free Shear Layer in Incompressible Flow," *Proc. Heat Transfer Mech. Inst*, 1965, pp. 157–167.

5 Ota, T. and Itasaka, M., "A Separated and Reattached Flow on a Blunt Flat Plate," ASME *Journal of Fluid Mechanics*, Vol. 98, Mar. 1976, pp. 79–86.

6 Ota, T., and Kon, N., "Heat Transfer in the Separated and Reattached Flow on a Blunt Flat Plate," ASME JOURNAL OF HEAT TRANSFER, Vol. 96, Nov. 1974, pp. 459–462.

7 Ota, T., and Kon, N., "Heat Transfer in the Separated and Reattached Flow Over Blunt Flat Plates—Effects of Nose Shape," *International Journal of Heat and Mass Transfer*, Vol. 22, 1979, pp. 197–206.

8 Kottke, V., Blenke, H., and Schmidt, K. G., "Determination of the Local and Average Mass Transfer on Thick Plates in Parallel Flow With Flow Separation and Reattachment," *Warme-und Stoffubertragung*, Vol. 10, 1977, pp. 217–232.

9 Ota, T., "An Axisymmetric Separated and Reattached Flow on a Longitudinal Blunt Circular Cylinder," ASME *Journal of Applied Mechanics*, Vol. 42, June 1975, pp. 311–315.

10 Ota, T. and Kon, N., "Heat Transfer in an Axisymmetric Separated and Reattached Flow Over a Longitudinal Blunt Circular Cylinder," ASME JOURNAL OF HEAT TRANSFER, Vol. 99, Feb. 1977, pp. 155–157.

11 McCormick, D. C., "Effect of Free-Stream Turbulence and Separated Flow on Heat Transfer," M.S. thesis, Department of Mechanical Engineering, University of Rhode Island, Feb. 1983.

12 Abernathy, F. H., "Flow Over an Inclined Plate," Pratt and Whitney Research Report, No. 151, Aug. 1958.

13 Sogin, H. H., "A Summary of Experiments on Local Heat Transfer From the Rear of Bluff Obstacles to a Low Speed Airstream," ASME JOURNAL OF HEAT TRANSFER, Vol. 86, May 1964, pp. 200–202.

14 Mueller, T. J., Korst, H. H., and Chow, W. L., "On the Separation, Reattachment, and Redevelopment of Incompressible Turbulent Shear Flow," *Journal of Basic Engineering*, Vol. 86, June 1964, pp. 221–226.

15 Hart, D., and Lessmann, R. C., "Visualization of Separated Flow on a Rectangular Prism," Technical Report NSF Grant CME-796890, June 1981.

16 Kays, W. M., and Crawford, M. E., *Convective Heat and Mass Transfer*, 2nd ed., McGraw-Hill, New York, 1980, pp. 149–150.

K. Chen
Assistant Professor,
Department of Mechanical and Industrial Engineering,
University of Utah,
Salt Lake City, Utah 84112
Assoc. Mem. ASME

M. M. Chen
Professor,
Department of Mechanical and Industrial Engineering,
University of Illinois,
Urbana, Ill. 61801
Mem. ASME

Thermal Instability of Forced Convection Boundary Layers

Thermal instability of forced convection boundary layers with nonzero streamwise pressure gradient is examined for moderate to high Prandtl numbers. The analysis is carried out for the family of Falkner-Skan flows, here viewed as the lowest order local similarity approximation of general forced convection boundary layers. Calculated critical Rayleigh numbers and wave numbers are found to be independent of the streamwise pressure gradient in the limiting case of infinite Prandtl number, and only weakly dependent on the streamwise pressure gradient for finite Prandtl number cases when the conduction thickness is employed as the reference length scale.

1 Introduction

The stability analysis of a forced convection boundary layer above a heated surface is an important problem for a large number of engineering and scientific disciplines. The recent interest in low Reynolds/Peclet number heat transfer, particularly relating to applications in solar and electronic heat transfer and nuclear safety, focuses new attention to this fundamental problem.

Although the study of thermal instability in quiescent, bottom-heated layers has had a long history, most of the previous studies concerning flowing fluids have been restricted to confined layers [1-3] or natural convection boundary layers [4-6]. Most of the existing studies on forced and mixed convection boundary layers [7-10] were concerned with the horizontal flat plate boundary layer without streamwise pressure gradient or with buoyancy-induced streamwise pressure gradient only. Most of the theoretical studies neglected streamwise variations of the perturbations. The study on stagnation boundary layers by the present authors [11], on the other hand, was exact in that boundary layer assumptions were not necessary and the perturbations were truly independent of x.

The present investigation is concerned with the effects of streamwise pressure gradient on the onset of thermal instability for general forced convection boundary layers. In this regard, the family of wedge flow boundary layers (Falkner-Skan flows) is particularly interesting, partly because of its mathematically convenient properties. More importantly, the Falkner-Skan flows can be viewed as the lowest order "local similarity" approximation of general boundary layers [12]. Several expansion schemes have been proposed to account for the higher order effects [13-15]. Enough examples have been worked out in these studies to show that the lowest order result (i.e., Falkner-Skan) gives a reasonably accurate account of the boundary layer structure, the shear stress, and heat flux for a wide range of wedge parameters (i.e., m, see below) and Prandtl numbers. It is reasonable to expect that calculations carried out for Falkner-Skan flows would provide a good estimate of the thermal instability of general forced convection boundary layers.

2 Mathematical Formulation

The coordinate system employed here is shown in Fig. 1. Note that the gravity force is perpendicular to the flow direction, the vortex instability dominates in this case [6]. The complete governing equations under the Boussinesq approximation and linear equation of state assumption are:

$$\nabla \cdot \mathbf{V} = 0 \tag{1}$$

$$\frac{\partial \mathbf{V}}{\partial \tau} + \mathbf{V} \cdot \nabla \mathbf{V} = -\frac{1}{\rho} \nabla p - \mathbf{g}\beta(t - t_\infty) + \nu \nabla^2 \mathbf{V} \tag{2}$$

$$\frac{\partial t}{\partial \tau} + \mathbf{V} \cdot \nabla t = \alpha \nabla^2 t \tag{3}$$

The solutions outside the viscous boundary layer are characterized by

$$u = u_\infty = cx^m \tag{4}$$

$$t = t_\infty \tag{5}$$

Both c and t_∞ are constants, while m is the Falkner-Skan parameter. For flows which are not true wedge flows, m may be evaluated from the expression [14]

$$\frac{m}{m+1} = \frac{d\ln u_\infty}{d\ln \xi} \quad \text{where } \xi = \int_o^x u_\infty(x)\,dx$$

An obvious scheme for nondimensionalization would employ L_o, the body dimension which is of the order of the x's encountered in the problem, and $u_o (= cL_o^m)$ the corresponding velocity, as reference scales for all the variables. Such a scheme, however, does not properly address the physics involved. While L_o is the proper length scale for streamwise variations, it is not the proper length scale for transverse buoyancy effects, which is responsible for the instability and is confined within the thermal boundary layer. Since it is known that the thermal boundary layer thickness varies approximately as $L_o\,\mathrm{Re}^{-1/2}\mathrm{Pr}^{-1/3}$ for $1 < \mathrm{Pr} < \infty$ and exactly for $\mathrm{Pr} \to \infty$, this will be chosen as the reference length scale for normal variations. (See equations (7) through (11) below). This corresponds to the "inner scale" in the jargon of inner-outer expansion techniques:

$$\delta_T = L_o \mathrm{Re}^{-1/2}\mathrm{Pr}^{-1/3} \tag{6}$$

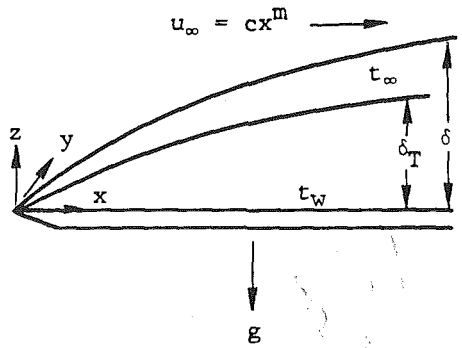

Fig. 1 Forced convection boundary layer over a heated surface

Contributed by the Heat Transfer Division for publication in the JOURNAL OF HEAT TRANSFER. Manuscript received by the Heat Transfer Division October 1, 1982.

Using this scale for normal and transverse variations, the dimensionless variables are

$$(x^+, y^+, z^+) = (x, y\mathrm{Re}^{1/2}\mathrm{Pr}^{1/3}, z\mathrm{Re}^{1/2}\mathrm{Pr}^{1/3})/L_o \quad (7)$$

$$(u^+, v^+, w^+) = (u\mathrm{Pr}^{1/3}, v\mathrm{Re}^{1/2}\mathrm{Pr}^{2/3}, w\mathrm{Re}^{1/2}\mathrm{Pr}^{2/3})/u_o \quad (8)$$

$$\tau^+ = L_o\mathrm{Pr}^{1/3}/u_o \quad (9)$$

$$(t^+ = \bar{t}^+ + \tilde{t}^+ = \theta^+ + \tilde{t}^+) = ((\bar{t} - t_\infty)/\Delta t + \tilde{t}/\Delta t) \quad (10)$$

$$p^+ = p/(\rho u_o{}^2\mathrm{Re}^{-1}\mathrm{Pr}^{-4/3}) \quad (11)$$

After decomposing each quantity into a base flow quantity (designated by an over-bar) and a disturbance quantity (designated by an over-tilde) and neglecting the high order terms, the dimensionless equations governing the disturbances can be obtained:

$$\frac{\partial \tilde{u}^+}{\partial x^+} + \frac{\partial \tilde{v}^+}{\partial y^+} + \frac{\partial \tilde{w}^+}{\partial z^+} = 0 \quad (12)$$

$$\frac{1}{\mathrm{Pr}}\left(\frac{\partial \tilde{u}^+}{\partial \tau^+} + \bar{u}^+\frac{\partial \tilde{u}^+}{\partial x^+} + \tilde{u}^+\frac{\partial \bar{u}^+}{\partial x^+} + \bar{w}^+\frac{\partial \tilde{u}^+}{\partial z^+} + \tilde{w}^+\frac{\partial \bar{u}^+}{\partial z^+}\right) = \frac{-1}{\mathrm{RePr}^{5/3}}\frac{\partial \tilde{P}^+}{\partial x^+} + \frac{1}{\mathrm{RePr}^{2/3}}\frac{\partial^2 \tilde{u}^+}{\partial x^{+2}} + \frac{\partial^2 \tilde{u}^+}{\partial y^{+2}} + \frac{\partial^2 \tilde{u}^+}{\partial z^{+2}} \quad (13)$$

$$\frac{1}{\mathrm{Re\ Pr}}\left(\frac{\partial \tilde{v}^+}{\partial \tau^+} + \bar{u}^+\frac{\partial \tilde{v}^+}{\partial x^+} + \bar{w}^+\frac{\partial \tilde{v}^+}{\partial z^+}\right) = \frac{1}{\mathrm{Re}}\left(\frac{-1}{\mathrm{Pr}}\frac{\partial \tilde{P}^+}{\partial y^+} + \frac{1}{\mathrm{Re\ Pr}^{2/3}}\frac{\partial^2 \tilde{v}^+}{\partial x^{+2}} + \frac{\partial^2 \tilde{v}^+}{\partial y^{+2}} + \frac{\partial^2 \tilde{v}^+}{\partial z^{+2}}\right) \quad (14)$$

$$\frac{1}{\mathrm{Re\ Pr}}\left(\frac{\partial \tilde{w}^+}{\partial \tau^+} + \bar{u}^+\frac{\partial \tilde{w}^+}{\partial x^+} + \tilde{u}^+\frac{\partial \bar{w}^+}{\partial z^+} + \bar{w}^+\frac{\partial \tilde{w}^+}{\partial z^+} + \tilde{w}^+\frac{\partial \bar{w}^+}{\partial z^+}\right) = \frac{1}{\mathrm{Re}}\left(\frac{-1}{\mathrm{Pr}}\frac{\partial \tilde{P}^+}{\partial z^+} + \frac{1}{\mathrm{RePr}^{2/3}}\frac{\partial^2 \tilde{w}^+}{\partial x^{+2}} + \frac{\partial^2 \tilde{w}^+}{\partial y^{+2}} + \frac{\partial^2 \tilde{w}^+}{\partial z^{+2}} + \mathrm{Ra}_o{}^+\tilde{t}^+\right) \quad (15)$$

$$\frac{\partial \tilde{t}^+}{\partial \tau^+} + \bar{u}^+\frac{\partial \tilde{t}^+}{\partial x^+} + \tilde{u}^+\frac{\partial \bar{t}^+}{\partial x^+} + \bar{w}^+\frac{\partial \tilde{t}^+}{\partial z^+} + \tilde{w}^+\frac{\partial \bar{t}^+}{\partial z^+} = \frac{1}{\mathrm{Re\ Pr}^{2/3}} + \frac{\partial^2 \tilde{t}^+}{\partial x^{+2}} + \frac{\partial^2 \tilde{t}^+}{\partial y^{+2}} + \frac{\partial^2 \tilde{t}^+}{\partial z^{+2}} \quad (16)$$

where

$$\mathrm{Re} = \frac{u_o L_o}{\nu},$$

$$\mathrm{Ra}_o^+ = \frac{g\beta\Delta t\delta_T{}^3}{\nu\alpha}$$

The base flow solutions, $\bar{u}^+$ and so on, constitute the coefficients. In the present investigation, the base flows are the two-dimensional, nonparallel flows governed by the familiar Falkner-Skan equations:

$$\phi^{+\prime\prime\prime} + \frac{1}{\mathrm{Pr}}\left(\phi^+\phi^{+\prime\prime} - \frac{2m}{m+1}\phi^{+\prime}\phi^{+\prime}\right) + \frac{1}{\mathrm{Pr}^{1/3}}\frac{2m}{m+1} = 0 \quad (17)$$

$$-\phi^+\theta^{+\prime} = \theta^{+\prime\prime} \quad (18)$$

with boundary conditions given by

$$\phi^+(0) = \phi^{+\prime}(0) = \theta^+(\infty) = 0$$
$$\phi^{+\prime}(\infty) = \theta^+(0) = 1 \quad (19)$$

where the primes indicate differentiations with respect to the similarity variable η^+. The definition of η^+ and relations between ϕ^+ and $\bar{u}^+$, $\bar{w}^+$ are shown as follows:

$$\eta^+ = \left(\frac{m+1}{2}x^{+m-1}\right)^{1/2} z^+ = \left[\frac{m+1}{2}\left(\frac{x}{L_o}\right)^{m-1}\right]^{1/2} z\mathrm{Re}^{1/2}\mathrm{Pr}^{1/3}/L_o \quad (20)$$

$$\bar{u}^+ = x^{+m}\phi^{+\prime} \quad (21)$$

Nomenclature

c = constant in equation (4)
g = gravitational acceleration
h = heat transfer coefficient
K_o = wave number
K = modified wave number, $K^+ = K_0^+\left[\frac{2}{m+1}x^{+1-m}\right]^{1/2}$
L_o = a constant characteristic length
m = wedge angle parameter
p = reduced pressure
P = amplitude function for perturbed pressure
Pr = Prandtl number, ν/α
Ra = Rayleigh number, $\frac{g\beta\Delta t x^3}{\alpha\nu}$, $\mathrm{Ra}^+ = \frac{g\beta\Delta t\delta_T{}^3}{\alpha\nu}\left(\frac{2}{m+1}x^{+1-m}\right)^{3/2}$, $\mathrm{Ra}^* = \mathrm{Ra}^+\left(\frac{\delta_c}{\delta_T}\right)^3$
Re = Reynolds number, $u_o L_o/\nu$
t = temperature
t_w = wall temperature
t_∞ = free stream temperature
Δt = temperature difference, $\Delta t = t_w - t_\infty$
T = amplitude function for perturbed temperature
u_o = a constant characteristic velocity
u,v,w = velocities in x, y, z directions, respectively
U,V,W = amplitude functions for perturbed velocities in x, y, z directions, respectively
$\mathbf{V}$ = velocity vector
x,y,z = spatial coordinates (see Fig. 1)
α = heat diffusivity
β = coefficient of thermal expansion
δ_c = conduction thickness (see equation (34))
δ_T = thermal boundary layer scale, $\delta_T = L_o\mathrm{Re}^{-1/2}\mathrm{Pr}^{-1/3}$
η = normal coordinate after similarity transformation
θ = temperature function in two-dimensional Falkner-Skan flow
ν = kinematic viscosity
ρ = density
σ = growth factor of disturbance
τ = time
ϕ = velocity function in two-dimensional Falkner-Skan flow

Subscript

∞ = free stream quantities
c = critical
min = minimum

Superscript

$'$ = differentiation with respect to η^+ or η^*
$+$ = dimensionless quantities based on thermal length scale
$*$ = dimensionless quantities based on conduction thickness
$-$ = mean quantities
$\sim$ = perturbed quantities

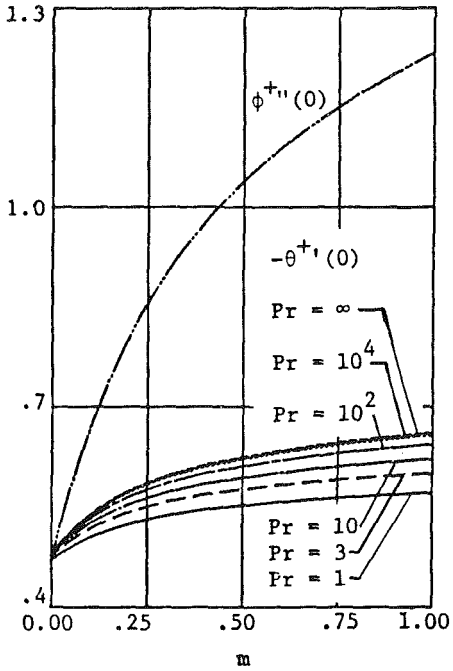

Fig. 2 Base flow boundary conditions, $\phi^{+\prime\prime}(0)$ and $-\theta^{+\prime}(0)$, for various wedge parameters and Prandtl numbers

$$\tilde{w}^+ = -\left(\frac{m+1}{2}x^{+m-1}\right)^{1/2}\left(\phi^+ + \frac{m-1}{m+1}\eta^+\phi^{+\prime}\right) \tag{22}$$

When the body force is perpendicular to the heated surface, the buoyancy force term in the base flow equations is of the order of 1/Re and thus can be neglected based on boundary-layer approximations. The base flow results have been solved and tabulated in many standard textbooks. The calculated heat fluxes and shear stresses at the heated surface for all the cases studied in the present investigation are shown in Fig. 2.

All previous investigations of thermal instability with shear have shown that the dominant mode of instability near the critical Rayleigh number is in the form of stationary streamwise vortices. The present investigation will be restricted to this mode, which is periodic in the spanwise direction. The disturbances are decomposed into Fourier components in the y-direction, with initial exponential growth, as follows:

$$\begin{bmatrix}\tilde{u}^+\\ \tilde{v}^+\\ \tilde{w}^+\\ \tilde{p}^+\\ \tilde{t}^+\end{bmatrix} = \begin{bmatrix}\frac{2}{m+1}x^{+m}U^+(\eta^+)\\ \left(\frac{2}{m+1}x^{+m-1}\right)^{1/2}V^+(\eta^+)\\ \left(\frac{2}{m+1}x^{+m-1}\right)^{1/2}W^+(\eta^+)\\ x^{+m-1}P^+(\eta^+)\\ \frac{2}{m+1}T^+(\eta^+)\end{bmatrix}\cdot e^{iK_o{}^+y^+ + \sigma^+\tau^+} \tag{23}$$

where σ^+ is the growth factor, and $K_o{}^+$ is real and represents the transverse periodic wave number of disturbances.

Most studies on boundary layer instability have neglected the x-dependence of the disturbances. This assumption neglects the convective terms $\bar{u}\partial/\partial x$. In a study of the stability of free convection boundary layer in porous media, Hsu, Cheng, and Homsy [16] carried out a careful order-of-magnitude analysis and showed that because of the large base flow velocity in the x-direction, these terms are actually of the same order as the other terms. Furthermore, they argued that since the scales of the disturbance parameters must vary with the boundary layer thickness and velocity scales of the base flow, the wave length and the velocity amplitudes must vary in the same manner as similar parameters in the base flow. The same arguments also apply here. This accounts for the presence of powers of x in equation (23). This in fact amounts to a quasi-similarity transformation, as is in the case of reference [16]. In so doing, the variables in the resulting disturbance equations are separable. A lower critical Rayleigh number would be obtained if the x-dependence of the disturbance amplitudes were neglected. As was stated in reference [16], the convective terms associated with $\bar{u}$ have a stabilizing effect on the flow field.

Substituting the assumed forms of disturbances into equations (12) through (16) and invoking the boundary layer assumption (i.e., setting $\mathrm{Re}\to\infty$ and $\mathrm{Re}\,\mathrm{Pr}^{2/3}\to\infty$), the resultant equations, after eliminating V^+ and P^+, become

$$U^{+\prime\prime} - K^{+2}U^+ = \left(\frac{4m}{m+1}U^+\phi^{+\prime} - \phi^+U^{+\prime} + \frac{m-1}{m+1}\eta^+\phi^{+\prime\prime}U^+ + W^+\phi^{+\prime\prime}\right)\Big/\mathrm{Pr} \tag{24}$$

$$\begin{aligned}W^{+\prime\prime\prime\prime} &- 2K^{+2}W^{+\prime\prime} + K^{+4}W^+ + \frac{m-1}{m+1}\eta^+U^{+\prime\prime\prime}\\ &+ \frac{5m-3}{m+1}U^{+\prime\prime\prime} - \frac{m-1}{m+1}\eta^+K^{+2}U^{+\prime\prime} - \frac{3m-1}{m+1}K^{+2}U^{+\prime}\\ &= K^{+2}\mathrm{Ra}^+T^+ + \frac{1}{\mathrm{Pr}}\left\{-\phi^+W^{+\prime\prime\prime} - \frac{2}{m+1}\phi^{+\prime}W^{+\prime\prime}\right.\\ &+ \left(\frac{m-1}{m+1}\phi^{+\prime\prime} + \phi^+K^{+2}\right)W^{+\prime}\\ &+ \left(\phi^{+\prime}K^{+2} + \frac{m-1}{m+1}\eta^+\phi^{+\prime\prime}K^{+2}\right)W^+\\ &- \frac{m-1}{m+1}\eta^+\phi^+U^{+\prime\prime\prime} - \left[\frac{4m-2}{m+1}\phi^+\right.\\ &+ \left.\frac{2m-2}{(m+1)^2}\eta^+\phi^{+\prime}\right]U^{+\prime\prime}\\ &- \left[\frac{6m-2}{(m+1)^2}\phi^{+\prime} - \frac{(m-1)^2}{(m+1)^2}\eta^+\phi^{+\prime\prime}\right]U^{+\prime}\\ &+ \left[\frac{2m^2-2m}{(m+1)^2}\phi^{+\prime\prime} + \frac{m-1}{m+1}\phi^+K^{+2}\right.\\ &+ \frac{3m^2-4m+1}{(m+1)^2}\eta^+\phi^{+\prime}K^{+2}\\ &\left.\left.+ \frac{(m-1)^2}{(m+1)^2}\eta^{+2}\phi^{+\prime\prime}K^{+2}\right]U^+\right\}\end{aligned} \tag{25}$$

$$\frac{m-1}{m+1}\eta^+U^+\theta^{+\prime} + W^+\theta^{+\prime} - \phi^+T^{+\prime} = T^{+\prime\prime} - K^{+2}T^+ \tag{26}$$

with boundary conditions

$$\begin{aligned}U^+ = W^+ = W^{+\prime} = T^+ = 0 \quad &\text{at } \eta^+ = 0\\ U^+, W^+, W^{+\prime}, T^+ \to 0 \quad &\text{as } \eta^+ \to \infty\end{aligned} \tag{27}$$

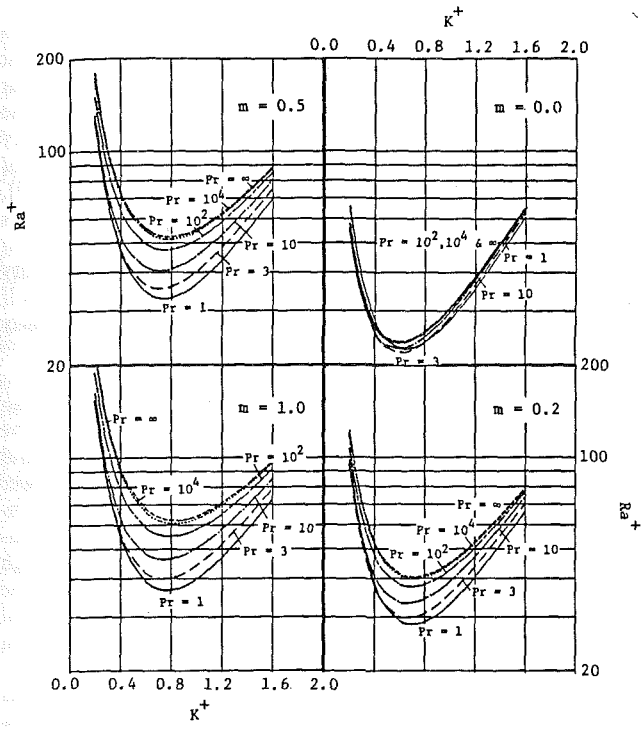

Fig. 3 Neutral stability curves plotted in thermal scale

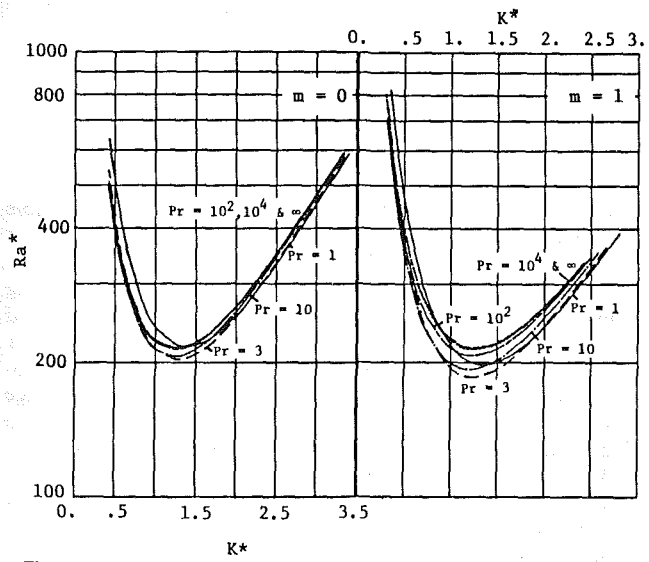

Fig. 4 Neutral stability curves based on the conduction thickness

where

$$K^+ = K_o + \left(\frac{2x^{+\,1-m}}{m+1}\right)^{1/2} \tag{28}$$

$$\mathrm{Ra}^+ = \mathrm{Ra}_o + \left(\frac{2}{m+1}x^{+\,1-m}\right)^{3/2} \tag{29}$$

That is, the boundary layer variation is combined with the wave number and Rayleigh number to form the modified wave number K^+ and Rayleigh number Ra^+.

Strictly speaking, the transformation performed above is a "quasi-similarity" transformation since the x-influences still exist in the coefficients of the resultant equations (except for $m=1$). The results of this analysis are therefore applicable to the vicinity of a given streamwise location x, unless the boundary layer variation along the streamwise direction is negligible.

In the limiting case of $\mathrm{Pr}\to\infty$, the velocity perturbation in the streamwise direction disappears. The problem reduces to a sixth-order eigenvalue problem with wedge parameter influence existing in the base flow only. By employing the conduction thickness δ_c instead of δ_T as the reference length scale, the resultant eigenvalue problem is universal for different wedge parameters as shown below. Note that the superscript * denotes dimensionless variables based on the conduction thickness.

$$\phi^* = 3[(1/3)!]^3\eta^{*2} \tag{30}$$

$$\theta^* = 1 - \int_o^{\eta^*} \exp\{-[(1/3)!]^3\zeta^3\}d\zeta \tag{31}$$

$$W^{*\,\prime\prime\prime\prime} - 2K^{*2}W^{*\,\prime\prime} + K^{*4}W^* = K^{*2}\mathrm{Ra}^*T^* \tag{32}$$

$$W^*\theta^{*\,\prime} - \phi^*T^{*\,\prime} = T^{*\,\prime\prime} - K^{*2}T^* \tag{33}$$

where

$$\delta_c = -\frac{\delta_T}{\theta^{+\,\prime}(0)} \tag{34}$$

$$\eta^* = \eta^+\frac{\delta_T}{\delta_c} \tag{35}$$

$$(T^*,\theta^*) = (T^+,\theta^+) \tag{36}$$

$$(\phi^*,W^*,K^*,\mathrm{Ra}^{*1/3}) = (\phi^+,W^+,K^+,\mathrm{Ra}^{+\,1/3})\frac{\delta_c}{\delta_T} \tag{37}$$

Therefore, it is expected to have a universal critical Rayleigh number based on the conduction thickness for flows with various pressure gradients in this limiting case.

3 Numerical Method

The resultant mathematical formulation for finite Pr cases is an eighth-order eigenvalue problem in a semi-infinite domain. The numerical technique employed to solve it is the outward shooting scheme, briefly described below. For a given wave number, a set of trial values for the eigenvalue and three unknown boundary conditions are assigned at the solid boundary. An additional nonhomogeneous boundary condition can be assigned arbitrarily because the problem is homogeneous. These, together with the four known homogeneous boundary conditions, permit the integration to proceed outward by Runge-Kutta or a similar marching scheme. At a preselected computing depth, the solution is tested to see if it satisfies the four vanishing velocities and temperature conditions. If not, corrected trial values are obtained using the multivariable Newton-Raphson iteration scheme. When the iteration converges, the computing depth is increased by a predetermined amount and the computation is repeated. It was shown in [17] that the perturbations decay exponentially outside the boundary layer. As a consequence, the incremental change of the eigenvalue for each successive increase in computing depth decays exponentially with the computing depth. This behavior permits an accurate extrapolation of the infinite depth result. Since the extrapolation was performed when the incremental change was less than 10^{-10}, the extrapolation error was expected to be considerably less. Tests with different step sizes and with double precision arithmetic were also performed. The total for the truncation and round-off errors was estimated to be 10^{-5}. A detailed discussion of the numerical scheme can be found in reference [17]. Trial computations were also carried out using the matching scheme developed by Nachtsheim [4] and agreement was satisfactory.

4 Results and Discussion

The calculated neutral stability curves with Pr ranging from one through infinity for four different wedge parameters are plotted in Fig. 3. The familiar fingerprint patterns are observed here. If the problem were nondimensionalized by the

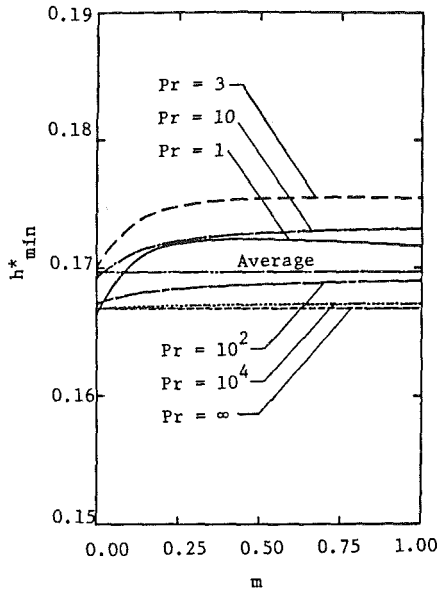

Fig. 5 Minimum heat transfer coefficients for stable boundary layers

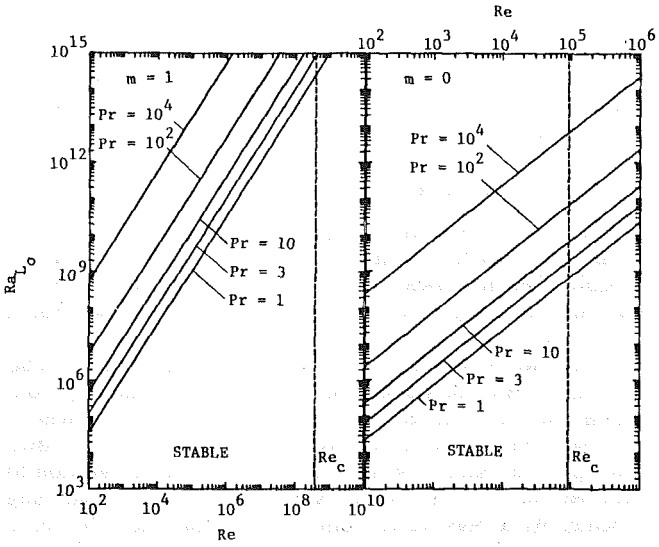

Fig. 6 Stability limits for thermal instability and shear flow instability in Blasius flows ($m = 0$) and stagnation flows ($m = 1$)

viscous variables instead of thermal variables, as in previous investigations [7, 10], these neutral stability curves would be dispersed and the results of infinite Pr cases could never be presented. The results for $m = 1$ are identical to that of the stagnation flow [11] presented before. But the latter problem yields an exact solution without applying the boundary layer simplification.

The influence of Pr on the neutral stability curves, though slight when the thermal layer thickness δ_T was employed as the reference length scale, can still be observed in these figures, especially for large wedge parameter cases. Comparing the observation here with the base flow boundary conditions shown in Fig. 2, we may conclude that this simple reference thermal scale δ_T cannot accurately account for the Prandtl number effect on the thermal boundary layer thickness. Thus, when the conduction thickness δ_c, which contains more information about thermal boundary layer thickness than δ_T does, is employed as our reference length scale, it is not surprising that the influence of Pr is nearly completely eliminated, as shown in Fig. 4. Although the conduction thickness concept was derived in the limiting case of infinite Pr, the calculated results show that this scale is still appropriate even for Pr down to unity. A critical Rayleigh number of about 200 and wave number of about 1.3, both based on the conduction thickness, are applicable to almost all of the cases studied in the present investigation. This result also reveals that thermal instability is mainly dependent on the temperature field instead of the velocity field in boundary layer flows. In view of the thermal instability analyses of Couette flow [1] and fully developed Poiseuille flow [3], which both show the same critical conditions as that in a quiescent fluid layer, it could be inferred that the effect of streamwise velocity profile on the onset of thermal instability is relatively insignificant in parallel or boundary layer flows if a reference length scale is employed which properly demonstrates the features of the temperature field.

The calculated Rayleigh number and wave number at critical point in Blasius flow have been compared with previous experimental results reported by Gilpin et al. [9]. The predicted wave number agrees well with the experimental observation. The calculated Rayleigh number is slightly lower than what was observed in the experiments. Since the instability must grow for a finite disturbance before its amplitude is large enough to be observed, and since the Rayleigh number is proportional to the cube of the reference length, the experimental results may have overestimated the critical Rayleigh number. A detailed comparison can be found in reference [17].

The existence of a critical Rayleigh number also suggests that there exists a minimum heat transfer coefficient below which the thermal boundary layer is unstable. The dimensionless heat transfer coefficient h^* is defined as

$$h^* \equiv \left(\frac{-\left.\frac{\partial t}{\partial z}\right|_{z=0}}{\Delta t} \right) \Big/ \left[\left(\frac{g\beta\Delta t}{\alpha\nu} \right)^{1/3} \left(\frac{m+1}{2x^{+1-m}} \right)^{1/2} \right]$$

The minimum heat transfer coefficients to maintain stable boundary layers for various Pr and m are shown in Fig. 5. It is noted that an average value of $h^*_{\min}$ about 0.170 ± 0.004 is applicable for Pr ranging from one to infinity and m ranging from 0 to 1. This gratifying result is very convenient and useful from a practical point of view since the heat transfer coefficient is an important design factor in engineering applications, and the maximum deviation from the average value of the minimum heat transfer coefficient is observed to be as small as only 5 percent for all the cases studied here.

When a shear flow is subjected to an unstable temperature gradient, both shear flow instability and thermal instability may occur. To complete the present investigation, it is useful to indicate the region of parameters where thermal instability may dominate, relative to the more familiar shear flow instability. The comparisons between these two instabilities for stagnation flow and Blasius flow are shown in Fig. 6. Shear flow instability is governed by the Reynolds number alone. Thermal instability is governed by three independent parameters: the Reynolds number, the Prandtl number, and the modified Rayleigh number Ra_{L_o} $(= \mathrm{Ra}^+ \mathrm{Re}^{3/2}\ \mathrm{Pr})$ based on a constant length L_o. The comparisons neglect the influence of the temperature profile on the onset of Tollmien-Schlichting waves and is valid only when the overall Richardson number is small [18]. It is important to note from this figure that the flow at small Re is more susceptible to thermal instability than at large Re. Therefore, a large Reynolds number may suppress the occurrence of thermal instability in forced convection problems, due primarily to its influence on the boundary layer thickness.

References

1 Ingersoll, A. P., "Convective Instabilities in Plane Couette Flow," *Phys. Fluids*, Vol. 9, No. 4, 1966, pp. 682-689.

2 Weber, J. E., "On Thermal Convection Between Nonuniformly Heated Planes," *Int. J. Heat Mass Transfer*, Vol. 16, 1973, pp. 961–970.

3 Cheng, K. C., and Wu, R. S., "Axial Heat Conduction Effects on Thermal Instability of Horizontal Plane Poiseuille Flows Heated From Below," ASME JOURNAL OF HEAT TRANSFER, Vol. 98, No. 4, Nov. 1976, pp. 564–569.

4 Nachtsheim, P. R., "Stability of Free Convection Boundary Layer Flows," NASA TN D-2089, 1963.

5 Gebhart, B., "Natural Convection Flow, Instability and Transition," ASME JOURNAL OF HEAT TRANSFER, Vol. 91, No. 3, Aug. 1969, pp. 293–309.

6 Haaland, S. E., and Sparrow, E. M., "Vortex Instability of Natural Convection Flow on Inclined Surfaces," *Int. J. Heat Mass Transfer*, Vol. 16, 1973, pp. 2355–2367.

7 Wu, R. S., and Cheng, K. C., "Thermal Instability of Blasius Flow Along Horizontal Plates," *Int. J. Heat Mass Transfer*, Vol. 19, 1976, pp. 907–913.

8 Chen, T. S., and Mucoglu, A., "Wave Instability of Mixed Flow Over a Horizontal Flat Plate," *Int. J. Heat Mass Transfer*, Vol. 22, 1979, pp. 185–196.

9 Gilpin, R. R., Imura, H., and Cheng, K. C., "Experiments on the Onset of Streamwise Vortices in Horizontal Blasius Flow Heated From Below," *Int. J. Heat Mass Transfer*, Vol. 100, 1978, pp. 71–77.

10 Moutsoglou, A., Chen, T. S., and Cheng, K. C., "Thermal Instability of Mixed Convection Flow Over a Horizontal Flat Plate," Joint ASME/AIChE National Heat Transfer Conference, Orlando, Florida, July 27–30, 1980.

11 Chen, M. M., Chen, K., and Sohn, C. W., "The Thermal Instability of Stagnation Point Boundary Layers," ASME Paper No. 80-HT-76, 1980.

12 Meksyn, D., *New Methods in Laminar Boundary-layer Theory*, Oxford, Pergamon Press, 1961, Chapters 6, 7, and 9.

13 Gortler, H., "A New Series for the Calculation of Steady Laminar Boundary Layer Flows," *J. Math. Mech.*, Vol. 6, 1957, pp. 1–66.

14 Chao, B. T., and Fagbenle, R. O., "On Merk's Method of Calculating Boundary Layer Transfer," *Int. J. Heat Mass Transfer*, Vol. 17, 1974, pp. 223–240.

15 Sparrow, E. M., Quack, H., and Boerner, C. J., "Local Nonsimilarity Boundary-Layer Solutions," *AIAA Journal*, Vol. 8, No. 11, 1970, pp. 1936–1942.

16 Hsu, C. T., Cheng, P., and Homsy, G. M., "Instability of Free Convection Flow Over a Horizontal Impermeable Surface in a Porous Medium," *Int. J. Heat Mass Transfer*, Vol. 21, 1978, pp. 1221–1228.

17 Chen, K., "Thermal Instability of Wedge Flows," Ph.D. thesis, Department of Mechanical and Industrial Engineering, University of Illinois at Urbana-Champaign, 1981.

18 Gage, K. S., and Reid, W. H., "The Stability of Thermally Stratified Plane Poiseuille Flow," *J. Fluid Mech.*, Vol. 33, Part I, 1968, pp. 21–32.

Heat Transfer From Rods or Fins Which Extend Radially Outward From a Rotating Shaft

E. M. Sparrow
Fellow ASME

D. S. Kadle

Department of Mechanical Engineering,
University of Minnesota,
Minneapolis, Minn. 55455

The heat transfer characteristics of spokelike rods that extend outward from a rotating shaft have been determined experimentally. The experiments encompassed a number of geometrical parameters, including the length and diameter of the rods, the number of rods deployed around the circumference of the shaft, and the distance between the rods and the free end of the shaft. Also varied during the experiments was the rotational Reynolds number. Per-rod Nusselt numbers were evaluated from the experimental data. By incorporating the rod dimensions in the definition of the characteristic velocity that appears in the Reynolds number, a universal Nusselt–Reynolds–Prandtl correlation was obtained which is independent of the dimension ratios of the problem. It was also found that the Nusselt number results are independent of the number of rods in the circumferential array and are very weakly dependent on the distance from the rods to the free end of the shaft. The final correlation is conveyed by equations (18) and (19), with the Reynolds number defined by equations (7) and (10).

Introduction

In this paper, experiments are described for determining the convective heat transfer characteristics of spokelike rods that extend radially outward from a rotating shaft. Such rods may be employed as pin fins to improve the heat transfer from the shaft to the surrounding fluid. They may also serve as spokes whose outer extremities mate with a wheel. Even in their capacity as spokes, the rods may act as *de facto* fins. Furthermore, rotating shafts often have surface protuberances that, in effect, function as short pin fins.

A review of the literature did not reveal any prior study of the heat transfer characteristics of rods that extend radially outward from the surface of a rotating shaft. Information is available for heat transfer at the surface of a rotating shaft without rods or protuberances [1–3], but that has little or no relationship to the characteristics of radially extended rods. In view of this, the results to be presented here appear to be the first contribution to the rotating rod problem.

A schematic view of the physical problem is presented in Fig. 1. The figure portrays a cross section that cuts through the rods and the shaft in such a way as to show the rod diameter. Also shown in the figure are a number of physical parameters that, together with the thermophysical properties of the fluid, govern the heat transfer coefficient for the rods. There are four geometric parameters: the rod diameter, D, and its base-to-tip length, L, the shaft diameter, D_s, and the number of rods, N (or alternately, the angle between rod centers). In addition, the angular velocity, ω, can be varied parametrically. For all of the experiments performed here, the rods were situated in a common cross section, as in Fig. 1.

As will be demonstrated later, dimensional analysis yields a total of five dimensionless groups that constitute the independent variables of the problem. These include the rod Reynolds number, the Prandtl number, two ratios of dimensions (e.g., L/D and D_s/D), and the number of rods. Aside from the Prandtl number, which was fixed, all of the other four groups were varied during the course of the experiments. In addition, supplementary experiments were carried out to investigate whether the heat transfer coefficients for the rods are affected by the proximity of the end of the shaft.

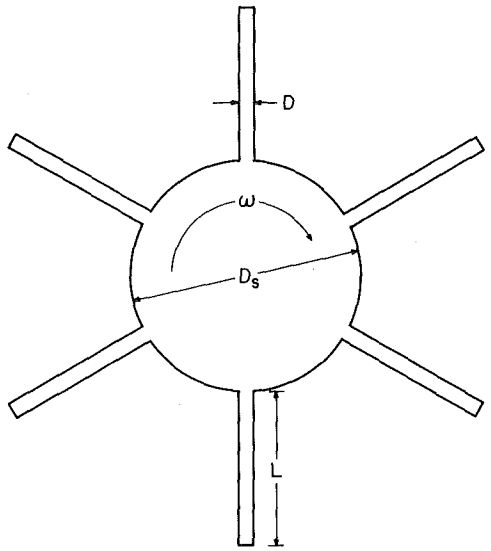

Fig. 1 Cross section through the rods and the rotating shaft

In each data run, measurements were made which enabled the per-rod heat transfer coefficient and Nusselt number to be evaluated. In the data reduction, ways were sought to reduce the number of dimensionless groups needed to correlate the Nusselt number. By a proper choice of the characteristic velocity that appears in the Reynolds number, it was found possible to eliminate the dimension ratio, L/D, from the correlation. Also, the insensitivity of the results to the number of rods eliminated still another parameter. Thus, in the final correlation, the Nusselt number was represented as a function of a reduced number of dimensionless groups.

The absence of any prior work on the class of problems investigated here precludes direct comparisons with the literature. Because of this, comparisons were sought with related physical situations—in particular, with Nusselt number correlations which might have been used to obtain approximate heat transfer results for the present problem prior to the availability of the Nusselt numbers measured

Contributed by the Heat Transfer Division for publication in the JOURNAL OF HEAT TRANSFER. Manuscript received by the Heat Transfer Division January 6, 1983.

here. The two cases that seem most appropriate in this regard are the in-line tube bank and the single cylinder in crossflow. There are major differences between the fluid flow patterns for those cases and that for the present configuration. One of these is the linear variation of the velocity along the length of the present rods in contrast to the axially uniform velocities for the comparison cases. Another is the presence and absence of centrifugal forces in the respective rotating and nonrotating flows.

The Experiments

To facilitate the attainment of the research objectives set forth in the Introduction, the experiments were performed using the naphthalene sublimation technique rather than by direct heat transfer measurements. The dimensionless mass transfer results (Sherwood numbers) obtained from the naphthalene technique can be transformed to Nusselt numbers for heat transfer via the analogy between the two processes. In addition to greater measurement precision, the naphthalene technique offers several special advantages in the present problem. It provides great flexibility in that the length, diameter, and number of rods can be varied with relative ease. Furthermore, it completely avoids the complexities of passing electric current through rotating contacts into separate heating circuits for the individual rods, as well as the difficulties of temperature measurement in a rotating body. Extraneous losses (such as those due to conduction in the corresponding heat transfer problem) are virtually absent. A final advantage of the technique is the easy attainment of a standard boundary condition (analogous to uniform wall temperature).

Experimental Apparatus. The rotating shaft used in the experiments was driven by a vertical milling machine situated in a laboratory setting. For the experiments, a collet was implanted in the rotating head of the milling machine, and a special fixture was used to mate the end of the shaft with the collet. With this setup, the axis of the shaft was colinear with the axis of the rotation of the milling machine. The milling machine was operated at rotational speeds between 265 and 1880 rpm in eight discrete steps. These speeds were verified periodically with a five-figure digital tachometer.

The experimental apparatus is shown schematically in the left-hand diagram of Fig. 2. As seen there, the rotating shaft is an assembly of several cylindrical sections which had been turned together on a lathe in order to ensure their precise alignment. The diagram is to scale, and all dimensions of the rotating shaft can be inferred from the 5.017-cm shaft diameter.

The upper section, which mated with the collet of the milling machine, was made of steel for strength. The next section was of Delrin, a free-machining plastic. A plastic was used for this section rather than a metal to minimize the thermal interaction between the rotating head of the milling machine and the naphthalene-coated rods. Due to the presence of the plastic and to the hardly perceptible temperature rise of the rotating head, the equilibrium temperature of the naphthalene (which controls its vapor pressure) was unaffected by the milling machine.

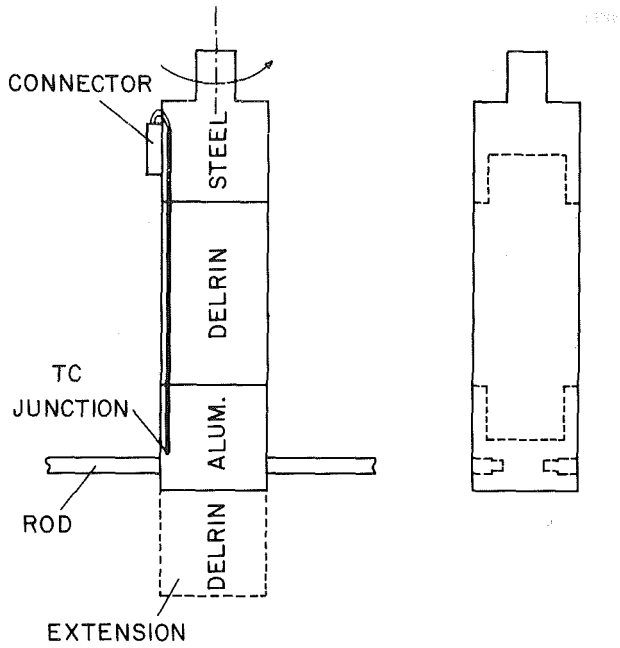

Fig. 2 Experimental apparatus. External view at left; internal view at right.

An aluminum section situated next to the Delrin served as the host for the rods, whose transfer characteristics are the focus of the experiments. The use of aluminum was motivated by its high thermal conductivity and its relatively light weight (compared with other highly conducting metals). The high conductivity aided in the attainment of temperature uniformity throughout the section and promoted temperature equality between the section and the rods which it hosted. As will be described shortly, the temperature of the rods was measured by a thermocouple embedded in the aluminum immediately adjacent to one of the rods.

The rods were accommodated in holes of appropriate diameter and depth drilled radially into the aluminum section adjacent to its base, as shown schematically in Fig. 2. All told, there were six such holes deployed at 60-deg intervals around the circumference of the section. Data runs were performed with various numbers of rods in place (ranging from one to six rods). When fewer than six rods were employed, the unused holes were covered with thin (0.005-cm-thick) pressure-sensitive tape.

Two sets of rods with respective diameters of 0.635 and 0.953 cm were employed in successive series of experiments. The first series of experiments were performed with the

Nomenclature

D = diameter of rod
D_s = diameter of shaft
$\mathfrak{D}$ = diffusion coefficient
K = per-rod mass transfer coefficient, $\dot{m}/(\rho_{nw} - \rho_{n\infty})$
L = length of rod
$\dot{m}$ = per-rod mass flux
N = number of rods
Nu = per-rod Nusselt number
Pr = Prandtl number
Re = Reynolds number, $(R^*\omega)D/\nu$
R_s = radius of shaft
R^* = radius for characteristic velocity, equation (10)
Sc = Schmidt number
Sh = per-rod Sherwood number, $KD/\mathfrak{D}$
V^* = characteristic velocity, $R^*\omega$
α = factor in definition of R^*, equation (6)
μ = viscosity
ν = kinematic viscosity
ρ = density
ρ_{nw} = naphthalene vapor density at surface
$\rho_{n\infty}$ = naphthalene vapor density in ambient
ω = angular velocity

smaller diameter rods, and when these runs were completed the radial holes were enlarged to accommodate the larger diameter rods. To ensure positive seating of the rods, the inner reaches of the holes were stepped, as were the mating ends of the rods. The rods were held in place by Allen-head screws recessed into the lower face of the aluminum section.

Whereas the foregoing sections of the rotating shaft were permanently interconnected, the lowermost section, termed the extension in Fig. 2, was made readily removable. The purpose of this section was to provide a length of shaft between the rods and the end face of the shaft. By performing experiments with and without the extension section in place, an assessment was made of the sensitivity of the rod mass (heat) transfer characteristics to the hydrodynamic end effects associated with the free end of the rotating shaft. The extension section was made of Delrin, and its length was equal to the diameter of the shaft (5.017 cm).

Whereas the left-hand diagram of Fig. 2 provides an external view of the rotating shaft, an internal view showing constructional details is provided by the right-hand diagram. As seen there, the permanently attached portions of the shaft were mated via tongue-in-groove type fits. This arrangement ensured the alignment of the sections even when subjected to force imbalances caused by unsymmetrical placement of the rotating rods (e.g., when only one rod was employed).

The temperature of the rods was measured by a calibrated, 30-gage, chromel-constantan thermocouple whose junction was embedded in a shallow depression in the aluminum surface at a distance of about 0.635 cm from one of the implanted rods. The placement of the junction is illustrated in the left-hand diagram of Fig. 2. The thermocouple lead wires were laid in a shallow groove which extended from the junction to the steel section of the rotating shaft. The groove was filled with body putty, after which the surface was sanded and then lapped to provide perfect continuity.

As seen in the figure, the thermocouple leads emanating from the upper end of the groove terminated in the socket portion of a sub-miniature, quick-connect connector which was securely taped to the side of the shaft. During rotation, the plug portion of the connector was not attached to the socket, so that the thermocouple circuit, of which the plug was a part, was not closed. The technique for temperature measurement will be elaborated as part of the description of the experimental procedure.

Naphthalene-Coated Rods. As was noted earlier, naphthalene-coated rods of two different diameters (D = 0.635 and 0.953 cm) were employed during the course of the experiments. For each diameter, three different rod lengths, L, were investigated, respectively, L/D_s = 0.5, 1, and 2 (D_s = 5.017 cm). Since experiments were run with arrays containing as many as six rods, thirty-six naphthalene-coated rods were utilized.

The experiments were sequenced so that the longest rods (i.e., L/D_s = 2) of a given diameter were fabricated first and the corresponding experiments executed. Then the rods were reduced in length (i.e., to L/D_s = 1) and the experiments performed. Finally, another reduction to L/D_s = 0.5 was made and the final set of experiments carried out.

Each rod was a composite consisting of a metallic core with an overcoating of naphthalene. The core was a length of drill rod of original diameter equal to that of the finished naphthalene-coated rod. To make place for the coating, the drill rod was undercut by about 0.065 cm on the diameter and was also shortened by about the same amount to accommodate the coating of the tip. On the undercut portion of the drill rod, a screw thread was machined in order to provide cavities to aid in the adhesion of the naphthalene.

The coating of a rod was a two-step process. In the first step, the rod was dipped into a container of molten naphthalene, the dipping being performed in several stages to avoid remelting the naphthalene that had already solidified. During the dipping, the end of the rod that is subsequently to be mated with the shaft is protected by a Teflon cap which keeps it free of naphthalene. Once a sufficiently thick coating has been built up, the coated rod is inserted into a lathe and machined until the proper dimensions are obtained for its length and diameter. Naphthalene machines easily, and the machined surface feels very smooth to the touch.

Instrumentation and Experimental Procedure. The per-rod rate of mass transfer during a data run was determined by differencing the mass of the rod measured both before and after the run. The mass measurements were made with a Sartorius ultra-precision electronic analytical balance capable of being read to 10^{-5} g and having a capacity of 166 g. Another quantity needed in the determination of the mass transfer coefficient is the temperature of the naphthalene, which, in conjunction with a vapor pressure-temperature relation, yields the naphthalene vapor pressure. To measure the temperature of the rotating rods, the milling machine was braked to an abrupt halt, and the plug portion of the connector was mated with the socket portion. With experience, these operations could be performed and the display of a digital voltmeter read, all within about 5 s. Because of the large thermal mass of the aluminum section, the temperature did not change in the 5-s interval. The accuracy of the temperature measurement is believed to be about 0.03°C.

To prepare for a data run, the rods to be employed during the run (all the rods were naphthalene coated) were weighed and then immediately covered with tight-fitting Teflon jackets. Then the rods were mated with the shaft, and a period of thermal equilibration was initiated. During this period, the rods were covered with the Teflon jackets to suppress sublimation, while the shaft was rotated at the rpm designated for the data run. Also, during this period, the temperature was read at regular intervals, and this was continued until the temperature became steady. At that point, the Teflon jackets were removed and the data run proper was initiated.

The duration of the run was selected so that the change in diameter of the rod due to sublimation would not exceed 0.0025 cm. At the termination of the run, the rotation was abruptly halted, the temperature was measured, and the Teflon jackets slipped over the rods. Then the rods were reweighed (with the Teflon jackets removed).

Supplementary experiments showed that the extraneous sublimation which occurred during the period when the rods were covered by the Teflon jackets did not exceed a half-percent of the mass sublimed during the data run proper.

The experiments were performed in a very large laboratory room (volume ~ 300 m^3), so that possible accumulations of naphthalene vapor were negligible. Several hours prior to the initiation of a data run, the windows of the laboratory were covered with sheets of polystyrene. Entrance to the laboratory was prohibited both prior and during the run. These measures provided a very stable ambient that aided in the attainment of data, which were both highly reproducible and virtually free of scatter.

The experimental technique was verified in companion experiments on mass transfer from a rotating disk [6]. Agreement of the data with the exact solution was within 2-3 percent.

Data Reduction

As mentioned earlier, the amount of mass transferred from a rod during a data run was determined by measuring the mass of the rod both before and after the run. In multiple-rod experiments, the mass transfer at the various rods generally agreed to within a half-percent or better. The rod-average

mass flux, $\dot{m}$, was then obtained by dividing the transferred mass by the duration time of the run and the naphthalene surface area (i.e., the cylindrical and tip surfaces of the rod). From this, the per-rod mass transfer coefficient, K, was evaluated from its definition

$$K = \dot{m}/(\rho_{nw} - \rho_{n\infty}) \tag{1}$$

The naphthalene vapor density, ρ_{nw}, at the subliming surface was calculated from the Sogin vapor pressure relation and the perfect gas law, using the measured temperature of the rod as input. For the operating conditions of the experiments, $\rho_{n\infty} = 0$.

To aid in the attainment of a compact dimensionless correlation of the mass transfer coefficient, K, the functional dependence of K on the other parameters of the problem may be written as

$$K = f(D, L, D_s, \omega, N, \rho, \mu, \mathfrak{D}) \tag{2}$$

where ω is the angular velocity ($\sim$ rpm), N is the number of rods, and $\mathfrak{D}$ is the mass diffusion coefficient. By employing dimensional analysis, there follows

$$KD/\mathfrak{D} = f(L/D, D_s/D, D^2\omega/\nu, N, \nu/\mathfrak{D}) \tag{3}$$

Among these, the Sherwood number, Sh, and the Schmidt number, Sc, can be identified as

$$\mathrm{Sh} = KD/\mathfrak{D},\ \mathrm{Sc} = \nu/\mathfrak{D} \tag{4}$$

The group $D^2\omega/\nu$ has the shape of a Reynolds number, with D as characteristic dimension and $D\omega$ having the units of velocity.

In reality, the velocity of a rod varies from $R_s\omega$ at its root ($R_s = \frac{1}{2}D_s$) to $(R_s + L)\omega$ at its tip. Therefore, an appropriate characteristic velocity, V^*, for a rod might be written as

$$V^* = R^*\omega \tag{5}$$

where

$$R^* = R_s + \alpha L,\ 0 \le \alpha \le 1 \tag{6}$$

and, with this, the Reynolds number can be defined as

$$\mathrm{Re} = (R^*\omega)D/\nu \tag{7}$$

or

$$\mathrm{Re} = (D^2\omega/\nu)[\tfrac{1}{2}(D_s/D) + \alpha(L/D)] \tag{8}$$

Thus, the Reynolds number defined by equation (7) contains three of the dimensionless groups that appear in the functional dependence indicated in equation (3).

A careful analysis was made of the Sherwood number data to determine whether the use of the Reynolds number definition (7) might yield a functional dependence involving fewer dimensionless groups than appear on the right-hand side of equation (3). In this regard, consideration was given to the parameter α which fixes the characteristic velocity V^*. Several values of α were selected and the corresponding Sherwood number correlations examined. With $\alpha = 0.3$ as input to the Reynolds number definition of equation (7), it was found that the explicit dependence of Sh on L/D was eliminated altogether, while only a slight explicit dependence on D_s/D remained.

It is noteworthy that with $\alpha = 0.3$, the characteristic velocity corresponds to a radial position nearer to the rotating shaft than to the tip of the rod. This is not unexpected in view of the relatively large surface area of the shaft.

Based on the aforementioned simplification associated with the use of Re and $\alpha = 0.3$, equation (3) can be recast in the form

$$\mathrm{Sh} = f(\mathrm{Re}, D_s/D, N, \mathrm{Sc}) \tag{9}$$

with

$$R^* = R_s + 0.3L \tag{10}$$

used in conjunction with equation (7).

To evaluate the Sherwood number from the experimental data, it is convenient to write

$$\mathrm{Sh} = (KD/\nu)(\nu/\mathfrak{D}) = (KD/\nu)\mathrm{Sc} \tag{11}$$

For the naphthalene-air system, Sc = 2.5. The kinematic viscosity, ν, that is needed as input to equation (11) and for the evaluation of the Reynolds number was taken as that for pure air.

To apply the mass transfer results to heat transfer, the correlation equation (9) for the Sherwood number is rewritten as

$$\mathrm{Nu} = f(\mathrm{Re}, D_s/D, N, \mathrm{Pr}) \tag{12}$$

where f is the very same function as that of equation (9). The present experimental results correspond to a specific Schmidt number and do not provide the variation of Sh with Sc (or the variation of Nu with Pr). Therefore, in keeping with accepted practice, a power-law dependence will be adopted, as will be described later.

Results and Discussion

Sherwood Number Results. Per-rod Sherwood numbers encompassing all of the investigated rod lengths and diameters are plotted in Fig. 3 as a function of the Reynolds number defined by equations (7) and (10). The data presented in this figure correspond to experiments in which there was only one rod in place (i.e., $N = 1$) and in which the extension of the rotating shaft was not used. However, as will be documented later, the per-rod Sherwood number is virtually independent of the number of rods within the range investigated ($N = 1$ through $N = 6$). Similarly, the Sherwood number is hardly affected by whether or not the extension is in place. Therefore, Fig. 3 may be regarded as representing all of the investigated operating conditions.

The data appearing in Fig. 3 are identified according to rod diameter (i.e., according to D/D_s) by either filled or open data symbols, respectively, for $D/D_s = 0.126$ and 0.190. For each rod diameter, the various rod lengths, characterized by L/D, are distinguished by circles, squares, and triangles.

For each fixed D/D_s, it is seen that the Sherwood-Reynolds relation is independent of L/D, that is, the data for the various L/D fall along a common line for a given D/D_s. Thus the data of Fig. 3 affirm the earlier assertion that the Reynolds number definition of equation (7) with the R^* of equation (10) eliminates the explicit dependence of Sh on L/D. This independence from L/D is a significant generalization of the present results and enables them to be applied for any L/D in the investigated range (2.5 to 16) and, if necessary, somewhat beyond. In this regard, it may be noted that the investigated range of L/D encompasses practical values for both pin fins and spokes.

The lines passing through the data in Fig. 3 are least-squares fits of the form

$$\mathrm{Sh} = C\mathrm{Re}^n \tag{13}$$

where the numerical values of C and n are listed in Table 1. The excellence of the fits is affirmed by the fact that the data deviations from the respective fitted lines are on the order of 1 percent or less. For each D/D_s, the data appear to fall along

Table 1 Values of C and n for equation (13)

D/D_s	Re	C	n
0.126	<1500	0.832	0.532
0.126	>1500	0.327	0.658
0.190	<1500	0.696	0.566
0.190	>1500	0.346	0.658

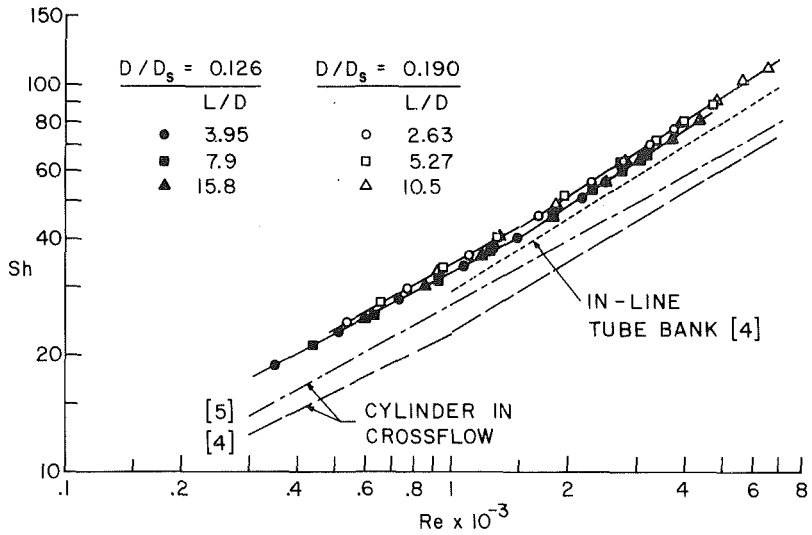

Fig. 3 Per-rod Sherwood numbers (single rod, no shaft extension)

lines which display a change of slope at Re = 1500. In actuality, the change of slope is probably continuous (rather than discrete), but for an algebraic representation, a two-part, linear fit is simpler than a continuous, higher-order fit.

The Sherwood numbers display a modest dependence on D/D_s. For Re < 1500, the overall spread of the data with D/D_s is 6 percent, while at lower Reynolds numbers the dependence on D/D_s tends to disappear as the two sets of data merge. A representation of the results that is valid for both of the investigated D/D_s may be written as

$$\mathrm{Sh} = 0.751\mathrm{Re}^{0.550},\ \mathrm{Re} < 1500 \tag{14}$$

$$\mathrm{Sh} = 0.337\mathrm{Re}^{0.658},\ \mathrm{Re} > 1500 \tag{15}$$

The maximum deviation of the data from these equations is only 3 percent. The equations are applicable for a Schmidt number (or Prandtl number) of 2.5. They will shortly be generalized so as to predict the heat transfer for arbitrary Prandtl numbers.

As discussed in the Introduction, the absence of prior work on the problem considered here precludes direct comparisons with the literature. In the absence of the present data, it is likely that available information for the cylinder in crossflow or for the in-line tube bank would have been employed to calculate heat transfer at rotating rods. It is, therefore, of interest to compare the present results with those cases, and this has been done in Fig. 3.

Among the correlations for heat transfer from cylinders in crossflow, both those of Zukauskas [4] and of Whitaker [5] are based on data for both air (Pr = 0.7) and for various liquids that cover a range of higher Prandtl numbers. For comparison with the present data (Sc = Pr = 2.5), these correlations are believed to be preferable to others that are based on air data alone. For this same reason, the Zukauskas correlation for the in-line tube bank [4] was selected from among those available. In applying the correlations, Nu was replaced by Sh, Pr was replaced by Sc, and Sc was set equal to 2.5. The resulting Sherwood numbers are presented in Fig. 3.

From the figure, it is seen that the tube bank results deviate only moderately (~10–15 percent) from the present data, while the cylinder in crossflow results show greater deviations. This ordering might, at first, appear inverted, since the data presented in the figure are for a single rod, not for an array of rods. However, owing to the fact that a rotating rod continuously encounters its own wake, it may be better modeled by an in-line array of stationary cylinders than by the single cylinder in crossflow. Despite this rationalization, whatever the level of agreement, it may be somewhat fortuitous because of basic differences in the patterns of fluid flow.

With regard to the Schmidt (Prandtl) number dependence of the results, guidance may be taken from the aforementioned tube bank and crossflow results, which respectively vary as $\mathrm{Pr}^{0.36}$, $\mathrm{Pr}^{0.37}$, and $\mathrm{Pr}^{0.4}$ [4, 5]. If the 0.37-power dependence is taken as a compromise, then equations (14) and (15) become

$$\mathrm{Sh} = 0.535\mathrm{Re}^{0.550}\mathrm{Sc}^{0.37},\ \mathrm{Re} < 1500 \tag{16}$$

$$\mathrm{Sh} = 0.240\mathrm{Re}^{0.658}\mathrm{Sc}^{0.37},\ \mathrm{Re} > 1500 \tag{17}$$

Equations (16) and (17) may be regarded as the most general form of the results of this investigation.

Effect of Number of Rods and Shaft Extension. The Sherwood number results that were presented in Fig. 3 were obtained in experiments in which there was only one rod and where the extension of the rotating shaft was not employed. An extensive set of experiments was performed for multirod arrays (up to six), encompassing the same range of D/D_s, L/D, and Re that was investigated for the single-rod case. These experiments were carried out without the extension in place. Still another set of experiments was performed to study the effect of extending the rotating shaft so as to increase the distance between the rod(s) and the end of the shaft. For these experiments, the full range of D/D_s, L/D, and Re was investigated for the one-rod case. The results of these two sets of experiments indicated that there was no need for further experiments involving both multiple rods and an extension of the shaft.

Only a portion of the available results will be presented here because of space limitations. In particular, the multiple-rod issue will be dealt with via comparisons between the results for the one-rod and six-rod cases. Also, owing to the similarity in the trends for the two investigated values of D/D_s (0.126 and 0.190), a somewhat abbreviated presentation is made for the latter.

The results for D/D_s = 0.126 are presented in Figs. 4–6, respectively, for L/D = 3.95, 7.9, and 15.8. Figures 7 and 8 convey results for D/D_s = 0.190 with L/D = 2.63 and 10.5 (the intermediate L/D is omitted). Each figure has a common structure. In the upper portion of the figure, the Sherwood numbers corresponding to the unextended and extended rotating shafts are compared for the one-rod case. The lower

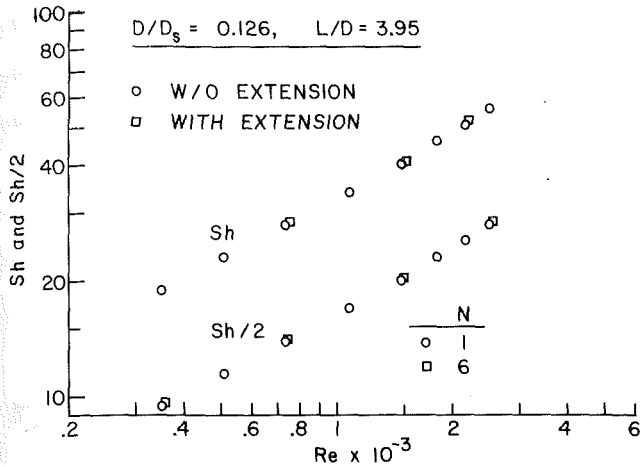

Fig. 4 Effect of number of rods and shaft extension on Sh, $D/D_s = 0.126, L/D = 3.95$

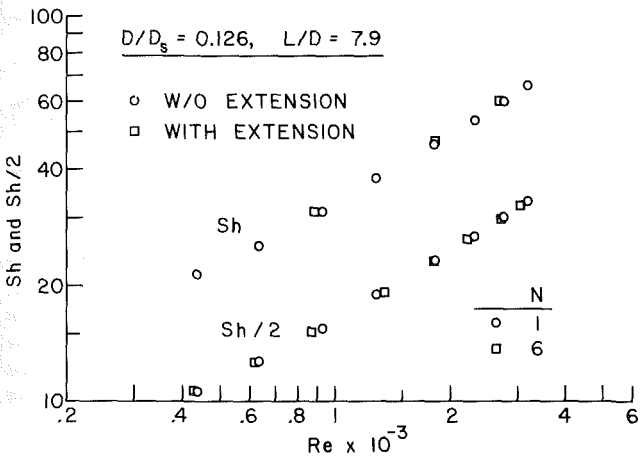

Fig. 5 Effect of number of rods and shaft extension on Sh, $D/D_s = 0.126, L/D = 7.9$

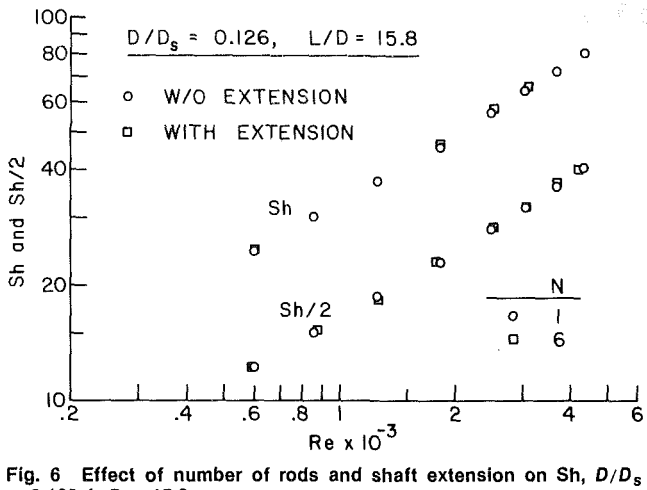

Fig. 6 Effect of number of rods and shaft extension on Sh, $D/D_s = 0.126, L/D = 15.8$

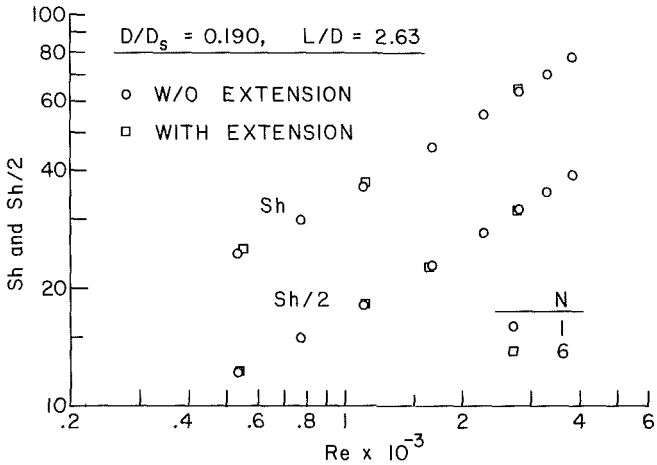

Fig. 7 Effect of number of rods and shaft extension on Sh, $D/D_s = 0.190, L/D = 2.63$

portion conveys a comparison between the Sherwood numbers for the one-rod and six-rod arrays for the case of the unextended shaft. In order to separate the two comparisons, the upper data are plotted as the Sherwood number itself, while the lower data are plotted as half the Sherwood number.

Attention is first focused on the one-rod, six-rod comparison. Careful inspection of Figs. 4–8 reveals that the data for the one-rod and six-rod arrays are virtually coincident for all of the investigated operating conditions. The deviations, if any, are in the 1–2 percent range, which is the expected accuracy of the experiments. This finding eliminates the functional dependence of the Sherwood number on the number of rods N, at least for values of $N \leq 6$, thereby affirming the generality of the Sherwood number correlations (16) and (17). Furthermore, since the $N = 6$ data show no tendency whatsoever to depart from the $N = 1$ data, it is not unreasonable to expect that the present correlations should continue to apply for substantially larger N, say, up to $N = 12$.

The just-discussed insensitivity of the per-rod Sherwood number to the number of rods suggests that it is immaterial whether a given rod encounters its own wake or that of another rod. While this finding was not expected, its demonstrated validity provides a great simplification in the correlation of the results.

Attention is next turned to the effect of extending the rotating shaft in order to increase the distance between the

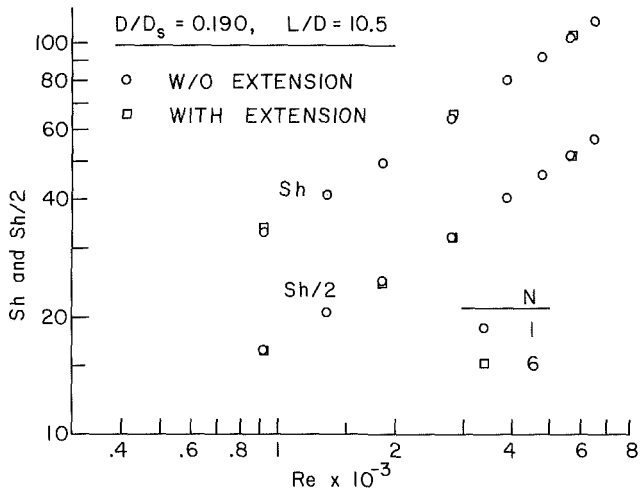

Fig. 8 Effect of number of rods and shaft extension on Sh, $D/D_s = 0.190, L/D = 10.5$

rods and the end of the shaft. From an examination of Figs. 4–8, it is seen that the extension distance yields a second-order increase in the Sherwood numbers relative to those for the unextended shaft. The increases, when they occur, are in the

2–3 percent range. These deviations are deemed too small to disturb the generality of the correlating equations (16) and (17).

Concluding Remarks

In this paper, seemingly for the first time, the heat transfer characteristics of rods which extend radially outward from the surface of a rotating shaft have been investigated. The experimental work was facilitated by the use of the naphthalene sublimation technique. During the course of the research, the diameter and length of the rods were varied, as was the number of rods. Another investigated geometric parameter was the distance between the rods and the free end of the rotating shaft. The angular velocity of the shaft was represented in dimensionless terms by the Reynolds number.

In view of the large number of governing parameters, it is noteworthy that a relatively simple correlation of the Sherwood number results was obtained. A key feature of the correlation is the choice of an appropriate characteristic velocity, V^*, on which to base the Reynolds number. With the proper choice of V^*, the dependence of the Sherwood number on L/D is altogether eliminated, and there is only a weak dependence on D/D_s. Furthermore, the data were found to be independent of the number of rods and to be very weakly dependent on the distance from the rods to the free end of the shaft. As a result of these simplifications, the final per-rod correlations, when phrased in heat transfer terms, are

$$\mathrm{Nu} = 0.535\mathrm{Re}^{0.550}\mathrm{Pr}^{0.37},\ \mathrm{Re} < 1500 \tag{18}$$

$$\mathrm{Nu} = 0.240\mathrm{Re}^{0.658}\mathrm{Pr}^{0.37},\ \mathrm{Re} > 1500 \tag{19}$$

The Reynolds number appearing in these equations is defined by equations (7) and (10).

Acknowledgment

This research was performed under the auspices of the National Science Foundation.

References

1 Etemad, G. A., "Free Convection Heat Transfer From a Rotating Horizontal Cylinder to Ambient Air with Interferometric Study of Flow," ASME *Transactions*, Vol. 77, 1955, pp. 1283–1289.

2 Dropkin, D., and Carmi, A., "Natural Convection Heat Transfer From a Horizontal Cylinder Rotating in Air," ASME *Transactions*, Vol. 79, 1957, pp. 741–749.

3 Kays, W. M., and Bjorklund, I. S., "Heat Transfer From a Rotating Cylinder With and Without Crossflow," ASME *Transactions*, Vol. 80, 1958, pp. 70–77.

4 Zukauskas, A. A., "Heat Transfer From Tubes in Crossflow," *Advances in Heat Transfer*, Vol. 8, 1972, Academic Press, New York, pp. 93–160.

5 Whitaker, S., *Elementary Heat Transfer Analysis*, Pergamon Press, Oxford, England, 1976.

6 Palsdottir, S., "Heat Transfer at and Adjacent to the Tip of a Rotating Cylinder," M. S. thesis, Department of Mechanical Engineering, University of Minnesota, Minneapolis, Minn., 1981.

Effects of Free Convection and Axial Conduction on Forced-Convection Heat Transfer Inside a Vertical Channel at Low Peclet Numbers

L. C. Chow

S. R. Husain[1]

A. Campo[2]

Department of Mechanical Engineering,
Washington State University,
Pullman, Wash. 99164

A numerical investigation was conducted to study the simultaneous effects of free convection and axial conduction on forced-convection heat transfer inside a vertical channel at low Peclet numbers. Insulated entry and exit lengths were provided in order to assess the effect of upstream and downstream energy penetration due to axial conduction. The fluid enters the channel with a parabolic velocity and uniform temperature profiles. A constant-property (except for the buoyancy term), steady-state case was assumed for the analysis. Results were categorized into two main groups, the first being the case where the channel walls were hotter than the entering fluid (heating), and the second being the reverse of the first (cooling). For each group, heat transfer between the fluid and the walls were given as functions of the Grashof, Peclet, and Reynolds numbers.

Introduction

The subject of laminar flow forced convection in ducts has been studied extensively and a comprehensive review was provided by Shah and London [1]. It is also recognized that free convection can interact with forced convection and may alter the heat transfer rate significantly. For forced flow in a vertical duct with heated or cooled walls, if the Reynolds number is low, free convection effects can be significant at even moderate Grashof numbers.

Combined forced and free convection, or mixed convection, inside a vertical tube has been considered by numerous researchers [2-15]. However, relatively few papers have been published for mixed convection between two vertical plates. Tao [16] considered fully developed laminar mixed convection in a vertical channel of constant axial wall temperature gradient, with or without heat generations. Bodoia and Osterle [17] investigated the flow development of mixed convection betwen heated vertical plates. The flow and heat transfer characteristics of the channel were studied and a development height was established. Savkar [18] considered the problem of developing laminar mixed convection between two vertical semi-infinite plates when energy was added at a uniform rate from the two plates. Quintiere and Mueller [19] presented approximate analytical solutions for free and forced convection between finite vertical parallel plates, covering a wide range of Rayleigh and Prandtl numbers.

For the case of forced convection, numerous investigations [20-22] have shown that the axial conduction term in the energy equation becomes significant at low Peclet number ($Pc < 50$). The inclusion of this term will realize the propagation of energy axially and thus affect the temperature profile of the fluid prior to its entry into the heat transfer section of the vertical duct. The importance of axial conduction should also be considered in the case of free and mixed convection for low Prandtl number fluids. However, the results of combined forced and free convection at low Peclet numbers are not available in the literature. Zeldin and Schmidt [12] included the axial conduction term in their analysis of developing flow with combined forced and free convection in an isothermal vertical tube. However, their calculations were restricted to a Peclet number of about 250, and axial conduction is expected to be negligible at such a high Peclet number. The only analytical prediction of free and forced convection heat transfer to a low Prandtl number fluid in vertical channel was presented by Quintiere and Mueller [19]. It is suspected that their analysis is incorrect at low Pr because they omitted the axial conduction term in their energy equation.

From the foregoing discussion, one can conclude that there is a need for further work on mixed convection at low Peclet numbers for both flows inside a vertical tube and in between two vertical plates. The authors have no knowledge of work done on predicting the simultaneous effects of free convection and axial conduction on forced convection heat transfer. This is the main motivation of the present study.

In this investigation, the hydrodynamics and heat transfer of low Peclet number flows in a symmetrically heated or cooled channel are studied. The schematic of the present problem is shown in Fig. 1. Insulated entry and exit lengths have been provided. The insulated entry length allows the axial penetration of energy due to axial conduction. The insulated exit length will allow the fluid velocity and temperature profiles to develop somewhat after the fluid has left the heat transfer region of the channel. The entry velocity profile in the insulated region is assumed to be fully developed (parabolic). This choice is made to focus on the distortion of the velocity profile due to free convection and axial conduction. The distortion of the velocity profile will, in turn, affect the heat transfer between the walls and the fluid. The flow is assumed to be two-dimensional and with constant properties (excepting the buoyancy term). The assumption of two-dimensional flow may be justified if the channel walls are sufficiently deep in the third dimension. The assumption of constant-property flow is acceptable provided that the

[1]Present address: Department of Mechanical Engineering, Texas A & M University, College Station, Texas 77843

[2]Present address: Departamento de Termodinamica, Universidad Simon Bolivar, Caracas, Venezuela

Contributed by the Heat Transfer Division and presented at the ASME Winter Annual Meeting, Washington, D.C., November 15-20, 1981. Manuscript received by the Heat Transfer Division April 20, 1983. Paper No. 81-WA/WT-66.

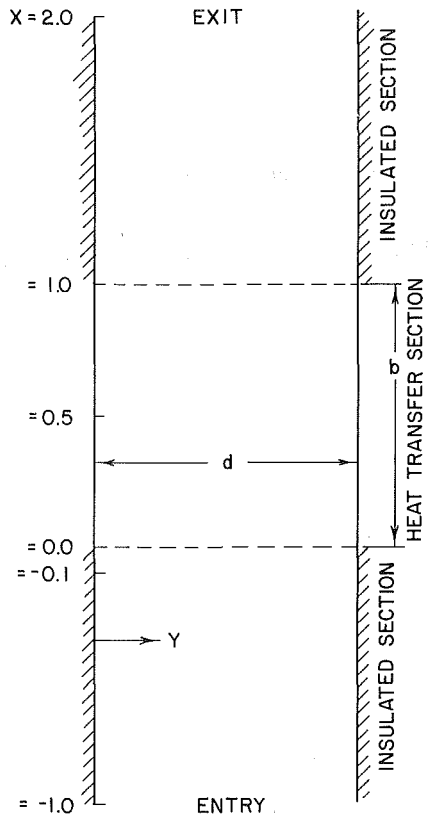

Fig. 1 Schematic of channel and reference locations

temperature difference between the walls and the fluid is not too large.

Problem Formulation

The situation considered is illustrated in Fig. 1. The channel has a width of d and a length of $b+2d$. It is open at both $x=-d$ and $x=b+d$. The first and last section of the channel ($-d \le x < 0$, and $b < x \le b+d$) is thermally insulated. The walls at midchannel ($0 \le x \le b$) are kept at a uniform temperature, t_w, either higher or lower than the fluid temperature. The fluid enters the channel at $x=-d$ with a uniform temperature, t_∞, and with a parabolic velocity profile. This choice for the velocity profile was made in order to eliminate the effects of hydrodynamic development. Consequently, any distortion of this profile downstream is a result of the combined effects of free convection and axial conduction.

Insulated entry and exit lengths have been provided to allow the propagation of energy both upstream and downstream from the heated or cooled section. Of particular interest is the insulated entry length that will accommodate the heating or cooling of the fluid prior to its entry to the heated or cooled section of the channel. For the Peclet numbers used in this work, it was tested that the upstream energy penetration length is less than the channel width. Hence an insulated entry length of d was used. Furthermore, this insulated entry length justifies the assumption of uniform entry temperature, t_∞, at $x=-d$.

By introducing a nondimensional stream function, vorticity, and temperature as dependent variables, and using the following definitions

$$X=\frac{x}{d} \qquad U=\frac{ud}{\nu} \qquad \psi=\frac{\Psi}{\nu}$$

$$Y=\frac{y}{d} \qquad V=\frac{vd}{\nu} \qquad \Omega=\frac{\omega d^2}{\nu}$$

and

$$T=(t-t_\infty)/(t_w-t_\infty)\text{(Heating)}$$
$$=(t-t_w)/(t_\infty-t_w)\text{(Cooling)} \tag{1}$$

the governing equations in nondimensional forms for the present problem are

$$U\frac{\partial\Omega}{\partial X}+V\frac{\partial\Omega}{\partial Y}=\frac{\partial^2\Omega}{\partial X^2}+\frac{\partial^2\Omega}{\partial Y^2}-\text{Gr}\frac{\partial T}{\partial Y} \tag{2}$$

$$\frac{\partial^2\psi}{\partial X^2}+\frac{\partial^2\psi}{\partial Y^2}=-\Omega=\frac{\partial U}{\partial Y}-\frac{\partial V}{\partial X} \tag{3}$$

$$U\frac{\partial T}{\partial X}+V\frac{\partial T}{\partial Y}=\frac{1}{\text{Pr}}\left[\frac{\partial^2 T}{\partial X^2}+\frac{\partial^2 T}{\partial Y^2}\right] \tag{4}$$

$$U=\frac{\partial\psi}{\partial Y} \text{ and } V=-\frac{\partial\psi}{\partial X} \tag{5}$$

Nomenclature

A = aspect ratio of heat transfer section of channel $= b/d$
b = length of heat transfer section of channel (m)
C_p = specific heat of fluid (kJ/kg°C)
d = channel width (m)
g = local acceleration due to gravity (m/s^2)
Gr = Grashof number $= |g\beta(t_w-t_\infty)d^3/\nu^2|$
k = thermal conductivity of fluid (kJ/s m°C)
Nu_x = local Nusselt number
$\overline{Nu}$ = overall Nusselt number
Pc = Peclet number = RePr
Pr = Prandtl number $= \nu/\alpha$
q = heat transfer rate to fluid per unit depth of channel from both walls (kJ/s m)
Q = dimensionless heat transfer rate $= q/k(t_w-t_\infty)$
Re = Reynolds number $= u_b d/\nu$
t = temperature (°C)
T = dimensionless temperature
u,v = vertical and horizontal velocities (m/s)
U,V = dimensionless vertical and horizontal velocities
x,y = Cartesian coordinates – vertical, horizontal (m)
X,Y = dimensionless Cartesian coordinates – vertical, horizontal
α = thermal diffusivity of fluid (m^2/s) $= k/\rho C_p$
β = coefficient of thermal expansion of fluid (°C^{-1})
μ = visocity of fluid (kg/s m)
ν = kinematic viscosity of fluid (m^2/s) $= \mu/\rho$
ρ = fluid density (kg/m^3)
Ψ = stream function (m^2/s)
ψ = dimensionless stream function
ω = vorticity (s^{-1})
Ω = dimensionless vorticity
τ = any field variable (ψ, Ω, or T)

Subscripts

b = bulk
e = exit plane
Max = maximum
w = at the wall
∞ = at the entrance of channel

Superscript

m = iteration counter

where $Gr = |g\beta(t_w - t_\infty)d^3/\nu^2|$ is the Grashof number and $Pr = \nu/\alpha$ is the Prantl number.

It should be noted that, with the definition of the nondimensional velocity U given in equation (1), the bulk Reynolds number, Re, at entrance is simply equal to the nondimensional bulk velocity U_b, where

$$U_b = \int_0^1 U\, dY \tag{6}$$

It should also be noted that the axial momentum and axial energy conduction terms are included in equations (2) and (4), respectively.

For the present study, the aspect ratio of the heat transfer section A was kept at unity. This choice is just for convenience only. Other values of the aspect ratio can be handled by the present analysis in the same manner. Since the problem is a spatially elliptic one, the values of ψ, Ω, and T must be specified at all the boundaries. The boundary conditions are

At entry: $(X = -1)$ $\psi = \mathrm{Re}\, Y^2(3-2Y)$

$$\Omega = \mathrm{Re}(12Y-6)$$

$$T = 0 \text{ (Heating)}$$

or

$$T = 1 \text{ (Cooling)} \tag{7a}$$

At left wall: $(Y=0)$ $\psi = 0$

$$\Omega = -\frac{\partial^2 \psi}{\partial Y^2} \tag{7b}$$

At right wall: $(Y=1)$ $\psi = \mathrm{Re}$

$$\Omega = -\frac{\partial^2 \psi}{\partial Y^2} \tag{7c}$$

At the heated or cooled section: $(0 \le X \le 1; \quad Y = 0 \text{ or } 1)$

$$T = 1 \text{ (Heating)}$$

or

$$T = 0 \text{ (Cooling)} \tag{7d}$$

At the unheated section: $(-1 < X < 0 \text{ or } 1 < X < 2;$ $Y = 0 \text{ or } 1)$

$$\frac{\partial T}{\partial Y} = 0 \tag{7e}$$

At exit: $(X = 2)$

$$\frac{\partial \psi}{\partial X} = \frac{\partial \Omega}{\partial X} = \frac{\partial T}{\partial X} = 0 \tag{7f}$$

The boundary condition at exit as shown may be justified if a sufficiently long insulated exit length is used. Numerical experiments were carried out to ascertain this length. It was found that with an insulated exit length equal to the channel width or longer, the dependent field variables in the channel are quite insensitive to the boundary condition at exit. In this investigation, the nondimensional insulated exit length was unity.

Method of Solution

Equations (2–5) were solved numerically subject to the boundary conditions given by equation (7). The governing equations were cast into finite difference form using a central difference scheme for the interior points in the domain. Discretized boundary conditions for the wall vortices and temeperature gradients at the walls were obtained by a one-sided expansion of second-order accuracy. The resulting set of equations were solved by successive relaxations of the ψ, Ω, and T fields until two successive iteration values of each field satisfied the following criterion

$$\frac{|\tau^{m+1} - \tau^m|_{\mathrm{Max}}}{\tau^m_{\mathrm{Max}}} < 10^{-4} \tag{8}$$

where $\tau = \psi$, Ω, or T.

The results reported in this paper were obtained with 31 and 21 grid spaces in the X- and Y-directions, respectively. Even this grid does not satisfy the cell Reynolds number criterion [23] everywhere in the flow field, but convergence and stability of the iterative process are still obtained. By employing a finer grid (61 by 41) for some of the computer runs, it was judged that the results given in the next section are correct to within 3 percent.

Upon obtaining the converged fields, the following dimensionless parameters were calculated

(*i*) The bulk temperature ($T_b(X)$)

$$T_b = \frac{\int_0^1 UT\,dY}{\int_0^1 U\,dY} \tag{9}$$

(*ii*) The local Nusselt number ($\mathrm{Nu}_X(X)$)

$$\mathrm{Nu}_X = \frac{\pm (\partial T/\partial Y)_w}{T_w - T_b} \tag{10}$$

where the minus and plus signs apply to the left and the right walls, respectively.

(*iii*) The total energy per unit depth received by the fluid from the heat transfer region of the walls

$$Q = \frac{q}{k(t_w - t_\infty)} = \int_0^1 \left[\left(\frac{\partial T}{\partial Y}\right)_{Y=1} - \left(\frac{\partial T}{\partial Y}\right)_{Y=0}\right] dX \tag{11}$$

By a simple energy balance, it can be shown that

$$Q = \mathrm{Pc}\, T_{be} \text{(Heating)}$$

$$= \mathrm{Pc}(1 - T_{be}) \text{(Cooling)} \tag{13}$$

where T_{be} is the exit bulk temperature and Pc is the Peclet number.

(*iv*) The overall Nusselt number in the heat transfer region

$$\overline{\mathrm{Nu}} = \int_0^1 \mathrm{Nu}_X dX \text{(either wall)} \tag{14}$$

Results and Discussion

Numerical results are obtained for two Reynolds numbers, namely, 50 and 100. The Grashof number ranges from 500 to 5×10^4. These dimensionless numbers are suitable for applications to compact heat exchangers, cooling of microelectronic devices, etc.

Heating. Plots of Q and $\overline{\mathrm{Nu}}$ as a function of the Grashof number with Peclet and Reynolds numbers as parameters are given in Fig. 2. It is clearly seen that both Q and $\overline{\mathrm{Nu}}$ increase with Gr for fixed values of Pc and Re. This indicates the enhancement of heat transfer due to free convection.

At low Grashof numbers (forced convection dominant), for the same Peclet number, the curves for the two different Reynolds numbers merge, indicating that the Peclet number is the only parameter needed to describe Q and $\overline{\mathrm{Nu}}$. On the other hand, at high Grashof numbers (free convection effects significant), both the Peclet and the Reynolds numbers are required as parameters to correlate Q and $\overline{\mathrm{Nu}}$ with Gr as

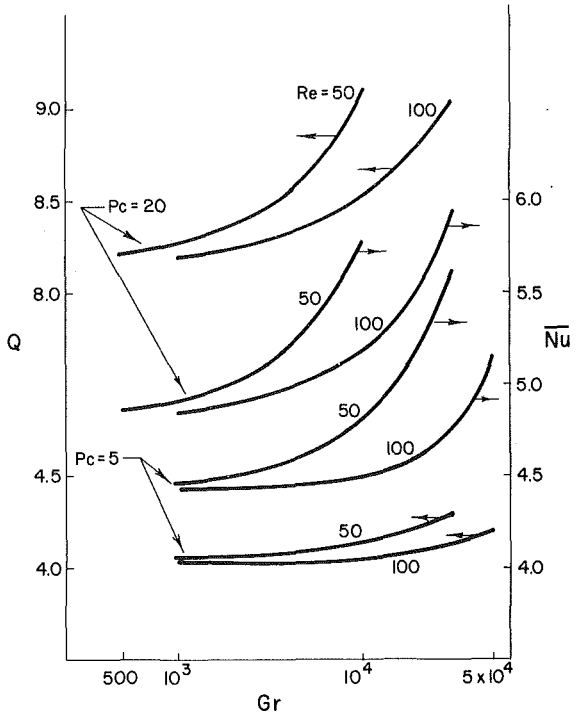

Fig. 2 Dimensionless heat transfer rate and overall Nusselt number as a function of Gr with Pc and Re as parameters (heating)

demonstrated by the split between the curves for different Re. This split may be regarded as the point where free-convection effects begin to assume a significant role for the lower Re case. In addition, for a fixed Peclet number, it is observed that in terms of Q and $\overline{Nu}$, the departure from pure forced convection occurs at higher Grashof numbers for higher Reynolds numbers.

It may also be noted from observing the curves of Q at different Peclet numbers that the increase of Q as Gr increases is more significant for Pc = 20 than for Pc = 5. This indicates that for lower Peclet numbers, the enhancement of heat transfer due to free convection is to a lesser extent compared to that for higher Peclet numbers. This is not surprising because a lower Peclet number implies a larger thermal diffusivity, which in turn causes the smoothing of the temperature profile. The temperature gradient, $\partial T/\partial Y$, constitutes the source of free-convection effects in the vorticity equation.

Figure 3 consists of dimensionless velocity profiles for Gr = 50000 at various X in the channel for Peclet number of 5. It is evident that flow is being distorted due to the effects of free convection. The distortion occurs even at $X = -0.1$, where the walls are insulated. This can be explained by the fact that energy has propagated upstream via the axial conduction term and set up temperature gradients in the insulated entry section, thereby perturbing the hydrodynamics of the flow. The distortion of the velocity profiles enhances the convective heat transfer from the channel walls which explains the upward trend of the curves in Fig. 2.

Dimensionless temperature profiles at various X-locations in the channel for Pc = 5 are shown in Fig. 4 for high and low Grashof numbers. Referring to Fig. 4, it is interesting to note that at $X = -0.1$, the temperatures near the walls are higher for Gr = 1000 than those for Gr = 50000. This can be explained by observing the velocity profiles in Fig. 3. At $X = -0.1$, the velocity profile near the walls has been substantially distorted from the initial parabolic shape in the case of Gr = 50,000 as compared to that for Gr = 1000, which is still essentially parabolic. On the basic of these observations, it may be inferred that due to increased free-convection effects

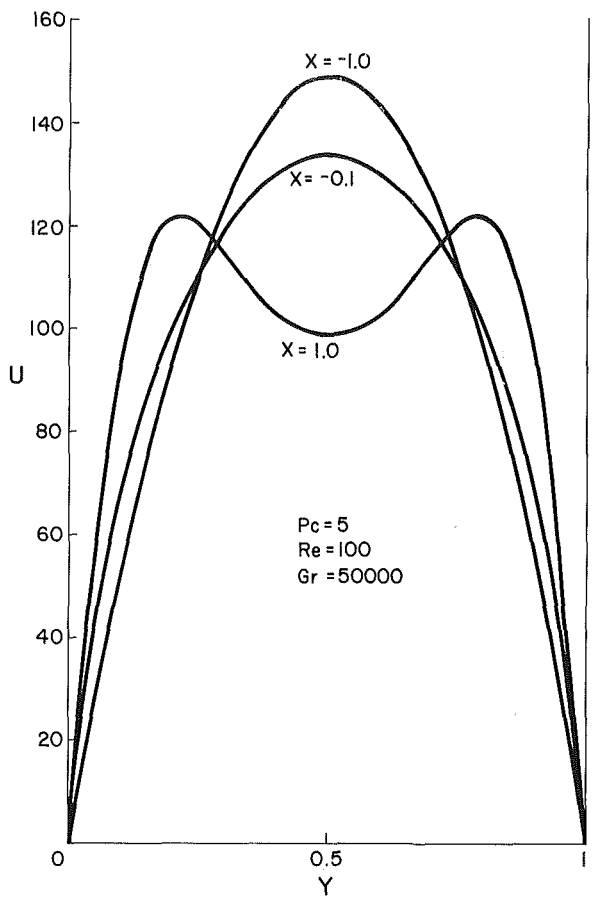

Fig. 3 Dimensionless velocity profiles at various X-locations in channel, Pc = 5, Gr = 50000, Re = 100 (heating)

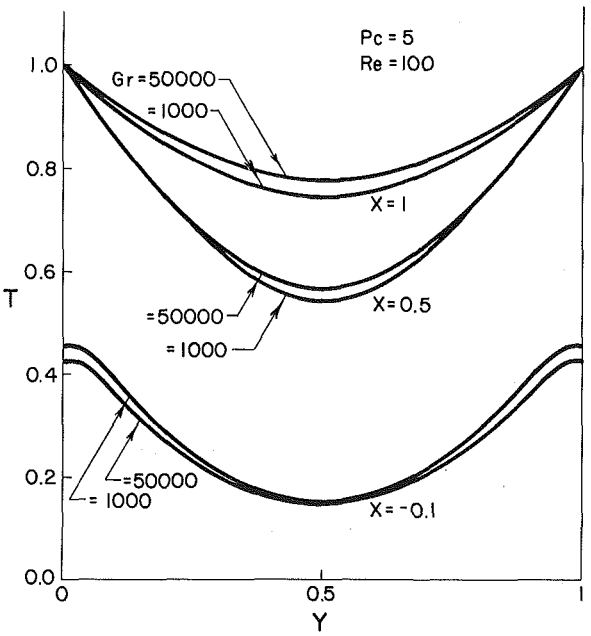

Fig. 4 Dimensionless temperature profiles at various X-locations in channel at high and low Gr, Pc = 5, Re = 100 (heating)

(Gr = 50,000), colder fluid is being drawn up near the walls at a faster rate and thus cools the region to a greater extent. In other words, the local Peclet number near the walls has been increased. This implies that free convection effects counter upstream axial conduction somewhat near the entrance to the heated section.

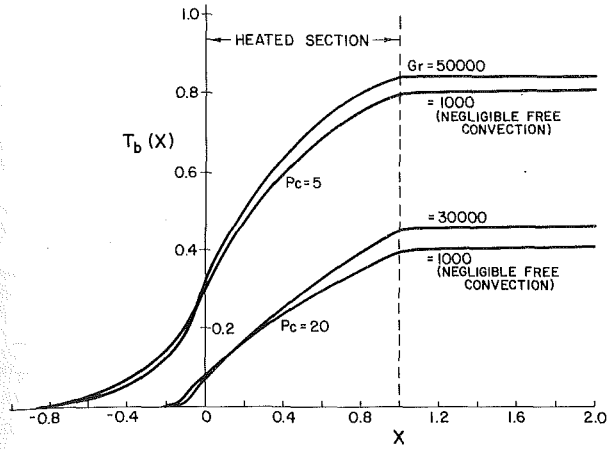

Fig. 5 Dimensionless bulk temperatures versus X at high and low Gr, Pc = 5 and 20, Re = 100 (heating)

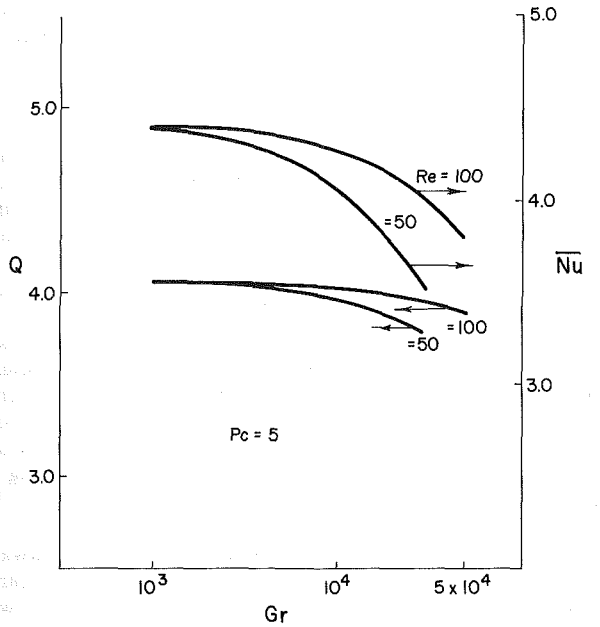

Fig. 6 Dimensionless heat transfer rate and overall Nusselt number as a function of Gr with Re as a parameter (cooling)

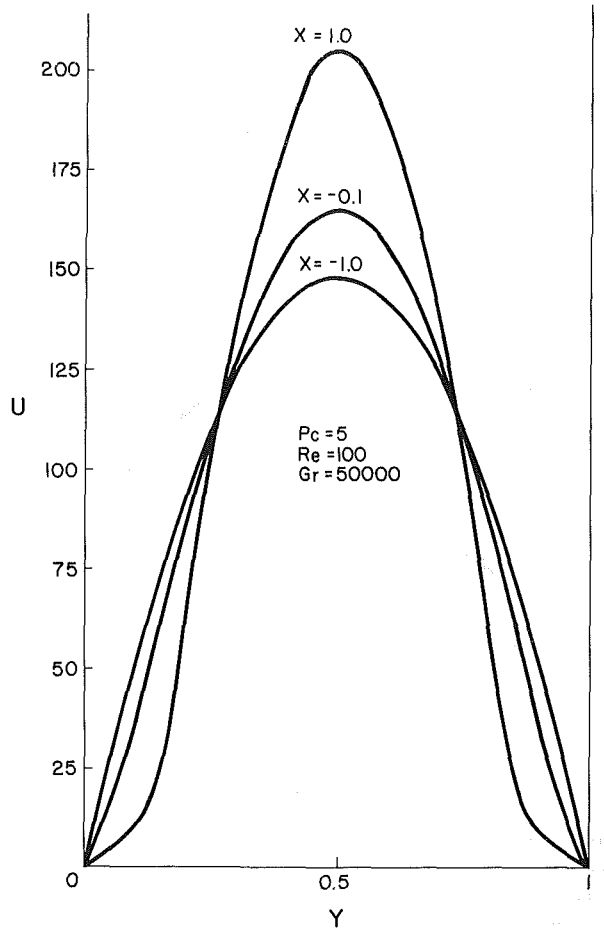

Fig. 7 Dimensionless velocity profiles at various X = locations in channel, Pc = 5, Gr = 50000, Re = 100 (cooling)

Figure 5 shows bulk temperatures as a function of X for different Peclet numbers for high and low Grashof numbers. The Reynolds number is fixed at 100. The bulk temperature for Pc = 5 rises to values approximately twice that for Pc = 20 at the end of the channel. An increase in the Grashof number for a particular Peclet number leads to an increase in the local bulk temperatures for $X > 0$, which demonstrates the increase in heat transfer to the fluid due to free convection effects. The reversal of the situation for $X < 0$ may be explained by the same line of reasoning used earlier, namely, free convection effects counter upstream axial conduction somewhat near the entrance to the heated section.

Upon comparing the bulk temperatures for $X < 0$ for the two Peclet numbers, it can be seen that the upstream energy penetration is significantly greater for the lower Peclet number fluid. It is observed that at $X = 0.0$, the lower Peclet number fluid has attained about 40 percent of its final or exit bulk temperature whereas the higher Pc fluid has reached only 17 percent of its exit bulk temperature. Upstream energy penetration via axial conduction therefore assumes increasing significance with decreasing Peclet numbers. However, the effect of upstream energy penetration decreases somewhat with increasing Grashof numbers. Had the axial conduction term been ignored, the heating of the fluid prior to its entry to the heated section of the channel would not occur.

Cooling. Figure 6 illustrates the variations of Q and $\overline{Nu}$ as a function of the Grashof number with the Peclet and the Reynolds numbers as parameters. It can be observed that both Q and $\overline{Nu}$ decrease as Gr increases, which is a trend opposite to that of the case of heating. This indicates that free convection reduces the heat transfer between the fluid and the walls of the channel.

At low Grashof numbers (forced convection dominant), for the same Peclet number, as in the case of heating, the curves of the two Reynolds numbers merge, indicating that the Peclet number is the only parameter required to describe Q and $\overline{Nu}$. However, when free convection effects begin to assume significance (high Grashof numbers), both the Peclet and the Reynolds numbers are needed to correlate Q and $\overline{Nu}$ as demonstrated by the split between the curves for different Re. As in the case of heating, this split may be regarded as the point where free convection effects begin to assume a significant role for the lower Re case. In addition, for a fixed Peclet number, it is observed that in terms of Q and $\overline{Nu}$, the departure from pure forced convection occurs at higher Grashof numbers for higher Reynolds numbers.

Figure 7 consists of dimensionless velocity profiles for Gr = 50,000 at various X in the channel. The distortion of the flow due to free convection effects varies markedly from that of the case of heating. Here the fluid near the walls is being

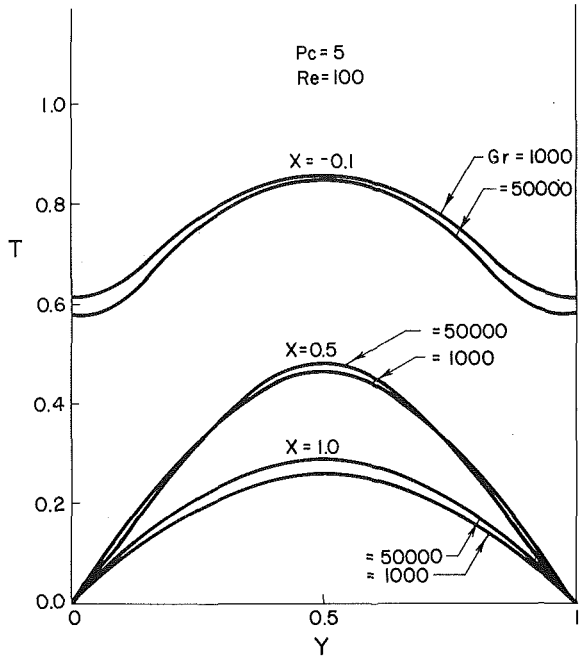

Fig. 8 Dimensionless temperature profiles at various X-locations in channel at high and low Gr, Pc = 5, Re = 100 (cooling)

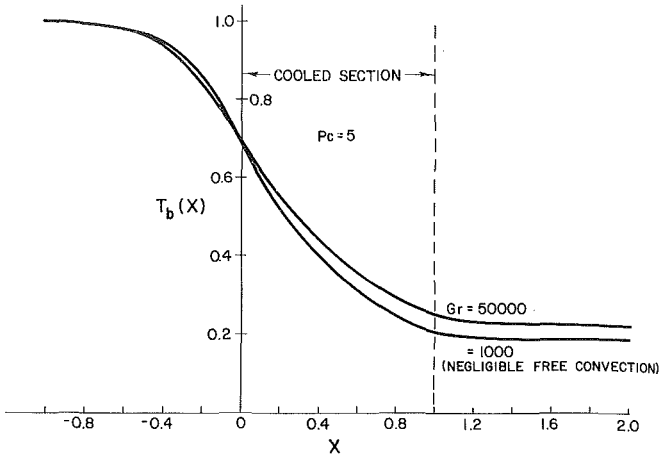

Fig. 9 Dimensionless bulk temperatures versus X at high and low Gr, Pc = 5, Re = 100 (cooling)

slowed down, whereas in heating, the same was being accelerated. Consequently, due to continuity requirements, the fluid near the channel centerline is being accelerated. It is the deceleration of the velocity near the walls that decreases the heat transfer from the fluid to the cooled portion of the channel walls. Furthermore, this distortion is observed even at $X = -0.1$ where the walls are insulated. This can be explained by the same line of reasoning used in the case of heating, except that axial conduction causes precooling of the fluid prior to its entry to the cooled region of the channel. The slowing down of the fluid near the walls is the key factor in reducing the heat transfer. This further explains the downward trend of the curves in Fig. 6.

Dimensionless temperature profiles at various X-locations in the channel for Pc = 5 are shown in Fig. 8 for high and low Grashof numbers. It is again of interest to note that $X = -0.1$, the temperatures near the walls are higher for Gr = 1000 than for Gr = 50,000. This can be explained by observing the velocity profiles in Fig. 7. At $X = -0.1$, for Gr = 50,000, the velocities near the walls have been substantially reduced (as compared to those for Gr = 1000). On the basis of these observations, it may be inferred that due to increased free convection effects (Gr = 50,000), hotter fluid is partially prevented from flowing near the walls and thus the region is kept cool to a greater extent. In other words, the local Peclet numbers near the walls have been decreased as opposed to the case of heating. This implies that free convection effects enhance upstream axial conduction and hence precooling near the entrance to the cooled section.

Figure 9 shows the variation of bulk temperature, T_b, as a function of X for high and low Grashof numbers. The Peclet number is 5, and the Reynolds number is 100. Since the cooling of the fluid is occurring, the bulk temperature drops from the value of unity to some exit bulk temperature, T_{be}. The increase in the Grashof number leads to an increase in the local bulk temperatures for $X > 0$, which implies the decrease in heat transfer from the fluid due to free-convection effects. The reversal of the situation for $X < 0$ may be explained by the fact that free convection effects enhance upstream axial conduction and hence precooling near the entrance to cooled section. The lowering of T_b for $X < 0$ indicates that precooling has occurred via the axial conduction term. Thus axial conduction is important for the Peclet number considered.

Summary and Conclusions

The effects of axial conduction at low Peclet numbers are significant both in the case of heating and cooling. However, this effect is greater in the case of cooling due to the lowering of local Peclet number near the entrance to the cooled section. For the case of heating, free convection effects counter axial conduction somewhat near the entrance to the heated section whereas in cooling, axial conduction is enhanced.

The combination of free convection and axial conduction distorts the velocity profile. In the case of heating, the fluid is accelerated near the walls whereas in cooling, the reverse holds true. The distortion occurs even prior to entry to the heated or cooled region of the channel. The distortion of the velocity profile in the case of heating enhances the heating of the fluid. On the other hand, the distortion occurring in the case of cooling reduces the heat transfer from the fluid.

The enhancement of heat transfer in heating is always observed when free convection effects become significant. However, this enhancement occurs to a lesser extent for lower Peclet numbers.

References

1 Shah, R. K., and London, A. L., *Laminar Flow Forced Convection in Ducts*, Academic Press, New York, 1978.

2 Pigfold, R. L., "Nonisothermal Flow and Heat Transfer Inside Vertical Tubes," *Chemical Engineering Progress Symposium Series*, No. 17, Vol. 51, 1955, pp. 79-92.

3 Jackson, T. W., Harrison, W. B., and Boteler, W. C., "Combined Free and Forced Convection in a Constant-Temperature Vertical Tube," ASME *Transactions*, Vol. 80, 1958, pp. 739-745.

4 Hallman, T. M., "Experimental Study of Combined Forced and Free Laminar Convection in a Vertical Tube," NACA Technical Note D-1104, 1961.

5 Hanratty, T. J., Rosen, E. M., and Kabel, R. C., "Effect of Heat Transfer on Flow Field at Low Reynolds Numbers in Vertical Tubes," *Ind. Engr. Chem.*, Vol. 50, 1958, pp. 815-820.

6 Kemeny, G. A., and Somers, E. V., "Combined Free and Forced-Convective Flow in Vertical Circular Tubes—Experiments With Water and Oil," ASME JOURNAL OF HEAT TRANSFER, Vol. 84, 1962, pp. 339-346.

7 Metais, B., and Eckert, E. R. G., "Forced, Mixed, and Free Convection Regimes," ASME JOURNAL OF HEAT TRANSFER, Vol. 86, 1964, pp. 295-296.

8 Worsøe-Schmidt, P. M., and Leppert, G., "Heat Transfer and Friction for Laminar Flow of Gas in a Circular Tube at High Heating Rate," *Int. J. of Heat Mass Transfer*, Vol. 8, 1965, pp. 1281-1301.

9 Iqbal, M., and Stachiewicz, J. W., "Influence of Tube Orientation on Combined Free and Forced Laminar Convection Heat Tranfer," ASME JOURNAL OF HEAT TRANSFER, Vol. 88, 1966, pp. 109-116.

10 Lawrence, W. T., and Chato, J. C., "Heat-Transfer Effects on the

Developing Laminar Flow Inside Vertical Tubes," ASME JOURNAL OF HEAT TRANSFER, Vol. 88, 1966, pp. 214–222.

11 Marner, W. J., and McMillan, H. K., "Combined Free and Forced Laminar Convection in a Vertical Tube With Constant Wall Temperature," ASME JOURNAL OF HEAT TRANSFER, Vol. 92, 1970, pp. 559–562.

12 Zeldin, B., and Schmidt, F. W., "Developing Flow With Combined Forced-Free Convection in an Isothermal Vertical Tube," ASME JOURNAL OF HEAT TRANSFER, Vol. 94, 1972, pp. 211–223.

13 Greif, R., "An Experimental and Theoretical Study of Heat Transfer in Vertical Tube Flows," ASME JOURNAL OF HEAT TRANSFER, Vol. 100, 1978, pp. 86–91.

14 Fukui, K., Nakajuma, M., Ueda, H., and Mizushina, T., "Flow Instability and Transport Phenomena in Combined Free and Forced Convection Between Vertical Parallel Plates," *Journal of Chemical Engineering of Japan*, Vol. 15, 1982, pp. 172–180.

15 Yao, L. S., "Free and Forced Convection in the Entry Region of a Heated Vertical Channel," *Int. J. Heat Mass Transfer*, Vol. 26, 1983, pp. 65–72.

16 Tao, L. N., "On Combined Free and Forced Convection in Channels," ASME JOURNAL OF HEAT TRANSFER, Vol. 82, 1960, pp. 233–238.

17 Bodoia, J. R., and Ostele, J. F., "The Development of Free Convection Between Heated Vertical Plates," ASME JOURNAL OF HEAT TRANSFER, Vol. 84, 1962, pp. 40–44.

18 Savkar, S. D., "Developing Forced and Free Convection Flows Between Two Semi-Infinite Parallel Plates," Fourth International Heat Transfer Conference, Paris-Versailles, 1970, Paper No. NC 3.8.

19 Quintiere, J., and Mueller, W. K., "An Analysis of Laminar Free and Forced Convection Between Finite Vertical Parallel Plates," ASME JOURNAL OF HEAT TRANSFER, Vol. 95, 1973, pp. 53–59.

20 Agrawal, H. C., "Heat Transfer in Laminar Flow Between Parallel Plates at Small Peclet Numbers," *Applied Scientific Research*, Vol. 9A, 1960, pp. 177–189.

21 Hennecke, D. K., "Heat Transfer by Hagen-Poiseuille Flow in the Thermal Development Region With Axial Conduction," *Wärme-und Stoffübertragung*, Vol. 1, 1968, pp. 177–184.

22 Schmidt, F. W., and Zeldin, B., "Laminar Heat Transfer in the Entrance Region of Ducts," *Applied Scientific Research*, Vol. 23, 1970, pp. 73–94.

23 Patankar, S. V., *Numerical Heat Transfer and Fluid Flow*, McGraw Hill, Washington, D.C., 1980, pp. 37, 81–83.

Mixed Convective Burning of a Fuel Surface With Arbitrary Inclination

C.-P. Mao

A. C. Fernandez-Pello
Mem. ASME

P. J. Pagni
Mem. ASME

Department of Mechanical Engineering,
University of California,
Berkeley, Calif. 94720

An analysis is developed for mixed, forced, and free convective combustion on a flat fuel surface of arbitrary inclination that makes use of the laminar boundary layer approximation to describe the gas flow and of the flame-sheet approximation to describe the gas-phase reactions. A mixed-convection parameter $(Re_x^n + Gr_x^m)^{1/2n}$ *that properly scales the dependent and independent variable fields and a mixed convection ratio* $(Gr_x^m/Re_x^n)^{1/2}$ *that plays the role of the downstream local similarity coordinate are introduced in the nondimensionalization of the equations. It is shown that these two parameters, rather than the standard Reynolds,* Re_x*, and Grashof,* Gr_x*, numbers are the optimum choice of governing nondimensional groups for this problem. The values of m and n are selected to obtain a similarity solution of the governing equations in the pure free convection limit for a vertical* ($m = 2$, $n = 4$) *and a horizontal* ($m = 2$, $n = 5$) *surface, which are the cases solved in this work. With this formulation, the solution of the problem provides for both cases smooth transition of all physical variables from one convective limit to the other. Results are obtained from numerical integration of the governing equations and from application of the local similarity approximation. It is shown that the range of validity of local similarity is extended beyond that obtained with alternate formulations and that the proper limits are approached. For use in practical applications, the results suggest that explicit expressions for the mass burning rate and for the fraction of unburnt pyrolyzate can be found that will suffice over the whole range of mixed-flow intensity.*

Introduction

In most practical situations, the combustion of fuel surfaces occurs under the combined influence of both natural and forced convection. The heat released by the chemical reaction taking place at the flame location induces a buoyant flow that reinforces any existing forced flow, e.g., from ventilation in compartment fires. Fundamental studies of boundary-layer convective combustion of a vertical or a horizontal fuel surface have been conducted by several authors for the pure forced, pure free, and mixed-convection cases [1-3]. Most analyses of mixed-mode combustion [1, 3-5] as well as those for the chemically inert, nongasifying systems [6-8], adopt the forced flow nondimensionalization of the governing boundary layer equations. Such formulations, however, fail to provide a smooth transition from the forced convection limit to the free-convection limit in that the solution becomes increasingly difficult to obtain as the latter limit is approached. In fact, the equations become singular at the limit. Similarly, the same difficulty would result close to the forced-convection limit if the natural convection nondimensionalization is used.

Recently, a unified mixed-flow parameter, $(Re^4 + Gr^2)^{1/8}$, has been introduced in the analysis of stagnation points [9]. This formulation not only brings a degree of symmetry to the problem, but more importantly, it provides solutions that are uniformly valid over the entire range of mixed-flow intensity, including the limits. Here the intrinsically nonsimilar problem of mixed-convective burning of a flat surface is examined using a mixed-flow parameter of the form $(Re_x^n + Gr_x^m)^{1/2n}$ to properly scale the dependent and independent variables and a mixed-convection ratio, $\xi = (Gr_x^m/Re_x^n)^{1/2}$, to index the distance x from the upstream leading edge of the fuel surface. The values of m and n are selected to obtain a similarity solution for the limiting cases of pure forced or pure free convection. This results in specific values of m and n for the vertical and horizontal cases. Because the singularity at one limit is removed and the governing equations become similar at both limits, it is shown that this nondimensionalization is more appropriate than the one based on Re_x or Gr_x. In addition, a locally similar solution of the boundary-layer equations is obtained which shows acceptable agreement with a numerical solution. This is to be contrasted with comparisons showing only limited range of agreement obtained using the previous formulation [4]. The mathematical solution of the nondimensionalized, laminar, reacting boundary-layer equations presented here follows standard procedures [1, 3-5]. Therefore, to avoid repetition, the reader is often referred to these references for the clarification of intermediate steps.

Problem Formulation

A schematic of the problem under consideration is shown in Fig. 1. The analysis considers the burning of the upper face of a flat combustible surface of arbitrary inclination once the initial transient burning has been completed. A laminar, forced-convection boundary layer is generated near the fuel surface by the forced oxidizing gas flow. In this boundary layer, adjacent to the actively pyrolyzing solid fuel, lies a diffusion flame that establishes an approximately constant elevated surface temperature through a balance between inward heat conduction from the flame and endothermic pyrolysis of the fuel. Some of the pyrolyzed fuel is transported locally to the flame via convection and diffusion, where it exothermically reacts with the oxidizer. The gaseous fuel not consumed by the flame at the location of its generation, excess pyrolyzate [10], is convected downstream between the flame and the fuel surface. The large difference

Contributed by the Heat Transfer Division and presented at the ASME/JSME Joint Thermal Engineering Conference, Honolulu, Hawaii, March 1983. Manuscript received by the Heat Transfer Division April 20, 1983.

between ambient density and that near the flame region generates a buoyant flow that reinforces the previously established forced flow. The characteristics of the resulting mixed-convection flow depend on the relative magnitude of the inertia and buoyant forces.

This analysis assumes that the burning surface is in equilibrium vaporization, i.e., that the activation energy of the surface pyrolysis reaction is sufficiently large that the variation in the surface mass flux, required by the boundary layer solution, can be accomodated with negligible change in the surface temperature. In addition, fast gas-phase chemical reactions are assumed to occur between fuel and oxidizer. Because the characteristic time of the gas-phase transport processes is much longer than the chemical kinetic time scale, the flame sheet approximation is used to describe the reacting flow. The effect of the net radiation between the surface and the flame on surface pyrolysis is incorporated by using an effective enthalpy of pyrolysis in the mass transfer number [10]. A more detailed incorporation of radiation in combusting boundary layers is available [11, 12]; however, since the analysis is already restricted to small scale, 0 (< 20 cm), by the laminar constraint, the radiation contribution for most fuels will be small [13, 14].

The governing boundary layer conservation equations are

$$\frac{\partial}{\partial x}(\rho u)+\frac{\partial}{\partial y}(\rho v)=0 \tag{1a}$$

$$\rho u\frac{\partial u}{\partial x}+\rho v\frac{\partial u}{\partial y}=\frac{\partial}{\partial y}\left(\mu\frac{\partial u}{\partial y}\right)+g\sin\sigma(\rho_\infty-\rho)-\frac{\partial p}{\partial x} \tag{1b}$$

$$\frac{\partial p}{\partial y}=g(\rho_\infty-\rho)\cos\sigma \tag{1c}$$

$$\rho u\frac{\partial h}{\partial x}+\rho v\frac{\partial h}{\partial y}=\frac{\partial}{\partial y}\left(\frac{\lambda}{c_p}\frac{\partial h}{\partial y}\right)+\dot{q}_v \tag{1d}$$

$$\rho u\frac{\partial Y_i}{\partial x}+\rho v\frac{\partial Y_i}{\partial y}=\frac{\partial}{\partial y}\left(\rho D\frac{\partial Y_i}{\partial y}\right)+\dot{m}_{iv} \tag{1e}$$

where $h\equiv\int_{T_\infty}^{T}c_p dT$ and $\dot{q}_v$ and $\dot{m}_{iv}$ are the volumetric heat and mass generation rates, respectively. Since the enthalpy and fuel concentration at the wall are constant, the boundary conditions are:

at $y=0$

$$u=0,\ h=h_w,\ Y_f=Y_{fw} \tag{2a}$$

and

$$\frac{\lambda}{c_p}\frac{\partial h}{\partial y}=\dot{m}_p L,\ \dot{m}_p=\frac{-\rho D\dfrac{\partial Y_f}{\partial y}}{Y_{fl}-Y_{fw}} \tag{2b}$$

at $y\to\infty$

$$u=u_\infty,\ h=0,\ Y_o=Y_{o\infty},\ p=p_\infty \tag{2c}$$

The mathematical analysis is simplified by introducing a stream function ψ satisfying

$$\rho u=\mu_\infty\frac{\partial\psi}{\partial y},\ \rho v=-\mu_\infty\frac{\partial\psi}{\partial x} \tag{3}$$

and the transformations

$$\xi=(\mathrm{Gr}_x{}^m/\mathrm{Re}_x^n)^{1/2} \tag{4a}$$

$$\eta=(\mathrm{Re}_x{}^n+\mathrm{Gr}_x{}^m)^{1/2n}\left(\int_0^y(\rho/\rho_\infty)dy\right)/x \tag{4b}$$

$$f(\xi,\eta)=(\mathrm{Re}_x{}^n+\mathrm{Gr}_x{}^m)^{-1/2n}\psi(x,y) \tag{4c}$$

$$J(\xi,\eta)=(\beta-\beta_\infty)/(\beta_w-\beta_\infty)=(\gamma-\gamma_\infty)/(\gamma_w-\gamma_\infty) \tag{4d}$$

$$H(\xi,\eta)=\mathrm{Gr}_x{}^{m/2n}(p-p_\infty)T_\infty/((T_w-T_\infty)g\cos\sigma\rho_\infty x) \tag{4e}$$

$$\theta(\xi,\eta)=h/h_w=(T-T_\infty)/(T_w-T_\infty) \tag{4f}$$

Nomenclature

B = mass transfer number, $B=[Q\ Y_{o\infty}/(\nu_o M_o)-c_p(T_w-T_\infty)]/L$
c_p = specific heat capacity
D = diffusivity
D_c = nondimensional heat of combustion, $D_c=Q\ Y_{o\infty}/(\nu_o M_o c_p(T_w-T_\infty))$
f = normalized stream function, equation (4c)
Gr_x = Grashof number, $\mathrm{Gr}_x=x^3 g(T_w-T_\infty)/(\nu_\infty{}^2 T_\infty)$
g = acceleration of gravity
H = normalized pressure function, equation (4e)
h = enthalpy
J = normalized Shvab-Zeldovich coupling function, equation (4d)
J_{fl} = value of J at the flame, $J_{fl}=r/(1+r)$
L = effective heat of pyrolysis
M = molecular weight
$\dot{M}$ = total mass flux
$\dot{m}$ = local mass flux, equation (10)
m = scaling exponential for the Grashof number $m=2$ vertical and horizontal
n = scaling exponential for the Reynolds number $n=4$ vertical, $n=5$ horizontal
Pr = Prandtl number, $\mathrm{Pr}=c_p\mu_\infty/\lambda_\infty$
P = pressure
$\dot{q}$ = local heat flux
Q = heat of combustion
Re_x = Reynolds number, $\mathrm{Re}_x=u_\infty x/\nu_\infty$
r = mass consumption number, $r=Y_{o\infty}s/Y_{fw}$
s = stoichiometric ratio, $\nu_f M_f/\nu_o M_o$
T = temperature
u = streamwise velocity
v = normal velocity
x = coordinate parallel to the fuel surface
Y_i = mass fraction of i species
y = coordinate normal to the fuel surface

Greek

β = Shvab-Zeldovich variable (species), equation (5)
γ = Shvab-Zeldovich variable (energy-species), equation (5)
η = local similarity variable, equation (4b)
θ = nondimensional temperature, equation (4f)
λ = thermal conductivity
μ = dynamic viscosity
ν = kinematic viscosity, or stoichiometric coefficient
ξ = mixed convection ratio equation (4a)
ρ = density
ψ = stream function, equation (4c)
τ = parameter, equation (6a), $\tau=(T_w-T_\infty)/T_\infty$
Δ = parameter, equation (6a), $\Delta=g(T_w-T_\infty)\nu_\infty/(T_\infty u_\infty{}^3)$

Subscripts

e = excess
f = fuel
fl = flame
i = species
o = oxygen
p = pyrolyzed
t = transferred
v = per unit volume
w = wall
∞ = ambient

The variables β and γ are the Shvab-Zeldovich coupling functions defined as

$$\beta = Y_F/(\nu_F M_F) - Y_o/(\nu_o M_o)$$
$$\gamma = -h/Q - Y_o/(\nu_o M_o) \tag{5}$$

with these variables and assuming Lewis number unity and constant values of $\rho\mu$, c_p, $\rho\lambda$, ρT, and $\rho^2 D$, the boundary-layer equations and their boundary conditions become

$$f''' + \frac{n+3m\xi^2}{2n(1+\xi^2)} ff'' - \frac{(3m-n)\xi^2}{n(1+\xi^2)} f'^2$$
$$= -\Delta^{(2m-n)/(3m-n)} \frac{\xi^{2/(3m-n)}}{(1+\xi^2)^{2/n}} \frac{\xi^{2/(3m-n)}}{(1+\xi^2)^{2/n}} \theta \sin\sigma$$
$$+ \Delta^{(5m-2n)/2(3m-n)} \frac{\xi^{(2n-3m)/n(3m-n)}}{(1+\xi^2)^{2/n}} \left(\left(1 - \frac{3m}{2n}\right)(H + \tau\theta H(\xi,0)) \right.$$
$$\left. - \frac{n-(3m-2n)\xi^2}{2n(1+\xi^2)} \eta H' + \frac{(3m-n)}{2} \left(\xi \frac{\partial H}{\partial \xi} + \tau\theta\xi \frac{\partial H(\xi,0)}{\partial \xi} \right) \right) \cos\sigma$$
$$+ \frac{3m-n}{2} \xi \left(f' \frac{\partial f'}{\partial \xi} - f'' \frac{\partial f}{\partial \xi} \right) \tag{6a}$$

$$H' = \frac{\xi^{1/n}}{(1+\xi^2)^{1/2n}} \theta \tag{6b}$$

$$\frac{J''}{\mathrm{Pr}} + \frac{n+3m\xi^2}{2n(1+\xi^2)} fJ' = \frac{3m-n}{2} \xi \left(f' \frac{\partial J}{\partial \xi} - J' \frac{\partial f}{\partial \xi} \right) \tag{6c}$$

subject to

$$f'(\xi,0) = 0, J(\xi,0) = 1,$$
$$f'(\xi,\infty) = (1+\xi^2)^{-1/n}, \tag{7a}$$
$$J(\xi,\infty) = 0$$

$$\xi \frac{\partial f(\xi,0)}{\partial \xi} + \frac{n+3m\xi^2}{n(3m-n)(1+\xi^2)} f(\xi,0)$$
$$= \frac{2}{(3m-n)} \frac{B}{\mathrm{Pr}} J'(\xi,0) \tag{7b}$$

$$H(\xi,\infty) = 0 \tag{7c}$$

where the prime indicates differentiation with respect to η at constant mixed-convection ratio $\xi = (\mathrm{Gr}_x{}^m/\mathrm{Re}_x{}^n)^{1/2}$ with the Reynolds number defined as $\mathrm{Re}_x = u_\infty x/\nu_\infty$ and the Grashof number as $\mathrm{Gr}_x = x^3 g(T_w - T_\infty)/(\nu_\infty{}^2 T_\infty)$. The non-dimensional temperature θ, is related to the normalized Shvab-Zeldovich function through its definition, resulting in

$$\theta = \begin{cases} D_c - (D_c - 1)J & \text{for } \eta \le \eta_{fl} \\ (D_c - (D_c - 1)J_{fl})J/J_{fl} & \text{for } \eta \ge \eta_{fl} \end{cases} \tag{8}$$

where $D_c = Q\, Y_o/\nu_o M_o\, c_p(T_w - T_\infty)$, and J_{fl} corresponds to the value of J at the position of the flame. Imposing the condition that at the flame $Y_o = Y_f = 0$ (flame sheet approximation) the resulting expression for J_{fl} is $J_{fl} = r/(1+r)$. In the foregoing expressions, $B = [Q\, Y_{o\infty}/(\nu_o M_o) - c_p(T_w - T_\infty)]/L$ is the mass transfer number, and $r = Y_{o\infty}\, \nu_f M_f/(Y_{fw}\nu_o M_o)$ is the mass consumption number. The fuel concentration at the solid surface, Y_{fw}, is obtained from the boundary conditions at the interface as $Y_{fw} = (BY_{fl} - Y_{o\infty}s)/(1+B)$.

Under the present formulation of the problem, the forced-convection limit ($\mathrm{Gr}_x = 0$) is obtained by setting $\xi = 0$ in the foregoing equations and the free-convection limit ($\mathrm{Re}_x = 0$) by setting $\xi \to \infty$. From equations (6) and their boundary conditions (equations (7)), it is seen that the governing equations for the forced-convection case [1, 15] are recovered for $\xi = 0$. For all m and n these equations have a similarity solution. For the free-convection limit, a similarity solution is found for the case of a vertical surface by setting in the foregoing equations $\xi \to \infty$, $\sigma = 90$ deg, $m = 2$ and $n = 4$, and for a horizontal surface burning on the top by setting $\xi \to \infty$, $\sigma = 0$, $m = 2$, and $n = 5$. The resulting equations and boundary conditions agree with those developed for the corresponding pure free-convection cases [1, 2, 16, 17]. The case of the underneath burning of a horizontal surface, although scaled by the same power of the Grashof number ($\mathrm{Gr}^{1/5}$), does not have a similarity solution [18] and will not be considered here. A local similarity solution [4, 19] of the combusting mixed-mode problem is obtained by neglecting the partial derivatives with respect to ξ.

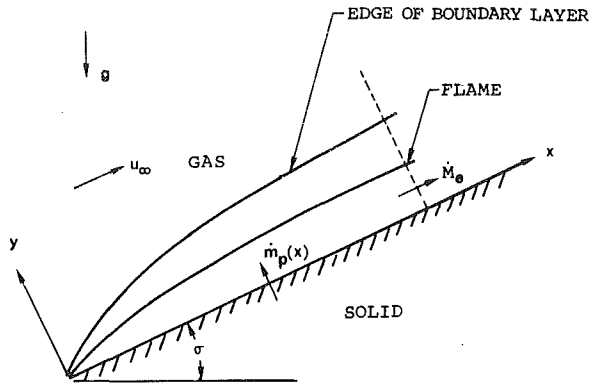

Fig. 1 Schematic diagram of the diffusion flame over a burning combustible in a flat plate boundary layer flow. The coordinate system employed is also indicated.

The solution for the vertical case is approximately valid for inclination angles of $30 < \sigma < 150$ deg [17], and the solution for the horizontal case for $\sigma < 10$ deg. An approximate solution for the intermediate inclinations can be obtained by interpolating between both solutions. A more rigorous solution is obtained by setting m and n equal to the values corresponding to either the vertical or horizontal case and solving the equations by a local similarity approach or by numerical integration of the partial differential equations.

The primary variables to be determined from this analysis are the velocity and temperature fields and the flame stand-off distance, the fuel pyrolysis rate, and the unburnt fraction of the fuel pyrolyzate. These variables can subsequently be used to calculate burning times of the material, flame heights, heat release rates, etc. The downstream velocity is readily deduced from the transformation definitions, equations (3) and (4), yielding

$$u = (\mathrm{Re}_x{}^n + \mathrm{Gr}_x{}^m)^{1/n} \nu_\infty f'/x \tag{9}$$

The local pyrolysis rate is obtained by applying energy conservation at the gas-solid interface, which results in

$$\dot{m}_p(x) = -(\mathrm{Re}_x{}^n + \mathrm{Gr}_x{}^m)^{1/2n} B\lambda_\infty J'(\xi,0)/c_p x \tag{10}$$

The unburnt fraction of the total fuel pyrolyzate from 0 to ξ is given by the ratio [1] of the excess pyrolyzate at x: $\dot{M}_e = \int_o^{y_{fl}} \rho u\, Y_f\, dy$, to the total fuel pyrolysis from 0 to x: $Y_{fl}\, \dot{M}_p = Y_{fl} \int_o^x \dot{m}_p\, dx$. Applying the definitions, we obtain

$$\frac{\dot{M}_e(\xi)}{Y_{fl}\dot{M}_p(\xi)} = -\frac{(3m-n)\mathrm{Pr}}{2(1+B+r)} \xi^{1/(3m-n)} (1+\xi^2)^{1/2n}$$
$$\times \frac{\int_o^{\eta_{fl}} (J(1+r)-r) f'\, d\eta}{Y_{fl} \int_o^\xi (1+\xi^2)^{1/2n} \xi^{1/(3m-n)-1} J'(\xi,0) d\xi} \tag{11}$$

The physical flame stand-off distance is obtained by inverting the transformation for η and integrating from the fuel surface to the flame location, giving

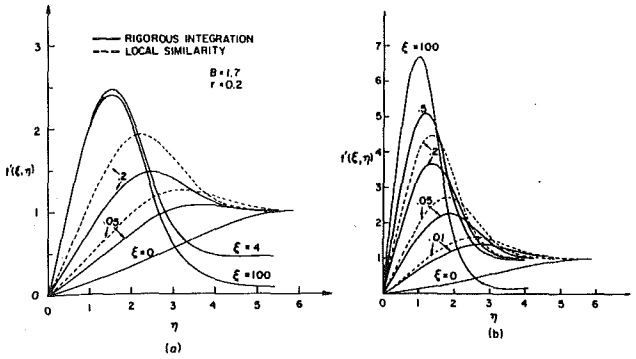

Fig. 2 Profiles of the nondimensional streamwise velocity $f' = ux/(\nu_\infty (\mathrm{Re}_x^n + \mathrm{Gr}_x^m)^{1/n})$ for several values of the mixed convection ratio $\xi = (\mathrm{Gr}_x^m/\mathrm{Re}_x^n)^{1/2}$, with $\eta = (\mathrm{Re}_x^n + \mathrm{Gr}_x^m)^{1/2n} (\int_0^y (\rho/\rho_\infty)dy)/x$: (a) vertical surface, $m = 2$, $n = 4$; (b) horizontal surface, $m = 2$, $n = 5$

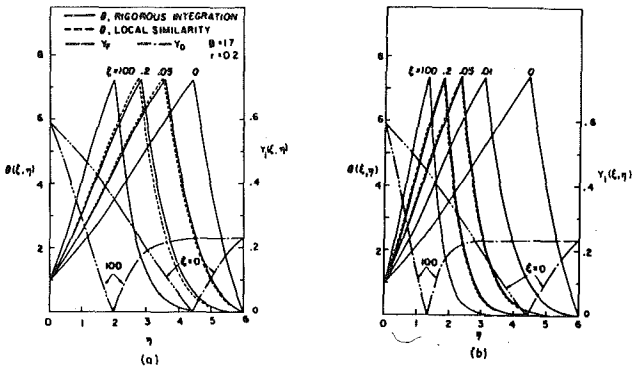

Fig. 3 Profiles of the normalized temperature $\theta = (T-T_\infty)/(T_W-T_\infty)$ for several values of the mixed convection ratio $\xi = (\mathrm{Gr}_x^m/\mathrm{Re}_x^n)^{1/2}$ with $\eta = (\mathrm{Re}_x^n + \mathrm{Gr}_x^m)^{1/2n} (\int_0^y (\rho/\rho_\infty)dy)/x$: (a) vertical surface, $m = 2$, $n = 4$; (b) horizontal surface, $m = 2$, $n = 5$. Profiles for the mass fraction of fuel Y_F and oxygen Y_O are also presented for the limiting cases of $\xi = 0$ and $\xi \to \infty$.

$$y_{fl} = (\mathrm{Re}_x{}^n + \mathrm{Gr}_x{}^m)^{-1/2n} x \int_o^{\eta_{fl}} \left(1 + \theta\left(\frac{T_w}{T_\infty} - 1\right)\right) d\eta \qquad (12)$$

What is exciting about equations (9–12) is that all the physical variables scale with $(\mathrm{Re}_x{}^n + \mathrm{Gr}_x{}^m)^{1/2n}$. So this parameter gives the magnitude of the profiles while their characters or shape is dictated by $\xi = (\mathrm{Gr}_x{}^m/\mathrm{Re}_x{}^n)^{1/2}$, i.e., $\xi \to 0$ more forcedlike, or $\xi \to \infty$ more freelike, as shown in the figures of the next section.

Results and Discussion

The set of partial differential equations (6) with their respective boundary conditions, equations (7), is solved numerically by first replacing the ξ-derivatives by a two-point backward differences, i.e., $\partial f/\partial\xi \simeq (f_m - f_{m-1})/\Delta\xi$, to give a set of coupled ordinary differential equations at each streamwise station. These are then integrated, using a quasi-linearization and iteration scheme [20, 21] with a Runge-Kutta-Gill fourth-order method. To obtain the local similarity approximation in the present formulation, the equations with all $\partial/\partial\xi$ equal to zero are also solved using the above quasilinearization scheme.

The streamwise velocity profiles may be inferred from the gradient of the normalized stream function, f'. Results obtained from the numerical and locally similar solutions, are presented for the vertical and horizontal cases, respectively, in Figs. 2(*a*) and 2(*b*) for several values of the mixed-convection ratio, ξ. The corresponding profiles for the nondimensional temperature θ are presented respectively in Figs. 3(*a*) and 3(*b*), as are two representative profiles of species concentrations. Because of the linear relationship between temperature and species concentration, and for clarity, only two species profiles are presented. The data used in the computation are those corresponding to polymethylmethacrylate (PMMA): Q = 13.57 kJ/gm of oxidizer, L = 1.59 kJ/gm of fuel, T_w = 663°K, $Y_{fl} = 1$, $M_f = 100$, $\nu_o/\nu_f = 6$. The Prandtl number is taken as constant with a value of Pr = 0.7. An ambient temperature of T_∞ = 295 K is assumed. All dependence on u_∞ is scaled out via $(\mathrm{Re}_x{}^n + \mathrm{Gr}_x{}^m)^{1/n}$ and ξ. The values of B and r correspond to PMMA burning in air. From the variation with ξ of the f' and θ profiles presented in Figs. 2 and 3, it appears that the present formulation of the problem provides a smooth transition from the forced $\xi \to 0$, to the natural convective limit, $\xi \to \infty$.

In interpreting the figures, it should be noted that the distance from the leading edge plays a critical role. The mixed-convection ratio is the ratio of the buoyant forces to the inertial forces $\xi = (g^m(T_w - T_\infty)^m/(T_\infty{}^m u_\infty{}^n \nu_\infty{}^{2m-n}))^{1/2} x^{(3m-n)/2}$. It is also the scaled distance from the fuel leading edge. Thus every flame with $u_\infty \neq 0$ makes a transition from inertia control to buoyancy control as one moves downstream. The combustion process is forced convection dominated near the fuel leading edge, with natural convection becoming more important as the distance from the leading edge increases. The results obtained in the present analysis can also be used to compare the predicted characteristics of the burning processes for vertical and horizontal surfaces. In comparing the values of the different variables, it should be taken into account that the variables are scaled differently by the mixed convection ratio according to whether the surface is horizontal or vertical.

Now move to a fixed distance from the fuel leading edge and consider the influence of environmental conditions, as shown in Figs. 2 and 3. It is seen that for fixed x and u_∞, an increase in buoyancy results in an increase of the gas velocity (inertia and buoyant effects are added) and in a decrease of the thickness of the boundary layer. The thinning of the boundary layer is the result of the increase in flow velocity, which counteracts the increase of fuel vapors added to the flow due to the increased heat flux at the fuel surface (Figs. 3(*a*) and 3(*b*)). As expected, it is the mixed region, where the results obtained from the rigorous integration and locally similar solutions show disagreement, particularly for the predicted flow velocity. If x and $g\,\Delta T$ are kept constant, it is seen from Figs. 2(*a*) and 2(*b*) that as u_∞ is increased, the overall streamwise velocity increases with the relative influence of buoyancy decreasing, i.e., the velocity profiles flatten, the location of the maximum velocity moves outward, the thickness of the boundary-layer increases, and the velocity profiles move closer to those for pure forced flow.

Comparison of the free convection ($\xi > 5$) results for vertical and horizontal surfaces presented in Figs. 2 and 3 show that the horizontal surface has, at low Grashof numbers ($\mathrm{Gr} < 10^3$), a boundary layer that is slightly thinner and a maximum streamwise velocity that is slightly larger than those for the vertical case. However, for $\mathrm{Gr} > 10^3$ the vertical boundary layer is thinner and the vertical streamwise velocity becomes larger than those in the horizontal case. The difference between the respective magnitudes increases as the Grashof number increases. For mixed convection, however, these differences decrease as the forced convection limit is approached.

The variation with the mixed convection ratio of the nondimensional shear stress, $f''(\xi, 0)$ and heat flux, $J'(\xi, 0)$, is shown in Figs. 4(*a*) and 4(*b*) for the vertical and horizontal cases, respectively. For comparison purposes, the results obtained from both the rigorous and local similarity integrations are presented in the figure. Here again it is seen that the present formulation of the problem provides a smooth

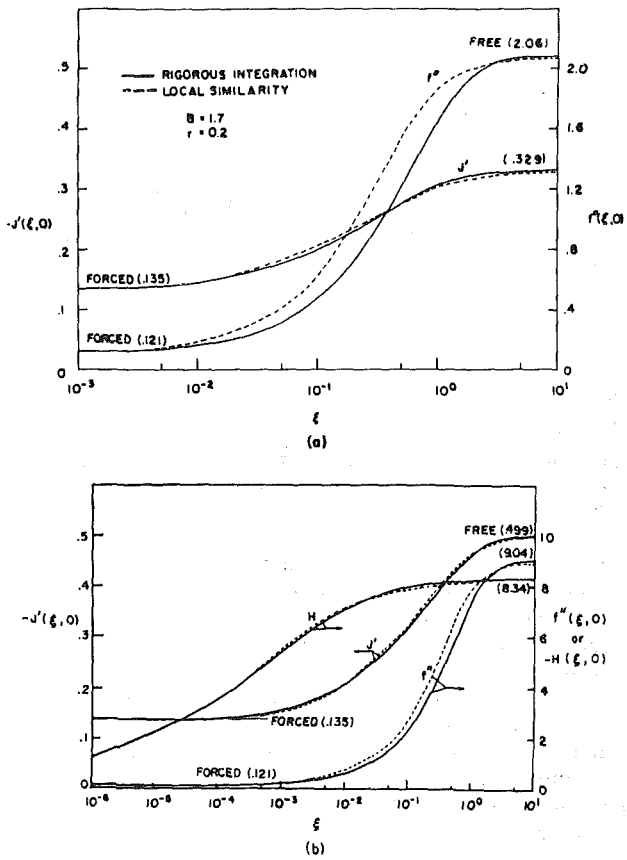

Fig. 4 Variation with the mixed convection ratio $\xi = (Gr_x^m/Re_x^n)^{1/2}$, of the nondimensional heat flux $J'_w = q_w c_p x/(\lambda_\infty L B(Re_x^n + Gr_x^m)^{1/2n})$, and nondimensional shear stress $f''_w = \tau_w x^2/(\rho_\infty \nu_\infty{}^2(Re_x^n + Gr_x^m)^{3/2n})$: (a) vertical surface $m = 2$, $n = 4$; (b) horizontal surface, $m = 2$, $n = 5$. The variation with ξ of the nondimensional pressure, H, is also presented for the case of a horizontal surface.

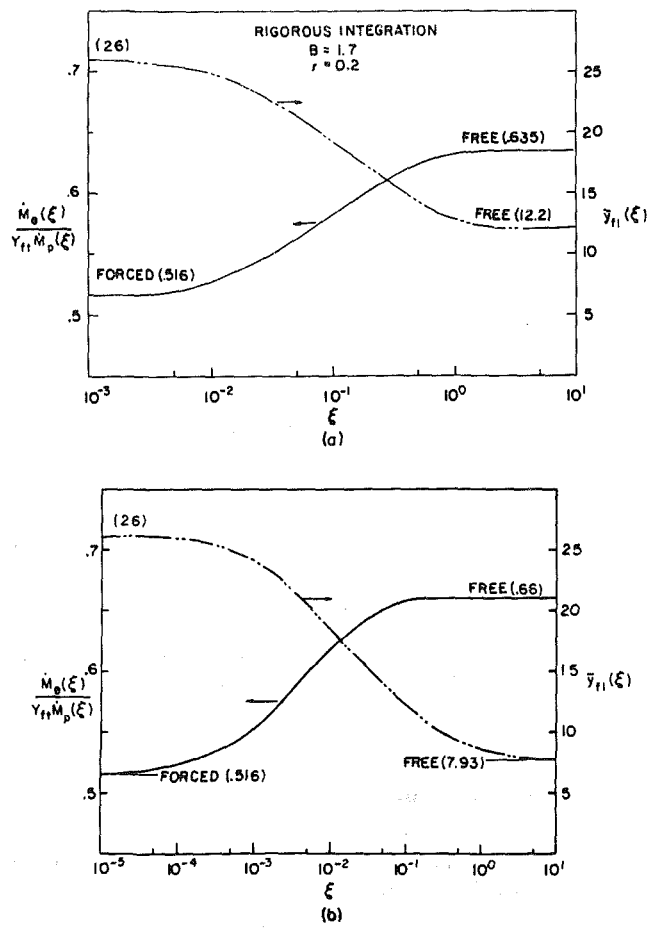

Fig. 5 Variation with the mixed convection ratio $\xi = (Gr_x^m/Re_x^n)^{1/2}$, of the unburnt fraction of the fuel pyrolyzate $\dot{M}_e/(Y_{ft}\dot{M}_p)$, and the normalized flame stand off distance $\bar{y}_{fl} = y_{fl}(Re_x^n + Gr_x^m)^{1/2n}/x$: (a) vertical surface, $m = 2$, $n = 4$; (b) horizontal surface, $m = 2$, $n = 5$

transition from one convective limit to the other. The slight disagreement observed between the two solutions for large values of ξ is believed to be due to accumulation of errors in the forward-marching integration technique used to solve the set of partial differential equations (6). The local similarity solution is actually more accurate at the $\xi \to \infty$ limit. The numerics can be readily improved.

The fuel pyrolysis rate is obtained by inputing to equation (10) the normalized surface heat flux given in Figs. 4(*a*) or 4(*b*). The good agreement observed between the heat fluxes predicted by the rigorous and local similarity solutions, in view of the simplification that the local similarity approximation introduces, suggests the use of this approximation for practical purposes. The potential for applying the local similarity approximation toward the solution of the problem under study is an important consequence of employing the nondimensionalization presented in this work. The conventional formulation of using only the Reynolds or Grashof numbers for the nondimensionalization of the governing equations results in a much less accurate local similarity solution [4].

The uniform behavior of $J'(\xi, 0)$ in Figs. 4(*a*) and 4(*b*) suggests a linear interpolation might be adequate to obtain the mixed-flow pyrolysis rate. In the forced- and free-flow limits $J'(0)$ is simply related to $f(0)$, which is known as a function of B and r from empirical fits to existing calculations [1]. Using equations (57, 59, 68) and (71) of [1] with equation (10) yields

$$\lim_{\xi \to 0} J'(0)_{\text{forced}} \approx -0.18 B^{-0.42 - 0.09\, lnB} \tag{13a}$$

$$\lim_{\xi \to \infty} J'(0)_{\text{free vertical}} \approx -0.34 r^{-0.05} B^{-0.23 - 0.05\, lnB} \tag{13b}$$

$$\lim_{\xi \to \infty} J'(0)_{\text{free horizontal}} \approx -0.538 r^{-0.0135} B^{-0.233 - 0.1\, lnB} \tag{13c}$$

Equation (13*c*) has been developed in the present work following the procedure indicated in [1].

Comparison of the predicted fuel pyrolysis rates for the free-convection vertical and horizontal cases shows that at low Grashof numbers the pyrolysis rate for the horizontal surface is slightly larger than that for the vertical surface. However for $Gr_x < 10^3$ the vertical pyrolysis rate is larger than the horizontal one. The difference between them increases with the Grashof number. This result is consistent with the previously indicated dependence on Gr_x of the boundary-layer thickness and consequently of the flame stand-off distance (Fig. 5(*a*) and 5(*b*)). For the mixed convection, the differences between both cases are reduced as the forced limit is approached.

Figures 5(*a*) and 5(*b*) show respectively for the vertical and the horizontal surfaces the unburnt fraction of the total pyrolyzate, $\dot{M}_e(\xi)/Y_{fl}\dot{M}_p(\xi)$, (equation (11)) and the normalized flame stand-off distance $\bar{y}_{fl} = y_{fl}(Re_x{}^n + Gr_x{}^m)^{1/2n}/x$, (equation (12)), as a function of the mixed-convection ratio. Since an integration must be performed from 0 to ξ (equation (11)) to calculate the unburnt fraction of the total pyrolyzate, the use of the local similarity approximation may not be justified here so that only the solution obtained from the numerical integration of the full equations (6) is presented. It is seen that at fixed B and r the flame stand-off distance decreases as the mixed-convection ratio increases because the boundary layer becomes thinner.

The total fuel pyrolyzate, the excess pyrolyzate, and the unburnt fraction of the total fuel pyrolyzate all increase as the mixed-convection ratio increases. The unburnt fraction of the total fuel pyrolyzate increases as the free limit is approached, since the peak in the streamwise velocity profile has not only increased, but also has moved into a region of higher fuel mass fraction, thus increasing the downstream fuel flux at the expense of local consumption. In addition, as ξ increases, the normal velocity changes sign on the fuel side of the flame, so that while convection aids fuel diffusion towards the flame at small ξ it opposes fuel diffusion at large ξ. This explains the increase indicated in Figs. 5(*a*) and 5(*b*) of the unburnt fraction of fuel pyrolyzate, in spite of the decrease in the flame stand-off distance as ξ increases.

Comparison of the flame stand-off distance for the free-convection horizontal and vertical cases show a similar dependence on the Grashof number as that predicted for the thickness of the boundary layer. At low values of Gr_x, the flame is closer to the surface for the horizontal case, while for $Gr_x > 10^3$, the flame is closer to the surface for the vertical case. The difference between the flame stand-off distances for these cases increases as the Grashof number increases. The predicted unburnt fractions of the total pyrolyzate are very similar for both vertical and horizontal surfaces. This is understandable, since it is a fraction of two magnitudes with similar dependency on Gr_x, and consequently it is insensitive to the variation of this parameter.

Concluding Remarks

The introduction of a mixed-convection parameter $(Re_x^n + Gr_x^m)^{1/2n}$, in the governing equations describing the mixed, free, and forced convective combustion of a fuel surface provides solutions that are uniformly valid over the entire range of mixed-flow intensities. The formulation of the nondimensional equations is such that the forced- and free-flow equations, for a vertical ($m = 2, n = 4$) or a horizontal ($m = 2, n = 5$) surface, are respectively recovered for values of the mixed-convection ratio, $\xi \to 0$ and $\xi \to \infty$. It is claimed, that for mixed-convection problems, the physical variables are best expressed in terms of these two nondimensional variables, $(Re_x^n + Gr_x^m)^{1/2n}$ and $\xi = (Gr_x^m/Re_x^n)^{1/2}$, rather than the standard Re_x and Gr_x. This solution of the problem provides a smooth transition from one convective lilmit to the other. Note that $(Re_x^n + Gr_x^m)^{1/2n}$ plays the role of a scale factor governing the appropriate magnitude of the physical variables, while ξ indicates whether the character of the variable profiles is more nearly forced or free.

From comparison of the results obtained from the rigorous integration solution and the local similarity approximation, it has been shown that under the present formulation of the problem, the locally similar solution provides reasonable results, thus suggesting its utility for practical applications where approximate results suffice. The better agreement obtained under the present formulation between the locally similar and rigorous integration solutions in comparison with other more conventional approaches to the problem is due primarily to the introduction of the foregoing mixed-convection parameter in the nondimensionalization. In the future, the fate of the converging streamline, which exists in the free limit but not in the forced limit, should be explored along with the normal velocity profiles, over the full range of ξ. Local radiation effects on mixed flow could be addressed. Also, it would be of interest to examine the problem of the spread of flames over a condensed fuel surface under the combined influence of forced and free convection.

Acknowledgments

This work was supported by the Center for Fire Research in the U.S.D.O.C. National Bureau of Standards under Grant No. NB 80-NADA-1064 (A.C.F.P.) and No. NB 80-NAG-E6839 (P.J.P.). The latter was also supported by the U.S.D.O.E. under Contract No. W-7405-ENG-48 administered by Lawrence Berkeley Laboratory of the University of California. Parts of this paper were presented at the 1983 ASME-JSME Thermal Engineering Conference, Honolulu, March 20–24.

References

1 Pagni, P. J., "Diffusion Flame Analyses," *Fire Safety Journal*, Vol. 3, 1980/81, pp. 273–285.

2 Clark, J. F., and Riley, N., "Free Convection and the Burning of a Horizontal Fuel Surface," *J. Fluid Mechanics*, Vol. 74, No. 3, 1976, pp. 415–431.

3 Lavid, M., and Berlad, A. L., "Gravitational Effects on Chemically Reacting Boundary Layer Flows over a Horizontal Flat Plate," *Sixteenth Symposium (International) on Combustion*, The Combustion Institute, 1976, pp. 1557–1568.

4 Shih, T. M., and Pagni, P. J., "Laminar Mixed-Mode Forced and Free Diffusion Flames," ASME JOURNAL OF HEAT TRANSFER, Vol. 100, 1978, pp. 253–259.

5 Kinoshita, C. M., and Pagni, P. J., "Laminar Wake Flame Heights," ASME JOURNAL OF HEAT TRANSFER, Vol. 102, 1980, pp. 104–109.

6 Lloyd, J. R., and Sparrow, E. M., "Combined Forced and Free Convection Flow on Vertical Surfaces," *Int. Journal of Heat and Mass Transfer*, Vol. 13, 1970, pp. 434–438.

7 Chen, T. S., Sparrow, E. M., and Mucoglu, A., "Mixed Convection in Boundary Layer Flow on a Horizontal Plate," ASME JOURNAL OF HEAT TRANSFER, Vol. 1, 1977, pp. 66–71.

8 Gryzagogridis, J., "Combined Free and Forced Convection from an Isothermal Vertical Plate," *Int. Journal of Heat and Mass Transfer*, Vol. 18, 1975, pp. 911–916.

9 Fernandez-Pello, A. C., and Law, C. K., "On the Mixed-Convection Flame Structure in the Stagnation Point of a Fuel Particle," accepted for publication, *Nineteenth Symposium (International) on Combustion*, The Combustion Institute, 1982, pp. 1037–1044.

10 Pagni, P. J., and Shih, T. M., "Excess Pyrolyzate," *Sixteenth Symposium (International) on Combustion*, The Combustion Institute, 1976, pp. 1329–1342.

11 Kinoshita, C. M., and Pagni, P. J., "Stagnation-Point Combustion With Radiation," *Eighteenth Symposium (International) on Combustion*, The Combustion Institute, 1981, pp. 1415–1425.

12 Beier, R. A., Pagni, P. J., and Okoh, C. I., "Soot and Radiation in Combusting Boundary Layers," *Emmons Conference on Fire Research*, August 23–25, 1983, N.B.S. Gaithersburg, Mo.

13 Beier, R. A., and Pagni, P. J., "Soot Volume Fraction Profiles in a Free Combusting Boundary Layer," ASME Paper No. 81-HT-1, 1981.

14 Beier, R. A., and Pagni, P. J., "Soot Volume Fraction Profiles in Forced Combusting Boundary Layers," ASME JOURNAL OF HEAT TRANSFER, Vol. 105, 1983, pp. 156–165.

15 Emmons, H. W., "The Film Combustion of Liquid Fuel," *Z. Agnew. Math. Mech.*, Vol. 36, 1956, pp. 60–71.

16 Kosdon, F. J., Williams, F. A., and Buman, C., "Combustion of Vertical Cellulosic Cylinders in Air," *Twelfth Symposium (International) on Combustion*, The Combustion Institute, 1969, pp. 253–264.

17 Kim, J. S. de Ris, J., and Kroesser, F. W., "Laminar Free Convective Burning of Fuel Surfaces," *Thirteenth Symposium (International) on Combustion*, The Combustion Institute, Pittsburgh, Pa., 1971, pp. 949–961.

18 Orloff, L., and de Ris, J., "Modeling of Ceiling Fires," *Thirteenth Symposium (International) on Combustion*, The Combustion Institute, Pittsburgh, Pa., 1971, pp. 979–992.

19 Sparrow, E. M., and Yu, H. S., "Local Nonsimilarity Thermal Boundary-Layer Solutions," ASME JOURNAL OF HEAT TRANSFER, Vol. 93, 1971, pp. 328–334.

20 Fernandez-Pello, A. C., "Fire Spread Over Vertical Fuel Surfaces Under the Influence of Externally Applied Thermal Radiation," Harvard University, Home Fire Project Technical Report No. 19, 1977.

21 Wu, X., Law, C. K., and Fernandez-Pello, A. C., "A Unified Criterion for the Convective Extinction of Fuel Particles," *Combustion and Flame*, Vol. 44, 1982, pp. 113–124.

Calculated Interaction of Sprays With Large-Scale Buoyant Flows

R. L. Alpert
Factory Mutual Research Corporation,
Norwood, Mass. 02062
Mem. ASME

Turbulent, recirculating gas flows resulting from interactions of water droplet sprays with large-scale buoyancy sources are difficult to predict without the use of numerical techniques, especially when spray-induced gas motion is considered. One such flow occurs when a negatively buoyant methane cloud, generated during LNG spills in a wind, is dispersed by a line water spray. Numerical predictions of the ratio of average methane vapor concentration downwind of the line spray to the upwind value correlate as a function of the ratio of methane momentum in the vapor cloud to water momentum in the spray. Warming of the cloud, which occurs when small drops in the spray freeze, leads to the production of positive cloud buoyancy and the possibility of cloud lift off from the ground. Numerical calculations have also been used to predict how a near-ceiling, downward-directed spray interacts with an opposed, buoyant jet issuing from floor level. Recirculating gas motion induced by droplet trajectories is again an important part of the problem. This opposed spray-plume arrangement, which is important in the process of fire suppression by automatic sprinklers, allows the effectiveness of spray cooling of the near-ceiling environment to be determined as a function of droplet injection characteristics. Because of the excessive amounts of computer time required for the solution of both turbulent, buoyant flow problems, it is concluded that much more efficient numerical techniques are needed.

1 Introduction

Recirculating, turbulent gas flow patterns resulting from interactions of water droplet sprays with large-scale buoyancy sources are difficult to predict without the use of numerical techniques. Such flows occur in the process of fire suppression by automatic sprinklers and in the dispersal of methane clouds generated during accidental liquefied natural gas (LNG) spills. The interaction of a droplet spray with a methane cloud is discussed in the first part of this paper. Cloud dispersal is an important problem because the negative buoyancy of the cold methane results in the spread of a combustible gas mixture for a considerable distance from the spill at windspeeds below 2 to 4 m/s. Higher windspeeds produce a less severe problem, due to natural atmospheric dispersal. Line water spray barriers positioned around sites of potential spills (e.g., LNG storage tanks) are capable of diluting the methane vapor with ambient air.

In the second part of the paper, the same numerical techniques applied to the methane dispersal problem are used to predict how a near-ceiling, downward-directed droplet spray interacts with an opposed, buoyant jet issuing upward from floor level. By changing the jet inflow velocity and temperature, conditions in the thermal plume above a fire can be simulated. Characteristics of ceiling-mounted sprinklers typically used for fire suppression are also simulated by adjustment of spray droplet size and initial trajectory angle distributions. The opposed spray-plume arrangement yields an axisymmetric flow which can be readily reproduced in a future laboratory experiment to check calculated results.

For both spray interaction problems, the computational mesh used to calculate the gas flow field contains from 16 to 22 nodal points in each of the two coordinate directions. Mesh spacing is variable to allow for greatest resolution near the spray origin and near the boundaries of the computational region. However, such improved resolution does not guarantee adequate solution accuracy. Recent work by Beier et al. [22] does suggest that at least two finite computational domains must exist in all flow regions containing significant fluid property gradients if at least 10 percent accuracy is to be achieved with the commonly used hybrid differencing [2] scheme. Although this condition is generally satisfied in the work described here, the resultant need for large variations in mesh spacing leads to a significant degradation of solution accuracy.

2 Wind-Vapor-Spray Interaction Calculations

Numerical solution techniques can be particularly valuable for finding those spray characteristics and spray orientations which are most effective for the dilution of a wind-driven methane cloud. Only one spray orientation (downward facing) is considered here but other orientations have been studied. In certain cases, especially with an upward-facing line spray near ground level, the presence of numerical instability makes the attainment of a solution rather costly in terms of computer time. Development of more efficient numerical algorithms would therefore be desirable for carrying out a complete line-spray optimization process.

The interaction of a line spray with a wind-driven vapor cloud is formulated as a steady-state planar, two-dimensional problem. Calculations are performed numerically in order to obtain quantitative estimates of wind effects, spray effects, and vapor cloud size effects on the diluted state of the cloud leaving the interaction region. This partially diluted cloud state is used as an input for three-dimensional, downwind atmospheric dispersion calculations described elsewhere [1].

2.1 Description of Calculation Technique. Gas motion due to wind and spray effects is solved by an iterative method similar to that of the TEACH-T computer code [2] for turbulent, recirculating, two-dimensional flow fields. This code incorporates a hybrid differencing scheme for the evaluation of convection terms in the conservation equations. A two-equation (k-ϵ) turbulence model is used to compute a value for the turbulent viscosity, which is added to the laminar viscosity to give an effective exchange coefficient for the conservation equations. Further details of the gas flow formulation, including gas conservation equations, the turbulence model modified for buoyancy and convergence tests can be found in [4] as well as in [23]. The droplet spray is coupled to this gas

Contributed by the Heat Transfer Division and presented at the ASME Winter Annual Meeting, Phoenix, Arizona, November 14-19, 1982. Manuscript received by the Heat Transfer Division March 7, 1983.

phase calculation by means of the Particle-Source-In-Cell (PSI-Cell) technique [3], whereby droplet evaporation, drag, and cooling act as sources of mass, momentum, and energy, respectively, for each grid cell of the gas calculations. Changes in droplet diameter, velocity, and enthalpy, which yield the source terms, are evaluated by use of the Reynolds number (based on the gas-droplet relative velocity) correlations for Sherwood number, drag coefficient, and Nusselt number, respectively, given in [3].

2.1.1 Boundary Conditions. Several different flow situations can be accommodated by the current numerical code. Two examples for the case of planar gas flow and planar droplet trajectories are: (*i*) a linear water curtain in quiescent air and (*ii*) a linear water curtain in wind-driven LNG vapor, which is the domain illustrated in Fig. 1. In both cases, the lower computational boundary or ground is adiabatic. A "law-of-the-wall" friction treatment is used to determine gas velocity and turbulence quantities adjacent to this boundary. When water droplets reach the ground plane, the droplet trajectory calculation is terminated.

To simplify the formulation and speed convergence of the iterative gas-droplet calculation scheme, an impervious, frictionless surface is taken as the upper boundary of the computational region in all cases. It has been found that the presence of this surface does not seem to affect results when the boundary height above the ground is more than three times the height above the ground of the downward directed spray curtain.

At the right, or downwind, vertical boundary (see Fig. 1), a zero gradient boundary condition is imposed for outflowing gases. Any air drawn into the computational region across this downwind boundary is assumed to be free of both turbulence and vorticity, with temperature and concentration levels equal to the undisturbed, ambient values. There are no qualitative changes in calculated results when the distance between the upwind and downwind boundaries is increased from 1.67 to 3.33 times the ground-level spray width in the flow plane.

The left, or upwind, vertical boundary is normally the entrance to the computational region for the wind and vapor. In this configuration, all flow properties are permanently fixed at prescribed values throughout the computation. Gas velocity parallel to the ground, gas temperature, gas concentration, and turbulence levels may be independently selected in the vapor cloud layer adjacent to the ground and in the air moving above the cloud.

When a line spray in quiescent (windless) air is to be simulated, the inflow left-hand boundary is switched to a symmetry plane, across which there is zero air flow. Gradients of gas temperature, concentration, turbulence quantities and the gradient of the gas velocity component normal to the ground are all set equal to zero across this boundary for the quiescent air condition.

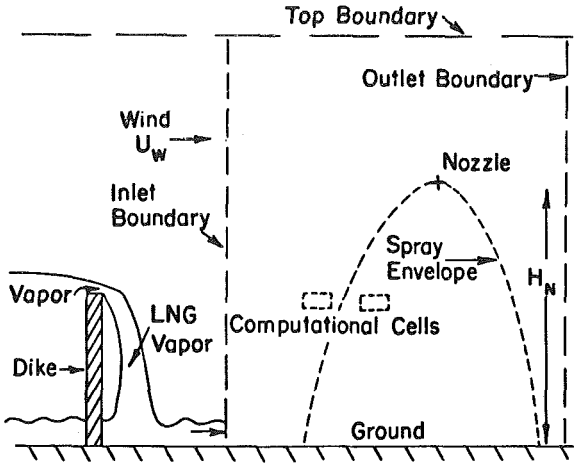

Fig. 1 Schematic of the calculation domain for wind-spray-vapor interaction

2.1.2 Inertial Relaxation of Body Force. The presence of gas-phase buoyancy forces comparable in strength to forces induced by the wind or by the spray has been found to cause numerical instability in certain cases, due to the coupling between the energy and vertical-direction momentum equations through the gas density. This instability, which is evident at windspeeds below 2 m/s for the methane dispersion problem, has been overcome in the present study by implementation of an inertial relaxation scheme described by Ideriah [5].

The relaxation scheme involves the insertion of a fictitious inertia force, which opposes the local buoyancy force by a term proportional both to the local density defect and to the change in vertical gas velocity between successive numerical iterations. When the gas-phase numerical iteration procedure has converged to a solution satisfying the conservation equations, changes in gas velocity from one iteration to the next will be negligible, and consequently, the opposing inertia force vanishes. Large changes in vertical gas velocity between successive iterations caused by changes in local buoyancy forces will be damped by this relaxation technique. Such numerical instability is most common at the beginning of the iteration process, when the gas phase calculations are far fom convergence.

2.2 Comparison of Calculated, Spray-Induced Flows With Experimental Data

Extensive calculations have been made previously [4] for

Nomenclature

b = plume radius based on $1/e$ of centerline V_p
d = droplet diameter
g = acceleration of gravity
H_N = height of line spray above ground
h_L = thickness of methane layer
$\dot{m}'$ = mass flow rate per unit length of dike or spray
$\dot{Q}$ = energy flow rate in plume or energy absorption rate by spray
T = absolute gas temperature
ΔT = $T - T_\infty$
U = horizontal component of gas velocity
V = vertical component of gas velocity
V_N = liquid injection velocity at spray origin
Y_i = mass fraction of component "i"
z = vertical distance above floor
ρ = gas density

Subscripts

$(\ )_{CJ}$ = ceiling-jet due to plume impingement
$(\ )_L$ = gas in partially diluted layer before spray interaction
$(\ )_m$ = mass median
$(\ )_N$ = liquid from nozzle
$(\ )_o$ = reference or ambient condition
$(\ )_p$ = buoyant plume
$(\ )_s$ = spray property
$(\ )_v$ = pure vapor to be dispersed
$(\ )_w$ = wind property
$(\ )_\infty$ = ambient condition

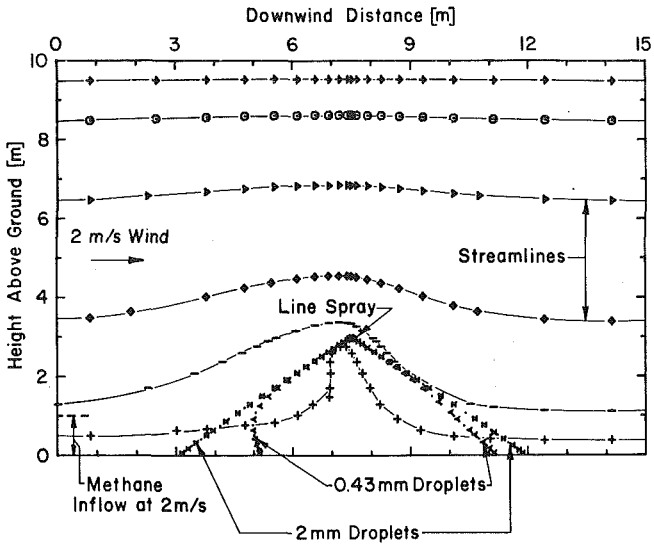

Fig. 2 Streamlines and outer trajectories of smallest and largest droplets—calculated with a 22 × 22 grid for a 3.0-m-high spray

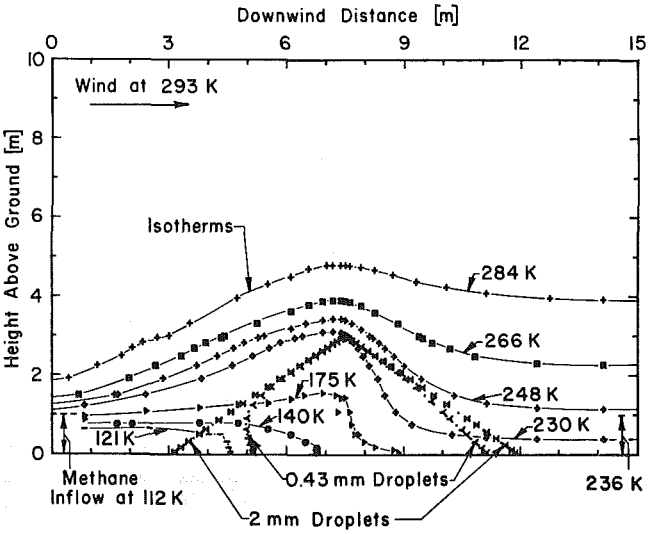

Fig. 3 Isotherms and outer droplet trajectories—calculated with a 22 × 22 grid for a 3.0-m-high spray

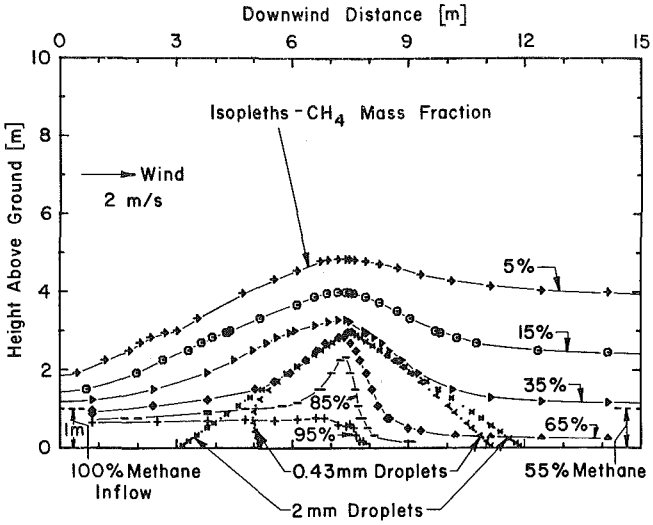

Fig. 4 Distribution of methane mass fraction calculated with a 22 × 22 grid for a 3.0-m-high spray

the case of a downward-facing, single-spray nozzle in an initially quiescent environment with ceiling and floor boundaries. The predicted axisymmetric flow induced by such a spray consists of air being drawn in radially and then directed downward toward the floor within the spray envelope. Calculations are in good agreement with measurements made by Heskestad et al. [6] for a range of nozzle pressures from 138–621 kPa (20–90) psi).

Measurements of air entrainment into a 5.3-m long, double water curtain under initially quiescent conditions have also been obtained by Heskestad et al. [7]. This water curtain is comprised of two staggered rows, one with four and the other with five downward facing Rockwood T-4-18 nozzles. The entrainment ratio (m^3 air/L water) within the sprays at a single location 4.12 m from the nozzles and 9 m below the ceiling is experimentally determined to be about 8.2 m^3/l. Calculated entrainment ratios for line sprays simulating such a double curtain (with both 16 × 16 and 22 × 22 computational grids) are found to increase to a peak value, 3 m from the spray origin, that is 30 percent less than the measured value. A possible explanation for the discrepancy may be the smaller lateral spray surface area available for entrainment with an idealized line spray compared to the actual three-dimensional spray curtain.

2.3 Physical Parameters. To analyze theoretically the effectiveness of a water curtain in the dispersal of LNG vapor, a hypothetical diked LNG spill is assumed [1], as illustrated in Fig. 1. Methane vapor will overflow the dike wall at rates per unit length of dike ranging up to about 3.45 kg/s•m for a 90 m × 90 m spill on an earth floor [9]. It is also assumed that the methane layer approaches the line spray mixed (due to dike overflow) with whatever quantity of ambient air is necessary to produce a specified layer thickness, h_L, vapor overflow rate, $\dot{m}_v'$ and layer motion matched to the windspeed. For instance, an assumed 1-m-thick methane layer moving at a 2 m/s windspeed will yield a 3.45 kg/s•m vapor overflow rate with an initial (or inlet) methane concentration close to 100 percent. However, higher windspeeds with the same layer thickness would only be consistent with partial dilution of the methane with warm, ambient air during dike overflow.

A simplified analysis of a two-dimensional adiabatic mixing process which would produce this required layer dilution is given in [21]. The analysis yields expressions for the temperature and the mass fraction of methane in the warmed and diluted incoming layer.

The water spray barrier is simulated in the calculations of vapor cloud dispersal by a line spray with droplet injection characteristics similar to those expected for real spray nozzles having a 40-mm-dia orifice. Obviously, flow details near such nozzles are not being calculated accurately. Droplets (assumed to be isothermal) are injected from the line source up to a maximum angle of 69 deg (1.2 rad) from the vertical along six uniformly distributed trajectories such that the water mass flow per unit angle of initial spray envelope is constant. A Rosin-Rammler [10] distribution of five discrete droplet sizes, each having 20 percent of total water mass flow, is used to represent a polydisperse water spray. Because of the low vapor cloud temperatures, freezing of spray droplets is monitored during the calculations so that heat released by ice formation can be taken into account in the gas phase energy equation.

2.4 Results: Methane Cloud Dispersal.

2.4.1 Calculated Flow Field. Figures 2, 3, and 4 show calculated streamlines, isotherms, and isopleths, respectively, for the set of boundary conditions listed in Table 1. The

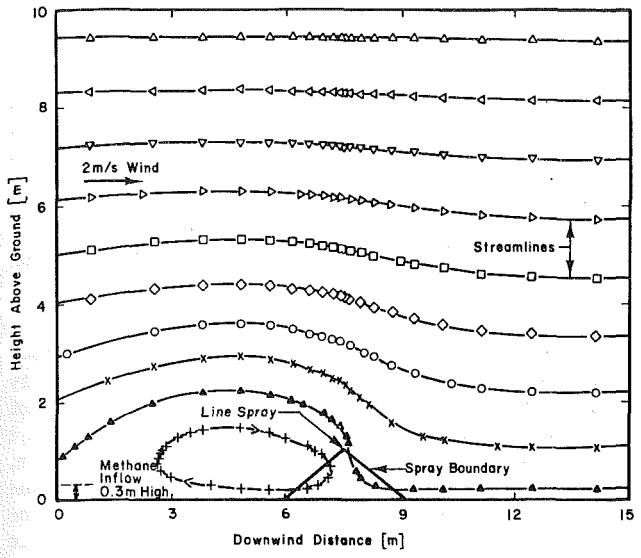

Fig. 5 Streamlines calculated with a 22 × 22 grid for a 1.0-m-high spray

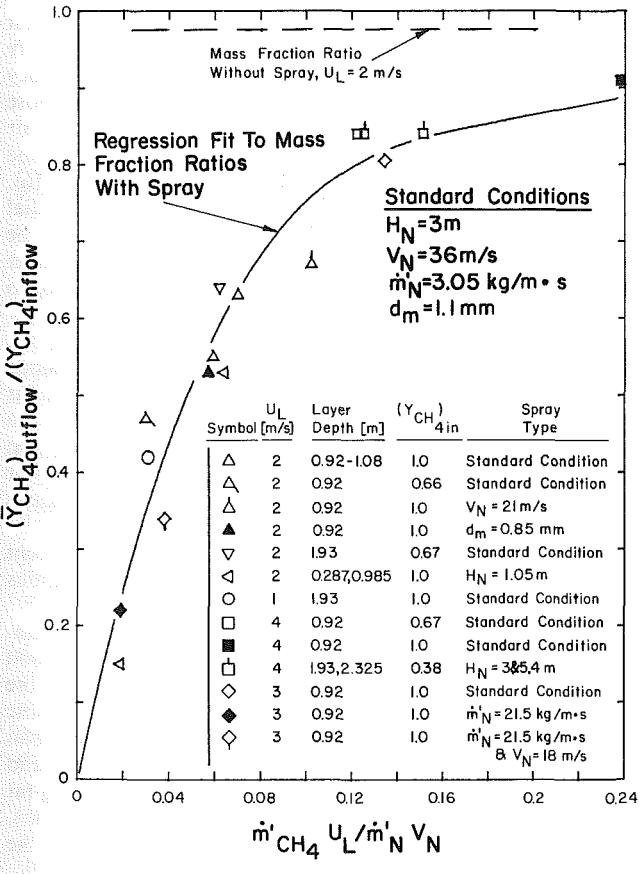

Fig. 6 Correlation of calculated methane mass fractions with ratio of methane inflow momentum to water injection momentum

computational cell size used consists of 22 × 22 grid nodes in a 15 m × 10 m domain. Figure 2 indicates that the methane layer is deflected upward on the upwind side of the spray and then redirected downward and diluted with entrained air on the downwind side of the spray. This upward layer deflection appears to be mainly due to the upwind force created by impingement on the ground of the spray-induced downward air flow. Streamline deflection is reduced considerably when the windspeed is increased from 2 to 4 m/s. At the higher windspeed, streamlines 0.5 m above the ground are virtually undisturbed by the water spray. More pronounced effects occur at lower windspeeds or for line sprays much closer to the ground. Figure 5 gives the gas streamlines calculated for the same windspeed of 2 m/s but a spray nozzle height of only 1 m. In this case, the upwind force created by spray impingement leads to an upwind ground jet, which recirculates the flow and strongly deflects ground level streamlines. A very similar streamline pattern results when windspeed is reduced to 1 m/s, but nozzle height is the usual 3 m value.

Warming of the layer as the result of the spray interaction is evident in Fig. 3, where it can be seen that the inflowing layer temperature of 112 K (−258°F) is increased to an average level of about 236 K (−35°F) in the lowest 1 m of outflowing gas. This same outflow layer is shown in Fig. 4 to contain an average methane mass fraction of 55 percent (69 percent by volume) due to spray dilution of the inflowing, 1-m-high layer of pure methane.

2.4.2 Predicted Effects of Windspeed, Vapor Flow Rate, and Spray Characteristics. Calculations have been performed with the 22 × 22 mesh to predict the effectiveness of spray dispersal for a range of methane vapor overflow rates. Results of these calculations are well-correlated in Fig. 6 by plotting the ratio of outflow methane mass fraction (averaged over the initial layer depth) to the inflow mass fraction versus the ratio of methane inflow momentum to the water momentum in the spray nozzle. The predicted dilution by the wind alone of a 1-m-thick pure methane layer moving at 2 m/s without a spray is also shown in the figure. It is clear from the figure that as the momentum ratio is decreased below about 0.1, the line spray becomes much more effective than the wind alone in diluting the methane layer. The mass fraction of methane in the ground level outflow is reduced to 20 percent of the inflow value, due to spray dilution, for a momentum ratio of about 0.02.

The correlation of calculated results should be very useful for the prediction of spray effectiveness, since in Fig. 6, variations in windspeed, layer thickness, initial (or inflow) layer dilution, water mass flow rate, $\dot{m}'_N$, and water injection velocity, V_N are incorporated. Results from a wind tunnel modeling study [19] of spray dispersion generally seem to confirm this correlation. It is not expected that the mass fraction ratio will depend only on the methane to nozzle momentum ratio when the inflowing layer is highly dilute and very thick due to mixing upstream of the spray barrier. However, such a dependence is found to be valid for initial CH_4 mass fractions down to 68 percent at a windspeed of 2 m/s and down to 38 percent at a windspeed of 4 m/s (see symbols in Fig. 6).

2.4.3 Increase In Vapor Cloud Buoyancy Due To Spray Heating. The warming of the methane during the spray interaction, which is evident in the isotherm plot of Fig. 3, results in an increase in vapor cloud buoyancy. In most cases, the cold, inflowing methane layer is heavier than air, even if partial dilution with ambient air is assumed during dike overflow. The methane layer outflow, however, after dilution and heating by the line spray, generally contains sufficient warmed methane to be lighter than air. This increase in layer buoyancy becomes most pronounced at values of methane to nozzle momentum ratio of about 0.04 to 0.12. Calculated values of the outflow excess gas density ($\rho - \rho_o$ averaged over the initial layer thickness) are found to be correlated by this momentum ratio when the mass median drop size is the assumed 1.1-mm value. Excess density ratios are predicted to be greater than zero (gas heavier than air) only for methane boil-off rates well above those of very large (90 m × 90 m) LNG spills [1] if a realistic spray is assumed.

Table 1 Practical parameters for calculation of methane dispersion

Methane vapor overflow rate	= 3.45 kg/s•m
Initial methane layer thickness	= 1 m
Initial methane mass fraction	= 1.0
Initial methane layer and windspeed	= 2 m/s
Line spray height	= 3 m
Water flow rate to spray	= 3.05 kg/s•m
Water injection velocity	= 36 m/s
Maximum drop trajectory angle	= 69 deg (1.2 rad) from vertical
Drop diameters	= 0.43, 0.79, 1.1 (mass median), 1.45, 2.0 mm
Initial drop temperature	= 286 K

Results for a mass median drop size, d_m, of 0.85 mm, instead of 1.1 mm, show a sharply increased outflow buoyancy, with an excess density, $\rho - \rho_o$, about 40 percent less than the correlated result for the standard drop size. Dilution of the methane layer in this particular case is virtually unaffected by the drop size reduction, as shown in Fig. 6 at a momentum ratio of about 0.06. There are several reasons for the insensitivity of layer dilution to a change in drop size. It is known [4, 6] that, for fixed nozzle geometry, effects of drop size on air entrainment rates are modest when the gravity force is a significant factor. Furthermore, induced air velocities within the spray at the momentum ratio of 0.06 are apparently not sufficient to really disperse the heavy methane layer, so changes in drop size are not going to change the success of this dispersal process significantly. However, heat transfer rates will be quite sensitive to the increased surface area to volume ratio of the smaller drops.

Heat transfer rates from the water droplets to the cold methane layer are enhanced by the predicted partial freezing of water droplets having a diameter of less than about 0.8 mm and complete freezing of the smallest droplets (diameter less than 0.4 mm) in the outer spray trajectories. The same Nusselt number correlation (square root of Reynolds number dependence) is used to compute heat transfer from both the isothermal liquid and the partially or completely frozen droplet. Calculations in which droplet heat transfer is "turned off" for the conditions of Table 1 reveal that both the cooling of the water droplets from an initial 286 K (55°F) down to 273 K (32°F) and the subsequent freezing of the smallest droplets is responsible for warming of the gas outflow from a heavier-than-air to a lighter-than-air condition. Without such droplet energy interactions, average outflow excess gas density is slightly positive (heavier than air), whereas the corresponding value is $-0.105\ \rho_o$ (lighter than air) with normal droplet heat transfer.

It is unlikely that dilution of the methane cloud down to a mass fraction of 2.8 percent (the lower flammability limit) will occur immediately downwind of a downward directed spray, although no attempt has been made to find an optimum set of spray characteristics. However, for the 1 to 4 m/s range of windspeeds, the flow 7 to 15 m downwind of the spray will have been warmed sufficiently to be lighter than air. Additional calculations by Zalosh et al. [1] show that this spray-warmed vapor cloud is likely to lift off the ground and rise as a buoyant plume for windspeeds below 4 m/s. Spray warming can thus reduce the ground level vapor cloud area at low windspeeds while natural atmospheric dispersion is more effective at higher windspeeds [1].

3 Plume-Spray Interaction

The axisymmetric flow induced by the impingement of a buoyant plume on a ceiling has been studied previously [11, 12, 13] in some detail, because such a flow is associated with hazardous fires in buildings. Plume impingement results in the development of a ceiling-jet of hot gas flowing radially outward from the plume axis. Automatic, fire-suppression sprinklers actuated by the ceiling-jet initiate a droplet spray which must cool the hot gas flow while providing a flux of liquid to the burning fuel. A classic problem in fire science is the prediction of sprinkler actuation patterns for given fuel geometries or even for fires of known intensity. Although the complete, three-dimensional problem is far too complex at present, a simpler, axisymmetric problem will be considered here to illustrate how the plume-induced flow is cooled by the spray. It will also be possible to investigate plume-induced modifications in droplet trajectories and floor-level water flux with this same axisymmetric flow.

3.1 Calculation Technique. A downward-facing spray is assumed to be located on the axis of a rising buoyant plume. The axisymmetric flow induced by this opposed plume-spray system is solved by the same iterative, numerical method used for the methane dispersion problem. Boundary conditions are identical to those applied to the quiescent air condition, previously discussed, except for the presence of a plume source at floor level on the symmetry axis (which replaces the symmetry plane of the previous problem). The plume source consists of a prescribed vertical inflow of hot gas over a limited floor radius. Froude numbers, based on this radius, are sufficiently small that a buoyancy dominated plume flow is developed close to the source.

3.2 Plume Calculations. Calculations are performed first with a plume source alone, without a spray, in order to verify the accuracy of the numerical technique for a buoyancy dominated flow. These calculations are similar to those described by Ideriah [14], who was able to reproduce with fair accuracy the measurements of mean and turbulent plume quantities obtained by George et al. [15] and Nakagome [16]. An upward air velocity of 4 m/s at 1000 K is fixed for a radial distance of 0.35 m from the symmetry axis as a test case in the present study. Such jet inlet conditions correspond to an inlet Froude number ($= V_0^2/g\ (\Delta T/T_\infty)\ b_o$) of 1.84, compared to a value of 1.6 used in the experiments of George et al.

In Fig. 7, values of centerline, upward plume velocity, V_p, and plume radius, b, (at which velocity falls to V_p/e) obtained with a 22 × 22 point mesh are shown. Results are very similar (within 10 percent) for the 16 × 16 point mesh. It can be seen that plume velocity accelerates to a peak value about 1 m above the floor and then decays as the expected $-1/3$ power of height, z, until the presence of the 10-m-high ceiling causes a more rapid decay. In the asymptotic plume region of $z^{-1/3}$ decay, the absolute magnitude of V_p is about 16 percent greater than that expected from the experimental correlations of George et al. [16] and Delichatsios [17].

A comparison of calculated excess centerline plume temperature with these same correlations again shows good agreement with the expected $z^{-5/3}$ decay about 1 m from the plume source. However, the absolute magnitude of the calculated excess temperature is about 50 percent higher than expected [17], probably due to poor turbulence modeling and the errors associated with a highly variable mesh spacing (at midheight on the plume axis, $\Delta x \approx 0.5$ m and $\Delta y \approx 0.1$ m). From 1 to 9 m above the floor, the calculations yield the following centerline temperature behavior:

$$\Delta T_p/T_\infty = 1.19 \times 10^{-3}[\mathrm{m}^{5/3}/\mathrm{W}^{2/3}]\dot{Q}_P^{2/3}(z+1.3)^{-5/3}$$

It is shown in Fig. 7 that the characteristic plume radius based on upward velocity is predicted to increase proportional to height z. The proportionality constant of 0.12 implies an entrainment constant for Gaussian profiles of 0.1, which is within 10 percent of values previously measured [18]. Calculations of plume radius based on excess temperature yield lower values than those based on velocity, with the characteristic temperature radius being about 10 percent of plume height. This result is also consistent with the measurements of George et al. [15].

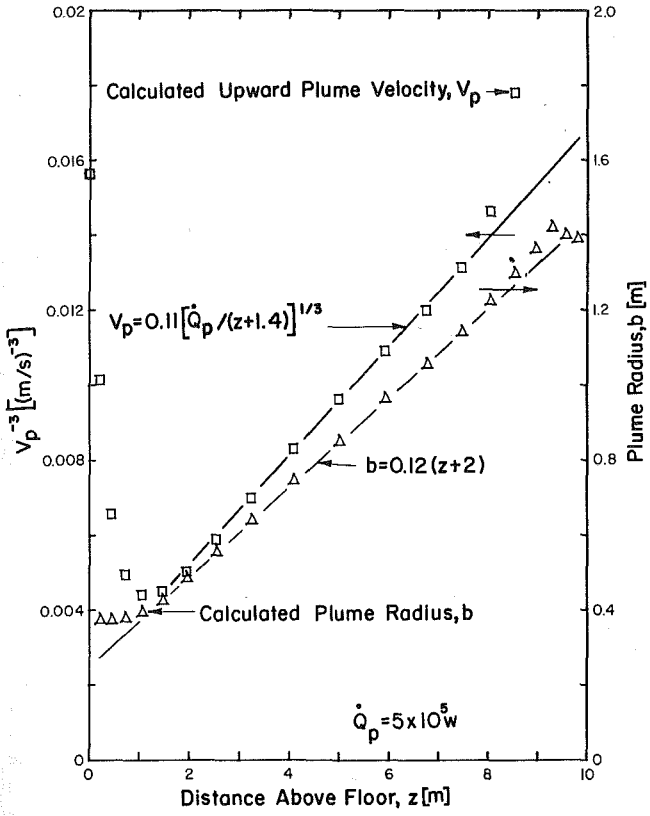

Fig. 7 Upward centerline velocity and characteristic velocity radius predicted for the plume above a 1000 K, 4 m/s, 0.7-m-dia. jet source in floor

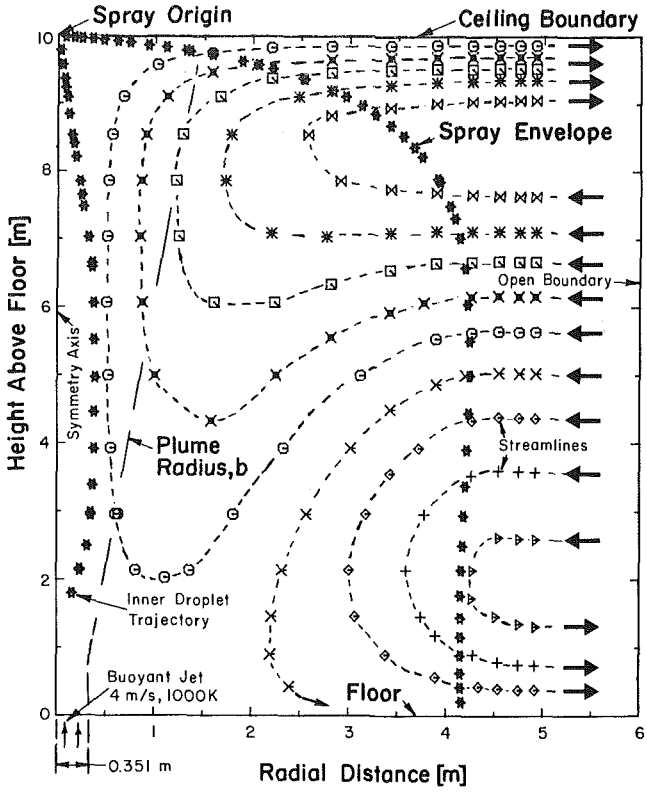

Fig. 8 Calculated gas streamlines and trajectories of 1-mm-dia. droplets induced by a spray on the axis of a plume. Plume radius shown is from Fig. 7.

3.3 Opposed Spray With Plume. A series of calculations have been performed for several different droplet sprays at the ceiling, on the plume axis. Spray calculations involve only mono-sized droplets injected downward along a discrete number of initial trajectory angles. Results are found to be relatively insensitive to variations in the number of initial trajectory angles from 8 (the standard case) up to 30. Polydisperse sprays were not investigated in this portion of the study.

3.3.1 Streamlines: Sprinkler Spray. To simulate the spray from a fire suppression sprinkler, droplet trajectories originate from a point source at the ceiling with uniformly distributed initial trajectory angles up to a maximum of 90 deg from the vertical. Details of the spray near the nozzle are obviously not simulated accurately. The liquid mass flow rate injected along each trajectory is adjusted to give a uniform mass flow per steradian in the spray envelope. As discussed in detail in [4], all droplets are injected at a single velocity determined by the characteristics of the spray device being simulated. A measurement [19] of the initial axial momentum of the spray from an automatic sprinkler with a 12.7-mm-dia orifice has been used to determine that this injection velocity should be about 12.4 m/s when the nozzle pressure drop is 207 kPa (corresponding to a water flow rate of 1.94 kg/s).

With the simulated sprinkler spray at the ceiling boundary and the plume source of the preceding test case (Fig. 7) at the floor boundary, a numerical solution is obtained for the resultant flow field. Induced air streamlines and droplet trajectories calculated with a 16 × 16 node mesh are shown in Fig. 8. Several interesting features of the spray-plume interaction can be observed in this figure. The ceiling-jet region formed by plume impingement, as well as the upward air flow in the plume itself, still exists in spite of the downward thrust of the droplet spray. However, the spray causes a widening of the plume upward velocity profile as well as a strong, downward deflection of air being entrained into both the plume and the spray from the ambient. This downward deflection by the spray leads to the formation of a radially outward floor-jet, thereby preventing inflow into the lower half of the computational region from ever reaching the plume.

Another feature of interest is the behavior of droplets only on the innermost trajectory of the spray. The downward motion of such droplets is completely stopped by the upward plume thrust within 2 m of the floor, as shown by the last trajectory symbol in Fig. 8. Thereafter, the 1-mm-dia droplet is carried up with the plume for several meters until the droplet begins falling again. This process can continue for many cycles due to the defined value of zero radial-direction gas velocity in the finite difference cell on the symmetry axis. More recent results have shown that use of gas velocities linearly interpolated between values at nodal points for the droplet calculations avoids such cyclic motion. For the solutions presented here, the droplet trajectory calculation is terminated once the initial downward motion stops in order to eliminate minor numerical instability caused by the complex droplet trajectory.

3.3.2 Spray Cooling. The effectiveness of a ceiling spray in cooling the test case plume has been studied by varying the spray thrust through changes in water flow rate and injection velocity. For this purpose, a narrower spray is used with eight initial trajectory angles uniformly distributed up to a maximum of 57 deg (1 radian) from the vertical symmetry axis. A truer simulation of a continuous spray is possible when this limited number of droplet trajectories is concentrated into the narrower spray envelope. Resultant gas flow streamlines are qualitatively very similar to those in Fig. 8.

Results obtained with the 16 × 16 point mesh are illustrated

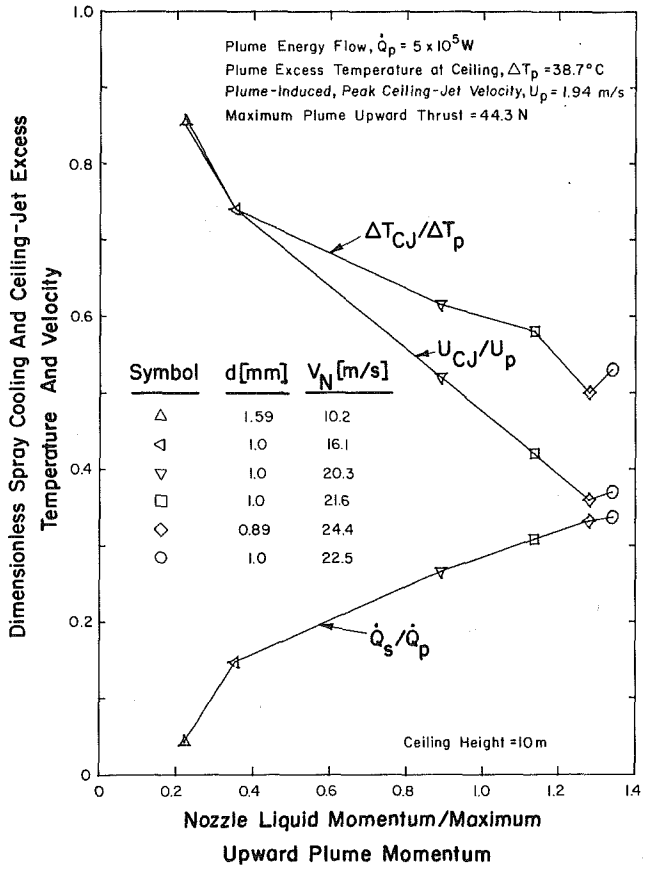

Fig. 9 Calculated effect of a spray on the maximum ceiling-jet temperature and velocity

in Fig. 9, where all quantities are compared to characteristic values in the undisturbed, test-case plume discussed in previous sections. Variations are made in nozzle liquid momentum (essentially, the downward thrust of the spray) from 0.2 to 1.4 times the maximum upward momentum of the undisturbed plume. Over this range of momentum ratios, the total thermal energy flow absorbed by the spray, $\dot{Q}_s$, increases from 4 to 34 percent of the total undisturbed plume energy flow. The peak gas velocity and excess gas temperature in the ceiling jet are also shown in Fig. 9 to be decreasing sharply in the plotted range of momentum ratios to 37 and 50 percent, respectively, of the corresponding undisturbed quantities.

All of these trends seem to continue for the 1-mm drop size when the momentum ratio is increased to 2.24 by increasing V_N to 25.6 m/s. In this case, complete solution convergence is not attained due to the presence of numerical instabilities, perhaps because the stronger spray begins a transition from a plume-dominated flow regime to one dominated by the spray-induced flow field. Significant changes from the general trends in ceiling jet velocity and excess temperature are seen to be caused by variations in droplet diameter from the 1-mm value. Information such as that provided by Fig. 9 should be very useful for the optimization of spray designs.

4 Conclusions

Two problems involving interactions of droplet sprays with buoyant flows have been solved numerically. Calculated properties of the interaction flow field in many cases appear to depend on a ratio of droplet spray momentum to that induced by the buoyancy source. It is expected that improved correlations of this type, developed from more extensive calculations, should prove to be useful for the optimization of water spray protection.

The numerical techniques used for the preceding spray interaction problems allow a description of spray-induced flow fields to be obtained, but at a considerable cost in computer time. For instance, about 120 to 150 iterations of the gas-phase equations are required to obtain a converged solution to the methane dispersion problem, even with a relatively coarse computational grid of 22 nodes in each of the two dimensions. This number of iterations translates into a central processor unit (CPU) time of 10 to 20 min on the IBM 370/158. Quantitative accuracy for such problems with large-scale flow domains probably demands the use of at least twice as many grid nodes, with a consequent order of magnitude increase in CPU time.

Much more efficient gas-phase algorithms are clearly needed to make accurate numerical solutions of buoyant turbulent flows in large-scale domains practical. Excessive CPU time is not the only manifestation of the need for such algorithms. Problems encountered with numerical stability in the solution of certain spray-plume and upward spray-methane layer interactions and the errors in predicting centerline plume temperatures and velocities also demonstrate the need for improvement. The TEACH-T computer program, used here for the gas-phase calculations, is capable of handling a wide range of physical flow situations, as demonstrated in the present work. Only a portion of the program handles the recirculating gas flow solution and it is in this area where improved algorithms can result in more accurate, stable calculations with sharply reduced CPU times. An effort to develope such algorithms is now in progress at Factory Mutual Research [22], the National Bureau of Standards [20], and at other institutions.

Acknowledgments

The help of Dr. Robert Zalosh, Dr. Gunnar Heskestad, and Ms. Mary K. Mathews in the performance of the LNG vapor calculations at Factory Mutual Research Corporation is deeply appreciated. These dispersion calculations were part of a contract from the Gas Research Institute (GRI Contract No. 5080-352-0386), which provided many helpful comments through the GRI Advisory Board, Mr. Sami Atallah, and Dr. Steve J. Wiersma. The support and encouragement of Dr. John de Ris of the FMRC Basic Research Department during the spray-plume work is gratefully acknowledged.

References

1 Zalosh, R. G., Alpert, R. L., and Heskestad, G., "Dispersal of LNG Vapor Clouds With Water Spray Curtains," Factory Mutual Research Corporation Report prepared for Gas Research Institute, FMRC J.I. OFOR6. RK, Dec. 1981.

2 Gosman, A. D., and Ideriah, F. J. K., "TEACH-T: A General Computer Program for Two-Dimensional, Turbulent Recirculating Flows," Imperial College of Science and Technology, Mechanical Engineering Department, London S.W. 7, England, June 1976.

3 Crowe, C. T., Sharma, M. P., and Stock, D. E., "The Particle-Source-In-Cell Model for Gas Droplet Flows," *Journal of Fluids Engineering*, June 1977, p. 325.

4 Alpert, R. L., and Mathews, M. K., "Calculation of Large-Scale Flow Fields Induced by Droplet Sprays," *Polyphase Flow and Transport Technology*, ASME, New York, 1980, pp. 115-128.

5 Ideriah, F. J. K., "An Inertial Relaxation Method of Curing Numerical Instability in Prediction of Flows Influenced by Severe Body Forces," *Journal of Mechanical Engineering Science*, Vol. 22, No. 3, 1980, pp. 153-156.

6 Heskestad, G., Kung, H. C., and Todtenkopf, N., "Air Entrainment Into Water Sprays and Spray Curtains," ASME Paper No. 76-WA/FE-40, 1976.

7 Heskestad, G., Kung, H. C., and Todtenkopf, N., "Air Entrainment Into Water Sprays," Factory Mutual Research Corporation Report RC77-TP-7, Nov. 1977.

8 Moodie, K., "Experimental Assessment of A Full-Scale Water Spray Barrier for Dispersing Dense Gases," *Proceedings: Symposium on The Containment and Dispersion of Gases by Water Sprays*, The Institution of Chemical Engineers, Manchester, England, Nov. 11, 1981.

9 Reid, R. C., "Boiling of LNG on Typical Dike Floor Materials," MIT LNG Research Center Report, NTIS #PB80-205362, March 1980.

10 Rosin, P., and Rammler, E., *Journal of Inst. Fuel*, Vol. 7, 1933, p. 29.

11 Alpert, R. L., "Turbulent Ceiling-Jet Induced by Large-Scale Fires," *Combustion Science and Technology*, Vol. 11, 1975, pp. 197–213.

12 You, H. Z., and Faeth, G. M., "Ceiling Heat Transfer During Fire Plume and Fire Impingement," *Fire and Materials*, Vol. 3, No. 3, 1979, pp. 140–147.

13 Zukoski, E. E., Kubota, T., and Veldman, C. C., "Experimental Study of Environment and Heat Transfer in a Room Fire," Technical Report No. 1 to NBS Center for Fire Research, Grant No. 5-9004, California Institute of Technology, Pasadena, Calif. 1975.

14 Ideriah, F. J. K., "Turbulent, Axi-Symmetric Buoyant Plumes in Uniform and Stably Stratified Surroundings," *Proceedings of the First International Conference on Numerical Methods in Thermal Problems*, Edited by R. W. Lewis and K. Morgan, Massachusetts Institute of Technology, 1979.

15 George, W. K., Jr., Alpert, R. L., and Tamanini, F., "Turbulence Measurements in an Axisymmetric Buoyant Plume," *International Journal of Heat and Mass Transfer*, Vol. 20, 1977, pp. 1145–1154.

16 Nakagome, H., and Hirata, M., "The Structure of Turbulent Diffusion in an Axi-Symmetrical Thermal Plume," *Symposium on Turbulent, Buoyant Convection*, Dubrovnik, Yogoslavia, 1976.

17 Delichatsios, M. A., "Time Similarity Analysis of Unsteady Buoyant Plumes in Neutral Surroundings," *Journal of Fluid Mechanics*, Vol. 93, pt. 2, 1979, pp. 240–250.

18 Morton, B. R., Taylor, G. I., and Turner, J. S., "Turbulent Gravitational Convection from Maintained and Instantaneous Sources," *Proceedings of the Royal Society A*, Vol. 236, 1956, p. 1.

19 Heskestad, G., Report No. GRI-83/0019, Gas Research Institute, Chicago, Ill., Nov. 1983.

20 Lewis, J. G., and Rehm, R. G., "The Numerical Solution of a Non-separable Elliptic Partial Differential Equation by Preconditioned Conjugate Gradients," *Journal of Research of the National Bureau of Standards*, Vol. 85, No. 5, Sept.-Oct. 1980, pp. 367–390.

21 Alpert, R. L., "Calculated Interaction of Sprays With Large-Scale Cross Flows and Buoyant Opposed Flows," Factory Mutual Research Corporation Technical Report, RC82-BT-3, J. I. No. OEOJ4.BU, July 1982.

22 Beier, R. A., de Ris, J., and Baum, H., "Accuracy of Finite Difference Methods in Recirculating Flows," *Numerical Heat Transfer*, Vol. 6, No. 3, 1983, pp. 283–302.

23 Markatos, N. C., and Malin, M. R., "Mathematical Modeling of Buoyancy-Induced Smoke Flow in Enclosures," *International Journal of Heat and Mass Transfer*, Vol. 25, No. 1, 1982, pp. 63–75.

Asymptotically Large Area Fires

R. D. Small

D. A. Larson

H. L. Brode

Pacific-Sierra Research Corporation,
Los Angeles, Calif. 90025

The fluid dynamics of large area fires is considered. The modeling of such fires using asymptotic plume theories, rotating plume theories, and hydrocode simulations is briefly reviewed, and a new model describing the strongly buoyant flow of the burning region and its transition to a weakly buoyant, free-convection column is presented. The new model simulates combustion processes by a volume heat addition, and allows large changes in density and temperature. Jump conditions applicable at the fire periphery are used to effect model problem closure, thus permitting calculation of the induced fire winds independent of a far-field analysis. Sample results show the turning and decay of a high-velocity inflow to form a nearly vertical flow, and illustrate how the generation of high-velocity fire winds is affected by the dimensions of the burning region, heat release, and the production of buoyancy and pressure gradients.

Introduction

Many area fires that destroyed large sections of cities have been documented. Such fires are characterized by large-aspect-ratio (radius/flame height) burning regions. For asymptotically large fires, the fuel bed dimension, column diameter, and scale height of the atmosphere may be of similar order. In addition to a source region characterized by a strongly buoyant flow and a large convection column, a high-velocity lower inflow layer, an upper outflow layer, and a far field can be distinguished.

The characteristics of the free-convection column are determined by the flow in the burning region. The heat release generates large temperature and density gradients (buoyancy) and corresponding radial and vertical pressure gradients. Those pressures govern the inflow of ambient air into the fire as well as the turning and transition of the flow to form a free-convection column. The pressure gradients are modified with altitude by the rapid decay of the column gas temperatures and densities to ambient values. That relaxation occurs within several flame heights of the burning region and is aided by radiation and turbulent mixing. The velocity and temperature profiles established at the convection column base thus depend strongly on the fire-generated buoyancy field.

For small free-burning fires (aspect ratio of order one), the fire-region inflow can be partially provided by viscous entrainment of ambient air. The presence of low-momentum, low-energy air at the fire-column edge encourages the development of narrow regions of high-velocity flow (thin plumes). For large area fires, entrainment of ambient air at the periphery contributes a much smaller fraction to the mass balance, and the flow is more directly governed by the buoyancy-induced pressures.

Asymptotic Theories

Classical plume theories [1, 2] assume a balance of forces that neglects dynamic pressure effects, equating buoyancy and turbulent diffusion with a sustained vertical flow. Entrainment of ambient air into the plume is taken as proportional to the centerline velocity, and profiles of velocity and density difference are similar at all heights. Radial velocities are of lower order than axial velocities. Thus the radial momentum equation appears only indirectly through the use of an empirical entrainment law. For order-one-aspect-ratio fires, radial and vertical velocities in the burning region are of similar magnitude. For large-aspect-ratio fires, mean radial velocities are of greater magnitude than mean vertical velocities. In either case, analysis of the flow near the burning region requires solution of a more complete momentum balance.

Asymptotic plume theories [3–12] best describe the weakly buoyant motion above a relatively small, free-burning fire. For large area fires that generate a convection column characterized by comparable radial and axial dimensions, a new description of the buoyant motion is required.

Swirling Flows

A noted feature of large area fires is the high-velocity influx that occurs at the fire boundary [13, 14] – estimated as high as 90 m/s [15]. However, measurements have not been made to either support those estimates or define the functional dependence of the induced inflows on fire size, heat release, and the characteristics of the atmosphere (moisture distribution, lapse rate, ambient winds).

For large area fires, entrainment of mass at the fire periphery cannot account for the high inflow velocities. Radial pressure gradients generated by the buoyancy field or imposed on the burning region by a large, swirling column [16] could reasonably produce inflow velocities of the magnitude observed. Whether a large fire will always generate a swirling column remains doubtful [17]. Documentation of catastrophic fires [18, 19] has not been precise enough to be conclusive. Controlled large-scale experiments have only infrequently exhibited a central rotating structure [20–22] and analysis has shown that such flows will rarely occur [23].

The creation of a swirling column depends on the concentration of ambient vorticity by the buoyancy-induced radial pressure gradient [17, 20, 23]. Sources of ambient vorticity include the earth's rotation (generally negligible for the scales considered) and wind shear produced by horizontal gradients in density and velocity.

The rotation of a rising buoyant column effectively reduces the radial entrainment of ambient air into the plume and thus the level of turbulent mixing [25–27]. A slower decay of the buoyancy with altitude results. The greater plume height implies a more persistent pressure and density difference and a correspondingly larger radial pressure gradient at the ground plane. Since the boundary layer at the ground reduces the rotation to zero, the pressure gradient induces a radially directed inflow. The magnitude of the fire winds depends to leading order on the pressure gradient.

Though the theories describing swirling free-convection plumes explain the high-velocity radial inflows generated by large fires, central swirling plumes have infrequently been observed. Numerical solutions of nonswirling flows as well as direct analysis of the source region have shown that high-velocity fire winds may also be generated by pressure gradients resulting solely from the production of buoyancy.

Contributed by the Heat Transfer Division for publication in the JOURNAL OF HEAT TRANSFER. Manuscript received by the Heat Transfer Division May 23, 1983.

Numerical Solutions

Conceptually, the full Navier-Stokes, energy, continuity, species, and combustion equations [28] can be solved numerically and the flow field defined in an infinite domain. For many problems of interest, current models of the burning processes, flow chemistry, and turbulent structure do not justify such a rigorous modeling. Accordingly, a number of simplifying assumptions have been used [29–33]. They include an isothermal boundary condition to model the heat release by combustion [29–31], the Boussinesq approximation [29–32], either a constant eddy diffusivity [29–31, 33] or k-ϵ model [32, 33] to describe the turbulent structure, simple radiative-loss models [32, 33], and a finite-volume heat source [33].

With the heat addition modeled by an isothermal condition at the ground, the production of buoyancy depends on the diffusion of energy from the boundary. Coupled with the Boussinesq approximation, use of an isothermal condition restricts the solution to weakly buoyant motions similar in principle to flows generated by urban heat islands [34, 35]. Though the fire-induced flow is represented more accurately as the distance from the source increases, the solution should describe at least qualitatively the momentum interchanges occurring near the fire.

Current solutions have shown that large inflow velocities are generated near the source region and depend on the amount of heating. Smith, Morton, and Leslie [30] relate the induced fire winds to the dynamic pressure field generated by the buoyancy. The pressure gradients are greatest in the neighborhood of the fire zone and decay rapidly with distance from the fire perimeter. The generation of a high-velocity inflow near the fire by pressure gradients rather than by viscous entrainment is consistent with the observations of Cox and Chitty [36].

An interesting feature of several large-scale solutions has been the development of well-defined vortex structures. Delage and Taylor [35] describe early-time roll motions above an urban heat island as well as the development of a mesoscale recirculation [34, 35]. Luti and Brzustowski [31] examine the generation of lee-side vortices by a heat source in crossflow.

Larson, Brode, and Small [33] consider the strongly buoyant flow produced by a large area fire (10-km radius) and describe the time history of several vortex motions. The volume heat addition generates several rotating cells in the source region. The continued, constant production of buoyancy generates a strengthening inflow that gradually imposes a radially directed flow in the source region. As the inflow strengthens, a strong vortex develops above the fire perimeter and is eventually shed. The outward motion of that vortex produces a stronger inflow that extends approximately one fire radius beyond the fire boundary. As the vortex moves to infinity, the inflow weakens and roll motions reappear in the burning region. The cycle repeats at approximately 20-min intervals.

The numerical simulations of large fires have improved understanding of the hydrothermodynamics of strongly buoyant flows. The high-velocity inflows generated by fire are related to the production of buoyancy and pressure gradients rather than to the viscous entrainment of ambient air. Vortex motions resulting from instabilities at the fire perimeter also influence the mass addition to the burning region as well as the fire dynamics.

Source Region

The high-velocity inflow generated by an area fire and the characteristics of the initial free-convection flow are determined by the burning-region interactions. Formulation of an appropriate equation set to describe the flow physics depends on the scale of the heat addition and the size of the burning region. As opposed to weakly heated flows controlled by the diffusion of momentum and energy, the volume heat addition implies a strong coupling of buoyancy forces and inertia.

The size of the burning region governs the ordering of terms in the conservation equations. For a heat addition volume defined by a mean flame height H and a fuel bed radius R, conservation of mass implies

$$\frac{u}{v} \sim \frac{R}{H} \tag{1}$$

If $R/H \sim 0(1)$, the radial (u) and axial (v) velocities and the corresponding acceleration terms are of similar order. For $R >> H$, the characteristic radial velocity is much greater than the mean axial velocity and the governing momentum equations may be simplified.

This section considers the class of flows generated by an asymptotically large fire ($R >> H$). An analytical model for the quasi-steady flow in and around the burning region is developed [37], and sample results illustrate the solution dependence on heat addition and fire size.

For the large fires considered, the turbulent motion is expected to limit the flame heights [38] such that a more or less uniform heating zone height H may be defined. A spatially dependent volume heat release function $Q_0 \times q(r, y)$ is thus used to model the combustion processes in a finite, axisymmetric region. Q_0 represents the mean rate of heat release, and $q(r, y)$ is an 0(1) variable describing its spatial distribution. Since 0(1) variations in temperature and density are expected, all density derivatives are retained.

The conservation equations are scaled using ambient (ground-level) thermodynamic values (P_a, ρ_a, T_a) and the characteristic burning region lengths, H and R. The asymptotically large burning region is thus represented by an order-one domain with comparable radial (r/R) and axial (y/H) dimensions. The disparate scaling lengths introduce a small parameter,

$$\epsilon = \frac{H}{R}, \quad \epsilon << 1 \tag{2}$$

which can be used to order terms. The burning-region aspect ratio is defined as ϵ^{-1}.

Radial velocities are scaled with an arbitrary velocity U, and in order to preserve the two-dimensional structure of the continuity equation, axial velocities are scaled by ϵU. Since a subsonic flow is expected, the thermodynamic pressure P is defined as

$$\frac{\hat{P}}{P_a} = 1 + \delta P, \quad \delta = \frac{U^2}{P_a/\rho_a} \tag{3}$$

where P represents a perturbation pressure. In scaled variables, the leading-order set of conservation and state equations [39] is

$$\frac{\partial}{\partial r}(r\rho u) + \frac{\partial}{\partial y}(r\rho v) = 0 \tag{4a}$$

$$\rho\left(u\frac{\partial u}{\partial r} + v\frac{\partial u}{\partial y}\right) = -\frac{\partial P}{\partial r} + M_1\left(\frac{1}{r}\frac{\partial}{\partial r}\left(r\frac{\partial u}{\partial r}\right) - \frac{u}{r^2}\right) + M_2\frac{\partial^2 u}{\partial y^2} \tag{4b}$$

$$\frac{\partial P}{\partial y} + A\rho = 0 \tag{4c}$$

$$\rho\left(u\frac{\partial T}{\partial r} + v\frac{\partial T}{\partial y}\right) = B(q(r,y) - \sigma(T^4 - 1))$$

$$+K_1\left(\frac{1}{r}\frac{\partial}{\partial r}r\frac{\partial T}{\partial r}\right)\Big)+K_2\frac{\partial^2 T}{\partial y^2} \tag{4d}$$

$$\rho T=1 \tag{4e}$$

where

$$A=\frac{gH}{U^2},\quad B=\frac{\gamma-1}{\gamma}\left(\frac{Q_0R}{P_aU}\right)$$

$$M_i=\frac{\epsilon^{3-2i}\mathcal{E}_i}{\rho_aUH},\quad K_i=\frac{\epsilon^{3-2i}k_i}{\rho_ac_pUH}$$

$$\sigma=4\pi\hat{\sigma}k^*\frac{T_a^4}{Q_0}=4\pi\hat{\sigma}T_a^4\left(\frac{k^*H}{Q_0H}\right) \tag{5}$$

$\mathcal{E}_i$ and k_i are dimensional mixing coefficients, the specific heat capacity c_p is assumed constant, $\hat{\sigma}$ is Stefan's constant, and k^* is the reciprocal of the radiation mean free path (assumed constant). In this formulation, eddy viscosities are used to model the turbulent transport of momentum and energy, and the graybody approximation [9] is used to specify the radiative cooling of the hot gas/smoke mixture.

An appropriate value for the radial velocity scale U is found by balancing the terms for convective transport and heat addition in the energy equation so as to properly represent the physics of a flow driven by combustive heating. Accordingly, setting $B = 1$, the characteristic fire-wind velocity is

$$U=\frac{\gamma-1}{\gamma}\left(\frac{Q_0R}{P_a}\right)\equiv\frac{\gamma-1}{\gamma}\left(\frac{Q_0H}{P_a\epsilon}\right) \tag{6}$$

Since an asymptotically large fire is considered, the axial momentum equation (4*c*) reduces to a hydrostatic balance. However, the density (buoyancy) depends directly on the temperature (equation (4*e*)), and hence on the combustive heating introduced in the energy equation. Because of the strong heating characteristic of large area fires, the density in the burning region exhibits an 0(1) variation, whereas the ambient density varies with height as $0(\epsilon^2)$. Equations (4) thus describe a flow driven by the strong heat release.

Boundary Conditions

The type of boundary value problems to be solved depends on the relative magnitudes of the coefficients M_i and K_i, $i = 1, 2$. When those coefficients are all 0(1), the energy and momentum equations are elliptic. Special cases arise for M_1, $K_1 << M_2, K_2$ and $M_2, K_2 << M_1, K_1$. With $M_2, K_2 << M_1, K_1$, the problem is essentially parabolic in the vertical direction though constrained, somewhat unusually, by conditions at infinity.

Measurements defining the magnitudes or relative values of the turbulent exchange coefficients have not been performed. However, observations of experimental burns simulating large urban area fires [29, 40] indicate that the flow is highly turbulent and that the level of turbulence influences the effective thickness of the axial column flow. For small fires with low levels of mixing, a thin, high-velocity plume is formed. For larger fires with increasing levels of turbulence, the column thickness approaches a value comparable to the fuel bed radius. These observations suggest a dependence of the turbulence levels on the heat release and burning-region dimensions as well as implying a strong interaction between the mixing and buoyancy-driven updraft. Mathematically, the second-derivative terms with respect to radius provide such a coupling and, further, allow the induced inflow at the boundary to depend on the extent and burning characteristics of the heating zone.

At the top of the source region, the flow should asymptote to the weakly buoyant flow characteristic of the free-convection column, implying that $M_2, K_2 \to 0$ while M_1, K_1 remain 0(1). Radial shear should also characterize the source region flow, at least near the center of the fire. Except in a thin sublayer near the ground, the radial diffusion of momentum and energy should dominate the axial diffusion. Accordingly, we assume $M_2, K_2 = 0$ and consider the solution of the nearly parabolic boundary value problem[1] prescribed by equations (4) and the following boundary conditions. The reduction to a parabolic equation set approximates the flow physics especially in the lower portion of the burning region. However, this model preserves the mathematical structure of the elliptic boundary value problem as well as producing a consistent and reasonable description of the mean fluid dynamics in the turning region ($r \lesssim 1$; $y \lesssim 10$).

At the symmetry axis and at the ground plane, the boundary conditions are

$$u=\frac{\partial T}{\partial r}=0 \quad \text{on } r=0 \tag{7a}$$

$$v=0 \quad \text{on } y=0 \tag{7b}$$

The boundary condition used at the top of the source region should reflect the restructuring of the high-velocity, high-temperature radial flow to a slower-moving, weakly buoyant, nearly vertical flow characteristic of the free-convection column. Based on a formal matching of asymptotic expansions [39] (in the limit $y\to\infty$, $\epsilon\to 0$) for the separate source region and convection column flows, it is found that

$$P+Ay\to 0 \text{ as } y\to\infty,\quad r\le 1 \tag{7c}$$

It can be shown that equation (7*c*) also implies $u\to 0$, $T\to 1$ as $y\to\infty$.

The edge boundary conditions should reflect the local flow dynamics as well as the characteristics of the source region. At the fire boundary ($R = 1$), the thermodynamic variables are discontinuous to leading order. In addition, the level of turbulence in the burning region should be much larger than comparable ambient values. This local behavior suggests the use of jump conditions to relate the ambient inflow to the source region flow. The jumps occur in a region ΔR, which may be associated with the turning region "pinch point" or edge streamline curvature. For the asymptotically large area fires considered, $\Delta R/R\to 0$.

Writing equations (4) in conservation form and integrating from $r = 1^-$ to $r = 1^+$ yields the following jumps in mass, momentum, and energy at the fire periphery

$$[\rho u]=0$$

$$[\rho u^2]=-[P]+\left[M_1\frac{\partial u}{\partial r}\right]$$

$$[\rho uT]=\left[K_1\frac{\partial T}{\partial r}\right]$$

where $[W] = W^+ - W^-$. In performing the integrations, it is assumed that, to leading order, u, v, P, and T remain finite at $r = 1$. Integrals of ρrv, ρruv, rv, rT^4, and P thus approach zero in the limit $\Delta r\to 0$. Since the leading-order ambient density and temperature are $\rho^+ = T^+ = 1$, integration of equation (4*c*) yields $P^+ = -Ay$ on $R = 1^+$. Expanding the jump conditions, using the leading-order thermodynamic properties, and assuming $M_1^+, K_1^+ << M_1^-, K_1^-$, the boundary conditions applicable at $r = 1$ are

$$\frac{\partial u}{\partial r}=\frac{1}{M_1}\{P+Ay+u^2(1-\rho)\}$$

$$\frac{\partial T}{\partial r}=\frac{1}{K_1}u(1-\rho) \tag{7d}$$

[1] The ordering of terms and the resulting types of boundary value problems are discussed in detail in [37].

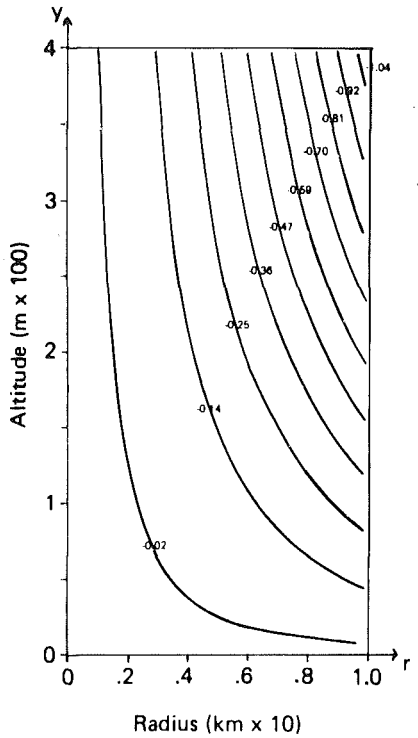

Fig. 1 Source region streamlines, 10-km-radius area fire

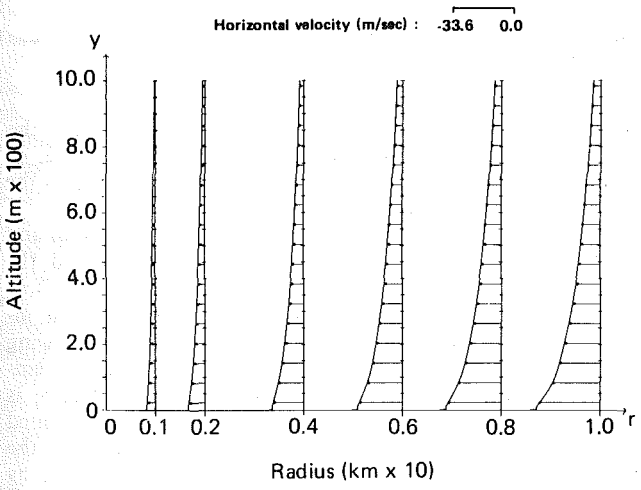

Fig. 2 Radial velocity profiles, 10-km-radius area fire

The boundary value problem – defined by equations (4) (with M_2, $K_2 = 0$) and the boundary conditions, equations (7) – is, to leading order, independent of both the far-field and the free-convection-column flows. Such an uncoupling implies that the mechanics of the source region are controlled principally by the heat release and the resulting pressure gradients produced by the strong buoyancy.

Results

Numerical solution of the boundary value problem involves repeated iteration to find a pressure distribution at $y = 0$, consistent with the asymptotic condition equation (7*c*) [41]. Results for several model fires and a detailed parameter study have been presented by Larson and Small [37, 41]. Several area fires were simulated including a Project Flambeau [29, 40] experimental fire ($\epsilon = 0.08$), the Hamburg firestorm ($\epsilon = 0.04$), and arbitrarily larger fires. The results obtained for the Flambeau and Hamburg fires agreed reasonably well with the

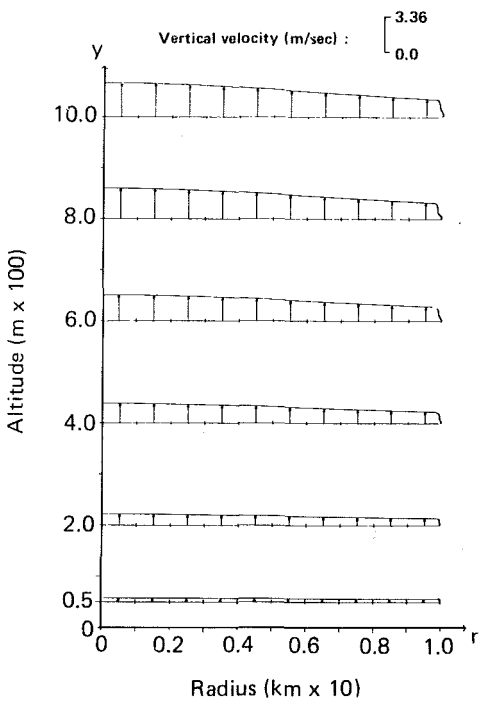

Fig. 3 Vertical velocity profiles, 10-km-radius area fire

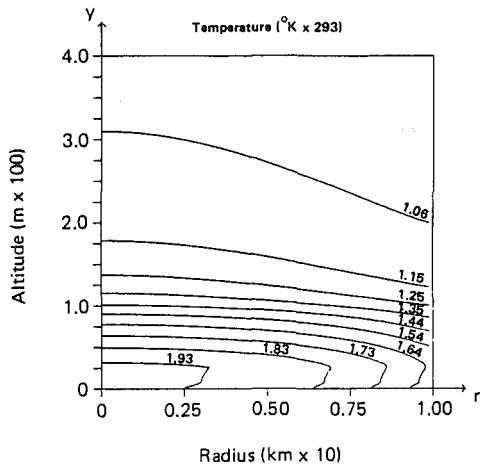

Fig. 4 Temperature contours, 10-km-radius area fire

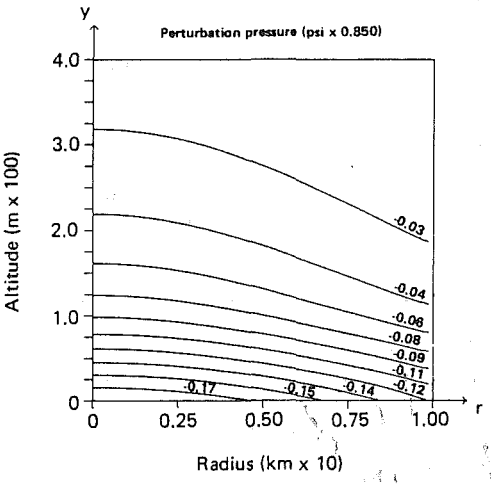

Fig. 5 Pressure contours, 10-km-radius area fire

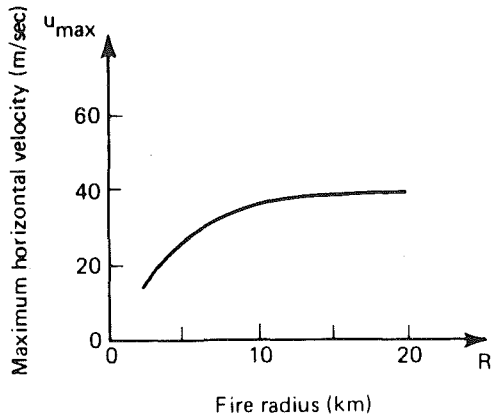

Fig. 6 Dependence of maximum radial velocity on fire radius

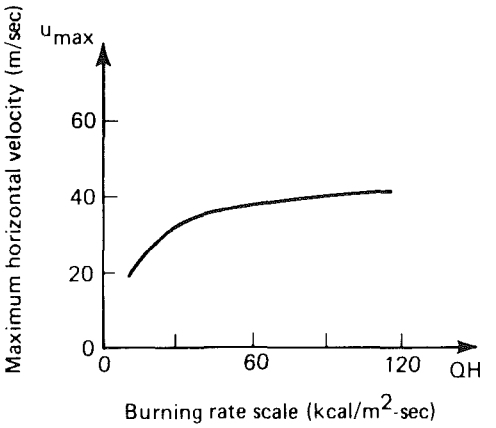

Fig. 7 Dependence of maximum radial velocity on burning rate scale

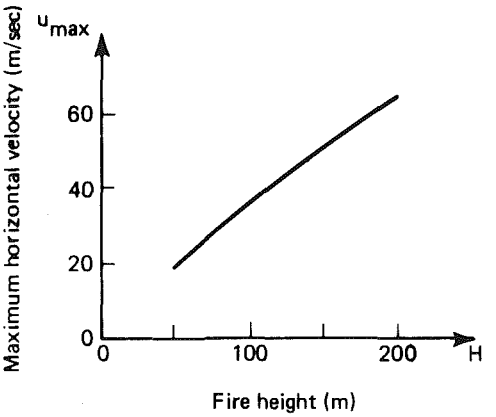

Fig. 8 Dependence of maximum radial velocity on burning-region height

available (relatively sparse) data, and duplicated the observed flow patterns.

Figures 1–5 show typical results[2] obtained for a 10-km-radius area fire [41]. For that case, the prescribed heating (Q_0 = 57 kcal/m^2-s) was applied in the region $r \leq 1$, $y \leq 1$ (H = 100 m, ϵ = 0.01). The radiation mean free path was taken as 20 m and M_1, K_1 as 0.2. For those values, the characteristic velocity is U = 67.2 m/s and the parameters A and σ are 0.217 and 0.110, respectively.

The streamline and velocity plots (Figs. 1–3) illustrate the turning of the induced fire winds to a nearly vertical flow at the top of the source region (Fig. 2). The development of the

[2] It should be noted that the radial scales are compressed by a factor of ϵ, thus distorting the representation of the streamlines and property contours.

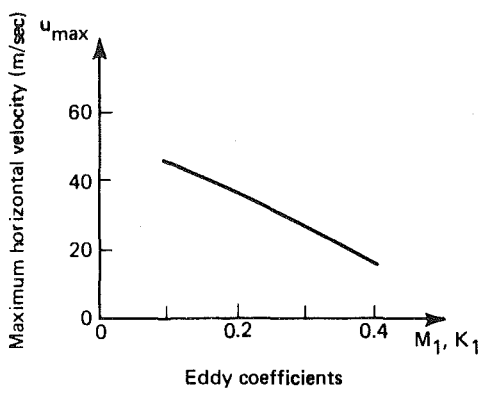

Fig. 9 Dependence of maximum radial velocity on eddy coefficient

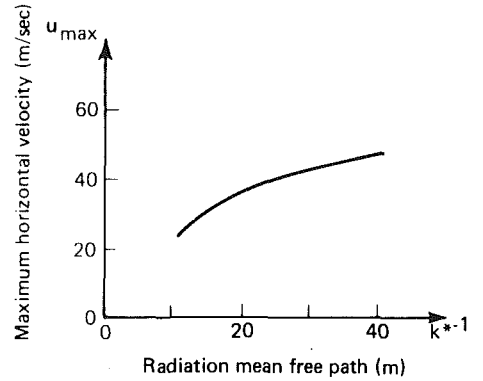

Fig. 10 Dependence of maximum radial velocity on radiation mean free path

axial velocity profiles in Fig. 3 appears to correlate with the nearly uniform temperature (buoyancy) contours in Fig. 4. Similarly, the rapid increase in magnitude is mirrored in the perturbation pressure contours shown in Fig. 5.

In the lower portion of the source region, strong radial and axial gradients in perturbation pressure decrease and the temperature increases as the high-velocity radial flow stagnates at the symmetry line (Fig. 2). Presumably, the increasing fluid residence time associated with the slowing radial flow allows additional heating and thus higher temperatures and locally increased buoyancy. Such behavior is consistent with the relatively larger axial velocities calculated near the centerline (Fig. 3). Above the source region, the radial velocities decay rapidly and the flow is characterized by fairly uniform contours of pressure and temperature. The flow achieves a state of weak buoyancy above four flame heights. A similar decay has been observed above small fires [42].

The dependence of radial velocity on the fire radius, heat release rate, and burning-region height is shown in Figs. 6–8. Initially, the velocity increases rapidly with either QH or R, and then asymptotes to a constant value. In both cases, the approach to a constant value is related to the slowing production of buoyancy per unit area. For QH and R fixed, greater heating zone heights produce larger maximum radial velocities. Though increasing H results in a lower energy density, the buoyancy per unit area increases directly with the burning region height. The strong dependence on H suggests that hydrocode simulations of a large area fire should use a volume heat source rather than a prescribed thermal condition.

The source region model assumes that turbulent mixing affects the transfer of momentum and thus the turning of the inflow. The second-derivative transfer terms prescribe the propagation of information across the source region. The

magnitude of the mixing coefficients thus influences the solution dependence on fire size and heat addition.

Figure 9 shows the variation of maximum radial velocity with changes in the coefficient M_1. Increasing the level of turbulent mixing slows the radial inflow, producing a broader, lower mean-velocity updraft. As the inviscid limit is approached, mean velocities increase and the vertical flow is confined to a thin, high-velocity plume. Similar variation of the eddy coefficient for heat transfer K_1 produces only small changes in characteristic values of velocity and temperature. The weak dependence on thermal diffusion implies that the energy balance is principally controlled by the net heat addition. The strong dependence on the eddy coefficient M_1 implies that the induction and turning of the fire-driven flow is principally governed by the balance of turbulent stresses and buoyancy-generated pressure gradients.

The influence of the radiative heat transfer on the maximum radial velocity is shown in Fig. 10. An increase in the radiation mean free path results in a decreased radiative flux and thus a higher mean temperature flow (see equation 4(*d*)). In this example, 500 K $\leq T_{max} \leq$ 650 K for 10 m $\leq k^{*-1} \leq$ 40 m. The higher energy level supports a greater buoyancy production. This in turn implies a larger pressure gradient (equation 4(*c*)) and a corresponding larger radial inflow (equation 4(*b*)).

Discussion

In this paper, we have briefly examined the physics of large area fires, outlining models that treat different component flows and presenting a new theory to describe the source region.

Classical plume theories assume a weakly buoyant flow and describe the motion of an asymptotically thin shear flow well above the source region. Such models are appropriate primarily for the upper-level flow above small free-burning fires, but may be used to describe the flow above moderately large fires, provided that the plume cross section is small relative to the height. These restrictions follow since the theories depend on the dissipation of buoyancy in the atmosphere by entrainment and diffusion of cold ambient air. For large free-convection columns, entrainment is an edge effect and so does not significantly diffuse the column buoyancy.

High-velocity inflows have been reported for several large area fires. One hypothesis relates those inflows to an organized rotational structure of the free-convection column. The swirl essentially limits the entrainment of ambient air to the buoyant column, leading to a greater rise of the plume in the atmosphere and hence an increased pressure deficit. At the ground, the pressure gradients induce a strong radial inflow. Though the current treatments assume an asymptotically thin plume, and it is not certain that large fire columns will always swirl, the results present a consistent explanation for the occurrence of high-velocity inflows. An alternative hypothesis relates the large inflow velocities to the production of buoyancy in the source region, as demonstrated in section 2.

A limited number of finite difference solutions of the conservation equations have been reported. They illustrate the relationship of buoyancy and dynamic pressure to the generation of high-velocity fire winds and describe a complex transient behavior involving the development and convection of vortex structures. Though employing several limiting approximations, those studies further our understanding of the mechanics and dynamics of area fires. More precise simulations of the large-fire environment should result from improved models of radiation transport processes, turbulent structure, and volume heat addition as well as a finer-grid resolution of the source region.

A new analytical procedure employing asymptotic methods to simplify the conservation equations has been used to describe the source region. Combustion processes are simulated by a finite-volume heat source, and large changes in temperature and density are allowed. A one-parameter, eddy-viscosity model is used to describe the turbulent stresses, and a graybody approximation is employed to represent hot gas and smoke radiation. Jump conditions are derived to describe the rapid changes in physical quantities at the fire periphery. Those conditions effect model problem closure, thus permitting direct calculation of the induced fire winds without extensive far-field computations. To leading order, the solution is independent of both the far field and the properties of the convection column.

Sample results illustrate the generation of high-velocity fire winds by the heat release and the resulting production of buoyancy. The inflow is turned in the source region and rapidly decays to a nearly vertical, weakly buoyant, free-convection flow. The effect of heating rate and burning-region dimensions on the fire-wind velocities is also described.

The analyses reviewed in this paper describe facets of the fluid dynamics of large area fires. The large-scale motions are generally understood, yet a few fundamental characteristics of the flow remain to be resolved. They include the radiative properties and turbulent structure of the fire-generated flow as well as the combustion dynamics. We have developed a simple model of the transient behavior of a large area fire and its interactions with the local atmosphere. The model is preliminary and incomplete; further research is needed for a more complete simulation of large area fires.

Acknowledgments

This paper was sponsored by the Defense Nuclear Agency and monitored by Dr. Michael J. Frankel. The model described in section 2 was developed under the sponsorship of the Federal Emergency Preparedness Agency.

References

1 Rouse, H., Yih, C. S., and Humphreys, H. W., "Gravitational Convection From a Boundary Source," *Tellus*, Vol. 4, 1952, pp. 201–210.

2 Morton, B. R., Taylor, G., and Turner, J. S., "Turbulent Gravitational Convection From Maintained and Instantaneous Sources," *Proceedings of the Royal Society*, Vol. 24, 1956, pp. 1–23.

3 Morton, B. R., "Forced Plumes," *Journal of Fluid Mechanics*, Vol. 5, 1959, pp. 151–163.

4 Morton, B. R., "Buoyant Plumes in a Moist Atmosphere," *Journal of Fluid Mechanics*, Vol. 2, 1957, pp. 127–144.

5 Murgai, M. P., "Radiative Transfer Effects in Natural Convection Above Fires," *Journal of Fluid Mechanics*, Vol. 12, 1962, pp. 441–448.

6 Smith, R. K., "Radiation Effects on Large Fire Plumes," *Eleventh International Symposium on Combustion*, The Combustion Institute, 1967, pp. 507–515.

7 Morton, B. R., "Modeling Fire Plumes," *Tenth International Symposium on Combustion*, The Combustion Institute, 1965, pp. 973–982.

8 Wilcox, D. C., "Model for Fires With Low Initial Momentum and Nongray Thermal Radiation," *AIAA Journal*, Vol. 13, 1975, pp. 381–386.

9 Murgai, M. P., and Emmons, H. W., "Natural Convection Above Fires," *Journal of Fluid Mechanics*, Vol. 8, 1960, pp. 611–624.

10 Lee, S. L., and Emmons, H. W., "A Study of Natural Convection Above a Line Fire," *Journal of Fluid Mechanics*, Vol. 11, 1961, pp. 353–368.

11 Lee, S. L., and Ling, C. H., "Natural Convection Plume Above a Circular Ring Fire," *Eleventh International Symposium on Combustion*, The Combustion Institute, 1967, pp. 501–506.

12 Nielsen, H. J., and Tao, L. N., "The Fire Plume Above a Large Free-Burning Fire," *Tenth International Symposium on Combustion*, The Combustion Institute, 1965, pp. 965–972.

13 Small, R. D., and Brode, H. L., "Physics of Large Urban Fires," Report 1010, Mar. 1980, Pacific-Sierra Research Corp., Los Angeles, Calif.

14 Brode, H. L., "Large-Scale Urban Fires," Note 348, Dec. 1980, Pacific-Sierra Research Corporation, Los Angeles, Calif.

15 Long, R. R., "Fire Storms," *Fire Research Abstracts and Reviews*, Vol. 9, 1967, pp. 53–68.

16 Emmons, H. W., "Fundamental Problems of the Free Burning Fire," *Tenth International Symposium on Combustion*, The Combustion Institute, 1965, pp. 951–964.

17 Morton, B. R., "The Physics of Fire Whirls," *Fire Research Abstracts and Reviews*, Vol. 12, 1970, pp. 1–19.

18 Bond, H. (ed.), *Fire and the Air War*, 1st ed., National Fire Protection Association, Boston, 1951.

19 Ebert, C. H. V., "The Meteorological Factor in the Hamburg Fire Storm," *Weatherwise*, Vol. 16, 1963, pp. 70–75.

20 Church, C. R., Snow, J. T., and Dessens, J., "Intense Atmospheric Vortices Associated with a 1000-MW Fire," *Bulletin of the American Meteorological Society*, Vol. 61, 1980, pp. 682–694.

21 Palmer, T. Y., "Large Fire Winds, Gases and Smoke," *Atmospheric Environment*, Vol. 15, 1981, pp. 2079–2090.

22 Williams, D. S., Adams, J. S., Batten, J. J., Whitty, G. F., and Richardson, G. T., "Operation Euroka, an Australian Mass Fire Experiment," Report 386, Sept. 1970, Australian Defense Scientific Service, Maribyrnong, Victoria, Australia.

23 Carrier, G. F., Fendell, F. E., and Feldman, P. S., "Firestorms," TRW Doc. No. 38163-6001-UT-00, 1982, TRW, Redondo Beach, Calif.

24 Emmons, H. W., and Ying, S. J., "The Fire Whirl," *Eleventh International Symposium on Combustion*, The Combustion Institute, 1967, pp. 475–488.

25 Lee, S. L., "Axisymmetrical Turbulent Swirling Natural-Convection Plume, Part 1, Theoretical Investigation," *Journal of Applied Mechanics*, Vol. 33, 1966, pp. 647–655.

26 Muraszew, A., Fedele, J. B., and Kuby, W. C., "The Fire-Whirl Phenomenon," *Combustion and Flame*, Vol. 34, 1979, pp. 29–45.

27 Ying, S. J., "The Fire Whirl," Ph.D. thesis, Harvard Univ., 1965.

28 Williams, F., "Scaling Mass Fires," *Fire Research Abstracts and Reviews*, Vol. 11, 1969, p. 1.

29 Nielsen, H. J., "Mass Fire Data Analysis," DASA Report No. 2018, Jan. 1970, IIT Research Institute, Chicago, Ill.

30 Smith, R. K., Morton, B. R., and Leslie, L. M., "The Role of Dynamic Pressure on Generating Fire Winds," *Journal of Fluid Mechanics*, Vol. 68, 1975, pp. 1–19.

31 Luti, F. M., and Brzustowski, T. A., "Flow Due to a Two-Dimensional Heat Source with Gross Flow in the Atmosphere," *Combustion Science and Technology*, Vol. 16, 1977, pp. 71–87.

32 Luti, F. M., "Some Characteristics of a Two-Dimensional Starting Mass Fire with Gross Flow," *Combustion Science and Technology*, Vol. 26, 1981, pp. 25–33.

33 Larson, D. A., Brode, H. H., and Small, R. D., "Time-Dependent Model of Flows Generated by Large Area Fires," Note 483, July 1982, Pacific-Sierra Research Corp., Los Angeles, Calif.

34 Estoque, M. A., and Bhumralkar, C. M., "Flow Over a Localized Heat Source," *Monthly Weather Review*, Vol. 97, 1969, pp. 850–859.

35 Delage, Y., and Taylor, P. A., "Numerical Studies of Heat Island Circulation," *Boundary Layer Meteorology*, Vol. 1, 1970, pp. 201–226.

36 Cox, G., and Chitty, R., "A Study of the Deterministic Properties of Unbounded Fire Plumes," *Combustion and Flame*, Vol. 39, 1980, pp. 191–209.

37 Larson, D. A., and Small, R. D., "Analysis of the Large Urban Fire Environment, Part I, Theory," Report 1210, Part I, July 1982, Pacific-Sierra Research Corp., Los Angeles, Calif.

38 Thomas, P. H., "The Size of Flames From Natural Fires," *Ninth International Symposium on Combustion*, The Combustion Institute, 1963, pp. 844–859.

39 Small, R. D., Larson, D. A., and Brode, H. L., "Analysis of Large Urban Fires," Report 1122, 1981, Pacific-Sierra Research Corp., Los Angeles, Calif.

40 Countryman, C. M., "PROJECT FLAMBEAU . . . An Investigation of Mass Fire (1964-1967)," Vol. 1, U.S. Forest Service, Berkeley, Calif., 1969.

41 Larson, D. A., and Small, R. D., "Analysis of the Large Urban Fire Environment, Part II, Parametric Analysis and Model City Simulations," Report 1210, Part II, Nov. 1982, Pacific-Sierra Research Corp., Los Angeles, Calif.

42 McCaffrey, B. J., "Purely Buoyant Diffusion Flames: Some Experimental Results," Report NBSIR 79-1910, 1979, National Bureau of Standards, Washington, D.C.

Observed Flow Reversals and Measured-Predicted Nusselt Numbers for Natural Convection in a One-Sided Heated Vertical Channel

E. M. Sparrow
Fellow ASME

G. M. Chrysler

L. F. Azevedo

Department of Mechanical Engineering,
University of Minnesota,
Minneapolis, Minn. 55455

A three-part study encompassing both experiment and analysis has been performed for natural convection in an open-ended vertical channel. One of the principal walls of the channel – the heated wall – was maintained at a uniform temperature, while the other principal wall was unheated. The experiments, which included flow visualization and Nusselt number measurements, were carried out with water in the channel and in the ambient which surrounds the channel. At Rayleigh numbers which exceeded a threshold value, the visualization revealed a pocket of recirculating flow situated adjacent to the unheated wall in the upper part of the channel. The recirculation was fed by fluid drawn into the top of the channel, adjacent to the unheated wall. Average Nusselt numbers for the heated wall were measured over a three orders of magnitude range of a single correlating parameter, which includes the Rayleigh number and the ratio of the channel length to the interwall spacing. The Nusselt numbers were found to be unaffected by the presence of the recirculation zone. Numerical solutions obtained via a parabolic finite difference scheme yielded Nusselt numbers in good agreement with those of experiment. The numerical results covered the Prandtl number range from 0.7 to 10.

Introduction

This paper sets forth a multifaceted experimental and analytical study of natural convection in an unsymmetrically heated, parallel-walled vertical channel open to ambient at the top and bottom. The heating conditions were such that one of the principal walls of the channel was maintained at a uniform temperature (elevated with respect to ambient), while the other principal wall was unheated. All of the experiments were performed in water, with the Prandtl number maintained approximately equal to 5.

The heretofore accepted pattern of the fluid flow in an unsymmetrically heated channel [1-3] is the same as that attributed to the more widely studied symmetrically heated channel. For both cases, fluid is drawn from the ambient into the bottom of the channel, from where it is assumed to flow vertically upward through the channel and to emerge from the top into the ambient. This model, which has been universally employed in analytical work on buoyant wall-heated channel flows, precludes a vertical downflow at any point in the channel and, in particular, requires that there be no inflow of fluid at the top of the channel. No direct verification of the aforementioned pattern of fluid flow appears to have yet been made, nor has its validity been challenged.

In the present investigation, flow visualization experiments have been performed to examine the fluid flow in a one-sided heated channel. The visualization was accomplished by the thymol blue method, whereby fluid particles which undergo a color change due to a local change in pH serve as a tracer. These experiments demonstrated that for certain operating conditions, fluid enters at the top of the channel adjacent to the unheated wall, while fluid exits the top adjacent to the heated wall. The fluid downflow adjacent to the unheated wall was documented photographically and a representative photograph will be presented later. Furthermore, the conditions marking the onset of the downflow were sought by systematic variations of the independent parameters – the Rayleigh number and the dimensionless interwall spacing. The values of these parameters which mark the onset may be regarded as critical or transition values – they will be reported in the presentation of results.

The next focus of the work was the experimental determination of heat transfer coefficients and Nusselt numbers for the one-sided heated channel. These experiments were undertaken both to assess the heat transfer ramifications of the aforementioned downflow and to provide heretofore unavailable heat transfer information for one-sided heating in a channel with water as the working fluid. The Nusselt number experiments were performed for parametric values of the Rayleigh number and of the dimensionless interwall spacing, and a universal correlation encompassing both parameters was obtained.

The final part of the work consisted of numerical solutions of the conservation equations for mass, momentum, and energy for the one-sided heated channel flow. These solutions were based on a model which does not account for vertical downflow, so that a comparison of the numerically predicted Nusselt numbers with the experimental data provides another means for assessing the importance of the observed downflow. The agreement between the predictions and the data was sufficiently good so that additional solutions (i.e., additional to those for $Pr = 5$) were carried out to cover the Prandtl number range from 0.7 to 10. Another outcome of the aforementioned comparison is the demonstration that the no-downflow model yields satisfactory predictions of practically useful heat transfer information.

With regard to the literature, the absence of direct flow field information has already been mentioned. Also absent

Contributed by the Heat Transfer Division for publication in the JOURNAL OF HEAT TRANSFER. Manuscript received by the Heat Transfer Division April 22, 1983.

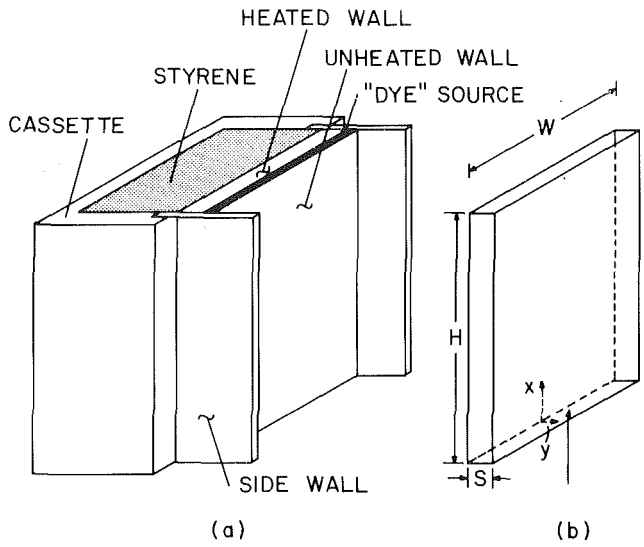

Fig. 1 Pictorial view of the experimental apparatus (left-hand diagram) and geometry of the flow channel (right-hand diagram)

are any experiments on natural convection in a vertical channel bounded on one side by an isothermal wall and on the other side by an unheated wall. Other unsymmetrical boundary conditions were employed in the experiments of [1], which were performed in air, in contrast to the water-related experiments performed here.

The Experiments

The description of the experimental apparatus is facilitated by reference to Fig. 1. In the figure, the left-hand diagram is a schematic pictorial view of the apparatus, while the right-hand diagram depicts the geometry of the flow channel and its dimensions. Other important features of the apparatus (not shown in Fig. 1 but to be discussed shortly) are the test chamber and the flow visualization system.

The heart of the apparatus is a 0.635-cm-thick copper plate, with a height, H, of 14.52 cm and a width, W, of 9.67 cm. In the rear face of the plate, there are twenty horizontal grooves distributed along the height. These grooves are used to accommodate Teflon-coated electrical resistance wire (0.0127-cm-dia chromel). The wire is potted in the grooves with copper oxide cement, and the entire rear face of the plate is overcoated with silicone rubber to provide a water-tight seal.

Three independently controlled heating circuits were used to enable temperature uniformity of the plate to be attained. The adjustment of the heating circuits was guided by the readings of eight thermocouples dispersed throughout the various heating zones. In an overwhelming majority of the data runs, temperature uniformity to better than 2½ percent of the plate-to-ambient temperature difference was achieved.

As a defense against extraneous heat losses, the plate was inset into a 3.2-cm-thick block of water-tolerant, closed-pore polystyrene. Special precautions were taken at the upper and lower edges of the plate to avoid contact between these edges and the water. In particular, only the front face of the plate, which comprised the heated wall of the channel, was exposed to the water. As seen in Fig. 1, the polystyrene was housed in a U-shaped container termed a cassette. The cassette was made of plexiglass.

The other principal wall of the flow channel (i.e., opposite the heated wall) was made of 0.635-cm-thick plexiglass. The side walls were also of plexiglass, this choice having been made to enable the motions of a tracer fluid to be observed. From the figure, it is seen that the lateral extent of the side walls was greater than that needed to bound the fluid. This feature facilitated the variation of the spacing, S, between the two principal walls. Once a spacing had been established by moving the unheated principal wall relative to the heated wall, it was fixed by a rigid locking mechanism (not shown). The spacing was set and verified with a dial-gage-equipped caliper with an accuracy of better than 0.0025 cm.

The assembly pictured in the left-hand diagram of the figure was supported from the floor of the test chamber by struts positioned so as not to inhibit or deflect the flow en route to the channel inlet. The inlet was situated 12.7 cm above the floor of the chamber, while the water level was maintained at 12.7 cm above the trailing edge of the channel.

Temperatures in the ambient water were sensed by three thermocouples deployed along a vertical line that was displaced laterally from the flow channel by about 30 cm. The three thermocouples were respectively situated at distances of 7.6, 17, and 24 cm above the floor of the test chamber. In the overwhelming majority of the data runs, the readings of the three thermocouples were uniform to better than a half percent of the heated plate-to-ambient temperature difference.

Test Chamber. The experiments were performed with the apparatus situated in a large, water-filled, open-topped plexiglass tank (73.7 × 43.2 × 45.7 cm, length × width × height). This tank – the test chamber – was situated within a still larger plexiglass tank having internal dimensions of 101.6 × 66 × 48.3 cm (length × width × height). The space between the tanks (both at the sides and at the bottom) was also filled with water. In addition, a temperature control and water circulating unit was installed in the intertank space. With this unit in place, the intertank space served as a thermal guard for the test chamber.

Nomenclature

Gr_s = Grashof number, $g\beta(T_w - T_\infty)S^3/\nu^2$
g = acceleration of gravity
H = channel height, Fig. 1(b)
h = average heat transfer coefficient for heated wall, $(Q/HW)/(T_w - T_\infty)$
k = thermal conductivity
Nu_s = average Nusselt number for heated wall, hS/k
P = dimensionless pressure difference, equation (7)
Pr = Prandtl number
p = pressure in channel
p_∞ = pressure in ambient
p' = pressure difference, $(p - p_\infty)$
Q = rate of heat transfer at heated wall
Ra_s = Rayleigh number, PrGr_s
S = interwall spacing, Fig. 1(b)
T = temperature
T_w = temperature of heated wall
T_∞ = ambient temperature
X,Y = dimensionless coordinates, equation (5)
x,y = coordinates, Fig. 1(b)
U,V = dimensionless velocity components, equation (6)
U_o = dimensionless inlet velocity
u,v = velocity components
u_0 = inlet velocity
W = channel width, Fig. 1(b)
β = coefficient of thermal expansion
Δ = deepest penetration of downflow into channel
θ = dimensionless temperature, $(T - T_\infty)/(T_w - T_\infty)$
ν = kinematic viscosity
ρ = density

Subscript

∞ = ambient

The effectiveness of the temperature control was heightened by the extensive use of insulation. All four sides of the outer tank were sheathed with polystyrene, while a sheet of polystyrene, lined with impermeable plastic, served as a cover that extended over the top of both tanks.

Distilled water was used in the test chamber, while tap water was used in the intertank space. Temperature equilibrium between the two fluids was monitored by 0.1°F ASTM-certified thermometers.

Experimental Procedure – Heat Transfer. Two conditions were imposed as prerequisites for the initiation of a data run. One is that the temperature of the water in the test chamber is uniform. The other is that the water in the chamber and that in the intertank space be at the same temperature. The fulfillment of these conditions guarantees the absence of extraneous buoyancy-related motions in the test chamber (i.e., extraneous with respect to the heated-plate-related buoyancy).

The attainment of thermal equilibrium between the water in the chamber and in the intertank space was a matter of time, and sufficient time was always allowed. Temperature uniformity within the chamber was achieved by manual stirring with a plexiglass paddle.

With intertank thermal equilibrium already established, the first preparatory step for a data run was to stir the water in the test chamber. Then, an hour was allowed for the motions induced by the stirring to die away. During this period, no power was supplied to the plate, but the voltage settings for the three plate heating circuits were dialed in to anticipate the beginning of the run. The relationships between the voltage settings appropriate to the attainment of temperature uniformity were known from experience gained in prior runs.

After the hour had elapsed, power was applied to the plate heating circuits and, thereafter, selected thermocouples were monitored to track the attainment of steady state. In all cases, steady state was achieved within 10 to 15 min. An additional 5 minutes was allowed and then the data were collected.

Then, the power was turned off and the test chamber was stirred. In this regard, it should be noted that the energy added to the water in the test chamber during a data run, when distributed uniformly by the stirring, caused a negligible temperature rise. Therefore, the intertank equilibrium was not disturbed and another run could be initiated after an hour's waiting period.

Flow Visualization. The thymol blue method [4] was used for the flow visualization. This is an electrochemical technique in which a change of color of the fluid occurs in response to a change in pH brought about by an impressed d-c voltage. The color change produces a neutrally buoyant blue fluid which faithfully follows natural convection motions. By use of suitable electrodes, the site of the color change can be localized. By observing the motions of the locally produced tracer fluid, the details of the flow pattern can be determined.

The flow visualization experiments were performed separately from the heat transfer experiments because of the chemicals added to the distilled water in the test chamber in order to facilitate the electrochemical reaction. Two groups of additives were employed. One group included an acid (hydrochloric acid) and a base (sodium hydroxide) used to tailor the pH of the solution, while the other included thymol blue – a pH indicator. The thymol blue is added first, and the solution is then titrated to the end point with the sodium hydroxide. Next, the solution is made very slightly acidic and red-yellow in color by the addition of hydrochloric acid. When a small d-c voltage (~6 V) is impressed between electrodes situated in such a solution, a proton transfer reaction occurs at the negative electrode, which changes the pH at that electrode from the acidic side to the basic side. This change in pH brings about a change of color from red-yellow to blue.

Since the blue "dye" is created at the negative electrode, the positioning of the electrode is critical with respect to the flow patterns that are to be observed. In the present instance, preliminary experiments had revealed the existence of a downflow adjacent to the unheated principal wall of the channel. It was this unexpected downflow that constituted the main focus of the visualization studies, and the negative electrode was positioned accordingly.

In the aforementioned preliminary experiments, the negative electrode was a wire that bridged between the principal walls at the top of the channel, midway between the side walls. Whereas this setup revealed both an upflow adjacent to the heated wall and a downflow adjacent to the unheated wall, its use was discontinued out of concern for the reliability of the results. In this regard, it should be noted that one portion of the wire was washed by the relatively hot upflow stream, while the other portion was washed by the relatively cool downflow stream. As a consequence, heat is transferred along the wire by conduction. This gives rise to local temperature differences between the wire and the fluid, which, in turn, create local buoyancy forces which tend to oppose the flow in the channel. Since the opposing buoyancy is extraneous, the bridging wire was not used for the definitive visualization experiments.

The adopted setup of the negative electrode is shown in the left-hand diagram of Fig. 1. The electrode is a 0.0024-cm-thick copper foil cemented to the upper edge of the unheated principal wall of the channel (the foil is depicted by the black strip labeled "dye" source). With the electrode in this position, the tracer fluid produced by the electrochemical reaction responds to the flow adjacent to the top of the unheated plate.

To obtain information on the nature of the gross fluid motion in the channel, a wire electrode which bridged between the principal walls at the bottom of the channel was employed. The anode was a large copper sheet which rested on the floor of the test chamber. To avoid the formation of flow-disturbing hydrogen bubbles at the negative electrode, the voltage was applied in discrete intervals rather than continuously.

The motion of the tracer fluid was observed through a narrow slit cut in the insulation that sheathed the outer tank. Lighting was from the side of the tank opposite the viewing slit, where another slit had been cut. The lighting was provided by a photo floodlight and diffused by a milk-white plastic plate.

The preparation for a flow visualization run was identical to that for a heat transfer data run, involving inter-tank equilibration, stirring, and an hour's settling period. Once the plate heaters were energized and 15 min allowed for the attainment of steady state, voltage was applied (intermittently) to the electrochemical circuit. The motion of the tracer fluid was carefully tracked during a 10–15 min period with the aid of a cathetometer. A special focus of these observations was to determine how far into the channel did the downflow penetrate. This distance was read with the cathetometer, which had a resolving power of 0.005 cm.

Penetration depths were measured for a range of Rayleigh numbers at each of three interplate spacings. The objective of these experiments was to determine the conditions marking the onset of the downflow. Observations were also made of the diffusive spreading of the tracer fluid when the channel was not heated.

Numerical Solutions

The numerical solutions which were carried out in support of the experimental work were based on a model that did not

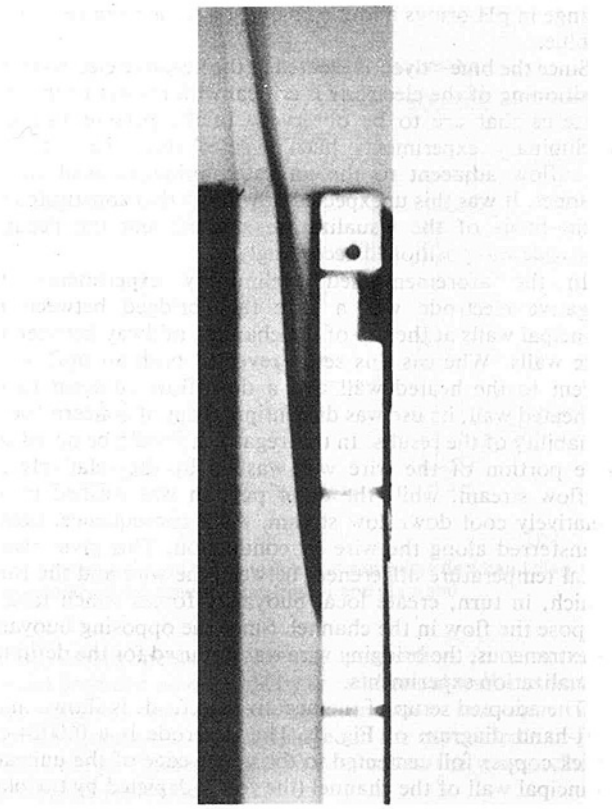

Fig. 2 Photographic illustration of the downflow and recirculation pattern

include downflow. As will be demonstrated shortly, the observed downflow is one leg of a pocket of recirculating flow adjacent to the unheated wall. The downflow is fed from the top of the channel, so that the nominal exit cross section of the channel includes both upflow and downflow (i.e., both outflow and inflow). To solve a fluid flow problem of this type requires that the solution domain encompass not only the channel but also the ambient fluid outside the channel. To deal with a problem of such magnitude requires extraordinary computing power, and even that is no guarantee that a meaningful solution will be obtained. Therefore, realistically, the numerical work should be based on a model which involves only the channel and not the ambient.

The model used here is the same as that of [3] aside from a slight change in boundary conditions. In view of this, only a brief outline of the analysis need be given, with emphasis on those features which aid in the interpretation of the results.

The analysis is two dimensional, and the x,y-coordinates are pictured in the right-hand diagram of Fig. 1 (the corresponding velocities are u and v). Streamwise second derivatives (i.e., $\partial^2/\partial x^2$) are neglected, and the pressure, p, is assumed to depend only on the axial coordinate, x. These assumptions are compatible with the adopted flow model, but could not be employed if a recirculation (i.e., downflow) zone were present. In the ambient fluid outside the channel, the temperature, T_∞, is uniform and the pressure, p_∞, varies linearly with x, that is, $p_\infty(x) = p_\infty(0) - \rho_\infty g x$, where the ambient density ρ_∞ is also a constant.

The analysis works with the local channel-to-ambient pressure difference $p'(x) = p(x) - p_\infty(x)$ and with the Boussinesq equation of state, $\Delta\rho = -\beta\rho\Delta T$, so that the buoyancy force which appears in the x-momentum equation becomes

$$-dp/dx - \rho g = -dp'/dx + g\beta\rho(T - T_\infty) \tag{1}$$

Once the buoyancy force has been transformed in accordance with equation (1), the thermophysical properties are assumed to be constant.

A key role in the analysis is played by the pressure boundary conditions. If u_o denotes the velocity entering the channel at $x=0$ (u_o is assumed uniform), then Bernoulli's equation gives

$$p'(0) = -\tfrac{1}{2}\rho u_o^2 \tag{2}$$

At the channel exit $x=H$, the channel pressure and the ambient pressure are assumed to be identical, so that

$$p'(H) = 0 \tag{3}$$

The neglect of the streamwise second derivatives and the $p=p(x)$ assumption enables a change of variables which eliminates the separate dependence of the results on the Grashof number and the aspect ratio, S/H. Instead, only a single composite parameter emerges

$$(S/H)\mathrm{Gr}_s, \quad \mathrm{Gr}_s = g\beta(T_w - T_\infty)S^3/\nu^2 \tag{4}$$

where T_w is the uniform temperature of the heated wall of the channel.

The change of variables which yields the minimum number of parameters is

$$X = (x/S)/\mathrm{Gr}_s, \quad Y = y/S \tag{5}$$

$$U = (uS/\nu)/\mathrm{Gr}_s, \quad V = vS/\nu \tag{6}$$

$$P = p'(S^2/\rho\nu^2)/\mathrm{Gr}_s^2, \quad \theta = (T - T_\infty)/(T_w - T_\infty) \tag{7}$$

from which the equations of continuity, x-momentum, and energy follow as

$$\partial U/\partial X + \partial V/\partial Y = 0 \tag{8}$$

$$U(\partial U/\partial X) + V(\partial U/\partial Y) = -dP/dX + \theta + \partial^2 U/\partial Y^2 \tag{9}$$

$$U(\partial\theta/\partial X) + V(\partial\theta/\partial Y) = (1/\mathrm{Pr})\partial^2\theta/\partial Y^2 \tag{10}$$

Equations (8-10) are to be solved subject to the boundary conditions that U and V are zero on the channel walls, that $\theta = 1$ on the isothermal heated wall ($Y=0$), and that $\partial\theta/\partial Y = 0$ on the adiabatic wall ($Y=1$). Also, at the inlet ($x=0$)

$$U = U_o, \quad V = 0, \quad P = -\tfrac{1}{2}U_o^2 \tag{11}$$

while at the exit ($X = (H/S)/\mathrm{Gr}_s$)

$$P = 0 \tag{12}$$

From an inspection of equations (8-12) and the related text, it appears that there are three prescribable parameters: $(S/H)\mathrm{Gr}_s$, Pr, and U_o. However, $(S/H)\mathrm{Gr}_s$ and U_o are not independent. To demonstrate this, a solution scenario will be described. In this regard, it is relevant to note that the computational problem is parabolic in nature, so that given sufficient information at $X=0$, the solution can be started there and marched forward in the direction of increasing X, without any note being taken of the channel exit. In the present instance, a value of U_o must be selected in order to start the solution. Then, during the marching procedure, the value of P is monitored. When the value $P=0$ is encountered, the solution is stopped, and the value of X at the stopping point is taken to be the exit of the channel. Since $1/X = (S/H)\mathrm{Gr}_s$ at the exit, it follows that for each U_0 there is a corresponding $(S/H)\mathrm{Gr}_s$ and vice-versa.

Thus, in light of the foregoing, there are only two prescribable parameters: $(S/H)\mathrm{Gr}_s$ and Pr. Furthermore, since the Rayleigh number Ra_s is equal to PrGr_s, the two parameters may equally well be specified as $(S/H)\mathrm{Ra}_s$ and Pr, and this practice has been followed for the present computations.

From the numerical solutions, an average Nusselt number for the heated plate was evaluated from

$$\mathrm{Nu}_s = hS/k, \quad h = (Q/HW)/(T_w - T_\infty) \tag{13}$$

where Q is the rate of heat transfer from the entire plate.

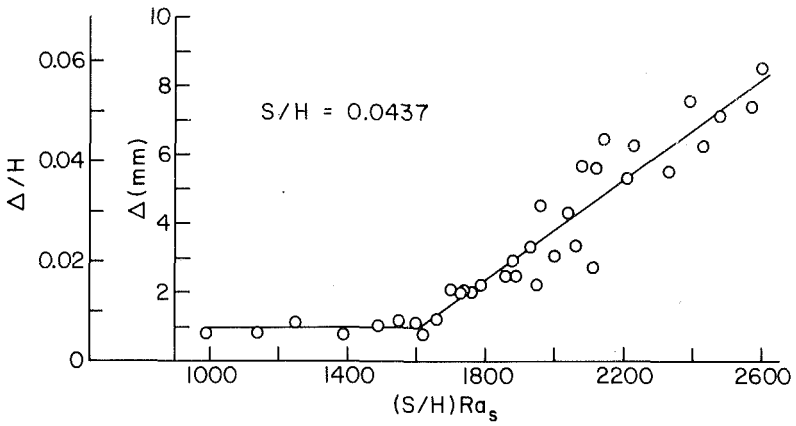

Fig. 3 Maximum penetration depth of downflow, $S/H = 0.0437$

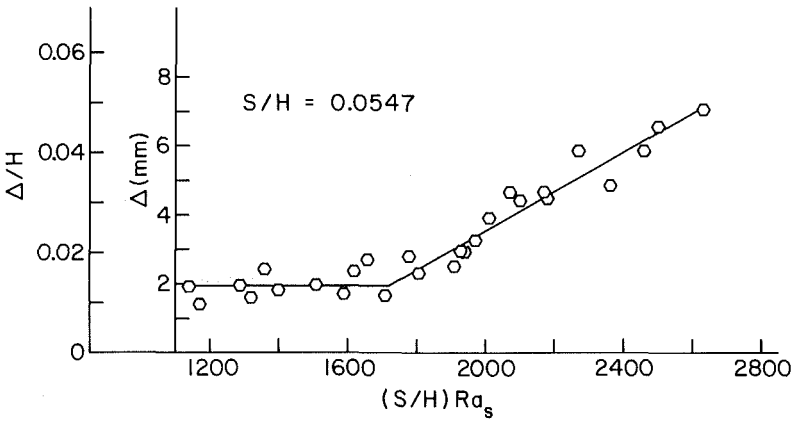

Fig. 4 Maximum penetration depth of downflow, $S/H = 0.0547$

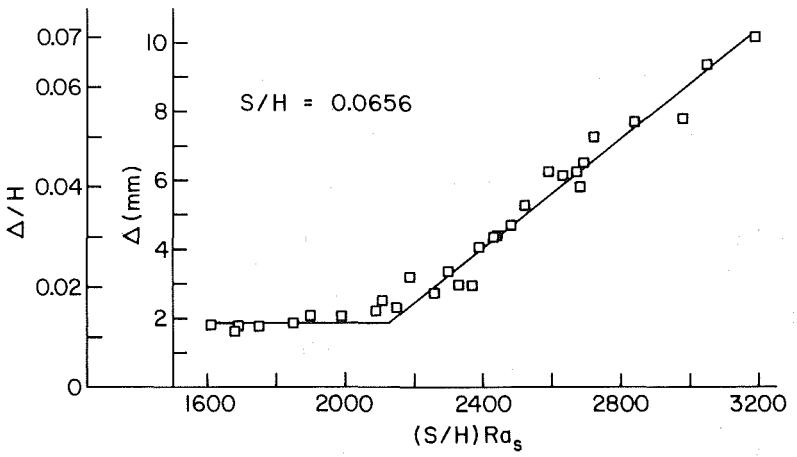

Fig. 5 Maximum penetration depth of downflow, $S/H = 0.0656$

To complement the experimental data, solutions were carried out for $(S/H)\mathrm{Ra}_s$ between 2×10^2 and 8×10^4. The experiments were performed at a nominal Prandtl number of 5, with small deviations. In view of this, the Prandtl number for the computer solutions was assigned values of 4.75, 5, and 5.25. However, at a fixed value of $(S/H)\mathrm{Ra}_s$, the Nusselt number results for the three Prandtl numbers were the same within plotting accuracy. In addition, to provide a more general set of results, solutions were also carried out for $\mathrm{Pr}=0.7$, 2, and 10.

Flow Visualization Results

A photograph illustrating the downflow and recirculation pattern that occurred in the flow channel is presented in Fig. 2. The photograph shows a side view of the upper part of the channel as well as the ambient space just above the channel. The black vertical strip at the left is the heated wall, while the white vertical strip at the right is the unheated wall. In the photograph, the blue tracer fluid appears black.

The recirculation zone is bounded by the black V-shaped

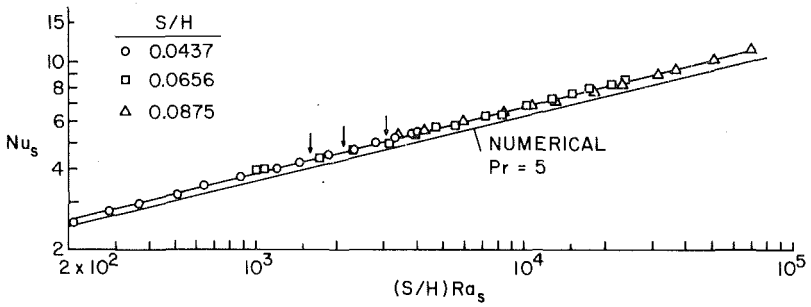

Fig. 6 Experimentally determined and numerically predicted average Nusselt numbers for the heated plate

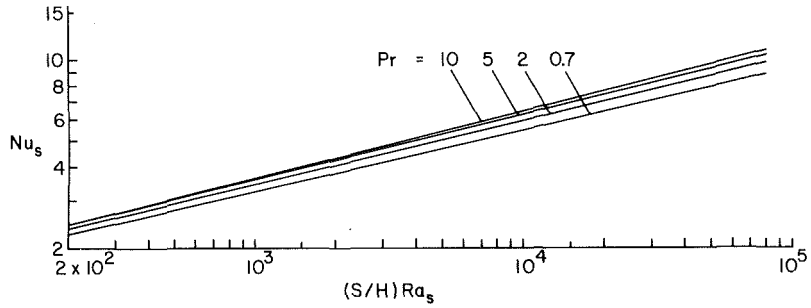

Fig. 7 Numerically predicted average Nusselt numbers for the heated plate, $0.7 \leq Pr \leq 10$

envelope formed by the tracer fluid adjacent to the upper portion of the unheated wall. The tracer, which is generated at the electrode atop the unheated wall, follows the fluid motion downward along the wall, as witnessed by the wall-adjacent black band (i.e., the right-hand leg of the V). For the case depicted in the photograph ($(S/H)\mathrm{Ra} \simeq 5270$, $S/H = 0.0656$), the downflow penetrates about 3.8 cm into the channel. Upon reaching its deepest penetration, the downflowing fluid turns and starts to rise toward the top of the channel while veering toward the heated plate, thereby producing the left-hand leg of the V. Within the region bounded by the V, fluid moves downward along the right-hand leg and upward along the left-hand leg.

To provide further perspectives about the flow pattern in the channel, observations made with the tracer-generating electrode positioned at the bottom of the channel may be mentioned. It was noted that as the fluid moved upward through the channel, it was drawn more and more toward the heated wall. It was also seen that the fluid near the heated wall accelerated as it ascended.

The observations of the preceding paragraph are useful in rationalizing the downflow and recirculation that are documented in Fig. 2. The heated wall is, in effect, a source of buoyancy, so that the fluid adjacent to it is accelerated upward. To satisfy mass conservation in the presence of the acceleration, fluid is drawn toward the heated wall. This progressively depletes the amount of upmoving fluid adjacent to the unheated wall. Ultimately, total depletion occurs (i.e., upflow ceases adjacent to the unheated wall) while, on the other hand, more fluid is needed to fulfill the mass requirements of the accelerating stream adjacent to the heated wall. This fluid is drawn into the top of the channel adjacent to the unheated wall. It recirculates as shown in the figure, being drawn toward the heated wall as needed for mass conservation.

The foregoing discussion suggests that the presence and extent of the downflow and recirculation will depend on the strength of the buoyancy – with stronger buoyancy making for a more deeply penetrating downflow. On the other hand, for sufficiently moderate buoyancy, no downflow need occur. This suggests that there is a transition from no downflow to downflow that is governed by a buoyancy-related parameter, for example, the Rayleigh number.

To examine this issue, experiments covering a range of Rayleigh numbers were performed at each of the three interwall spacings. At each Rayleigh number, the deepest penetration of the downflow into the channel was observed and recorded. These results are presented in Figs. 3–5, respectively for $S/H = 0.0437$, 0.0547, and 0.0656 ($S = 0.635$, 0.794, and 0.953 cm). The penetration depth, Δ, is plotted on the ordinate, both in dimensional and dimensionless form. The abscissa is $(S/H)\mathrm{Ra}_s$, with the fluid properties in Ra_s being evaluated at the mean of T_w and T_∞.

The data in all of the figures display a common behavior. In the range of lower Rayleigh numbers, Δ is very small and virtually constant. Then, at a certain Rayleigh number, there is a breakaway, and thereafter the penetration depth increases more or less linearly with increasing Rayleigh number over the moderate range covered in these figures (the straight lines passing through the data are least-squares fits). This behavior indicates that there is an identifiable Rayleigh-number-related transition from no downflow to downflow.

The transition values of $(S/H)\mathrm{Ra}_s$ from Figs. 3–5 ranged from 1600 to 2130, while the Rayleigh numbers ranged from about 31,500 to 36,500. Tentatively, the no-downflow/downflow transition Rayleigh number will be taken to be 35,000, subject to validation in other experiments which encompass a larger range of spacings.

In auxiliary experiments with no heating and with quiescent conditions in the test chamber, the tracer fluid tended to diffuse slowly away from its generating electrode in all directions. The depth to which the diffusing fluid penetrated into the channel during an observation period comparable to that used in the visualization data runs was noted. This depth

Table 1 Values of C and n for equation (16)

Pr	C	n
0.7	0.667	0.229
2	0.672	0.237
5	0.655	0.245
10	0.635	0.252

was approximately equal to those of Figs. 3–5 for Rayleigh numbers below the respective transition values.

Heat Transfer Results

Average heat transfer coefficients and Nusselt numbers for the heated plate were evaluated from equations (13) utilizing the measured power inputs, wall temperatures, and ambient temperatures. Also determined for each data run was the quantity $(S/H)\mathrm{Ra}_s$, where $\mathrm{Ra}_s = \mathrm{PrGr}_s$ and Gr_s is given by equation (4). All thermophysical properties appearing in Nu_s and Ra_s were evaluated at the mean of the wall and ambient temperatures.

The experimentally determined Nusselt numbers are plotted in Fig. 6 as a function of $(S/H)\mathrm{Ra}_s$, which spans a range of almost three orders of magnitude. The data are parameterized by the dimensionless interwall spacing S/H and identified by different data symbols. Also shown in the figure are a trio of arrows which respectively indicate, from left to right, the value of $(S/H)\mathrm{Ra}_s$ marking the onset of downflow for interwall spacings $S/H = 0.0437$, 0.0656, and 0.0875. The first two of these values were read directly from Figs. 3 and 5, while the third was computed using a no-downflow/downflow transition value of $\mathrm{Ra}_s = 35{,}000$. The line passing through the data is a least-squares fit having the equation

$$\mathrm{Nu}_s = 0.688[(\mathrm{S/H})\mathrm{Ra}_s]^{0.249} \tag{14}$$

The data will now be analyzed to evaluate the response of the heat transfer to the fluid flow processes that were described in the prior section of the paper. In this regard, consider first the data for any fixed interwall spacing, S/H. Each such set of data encompasses a factor of 20 in the Rayleigh number. By inspection of Fig. 6, it is seen that aside from slight scatter, the data points for each set lie along a straight line. Of greater significance is that there are no changes of slope or regions of data breakaway. Thus the lay of the data indicates no inkling of a change of flow pattern such as the onset of downflow or the progressively deeper penetration of the downflow into the flow channel. Indeed, the straight-line nature of the data lay is suggestive of an established flow regime.

The aggregate of the data for all three interwall spacings will now be examined. The most significant finding from such an examination is that the data do not display a separate dependence on S/H and on Ra_s. Rather, the data are very well correlated by the single group $(S/H)\mathrm{Ra}_s$. To extract the meaning of this finding, it is useful to reconsider the analysis of the problem as set forth earlier in the paper.

There, it was found that when the streamwise second derivatives and transverse pressure variation are neglected, the Nusselt number is a function of the $(S/H)\mathrm{Ra}_s$ group (and of Pr) but does not depend separately on (S/H) and Ra_s. If an analysis were to be made which accounts for recirculation and downflow, it would be necessary to include the streamwise second derivatives and the transverse pressure variation. In that case, the appropriate functional relation which emerges from an examination of the equations is that $\mathrm{Nu}_s = \mathrm{Nu}_s(\mathrm{Ra}_s, S/H, \mathrm{Pr})$. The fact that the experimental data for a fixed Prandtl number correlate as $\mathrm{Nu}_s = \mathrm{Nu}_s[(S/H)\mathrm{Ra}_s]$ rather than as $\mathrm{Nu}_s = \mathrm{Nu}_s(\mathrm{Ra}_s, S/H)$ suggests that Nu_s is insensitive to the presence of the backflow.

Attention is next turned to the Nusselt number results from the numerical solutions that are plotted in Fig. 6. These results correspond to $\mathrm{Pr} = 5$, but are equally applicable to $\mathrm{Pr} = 4.75$ and 5.25, which represent the extremes of the data. When the individual numerical results from the solutions were plotted in the figure, it was found that they fell on a straight line, with only a very slight deviation (~ 2 percent) at the lowest value of $(S/H)\mathrm{Ra}_s$. In view of this, a straight line representation was employed, the algebraic expression for which is

$$\mathrm{Nu}_s = 0.655[(S/H)\mathrm{Ra}_s]^{0.245} \tag{15}$$

A comparison of the numerical predictions and the experimental data (i.e., represented by the least-squares line (14)) yields agreement in the 7–11 percent range over the nearly three orders of magnitude spanned by the abscissa. When viewed in the context of numerous other comparisons between natural convection experiments and predictions, the aforementioned agreement is very good. Indeed, it is surprisingly good when note is taken of the fact that the numerical model does not include backflow and recirculation, while these features were present in various of the data runs (i.e, those to the right of the arrows in Fig. 6). Thus, the good agreement evidenced in Fig. 6 provides further backing for the finding that the Nu_s data were not affected by the backflow and recirculation.

The insensitivity of Nu_s to the backflow may be rationalized on various accounts. First, the backflow occurs adjacent to the unheated wall, while Nu_s pertains to the heated wall. Furthermore, in this regard, it should be noted that even when there is no backflow, the fluid adjacent to the unheated wall is slow moving. This means that both with or without the backflow, most of the channel throughflow passes adjacent to the heated wall. A second factor is that the effects of the backflow, whatever they might be, should be greatest in the upper portion of the channel and least in the lower portion. However, the rate of heat transfer at the heated wall is least in the upper portion of the channel and greatest in the lower portion. This mismatch between the most affected region and the region of highest heat transfer tends to mute the response of Nu_s to the downflow.

The final point has already been implied in the foregoing – namely, that Nu_s is an average over the entire heated plate. Therefore, it may be insensitive to events which occur at only part of the surface.

Having fully dealt with the downflow issue, certain other features of the results of Fig. 6 will now be addressed. With regard to the accuracy of the data, calculations of the conduction losses through the insulation backing of the heated plate indicated an extreme value of 1/2 percent of the power input. In addition, extraneous heat losses at the unheated principal wall were shown to be negligible with the aid of supplementary numerical solutions for the model described earlier in the paper. The supplementary solutions were performed with the "unheated" plate at the ambient temperature, whereas in the original solutions the unheated plate was adiabatic. The extreme difference in the Nu_s values from the two sets of solutions was 1 percent, which is a measure of the extraneous heat losses from the unheated principal wall.

With the foregoing estimates and with the care exercised in the design and execution of the experiments, the Nu_s data are expected to have an accuracy of 2 percent.

The good agreement of the numerical predictions shown in Fig. 6 with the experimental data encourages the use of the model to predict Nu_s information for other Prandtl numbers. Such solutions have been performed for $\mathrm{Pr} = 0.7$, 2, 5, and 10 (e.g., gases and water), and the corresponding Nu_s results are plotted in Fig. 7 for the same range of $(S/H)\mathrm{Ra}_s$ as was employed in Fig. 6. The results for each Prandtl number are well described by straight lines

$$\mathrm{Nu}_s = C[(S/H)\mathrm{Ra}_s]^n \tag{16}$$

where C and n are listed in Table 1.

As can be seen from both the table and the figure, there is a modest divergence among the Nu_s results for the various Prandtl numbers as $(S/H)Ra_s$ increases. Thus at $(S/H)Ra_s = 2 \times 10^2$, the spread of Nu_s with Pr is 8 percent, while at $(S/H)Ra_s = 8 \times 10^4$, the spread has increased to 23 percent. This increased sensitivity to Prandtl number reflects the greater role played by inertial effects at larger values of $(S/H)Ra_s$.

Concluding Remarks

The experiments performed here have, seemingly for the first time, revealed the presence of a pocket of downflow and recirculation in a buoyancy-driven flow in a heated vertical channel where, heretofore, pure upflow had been thought to prevail. The channel was open to the ambient at its upper and lower ends. One of the principal walls of the channel was maintained at a uniform temperature above that of the ambient, while the other principal wall was unheated. The experiments were performed with water at Prandtl number of about 5.

The downflow and recirculation pocket was observed with the aid of the thymol blue flow visualization technique. The pocket was situated adjacent to the unheated wall, in the upper portion of the channel. It was formed when fluid from the ambient entered the top of the channel adjacent to the unheated wall and passed downward along the wall. Upon attaining its deepest penetration into the channel, the downflowing fluid turned and headed back toward the top of the channel while veering toward the heated plate.

This type of flow pattern was found to exist for $Ra > \sim 35{,}000$. Its existence can be explained by taking note of the presence of a highly buoyant, accelerating stream adjacent to the heated wall. The acceleration draws mass toward the heated wall and, when insufficient mass is available within the channel, fluid is drawn into the top of the channel, adjacent to the unheated wall.

Average Nusselt numbers for the heated plate were measured over a range of nearly three orders of magnitude in $(S/H)Ra_s$ and were very well correlated by the relation $Nu_s = 0.688[(S/H)Ra_s]^{0.249}$. A careful analysis of the results indicated that they were not affected by the downflow and recirculation. Furthermore, numerical predictions for the Nusselt number based on a model without downflow and recirculation were in good agreement with the experimental results.

The aforementioned good agreement encouraged the use of the model to predict Nusselt number results for other Prandtl numbers, and such results were obtained over the range between 0.7 and 10 (e.g., gases and water). The Nusselt numbers for the individual Prandtl numbers were well correlated by power-law relations $Nu_s = C[(S/H)Ra_s]^n$, where the exponent n increases from 0.229 to 0.252 as Pr increases from 0.7 to 10.

References

1 Aung, W., Fletcher, L. S., and Sernas, V., "Developing Laminar Free Convection Between Vertical Flat Plates with Asymmetric Heating," *International Journal of Heat and Mass Transfer*, Vol. 15, 1972, pp. 2293–2308.

2 Carpenter, J. R., Briggs, D. G., and Sernas, V., "Combined Radiation and Developing Laminar Free Convection Between Vertical Flat Plates with Asymmetric Heating," ASME JOURNAL OF HEAT TRANSFER, Vol. 98, 1976, pp. 95–100.

3 Sparrow, E. M., Shah, S., and Prakash, C., "Natural Convection in a Vertical Channel: I. Interacting Convection and Radiation. II. The Vertical Plate With and Without Shrouding," *Numerical Heat Transfer*, Vol. 3, 1980, pp. 297–314.

4 Baker, D.J., "A Technique for the Precise Measurement of Small Fluid Velocities," *Journal of Fluid Mechanics*, Vol. 26, 1966, pp. 573–575.

Experimental Investigation of Natural Convection Losses From Open Cavities

C. F. Hess

R. H. Henze

Assoc. Mem.
Spectron Development Laboratories, Inc.,
Costa Mesa, Calif. 92626

Experimental results for natural convection in a cavity are reported. Both constrained and unconstrained cavity geometries were studied. Detailed velocity profiles were obtained using Laser doppler velocimetry for Rayleigh numbers between 3×10^{10} and 2×10^{11}, corresponding to a constant elevated wall temperature boundary condition. Characteristics of two-dimensional and three-dimensional flows obtained with dye flow visualization are discussed, including boundary layer transition to turbulence, flow patterns in the cavity, and flow outside of the cavity. Local Nusselt number is correlated with local Rayleigh number for constrained and unconstrained cavities.

1 Introduction

Natural convection flows in open cavities are receiving increased attention because of their applications in fire research, passive solar heating, energy conservation in buildings, and solar concentrating receivers. These flow patterns are typically complex, and considerable limitations exist in present modeling techniques that attempt to predict their momentum and heat transfer behavior. This is particularly true in the high Rayleigh number regimes representative of many actual flows.

Much research has been conducted to study flow and heat transfer in complete enclosures. References [1] and [2] provide excellent reviews of this topic. Parameters discussed include Rayleigh number, Prandtl number, aspect ratio, and inclination angle. Current work in buoyancy-driven flows in enclosures concentrates on modeling high Rayleigh number flows [3, 4].

Buoyancy-driven flows in cavities differ from those in complete enclosures where the boundary conditions can be well defined. In modeling cavity flows, assumptions must be made regarding the pressure or flow fields at the cavity aperture or at some plane outside of the cavity. Abrams and Greif [5] provide overall-type results, using a very simple approach solving Bernoulli's equation for a given set of assumptions. Several numerical models use a fully elliptic finite difference scheme with pressure and velocity as primitive variables [6, 7]. Ku et al. [6] apply this model in fire research to study the buoyant flows generated by fire in a corridor. To deal with the opening, they prescribe the pressure and assume the derivative of the velocity components normal to the free surface equal to zero. Thermal conditions at the aperture are assumed also. Experiments show good agreements between computed and measured temperature profiles when the proper assumptions are applied.

Recent work on high Rayleigh number buoyant flows in cavities is related to determining convective losses in solar concentrating receivers. Reference [8] provides an up-to-date report on several research programs, both numerical and experimental, in this area.

This paper presents the experimental results obtained from a research program conducted to study the heat transfer characteristics and flow fields of buoyancy-driven flows in an open cavity.

The cavity model (Fig. 1) consisted of a cubical cavity with one heated wall, an aperture at the opposite wall, and the remaining walls which were insulated. Water was used as the fluid in these experiments, because its properties allow high Rayleigh numbers ($Ra > 10^{11}$) to be obtained with a laboratory scale model. The low wall temperature necessary to achieve these conditions results in radiation-free boundary conditions.

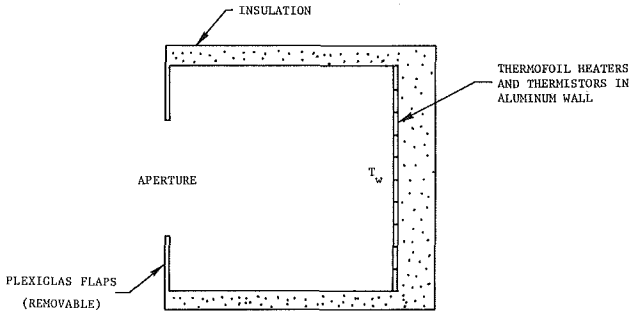

Fig. 1 Schematic representation of cavity

2 Description of Facility and Experimental Apparatus

A 2500-gal aluminum rectangular tank 2.9 m high, 3.05 m long, and 1.07 m wide was used to contain the water needed for the experiment. Centrally located on the tank's large side walls are transparent windows of 114 cm × 114 cm made of 3.8-cm-thick plexiglass. These allow optical access to the cavity.

A water circulation–filtration system is also part of this facility. Particles larger than 5 microns which could cause inaccuracies with LDV are eliminated with this filter.

A cubical cavity of 1 m on the side is centrally located inside the tank. A heated aluminum plate (12.5 mm thick) provides the thermal boundary condition to the system. The plate is heated with foil type heaters which are insulated from behind with 15 cm of closed cell polyurethane. The heaters can provide a maximum power of 17 kW. The top and bottom walls are made of plexiglass and are also insulated with polyurethane.

Power into the heaters is regulated by five independent temperature controllers, providing an accuracy of ± 0.1°C and monitored by true rms voltage meters. These measurements are inputed to the data acquisition computer.

An LDV system operating in the front-scattering mode was used to measure fluid velocities. To resolve the sign of the velocity, a very accurate Bragg cell driver (better than 5 ppm) was developed and built. To avoid multiplex signals from the same particle, an arbitrary time delay between signals can be imposed in the data acquisition software.

The LDV system is traversed across the transparent windows on motorized traverse mechanisms. Two mechanisms are necessary: one for the transmitter and the other for the receiver. Traverse position is tracked with digital counters with a resolution better than ± 0.001 in.

Contributed by the Heat Transfer Division for publication in the JOURNAL OF HEAT TRANSFER. Manuscript received by the Heat Transfer Division March 18, 1982.

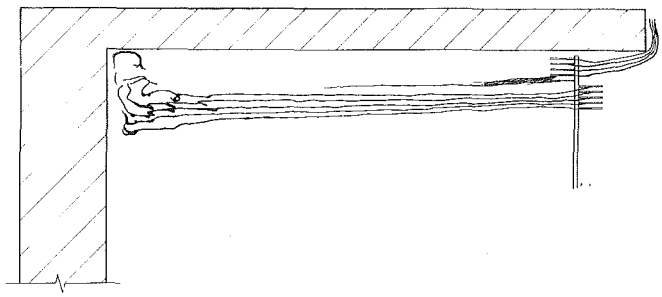

Fig. 2 Schematic of dye flow visualization in the unconstrained cavity

Temperature measurements were performed with thirty copper-constantan thermocouples (gauges 30 to 36) distributed in the aperture (18), plate (5), and boundary layer (7). The thermocouples are connected to an electronic scanner-linearizer-digitizer interfaced to the data acquisition computer. The thermocouples are periodically calibrated against NBS certified thermometers (± 0.05 C), both in a calibration tank and in situ. Temperature accuracy of ± 0.1 C is obtained with this arrangement. Qualitative information of the temperature fields was obtained with a wave shearing interferometer.

3 Description of Experiments

Two cavity geometries were studied. The first corresponded to a cubic cavity with an unrestricted aperture (aperture ratio: 1); in the second, the aperture was restricted with flaps extending from the top and bottom walls, leaving an effective aperture of half the size of the side of the cavity (aperture ratio: 0.5). In either case, only the wall parallel to the aperture was heated, and that heated wall was kept in the direction of the gravity force (inclination angle = 0).

As described earlier, the cavity was centered in the tank which was full with water. The water was filtered, then seeded with 3-μm polyvinyltoluene particles and then allowed to come to rest. At a time selected as zero, the heaters on the back of the aluminum plate were turned on, and a short time thereafter (about 2 min) the plate temperature was established. Constant wall temperature boundary conditions were imposed throughout the experiments. Temperature differences between the plate (wall temperature) and the initially cold fluid, between 2°C and 13°C were established ($Ra = 3 \times 10^{10}$ to 2×10^{11}).

Three types of experiments were performed. The first employed a dye (malachite green in a solution of water and alcohol) to visualize the flow field in particular at the aperture. The second used a wave shearing interferometer to visualize the temperature gradients. In the third type of experiment the velocity of the flow was measured with laser Doppler velocimetry (LDV). Initially, the LDV system was placed at a predetermined position where transient velocities were to be measured. After a steady state velocity condition was reached, the probe volume of the LDV was translated to resolve velocity profiles at various locations throughout the cavity. In all three cases, the temperature of the thermocouples and the power into the heaters were recorded as a function of time.

4 Results and Discussion

4.1 Unconstrained Cavity Case (Aperture Ratio of 1). The general characteristics of the flow areas follow: When the temperature of the vertical plate is raised to T_w, the fluid rises and is turned outward by the pressure gradient imposed by the top. For the Rayleigh numbers employed in these experiments, a boundary layer-type flow is established near the plate and the flow ascends for about 90 percent of the length of the heated plate before it is turned by the top wall. Considerable mixing was observed in this top corner region as the flow turns outward. This mixing region could be laminar or turbulent (as will be quantified later), depending on the Rayleigh number.

The hot flow then followed the top wall and escaped to the tank (atmosphere). In the process of running along the top wall, the flow became laminar again and well-defined laminar streamlines were observed near and at the aperture. Surprisingly, it was observed that a large portion of the incoming flow entered right below the escaping flow, forming a shear layer near the top of the aperture. This shear layer was more pronounced for high Rayleigh numbers. Visualization studies of this unconstrained case showed that the flow was two dimensional in nature.

Dye patterns of the incoming flow (Fig. 2) show that the streamlines are almost parallel and horizontal, and that this flow is entrained all the way into the plate and fed to the boundary layer. This phenomenon may be consistent with an increase of flow entrained into the boundary layer as it turns turbulent. However, it needs to be investigated and quantified.

Nomenclature

F_o = Fourier number $= \dfrac{\alpha_f t}{Y^2}$

g = acceleration of gravity
k = thermal conductivity
l = length from bottom of heated plate
L = length of heated plate

Nu_l = Nusselt number $= \dfrac{gl}{k_f(T_w - T_B)}$

q = heat flux

Ra_l = Rayleigh number $= \dfrac{g\beta_f l^3(T_w - T_B)}{\nu_f \alpha_f}$

T = temperature
u = velocity in the x-direction
u_c = characteristic convection velocity, $u_c = g\beta_f L(T_w - T_B)$
x = distance from heated plate
X = x-direction length of top wall
y = distance from top wall or top of aperture
Y = length of cavity or aperture in y-direction

Symbols

α = thermal diffusivity
β = volume expansion coefficient

θ = dimensionless temperature $\theta = \dfrac{T - T_B}{T_w - T_B}$

ν = kinematic viscosity

Subscripts

B = bulk or far field property

f = fluid property, evaluated at $T_f = \dfrac{T_w + T_B}{2}$

w = hot wall

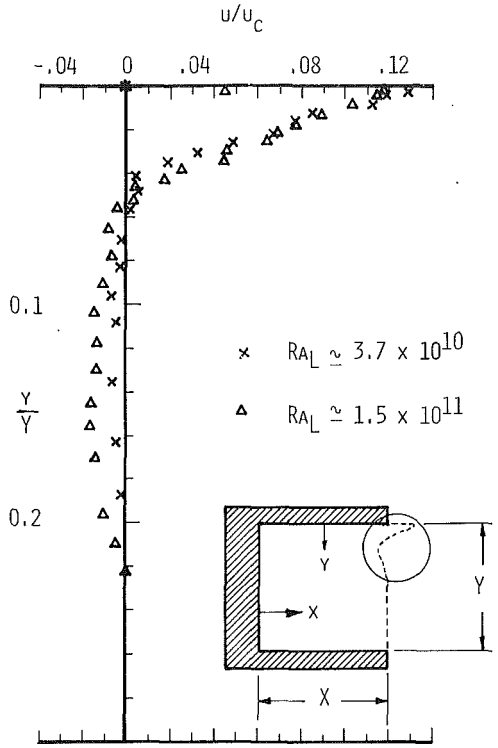

Fig. 3(*a*) Normalized velocity profiles at the aperture plane (x/X = 1.0) for the unconstrained cavity (Y/L = 1.0); (X) u_c = 7.3 cm/s, (Δ) u_c = 14.4 cm/s

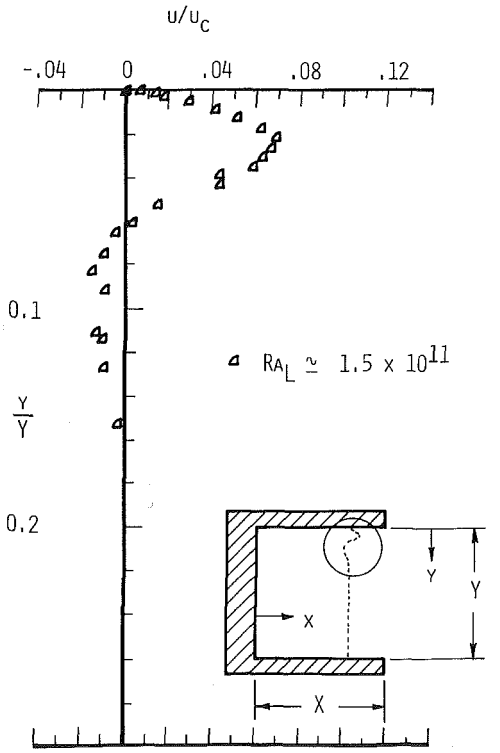

Fig. 3(*b*) Normalized velocity profile at x/X = .75 for the unconstrained cavity (Y/L = 1.0), u_c = 14.2 cm/s

4.1.1 Velocity Profiles. Figures 3(*a*) and (*b*) show normalized velocity profiles for the unconstrained cavity at steady-state conditions defined by no appreciable change in the velocity profile. These profiles quantitatively confirm the flow behavior seen in the flow visualization studies which

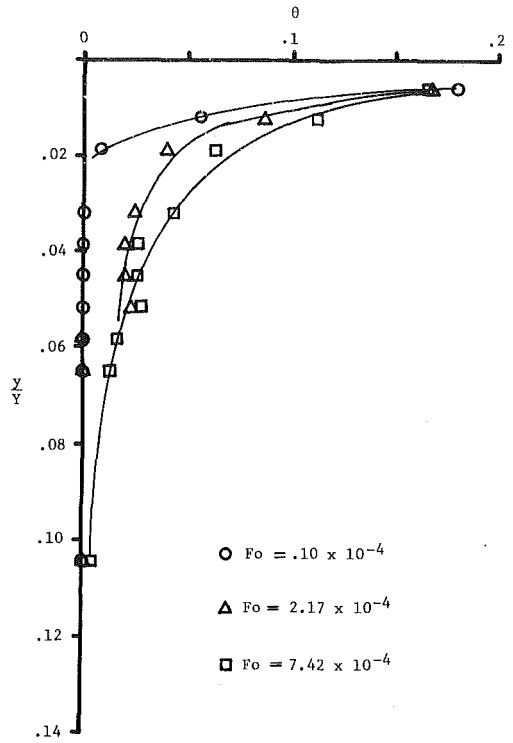

Fig. 4(*a*) Dimensionless temperature profiles at the aperture plane as a function of Fourier number, Ra = 3.7 x 10^{10}

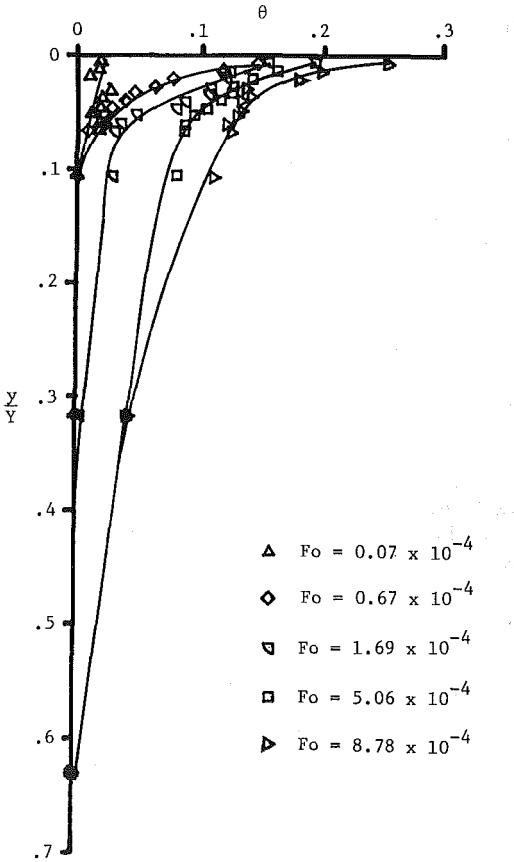

Fig. 4(*b*) Dimensionless temperature profiles at the aperture plane as a function of Fourier number, Ra = 1.5 x 10^{11}

show the presence of a shear layer near the top of the aperture (Fig. 2). Figure 3(*a*) compares the velocity profiles at the aperture for both high and low Rayleigh numbers. In both

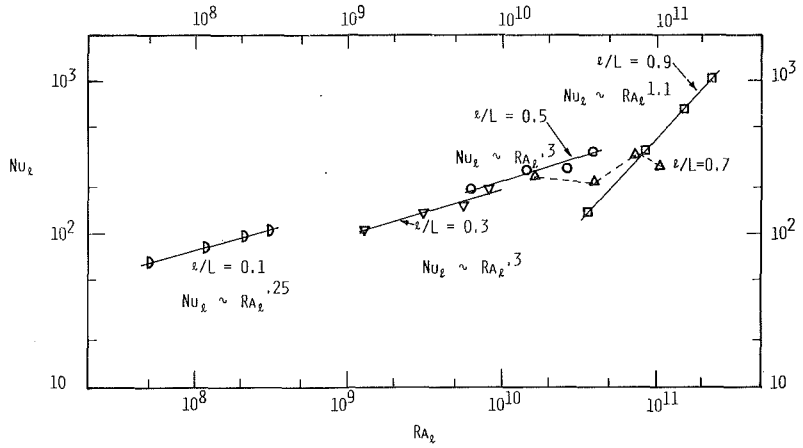

Fig. 5 Variation of local Nusselt number with local Rayleigh number at various heights (l/L) for the unconstrained cavity

cases, the inflection to negative velocities occurs at $y/Y = .055$ to .060. Integration of this region shows a normalized volume flow rate per unit width

$$\int_{y/Y=0}^{y/Y|_{\text{inf.}}} u/u_c d(y/Y)$$

of 3.00×10^{-3} for $\text{Ra}_L \simeq 1.5 \times 10^{11}$, and 2.86×10^{-3} for $\text{Ra}_L \simeq 3.7 \times 10^{10}$, a difference of less than 5 percent.

An important difference between the high and low Rayleigh number cases is the profile of the incoming flow. The low Rayleigh number case shows a slower and more uniform profile throughout the aperture, while the high Rayleigh number case has a stronger negative velocity region which ends at $y/Y \simeq .22$. Velocities below this point were generally too small to resolve with the LDV. Dye studies both inside the cavity and at the aperture showed either a very slow negative velocity or slow oscillations about zero velocity regions below $y/Y > .3$. Integration of the volume flow rate from $y/Y = 0$ to $y/Y = .3$ shows that an average inward velocity $\bar{u} \simeq .02$ cm/s (for either Rayleigh number) would be required throughout the remainder of the aperture to satisfy continuity. This velocity was below the resolution of our present LDV system.

Figure 3(*b*) shows the velocity profile of the high Rayleigh number case at $x/X = .75$. Note how the inflection point decreases with increasing X ($y/Y|_{\text{inf.}} = .061$ at $x/X = .75$, $y/Y|_{\text{inf.}} = .055$ at $x/X = 1.0$). The same effect is observed in the location of the maximum velocity ($y/Y|_{\text{max}} = .022$ at $x/X = .75$, $y/Y|_{max} = .003$ at $x/X = 1.0$), while its magnitude increases from $u/u_c = .070$ at $x/X = .75$, to $u/u_c = .116$ at $x/X = 1.0$. The velocity increases because the flow is being squeezed as it turns sharply upward when it reaches the aperture plane.

4.1.2 Transition to Turbulence. Dye experiments for several wall temperatures were performed at the boundary layer. The dye was introduced at $l/L \sim 0.3$ and was observed as it ascended along the vertical plate. Four different T_w were imposed corresponding to $\text{Ra}_L = 3 \times 10^{10}$, 9×10^{10}, 10^{11}, and 1.5×10^{11}. The first indications of disturbance were observed at a local Rayleigh number $\text{Ra}_l = 2 \times 10^{10}$ to 3×10^{10}. Vortex streets were initiated at $\text{Ra}_l \sim 4 \times 10^{10}$, and complete turbulence was observed at $\text{Ra}_l = 7 \times 10^{10}$ to 9×10^{10}. These results are consistent with those reported by the Lawrence Berkeley Laboratory [3], using a different configuration. They indicate that the transition to turbulence in enclosures is not well understood since many authors are still basing this transition on vertical flat plate data (Ra_l about 10^9). The aspect ratio will also affect the transition to turbulence; however, these studies remain to be conducted.

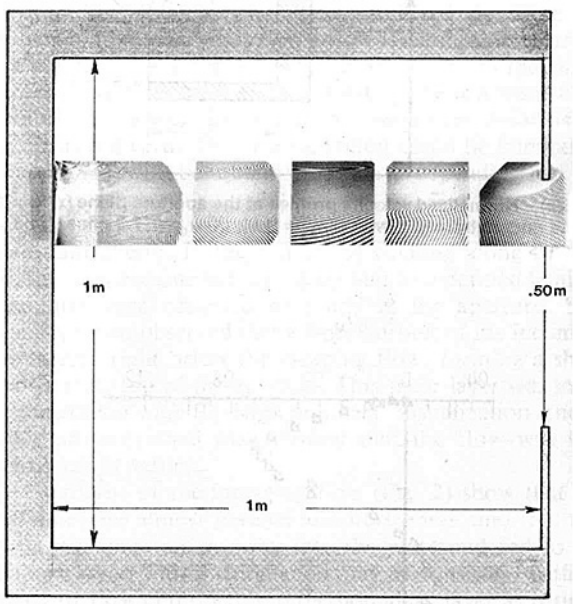

Fig. 6 Interferograms of thermocline in constrained cavity: $\text{Ra}_L = 1.5 \times 10^{11}$

4.1.3 Temperature Profiles. The time history of the dimensionless temperature profiles at the aperture plane are shown on Figs. 4(*a*) and 4(*b*) for the Rayleigh numbers of 3.7×10^{10} and 1.5×10^{11}.

The temperature profiles of either the high or low Rayleigh cases have a similar shape but they reflect a continuous increase in temperature. This behavior is more pronounced at the high Rayleigh number. In addition, for the high Rayleigh number case, temperatures larger than ambient are observed below the velocity inflection plane, except at very early times.

Several effects can be responsible for these results. Convective mixing through the shear layer of hot exiting flow and cold entraining flow can have a strong influence. Also important is the stratification of the water in the tank due to the accumulation of hot flow leaving the aperture and changes in the room temperature.

A thermal analysis indicates that for $\text{Ra} = 1.5 \times 10^{11}$, the thermocline of the tank will descend to the top of the cavity after $\text{Fo} = 8.5 \times 10^{-4}$ (90 min). This limits the time for data acquisition in a stable environment for this Rayleigh number to about one hour per run. This time is larger for lower Rayleigh numbers.

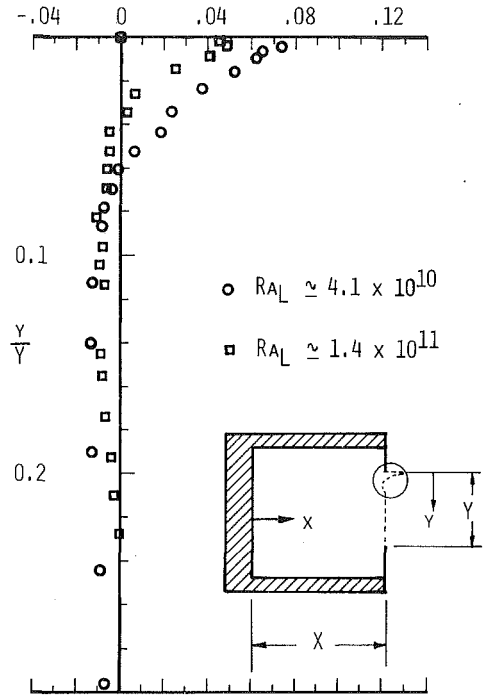

Fig. 7(*a*) Normalized velocity profiles at the aperture plane ($x/X = 1.0$) for the constrained cavity ($Y/L = 0.5$). (o) $u_c = 7.5$ cm/s, (□) $u_c = 14.0$ cm/s

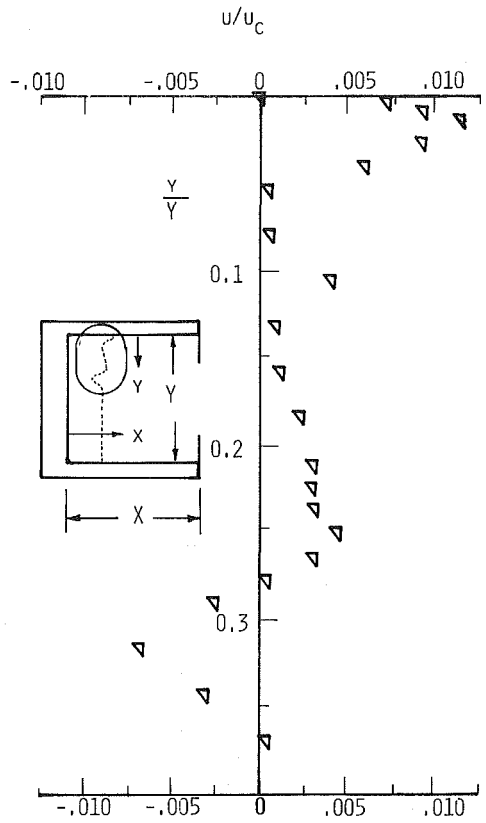

Fig. 7(*b*) Normalized velocity profile at $x/X = .25$ for the constrained cavity ($Y/L = 1.0$), $Ra_L = 2.2 \times 10^{11}$, $u_c = 16.9$ cm/s

4.1.4 The Nusselt Number. As described earlier, five independent heating circuits are used to heat the plate to a constant wall temperature boundary condition. The power input to each individual circuit is measured and corrected for losses in the line. A straightforward conduction analysis was used to estimate the heat losses through the insulation and ends of the plate. The results indicated that they could be neglected.

The Nusselt number was then computed using the expression

$$\mathrm{Nu}_l = \frac{\bar{q}_{w,i} l_i}{k_f (T_w - T_B)}$$

where $\bar{q}_{w,i}$ is the average heat flux output of each circuit, i, and l_i is the average height of this circuit measured from the bottom of the heated plate.

The results are shown in Fig. 5, where the local Nusselt number is plotted as a function of the local Rayleigh number. Note that near the bottom, the slope is close to the one predicted for vertical flat plates ($\mathrm{NU}_l \sim \mathrm{Ra}_l^{0.25}$). For $l/L = 0.7$, a more erratic behavior was observed which is partly due to the transition to turbulence. At $l/L = 0.9$ both the value and slope of Nu changed dramatically. Two phenomena are influencing this behavior. First the flow (except for the lowest point) was typically turbulent in this region. Second, the hot mixing region near the top helped reduce the heat flux into the fluid resulting in a lower Nu for the same Ra. That is this top region is affected more by recirculation than the lower regions.

4.2 Constrained Cavity Case (Aperture Ratio of 0.5). Flaps on the top and bottom of the aperture were added to produce a central opening with an aperture ratio of 0.5. The same Rayleigh numbers (based on length of heated plate) were run for this case. It was observed with the dye patterns that initially the flow is highly three dimensional. Three regimes were established as a function of time. Initially, the flow following the top wall bounces back from the upper flap and a slow oscillatory motion is generated. As more hot fluid is driven by the hot plate, a thicker region of hot fluid is accumulated on the top. The flow impinging on the top flap divides into two large swirls almost horizontal to the top wall. The swirling flows descend slowly due to the presence of the cooler side windows and the hotter fluid displacing them. A large double vortex is thus established on the top, and it keeps on rotating as a thermocline grows on the top. At the aperture plane, the velocity profile experiences oscillations at the early times, and then it is shaped similarly to the unconstrained case.

After an extended period of time, almost stagnant hot fluid fills the top of the cavity to the bottom of the upper flap. Interferometric measurements at this plane (Fig. 6) show the sharp change experienced by the temperature profile just below the region of exiting flow. This is evidenced by the changes in the fringe shape. Coarsely spaced fringes correspond to constant temperature fields. As hot fluid accumulates on the top, it deflects down the ascending boundary layer flow. This effectively reduces the aspect ratio and forms a well-defined (by the bottom of the upper flap) thermocline.

4.2.1 Velocity Profiles. Figures 7(*a*) and (*b*) show normalized velocity profiles for the constrained cavity during steady-state velocity conditions. Profiles of the initial transient flow regime and the double-vortex regime are not reported. Unlike the unconstrained cavity flow, which was two dimensional, the constrained cavity flow was observed to be significantly three dimensional in nature, even during steady-state conditions. The velocity profiles reported are for the center plane of the cavity width. Therefore, the quantitative values of velocity and the position of velocity inflection reported are not applicable to the entire cavity width.

Figure 7(*a*) compares the velocity profiles in the middle of the aperture for two Rayleigh numbers. The general behavior of the flow at the aperture plane is similar to that of the unconstrained cases; a small region of exiting flow at the top of the aperture, a shear layer caused by the incoming flow directly beneath the exiting flow, and maximum incoming

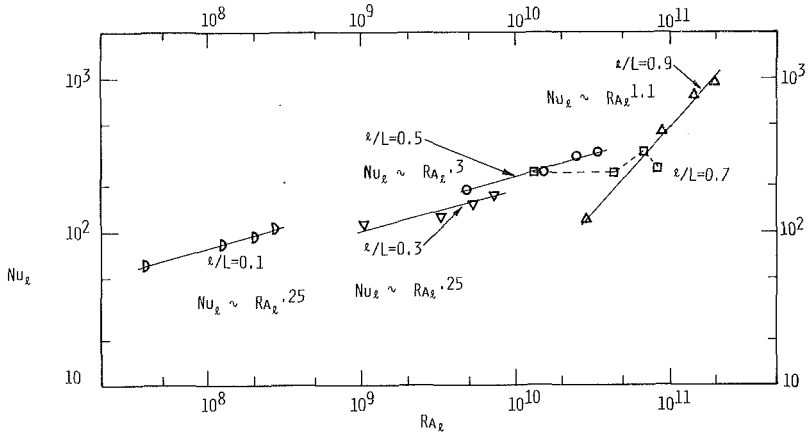

Fig. 8 Variation of local Nusselt number with local Rayleigh number at various heights (ℓ/L) for the constrained cavity

velocities in a region immediately below the shear layer. The constraining flap has caused a significant reduction in the momentum of the exiting flow, with a decrease in the maximum exiting velocity from $u/u_c = .130$ to $u/u_c = .073$ for the low Rayleigh number case and from $u/u_c = .116$ to $u/u_c = 0.5$ for the high Rayleigh number case.

The constrained profiles show similar trends to those found in the unconstrained profiles for the high and low Rayleigh number cases. That is, for the high Rayleigh number case, most of the incoming flow occurred between $y/Y = .036$ and $y/Y = .230$. Velocities below this region were unresolvable by the LDV and appeared to be slightly negative, or to fluctuate about zero. Notice that integration of the velocity profile at any aperture plane is meaningless because of the three-dimensional characteristics of the flow.

For the low Rayleigh number case, small incoming velocities of $u/u_c \simeq .002$ to .003 were measured from $y/Y = .3$ down to $y/Y = .95$. This requires a significant amount of exiting flow to be present at other planes in the cavity width to satisfy continuity, again pointing out the three-dimensional aspects of the flow. Note that the low Rayleigh number unconstrained cavity flow also demonstrated incoming velocities in the lower aperture region, and this effet does not appear to be as strong for the high Rayleigh number flows.

A complex velocity profile can be observed in Fig. 7(*b*). The upper portion corresponds to the hot boundary layer flow that penetrated the thermocline and moves along the top wall. The lower portion is characteristic of the shear layer, which is felt even close to the hot plate. A similar inflection in the velocity at $y/Y = .275$ was observed at $x/X = .75$, which indicates a horizontal entraining velocity from the aperature to the heated plate. Furthermore, flow visualization outside of the cavity showed that the incoming velocity was also traveling following a horizontal trajectory. As indicated, there is evidence of movement throughout the entire cavity with some small regions remaining almost stagnant. This has an effect in the heat transfer coefficient as will be discussed next.

4.2.2 The Nusselt Number. The local Nusselt numbers are plotted on Fig. 8 as a function of the local Rayleigh number. The results except near the top are almost identical to those of the unconstrained case. The total heat flux to the vertical wall was measured for the constrained and unconstrained apertures for four different wall temperatures. The results indicated a reduction of about 10 percent in the constrained case. This reduction is surprisingly small and could be attributed to the high Pr of the fluid. The slopes of the Nusselt numbers are also almost identical to those of Fig. 5.

It is expected that the heat transfer will be further reduced using smaller and/or off-centered apertures. However, this reduction will be limited because of the ability of the boundary layer flow (due to its large momentum) to penetrate and disrupt the thermocline.

Acknowledgment

Financial support for this research was provided by the U.S. Department of Energy under contract No. DE-AC01-79-ET21105.

References

1 Ostrach, S., "Natural Convection in Enclosures," *Advances in Heat Transfer*, Vol. 8, 1972, p. 161.

2 Buchberg, H., Catton, I., and Edwards, D. K., "Natural Convection in Enclosed Spaces — A Review of Application to Solar Energy Collection," ASME JOURNAL OF HEAT TRANSFER, Vol. 98, 1976, pp. 182–188.

3 Bauman, F., Gadgil, A., Kammerud, R., and Greif, R., "Buoyancy-Driven Convection in Rectangular Enclosures: Experimental Results and Numerical Calculations," ASME Paper 80-HT-66, July 1980.

4 Quon, C., "High Rayleigh Number Convection in an Enclosure — A Numerical Study," *The Physics of Fluids*, Vol. 15, No. 1, 1972, p. 12.

5 Abrams, M., and Greif, R., "A Simple Theory for Predicting the Natural Convective Energy Loss from Side-Facing Solar Cavity Receivers," SAND 81-8201, Jan. 1981.

6 Ku, A. C., Doria, M. L., and Lloyd, J. R., "Numerical Modeling of Unsteady Buoyant Flows Generated by Fire in a Corridor," *Proceedings of the 16th Symp. (Intl) on Combustion*, CI, 1976, pp. 1373–1384.

7 LeQuere, P., Humphrey, J. A. C., and Sherman, F. S., "Numerical Calculation of Thermally Driven Two-Dimensional Unsteady Laminar Flow in Cavities of Rectangular Cross Section," *Numerical Heat Transfer*, Vol. 4, 1981, pp. 249–283.

8 Department of Energy Solar Central Receiver Semiannual Meeting, Report No. SAND 80-8049, Jan. 1981, issued by Sandia National Laboratories.

Experimental Study of Three-Dimensional Natural Convection High-Rayleigh Number

M. S. Bohn
Solar Energy Research Institute,
Golden, Colo. 80401
Assoc. Mem. ASME

A. T. Kirkpatrick
Mechanical Engineering Department,
Colorado State University,
Ft. Collins, Colo.
Assoc. Mem. ASME

D. A. Olson
Mechanical Engineering Department,
Massachusetts Institute of Technology,
Cambridge, Mass.
Assoc. Mem. ASME

Natural convection in buildings is characterized by three-dimensional flow at high Rayleigh numbers ($Ra \sim 10^{10}$). At present, little is known about natural convection heat transfer in this regime, although a better understanding would allow more energy efficient usage of buildings. This paper presents results from the first phase of an experimental program aimed at improving our understanding of heat transfer and air flow in buildings. The experimental apparatus consists of a cubical enclosure filled with water in which each wall may be heated or cooled in a controlled manner. A transparent, adiabatic top and bottom provide flow visualization capability. Average heat transfer coefficients for the walls have been measured for several configurations of heating and cooling of the vertical isothermal walls. A unified Nu-Ra correlation has been computed which collapses the heat transfer coefficients of the various configurations to within 5.7 percent. The heat transfer and flow visualization results indicate that even at Rayleigh numbers as high as 6×10^{10}, the heat transfer mechanism is laminar boundary-layer convection from one wall to the bulk fluid.

Introduction

In this paper, we address the problem of three-dimensional natural convection in enclosures with differentially heated vertical walls at high Rayleigh numbers. The particular application of interest is passive solar heating and cooling of buildings, although the experimental data should be useful in many other applications as well. These include cryogenic storage tanks, building fires, nuclear reactor cooling, and solar cavity receivers. In addition, the data should be useful in three-dimensional numerical code validation and in determining the validity of the assumption of two-dimensionality in previous experiments.

The objective of the research is to determine the natural convection flow patterns and heat transfer coefficients between heated and cooled vertical walls in a cubical enclosure. This problem involves three-dimensional flow between perpendicular walls, as well as across parallel walls.

Natural convection heat transfer across fluid-filled enclosures has been the subject of many analytical, numerical, and experimental investigations. The flow regimes in the two-dimensional problem involving heat transfer between two parallel walls were first delineated by Batchelor [1] using a Rayleigh number criterion, and subsequently confirmed by Eckert and Carlson [2]. At Rayleigh numbers greater than 10^4 and aspect ratios near 1, the laminar boundary layer regime exists. The heat transfer mechanism is convection in boundary layers along the vertical walls surrounding a core region. The core region is relatively inactive, is isothermal in the horizontal direction, and has a linear temperature gradient in the vertical direction. Elder [3, 4] and Gill [5], for A, aspect ratios >1, where the aspect ratio is the ratio of enclosure height to length, have shown there is entrainment between the hot and cold wall boundary layers, due to the top and bottom surfaces of the enclosure, resulting in stable thermal stratification of the core. In addition, their results show that the boundary layer heat transfer is only weakly dependent on the Prandtl number of the fluid in the enclosure.

As the Rayleigh number is increased, the thickness of the velocity and temperature boundary layers decreases, since the boundary layer thicknesses are proportional to $A^{1/4}\ \mathrm{Ra}^{-1/4}$. Bejan [6] has extended Gill's laminar boundary layer solution for $A > 1$ to predict heat transfer rates. The resulting equation, valid as $A\ \mathrm{Ra}^{1/7} \to \infty$ is $\mathrm{Nu} = 0.364\ A^{-1/4}\ \mathrm{Ra}^{1/4}$. Simpkins and Dudderar [7] have experimentally checked Gill's boundary layer analysis for $0.25 < A < 9$. An approximate boundary layer analysis for aspect ratios > 5 was performed by Raithby et al. [8, 9], and an integral boundary layer analysis has been performed by Emery and Chu [10]. For a fluid with a Prandtl number of 3.5, the Raithby-Hollands analysis predicts $\mathrm{Nu} = 0.335 A^{-1/4}\ \mathrm{Ra}^{1/4}$. In summary, the previous boundary layer analyses for $A > 1$ predict $\mathrm{Nu} = (.3 \text{ to } .4)\ A^{-1/4}\ \mathrm{Ra}^{1/4}$. For turbulent flow, the Raithby-Hollands analysis predicts $\mathrm{Nu} = 0.044\ \mathrm{Ra}^{1/3}$. The two foregoing predictions are plotted in Fig. 1 for $A = 1$.

Numerical results for aspect ratios between 1 and 20, and Grashof number $< 10^5$ have been presented by Newell and

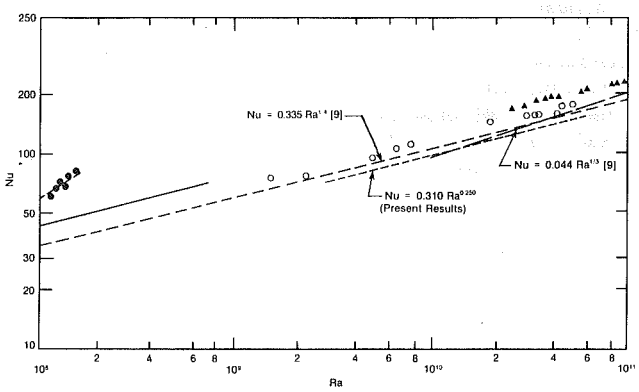

Fig. 1 Compilation of two-dimensional high Rayleigh number data and comparison with present results

- – – – Raithby-Hollands laminar boundary layer theory (9), $A = 1$, $Pr = 3.5$
- – – Raithby-Hollands turbulent boundary layer theory (9), $A = 1$, $Pr = 3.5$
- ——— Gadgil numerical analysis (23), $A = 1$, $Pr = 0.7$
- ○ Bauman et al. (27), $A = 0.5$, $Pr = 3.5$
- ▲ Nansteel and Greif (29), $A = 0.5$, $Pr = 3.5$
- ● Burnay et al. (18), $A = 1$, $Pr = 0.7$

Contributed by the Heat Transfer Division and presented at the ASME-JSME Joint Thermal Engineering Conference, Honolulu, Hawaii, March 1983. Manuscript received by the Heat Transfer Division May 2, 1983.

Schmidt [11] for aspect ratios between 0.1 and 20, by Boyack and Kearney [12] and aspect ratios between 0.05 and 1, and $Ra < 10^6$ by Inaba et al. [13]. Numerical results for $Ra < 10^7$ and aspect ratios of 1, 5, and 10 have been computed by Strada and Heinrich [14]. The numerical results predict a maximum Nusselt number near an aspect ratio of one, and as the aspect ratio approaches zero or infinity, the Nusselt number approaches unity, a trend also noted by Bejan [15]. Also, as the Rayleigh number is increased, the aspect ratio at which the maximum Nusselt number occurs decreases. In Inaba's [13] numerical analysis, the aspect ratio at which the Nusselt number was a maximum decreased from $A = 1.7$ at $Ra = 10^4$ to $A = 1.2$ at $Ra = 10^5$. Bejan [15] predicted that the maximum Nusselt number would occur at $A = 0.4$ for $Ra = 10^6$; $A = 0.25$ to $Ra = 10^7$; and $A = 0.18$ at $Ra = 10^8$. The data (from an experiment with $A = 0.5$) plotted on Fig. 1 follow the same trend, since they lie above the $A = 1$ predictions.

Limited two-dimensional experimental data exist for $Ra > 10^8$ and A near 1. MacGregor and Emery [16] found experimentally for constant heat flux conditions and aspect ratios from 10 to 40 that $Nu = 0.42 A^{-0.3} Pr^{0.012} Ra^{1/4}$ for $3 \times 10^4 < Ra < 3 \times 10^6$ and $Nu = 0.046 Ra^{1/3}$ for $3 \times 10^7 < Ra < 10^9$. For the aspect ratios of their experiment, they determined that the transition from fully laminar to fully turbulent boundary layer flow occurred in the range of Rayleigh numbers from 3×10^6 to 3×10^7. Dropkin and Sommerscales [17] reported experimental results for Rayleigh numbers from 5×10^4 to 7.2×10^8. Experimental data for air in a square enclosure with Rayleigh numbers from 1.2×10^8 to 1.7×10^8 have been presented by Burnay et al. [18]; however, the precision of their results is suspect since the correction for radiation heat transfer was of the same magnitude as the natural convection heat transfer. Measurements and correlation equations have been published by ElSherbiny et al. [19] for $A \geq 5$, and Rayleigh numbers from 10^2 to 2×10^7.

Increased attention has been focused recently on natural convection heat transfer in rectangular cavities with aspect ratios less than one. Bejan and Tien [20] have predicted that for $0.1 < A < 1$, $Nu = 0.623 A^{-2/5} Ra^{1/5}$. Shiralkar et al. [21] analytically and numerically show that for laminar flow and $A < 1$, as $Ra \rightarrow \infty$, $Nu \rightarrow 0.354 Ra^{1/4}$. The exponent of the Rayleigh number was shown to be not constant, but a decreasing function of Rayleigh number. Analytical and numerical calculations were performed by Tichy and Gadgil [22] for $A = 0.1$, 0.2, and $Ra > 10^6$. Numerical results have been reported by Gadgil [23] for $A = 1$ and $10^4 < Ra < 10^9$, and are plotted in Fig. 1.

Imberger [24] found experimentally that as $Ra \rightarrow \infty$, $Nu \rightarrow A Ra^{1/4}$ for $A = 0.01$, 0.02. Bejan et al. [25] reported that $Nu = 0.014 Ra^{0.38}$ for $A = 0.0625$ and $2 \times 10^8 < Ra < 2 \times 10^9$. Experimental results for the flow pattern in enclosures with aspect ratios between 0.1 and 10 have been reported by Sernas and Lee [26]. Experiments with a water filled cavity with $A = 0.5$ an Prandtl number variation from 2.6 to 6.8 have been reported by Bauman et al. [27], Gadgil et al. [28], and Nansteel and Greif [29] for Rayleigh numbers from 1.6×10^9 to 1.1×10^{11}. The data points from [27] and [29] are plotted in Fig. 1.

There are very few articles in the literature on three-dimensional flow in enclosures with differential side heating. Mallinson and deVahl Davis [30] numerically solved for the laminar temperature and velocity fields in a cubical enclosure with adiabatic endwalls. The endwalls induced a double spiral motion in the core, and decreased the average Nusselt number by about 3 percent relative to a two-dimensional case. The endwall effect decreased with increasing Rayleigh number, from a 4.8 percent difference at $Ra = 10^4$ to a 2.6 percent difference at $Ra = 10^6$. This small effect shows that in the laminar boundary layer regime, the overall heat transfer is not very sensitive to the flow pattern in the core region. As the endwalls are moved from an endwall aspect ratio of 1 to 5, the endwall effect on the Nusselt number decreases from 4.2 percent to 2.3 percent at a constant Rayleigh number of 1.5×10^5. A numerical study of three-dimensional turbulent flow in a ventilated room was performed by Hjertager and Magnussen [31]. Gadgil [23] numerically calculated a hot wall average Nusselt number of 145 for a cube with one of its vertical surfaces maintained at a uniformly higher temperature than the other five surfaces at $Ra = 1.15 \times 10^{10}$. Morrison and Tran [32] measured the effect of endwall conduction on the velocity and temperature profiles for $A = 5$, and $Ra = 5 \times 10^4$. A literature search did not reveal any results for perpendicular vertical walls.

Description of the Experiment

The test cell, Fig. 2, is a cubical enclosure, interior dimension 30.5 cm, constructed of eight 1.27-cm-thick aluminum plates. The four inner plates overlap one another and are screwed together with a neoprene gasket to form the enclosure. The four outer plates provide heating and cooling to the four enclosure walls as shown in Fig. 3. The outer plates are sealed and bolted to the inner plates.

Three of the walls have a centered thermocouple located to within 3 mm of the enclosure inner surface. The fourth wall has eight such thermocouples. These thermocouples are located on a horizontal line 5 cm above and 5 cm below the wall center and spaced on 5 cm centers from the wall vertical centerline. The wall thermocouples (copper-constantan) indicate the average wall temperature and spatial variation of the wall temperature across the plate. The spatial variation was less than 10 percent (typically 5 percent) of the overall

Nomenclature

A = aspect ratio, height to length ratio of a two-dimensional enclosure
A_w = area of enclosure wall (cm^2)
g = acceleration of gravity (cm/s^2)
H = height of a two-dimensional enclosure (cm)
h = average heat transfer coefficient of enclosure wall $= Q/A_w \lvert T_w - T_b \rvert$ ($W/cm^2 °C$)
k = thermal conductivity of test cell fluid ($W/cm °C$)
L = plate spacing of cubical enclosure (cm)
m = exponent of Ra (−)
Nu = Nusselt number $= hL/k$ (−)
Pr = Prandtl number of test cell fluid (−)
Q = heat transferred to or from wall (W)
Ra = Rayleigh number $= g\beta\Delta TL^3 Pr/\nu^2$ (−)
T = temperature (°C)

Subscript

b = bulk
c = cooled wall
h = heated wall
H = based on height dimension
x = based on distance from leading edge
w = wall

Greek Symbols

β = coefficient of thermal expansion ($°C^{-1}$)
ΔT_o = overall temperature difference $= T_h - T_c$ (°C)
ν = kinematic viscosity

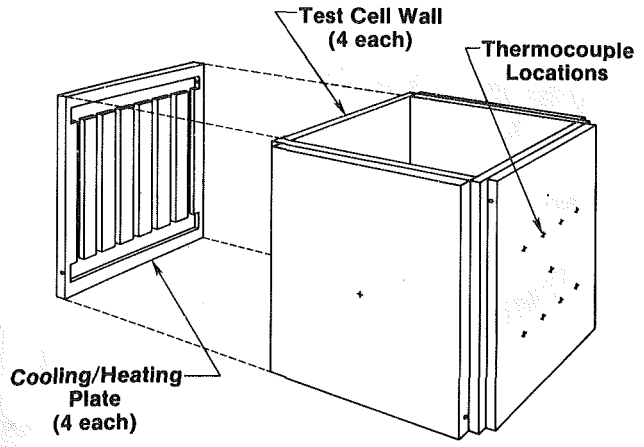

Fig. 2 Diagram of the cubical enclosure test cell. Interior dimensions of the cube are 30.5 cm.

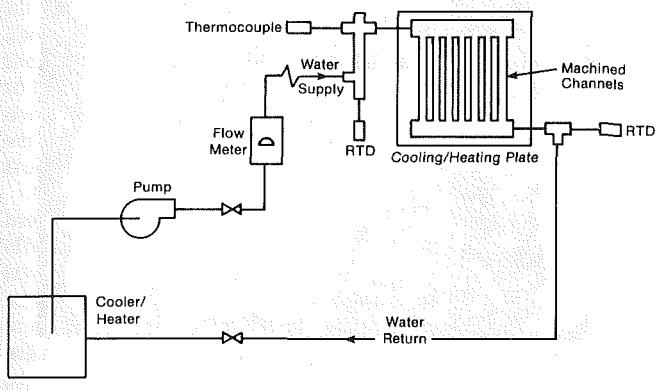

Fig. 3 Diagram of the cooling/heating circuits

temperature difference, $T_h - T_c$. Therefore, the heated and cooled walls may be considered isothermal.

For flow visualization purposes, the top and bottom of the enclosure consists of 1.27-cm-thick lucite plates screwed to the top surface of the inner plates with a neoprene gasket. The top plate has four compression fittings with rubber septums that allow hypodermic tubing to be inserted into the test cell. Diluted food coloring is used as the dye and injected through the hypodermic tubing into the test cell. The dye is injected through a micrometering valve for flow control at approximately 5 cc per hour flow rate. Total volume of injected dye for a typical 1-hr experiment from all four dye ports is therefore about 0.8 percent of the cell volume. Dye velocity at the tip of the needle is less than 3 mm/s, which is much less than flow velocity in the boundary layers and roughly the same as the core velocities. When the probe is inserted more than 10 cm into the cell, heat transfer from the dye, as it flowed through the needle to the test cell, appeared to bring the dye to thermal equilibrium with the test cell water. For insertions of less than 10 cm, the buoyant effect on the dye could be seen as it exited the tip of the needle. Under these conditions, the dye drifted upward (or downward in warm regions) for about 1 cm before appearing to move with the local flow. When dye was injected into the boundary layer, the probe was adjusted to approach the wall obliquely to create minimum flow disturbance, see Fig. 6. Although this method of flow visualization is far from ideal, it does offer many advantages and is very simple to implement.

The four aluminum test cell walls are insulated with urethane foam board insulation 8.3 cm thick, thermal resistance 4.6°C m^2/W. Heat loss from these four walls is estimated to be about 0.1 percent of the total heat transferred from the walls. The estimate is based on the wall temperature, the outer surface temperature of the insulation, and the thermal resistance of the insulation. Loss from the lucite top (which was usually not insulated) is estimated to be about 0.5 percent. This estimate was made from the highest temperature on the outer surface of the plate, ambient temperature and an assumed natural convection coefficient of 6 W/m^2 °C. The bottom lucite plate operates near ambient temperature and losses from that plate are estimated to be less than 0.2 percent. Therefore, the test cell top and bottom may be considered adiabatic. Heat transferred from a hot wall to a cold wall through the neoprene insulation is estimated to be about 0.8 percent.

Cooling or heating of the four enclosure walls is accomplished by pumping water through milled channels in the four outer aluminum plates, Fig. 3. Hot water is supplied by a 6-kW in-line electric heater, and a domestic hot water tank is used to store and buffer the hot water before it is pumped to the heated enclosure walls. The in-line heater is controlled by a proportional temperature controller that senses the water temperature as it leaves the hot water tank. In this way, water temperature delivered to the heated plates is controlled to within ±1/4°C. Cold water is supplied by pumping the water through a tank that contains a heat exchange coil. By pumping cold tap water through this coil, cold water delivered to the cooled enclosure walls is also controlled to ±1/4°C. A fitting at the channel inlet provides water inlets and outlets and fittings for insertion of a thermocouple in the inlet flow, an RTD probe in the inlet flow and a second RTD in either the inlet or outlet flow. This arrangement is used to measure the change in cooling or heating water temperature in the four walls. The RTD probes are placed in opposite arms of a Wheatstone bridge in such a way that the nominal probe resistance, 100 ohm, is cancelled and a bridge output voltage proportional to the temperature difference measured with this technique was determined by calibration to be ±1 percent for temperature differences greater than about 0.2°C.

Cooling and heating water flow rates, nominally 500 kg/hr, are measured with rotameters. These were calibrated by the stopwatch-and-bucket method to within ±0.5 percent for temperatures near ambient. For the highest temperatures the walls are operated, about 65°C, the flow meters tended to read high by about 2–3 percent, in addition to a decrease of approximately 1.5 percent in the water density (from 30 to 60°C). Partially offsetting those two errors is an error that increases to about 2 percent at 65°C due to nonlinearity of the temperature difference measuring method.

Frictional heating in the cooling/heating channels is responsible for about a 1 percent decrease (increase) in the magnitude of measured heat transfer from (to) the hot (cold) walls. An approximate error analysis based on all four sources of error, suggests that the heat transfer measurement for each wall is accurate to ±2 percent. Data are not corrected for conduction through the neoprene gasket from a hot wall to a cold wall (about 0.8 percent), nor for radiation heat transfer from the hot wall to the cold walls (about 1.6 percent). Overall heat balances in the test cell (total measured heat transfer from hot walls minus total measured heat transfer to the cold walls divided by total measured heat transfer from the hot walls) is typically better than ±2 percent, although for low Rayleigh number tests (less than 0.5×10^{10}) this increased to ±4 percent. Overall heat transfer measurement is expected to be within ±5 percent of the actual convective heat transfer from each wall.

The working fluid in the test cell is de-ionized water. To eliminate the formation of air bubbles in the test cell, the water was brought to a slow boil for two hours, allowed to cool, then poured slowly into the cell. Water used for diluting the food coloring dye is treated similarly. The test cell was carefully leveled with a bubble-type machinists level. Thermal

expansion of the test cell water is accommodated by a small expansion tank held about 20 cm above the test cell and connected by flexible tubing to the cell.

Properties of the water (thermal conductivity, dynamic viscosity, density, coefficient of thermal expansion) in the test cell are calculated at a temperature equal to the average of the four heated/cooled wall temperatures, referred to as the bulk temperature, T_b. Specific heat was taken as constant (4.19 J/gm°C). The length scale used in calculating the Nusselt number and Rayleigh number is $L = 30.5$ cm and, the area used to derive the heat transfer coefficient is $A_w = 930$ cm^2. The temperature difference used in deriving the Rayleigh number is the difference in temperatures of the hot and cold walls, i.e., the overall temperature difference.

$$\mathrm{Ra} = \frac{g\beta\Delta T_o L^3}{\nu^2}\mathrm{Pr} \tag{1}$$

The temperature difference used to calculate the heat transfer coefficient is the difference between the wall temperature and the bulk temperature

$$\mathrm{Nu} = \frac{hL}{k} \quad h = \frac{Q}{A_w|T_w - T_b|} \tag{2}$$

The four possible different configurations of heated/cooled walls were tested. These are denoted by CHCC, HHCC, HCHC, and HHHC. Here, H refers to a heated wall and C refers to a cooled wall. The wall with eight thermocouples is called wall #1 and is listed first in this scheme. Thus the first series of runs involved wall #1 being cooled, a heated wall adjacent to wall #1, a cooled wall opposite wall #1, and the remaining wall also being cooled.

For each configuration, at least 24 hours is initially allowed to reach steady state. The hot wall temperatures are set to produce several different Rayleigh numbers from 0.3 to 5.0 × 10^{10} with at least 3 hrs allowed to reach steady state between Rayleigh number settings. Steady state is indicated by a steady temperature difference (for constant flow rate) in the heating and cooling water for each wall, i.e., constant wall heat transfer. Generally, the first Rayleigh numbers run are in the middle of the range, then the higher ones are run in increasing order, then Rayleigh numbers decreasing below the first one tested. Results did not vary significantly with the order of testing, however. The Prandtl number varied from about 3.5 to 6 due to variation in the bulk temperature.

At the end of this series of four configurations which spanned a period of about one month, HCCC was run to compare with the first configuration, CHCC. The results for the hot wall for both configurations agreed to within ±5 percent for tests at three Rayleigh numbers ranging from 0.46 to 2.7 × 10^{10}.

Results

Flow visualization experiments confirm the existence of a relatively inactive core region for all configurations. A unique core flow pattern is set up for each configuration. An example is shown in Fig. 4 for the configuration HCHC at Ra = 2.9 × 10^{10}. In Fig. 4, dye is injected at a point about halfway between the top and bottom of the test cell through the port near the top of the photograph. The dye stream moves toward the warm wall, where it apparently splits. A small part of the stream seems to be entrained by the boundary layer as it moves vertically up the wall to approximately 2 cm below the top of the cell. At this point, the dye stream separates from the wall and disperses. The part of the stream moves in a helical pattern, clockwise viewed from above. (A shadow of the upper portion of the helix is projected on the cold wall.) At least one complete rotation of the helix is visible before the dye becomes too diffuse to be clearly seen. Even a portion of the first rotation near the wall is difficult to see. By symmetry,

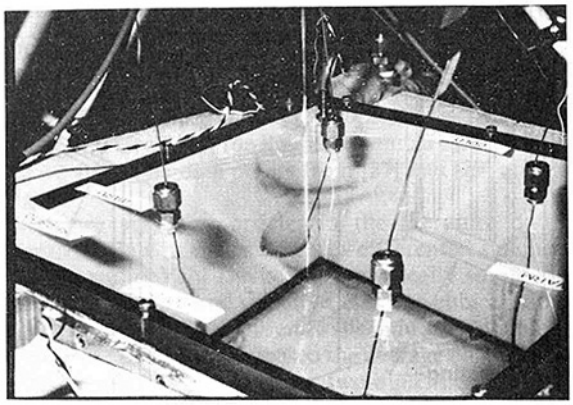

Fig. 4 Flow visualization for the configuration HCHC at Ra = 2.9 × 10^{10}

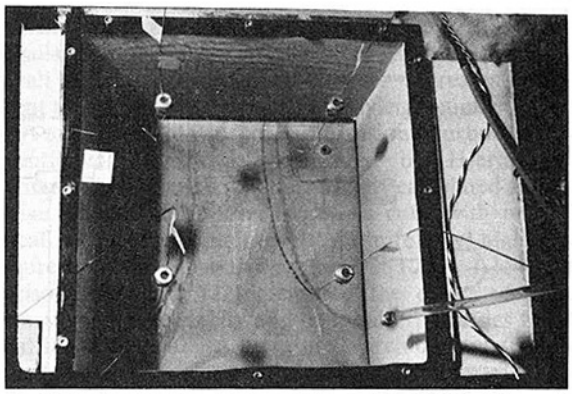

Fig. 5 Flow visualization for the configuration CHCC at Ra = 3.6 × 10^{10}

we assume the core flow consists of four such helices with the direction of rotation alternating from corner to corner. Flow velocity was not measured but was estimated by observing the movement of the dye. In the core, the velocity is such that one revolution of the helix in Fig. 4 required several minutes. Velocity in the boundary layers is of the order of 1 cm per s. A repeat of the visualization experiment shown in Fig. 4 for Ra = 0.8 × 10^{10} did not reveal the helical flow in the core. This change in the core flow could be related to a small change in the heat transfer results which will be discussed later in this section.

Figure 5 shows flow visualization results for the configuration CHCC at Ra = 3.6 × 10^{10}. The heated wall is near the top of the photograph. The core flow is depicted by the lower right dye probe, which is inserted to within 3 cm from the cell bottom. The dye stream bends in toward the plane of symmetry and impinges the heated wall normally before being entrained into the boundary layer and flowing upward. From the junction of the wall and the top, the dye proceeds across the top in a similar curved path until it reaches the cooled wall, where it flows downward with the wall boundary layer. Weak cellular structures, not shown in this photograph, were observed in the core near the top center of the two parallel cooled walls. The volume near the intersection of the cooled walls tends to be stagnant.

A cursory examination of the core temperature with copper constantan thermocouples revealed stratification with a nearly linear vertical temperature distribution and weak variations in a horizontal plane, consistent with previous work in two dimensions [1, 2]. The temperature distribution varies from this linear profile near the top and bottom of the cell where heated fluid (top) or cooled fluid (bottom) flowed in a boundary-layer-like flow to the cooled or heated vertical walls.

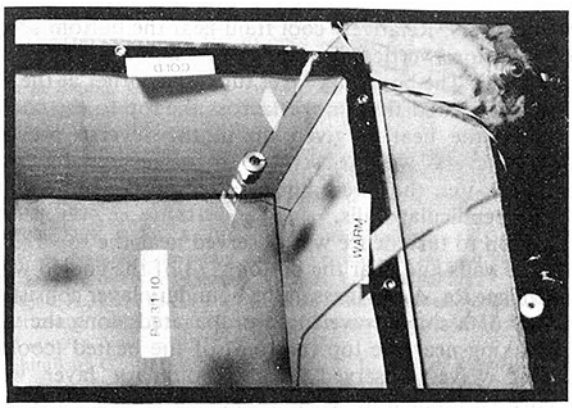

Fig. 6 Flow visualization for the configuration HHCC at Ra = 3.1 × 10^{10}

The probe near the top left of the photograph injects dye into the heated wall boundary layer near the bottom of the cell about 1 cm from the cooled wall. As seen in the photograph, the dye stream moves vertically upward and does not appear to be affected by the presence of the nearby cooled wall. The dye stream then moves diagonally across the cell top and vertically down the cooled wall boundary layer about 1 cm from the heated wall.

Also obvious in the photograph is the waviness on the heated wall. The waves are made visible by a shadowgraph effect and represent transition of the heated wall boundary layer. The waves appear to be of a well-defined, single wavelength (about 1 cm) and are essentially two dimensional in nature. The waves appear to break near the top of the test cell. The boundary layer relaminarized after turning the top corner. Similar flow visualization experiments at lower Ra (less than 10^{10}) did not reveal these waves.

The waviness in the boundary layer occurred at local Rayleigh numbers Ra_x, estimated to be between 10^8 and 10^9, where

$$\mathrm{Ra}_x = \frac{g\beta(T_w - T_b)x^3}{\nu^2}\,\mathrm{Pr}$$

This result is consistent with the experimental results by Elder [4], who gives the condition for the onset of boundary layer waves as $\mathrm{Ra}_x = 3 \times 10^8$ (for aspect ratios between 9 and 27). The linear stability theory calculations of Hieber and Gebhart [33] predict the growth of traveling wave disturbances at Ra_x above 3×10^6 Pr. The difference between the predicted and observed values is due to the vertical distance required for finite amplification of a natural disturbance [34].

Figure 6 also shows waviness, this time towards the bottom of a cooled wall. The probe near the upper right corner of the cell injected dye directly on the wall. The dye stream seems to split into two streams, one moving in a straight vertical path and the other stream moving in a wavy pattern. Observation of the dye streams from the top of the cell indicated that the first stream was very close to the wall, perhaps in the viscous sublayer, and the second dye stream was further from the wall, about 1 mm and probably in the outer part of the boundary layer undergoing transition, thus explaining the waviness.

The flow visualization results indicate that the inactive core does not play an important role in transferring heat from the heated walls to the cooled walls. The heat transfer is accomplished almost entirely by flow in the boundary layers up the heated walls, across the top, and down the cooled walls. One would then expect that heat transfer results would not be very sensitive to which walls are heated and which walls are cooled. This is borne out by the measurements of the heat transfer coefficients for each wall. For example, the three cold

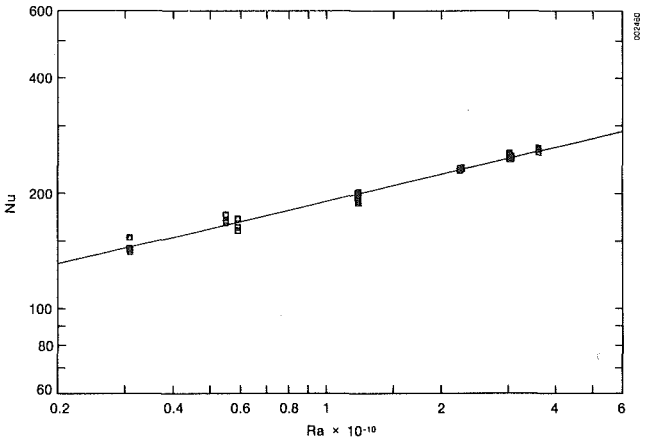

Fig. 7 Heat transfer data for the configuration HHCC

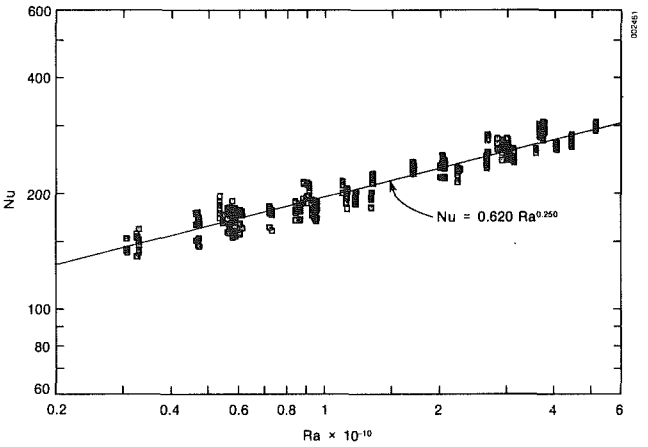

Fig. 8 Heat transfer data for all walls, all configurations

walls in the configuration CHCC have approximately equal heat transfer coefficients, likewise, the three hot walls in the configuration HHHC have approximately equal heat transfer coefficients.

Initially, the heat transfer coefficients were calculated using the overall temperature differences ΔT_o. This yielded a larger Nu (at fixed Ra) for a single wall of given temperature in a configuration with three walls of given temperature, e.g., the hot wall in CHCC had a Nu about three times that for the cold walls. Since flow visualization studies showed that the flow is essentially a boundary-layer flow that must be driven by the temperature difference between the wall and the core, it seemed more appropriate to use that temperature difference to derive the heat transfer coefficient. The core temperature was taken to be the bulk temperature, T_b, the average of the four wall temperatures.

Results for the configuration HHCC are shown in Fig. 7. The four points at each Ra represent the Nu for each of the four walls. The difference in Nu for a given Ra for the walls is quite small so the same symbol has been plotted in the figure for all four points. Some fine detail is revealed for each wall and for each configuration, although the correlation is obviously of the form $\mathrm{Nu} \sim \mathrm{Ra}^m$. For example, in the configuration HHHC, the Nu at $\mathrm{Ra} > 10^{10}$ tends to lie above a correlation line passed through the higher Ra points by about 12 percent. Since the core flow could weakly influence the boundary layer flow, it is possible that this was due to the observed change in the core flow pattern as Ra was increased beyond 10^{10} as discussed in the first part of this section. These

details produce only minor variations in the Nu from an expected value (from a correlation equation for example) and should be the subject of further study.

For developing a useful correlation of reasonable accuracy, data points for all walls and all configurations (416 data points) are plotted in Fig. 8. A regression analysis gave the correlation

$$\mathrm{Nu} = 0.620\ \mathrm{Ra}^{0.250} \tag{3}$$

for $0.3 < \mathrm{Ra} < 6 \times 10^{10}$. The standard deviation from this correlation equation is ± 5.7 percent. Notwithstanding the transition to turbulence at the higher Ra as evidenced by flow visualization, the Nu data correlate well with a 1/4 power of Ra as predicted from laminar boundary layer theory. The power of the Ra in equation (3) was calculated from the regression analysis and is not an assumed value of 1/4. This further confirms that the heat transfer mechanism is laminar convection in the boundary layers along vertical walls surrounding the core region as observed by flow visualization and as previously discussed for two dimensional flow. Since transition occurs in a region where the local heat transfer coefficient is significantly less than the average value (due to a smaller local temperature gradient from the wall to the stratified bulk fluid) as discussed in [23], the effect of transition on the average Nu is suppressed. The $\mathrm{Ra}^{1/4}$ dependence may be expected to hold until a substantial portion of the wall boundary layer is turbulent. Boundary layer waviness was observed in only the upper 1/3 of the hot wall for $\mathrm{Ra} > 3 \times 10^{10}$ in these experiments.

The leading constant in equation (3) is partially an artifact of the temperature difference used to calculate the heat transfer coefficient. The choice of wall-to-bulk temperature difference collapses all results to one correlation curve, equation (3), because the heat transfer mechanism is boundary layer convection, and as demonstrated by the flow visualization experiment, the boundary layer flow is not disturbed by the presence of adjacent walls and is thus configuration independent, at least for aspect ratios near one. Numerical results [23] show that the variation in heat transfer across the wall in the horizontal direction is negligible. This choice of temperature difference, however, requires some care when making comparison with previous work. If previous two-dimensional analyses and experiments has been based on the wall-to-bulk temperature rather than the overall temperature difference, the coefficient of the Rayleigh number would double (since the bulk temperature is the average of hot and cold wall temperatures). From the discussion presented in the Introduction, most of the analyses and experiments would then yield $\mathrm{Nu} = (.6 \text{ to } .8)\ \mathrm{Ra}^{1/4}$. For comparison purposes, we have plotted in Fig. 1 Nu/2 for the present three-dimensional work, i.e., $\mathrm{Nu} = 0.310\ \mathrm{Ra}^{0.250}$, and that the comparison can be seen to be quite favorable with the two-dimensional analyses and experiments (see Fig. 1). It should also be noted that the experimental ($A = 0.5$) data of [27] and [29] are slightly higher than the present results, as predicted by numerical results of [13] and [14].

Conclusions

Flow visualization experiments and heat transfer measurements have been completed for three-dimensional natural convection in a cubical enclosure at high Rayleigh number, $0(10^{10})$. The test cell has an adiabatic top and bottom and isothermal vertical walls. Four combinations of heating and cooling the isothermal walls were tested.

The flow visualization experiments verified the existence of a relatively inactive core surrounded by boundary layers on each of the four vertical walls. Transport of heat from the heated walls to the cooled walls is carried out by flow in the boundary layers. Relatively cool fluid near the bottom of the heated wall flows vertically up the heated wall absorbing heat from the wall. The boundary layer turns the corner at the cell top, and the heated fluid moves across the top to the cooled wall where the heat is given up in the reverse process. Boundary layers were observed to be essentially two-dimensional, i.e., they were not affected by the presence of nearby perpendicular walls.

Transition to turbulence was observed near the top 1/3 of the heated walls and near the bottom 1/3 of the cooled walls for the higher Ra. A waviness in the boundary layer consisting essentially of a single wavelength propagated along the wall until breaking near the top (bottom) of the heated (cooled) wall. The waves observed in the boundary layer were essentially two-dimensional, i.e., they extended across the wall from one edge to the other in a horizontal line.

Heat transfer measurements consist of average heat transfer coefficients for each wall and for each of four configurations of heated wall and cooled walls. The Ra was varied from about 0.3 to 6×10^{10}, and the Prandtl number was in the range of 3.5 to 6.0. Data were plotted in the form of Nu versus Ra on a log-log plot to reveal a straight line relationship. When heat transfer coefficients were based on the wall-to-bulk temperature difference, data for all walls and for all configurations collapsed to a single correlation equation, which agrees quite favorably with analyses and experiments in two-dimensional enclosures. The heat transfer mechanism is convection in the boundary layers that are not affected by the different core flows set up for the different configurations. The correlation indicates a laminar boundary-layer flow heat transfer mechanism, even though transition to turbulence was observed in the higher Ra experiments.

References

1 Batchelor, G. K., "Heat Transfer by Free Convection Across a Closed Cavity Between Vertical Boundaries at Different Temperatures," *Quarterly of Applied Mathematics*, Vol. 12, 1954, pp. 209–233.

2 Eckert, E. R. G., and Carlson, W. D., "Natural Convection in an Air Layer Enclosed Between Two Vertical Plates With Different Temperatures," *International Journal of Heat and Mass Transfer*, Vol. 2, 1961, pp. 106–120.

3 Elder, J. W., "Laminar Free Convection in a Vertical Slot," *Journal of Fluid Mechanics*, Vol. 23, 1965, pp. 77–98.

4 Elder, J. W., "Turbulent Free Convection in a Vertical Slot," *Journal of Fluid Mechanics*, Vol. 23, 1965, pp. 99–111.

5 Gill, A. E., "The Boundary-Layer Regime for Convection in a Rectangular Cavity," *Journal of Fluid Mechanics*, Vol. 26, 1966, pp. 515–536.

6 Bejan, A., "Note on Gill's Solution for Free Convection in a Vertical Enclosure," *Journal of Fluid Mechanics*, Vol. 90, 1979, pp. 561–568.

7 Simpkins, P. G., and Dudderar, T. D., "Convection in Rectangular Cavities with Differentially Heated End Walls," *Journal of Fluid Mechanics*, Vol. 110, 1981, pp. 433–456.

8 Raithby, G. D., and Hollands, K. G. T., "A General Method of Obtaining Approximate Solutions for Laminar and Turbulent Free Convection Problems," *Advances in Heat Transfer*, Academic Press, Vol. 11, 1975, pp. 265–315.

9 Raithby, G. D., Hollands, K. G. T., and Unny, T. E., "Analysis of Heat Transfer by Natural Convection Across Vertical Fluid Layers," ASME JOURNAL OF HEAT TRANSFER, Vol. 99, 1977, pp. 287–293.

10 Emery, A., and Chu, N. C., "Heat Transfer Across Vertical Layers," ASME JOURNAL OF HEAT TRANSFER, Vol. 87, 1965, pp. 110–116.

11 Newell, M. E., and Schmidt, F. W., "Heat Transfer by Laminar Natural Convection Within Rectangular Enclosures," ASME JOURNAL OF HEAT TRANSFER, Vol. 92, 1970, pp. 159–165.

12 Boyack, B. E., and Kearney, D. W., "Heat Transfer by Laminar Natural Convection in Low Aspect Ratio Cavities," ASME Paper No. 72-HT-52, 1972.

13 Inaba, H., Seki, N., Fukusako, S., and Kanayama, K., "Natural Convective Heat Transfer in a Shallow Rectangular Cavity With Different End Temperatures," *Numerical Heat Transfer*, Vol. 4, 1981, pp. 459–468.

14 Strada, M., and Heinrich, J. C., "Heat Transfer in Natural Convection at High Rayleigh Numbers in Rectangular Enclosures: A Numerical Study," *Numerical Heat Transfer*, Vol. 5, 1982, pp. 81–93.

15 Bejan, A., "A Synthesis of Analytical Results for Natural Convection Heat Transfer Across Rectangular Enclosures," *International Journal of Heat and Mass Transfer*, Vol. 23, 1980, pp. 723–726.

16 MacGregor, R. K., and Emery, A. F., "Free Convection Through

Vertical Plane Layers—Moderate and High Prandtl Number Fluids," ASME JOURNAL OF HEAT TRANSFER, Vol. 91, 1969, pp. 391–403.

17 Dropkin, D., and Somerscales, E., "Heat Transfer by Natural Convection in Liquids Confined by Two Parallel Plates Which are Inclined at Various Angles with Respect to the Horizontal," ASME JOURNAL OF HEAT TRANSFER, Vol. 87, 1965, pp. 77–84.

18 Burnay, G., Hannay, J., and Portier, J., "Experimental Study of Free Convection in a Square Cavity," *Heat Transfer and Turbulent Buoyant Convection*, Vol. II, edited by D. B. Spalding and N. Afgan, Hemisphere Publishing, 1977, pp. 807–811.

19 ElSherbiny, S. M., Raithby, G. D., and Hollands, K. G. T., "Heat Transfer by Natural Convection Across Vertical and Inclined Air Layers," ASME JOURNAL OF HEAT TRANSFER, Vol. 104, 1982, pp. 96–102.

20 Bejan, A., and Tien, C. L., "Laminar Natural Convection Heat Transfer in a Horizontal Cavity With Different End Temperatures," ASME JOURNAL OF HEAT TRANSFER, Vol. 100, 1978, pp. 641–647.

21 Shiralkar, G., Gadgil, A., and Tien, C. L., "High Rayleigh Number Convection in Shallow Enclosures With Different End Temperatures," *International Journal of Heat and Mass Transfer*, Vol. 24, 1981, pp. 1621–1629.

22 Tichy, J., and Gadgil, A., "High Rayleigh Number Laminar Convection in Low Aspect Ratio Enclosures With Adiabatic Horizontal Walls and Differentially Heated Vertical Walls," ASME JOURNAL OF HEAT TRANSFER, Vol. 104, 1982, pp. 103–110.

23 Gadgil, A., "On Convective Heat Transfer in Building Energy Analysis," Ph.D. thesis, Department of Physics, University of California, Berkeley 1979; also LBL-10900, Lawrence Berkeley Laboratory Report.

24 Imberger, J., "Natural Convection in a Shallow Cavity With Differentially Heated End Walls. Part 3. Experimental Results," *Journal of Fluid Mechanics*, Vol. 65, 1974, pp. 247–260.

25 Bejan, A., Al-Homoud, A. A., and Imberger, J., "Experimental Study of High Rayleigh-Number Convection in a Horizontal Cavity With Different End Temperatures," *Journal of Fluid Mechanics*, Vol. 109, 1981, pp. 283–299.

26 Sernas, V., and Lee, E. I., "Heat Transfer in Air Enclosures of Aspect Ratio Less than One," ASME JOURNAL OF HEAT TRANSFER, Vol. 103, 1981, pp. 617–622.

27 Bauman, F., Gadgil, A., Kammerud, R., and Greif, R., "Buoyancy-Driven Convection in Rectangular Enclosures: Experimental Results and Numerical Calculations," ASME Paper No. 80-HT-66, 1980.

28 Gadgil, A., Bauman, F., and Kammerud, R., "Natural Convection in Passive Solar Buildings: Experiments, Analysis, and Results," *Passive Solar Journal*, Vol. 1, 1982, pp. 28–40.

29 Nansteel, M., and Greif, R., "Natural Convection in Undivided and Partially Divided Rectangular Enclosures," ASME JOURNAL OF HEAT TRANSFER, Vol. 103, 1981, pp. 623–629.

30 Mallinson, G. D., and deVahl Davis, G., "Three-Dimensional Natural Convection in a Box: A Numerical Study," *Journal of Fluid Mechanics*, Vol. 83, 1977, pp. 1–31.

31 Hjertager, B. H., and Magnussen, B. F., "Numerical Prediction of Three-Dimensional Turbulent Buoyant Flow in a Ventilated Room," *Heat Transfer and Turbulent Buoyant Convection*, Vol. II, edited by D. B. Spalding and N. Afgan, Hemisphere Publishing, 1977, pp. 429–441.

32 Morrison, G. L., and Tran, V. Q., "Laminar Flow Structure in Vertical Free Convective Cavities," *International Journal of Heat and Mass Transfer*, Vol. 21, 1978, pp. 203–213.

33 Hieber, C., and Gebhart, B., "Stability of Vertical Natural Convection Boundary Layers: Some Numerical Solutions" *Journal of Fluid Mechanics*, Vol. 48, 1971, pp. 625–646.

34 Gebhart, B., *Heat Transfer*, ch. 8, 2d ed., McGraw-Hill, New York, 1971.

M. E. Franke
Professor,
Air Force Institute
of Technology,
Mem. ASME

K. E. Hutson
Chief,
Programming and Planning,
Airlift Systems,
Aeronautical Systems Division,

Wright-Patterson AFB,
Ohio 45433

Effects of Corona Discharge on Free-Convection Heat Transfer Inside a Vertical Hollow Cylinder[1]

Vortex rolls induced inside a vertical hollow cylinder are found to increase the free-convection heat transfer rate from the inside surface. The vortex rolls are induced by the corona wind generated between 0.05-mm-dia wire electrodes placed vertically on the inside surface of the vertical hollow cylinder. The increase in heat transfer rate is determined experimentally and is based on the heat input required to maintain the inside surface of the cylinder at constant temperature. The experimental results without corona discharge are compared with an analytical heat balance. A Mach-Zehnder interferometer is used for boundary layer visualization.

Introduction

Vortex rolls in forced flows have been shown to increase the heat transfer rate in a number of studies [1–4]. Similarly, in free convection, it has been shown that columnar, counterrotating vortex rolls induced in the boundary layer will increase the heat transfer rate [5, 6]. DeGraaf and van der Held [5] obtained the vortex rolls through instability while Franke [6] induced the vortex rolls from the corona wind resulting from corona discharge on small diameter wires placed vertically on a phenolic flat plate. This latter study [6] described how the vortex rolls are formed by the corona wind and showed that the vortex rolls could more than double the free-convection heat transfer rate.

A number of other studies have used electrostatic corona discharge and the resulting corona wind to increase the heat transfer rate (for example, [7–14]). Several of these studies involved induced secondary flows and longitudinal rolls [10–14]. Velkoff and Godfrey [10] found that streamwise secondary flow induced by corona electrostatic discharge enhanced the heat transfer as long as the stream velocity was on the order of the corona wind velocity or less. Velkoff et al. [11] also found that electrostatically induced longitudinal rolls in a channel increased the heat transfer and affected the pressure drop. Additional studies [12–14] have described the effects of ion motion on friction factor, velocity profile, and heat transfer for gas flowing in a channel. Also a number of references [15–21] are available that describe the corona wind phenomenon and how the corona wind is caused by migration of positive ions and collisions of these ions with neutral molecules of air.

The purpose of this study was to extend the flat-plate study [6] to determine the effect of vortex rolls induced by the corona wind on the free-convection heat transfer rate on the inside surface of a vertical hollow cylinder. The specific objectives were: (*i*) to determine experimentally the increase in heat transfer rate at various electric field power levels and to compare the increase obtained with the power expended to effect the increase, (*ii*) to obtain an analytical heat balance for the cylinder without corona discharge and compare with experimental results, and (*iii*) to view the thermal boundary layers using a Mach-Zehnder interferometer.

Experimental Apparatus

The 0.127-m-i.d. by 0.26-m-long (5-in. by 10½-in.) hollow cylinder was constructed as shown in Fig. 1. The cylinder wall consisted of an inner surface of 3.18-mm (1/8-in.)-thick phenolic that was backed up by 16 gage aluminum. The aluminum sleeve was surrounded with Nichrome heater wires, insulating tape, and fiberglass insulation. The phenolic material was used for the inside surface to prevent the bare wire electrodes from shorting. The aluminum plate was used to provide a more uniform wall temperature distribution. There were four electrical heaters; each individually controlled. The plate heater power was obtained from a 115-V, a-c line, and power input measurements were made with a voltmeter and an ammeter.

The 0.05-mm (0.002-in.)-dia wires used for corona discharge were placed directly on the phenolic surface. The

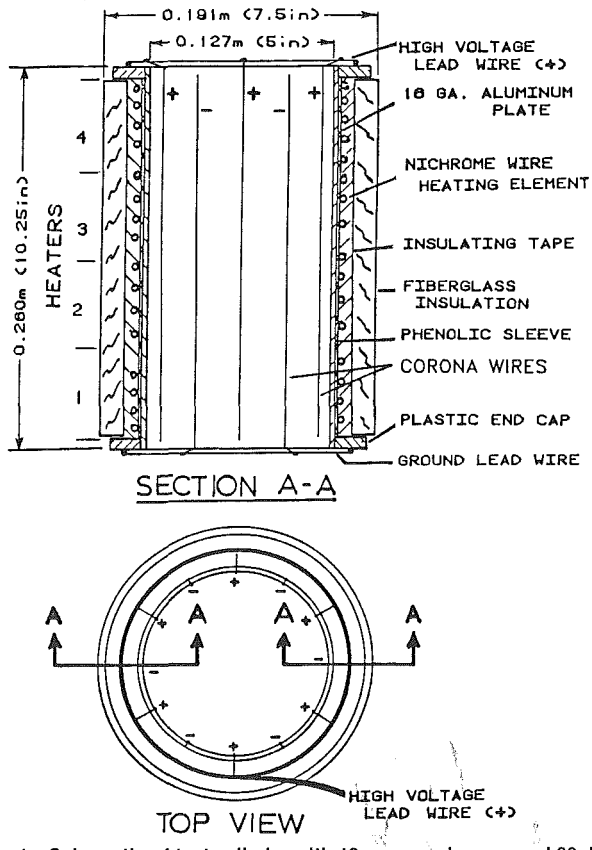

Fig. 1 Schematic of test cylinder with 12 corona wires spaced 30 deg apart

[1] The views expressed herein are those of the authors and do not necessarily reflect those of the United States Air Force or the Department of Defense.

Contributed by the Heat Transfer Division and presented at the ASME Winter Annual Meeting, Phoenix, Arizona, Novermber 14–19, 1982. Manuscript received by the Heat Transfer Division January 7, 1983. Paper No. 82-WA/HT-20.

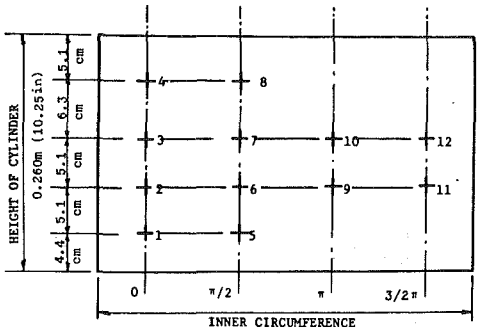

Fig. 2 Thermocouple locations

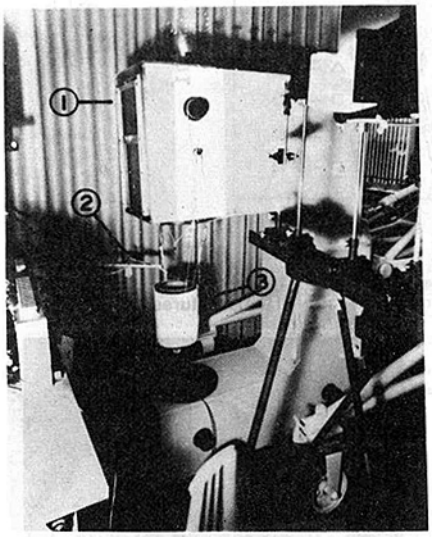

Fig. 3 Test cylinder apparatus: (1) optical interferometer, (2) high-voltage lead wire, (3) test cylinder

wires were aligned vertically and arranged around the inside surface with alternate polarity as shown in Fig. 1. Three wire configurations were used: 8 wires spaced 45 deg apart, 12 wires spaced 30 deg apart, and 16 wires spaced 22.5 deg apart. The positive polarity wires were connected to the high-voltage lead wire at the top of the cylinder and the negative wires were connected to the ground lead wire at the bottom of the cylinder. A high-voltage, d-c power supply provided the power for the electrostatic field and the corona discharge. The voltage and current were measured with an electrostatic voltmeter and a milliammeter.

Twelve copper-constantan thermocouples were located around the inside surface of the cylinder, Fig. 2. The thermocouples were embedded in the phenolic to within 0.8 mm (1/32 in.) of the inside surface. The inner aluminum sleeve was grounded so that the electrostatic field had only a small influence on the thermocouple readings. Two thermocouples were used to measure the temperature of the outer surface (insulation) of the cylinder.

Figure 3 is a photograph of the test cylinder positioned in the test section of the interferometer.

Experimental Procedures

The tests were run at a uniform cylinder wall temperature. The inside wall temperature was stabilized at a predetermined temperature above ambient by adjusting the power input to the four individual heating elements. Temperature stabilization was verified by serially polling the thermocouples located throughout the cylinder and recording the results on a strip chart recorder. When steady state was obtained, heater power input readings provided the total heat loss from the hollow cylinder under free-convection conditions without corona discharge.

The electric-field strength on the wire electrodes was then increased by raising the voltage on the positive wires. Corona discharge occurred above a threshold value of voltage. At each level of corona discharge, heater power input readings were recorded after the inside wall temperature had stabilized at the initial uniform temperature. The increase in heater power required with corona discharge determined the increase in heat transfer rate due to the corona wind.

By maintaining the temperature of the cylinder essentially constant as the electric field voltage was increased, it was assumed that all heat losses except the convection losses from the inside wall remained essentially constant. Thus the increase in convection losses along the inner wall was approximated by the measured increase in heater power input.

The tests were run at wall temperature differences relative to ambient of approximately 6°C (11°F), 16°C (29°F), 29°C (53°F), and 44°C (80°F).

Analytical Heat Balance

An analytical heat balance was made for the entire cylinder with no applied electric field. Generally accepted relations were used to obtain the total heat loss. The heat losses considered in the heat balance were: convection from the inside surface Q_{ci}, convection from the outside surface Q_{co}, radiation from the inside surface Q_{ri}, radiation from the outside surface Q_{ro}, losses through the ends Q_e, and electrical heater wire lead losses Q_l.

For other than very long or small diameter cylinders, it has been shown that the average heat transfer rate from a vertical cylinder should closely approach that of a vertical plate [22, 23]. Free-convection losses from the inside and outside vertical surfaces were calculated using the average heat transfer coefficient $\bar{h}$ obtained from the average Nusselt number

$$\overline{\mathrm{Nu}} = \frac{\bar{h}L}{k} = 0.555(\mathrm{Gr}\,\mathrm{Pr})^{1/4} \tag{1}$$

Nomenclature

A = surface area
C_p = specific heat at constant pressure
D = inside diameter of cylinder
F_A = radiation configuration factor
F_ϵ = radiation emissivity factor
g = acceleration of gravity
Gr = average Grashof number, $\rho^2 g\beta L^3 \Delta T/\mu^2$
$\bar{h}$ = average heat transfer coefficient
k = thermal conductivity
L = length of cylinder
$\bar{\mathrm{N}}\mathrm{u}$ = average Nusselt number, $\bar{h}L/k$
Pr = Prandtl number, $\mu C_p/k$
Q = heat transfer rate
T = temperature
β = coefficient of volumetric expansion
ϵ = emissivity
μ = viscosity
ρ = fluid density
σ = Stefan-Boltzmann constant

Subscripts

a = ambient
c = convection
e = end
f = film
i = inside
l = leads
m = measured
o = outside
r = radiation
t = total
w = wall

Table 1 Values of heat loss with no applied field for typical values of wall temperature

T_{wi},°C	T_a,°C	Q_t,W	Q_{tm},W	Q_{ci},W
32	26	4.8	4.9	2.1
44	28	12.8	13.5	6.8
56	27	26.5	25.3	14.2
69	25	41.9	41.2	23.7

where the fluid properties were evaluated at the average film temperature

$$T_f = (T_a + T_w)/2 \tag{2}$$

The heat transfer coefficient $\bar{h}$ was then used to obtain the convection losses

$$Q_c = \bar{h}A(T_w - T_a) \tag{3}$$

Radiation losses were calculated using the equation

$$Q_r = AF_A F_\epsilon \sigma (T_w^4 - T_a^4) \tag{4}$$

For radiation from the outside surface, the cylinder was considered a completely enclosed gray body where $F_A = 1$, $F_\epsilon = \epsilon$. Various material property references give emissivity values for paper and phenolic materials in the range of 0.85 to 0.95. A value of $\epsilon = 0.9$ was assumed for both the outside paper tape surface and the inner phenolic sleeve. For the inside surface, the configuration factor given by Bien [24] for the inside wall of a cylindrical cavity radiating to space was used

$$F_A = [(L/D)^2 + 1]^{1/2} - (L/D) \tag{5}$$

Following Hsu [25], an approximate value for F_ϵ for interchange of radiation between the inner wall of the cylinder and the surroundings is the product of the emissivities of both radiating surfaces. Assuming the emissivity of the interferometer glass and paint equal to 0.9, $F_\epsilon = 0.81$ for this interchange.

Temperature of the end cap surfaces remained very close to the temperature of the outside surface, and furthermore, the combined surface area of both caps was only about 16 percent of the vertical outside surface. Therefore, the end losses were estimated based on area ratio. The electrical resistance of each heater lead was measured, and the I^2R losses were calculated from these measurements. The lead losses were less than 1 percent.

Results

Values of the calculated total heat loss without an applied electric field, Q_t, which includes all of the losses identified in the analytical heat balance, are shown in Table 1 for several typical values of inside wall temperature. Values of the measured total heat input Q_{tm} to the heater elements are also given in Table 1. The differences between Q_t and Q_{tm} were generally 5 percent or less, except in one case (not shown) where the difference was 8 percent.

The close agreement between the measured and calculated values of the total heat transfer from the cylinder suggests that the heat balance calculations were good approximations for the individually calculated radiation and convection heat transfer rates. The calculated values of the convection heat transfer from the inside surface Q_{ci} were therefore used as references values for the increase in heat transfer due to the effects of corona discharge. Typical values of Q_{ci} are shown in Table 1. Convection heat transfer Q_{ci} accounted for approximately 45 to 55 percent of Q_t, whereas Q_{co} was only 8 to 10 percent due to the insulated outer surface. Radiation losses from all surfaces were approximately 30 to 40 percent of Q_t. The range in values depended on the temperature.

When voltage was applied to the positive wires nothing happened until a potential was reached where ionization began and there was current flow. The potential required for incipient current varied from 1 to 3 kV with the higher potential required for greater wire spacing. There were two

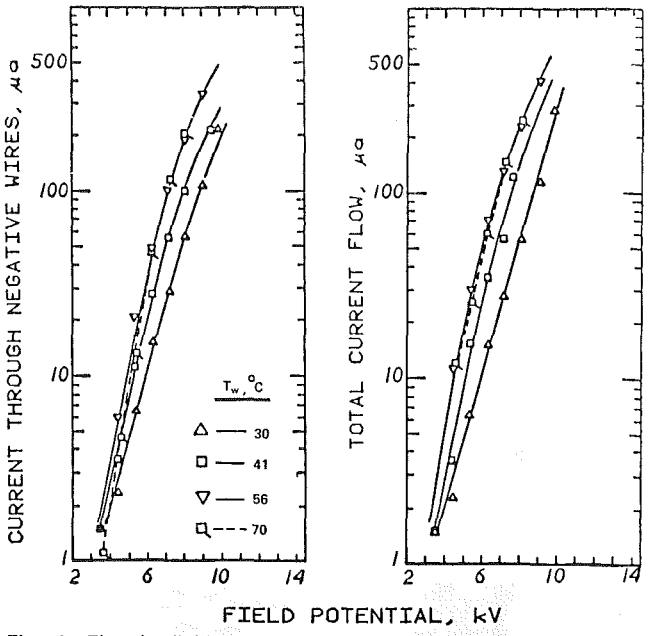

Fig. 4 Electric field voltage—current characteristics for 12-wire configuration at various wall temperatures

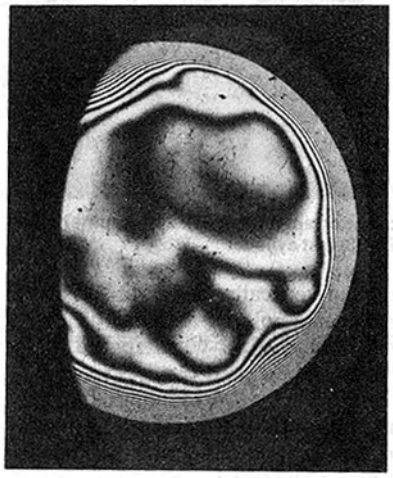

Fig. 5 Interference photograph of thermal boundary layer with 0 kV on corona wires, ΔT = 44°C

paths for current flow: (*i*) through the grounded (negative) wire electrodes and (*ii*) through the grounded aluminum sleeve behind the phenolic wall. The intended path was through the negative wires. The current distribution between the two paths depended on wire spacing, wall temperature, and positive wire potential. The current through the grounded (negative) wires as a percentage of the total current generally decreased with increasing wall temperature or wire spacing, but increased with increasing wire potential (above 3 kV). The relatively higher percentage of current through the plate with increasing wall temperature is believed due, in part, to the decrease in electrical resistivity of phenolic resins with increase in temperature.

For the 12- and 16-wire configurations, the current through the wires was approximately 50 percent of the total current in the 3- to 4-kV range and proportionately increased with voltage increase to approximately 80 percent at 9 kV. For the 8-wire configuration, the current through the negative wires varied from approximately 10 to 30 percent (depending on temperature) in the 3- to 4-kV range to approximately 25 to 60 percent (depending on temperature) at 8 kV.

The current leakage to the inner aluminum plate could

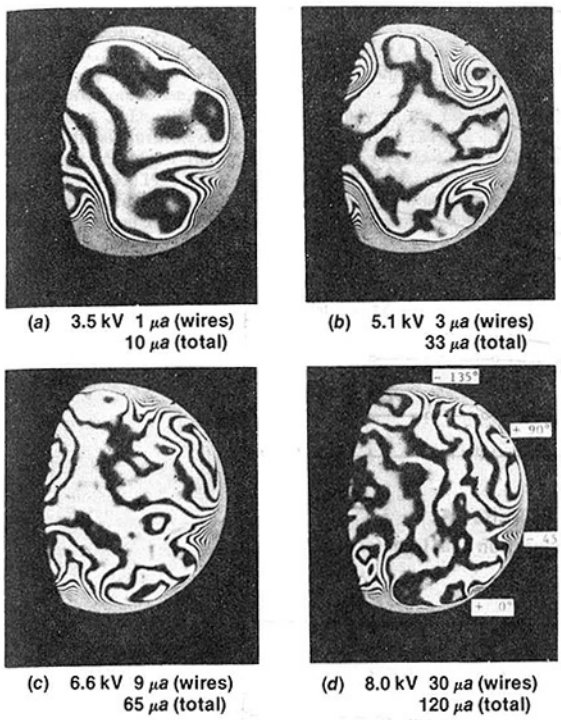

Fig. 6 Interference photographs of the effect of corona discharge on thermal boundary layer with 8 wires spaced 45 deg apart, ΔT = 44°C

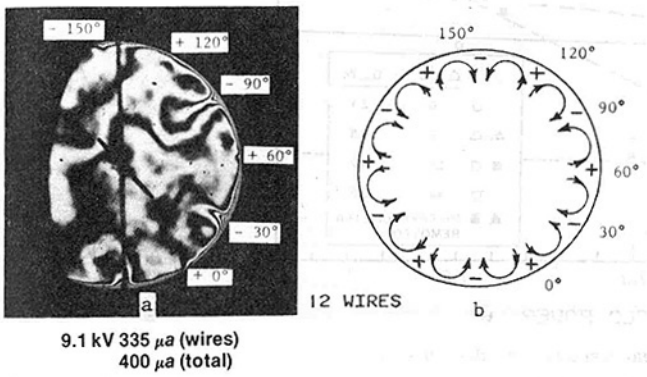

Fig. 7 Interference photograph of boundary layer and schematic diagram of proposed flow distribution

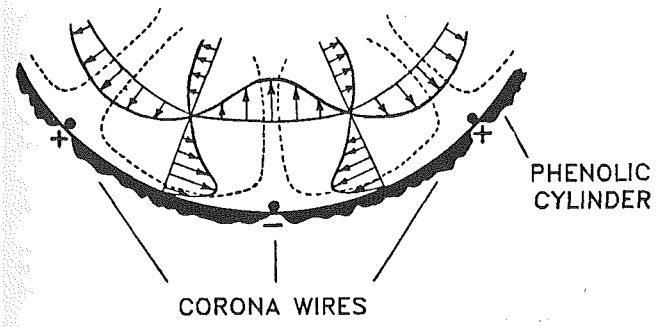

Fig. 8 Suggested velocity profiles

probably be reduced by better design and material selection. No attempt was made to do this in this study. Voltage–current curves for the 12-wire configuration are shown in Fig. 4.

The heat transfer rate also was unaffected by the electric field until current flowed through the negative wires to ground. An interference photograph (vertical view) of the hollow cylinder is shown in Fig. 5. This view shows the free-convection boundary layer without an applied electrostatic field at a temperature difference between the inner wall and room ambient of 44°C (80°F). This view is also typical with an applied field at low voltage prior to current flow. The entire i.d. of the cylinder is not shown in the photographs due to the size of the mirrors in the interferometer.

When the voltage on the positive wires was raised to a value where there was current flow, the boundary layer was affected and the heat transfer rate increased. Figure 6 shows the effect of the corona discharge on the free-convection boundary layer. The results shown in Fig. 6 were obtained with a wire configuration, consisting of 8 wires spaced 45 deg apart and a temperature difference of 44°C, which corresponds to the ΔT in Fig. 5. Increases in input heater power were required to maintain the inner wall at a ΔT of 44°C as the voltage was increased. The decrease of the boundary layer thickness also illustrates the increase in heat transfer rate due to the corona wind. Wire locations and polarity as illustrated in Fig. 6(*d*) are the same for all photographs in Fig. 6. Also it can be seen in Fig. 6 that the heat transfer rate was highest near the positive wires. This was the same as found by Franke [6]. Corresponding voltage-current values are identified with each photograph. The corona discharge was also visible on the wires at the higher voltage levels during the tests.

From the results shown in Fig. 6, it is possible to conclude that there was air flow inward (toward the surface) at the positive wires and outward at the negative wires. This flow distribution is further substantiated since, based on the mobility study of Ratner [20], one would expect a net flow of corona wind from the positive wires towards the negative wires. The proposed flow distribution around the periphery of the inner wall is further illustrated in Fig. 7, where an interference photograph with the 12-wire configuration is shown in Fig. 7(*a*) and a corresponding schematic diagram of the proposed flow distribution at a given cross section is shown in Fig. 7(*b*). Wire locations and polarity are correlated in Figs. 7(*a*) and 7(*b*). The suggested (not verified) velocity profiles are illustrated in Fig. 8. The flow condition described leads to columnar, counterrotating, vertical vortex rolls in the hollow cavity as the heated air rises.

Calculated values of the free-convection heat transfer rate and the increases in the heat transfer rate as a result of the corona wind are shown in Figs. 9 and 10. The results are presented at constant values of ΔT. As previously discussed, the temperature of the cylinder was held constant as the electric field voltage on the corona wires was increased. Consequently, the increase in heater power required to maintain the temperature constant was a direct measure of the increase in convection heat transfer on the inside wall due to the corona wind. In general, the convection heat transfer rate was almost doubled due to the corona wind. These results were not quite as high as those reported for a flat plate [6]. This is probably due to the temperature increase of the air within the cylinder. Temperature differences as much as 6°C were found along the centerline of the cylinder from the bottom to the top.

The power expended to effect the increase in heat transfer was considerably less than the increase in the heat transfer itself. Figure 10 shows lines of constant ratio of heat transfer increase to electric field power. At low field power levels, the ratio was generally greater than 25/1. The heat transfer rate did not increase significantly for values of electric field power greater than about 10 percent of the increase in heat transfer rate, Fig. 10.

Conclusions

The convection heat transfer rate was nearly doubled along the inside surface of a hollow vertical cylinder due to the effect of the corona wind. The development of vortex rolls in

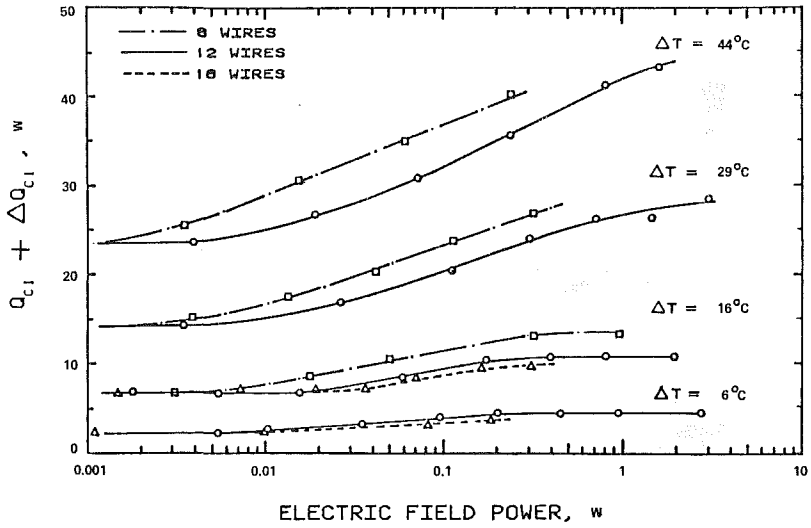

Fig. 9 Effect of corona discharge on free-convection heat transfer rate

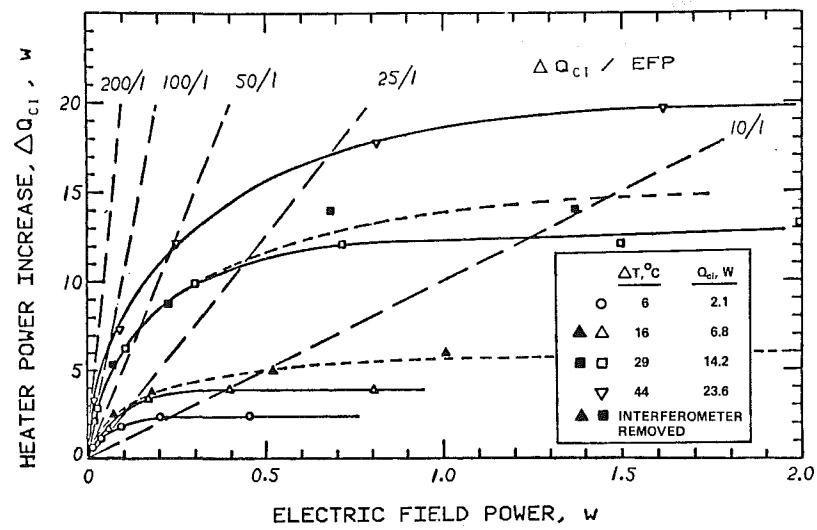

Fig. 10 Increases in convection heat transfer rate due to corona discharge with 12-wire configuration

the free-convection boundary layer leads to significant increases in the heat transfer rate.

References

1 Ginoux, J. J., "Experimental Evidence of Three-Dimensional Perturbations in the Reattachment of a Two-Dimensional Boundary Layer at Mach 2.05," TN-1, Training Center for Experimental Aerodynamics, Belgium, 1958.

2 Sutera, S. P., "Vorticity Amplification in the Stagnation-Point Flow and Its Effect on Heat Transfer," *Journal of Fluid Mechanics*, Vol. 21, pt. 3, 1965, pp. 513–534.

3 Persen, L. N., "A Simplified Approach to the Influences of Görtler-Type Vortices on the Heat Transfer from a Wall," Report ARL 65-88, Aerospace Research Laboratories, Wright-Patterson Air Force Base, Ohio, 1965.

4 Mori, Y., and Uchida, Y., "Forced Convective Heat Transfer Between Horizontal Flat Plates," *International Journal of Heat Mass Transfer*, Vol. 9, 1966, pp. 803–817.

5 DeGraaf, J. G. A., and van der Held, E. F. M., "The Relation Between the Heat Transfer and the Convection Phenomena in Enclosed Plane Air Layers," *Applied Scientific Research*, Section A, Vol. 3, 1953, pp. 393–409.

6 Franke, M. E., "Effects of Vortices Induced by Corona Discharge on Free-Convection Heat Transfer From a Vertical Plate," ASME JOURNAL OF HEAT TRANSFER, Vol. 91, 1969, pp. 427–433.

7 Velkoff, H. R., "Electrofluidmechanics: Investigation of the Effects of Electrostatic Fields on Heat Transfer and Boundary Layers," ASD-TDR-62-650, Propulsion Laboratory, Wright-Patterson Air Force Base, Ohio, 1962.

8 Marco, S. M., and Velkoff, H. R., "Effect of Electrostatic Fields on Free-Convection Heat Transfer From Flat Plates," ASME Paper No. 63-HT-9, 1963.

9 O'Brien, R. J., and Shine, A. J., "Some Effects of an Electric Field on Heat Transfer from a Vertical Plate in Free Convection," ASME JOURNAL OF HEAT TRANSFER, Vol. 89, 1967, pp. 114–115.

10 Velkoff, H. R., and Godfrey, R., "Low Velocity Heat Transfer to a Flat Plate in the Presence of a Corona Discharge in Air," ASME JOURNAL OF HEAT TRANSFER, Vol. 101, 1979, pp. 157–163.

11 Velkoff, H. R., Pejack, E. J., and Chuang, T. H., "Electrostatically Induced Secondary Flows in a Channel," Sixty-Ninth National Meeting, AIChE, Cincinnati, Ohio, May 1971.

12 Velkoff, H. R., "The Effects of Ionization on the Flow and Heat Transfer of a Dense Gas in a Transverse Electrical Field," *Proceedings of the 1964 Heat Transfer and Fluid Mechanics Institute*, Berkeley, Calif., Stanford University Press, 1964.

13 Velkoff, H. R., "An Exploratory Investigation of the Effects of Ionization on the Flow and Heat Transfer with a Dense Gas," Aero Propulsion Laboratory Report ASD-TDR-63-842, Wright-Patterson Air Force Base, Ohio, 1963.

14 Pejack, E., and Velkoff, H. R., "The Effect of Transverse Ion Current on the Flow of Air in a Flat Duct," Technical Report #2, Contract DA-31-124-ARO-D-246, U.S. Army Research Office–Durham, Durham, N.C., 1967.

15 Robinson, M., "Movement of Air in Electric Wind of the Corona Discharge," *AIEE Transactions*, Vol. 80, pt. I (Comm. and Electronics) no. 54, 1961, pp. 143–150.

16 Cobine, J. D., *Gaseous Conductors*, Dover Publications, New York, 1958.

17 Loeb, L. B., *Fundamental Processes of Electrical Discharge in Gases*, John Wiley & Sons, New York, 1939.
18 Velkoff, H. R., "Electrofluidmechanics: A Study of Electrokinetic Actions in Fluids," ASD-TR-61-642, Propulsion Laboratory, Wright-Patterson Air Force Base, Ohio, 1962.
19 Harney, J. D., "An Aerodynamic Study of the Electric Wind," M.S. thesis, California Institute of Technology, 1957, AD 134 400.
20 Ratner, S., "On the Mobility of the Negative Ion," *Philosophical Magazine*, Vol. 32, 1916, pp. 441–461.
21 Yabe, A., Mori, Y., and Hijikata, K., "EHD Study of the Corona Wind Between Wire and Plate Electrodes," *AIAA Journal*, Vol. 16, No. 4, Apr. 1978, pp. 340–345.
22 Elenbass, W., "Dissipation of Heat by Free Convection," Philips Research Report 3, N.V. Philips' Gloeilampenfobrienken, Eindhoben, Netherlands, 1948, pp. 338–360 and 450–465.
23 Sparrow, E. M., and Gregg, J. R., "Free Convection Heat Transfer From the Outer Surface of a Vertical Circular Cylinder," ASME *Transactions*, Vol. 78, No. 8, Nov. 1956, pp. 1823–1829.
24 Bien, D. D., "Configuration Factors for Thermal Radiation from Isothermal Inner Walls of Cones and Cylinders," *Journal of Spacecraft Rockets*, Vol. 3, No. 1, 1966, p. 155.
25 Hsu, S. T., *Engineering Heat Transfer*, D. Van Nostrand Co., New York, 1963.

Matrix Formalism for Complex Heat Exchangers

A. Pignotti
Techint S. A.,
Buenos Aires 1001,
Argentina

The matrix formalism introduced by Domingos for the calculation of the effectiveness of assemblies of heat exchangers is extended to the case of complex exchangers, for which the restriction of complete mixing for each fluid in the inlet and outlet streams is relaxed. Rectangular matrices are used to relate the inlet and outlet temperatures, and their properties are discussed. The method can be used to find explicit solutions for configurations of practical interest, which are analyzed as assemblies of simpler units, coupled together in various ways. The formalism is illustrated by a model calculation of a 1-2 shell-and-tube exchanger with a finite number of baffles, for TEMA E (normal flow) and TEMA J (divided flow) types of shells.

1 Introduction

Under the assumptions of constancy of heat capacities and heat transfer coefficients (no change of phase, uniform inlet and outlet temperature distributions, and no heat losses), the thermal behavior of a heat exchanger can be characterized by a matrix M which relates the inlet and outlet temperature vectors through the equation [1][1]

$$\begin{vmatrix} t' \\ T' \end{vmatrix} = \begin{vmatrix} M_{11} & M_{12} \\ M_{21} & M_{22} \end{vmatrix} \begin{vmatrix} t \\ T \end{vmatrix} \tag{1}$$

The matrix elements M_{ij} are not independent. Translational invariance of the heat transfer equations in the temperature variable requires equation (1) to hold if all temperatures are incremented in the same constant amount, which implies

$$\sum_{j=1}^{2} M_{ij} = 1, \quad i = 1,2 \tag{2}$$

The second law of thermodynamics requires M_{ij} to be nonnegative, and from equation (2)

$$0 \le M_{ij} \le 1 \tag{3}$$

In addition, heat conservation can be expressed in the form

$$wc(t' - t) = WC(T - T') \tag{4}$$

whence

$$M_{11} + M_{21}/R = 1 \tag{5}$$

and

$$R\,M_{12} + M_{22} = 1 \tag{6}$$

From equations (2) and either (5) or (6), we obtain

$$M_{21} = R\,M_{12} \tag{7}$$

The elements M_{12} and M_{21} can readily be identified as the shell-and-tube fluid effectivenesses, so that M can be written as

$$M = \begin{vmatrix} 1-P & P \\ \mathbf{P} & 1-\mathbf{P} \end{vmatrix} \tag{8}$$

In the following, an exchanger characterized by the foregoing equations is called a basic heat exchanger. Domingos has shown how two or more of such exchangers can be assembled together in various ways to form new basic heat exchangers, the properties of which are related to those of the constituting elements [1].

The matrix formalism just described is generalized to the case of complex heat exchangers, in which arbitrary numbers of inlet and outlet streams, each characterized by its temperature and heat capacity rate, are possible for both the shell fluid and the tube fluid. The purpose of this extension is twofold: on one hand, it allows a more realistic treatment of exchangers in which one or both of the inlet and/or the outlet fluids are not completely mixed, and, on the other one, it provides a framework for the calculation of the properties of configurations of practical interest, which are obtained as assemblies of such multistream units. An example of a model calculation of a 1-2 shell-and-tube heat exchanger with a finite number of baffles using these techniques is given in section 6 for TEMA E shells, and in section 7 for TEMA J shells.

2 Generalized Matrix Formalism

In the case of complex exchangers, the dimensions of the inlet and outlet temperature vectors are $(n+N)$ and $(n'+N')$, respectively, and M becomes an $(n'+N')\times(n+N)$ rectangular matrix, such that

$$\begin{vmatrix} t'_1 \\ \vdots \\ t'_{n'} \\ T'_1 \\ \vdots \\ T'_{N'} \end{vmatrix} = \begin{vmatrix} M_{1,1} & \cdots & M_{1,n} & M_{1,n+1} & \cdots & M_{1,n+N} \\ \vdots & & \vdots & \vdots & & \vdots \\ M_{n',1} & \cdots & M_{n',n} & M_{n',n+1} & \cdots & M_{n',n+N} \\ M_{n'+1,1} & \cdots & M_{n'+1,n} & M_{n'+1,n+1} & \cdots & M_{n'+1,n+N} \\ \vdots & & \vdots & \vdots & & \vdots \\ M_{n'+N',1} & \cdots & M_{n'+N',n} & M_{n'+N',n+1} & \cdots & M_{n'+N',n+N} \end{vmatrix} \begin{vmatrix} t_1 \\ \vdots \\ t_n \\ T_1 \\ \vdots \\ T_N \end{vmatrix} \tag{9}$$

For the same reasons mentioned in the Introduction, the matrix elements M_{ij} again satisfy the constraints

$$\sum_{j=1}^{n+N} M_{ij} = 1, \quad i = 1, \ldots, n'+N' \tag{10}$$

and

$$0 \le M_{ij} \le 1. \tag{11}$$

[1] For concreteness, throughout this work t and T will be referred to as shell and tube fluid temperatures, respectively. The results also apply, however, to exchangers in which such identification is not warranted, such as air coolers, in which there is no actual shell, or compact exchangers with neither tubes nor shell. In such cases, any other fluid identification based on the physical description of the apparatus is equally valid.

Contributed by the Heat Transfer Division for publication in the JOURNAL OF HEAT TRANSFER. Manuscript received by the Heat Transfer Division November 10, 1982.

Heat conservation can be written now as

$$c\left[\sum_{i=1}^{n'} w_i' t_i' - \sum_{i=1}^{n} w_i t_i\right] = C\left[\sum_{i=1}^{N} W_i T_i - \sum_{i=1}^{N'} W_i' T_i'\right] \quad (12)$$

Substitution of the outlet temperatures from equation (9) into (12) leads to a homogeneous equation in the variables t_i and T_i, which, in order to be satisfied for all possible values of the inlet temperatures, requires the corresponding coefficients to vanish. From this, we obtain $n+N$ relations which are the generalizations of equations (5) and (6) and can be written in the form

$$\sum_{j=1}^{n'+N'} \hat{M}_{ij} = 1, \quad i = 1, \ldots, n+N \quad (13)$$

where

$$\hat{M} = D^{-1}\tilde{M}D' \quad (14)$$

Here the tilde denotes transposition, and D and D' are the inlet and outlet heat capacity rate diagonal matrices of dimensions $(n+N)\times(n+N)$ and $(n'+N')\times(n'+N')$, respectively, such that

$$D_{ii} = \begin{cases} c\, w_i & 1 \le i \le n \\ C\, W_{i-n} & n+1 \le i \le n+N \end{cases} \quad (15)$$

and similarly for D'. Observe that the inlet and outlet flow rates of individual streams need not be the same, and are only restricted by the constraints of flow conservation.

The matrix $\hat{M}$, which satisfies equation (13), quite analogous to equation (10), can be interpreted as the matrix describing the "flow reversed" process, i.e., a physical process with the same geometry, fluids, and flowrates as the one described by M, but in which the directions of flow of all streams are reversed (and, therefore, inlet flow rates become outlet flowrates, and vice versa). The proof of this statement requires, however, an elaboration that is presented in [2].

The matrix M can be rewritten in the form

$$M = \begin{vmatrix} \delta_1(1-P_{1,1}) & \ldots & \delta_n(1-P_{1,n}) & \Delta_1 P_{1,n+1} & \ldots & \Delta_N P_{1,n+N} \\ \vdots & & \vdots & \vdots & & \vdots \\ \delta_1(1-P_{n',1}) & \ldots & \delta_n(1-P_{n',n}) & \Delta_1 P_{n',n+1} & \ldots & \Delta_N P_{n',n+N} \\ \delta_1 \mathbf{P}_{n'+1,1} & \ldots & \delta_n \mathbf{P}_{n'+1,n} & \Delta_1(1-\mathbf{P}_{n'+1,n+1}) & \ldots & \Delta_N(1-\mathbf{P}_{n'+1,n+N}) \\ \vdots & & \vdots & \vdots & & \vdots \\ \delta_1 \mathbf{P}_{n'+N',1} & \ldots & \delta_n \mathbf{P}_{n'+N',n} & \Delta_1(1-\mathbf{P}_{n'+N',n+1}) & \ldots & \Delta_N(1-\mathbf{P}_{n'+N',n+N}) \end{vmatrix} \quad (16)$$

Nomenclature

A = heat transfer area, m^2
c,C = out-of-tube (shell) and tube fluid specific heats, J/kg°C
D,D' = inlet and outlet heat capacity rate matrices, J/s°C
F = logarithmic mean temperature difference correction factor, dimensionless
H,I,K = matrices relating the set of temperatures chosen as dependent to the set of independent temperatures, when different from outlet and inlet sets, respectively, dimensionless
M = matrix relating the outlet to the inlet temperatures, dimensionless
$\tilde{M}$ = transpose of matrix M, dimensionless
$\hat{M}$ = auxiliary matrix defined in equation (14), dimensionless
n,n' = number of inlet and outlet shell fluid streams, dimensionless
N,N' = number of inlet and outlet tube fluid streams, dimensionless
N_B = number of baffles in E shell exchangers or number of baffles in each half of the J type exchangers, not counting the central baffle
N_{tu} = UA/wc, number of heat transfer units, referred to the shell fluid, for the whole exchanger, dimensionless
P = $(t'-t)/(T-t)$, shell fluid effectiveness, dimensionless
$\mathbf{P}$ = $(T-T')/(T-t)$, tube fluid effectiveness, dimensionless
$P_i,\mathbf{P}_i$ = partial shell and tube fluid effectiveness, defined in equation (21), dimensionless
$P_{ij},\mathbf{P}_{ij}$ = parameters defined in equation (16), dimensionless
R = wc/WC, heat capacity rate ratio, dimensionless
t,t' = inlet and outlet shell fluid temperatures, °C
T,T' = inlet and outlet tube fluid temperatures, °C
U = heat transfer coefficient, J/s°C m^2
w,w' = inlet and outlet shell fluid flowrates, kg/s
W,W' = inlet and outlet tube fluid flowrates, kg/s
x,y = dimensionless axial coordinates of the tubes varying from 0 to 1 in the direction of tube flow
α,β,γ = auxiliary functions of N_{tu} and R defined in equation (60)
δ,δ' = inlet and outlet shell fluid flowrate fractions, dimensionless
Δ,Δ' = inlet and outlet tube fluid flowrate fractions, dimensionless
λ = function of R and ρ defined in equation (33)
ρ = function of N_{tu} and N_B defined in equation (34)

Subscripts

a,A,b,B = block labels in block decomposition of exchanger
F = final or outlet off-tube temperature distribution in crossflow exchange
I = initial or inlet off-tube temperature distribution in crossflow exchange
$i,j,1,2,3$ = stream labels or matrix indices
R = indicates reduced matrix

where δ_i and Δ_i are the inlet flow rate fractions of the shell and tube fluids, respectively, defined as

$$\delta_i = w_i \Big/ \sum_{j=1}^{n} w_j \qquad \Delta_i = W_i \Big/ \sum_{j=1}^{N} W_j \tag{17}$$

such that

$$\sum_{i=1}^{n} \delta_i = \sum_{i=1}^{N} \Delta_i = 1$$

The relation between the parameters P_{ij} and $\mathbf{P}_{ij}$ defined by equation (16) and the effectiveness of basic exchangers will be apparent after the discussion of the examples presented in the following section.

3 Examples

(a) $n=N=1$, **No Actual Heat Exchange.** An "exchanger" of this type is just an inlet stream divider which partitions the inlet shell and tube fluid streams into n' and N' separate streams, respectively, with no heat transfer among them. In this trivial case, $P_{ij}=\mathbf{P}_{ij}=0$, $\delta_1=\Delta_1=1$, and the matrix elements of M are

$$M_{ij}=\begin{cases} 1 \text{ for } 1\le i\le n', & j=1 \\ 1 \text{ for } (n'+1)\le i\le (n'+N'), & j=2 \\ 0 \text{ otherwise} \end{cases} \tag{18}$$

(b) $n'=N'=1$, **No Actual Heat Exchange Between Tube and Shell Fluids.** This is just a mixer which yields a singlet outlet shell fluid stream and a single outlet tube fluid stream from arbitrary inlet streams. Again, $P_{ij}=\mathbf{P}_{ij}=0$, and M is given by

$$M=\begin{vmatrix} \delta_1 \ldots \delta_n & 0 \ldots 0 \\ 0 \ldots 0 & \Delta_1 \ldots \Delta_N \end{vmatrix} \tag{19}$$

(c) $n=N=1$, $n'>1$, $N'>1$. This corresponds to the case of mixed inlet and unmixed outlet fluids. In this case, M adopts the form

$$M=\begin{vmatrix} 1-P_1 & P_1 \\ \cdot & \cdot \\ \cdot & \cdot \\ 1-P_{n'} & P_{n'} \\ \mathbf{P}_1 & 1-\mathbf{P}_1 \\ \cdot & \cdot \\ \cdot & \cdot \\ \mathbf{P}_{N'} & 1-\mathbf{P}_{N'} \end{vmatrix} \tag{20}$$

where P_i and $\mathbf{P}_i$ are the partial shell-and-tube fluid effectiveness, respectively, and in terms of the inlet and outlet temperatures are given by

$$P_i=(t'_i-t)/(T-t) \qquad \mathbf{P}_i=(T-T'_i)/(T-t) \tag{21}$$

$$P_i=\sum_{j=1}^{n}\delta_j P_{ij}=\sum_{j=1}^{N}\Delta_j P_{i,n+j}, \quad i=1,\ldots,n' \qquad \mathbf{P}_i=\sum_{j=1}^{n}\delta_j \mathbf{P}_{n'+i,j}=\sum_{j=1}^{N}\Delta_j \mathbf{P}_{n'+i,n+j} \quad i=1,\ldots,N' \tag{22}$$

(d) $n=N=n'=N'=1$. This is just the case of a basic exchanger, for which M is given by equation (8). If such an exchanger is obtained by separately mixing the outlet tube-and-shell fluids from the previous example, equation (8) results from the product of equations (19) and (20) with the identification

$$P=\sum_{i=1}^{n'}\delta'_i \quad P_i \qquad \mathbf{P}=\sum_{i=1}^{N'}\Delta'_i \quad \mathbf{P}_i \tag{23}$$

where δ'_i and Δ'_i are the outlet shell-and-tube fluid flow rate fractions for the complex exchanger and, therefore, the inlet fractions of the mixer.

From equations (22) and (23), if a basic exchanger is assembled by preceding and following a complex exchanger by adequate inlet stream divisor and outlet stream mixer, respectively, the effectiveness of the resulting exchanger can be written as

$$P=\sum_{i=1}^{n'}\sum_{j=1}^{n}\delta'_i \quad \delta_j P_{ij}, \qquad \mathbf{P}=\sum_{i=1}^{N'}\sum_{j=1}^{N}\Delta'_i \quad \Delta_j \mathbf{P}_{i+n',j+n} \tag{24}$$

4 Partial Inversion

In this and the following section, we describe some operations which are useful when performing calculations of heat exchangers effectiveness. Unlike equation (1), equation (9) cannot be inverted in general because, for a given complex exchanger, there may be infinitely many sets of inlet temperatures that lead to the same outlet values. The set of inlet temperatures is not, however, the only set that completely defines the problem. It is possible to choose alternate complete sets of independent variables such that, when their values are known, all the remaining temperatures are determined. We show in an example how to find one such alternate set; others can be found by iterating the procedure.

Let $n=2$, $n'=N=N'=1$. Starting with the set of independent inlet variables t_1, t_2, T, such that

$$\begin{vmatrix} t' \\ T' \end{vmatrix} = \begin{vmatrix} M_{11} & M_{12} & M_{13} \\ M_{21} & M_{22} & M_{23} \end{vmatrix} \begin{vmatrix} t_1 \\ t_2 \\ T \end{vmatrix} \tag{25}$$

we can replace t_2 by t' as an independent variable provided M_{12}, the coefficient of t_2 in the expansion of t', is different from zero. Solving for t_2 from the first component of equation (25) and substituting into the expression for T', we obtain

$$\begin{vmatrix} t_2 \\ T' \end{vmatrix} = \begin{vmatrix} -M_{11}/M_{12} & 1/M_{12} & -M_{13}/M_{12} \\ M_{21}-M_{11}M_{22}/M_{12} & M_{22}/M_{12} & M_{23}-M_{13}M_{22}/M_{12} \end{vmatrix} \begin{vmatrix} t_1 \\ t' \\ T \end{vmatrix} = H \begin{vmatrix} t_1 \\ t' \\ T \end{vmatrix} \tag{26}$$

An exchanger of this type can be constructed by matching an inlet stream divider (example *a*) to a general complex exchanger. In such a case, the matrix (20) is obtained as the product of the general matrix of equation (16) times that of equation (18). The partial effectivenesses (21) are then related to the elements of (16) by

The new matrix H in equation (26) is as complete a characterization of the heat exchanger as the original one of equation (25), and may be more convenient to use in some cases, as will be apparent from the examples of sections 6 and 7. The matrix elements of H still satisfy the constraint (10), but their values are not restricted to the interval between 0 and

1. In the following, the temperature variables that appear in equations such as (26) are referred to as right-hand or independent variables, and left-hand or dependent ones.

5 Reduction

In the construction of assemblies of heat exchangers such as discussed in sections 6 and 7, the following problem arises: given a heat exchanger with a known matrix M, which has an outlet stream with the same flow rate as an inlet stream of the same fluid, we want to know the matrix describing the "reduced" exchanger, in which a bypass is established between the inlet and outlet streams just mentioned. How to perform this reduction is best shown by an example, such as that of Fig. 1, in which we assume $w'_1 = w_1$. In it, the original exchanger is described by a matrix M such that

$$\begin{vmatrix} t'_1 \\ t'_2 \\ T' \end{vmatrix} = \begin{vmatrix} M_{11} & M_{12} & M_{13} \\ M_{21} & M_{22} & M_{23} \\ M_{31} & M_{32} & M_{33} \end{vmatrix} \begin{vmatrix} t_1 \\ t_2 \\ T \end{vmatrix} \tag{27}$$

and we want to perform a reduction of the streams of temperatures t_1 and t'_1.

The case of $M_{11} = 1$ is trivial, because from equations (10) and (11) we obtain $M_{12} = M_{13} = 0$ and, from equations (13) and (14), with the condition $w'_1 = w_1$, $M_{21} = M_{31} = 0$. This corresponds to the fact that the inlet stream 1 goes into the outlet stream 1′ without fluid or heat exchange with the other streams, and the reduced exchanger is just described by a submatrix of the original matrix. For $M_{11} < 1$, setting $t_1 = t'_1$ and solving the first component of equation (27) for t_1, yields

$$t_1 = t_2 M_{12}/(1 - M_{11}) + T M_{13}/(1 - M_{11}) \tag{28}$$

Replacing this expression into the second and third components of equation (27) gives the following expression for the reduced exchanger

$$\begin{vmatrix} t'_2 \\ T' \end{vmatrix} = \begin{vmatrix} M_{22} + M_{21}M_{12}/(1 - M_{11}) & M_{23} + M_{21}M_{13}/(1 - M_{11}) \\ M_{32} + M_{31}M_{12}/(1 - M_{11}) & M_{33} + M_{31}M_{13}/(1 - M_{11}) \end{vmatrix} \begin{vmatrix} t_2 \\ T \end{vmatrix} \tag{29}$$

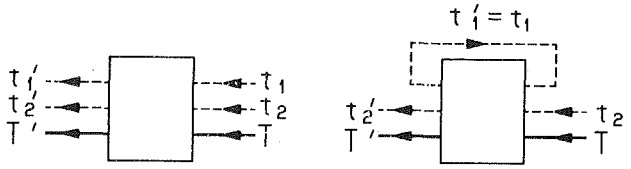

Fig. 1 Reduction operation on a complex heat exchanger

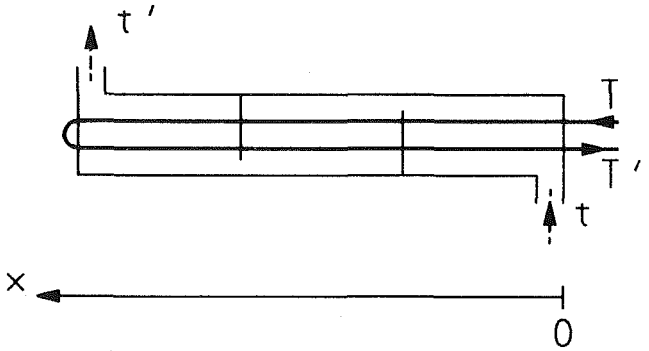

Fig. 2 TEMA E 1-2 shell-and-tube heat exchanger

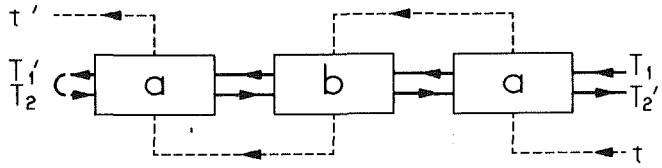

Fig. 3 Block decomposition of the exchanger of Fig. 2

6 TEMA E Shell-and-Tube Exchanger

As a first example of possible applications of the formalism developed in the previous sections, we present a model calculation of a 1-2 shell-and-tube heat exchanger of the TEMA E shell type, with a finite number of baffles. The exchanger is shown in Fig. 2, in which, for clarity, only two baffles are drawn.

In the usual approximation [3], the shell fluid is assumed to mix completely at each value of the longitudinal coordinate x, which corresponds to the limit of an infinite number of baffles. Here we adopt an alternate model in which, within each of the sections that are separated by the baffles, we assume the shell fluid not to mix and to exchange heat in crossflow with the tube fluid. At the outlet of each section, the shell fluid is assumed to mix completely. Such a description has been used by Caglayan and Buthod to calculate the correction factors for one-shell-pass exchangers [4], but our treatment differs from theirs in several respects: (*i*) The shell fluid is treated as a continuum, as opposed to the approximate discrete treatment of [4]; (*ii*) an explicit expression that requires no iteration is obtained here for the effectiveness, and (*iii*) the present treatment makes it possible to handle more than one shell pass (expressions for two shell passes are derived later). Gardner and Taborek [5] have also used a description quite similar to the present one to evaluate the effect of having a small number of baffles in a 1-2 TEMA E exchanger. They also use a block decomposition of the exchanger, but because they do not handle multistream blocks, they are forced to mix the shell fluid between tube passes, which is not done in the present calculation. There is also a difference in the tube mixing assumptions between our treatment and that in [5]. In the latter, the tube fluid is assumed to be unmixed within each section (i.e., between adjacent baffles), and to mix completely between each pair of consecutive sections. We assume it to be mixed throughout, but in our treatment we can also allow for partial mixing in a consistent way by including more than two tubes in the building blocks of Fig. 4 and increasing the dimensionality of the corresponding matrix.

The calculation of the effectiveness of the exchanger as a function of the heat capacity rates ratio R and the number of transfer units N_{tu} proceeds in the following way (see Fig. 3): Starting at the shell inlet, each section is described by a 3 × 3 matrix relating the left-hand variables (one shell and two tube fluid temperatures at the left end of the section) to the right-hand temperatures at the other end. Left-hand variables for a section become right-hand variables for the following one. By such a concatenation, the shell outlet is reached. At this stage, partial inversion (see section 4) is used to switch the tube outlet temperature T_2' to the left-hand side and T_2 to the right-hand side, and reduction in the $T_1' - T_2$ pair (section 5) to account for the continuity of the tube fluid at the left end of the exchanger.

The basic building blocks are therefore shown in Figs. 4(*a*) and 4(*b*). For the first one, we write

$$\begin{vmatrix} t' \\ T_1' \\ T_2 \end{vmatrix} = H_a \begin{vmatrix} t \\ T_1 \\ T_2' \end{vmatrix} \tag{30}$$

where H_a is obtained by integration of the crossflow differential equations which give [6]

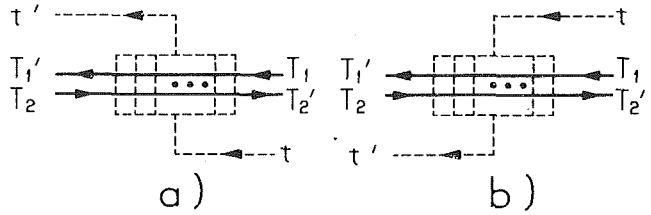

Fig. 4 Building blocks for the exchanger of Fig. 2. The dashed line represents the shell fluid that is divided into infinitely many streams. These elementary streams are recombined into a single outlet stream after having exchanged heat in crossflow with the tube fluid.

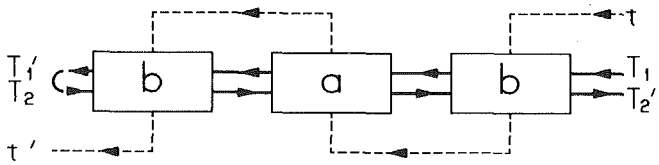

Fig. 5 Block decomposition of the exchanger of Fig. 2, after reversal of the tube fluid and a 180 deg rotation around the longitudinal axis

$$T(x)=\exp(-\lambda x)\left[T(0)+\lambda\int_0^x \exp(\lambda y)t_I(y)\,dy\right] \tag{31}$$

and

$$t_F(x)=\rho t_I(x)+(1-\rho)T(x) \tag{32}$$

where

$$\lambda=R(1-\rho) \tag{33}$$

and

$$\rho=\exp[-N_{tu}/(2N_B+2)] \tag{34}$$

Successsive application of these equations, starting from a constant inlet shell temperature distribution $t_I(x)=t$, using the outlet shell temperature distribution for one row $t_F(x)$ as inlet distribution for the following row (with appropriate coordinate inversion when the direction of flow is reversed), and averaging over the outlet shell temperature distribution for the final row, makes it possible to construct H_a for any finite number of rows. For the case at hand, we obtain

$$H_a=\begin{vmatrix} 1-(1+\rho)(\sinh\lambda)/R & [1-\exp(-\lambda)]/R & (\rho\sinh\lambda+\cosh\lambda-1)/R \\ 1+\rho\sinh\lambda-\cosh\lambda & \exp(-\lambda) & (1-\rho)\sinh\lambda \\ 1-\exp\lambda & 0 & \exp\lambda \end{vmatrix} \tag{35}$$

Similarly, the middle section in the exchanger of Fig. 3 is described by the matrix

$$H_b=\begin{vmatrix} 1-(1+\rho)(\sinh\lambda)/R & (1+\rho\sinh\lambda-\cosh\lambda)/R & (\exp\lambda-1)/R \\ 1-\exp(-\lambda) & \exp(-\lambda) & 0 \\ 1-\rho\sinh\lambda-\cosh\lambda & -(1-\rho)\sinh\lambda & \exp\lambda \end{vmatrix} \tag{36}$$

For the combination of the three sections of Fig. 3, we can write an expression like that of equation (30) but with H_a replaced by

$$H_A=H_aH_bH_a \tag{37}$$

Partial inversion leads to

$$\begin{vmatrix} t' \\ T'_1 \\ T'_2 \end{vmatrix} = M \begin{vmatrix} t \\ T_1 \\ T_2 \end{vmatrix} \tag{38}$$

After reduction of the $T'_1 - T_2$ pair, we are left with

$$\begin{vmatrix} t' \\ T'_2 \end{vmatrix} = M_R \begin{vmatrix} t \\ T_1 \end{vmatrix} \tag{39}$$

where, from comparison with equation (8), we obtain for the effectiveness of the whole exchanger

$$P=(M_R)_{12} \tag{40}$$

Alternatively, when H_A has been obtained by the matrix multiplication of equation (37), the following shortcut can be used to obtain the effectiveness P in terms of R and the matrix elements of H_A. Because P is independent of the inlet temperatures, we can set $t=0$, $T_1=1$, and write P and R as functions of T'_2

$$P=(t'-t)/(T_1-t)=H_{A_{12}}+H_{A_{13}}T'_2 \tag{41}$$

$$R=(T_1-T'_2)/(t'-t)=(1-T'_2)/P. \tag{42}$$

Hence

$$T'_2=1-RP$$

and

$$P=(1-H_{A_{11}})/(1+RH_{A_{13}}) \tag{43}$$

It is interesting to examine what happens if the direction of flow of the tube fluid is reversed. If an additional 180 deg rotation of the exchanger around its longitudinal axis is performed, we are left with the configuration of Fig. 5, from which it is clear that the only change in the previous analysis is the substitution of H_A given by equation (37) by

$$H_B=H_bH_aH_b \tag{44}$$

Equations (33-37), (43), and (44) give explicit expressions for the effectiveness of the exchanger as a function of R and N_{tu} for the case of two baffles. The corresponding LMTD correction factor F follows immediately as a function of the same variables. In Fig. 6 the usual plot of F versus P at constant R is shown for two up to five baffles, for the two possible directions of tube flow. The results for different values of N_B are obtained by varying the number of matrix factors in equations (37) and (44), in which H_a and H_b appear in alternating order. The total number of factors is N_B+1, and the rightmost factor is H_a in equation (37) and H_b in equation (44). It is clear that as the number of baffles increases, the effect of the tube flow inversion becomes smaller. The limiting case for $N_B\to\infty$ shown in Fig. 9 is described in the next section, after the divided-flow example. It is worth pointing out that, in spite of the differences mentioned earlier between the mixing assumptions in our calculations and those of Gardner and Taborek [5], the curves shown in [5] for $R=1$, variable number of baffles, and both orientations of tube return flow, are quite close to those presented here.

7 TEMA J Shell-and-Tube Exchanger

Figure 7 shows the building-block decomposition of a divided-flow shell-and-tube exchanger, for which schematic diagrams and F curves are given in Fig. 8. If blocks A and B are described by the model presented in the previous section with N_B baffles each, the divided-flow exchanger has $2N_B+1$

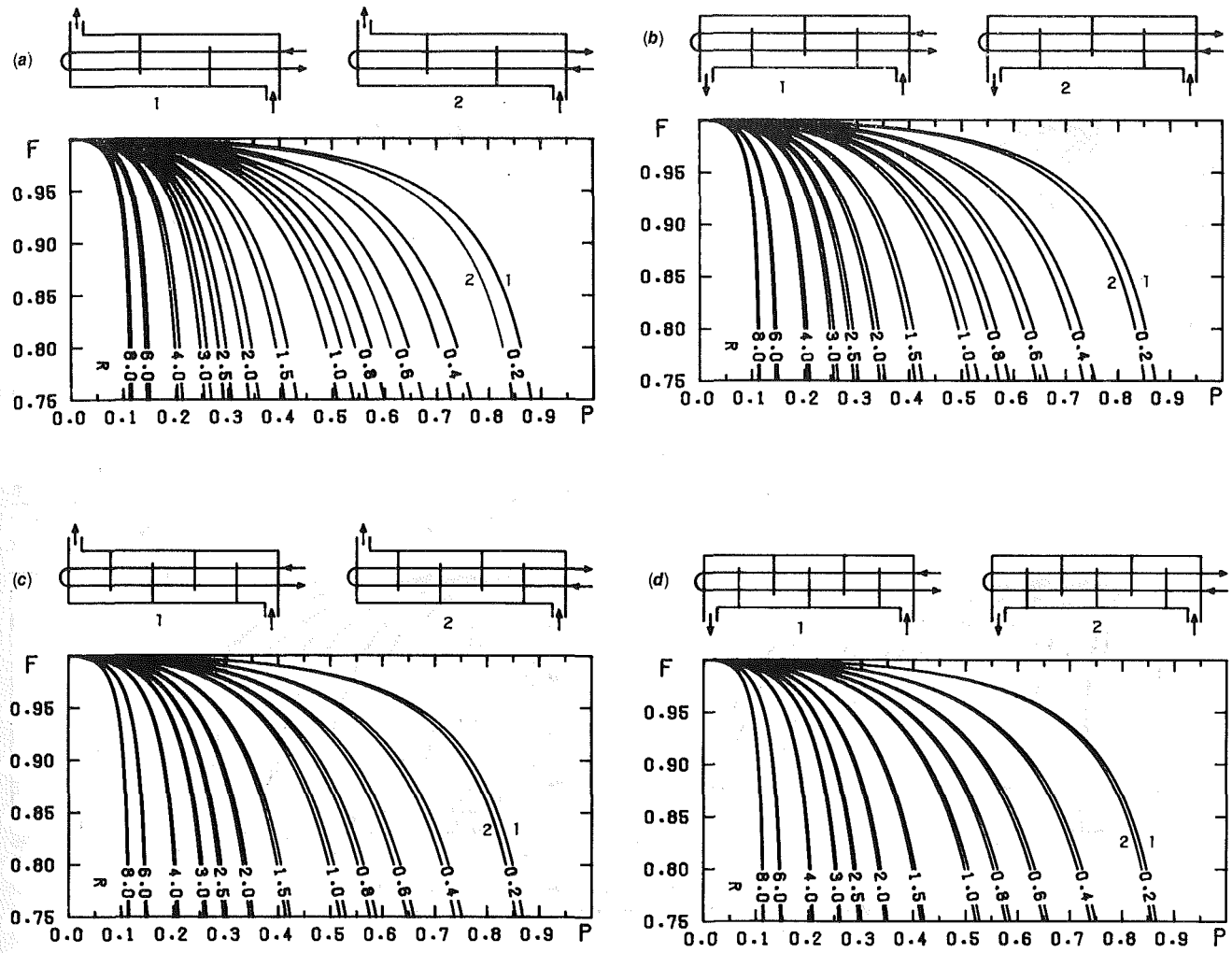

Fig. 6 LMTD correction factors for TEMA E 1-2 shell-and tube exchanger, for both directions of tube flow, with (*a*) 2 baffles, (*b*) 3 baffles (*c*) 4 baffles, and (*d*) 5 baffles

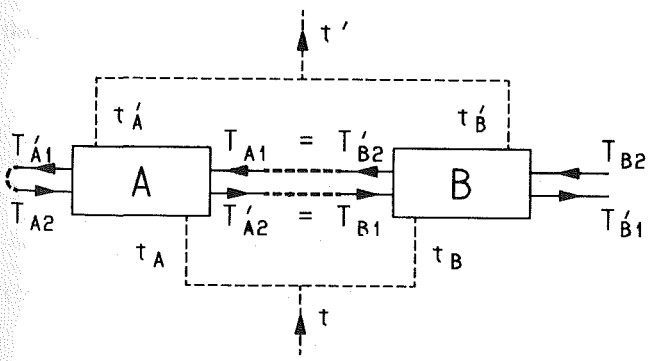

Fig. 7 Block decomposition of TEMA J 1-2 shell-and-tube exchanger

baffles. For $N_B = 2$, block A is precisely given in the combination shown in Fig. 3, whereas block B can be obtained from Fig. 5 by a 180 deg rotation in the plane of the drawing and the suppression of the reduction in the $T_1' - T_2$ variables. We can therefore write

$$\begin{vmatrix} t'_A \\ T'_{A1} \\ T_{A2} \end{vmatrix} = H_A \begin{vmatrix} t_A \\ T_{A1} \\ T'_{A2} \end{vmatrix} \tag{45}$$

$$\begin{vmatrix} t'_B \\ T'_{B1} \\ T_{B2} \end{vmatrix} = H_B \begin{vmatrix} t_B \\ T_{B1} \\ T'_{B2} \end{vmatrix} \tag{46}$$

$$\begin{vmatrix} t_B \\ T_{B1} \\ T'_{B2} \end{vmatrix} = I_B \begin{vmatrix} t'_B \\ T'_{B1} \\ T_{B2} \end{vmatrix} \tag{47}$$

and

$$\begin{vmatrix} t'_B \\ T_{B1} \\ T'_{B2} \end{vmatrix} = K_B \begin{vmatrix} t_B \\ T'_{B1} \\ T_{B2} \end{vmatrix} \tag{48}$$

where

$$I_B = H_B^{-1} \tag{49}$$

and K_B can be obtained from I_B through partial inversion in the variables $t_B - t'_B$. With these elements, the aim is to obtain a matrix H such that

$$\begin{vmatrix} t' \\ T'_{A1} \\ T_{A2} \end{vmatrix} = H \begin{vmatrix} t \\ T_{B2} \\ T'_{B1} \end{vmatrix} \tag{50}$$

from which the same derivation used to obtain equation (43) yields

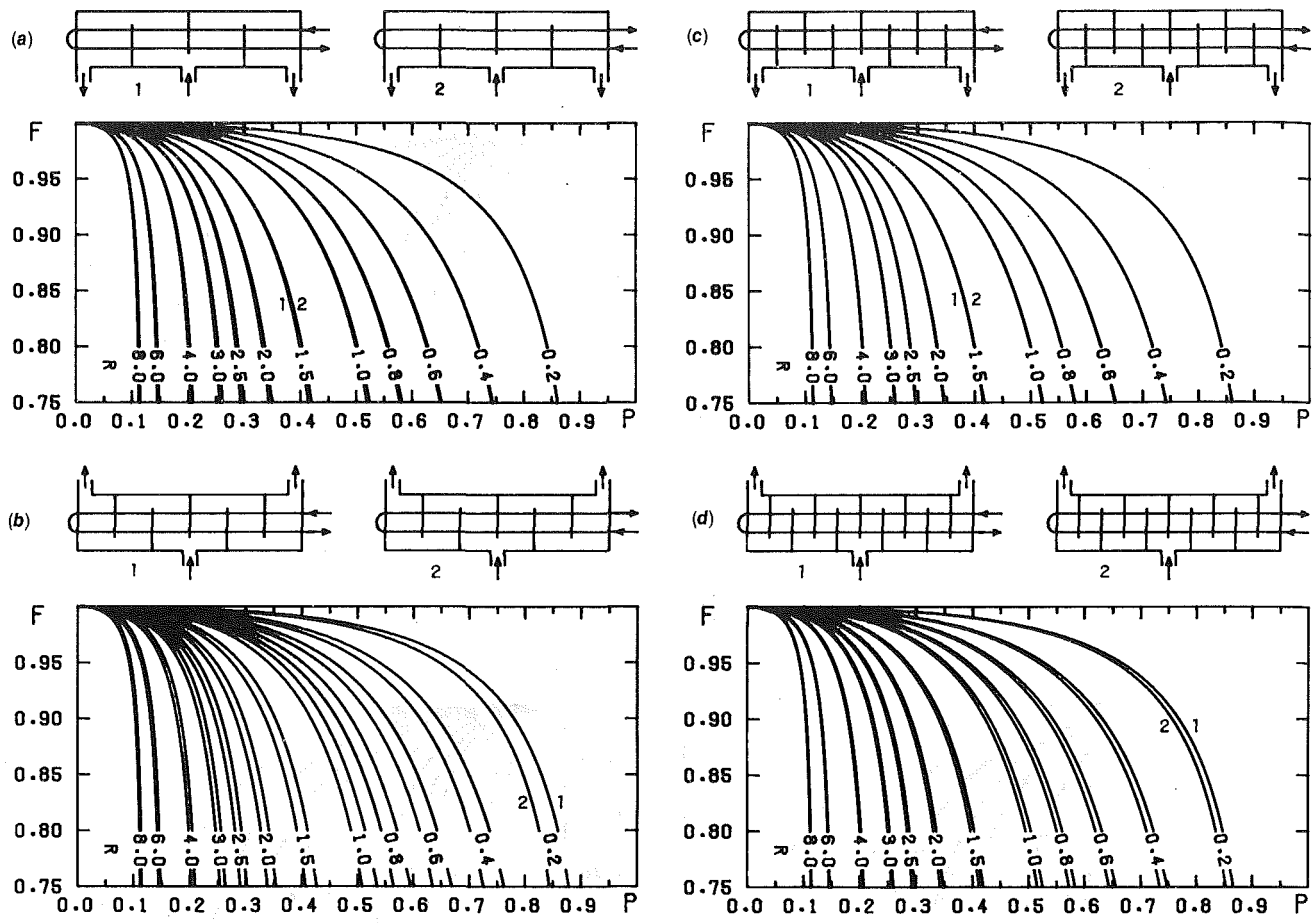

Fig. 8 LMTD correction factors for TEMA J 1-2 shell-and-tube exchanger for both directions of tube flow, with (*a*) 3 baffles, (*b*) 5 baffles, (*c*) 7 baffles, and (*d*) 9 baffles

$$P=(1-H_{11})/(1+RH_{13}) \tag{51}$$

The expression for H is obtained through the following steps:

1 The variable t'_B is added to equation (45)

$$\begin{vmatrix} t'_A \\ T'_{A1} \\ T_{A2} \\ t'_B \end{vmatrix} = \begin{vmatrix} H_A & \begin{matrix}0\\0\\0\end{matrix} \\ 0\,0\,0 & 1 \end{vmatrix} \begin{vmatrix} t_A \\ T_{A1} \\ T'_{A2} \\ t'_B \end{vmatrix} \tag{52}$$

2 The variables T_{A1} and T'_{A2} are substituted by the corresponding values T'_{B2} and T_{B1} and written in terms of T'_{B1} and T_{B2}

$$\begin{vmatrix} t_A \\ T_{A1} \\ T'_{A2} \\ t'_B \end{vmatrix} = \begin{vmatrix} 1&0&0&0 \\ 0&0&0&1 \\ 0&0&1&0 \\ 0&1&0&0 \end{vmatrix} \begin{vmatrix} t_A \\ t'_B \\ T_{B1} \\ T'_{B2} \end{vmatrix} =$$

$$\begin{vmatrix} 1&0&0&0 \\ 0&0&0&1 \\ 0&0&1&0 \\ 0&1&0&0 \end{vmatrix} \begin{vmatrix} 1&0&0&0 \\ 0&0&0&1 \\ 0&0&1&0 \\ 0&1&0&0 \end{vmatrix} \begin{vmatrix} t_A \\ t_B \\ T'_{B1} \\ T_{B2} \end{vmatrix} \tag{53}$$

3 The variables T'_{B1} and T_{B2} are interchanged, and t_A and t_B are just set equal to t by substituting

$$\begin{vmatrix} t_A \\ t_B \\ T'_{B1} \\ T_{B2} \end{vmatrix} = \begin{vmatrix} 1&0&0 \\ 1&0&0 \\ 0&0&1 \\ 0&1&0 \end{vmatrix} \begin{vmatrix} t \\ T_{B2} \\ T'_{B1} \end{vmatrix} \tag{54}$$

4 The outlet shell streams are mixed

$$\begin{vmatrix} t'_A \\ T'_{A1} \\ T_{A2} \end{vmatrix} = \begin{vmatrix} 1/2&0&0&1/2 \\ 0&1&0&0 \\ 0&0&1&0 \end{vmatrix} \begin{vmatrix} t'_A \\ T'_{A1} \\ T_{A2} \\ t'_B \end{vmatrix} \tag{55}$$

Combining equations (52–55) and comparing with (50), we obtain

$$H= \begin{vmatrix} 1/2&0&0&1/2 \\ 0&1&0&0 \\ 0&0&1&0 \end{vmatrix} \begin{vmatrix} \begin{vmatrix} H_A & \begin{matrix}0\\0\\0\end{matrix} \\ 0\,0\,0 & 1 \end{vmatrix} \begin{vmatrix} 1&0&0&0 \\ 0&0&0&1 \\ 0&0&1&0 \\ 0&1&0&0 \end{vmatrix} \begin{vmatrix} 1&0&0&0 \\ 0&\begin{matrix}0\\0\\0\end{matrix}&K_B \end{vmatrix} \begin{vmatrix} 1&0&0 \\ 1&0&0 \\ 0&0&1 \\ 0&1&0 \end{vmatrix} \tag{56}$$

whence, after writing the matrix elements of K_B in terms of those of I_B, one obtains

$$H_{11} = \frac{1}{2I_{B_{11}}} (H_{A_{11}} I_{B_{11}} + H_{A_{12}} I_{B_{31}} + H_{A_{13}} I_{B_{21}} + 1) \quad (57)$$

and

$$H_{13} = \frac{1}{2I_{B_{11}}} [H_{A_{12}} (I_{B_{11}} I_{B_{32}} - I_{B_{31}} I_{B_{12}}) + H_{A_{13}} (I_{B_{11}} I_{B_{22}} - I_{B_{21}} I_{B_{12}}) - I_{B_{12}}] \quad (58)$$

From these expressions and equation (51), the effectiveness of the divided-flow exchanger is obtained explicitly in terms of the matrices that describe the normal shell exchanger and only requires the inversion of a 3 × 3 matrix of equation (49). All these operations can be easily performed in an electronic calculator, and there is no point in carrying out the algebraic manipulations required by matrix multiplication and inversion if, eventually, the final analytical expression is not going to be calculated by hand, anyway. Observe, however, that whereas the number of transfer units for the whole exchanger is the same as for each of the sections A and B into which we have divided it, the heat capacity rate ratio is twice as large. Therefore, when using equations (57) and (58), the expressions for H_A and H_B should be evaluated for $R_A = R_B = R/2$.

Figure 8 shows the F-curves for divided-flow exchangers with 3, 5, 7, and 9 baffles, for both directions of tube flow. Again we verify that, as the number of baffles grows, the effect of the tube direction of flow becomes less important. There is a difference, however, between the cases in which the number of baffles N_B in each half of the exchanger (not counting the central baffle) is even or odd. For even values, there is still a clear effect for $N_B = 4$ (see Fig. 8(d)), whereas for odd values, the effect is already very small for at $N_B = 1$ (Fig. 8(a)). This is so because for even values of N_B both halves of the exchanger are more effective for the same tube flow direction, whereas for odd N_B the flow direction that yields a higher effectiveness in one half of the exchanger gives a lower one in the other half, and vice versa, with a net result of near independence on the tube fluid direction of flow. In the preceding argument, by effectiveness of one half of the exchanger we mean the effectiveness that the exchanger would have if the heat transfer coefficient of the other half was "switched off," i.e., was set equal to zero.

The limit for N_B tending to infinity can be obtained for both E shells and J shells, and we include it here for completeness, even though the results are known from the works of Underwood [3] and Jaw [7], respectively. In this limit, perfect mixing is achieved for the shell fluid in the transverse direction, and the treatment of Underwood [3] can be used to derive the following expressions for the matrices H_A and H_B, which turn out to coincide

$$H_A = H_B = \begin{vmatrix} 1-2\alpha & [1-\beta+(R-1)\alpha]/R & [\beta-1+(R+1)\alpha]/R \\ 1-\beta+(R-1)\alpha & [1+(R-1)\beta+(R-1-R^2)\alpha]/R & (\beta-1+\alpha)/R \\ 1-\beta-(R+1)\alpha & (1-\beta-\alpha)/R & [\beta(1+R)-1+\alpha(1+R+R^2)]/R \end{vmatrix} \quad (59)$$

where

$$\alpha = \exp(-N_{tu/2}) \text{singh}(\gamma N_{tu}/2)/$$
$$\beta = \exp(-N_{tu}/2)\cosh(\gamma N_{tu}/2) \quad (60)$$
$$\gamma = \sqrt{1+R^2}$$

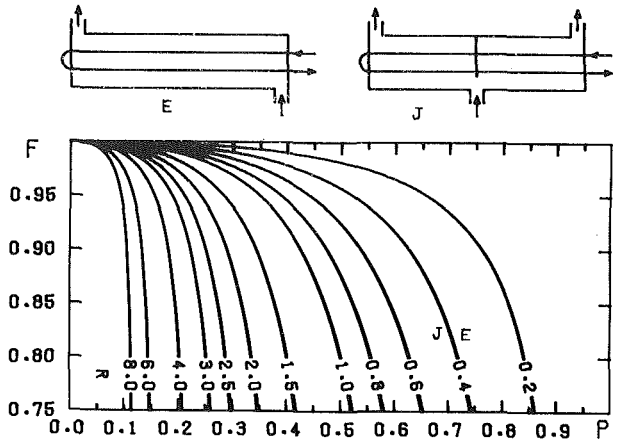

Fig. 9 LMTD correction factors for TEMA E and TEMA J shells in the limit of large numbers of baffles. Both sets of curves almost coincide, but the TEMA E curves are slightly higher. The same curves apply if the tube flows are reversed.

With these expressions, we perform again the analysis of the 1-2 E and J shell-type exchangers. The corresponding F-curves are plotted in Fig. 9 and show that there is no significant difference between the two types of shells in this limit of large number of baffles.

The comparison of Figs. 6, 8, and 9 leads to the conclusion that the correction factor for the TEMA J shells with $2N_B + 1$ baffles are closely represented by the TEMA E values, with the following rule: for even values of N_B, the TEMA E shell with N_B baffles should be used; for odd values of N_B, the limiting value for large number of baffles should be used for the E shell.

In the analysis of this and the preceding sections, the tube fluid has been assumed to be totally mixed. By using matrices of higher dimensionality each tube pass can be described as formed by one or more rows, with each row fully mixed. In this treatment, there is no need to mix fluids of different tubes between neighboring sections.

8 Concluding Remarks

From the preceding discussion, it should be clear that the generalized matrix formalism is a powerful tool to handle calculations of heat exchangers that incorporates in a natural way the basic properties of linearity, heat conservation, and translational invariance of the heat transfer equations. This has been illustrated through the discussion of the 1-2 shell-and-tube heat exchangers with variable number of baffles, normal or divided shell flow, and two possible directions of tube flow. These examples by no means exhaust the possible applications of the formalism, but should be sufficient to show the interested designer how to apply the formalism to other configurations of his immediate concern.

9 Acknowledgments

The author is indebted to Professor Guillermo Cordero for fruitful discussions.

References

1 Domingos, J. D., "Analysis of Complex Assemblies of Heat Exchangers," *Int. J. Heat Mass Transfer*, Vol. 12, 1969, pp. 537–548.

2 Pignotti, A., "Flow-Reversibility of Heat Exchangers," ASME JOURNAL OF HEAT TRANSFER, Vol. 106, No. 2, pp. 361–368.

3 Underwood, A. J. V., "The Calculation of the Mean Temperature Difference in Multipass Heat Exchangers," *J. Inst. Petroleum Technol.*, Vol. 20, 1934, pp. 145–158.

4 Caglayan, A. N., and Buthod, P., "Factors Correct Air-Cooler and S&T Exchanger LMTD," *Oil and Gas Journal*, Vol. 74, 1976, pp. 91–94.

5 Gardner, K., and Taborek, J., "Mean Temperature Difference: A Reappraisal," *AIChE Journal*, Vol. 23, 1977, pp. 777–786.

6 Pignotti, A., and Cordero, C., "Mean Temperature Difference in Multipass Crossflow," ASME JOURNAL OF HEAT TRANSFER, to be published.

7 Jaw, L., "Temperature Relations in Shell and Tube Exchangers Having One Pass Split-Flow Shells," ASME JOURNAL OF HEAT TRANSFER, Vol. 86, 1964, pp. 408–416.

Flow Reversibility of Heat Exchangers

A. Pignotti
Techint S. A.,
Buenos Aires 1001, Argentina

A symmetry property which relates the thermal behavior of a heat exchange process to that of the reverse process, in which the directions of flow of both fluids are reversed, is demonstrated for the ideal case of no change of phase, no heat losses, and temperature-independent heat transfer coefficients and heat capacities. The symmetry is formulated in terms of a relation between the matrices that describe the direct and reverse process, which can be used to obtain one of them if the other is known. The formalism used does not require the inlet and outlet streams to be completely mixed, but when this is the case, both matrices coincide, and therefore, the effectiveness is the same for both processes. The consequences of the symmetry are ilustrated by the discussion of a three-row, two-pass air cooler, and the TEMA G split flow shell-and-tube heat exchanger.

1 Introduction

It is well-known that in the approximations commonly used for the calculation of the mean temperature difference in a 1-2 shell-and-tube heat exchanger, the four different configurations of Figs. 1(*a–d*) yield the same result [1]. However, Gardner and Taborek [2] have shown that the equivalence of the configurations of Figs. 1(*a*) and 1(*c*), which differ from each other in the inversion of the direction of the tube flow, disappears if the assumption of complete transverse mixing of the shell fluid is dropped, and a model which takes into account the finite numer of baffles present is used. They have also pointed out that if the same model is applied to the cases of Figs. 1(*b*) and 1(*d*), it is found that case 1(*a*) still coincides with 1(*b*), and 1(*c*) with 1(*d*). This is still true in a very similar model, with different mixing assumptions, described in [3].

Is the coincidence just described accidental, can it be removed by a further refinement of the model, or will it persist because of some deeper reason? Does it happen only in this case, or is this just a particular example of a much more general property? It is tempting to conjecture that it is the manifestation of a hidden symmetry property, i.e., of the invariance of a phsycial quantity (such as the effectiveness of the exchanger) under a transformation that changes one configuration (for instance, that of Fig. 1(*a*)), into a thermally equivalent configuration (in our example, that of Fig. 1(*b*)).

Examination of the examples of Fig. 1 shows that in both cases in which the coincidence exists, the two equivalent configurations differ from each other only in the inversion of *both* fluids. Gardner and Taborek did point out the inversion of the shell fluid, but for the following argument it is crucial to realize that the tube fluid is *also* inverted when going from Fig. 1(*a*) to 1(*b*) or from Fig. 1(*c*) to 1(*d*), while the geometry of the exchanger is kept precisely the same. Therefore, one might suspect that, not only in the present case, but for all possible exchangers, when this double inversion occurs and the inlet temperatures are kept the same, the outlet temperatures are also the same. This is schematically shown in Fig. 2(*a*).

In the following, we show that this is indeed the case for heat exchangers with two inlet and two outlet streams, and we call this property flow reversibility. It should be pointed out that it is a property related to reversing the direction of both fluids, and it is *not* related to entropy production in the exchanger.

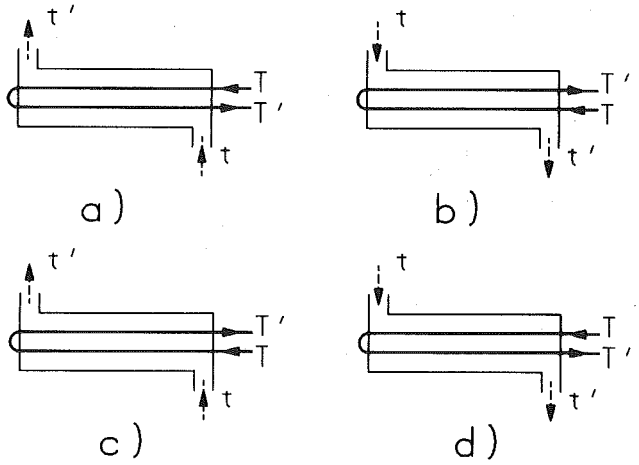

Fig. 1 Four different flow arrangements for 1-2 shell-and-tube heat exchanger that are equivalent if complete transverse mixing of the shell fluid is assumed

The symmetry property discussed in this article is by no means trivial, except in cases that have a special geometrical symmetry. What makes it more intriguing is that it only applies in a global sense, i.e., to the inlet and outlet temperatures, but not to intermediate ones, such as the temperatures at the tube return points between passes 1 and 2 in Figs. 1(*a*) and 1(*b*), which do not coincide. It turns out that, in order to prove flow reversibility for basic exchangers (those with no more than two inlet and two outlet streams), we have to consider what happens when all the flows are reversed in the more general case of complex exchangers, in which more than two inlet and/or two outlet streams are present. By analogy, we might attempt to generalize the flow-reversibility concept by asking whether it is true that, when all the flows in the exchanger are reversed, and the same inlet temperatures are used, the outlet temperatures remain the same. However, it is readily seen that this generalization in untenable. In the first place, it is impossible to assign the proper inlet and outlet temperatures to the reversed configuration when the numbers of the inlet and outlet streams do not coincide. Second, even when they do coincide, we can show by the simple example of Fig. 2(*b*), in which two flow-reversible basic heat exchangers A and B are coupled, that the final temperatures in the reversed configuration may be different from those in the original one. This difference is only removed when the inlet and outlet streams of the tube fluid are mixed, such as shown in Fig. 2(*c*), in which case we no longer deal with a complex heat exchanger.

We have, therefore, apparently failed in our attempt to generalize the concept of flow reversibility to complex heat

Contributed by the Heat Transfer Division for publication in the JOURNAL OF HEAT TRANSFER. Manuscript received by the Heat Transfer Division November 10, 1982.

exchangers. But we failed only because the generalization attempted was naive and inconsistent. It turns out that it is possible to formulate this generalization in a precise and correct form, which enables us to relate the thermal properties of any complex configuration to those of the flow-reversed one. The formulation is not done in terms of the inlet and outlet temperatures but, rather, in terms of the matrices that describe the thermal behavior of each configuration, and that uniquely determine the outlet temperatures when the inlet ones are given [3].

In this formulation, flow reversibility is just seen as the transformation property of thermal matrices under flow reversal. This is probably more abstract than what most readers are readily willing to accept, but it should be remarked that when a symmetry operation is performed, only the simplest physical quantities remain invariant, while more complex ones undergo specific transformations. To quote a familiar example, scalar quantities are unchanged when the coordinate axes are rotated, whereas vector or tensor quantities are transformed according to prescribed laws. These transformation properties are the expression of the isotropy of space. In our case, the symmetry operation is flow reversal, and a simple invariant quantity is the effectiveness of a basic heat exchanger, while the matrices that describe complex exchangers undergo specific transformations. And these transformations are the correct expression of the flow-reversibility property of heat exchange processes. It is in this deeper sense that we claim that the exchanger of Fig. 2(*b*) is flow reversible, and the example will be discussed from this point of view in more detail in section 3.

The transformation properties of thermal matrices under flow reversal are stated in section 2, are illustrated through some simple examples in section 3, and are proved in section 5. The proof is based on two theorems formulated in section 4 and proved in the Appendix. Sections 6 and 7 deal with applications of flow reversibility and the conclusions are summarized in section 8.

2 General Statement of Flow Reversibility

In this section, we formulate the general property of flow reversibility, the proof of which is given in section 5. Following the Nomenclature of [3], we call a heat exchanger

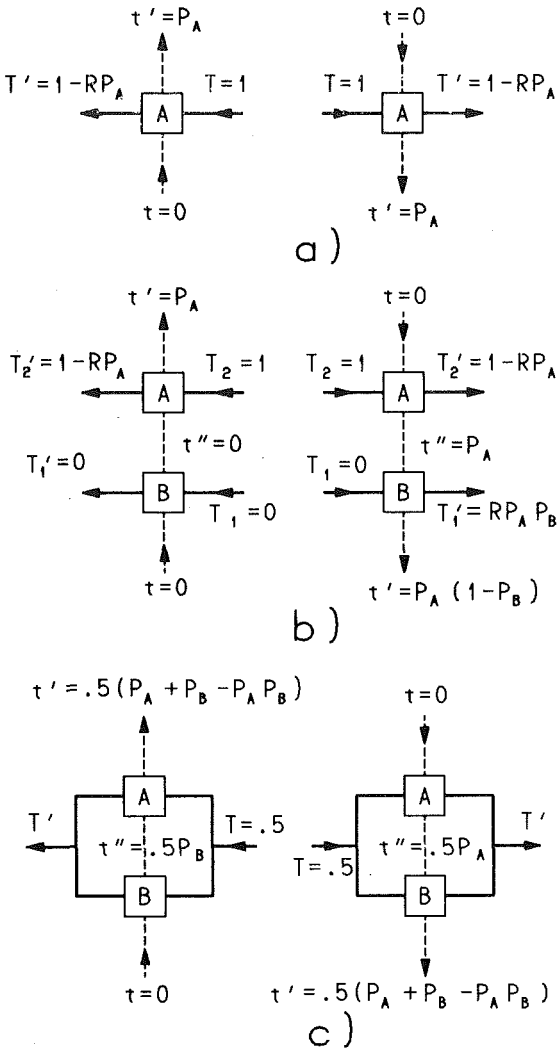

Fig. 2 Three examples of the effect of reversing the motion of both fluids. The exchangers represented by boxes labeled *A* and *B* are assumed to be flow-reversible.

Nomenclature

A = heat transfer area, m^2
c, C = shell and tube[1] fluid specific heats, J/kg °C
D, D' = inlet and outlet heat capacity rate matrices, J/s °C
F = logarithmic mean temperature difference correction factor, dimensionless
M = matrix relating the outlet to the inlet temperatures, dimensionless
$\tilde{M}$ = transpose of matrix M, dimensionless
$\hat{M}$ = matrix relating the outlet to the inlet temperatures for the reverse process, dimensionless
n, n' = number of inlet and outlet shell fluid streams, dimensionless
N, N' = number of inlet and outlet tube fluid streams, dimensionless
N_{tu} = UA/wc, number of heat transfer units, referred to the shell fluid, for the whole exchanger, dimensionless
P = $(t'-t)/(T-t)$, shell fluid effectiveness, dimensionless
$\mathbf{P}$ = $(T-T')/(T-t)$, tube fluid effectiveness, dimensionless
R = wc/WC heat capacity rates ratio, dimensionless
t, t' = inlet and outlet shell fluid temperatures, °C
T, T' = inlet and outlet tube fluid temperatures, °C
U = overall heat transfer coefficient, $W/°C\,m^2$
w, w' = inlet and outlet shell fluid flowrates, kg/s
W, W' = inlet and outlet tube fluid flowrates, kg/s
α, β = auxiliary functions defined in equation (18)
δ_i = $w_i \Big/ \sum_{j=1}^{n} w_j$, shell fluid flowrate fraction of the ith inlet stream, dimensionless

Subscripts

A, B = block labels in block decomposition of exchanger
$i, j, 1, 2, 3$ = stream labels or matrix indices
L = indicates lower half of the split-flow exchanger
R = indicates reduced matrix
U = indicates upper half of the split-flow exchanger

[1] In exchangers in which "shell" and "tube" are not precise characterizations of the fluids, any other descriptions in terms of physical characteristics of the apparatus are equally valid.

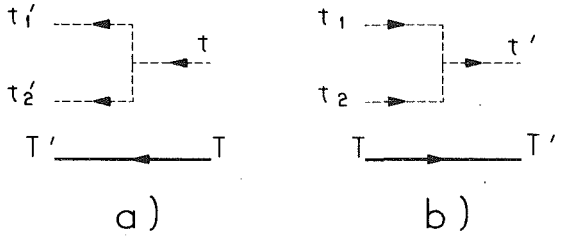

Fig. 3 Shell fluid divider/mixer

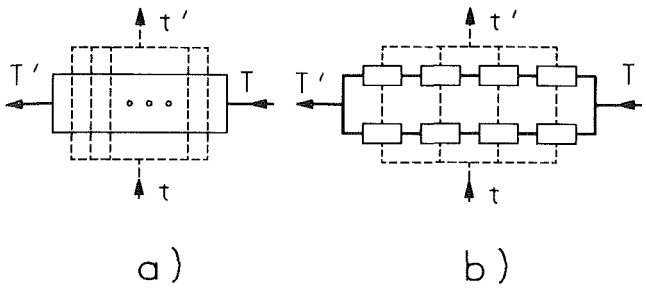

Fig. 4 (a) Schematic representation of a one-pass, two-row air cooler with no intermediate air mixing, and (b) decomposition of the same exchanger into eight coupled elementary exchangers

basic if the inlet and outlet streams of both fluids are perfectly mixed and complex if at least one of those streams is subdivided into two or more streams of uniform temperature. We begin by stating the property of flow reversibility for basic heat exchangers, in the approximations of no heat losses, constant heat capacities and heat transfer coefficients, and no change of phase.

In the case considered, the relation between the outlet and inlet temperatures can be expressed in the following matrix form [4]

$$\begin{vmatrix} t' \\ T' \end{vmatrix} = \begin{vmatrix} M_{11} & M_{12} \\ M_{21} & M_{22} \end{vmatrix} \begin{vmatrix} t \\ T \end{vmatrix}, \tag{1}$$

where M is a 2×2 matrix which characterizes the exchanger used. If we now take the same apparatus, but let both fluids flow through it in reverse directions, we have, in principle, a different heat exchange process, for which an expression like equation (1) can be written, with a matrix that we call $\hat{M}$. The statement of flow reversibility for basic heat exchangers is simply

$$\hat{M} = M \tag{2}$$

Care should be taken not to confuse the inversion of flows discussed here, which is a physical inversion, with the mathematical inversion of equation (1), which is discussed in [4], and is used to express the inlet variables as dependent and the outlet ones as independent for the same physical process described by equation (1). Here we are saying that the same matrix describes both the direct and the reverse physical process which, in general, look quite different from each other, if, in each case, the outlet variables are the dependent ones.

In the same approximations, a complex heat exchanger is described by an $(n'+N') \times (n+N)$ temperature-independent rectangular matrix M, which relates the outlet to the inlet temperatures in an expression entirely analogous to equation (1) [3]. The reverse process is in turn described by an $(n+N) \times (n'+N')$ matrix which we denote $\hat{M}$, and flow reversibility can be expressed as

$$\hat{M} = D^{-1} \tilde{M} D' \tag{3}$$

where the tilde denotes transposition. D is a diagonal matrix, the nonvanishing elements of which are the heat capacity rates of the inlet streams of the direct process (i.e., of the outlet streams of the reversed process), and D' is the analogous one for the direct process outlet streams

$$D = \begin{vmatrix} w_1 c & & & & & \\ & \ddots & & & & \\ & & w_n c & & & \\ & & & W_1 C & & \\ & & & & \ddots & \\ & & & & & W_N C \end{vmatrix} \tag{4}$$

$$D' = \begin{vmatrix} w'_1 c & & & & & \\ & \ddots & & & & \\ & & w'_{n'} c & & & \\ & & & W'_1 C & & \\ & & & & \ddots & \\ & & & & & W'_{N'} C \end{vmatrix} \tag{5}$$

The proof of equation (3) is given in section 5. Here we only show that $\hat{M}$, as given by equation (3), satisfies three conditions that are necessary if it is to be interpreted as the matrix which describes the reverse process. In the first place, equation (2) can be easily obtained as a particular case of equation (3) for basic heat exchangers ($n = n' = N = N' = 1$). This can be verified by direct substitution. Second, $\hat{M}$ satisfies the constraints of translational invariance in the temperature variable [3] and of heat conservation for the reversed process. Indeed, the known property of $\hat{M}$, which follows from heat conservation for the direct process [3]

$$\sum_{i=1}^{n'+N'} \hat{M}_{ij} = 1, \quad i = 1, \ldots, n+N \tag{6}$$

is precisely what is needed for $\hat{M}$ to satisfy the contraints of translational invariance. Reciprocally, translational invariance of M guarantees that $\hat{M}$ satisfies the contraint of heat conservation for the reversed process. The fact that the matrix $\hat{M}$, given by equation (3) automatically satisfies these three constraints, does not constitute a proof that it is the matrix which describes the flow-reversed process, but is highly suggestive that we are on the right track.

3 Elementary Examples

We discuss in this section three simple examples which, however, provide some elements needed for the proof of the flow reversibility property expressed by equation (3).

(a) Stream Divider/Mixer. The "apparatus" of Fig. 3(*a*), in which the sole effect is to divide one of the inlet streams into two, is a shell fluid divider, for which

$$M = \begin{vmatrix} 1 & 0 \\ 1 & 0 \\ 0 & 1 \end{vmatrix} \tag{7}$$

Figure 3(*b*) shows the process obtained by inverting the flows in the same "exchanger," for which we now have from equations (3), (4), (5), and (7)

$$\hat{M} = \begin{vmatrix} \delta_1 & \delta_2 & 0 \\ 0 & 0 & 1 \end{vmatrix} \tag{8}$$

where δ_i are the inlet fluid flowrate fractions. The matrix given by equation (8) correctly describes the fluid mixer of Fig. 3(*b*). Therefore, this divider/mixer combination can be formally considered a flow-reversible heat exchanger even though no heat is actually exchanged from one fluid to the other.

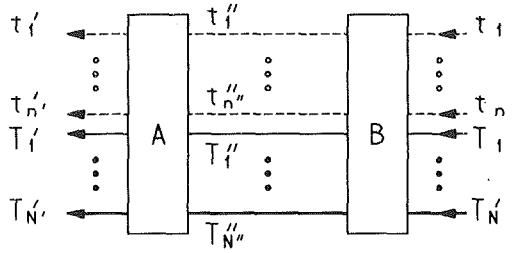

Fig. 5 Concatenation of two exchangers

(*b*) **Geometrically Symmetric Basic Heat Exchangers.** Basic heat exchangers with appropriate geometrical symmetry, such that they look the same when viewed from either the inlet or outlet end, as that of Fig. 4(*a*), clearly satisfy equation (2) and, therefore, are trivially reversible. Figure 4(*a*) represents a crossflow air cooler with one two-row pass on the tube side. The air flow is represented by dashed lines that show an inlet stream of uniform temperature t that is subdivided into infinitely many intermediate streams. After exchanging heat with the tubes, these elementary air streams are combined back together into a stream of temperature t' at the exchanger outlet. Note that if both rows are not exactly equal, the exchanger is no longer *a priori* reversible. In such a case, however, we can break it up into a collection of flow-reversible basic heat exchangers with any desired degree of accuracy by subdividing each tube into sufficiently small consecutive segments, such that for each one of them the inlet and outlet air temperatures can be approximated by constants (see Fig. 4(*b*)). The flow reversibility of each little piece follows from geometrical considerations, and this is the basis for the proof of the same property for the whole exchanger which is given in subsequent sections.

(*c*) **Combination of Two Reversible Basic Heat Exchangers of Fig. 2(*b*).** The matrix which describes the direct process for this case can be written as the following product of two matrices

$$M = \begin{vmatrix} 1-P_A & 0 & P_A \\ 0 & 1 & 0 \\ RP_A & 0 & 1-RP_A \end{vmatrix} \begin{vmatrix} 1-P_B & P_B & 0 \\ RP_B & 1-RP_B & 0 \\ 0 & 0 & 1 \end{vmatrix}$$

$$= \begin{vmatrix} (1-P_A)(1-P_B) & (1-P_A)P_B & P_A \\ RP_B & 1-RP_B & 0 \\ (1-P_B)RP_A & RP_AP_B & 1-RP_A \end{vmatrix} \quad (9)$$

The right-hand matrix factor in the preceding equation describes the effect of the exchanger labeled B, in which two of the inlet streams are involved, and the third one is a spectator. This is represented by a 2×2 submatrix with nonvanishing elements and the addition of one row and one column the elements of which are zero, except for a diagonal matrix element equal to one. In an analogous fashion, the left-hand matrix factor incorporates the effect of the exchanger labeled A, in which the spectator is the second component of the temperature vector.

The same reasoning can be used to obtain the matrix which describes the flow-reversed process. Because the exchangers A and B are assumed to be flow reversible, the reversed process is described by the product of the same matrices in reversed order

$$\hat{M} = \begin{vmatrix} 1-P_B & P_B & 0 \\ RP_B & 1-RP_B & 0 \\ 0 & 0 & 1 \end{vmatrix} \begin{vmatrix} 1-P_A & 0 & P_A \\ 0 & 1 & 0 \\ RP_A & 0 & 1-RP_A \end{vmatrix}$$

$$= \begin{vmatrix} (1-P_A)(1-P_B) & P_B & P_A(1-P_B) \\ (1-P_A)RP_B & 1-RP_B & RP_AP_B \\ RP_A & 0 & 1-RP_A \end{vmatrix} \quad (10)$$

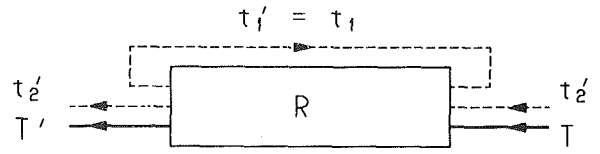

Fig. 6 Effect of a reduction operation on a three-inlet-stream, three-outlet stream exchanger.

From these expressions, equation (3) can be easily verified, which proves that even though the combined exchanger did not satisfy the naive flow-reversibility criterion discussed in the Introduction, it actually does satisfy equation (3), which is the correct generalization of the statement of flow reversibility to complex heat exchangers. In order words, flow-reversibility is the ability to predict the thermal behavior after the flows are reversed, from the knowledge of the direct process. The prediction is formulated mathematically through equation (3) and, as long as this relation is satisfied, we claim that flow reversibility holds.

4 Two Theorems on Flow Reversibility

The proof of equation (3) hinges on two theorems that are stated here and proved in the Appendix.

Theorem I: Flow-reversibility is preserved by concatenation, i.e., if A and B are two exchangers satisfying equation (3) and having matched flowrates, the exchanger described by the matrix $M = M_A M_B$ and obtained using the outlet streams of B as inlet streams for A (see Fig. 5) also satisfies equation (3).

Theorem II: The operation of reduction preserves flow-reversibility: if equation (3) holds for a given process, it also holds for the reduced process in which a bypass is established between one of the outlet streams of the original process and a matching inlet stream (see Fig. 6). The theorems just mentioned also cover the cases of partial and mixed concatenation. The first one corresponds to the case in which only some of the outlet streams of B are inlet to A, whereas the remaining ones do not participate in the A heat exchange process. Such "spectators" can be incorporated into the matrix M_A by expanding it with the addition of appropriate rows and columns as was already done in equation (9) for the tube fluid stream number 1 (see Fig. 2(*b*)). This addition does not alter the reversibility property of the A process and, therefore, the theorem remains valid. Spectators can also be added to B if part of the inlet streams of A is not present in the B outlet. We have also seen this happen in the example just quoted.

Mixed concatenation occurs when some outlet streams of B are inlet to A and, simultaneously, some outlet streams of A are inlet to B. In such case, we proceed in two stages: in the first one we concatenate the outlet streams of B with the corresponding inlet streams of A, and thus prove reversibility for the partially concatenated assembly. After the two exchangers have thus become a single entity, the second part of the concatenation is just a simple reduction, which is covered by theorem II.

5 Proof of Flow Reversibility

With the foregoing elements, we can now prove the following proposition: any heat exchanger, whether basic or complex, formed by an arbitrary combination of a finite number of divider/mixers and flow-reversible heat exchangers, is also flow-reversible. The proof starts from the trivially flow-reversible exchanger constituted by just the inlet streams, with no heat exchange, mix, or division whatsoever, which is described by a matrix M that is equal to the unit matrix. Proceeding along the inlet streams, the various constituting parts of the exchanger are found. As each one is

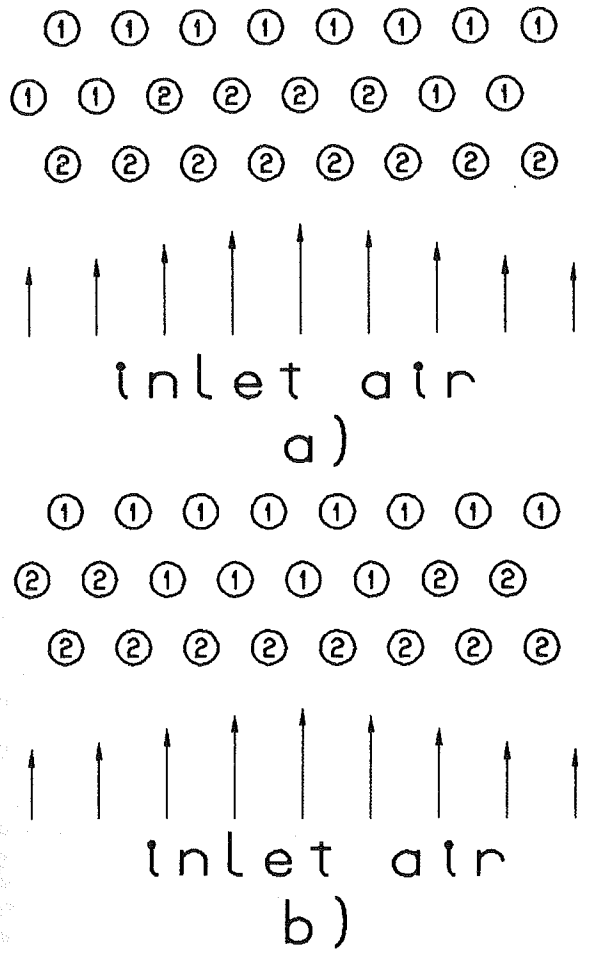

Fig. 7 Cross section of a three-row tube bundle used for a two-pass air cooler. The pass assignment for each tube is indicated inside the tube section. Two possible configurations are shown in (*a*) and (*b*). The arrows indicate an air velocity distribution peaked at the central part of the exchanger.

encountered, it is incorporated into M by matrix multiplication, with the provision that whenever an inlet stream of a new element is not already present as an outlet stream of M, M is first expanded to incorporate it as a spectator. After all the outlet streams of the exchanger have been reached, the only task left is to perform the reduction of all the inlet lines that were introduced as spectators with the matching lines that the process has generated, thus reconstructing the correct topology for the exchanger. Throughout this operation flow reversibility is preserved, and therefore, the property is valid for the whole exchanger.

The proof just presented has the apparent limitation of being valid only for exchangers constructed by assembling a finite number of flow reversible constituents. The elements for such a construction are obtained by recursively subdividing a given exchanger into constituent parts until the flow reversibility of each component follows from geometric symmetry considerations. The most elementary of such parts or "cells" are flat conducting surface elements in thermal contact with the two fluids. However, the decomposition of the exchanger into trivially symmetrical parts need not always be carried out to this level, because, as we have discussed in the example *b* of section III, more elaborate constituents such as pipe elements exchanging heat in crossflow (or cocurrent flow, or counterflow, or flow at any other angle), are also geometrically symmetric. Therefore, we claim that any exchanger of physical interest, no matter how complex, can be approximated to any desired degree of accuracy by such a construction, provided a sufficiently large number of elements is chosen. The validity of the flow-reversibility property is therefore only limited by the conditions of validity of the matrix formalism used, which preclude change of phase, heat losses, and temperature dependence of heat capacities and heat transfer coefficients.

6 Air Cooler Example

We present here an example of the application of the flow-reversibility property to the domain of air coolers. Suppose that we have a three-row tube bundle with eight tubes per row (any multiple of four will do equally well). To make the example more realistic, assume that the inlet and outlet air velocity distribution is not uniform, but is instead peaked at the central part of the exchanger. We do, however, assume the same velocity distribution for the inlet and outlet air. With these elements, we want to construct a two-pass crossflow air cooler and we wonder which one of the two configurations shown in Figs. 7(*a*) and 7(*b*) has a higher effectiveness. We might be tempted to make a choice on the basis of qualitative physical arguments, or even perform and compare two finite element computer calculations. However, we observe that reversing the flow directions of the inlet air and the tube fluid (which interchanges 1's and 2's in Fig. 7(*a*)), we obtain the arrangement of Fig. 7(*b*). Thus the two configurations are the flow reversed of each other, and therefore, they have exactly the same tube fluid effectiveness, P. Strictly speaking, in order to reach this conclusion we should have a basic heat exchanger, i.e., we should mix thoroughly the outlet air. The conclusion, of course, is still true, even if we do not mix the outlet air, because the tube fluid outlet temperature is not influenced by what happens to the outlet air.

In the preceding example, we have not even attempted to calculate the effectiveness, which is no simple task because the configuration is complicated (the middle tube row is shared by two different passes), and the velocity distribution is not uniform. In spite of that, we have been able to predict that two such configurations, which do not look equal to each other, are actually thermally equivalent. This is precisely what is meant by a symmetry property.

If, however, in the foregoing example the inlet and outlet air velocity distributions are not exactly the same, the exchangers of Figs. 7(*a*) and 7(*b*) are no longer precisely the flow reversed of each other, and the corresponding effectiveness need not be exactly equal. Multiple examples of applications of the flow-reversibility property similar to the one discussed can be found in the practice of heat exchanger design.

7 TEMA G Split Flow Shell-and-Tube Exchanger

In order to exhibit an application of the flow-reversibility symmetry to an exchanger (or, actually, a fraction thereof) described by a truly rectangular matrix, we discuss the split-flow shell-and-tube exchanger shown in Fig. 8(*a*) (TEMA G shell). Figure 8(*b*) shows a block decomposition of the exchanger, in which blocks labeled A represent a heat exchange process between shell and tube fluids which, if the number of baffles is sufficiently large, can be described by counterflow exchange. Conversely, in the same approximation, B can be described by pure cocurrent flow exchange. Alternatively, both A and B may be split into several crossflow exchangers, each one describing a section between two transverse baffles. For our present purpose of illustrating flow reversibility, both approaches are equally valid, and for simplicity, we stick to the first one, which corresponds to the limit of infinitely many baffles.

We begin by finding the 3×2 matrix M_L which describes the lower half of the exchanger, shown in Fig. 9(*a*), such that

$$\begin{vmatrix} t'_1 \\ t'_2 \\ T'_L \end{vmatrix} = M_L \begin{vmatrix} t \\ T_L \end{vmatrix} \tag{11}$$

For the A and B blocks, we define as usual the matrices M_A and M_B through the relations

$$\begin{vmatrix} t'_1 \\ T''_L \end{vmatrix} = M_A \begin{vmatrix} t_A \\ T_L \end{vmatrix}, \quad \begin{vmatrix} t'_2 \\ T'_L \end{vmatrix} = M_B \begin{vmatrix} t_B \\ T''_L \end{vmatrix} \tag{12}$$

Hence, we can write

$$\begin{vmatrix} t'_1 \\ t'_2 \\ T'_L \end{vmatrix} = \left|\begin{array}{c|cc} 1 & 0 & 0 \\ \hline 0 & & \\ 0 & \multicolumn{2}{c}{M_B} \end{array}\right| \begin{vmatrix} t'_1 \\ t_B \\ T''_L \end{vmatrix}$$

$$= \left|\begin{array}{c|cc} 1 & 0 & 0 \\ \hline 0 & & \\ 0 & \multicolumn{2}{c}{M_B} \end{array}\right| \begin{vmatrix} 1 & 0 & 0 \\ 0 & 0 & 1 \\ 0 & 1 & 0 \end{vmatrix} \begin{vmatrix} t'_1 \\ T''_L \\ t_B \end{vmatrix}$$

$$= \left|\begin{array}{c|cc} 1 & 0 & 0 \\ \hline 0 & & \\ 0 & \multicolumn{2}{c}{M_B} \end{array}\right| \begin{vmatrix} 1 & 0 & 0 \\ 0 & 0 & 1 \\ 0 & 1 & 0 \end{vmatrix} \left|\begin{array}{cc|c} & & 0 \\ \multicolumn{2}{c|}{M_A} & 0 \\ \hline 0 & 0 & 1 \end{array}\right| \begin{vmatrix} 1 & 0 \\ 0 & 1 \\ 1 & 0 \end{vmatrix} \begin{vmatrix} t \\ T_L \end{vmatrix} \tag{13}$$

and, comparing with equation (11), we obtain

$$M_L = \begin{vmatrix} M_{A_{11}} & & M_{A_{12}} & \\ M_{A_{21}} & M_{B_{12}} + M_{B_{11}} & M_{B_{12}} & M_{A_{22}} \\ M_{A_{21}} & M_{B_{21}} + M_{B_{11}} & M_{B_{22}} & M_{A_{22}} \end{vmatrix} \tag{14}$$

The expressions for M_A and M_B are obtained by solving the elementary counterflow and cocurrent flow differential equations, respectively, which give for $R_A \neq 1$

$$M_A = \frac{1}{R_A \alpha - 1} \begin{vmatrix} (R_A - 1)\alpha & \alpha - 1 \\ R_A(\alpha - 1) & R_A - 1 \end{vmatrix} \tag{15}$$

and for $R_A \neq 1$

$$M_A = \frac{1}{1 + N_{tu_A}} \begin{vmatrix} 1 & N_{tu_A} \\ N_{tu_A} & 1 \end{vmatrix} \tag{16}$$

whereas

$$M_B = \frac{1}{1 + R_B} \begin{vmatrix} R_B + \beta & 1 - \beta \\ R_B(1 - \beta) & 1 + R_B\beta \end{vmatrix} \tag{17}$$

with

$$\alpha = \exp[(R_A - 1)\, N_{tu_A}]$$
$$\beta = \exp[-(R_B + 1)\, N_{tu_B}] \tag{18}$$

From the foregoing expressions, M_L can be immediately calculated. It should be kept in mind, however, that the values of R_A, R_B, N_{tu_A}, and N_{tu_B} are related to R and N_{tu} for the whole exchanger through the relations

$$R_A = R_B = R/2$$
$$N_{tu_A} = N_{tu_B} = N_{tu}/2 \tag{19}$$

For M_L, one obtains for $R_A = R_B \neq 1$

$$M_L = \frac{1}{(\alpha R_A - 1)(R_A + 1)} \begin{vmatrix} (R_A{}^2 - 1)\alpha & (R_A + 1)(\alpha - 1) \\ R_A(\alpha - 1)(1 - \beta) + (R_A + \beta)(R_A\alpha - 1) & (1 - \beta)(R_A - 1) \\ R_A(\alpha - 1)(1 + R_A\beta) + R_A(1 - \beta)(R_A\alpha - 1) & (1 + R_A\beta)(R_A - 1) \end{vmatrix} \tag{20}$$

and for $R_A = R_B = 1$.

$$M_L = \frac{1}{1 + N_{tu_A}} \begin{vmatrix} 1 & N_{tu_A} \\ N_{tu_A} + (1 + \beta)/2 & (1 - \beta)/2 \\ N_{tu_A} + (1 - \beta)/2 & (1 + \beta)/2 \end{vmatrix} \tag{21}$$

The following step is to calculate the 2×3 matrix M_U, which describes the upper half of the exchanger, shown in Fig. 9(*b*), for which we write

$$\begin{vmatrix} t' \\ T'_U \end{vmatrix} = M_U \begin{vmatrix} t_1 \\ t_2 \\ T_U \end{vmatrix} \tag{22}$$

We observe, however, that this upper half can be obtained by applying the flow-reversal transformation to the lower half, and therefore have

$$M_U = \hat{M}_L = \begin{vmatrix} 1/wc & 0 \\ 0 & 1/WC \end{vmatrix} \begin{vmatrix} M_{L_{11}} & M_{L_{21}} & M_{L_{31}} \\ M_{L_{12}} & M_{L_{22}} & M_{L_{32}} \end{vmatrix} \begin{vmatrix} wc/2 & 0 & 0 \\ 0 & wc/2 & 0 \\ 0 & 0 & WC \end{vmatrix}$$

$$= \begin{vmatrix} M_{L_{11}}/2 & M_{L_{21}}/2 & M_{L_{31}}/R \\ RM_{L_{12}}/2 & RM_{L_{22}}/2 & M_{L_{32}} \end{vmatrix} \tag{23}$$

Thus the flow-reversibility property allows us to calculate M_U from the previously derived expression for M_L.

Having proceeded so far, we might as well complete the calculation of the effectiveness of the split-flow exchanger. The upper and lower halves can be combined by matrix multiplication using the trick already employed in section 3, example (*c*), of incorporating rows and columns with vanishing elements except for elements equal to one along the matrix diagonal, whenever spectators are present. In addition, when the order in which two temperatures appear in a given temperature vector is not the one for which a matrix has been constructed, the vector components can be rearranged by multiplication by an adequate "rearrangement matrix." Such a matrix is just the unit matrix in which two or more rows have been permuted. In this fashion, we can write

$$\begin{vmatrix} t' \\ T'_U \\ T'_L \end{vmatrix} = \left|\begin{array}{ccc|c} & M_U & & 0 \\ & & & 0 \\ \hline 0 & 0 & 0 & 1 \end{array}\right| \begin{vmatrix} 1 & 0 & 0 & 0 \\ 0 & 1 & 0 & 0 \\ 0 & 0 & 0 & 1 \\ 0 & 0 & 1 & 0 \end{vmatrix} \left|\begin{array}{cc|c} & & 0 \\ \multicolumn{2}{c|}{M_L} & 0 \\ & & 0 \\ \hline 0 & 0 & 1 \end{array}\right| \begin{vmatrix} t \\ T_L \\ T_U \end{vmatrix} = M \begin{vmatrix} t \\ T_L \\ T_U \end{vmatrix} \tag{24}$$

and reduction in the $T'_U - T_L$ pair gives

$$\begin{vmatrix} t' \\ T'_L \end{vmatrix} = M_R \begin{vmatrix} t \\ T_U \end{vmatrix} \tag{25}$$

where

$$M_{R_{12}} = P = M_{13} + M_{12}M_{23}/(1 - M_{22}) \tag{26}$$

The effectiveness of the exchanger can therefore be written in terms of the matrix elements of M which, through equations (23) and (24), are expressed in terms of the matrix elements of M_L, namely

$$M_{12} = (M_{L_{11}}\ M_{L_{12}} + M_{L_{21}}\ M_{L_{22}})/2$$
$$M_{13} = M_{L_{31}}/R$$
$$M_{22} = R(M_{L_{12}}{}^2 + M_{L_{22}}{}^2)/2 \tag{27}$$
$$M_{23} = M_{32} = M_{L_{32}}$$

If we want to analyze the effect of inverting the tube flow, we need only perform instead the reduction of the matrix M in the $T'_L - T_U$ pair, which leads to the result

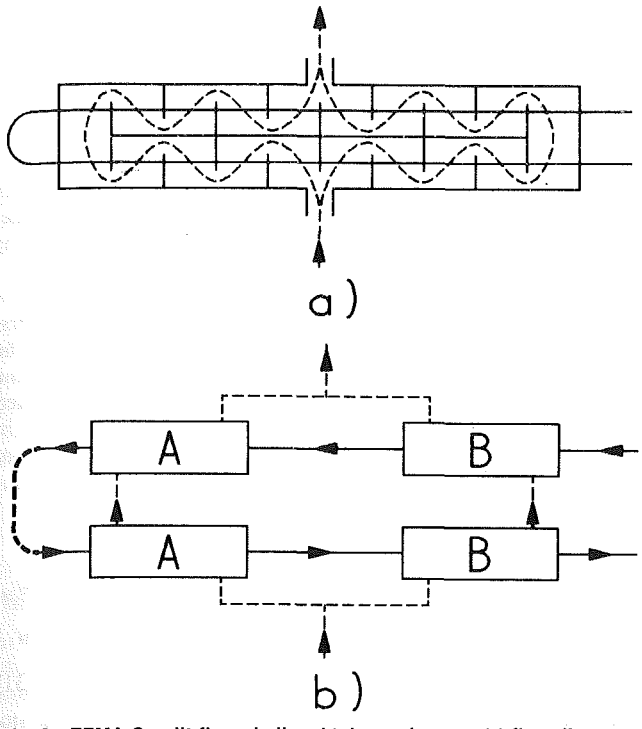

Fig. 8 TEMA G split flow shell-and-tube exchanger: (*a*) flow diagram, (*b*) block decomposition

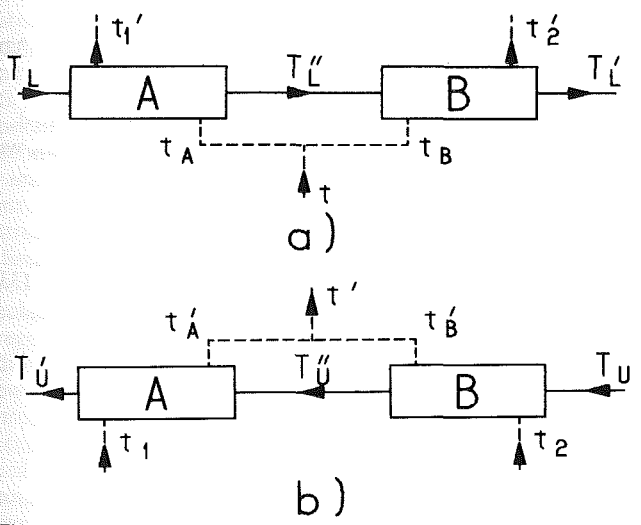

Fig. 9 (*a*) Lower half of the exchanger of Fig. 8 and (*b*) upper half of the same exchanger

$$P = (M_{L_{11}}\ M_{L_{12}} + M_{L_{21}}\ M_{L_{22}})/2 + M_{L_{31}}\ M_{L_{32}}/R \quad (28)$$

The corresponding LMTD correction factors are plotted in Fig. 10, which shows that, as expected, the split-flow exchanger has a much higher correction factor if the tube inlet is on the shell outlet side than if it is on the shell inlet side. Our solution for the former case coincides with that obtained by Schindler and Bates [5] under the same assumptions, whereas we know of no published solution for the other configuration, which is obtained from the previous one by inversion of the direction of one of the fluids.

8 Conclusions

The concept of flow reversibility discussed in the present paper has two basic appeals. In the first place, it is a labor saving device. We need only calculate one half of all possible nongeometrically symmetric configurations, and the other

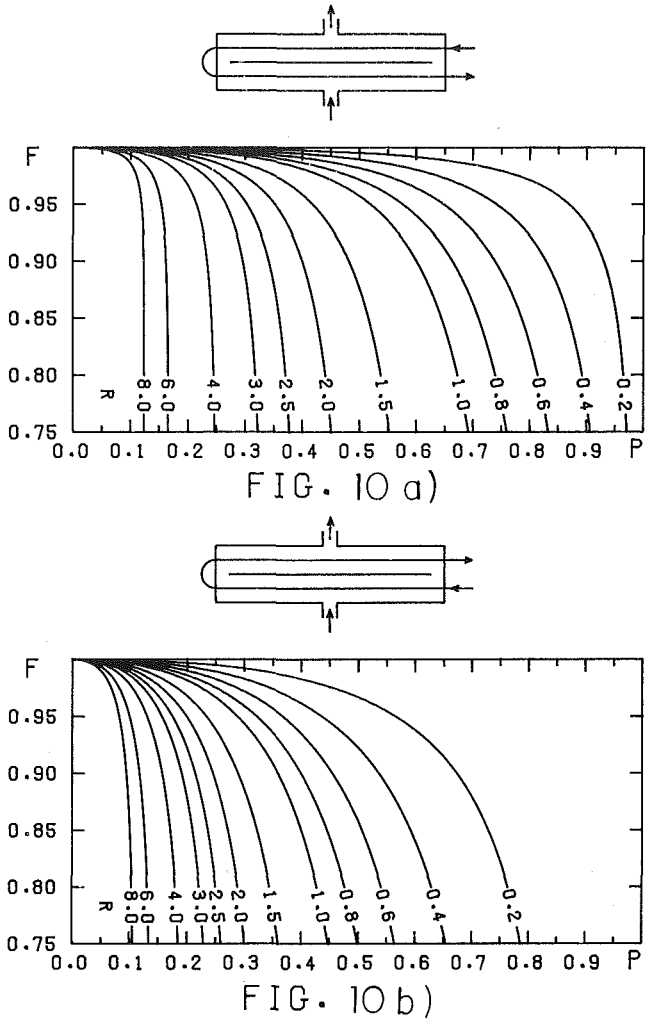

Fig. 10 LMTD correction factors for TEMA G split flow shell-and-tube exchanger for large number of baffles with (*a*) tube inlet on shell outlet side and (*b*) tube inlet on shell inlet side

half is taken care of by flow reversibility. This was illustrated by the example of the split-flow exchanger of section 7, in which there is no need to calculate the matrix which describes the upper half of the exchanger, because after the flow-reversal operation is performed, the upper half coincides with the lower half. Of course, it may be argued that if we are able to calculate the lower half in the first place, we can also calculate the upper one, and that is quite right: flow-reversibility does not help solving otherwise unsolvable problems. It just allows one to solve half as many of the (nongeometrically symmetric) solvable ones. Moreover, in the case of geometrically symmetric exchangers, for which flow reversibility appears as a trivial statement, we still learn something, namely, that for such cases $\hat{M} = D^{-1}\tilde{M}D' = M$. This relation implies constraints on the matrix elements of M which may facilitate their determination for complex exchangers.

The second and possibly more important aspect of the flow-reversibility concept is that it is a symmetry property which follows from the basic properties of linearity, heat conservation, and translational invariance in the temperature variable of the heat transfer equations. Therefore, it applies to all exchangers for which these properties are valid. Within this restricted domain, which rules out change of phase, heat losses, and temperature dependence of the heat transfer coefficients and heat capacities, this symmetry property states that two physically different processes, which are related through a well-defined transformation, are basically ther-

mally equivalent. We thus conclude, for instance, that the coincidence pointed out by Gardner and Taborek [2] between the effectivenesses of the exchangers of Figs. 1(*a*) and 1(*b*) is neither a fortunate accident, nor the consequence of some particular assumption of the model used, but that it will hold true in any other model, no matter how elaborate, within the domain of validity stated above. Thus, we are able to make predictions for cases which may be too complicated to solve analytically, and even too costly to solve numerically and that involve exchangers with arbitrary numbers of inlet and outlet streams. In other words, through the flow-reversibility analysis we obtain, in addition to a labor saving scheme, a new insight into heat transfer processes based on a hitherto overlooked symmetry property of significant predictive capability.

7 Acknowledgment

Illuminating discussions with Professor Guillermo Cordero are gratefully acknowledged.

References

1 Kern, D. Q., *Process Heat Transfer*, McGraw-Hill, 1950, pp. 140–145.[2]
2 Gardner, K., and Taborek, J., "Mean Temperature Difference: A Reappraisal," *AIChE Journal*, Vol. 23, 1977, pp. 777–786.
3 Pignotti, A., "Matrix Formalism for Complex Heat Exchangers," ASME JOURNAL OF HEAT TRANSFER, Vol. 106, No. 2, pp. 352–360.
4 Domingos, J. D., "Analysis of Complex Assemblies of Heat Exchangers," *Int. J. Heat Mass Transfer*, Vol. 12, 1969, pp. 537–548.
5 Schindler, D. L., and Bates, H. T., "True Temperature Difference in a 1-2 Divided-Flow Heat Exchanger," *Chemical Engineering Progress Symposium Series*, No. 30, Vol. 56, pp. 203–206.

APPENDIX

Theorem I: Let A and B be two flow-reversible heat exchangers, such that outlet streams of B are inlet streams of A. The composite exchanger described by the matrix $M = M_A\, M_B$ is also flow reversible. Proof: For the reversed process we have

$$\hat{M} = \hat{M}_B\, \hat{M}_A \tag{29}$$

Because both A and B are reversible, using equation (3)

$$\tilde{M} = D^{-1}\tilde{M}_B D'' D''^{-1}\tilde{M}_A D' = D^{-1}\tilde{M}_B\tilde{M}_A D' = D^{-1}\tilde{M}D' \tag{30}$$

which is the desired result.

Theorem II: Let R be a flow-reversible heat exchanger such that, for one of the fluids, the flow rates of an inlet and outlet stream coincide. The reduced exchanger obtained by bypassing those two streams is also flow reversible.

For clarity, we are going to present the proof of $n = n' = 2$, $N = N' = 1$, with the reduction performed on the first inlet and outlet shell streams, such as shown in Fig. 6. The generalization to other cases is straightforward. We assume $M_{11} \neq 1$ because otherwise the shell stream 1 is decoupled from the rest of the exchanger and the reduction consists in eliminating the first row and column from the matrix M, from which flow reversibility of the reduced process follows immediately.

For the direct process, the reduced matrix is [3]

$$M_R = \begin{vmatrix} M_{22}+M_{21}\ M_{12}/(1-M_{11}) & M_{23}+M_{21}\ M_{13}/(1-M_{11}) \\ M_{32}+M_{31}\ M_{12}/(1-M_{11}) & M_{33}+M_{31}\ M_{13}/(1-M_{11} \end{vmatrix} \tag{31}$$

Since the direct process was assumed to be flow reversible, the full matrix for the reversed process can be obtained from equation (3) as follows.

$$\hat{M} = \begin{vmatrix} M_{11} & M_{21}w_2/w_1 & M_{31}WC/w_1c \\ M_{12}w_1/w_2 & M_{22} & M_{32}WC/w_2c \\ M_{13}w_1c/WC & M_{23}w_2c/WC & M_{33} \end{vmatrix} \tag{32}$$

where the relations $w_1 = w'_1$ and $w_2 = w'_2$ have been used.

If we now perform the reduction on the reverse process, we obtain

$$(\hat{M})_R = \begin{vmatrix} M_{22}+M_{12}\ M_{21}/(1-M_{11}) & [M_{32}+M_{12}\ M_{31}/(1-M_{11})]WC/w_2c \\ [M_{23}+M_{21}\ M_{13}/(1-M_{11})]w_2c/WC & M_{33}+M_{31}\ M_{13}/(1-M_{11}) \end{vmatrix} \tag{33}$$

From equations (3), (31), and (33), the relation

$$(\hat{M}_R) = (\hat{M})_R$$

is verified, which completes the proof.

[2]The cases of Figs. 1(*a*) and 1(*b*) are discussed in this reference in addition to other references. Because complete transverse mixing of the shell fluid is assumed, the same results apply to the arrangements of Figs. 1(*c*) and 1(*d*).

Recirculation of Purged Flow in an Adiabatic Counterflow Rotary Dehumidifier

J. J. Jurinak
Assoc. Mem. ASME

J. W. Mitchell
Mem. ASME

University of Wisconsin
Solar Energy Laboratory,
Madison, Wis. 53706

The average process stream outlet humidity ratio of an adiabatic counterflow dehumidifier can be lowered if a portion of the process outlet stream is purged from the bulk flow. The purged stream can be recirculated and introduced at the inlet of the regenerating period. In this paper, the performance of such a purged counterflow dehumidifier is studied. Two purge geometries that result in a spatially nonuniform inlet condition in the regenerating period are considered. Wave diagram solutions for the limiting case of infinite heat and mass transfer coefficients are used to qualitatively predict the behavior of the purged dehumidifier. A finite difference solution is used to verify the general trends of the approximate wave diagram solutions. The effect of the recirculated purge on the process stream outlet states of high performance silica gel dehumidifiers with low and high thermal capacitance matrices operated at nearly optimal rotational speeds is evaluated.

Introduction

Counterflow rotary dehumidifiers are used in industrial air driers [1] and in energy-efficient, open-cycle desiccant air conditioners [2–5]. Considerable effort has been made to optimize the dehumidifier performance [4–8].

The performance of the adiabatic rotary dehumidifier can be improved by purging high-temperature, wet air from the dehumidified air stream, as shown schematically in Fig. 1. In steady-state operation, the air streams emerging from the dehumidifier have circumferential distributions of temperature and humidity ratio [9–11]. The air that exits in the first 10 to 20 percent of the rotational arc of the process period is considerably hotter and wetter than the rest of the dehumidified air stream. If this hot and wet air is physically removed from the process stream before mixing occurs, the mean temperature and humidity ratio of the process outlet air stream can be lowered. The purged air stream may be discarded, but since it is at high temperature, it can be recirculated and used in the regenerating period. The recirculated purge stream may either be mixed with the bulk regenerating stream or used to produce a locally nonuniform distribution in the regenerating period inlet. Recirculation of purged flow can both increase the dehumidification in the process stream and decrease the energy input to the regenerating stream. In addition, if the regenerating stream is heated by an open flame, the purge section can prevent contamination of the process air stream with combustion byproducts. The purged rotary dehumidifier has been used in prototype, open-cycle, desiccant air-conditioning systems developed by the Garrett Corporation and the Institute of Gas Technology [4, 5]. The effect of purging on open-cycle desiccant cooling system performance has been studied [13].

Adiabatic counterflow dehumidifiers with purged air recirculation and a spatially nonuniform regenerating stream inlet state are analyzed in this paper. Only balanced (equal v_{jk}) and symmetric (equal θ_j) dehumidifiers are considered. The limiting case of a dehumidifier with infinite heat and mass transfer coefficients is studied first, using an approximate analogy with heat transfer regenerators. This analysis qualitatively shows the effect of purge recirculation on the dehumidifier performance. A finite difference model of the dehumidifier is then used to determine the outlet and purge states of a counterflow silica gel dehumidifier with finite transfer coefficients. Typical silica gel properties are used, and the heat and mass transfer rates are assumed to be limited by convection. Both low and high thermal capacitance matrices are modeled, corresponding to matrices with small and large proportions of nonadsorbing structural materials. The numerical results are used to verify the trends suggested by the analogy analysis and to indicate the improvement in dehumidification and reduction in energy input obtained with recirculated purge in comparison to an unpurged counterflow dehumidifier.

The Purged Dehumidifier Model

In the recirculation pattern illustrated in Fig. 1, flow from the outlet of subperiod 1 of period 1 is recirculated to the inlet of subperiod 1 of period 2 and is referred to as the preconditioning purge or recirculation pattern. A postconditioning purge geometry, with recirculation to subperiod 2 of the regenerating period, is also considered. The fractional subperiod boundaries are described by $\beta_{jk} = \phi_{jk}/\Phi_j$. For example, $\beta_{11} = 0.10$ implies that the purge section occupies 10 percent of the total arc of period 1.

In this study, the following assumptions concerning the flow and transfer processes in the counterflow rotary dehumidifier are made: (*i*) the flow in each subperiod is at constant pressure and velocity; (*ii*) the flow at each subperiod inlet is at uniform temperature and humidity ratio; (*iii*) there is negligible axial diffusion of heat or moisture in the matrix and air; (*iv*) the thermal and moisture capacitances of the air in the matrix interstices are negligible compared to the matrix capacitances; (*v*) there is no transfer flux coupling by thermo-

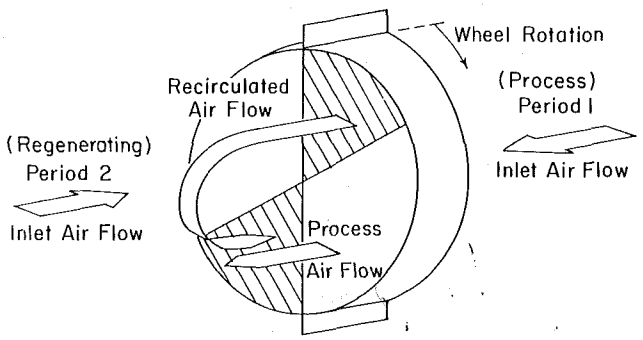

Fig. 1 Counterflow dehumidifier with preconditioning recirculation of purged flow

Contributed by the Heat Transfer Division for publication in the JOURNAL OF HEAT TRANSFER. Manuscript received by the Heat Transfer Division August 30, 1982.

diffusion or Dufor processes; (*vi*) the transfer processes between the air and the matrix can be described by composite transfer coefficients.

The conservation equations written with respect to a coordinate system moving with the matrix are [9, 10]:

Mass

$$\frac{\partial w}{\partial x'} + \beta_{jk}\theta_j'(\mu\kappa)_{jk}\frac{\partial W}{\partial \theta'} = 0 \qquad j,k = 1,2 \qquad (1)$$

Energy

$$\frac{\partial i}{\partial x'} + \beta_{jk}\theta_j'(\mu\kappa)_{jk}\frac{\partial I}{\partial \theta'} = 0$$

The transfer rate equations for mass and heat are

Mass

$$\frac{\partial w}{\partial x'} = \Lambda_{jk}(w_m - w_f) \qquad j,k = 1,2 \qquad (2)$$

Energy

$$\frac{\partial i}{\partial x'} = \Lambda_{jk}(\mathrm{Le}_o c_f(t_m - t_f) + i_{wv}(w_m - w_f))$$

Since the coordinate system is fixed with respect to the matrix, the rotary nature of the dehumidifier is modeled using periodic boundary conditions. The counterflow geometry is reflected by a reversal in flow direction at the beginning of each period. The recirculation condition is imposed by taking the spatial average of the outlet temperature and humidity ratio in the purge section to be the inlet condition for the appropriate subperiod in the regeneration period. The conservation of mass requires that $\mu\kappa$, the ratio of matrix rotational mass flow rate to air flow rate, in the two purge subperiods be equal (e.g., $\mu\kappa_{11} = \mu\kappa_{21}$ for the preconditioning purge).

Equilibrium Analysis of the Purged Dehumidifier

If the transfer coefficients in equations (2) are infinite, then equations (1) describe equilibrium changes in the local air and matrix moisture and enthalpy. Analysis of the equilibrium system provides both an intuitive understanding of the dehumidifier operation and an upper bound to dehumidifier performance.

Banks and Maclaine-cross have shown that by proper definition of combined heat and mass transfer potentials, F_1 and F_2, and combined capacitance ratios, γ_1 and γ_2, equations (1) can be transformed to

$$\frac{\partial F_i}{\partial x'} + \theta_j'\beta_{jk}C_{i,jk}\frac{\partial F_i}{\partial \theta'} = 0 \qquad \begin{matrix} i = 1,2 \\ j = 1,2 \end{matrix} \qquad (3)$$

where $C_{i,jk} = \mu\kappa_{jk}\gamma_i$ [9, 14–16]. The combined potentials, F_1 and F_2, and the combined capacitance ratios, γ_1 and γ_2, are functions of the equilibrium thermal and sorption properties of the moist air-adsorbent system. Equations (3) are first-order kinematic wave equations that are exactly similar to the wave equation that describes the equilibrium heat transfer in a rotary sensible regenerator [12, 14]. Wave diagrams drawn on an $x' - \theta'$ coordinate system can be used to solve wave equations of this form [12, 14, 15]. The F_i wave fronts propagate with velocities $V_{i,jk} = 1/(\theta_j'\beta_{jk}C_{i,jk})$. Since for all desiccants, $\gamma_1 < \gamma_2$, an F_1 change wave traverses the matrix more rapidly than an F_2 wave. If the γ_i are constant, F_i changes propagate as sharp discontinuities through the matrix, represented by a straight line on the wave diagram. For most sorbents, the γ_i are not constant, so that the velocity of the F_i wave fronts vary with matrix state and the fronts can change shape. A broadening wave front is represented by a fan of lines on the wave diagram. Finite transfer coefficients tend to broaden or smear the wave fronts [9, 12, 14, 15].

Wave diagrams for F_1 and F_2 have previously been used to solve equations (3) for dehumidifiers with uniform [9, 14, 15] and spatially nonuniform [18, 19] air inlet states. The qualitative description of unpurged dehumidifier operation provided by this solution technique has been verified by comparison with the results of finite difference models [9, 13–15]. The equilibrium F_i wave diagram solutions for the purged dehumidifier are given here, and are later substantiated and refined by presentation of the results of a finite difference model.

It is assumed that the desiccant properties of the balanced and symmetric dehumidifier are constant. Therefore, $\beta_{jk}C_{i,jk} = C_{i,j}$, the wave velocities in each subperiod are equal, $V_{i,jk} = V_{i,j} = V_i$, and F_i lines on wave diagrams do not change slope at subperiod boundaries. For convenience in discussion, the subscripts on β_{11}, the fractional purge angle, will be dropped.

The hot and wet air in the initial portion of the dehumidified air stream is due to an F_1 wave at the

Nomenclature

c_f = moist air thermal capacitance [energy/(dry mass-temperature)]
c_m = matrix thermal capacitance [energy/(dry desiccant mass-temperature)]
$C_{i,j}$ = $(\mu\kappa)_j\gamma_i$ analogous rotational capacity rate of period j [dimensionless].
$C_{i,jk}$ = $(\mu\kappa)_{jk}\gamma_i$ subperiod k of period j analogous rotational capacity rate ratio for the F_i potential [dimensionless]
F_i = ith combined heat and mass transfer potential [dimensions arbitrary]
i = moist air enthalpy [energy/dry mass]
i_{wv} = water vapor enthalpy [energy/mass]
I = matrix enthalpy [energy/dry mass]
$J_{t,j}$ = $4h/(\rho' d_h c_f)$, where h is the heat transfer coefficient, ρ' is the dry fluid density, d_h is the hydraulic diameter. The lumped matrix-fluid transfer coefficient per unit mass of fluid [time^{-1}]
$J_{w,j}$ = $4h_w/(\rho' d_h)$, where h_w is the mass transfer coefficient, ρ' is the dry fluid density, and d_h is the hydraulic diameter. The lumped matrix-fluid mass transfer coefficient per unit mass of fluid [time^{-1}]
L = axial flow length through the matrix [length]
Le_o = $J_{t,j}/J_{w,j}$, overall Lewis number [dimensionless]
$t_{jk,l}$ = temperature at face l of subperiod k of period j
v_j = air velocity in period j [length/time]
v_{jk} = air velocity in subperiod k of period j [length/time]
$V_{i,jk}$ = $1/\theta_j'\beta_{jk}C_{i,jk}$, velocity of the F_i change wave in subperiod k of period j [dimensionless]
w = moist air humidity ratio [dimensionless]
$w_{j,l}$ = spatial average humidity ratio at face l of period j [dimensionless]
$w_{jk,l}$ = spatial average humidity ratio at face l of subperiod k of period j [dimensionless]
W = matrix water content [dimensionless]
x = axial displacement through matrix measured from period entrance [length]
x' = x/L, dimensionless axial position [dimensionless]
β = ϕ_{11}/Φ_1, fractional purge angle
β_{jk} = ϕ_{jk}/Φ_j, fraction of period j occupied by subperiod k [dimensionless]

regenerating state (F_{1r}) [9, 13-15]. Therefore, there are two solutions to consider for each purge geometry, corresponding to whether or not the F_{1r} wave passes through the matrix within the arc of the purge section. If $\beta < C_{1,1}$ (i.e., $C_{1,11} < 1$), the F_{1r} wave is not completely purged; conversely, if $\beta \geq C_{1,1}$ ($C_{1,11} \geq 1$), the F_{1r} wave is entirely within the purge section. In each case, it is assumed that the purged air is fully mixed prior to introduction at the inlet of a subperiod in period 2. Thus, the distribution of the purged outlet state is destroyed, but the mean purge state creates a nonuniform inlet condition in the regenerating period. The F_1 and F_2 wave diagrams for these four cases are illustrated in Figs. 2-5. Figures 2 and 4 are for $\beta \leq C_{1,1}$, corresponding to an incomplete purge of the regeneration F_1 state, while Figs. 3 and 5 illustrate $\beta > C_{1,1}$ cases. In all of these diagrams, p is the process inlet state, pr is the purge state, r is the regenerating state, and o is the process outlet state.

Figure 2 shows the wave diagrams for the preconditioning recirculation pattern with $\beta \leq C_{1,1}$. The purge state is the regenerating inlet state. The mean period 1 outlet state and the θ' distribution of period 1 outlet states are unaffected by the purge recirculation and are the same as for an unpurged dehumidifier. The preconditioning purge with $\beta \leq C_{1,1}$ shifts the process outlet state toward the period 1 intersection point, corresponding to improved dehumidification.

The F_i wave diagrams for the preconditioning recirculation with $\beta > C_{1,1}$ are shown in Fig. 3. The purge state is between the period 1 intersection point and the regenerating inlet state. The distribution and mean of the period 1 outlet states are identical to those for the preconditioning purge with $\beta \leq C_{1,1}$. The process outlet state is at the intersection point of the F_{1p} and F_{2r} lines, and maximum dehumidification is obtained.

The solution for the postconditioning recirculation pattern with $\beta \leq C_{1,1}$ is shown in Fig. 4. For constant γ_i, the F_i purge states are recycled through the matrix and are completely arbitrary. In a system with variable γ_i or finite transfer coefficients, the wave fronts smear, and the purge state, rather than being arbitrary, tends to the regenerating state. In this case, the postconditioning recirculation with $\beta \leq C_{1,1}$ results in the same distribution of period 1 outlet states as the preconditioning recirculation with $\beta \leq C_{1,1}$. Regardless of the purge state, the process outlet state is identical to that for the preconditioning purge with $\beta \leq C_{1,1}$.

The postconditioning purge with $\beta > C_{1,1}$ is illustrated in Fig. 5. The F_{2pr} state is again completely arbitrary. However, $F_{1pr} = F_{1p}$, and the matrix is uniformly at F_{1p} during period 1. If the wave fronts broaden, then $F_{2pr} = F_{2r}$, and the period 1 outlet is uniformly at the intersection point of the F_{1p} and F_{2r} characteristics. The process outlet state is at the period 1 intersection point, as it is for the preconditioning purge with $\beta > C_{1,1}$.

The equilibrium analysis of the recirculated purge dehumidifier indicates that while the θ' distribution of the period 1 outlet states is influenced by the recirculation geometry, the process outlet state ($t_{12,2}, w_{12,2}$) depends only on the magnitude of the purge angle β in relation to $C_{1,1}$. As β increases, the fraction of the flow through period 1 of the dehumidifier that goes to the process decreases. At $\beta = C_{1,1}$, just as the regenerating state F_1 is completely purged, the minimum outlet humidity ratio is obtained. For $\beta > C_{1,1}$, there is no change in process outlet state, but the useful process flow rate is decreased. This suggests that the optimum purge angle regardless of the recirculation pattern is $\beta = C_{1,1}$.

Numerical Analysis of the Purged Dehumidifier

In a dehumidifier, the transfer coefficients are finite and the γ_i are not constant. Therefore, an equilibrium analysis is only of qualitative utility, and a numerical solution of equations (1, 2) is required to fully investigate the performance of the purged dehumidifier. The finite difference solution used in this study was derived from a method developed by Maclaine-cross [9] that was previously used by the authors [6, 13, 17]. The difference equations are second order. Solutions are obtained for three grid sizes, and the results are quadratically extrapolated to zero grid size. The extrapolated solution is fourth order [9]. For the results given here, the errors in the system moisture and energy balances are less than 0.01 percent of the changes in humidity ratio or enthalpy from period inlet to outlet.

A symmetric and balanced counterflow silica gel dehumidifier is studied. The overall Lewis number is assumed to be unity, a condition satisfied if convection controls the heat and mass transfer rates. Typical silica gel properties are employed to characterize the desiccant [13, 17]. Results are presented for two matrices. In one, there is negligible contribution by the structural materials to the matrix thermal capacity, and the bulk specific heat of silica gel applies ($c_m = 921$ J/kg-°C). A matrix that is 50 percent mylar or 44 percent aluminum by volume is also considered ($c_m = 3350$ J/kg-°C) [6]. Solutions are presented for high-performance dehumidifiers with $\Lambda_{jk} = 20.0$. The ratios of matrix rotational mass flow rate to air mass flow rate considered are

Nomenclature (cont.)

γ_i = analogous capacitance ratio for the F_i potential [dimensionless]
η_{wp} = $(w_{1,1} - w_{12,2})/(w_{1,1} - w_{1,\text{int}})$ normalized dehumidification per unit process period flow [dimensionless]
η^*_{wp} = $(1 - \beta_{11})\eta_{wp}$ normalized dehumidification per unit total period flow [dimensionless]
θ = time from the beginning of period 1
θ_j = duration of period j [time]
θ_{jk} = duration of subperiod k of period j [time]
θ' = θ/T rotational time divided by time for a complete revolution [dimensionless]
θ'_j = θ_j/T fractional rotational time of period j [dimensionless]
κ_{jk} = $L/(v_{jk}\theta_{jk})$, carry-over ratio [dimensionless]
Λ_{jk} = $J_{w,jk}L/v_{jk}$, dimensionless mass transfer length [dimensional]
μ_j = dry period j matrix mass divided by dry fluid mass contained in matrix in period j [dimensionless]
ϕ_{jk} = angle associated with subperiod k of period j [radians]
Φ_j = angle associated with period j [radians]
T = time required for a complete wheel revolution

Subscripts

f = evaluated at fluid state
i = combined potential index
int = evaluated at intersection point of F_1 characteristic through the period j inlet state and the F_2 characteristic through the period 3-j inlet state
j = period index
k = subperiod index
l = face index 1 = inlet, 2 = outlet
m = evaluated at, or in equilibrium with, the matrix state
o = time or spatial average process outlet state
p = evaluated at the process inlet state
pr = evaluated at the time or spatially averaged purge state
r = evaluated at the regenerating inlet state

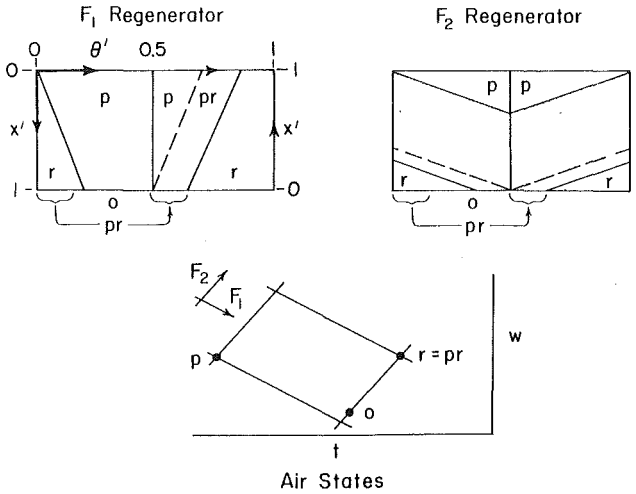

Fig. 2 Wave diagrams for the preconditioning purge with $\beta \leq C_{1,1}$

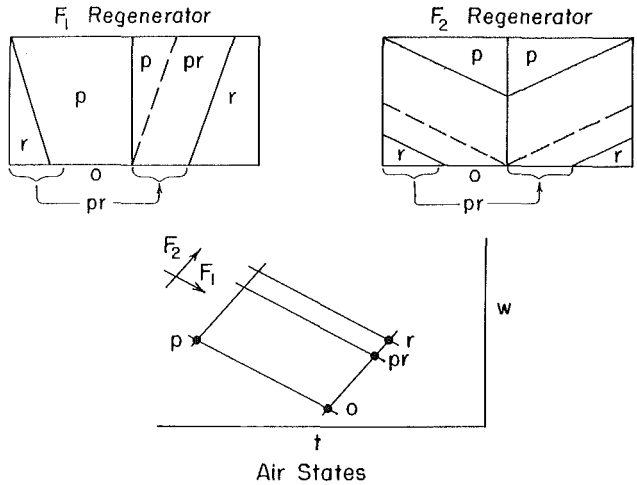

Fig. 3 Wave diagrams for the preconditioning purge with $\beta > C_{1,1}$

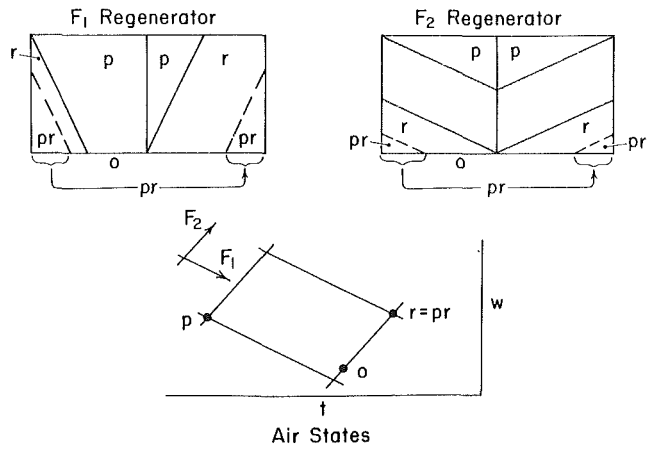

Fig. 4 Wave diagrams for the postconditioning purge with $\beta \leq C_{1,1}$

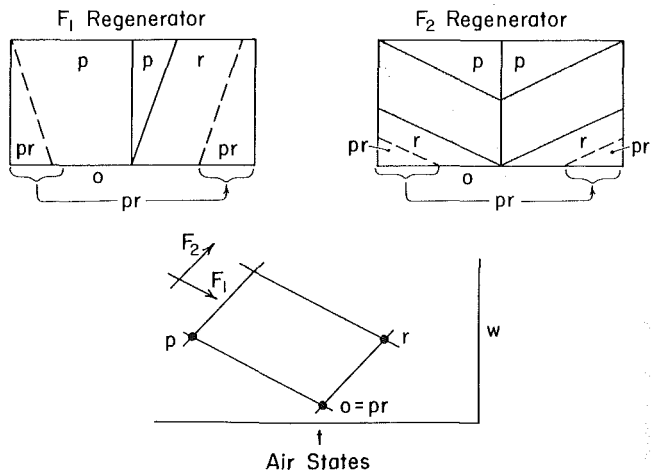

Fig. 5 Wave diagrams for the postconditioning purge with $\beta > C_{1,1}$

Table 1 Inlet states, and the corresponding period 1 F_i intersection points and outlet states for an unpurged dehumidifier with a low or high thermal capacitance matrix

	Inlet States (°C,g/kg)		
	Process	Regenerating	
1	(35,14.2)	(85,14.2)	
2	(26.7, 11.1)	(85,18.8)	
inlet state	matrix c_m	$(t_{1,\text{int}}, w_{1,\text{int}})$	$(t_{1,2}, w_{1,2})^a$
	(J/kg-°C)	(°C, g/kg)	(°C, g/kg)
1	921	(65.51, 3.846)	(66.0, 5.17)
	3350	(74.76, 3.959)	(70.2, 6.47)
2	921	(52.16, 2.151)	(55.6, 3.52)
	3350	(61.49, 1.219)	(62.6, 4.22)

[a] $\Lambda = 20.0$, $\text{Le}_o = 1$, $\mu\kappa = 0.20$ and 0.125 for low and high thermal capacitance matrices, respectively.

$\mu\kappa = 0.20$ for the bulk silica gel dehumidifier and $\mu\kappa = 0.125$ for the high thermal capacity matrix. These $\mu\kappa$ result in nearly maximum dehumidification of the process air stream in unpurged operation of the respective matrices [6, 17]. Two pairs of inlet states relevant to air conditioning processes are used. These are given in Table 1, along with the period 1 F_i intersection points $(t_{1,\text{int}}, w_{1,\text{int}})$ and the process outlet states $(t_{1,2}, w_{1,2})$ for an unpurged dehumidifier with either the low or high thermal capacitance matrix.

The qualitative accuracy of the equilibrium analogy solutions is demonstrated by the period 1 outlet air temperature and humidity ratio distributions shown in Figs. 6 and 7 for the preconditioning and postconditioning recirculation patterns. A low thermal capacitance dehumidifier with inlet state pair 1 and $\mu\kappa = 0.20$ is considered. For this case, $C_{1,1} \simeq 0.0875$ [17], so that the selected range of β spans incomplete and complete purging of the F_{1r} state. Table 2 gives the period 1 mean outlet state, the mean purge state, and the mean process outlet state for the cases considered.

The equilibrium solutions indicate that the purge angle β does not affect the period 1 outlet temperature and humidity ratio distributions in the preconditioning purge geometry. This is substantiated by the finite difference results given in Fig. 6 and Table 2. The variation with β of the spatial average

Table 2 Finite difference solution for the purged dehumidifier with $\beta < C_{1,1}$, $\beta = C_{1,1}$, and $\beta > C_{1,1}$ for inlet state pair 1

	Period 1 mean		Purge		Process	
	t(°C)	w(g/kg)	t(°C)	w(g/kg)	t(°C)	w(g/kg)
Precond.						
$\beta = 0.025$	65.96	5.167	84.96[a]	14.164	65.46	4.937
0.0875	65.94	5.171	81.50	11.564	64.43	4.558
0.150	65.86	5.187	76.73	8.945	63.93	4.524
Postcond.						
$\beta = 0.025$	65.95	5.164	84.85	14.064	65.46	4.936
0.0875	65.11	4.689	72.98	6.438	64.35	4.521
0.150	64.34	4.478	66.71	4.271	63.92	4.515

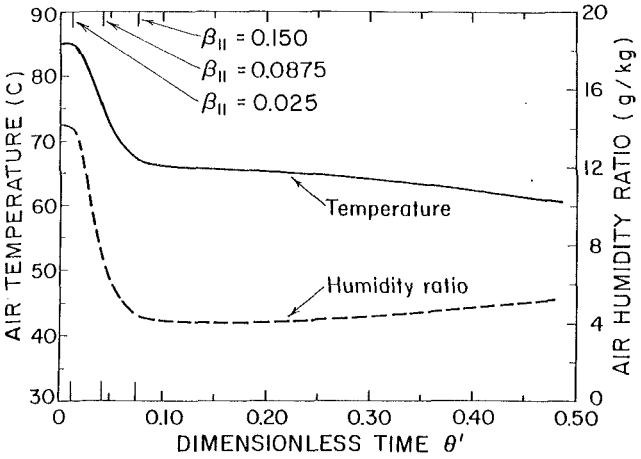

Fig. 6 Period 1 outlet temperature and humidity ratio distributions for the preconditioning purge dehumidifier with inlet state pair 1

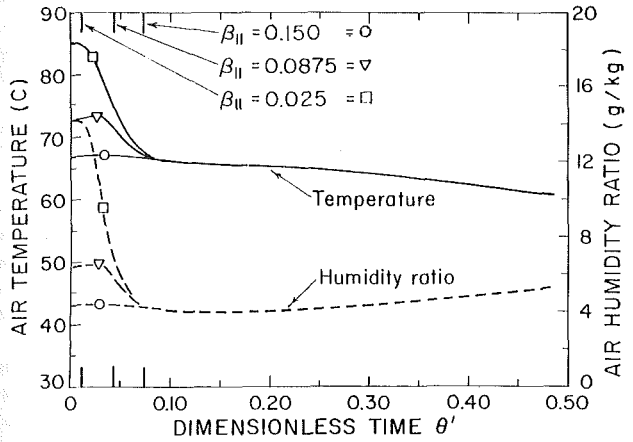

Fig. 7 Period 1 outlet temperature and humidity ratio distributions for the postconditioning purge dehumidifier with inlet state pair 1

period 1 outlet temperature and humidity ratio in this case is much less than 1 percent of the total change in period 1 air state from the inlet conditions. In contrast, the equilibrium solutions for the postconditioning purge showed an effect of β on the period 1 outlet state distributions. The predicted effect is evident in the numerical results given in Fig. 7 and Table 2. For $\beta = 0.025 < C_{1,1}$, the postconditioning purge outlet state distributions are essentially identical to those for the preconditioning purge, while for $\beta = 0.15 > C_{1,1}$ the period 1 outlet temperature and humidity ratio distributions are nearly constant with θ' at values near those of the period 1 intersection point. Also in confirmation of the analogy prediction, the data in Table 2 show that a given purge angle there is little difference in the process outlet states for the two geometries. The only feature of the equilibrium solution that is in distinct variance with the finite difference results is the prediction that a minimum in outlet humidity ratio is obtained at $\beta = C_{1,1}$. The numerical results show that the minimum process outlet humidity ratio is obtained at a value of β greater than $C_{1,1}$. This result is due to the continuous nature of the outlet state distributions. On the whole, however, these comparisons of the analogy solutions with the results of the finite difference model confirm the qualitative utility of the equilibrium analysis using the analogy method.

The numerical results show that the process stream outlet humidity ratio decreases with increasing β, which suggests that there is a purge angle which maximizes the dehumidification of the process air stream. However, performance of purged dehumidifiers can be compared on the basis of either constant total flow through the dehumidifier or

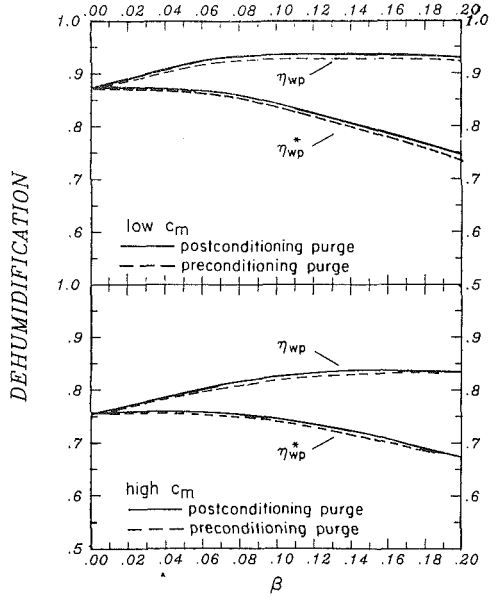

Fig. 8 Normalized dehumidification η_{wp} and η^*_{wp} for low and high thermal capacitance purged dehumidifiers with inlet state pair 1

constant process stream flow rate as the purge fraction is changed.

If the process air flow rate is kept constant as β is increased, then the total flow through the dehumidifier must increase as $(1-\beta)^{-1}$. The wheel radius must increase as $(1-\beta)^{-1/2}$ to keep $\mu\kappa$ and Λ constant. For constant dehumidifier process stream flow, the dehumidifier efficiency is

$$\eta_{wp} = \frac{w_{1,1} - w_{12,2}}{w_{1,1} - w_{1,\text{int}}} \tag{4}$$

where $w_{1,\text{int}}$ is the humidity ratio at the period 1 F_i intersection point. This is a measure of dehumidifier performance provided that the dehumidifier size and the power to pump air through the dehumidifier are unimportant.

If the total air flow through the dehumidifier is kept constant as β is increased, then the dehumidified air flow rate decreases as $(1 - \beta)$. In this case, the effective humidification per unit total process period flow is

$$\eta^*_{wp} = (1-\beta)\,\eta_{wp} = (1-\beta)\,\frac{w_{1,1} - w_{12,2}}{w_{1,1} - w_{1,\text{int}}} \tag{5}$$

This figure of merit is appropriate if the dehumidifier is of specified diameter or if the power requirement to pump air through the matrix is important.

The effects of purge angle β and purge geometry on the efficiencies η_{wp} and η^*_{wp} for a purged dehumidifier with inlet state 1 are illustrated in Fig. 8. The data show that the postconditioning recirculation pattern consistently results in a slightly drier process outlet state than does the preconditioning purge. For both the low and high thermal capacitance dehumidifiers, a minimum in process stream humidity ratio is obtained at $\beta = 0.125$. This purge angle is greater than the optimum predicted by the equilibrium analogy analysis for either matrix. The maxima in dehumidification per unit process flow rate, η_{wp}, for the low and high thermal capacitance dehumidifiers are respectively 7 percent and 11 percent greater than the η_{wp} obtained with unpurged operation. Although the high thermal capacitance dehumidifier benefits more from purging than does the low thermal capacitance dehumidifier, the low thermal capacitance matrix still results in the greater dehumidification. Also, while there are maxima in η_{wp} for the two matrices, the η^*_{wp} decrease monotonically with increasing β. For inlet state pair 1, at fixed total flow through the matrix,

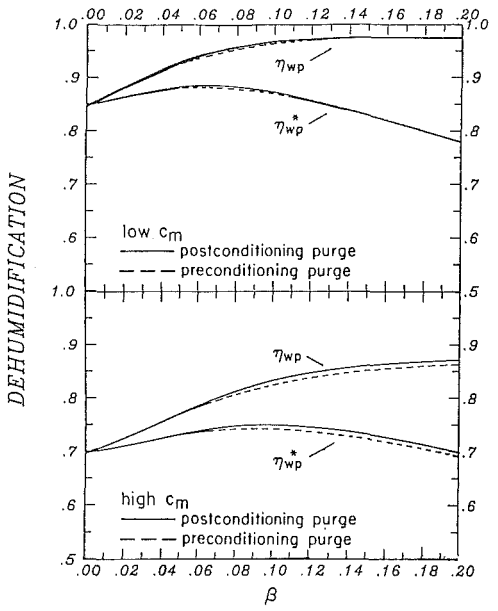

Fig. 9 Normalized dehumidification η_{wp} and η^*_{wp} for low and high thermal capacitance purged dehumidifiers with inlet state pair 2

the process stream flow rate decreases more rapidly with increasing purge angle than does the outlet humidity ratio, resulting in a net decrease in useful dehumidification.

The corresponding results for inlet state pair 2 are illustrated in Fig. 9. The postconditioning recirculation again results in slightly greater dehumidification than does the preconditioning purge. The minima in process stream outlet humidity ratio occur at $\beta \simeq 0.175$ and $\beta > 0.20$ for the low and high thermal capacitance matrices, respectively. These angles are greater than those required for inlet state pair 1, and are nearly twice the optimum values predicted by the equilibrium analogy. The corresponding maxima in η_{wp} are 15 and 25 percent greater than obtained with an unpurged dehumidifier. As was the case previously, the high thermal capacitance matrix results in poorer dehumidification than the low thermal capacitance matrix. However, in contrast to the results for inlet state pair 1, there are also maxima in the dehumidification per unit total period 1 flow, η^*_{wp}. These maxima are 4 and 8 percent greater than the $\beta=0.0$ values for the two matrices, and occur at values of β less than those corresponding to the maxima in process stream outlet humidity ratio.

The finite difference solution indicates that the recirculated purge improves the dehumidifier performance for inlet state pair 2 more than for inlet state pair 1. This is due to the much greater difference between regenerating inlet and the process inlet humidity ratios for inlet state pair 2. The significance of these improvements in dehumidifier performance depends on the constraints imposed on the dehumidifier design and operating conditions.

For example, suppose that the inlet states are fixed at state pair 2, and the dehumidifier performance can only be modified by changing the flow length, Λ_{jk}. For both the low and high thermal capacitance matrices, Λ_{jk} must be increased to more than 80 in order for an unpurged ($\beta=0$) dehumidifier to have the same dehumidification per unit period flow as the optimum purged dehumidifier with $\Lambda_{jk} = 20$. This represents a substantial change in dehumidifier geometry.

Alternatively, if the dehumidifier dimensions and flow rates are fixed, the regeneration temperature of the unpurged low thermal capacitance dehumidifier must be boosted from 85 to 88.5°C in order to give the same performance as the optimum purged dehumidifier with an 85°C regeneration temperature. Similarly, the regeneration temperature of the unpurged high thermal capacitance dehumidifier must be increased from 85 to 89.5°C. The unpurged dehumidifier requires a greater input of thermal energy to the regenerating stream to match purged dehumidifier performance, not only because the required regeneration temperatures are higher, but because the regenerating flow rate is greater than in the purged dehumidifier by a factor of $(1-\beta)^{-1}$. For inlet state pair 2, the energy requirement for an unpurged flow capacitance dehumidifier is at least 6 percent greater than that of the optimum purged dehumidifier, while the unpurged high capacitance dehumidifier requires over 10 percent more energy input than the equivalent purged dehumidifier. If the purged dehumidifier is coupled with a regenerative heat exchanger, the proportional energy savings can be greater than those indicated here.

Summary and Conclusions

The performance of a purged counterflow dehumidifier with recirculation of purged flow to produce a spatially nonuniform inlet condition in the regenerating period inlet was studied using both an equilibrium analysis and a finite difference model of the dehumidifier.This study has quantitatively shown that dehumidifier performance can be improved by purge recirculation.

The wave diagram solutions show that in an equilibrium system, the process stream outlet state is independent of the purge geometry and depends only on the purge angle. The period 1 outlet state distribution is not affected by the preconditioning purge recirculation but is changed by the postconditioning purge flow. A minimum in the process stream outlet humidity ratio occurs at $\beta = C_{1,1}$.

The finite difference model of the dehumidifier verified the trends predicted by the equilibrium analysis. The numerical solution shows that the dehumidifier performance is affected by the purge angle but is only slightly influenced by purge geometry. The postconditioning purge geometry consistently results in slightly lower process stream outlet humidity ratios than can be obtained with the preconditioning flow. The period 1 outlet state distribution is insensitive to purge angle β in the predconditioning purge but varies with β in the postconditioning purge recirculation. The minimum in process stream outlet humidity ratio occurs at values of β greater than predicted by the equilibrium analysis.

For silica gel dehumidifier with $Le_o = 1$ and with either a low or high thermal capacitance matrix, the recirculated purge dehumidifier has lower process stream outlet humidity ratios than the unpurged dehumidifier. However, for a constant total air flow rate, purged operation improves dehumidification capacity only if the regenerating inlet state humidity ratio is considerably greater than the process stream inlet humidity ratio. For the two inlet states considered, the maximum increase in dehumidification per unit period flow rate was 4 percent for the low thermal capacitance dehumidifier and 8 percent for the high thermal capacitance dehumidifier. The purged high thermal capacitance dehumidifier results in poorer dehumidification than can be obtained with the low thermal capacitance matrix.

Acknowledgments

The authors thank Drs. D. J. Close, P. J. Banks, and J. G. van Leersum of CSIRO Division of Energy Technology, Dr. M. J. Brandemuehl of Carrier Corporation, and Professor W. A. Beckman, University of Wisconsin, for their comments on this work. This project was supported by the Solar Heating and Cooling Research and Development Branch, Office of Conservation and Solar Applications, U.S. Department of Energy.

References

1 Product literature, TB-75, 330, Cargocaire Engineering Corp., Amesbury, Mass.

2 Nelson, J. S., Beckman, W. A., Mitchell, J. W., and Close, D. J., "Simulation of the Performance of Open-Cycle Desiccant Systems Using Solar Energy," *Solar Energy*, Vol. 21, 1978, pp. 273–278.

3 Jurinak, J. J., Mitchell, J. W., and Beckman, W. A., "Open-Cycle Desiccant Air Conditioning as an Alternative to Vapor Compression Cooling in Residential Application," *Solar Eng. 1983, Proc. ASME Solar Energy Div., 5th Annual Conf.*, Orlando, Fl., Apr. 1983, pp.1–9.

4 Macriss, R. A., and Zawacki, T. S., "High COP Rotating Wheel Solid Desiccant System," *Proc. 9th Energy Technology Conf.*, Washington, D.C., Feb. (1982).

5 Gunderson, M. E., Huang, K. C., and Railing, S. M., "Development of a Solar Desiccant Dehumidifier, Vol. 1 and 2," SAN-1591-1, Mar. 1978.

6 Jurinak, J. J., and Mitchell, J. W., "Effect of Matrix Properties on the Performance of a Counterflow Rotary Dehumidifier," *Heat Transfer in Porous Media*, ASME 1982 Winter Annual Meeting, Vol. HTD-22, Nov. 1982, pp. 69–79; accepted for publication in the ASME JOURNAL OF HEAT TRANSFER.

7 Barlow, R. S., and Collier, R. K., "Optimizing the Performance of Desiccant Beds for Solar Regenerated Cooling," *Proceedings of the 1981 Annual Meeting of AS/ISES*, Philadelphia, 1981.

8 Mei, V., and Lavan, Z., "Performance of Cross-Cooled Desiccant Dehumidifiers," Paper No. 80-WA/Sol-34, ASME Winter Annual Meeting, Chicago, Nov. 1980.

9 Maclaine-cross, I. L., "A Theory of Combined Heat and Mass Transfer in Regenerators," PhD thesis, Department of Mechanical Engineering, Monash University, Clayton, Victoria, Australia, 1974.

10 Holmberg, R. B., "Combined Heat and Mass Transfer in Regenerators with Hygroscopic Materials," ASME JOURNAL OF HEAT TRANSFER, Vol. 101, May 1979, pp. 205–210.

11 Barlow, R. S., "Analysis of the Adsorption Process and of Desiccant Cooling Systems—Pseudo-Steady-State Model for Coupled Heat and Mass Transfer," SERI/TR-631-1330, Dec. 1981.

12 Brandemuehl, M. J., and Banks, P. J., "Rotary Heat Exchangers with Time Varying or Nonuniform Inlet Temperatures," *Regenerative and Recuperative Heat Exchangers*, HTD-21, ASME 1981 Winter Annual Meeting, Nov. 1981.

13 Jurinak, J. J., "Open-Cycle Solid Desiccant Cooling—Component Models and System Simulations," PhD thesis, Department of Mechanical Engineering, University of Wisconsin-Madison, 1982.

14 Maclaine-cross, I. L., and Banks, P. J., "Coupled Heat and Mass Transfer in Regenerators-Prediction Using an Analogy With Heat Transfer," *Int'l Jour Heat Mass Trans.*, Vol. 15, 1972, pp. 1225–1242.

15 Banks, P. J., "Prediction of Heat and Water Vapour Exchanger Performance from That of a Similar Heat Exchanger," *Compact Heat Exchanger—History, Technological Advancement and Mechanical Design Problems*, HTD-10, ASME 1980 Winter Annual Meeting, Nov. 1980, pp. 57–64.

16 Banks, P. J., "Coupled Equilibrium Heat and Single Adsorbate Transfer in Fluid Flow through a Porous Medium: 1. Characteristic Potentials and Specific Capacity Ratios," *Chem. Eng. Sci.*, Vol. 27, May 1972, pp. 1143–1150.

17 Jurinak, J. J., and Banks, P. J., "An Evaluation of Two Analogy Solutions for a Counterflow Rotary Silica Gel Dehumidifier," *Heat Transfer in Porous Media*, Vol. HTD-22, ASME 1982 Winter Annual Meeting, Nov. 1982, pp. 57–68.

18 Close, D. J., CSIRO Div. Energy Technology, Highett, Vic. Australia, personal communication, 1981.

19 Brandemuehl, M. J., "Analysis of Heat and Mass Transfer Regenerators with Time Varying or Spatially Nonuniform Inlet Conditions," PhD thesis, Department of Mechanical Engineering, University of Wisconsin-Madison, 1981.

Melting Around a Horizontal Heated Cylinder: Part I—Perturbation and Numerical Solutions for Constant Heat Flux Boundary Condition

J. Prusa
Department of Mechanical Engineering,
Iowa State University,
Ames, Iowa 50011
Assoc. Mem. ASME

L. S. Yao
Department of Mechanical
and Aerospace Engineering,
Arizona State University,
Tempe, Arizona 85203
Mem. ASME

The melting of a solid about a heated cylinder presents an irregularly shaped, moving boundary problem. A transformation is used to immobilize this boundary—replacing the problem of variable geometry by one of constant geometry. A constant heat flux boundary condition is used along the cylinder surface. Using perturbation and numerical methods, several solutions for this transient problem are generated for Stefan, Rayleigh, and Prandtl numbers of $St_q = 0.374$, $Ra = 5000$, and $Pr = 54$. St_q is the ratio of heat transfer rate to the thermal energy needed to melt the solid. $Ra \cdot B^3$ is the measure of the magnitude of the natural convection effect, where B is a dimensionless measure of the size of the melt region called the gap function. Ra itself can be thought of as a dimensionless heat flux, since it does not take the size of the melt region into account. The dimensionless groups St_q and Ra (based upon the surface heat flux) are used to determine two parameter expansions of the dependent variables for the regular perturbation method. The first three terms of the series solutions are determined. They provide accurate solutions for short times after the start of melting, for small values of Stefan and Rayleigh numbers. The accuracy of the perturbation method is verified using a numerical method, which is not limited to short initial time intervals or to small values of Stefan and Rayleigh numbers. Detailed predictions of the melt volume, shape, temperature field, global and local heat transfer rates are given for representative cases. Comparisons with earlier experimental results are made.

Introduction

Many important problems in engineering science involve very irregularly shaped boundaries that move with time. Such problems require that the position of the boundaries be determined as part of the solution. Obvious examples can be found in the growth of crystals, in phase-change, bubble dynamics, cavitation, surface waves, combustion, and in compressible flow problems. This study solves a typical engineering problem that involves an irregular moving boundary – the melting of a solid about a heated horizontal cylinder. A way to effectively negate the complications introduced by irregular moving boundaries is to use a transformation method. The boundaries in the physical plane are mapped into simple fixed geometric shapes in a transformed plane. Analysis is done in the simple fixed geometry of the transformed plane using coordinate systems such as polar or Cartesian coordinates. In the physical plane, the Cartesian or polar coordinates of the transformed plane form a curvilinear coordinate (generally nonorthogonal) system that grows with and precisely matches the irregular moving shapes of the boundaries. The curvilinear coordinates are called "natural coordinates" [1–3].

The most widely known contemporary method of generating natural coordinates is the "body-fitted coordinate" method of Thompson, Thames, and Mastin [1–3]. In their method, problems of arbitrary, enclosed, two-dimensional geometry are mapped into simply connected rectangular domains in a transformed plane. The natural coordinate system is determined by solving numerically a system of elliptic partial differential equations. A system of N governing equations with an irregular transient geometry is replaced by a system of $N + 2$ partial differential equations with a simple fixed geometry. The method is quite general and provides an extremely powerful tool in a number of problems with irregularly shaped boundaries.

This study uses a radial transformation method [4–9] to generate natural coordinate systems for problems in doubly connected regions (one closed boundary surrounded by another). Either boundary can be irregular and may move with time. In two dimensions, the transformation works by mapping the irregular moving physical domain into concentric circles in the transformed plane. Consequently, polar coordinates (r, ψ) can be used in the transformed plane to precisely match the boundaries of the problem. The physical plane is defined using the polar coordinates $(\bar{r}, \bar{\psi})$. The radial transformation used to determine the natural coordinates has the following form

$$r = \frac{\bar{r} - R_i}{R_o - R_i} + c \text{ and } \psi = \bar{\psi}$$

R_i and R_o are the radii of the inner and outer boundaries. In general, $R_i = R_i(\bar{\psi}, \bar{t})$ and $R_o = R_o(\bar{\psi}, \bar{t})$. c is a constant that determines the radii of the circular boundaries in the transformed plane.

The natural coordinate system that is generated by the radial transformation is equivalent to the system generated by the body-fitted coordinate method. However, since the radial transformation is so simple, its use is not limited to numerical methods. It can be useful even in analytical methods. This simplicity also means that in a numerical method, the exact calculation of the coordinate system requires an insignificant amount of computer time. This is in direct contrast to the body-fitted coordinate method. Finally, if R_i or R_o have fixed

Contributed by the Heat Transfer Division for publication in the JOURNAL OF HEAT TRANSFER. Manuscript received by the Heat Transfer Division April 4, 1983. Paper No. 83-HT-18.

circular or spherical shapes, fewer extra terms are added to the transformed governing equations. Clearly, for enclosed geometries the radial transformation can exhibit greater efficiency than the method of body-fitted coordinates.

The radial transformation is demonstrated in this study by solving the problem of melting about a heated horizontal cylinder. This trial case is also a problem of considerable importance in its own right – heat transfer with phase-change is encountered often in modern technology. Examples range from the solidification of castings, to ice formation (and melting, and the ablation of surfaces due to aerodynamic heating (e.g., spacecraft reentry), More examples are found in the purification of materials, in the freeze drying of foodstuffs, and in geophysics. Solid-liquid, phase-change problems involved in low and moderate temperature thermal storage systems are also of keen interest in our energy conscious world. Typically, these thermal storage problems occur in solar energy applications and in spacecraft thermal control systems.

Early works (10–14) using analytical and numerical methods avoided the difficulty of irregularly shaped moving boundaries by considering only one-dimensional phase change. These works have contributed to our physical understanding of the basic problem. However marked, qualitative changes occur in the phase-change solution – the direct results of natural convection and an irregularly shaped melting front – when the domain becomes multidimensional.

The effects of natural convection in a spatial phase-change problem has been clearly observed in several independent experiments [15–17]. In these studies, the melting region produced by horizontal heated cylinders grew most rapidly above the heated cylinder. This produced an elongated melt region with the heated cylinder towards the bottom. The melt region appeared symmetrical with respect to the vertical. The development of a nonconcentric melt region was attributed directly to natural convection.

Sparrow, Patankar, and Ramadhyani [4] computed a numerical solution for melting around vertical cylinders with no subcooling using a radial transformation. However, higher order curvature terms for the interface and terms resulting from the motion of the interface were thrown away. This limits the validity of their method to cases where the buoyancy forces and heat transfer rates are small. Solidification in rectangular domains [18] and melting inside horizontal cylinders [19] have also recently been studied using radial transformations in numerical methods. Rieger, Projahn, and Beer [20] considered melting around a heated horizontal cylinder using the method of body-fitted coordinates in a numerical method.

Yao and Chen [7] solved the melting of a solid about a horizontal heated cylinder. They determined a double perturbation series solution in terms of the Rayleigh and Stefan numbers. Yao and Cherney [8] solved this problem with the effects of subcooling added using an integral method. The initial singularity in the governing equations was removed by using a similarity transformation. Subcooling was found to suppress free convection heat transfer. Both analytical methods used a radial transformation to immobilize the irregular moving boundary formed by the melting front.

The present work is primarily motivated by interest in demonstrating the use of a radial transformation method in engineering problems characterized by doubly-connected regions. The transformation is very simple and can be used to generate natural coordinates for analytical methods. In the present melting problem, the transformation is used to generate natural coordinates for perturbation and numerical methods. The perturbation solution is based upon the observation that conduction dominates the beginning of the melting process [7, 8, 15–17]. Natural convection is only a perturbation on this heat transfer process. The numerical method generates information on the melting process far beyond the initial period (and values of Rayleigh and Stefan numbers) for which the perturbation solution is valid. It clearly indicates the usefulness of the perturbation method as well as its limits. The two solutions augment each other and enhance the comparisons with the experimental results of [15] and [17].

Analysis

The analysis begins by considering the basic equations for unsteady laminar flow in polar coordinates. The dependent

Nomenclature

a = inner cylinder radius
c = specific heat (c_l = 2185 J/kg°C for $C_{18}H_{36}$ at 33°C)
f = $\bar{f}/\alpha$, dimensionless stream-function
g = acceleration of gravity
h_{sl} = latent heat of fusion (h_{sl} = 244 KJ/kg for $C_{18}H_{36}$)
k = thermal conductivity (k_l = .149 W/m°C for $C_{18}H_{36}$ at 33°C)
q = local heat flux
r = $(\bar{r}-a)/(R-a)$, dimensionless radial coordinate
s = $1 + rB_{00}$
t = $\bar{t}/(a^2/\alpha)$, dimensionless time
B = $(R-a)/a$, dimensionless gap function
F = average ratio of R/a
Pr = ν/α, Prandtl number (Pr = 54 for $C_{18}H_{36}$ at 33°C)
R = radius of the outer boundary as measured from the pole
Ra = $g\beta a^4 q/\alpha\nu k$, constant flux Rayleigh number
St_q = $c_l q a \rho_l / h_{sl} k_l \rho_s$, constant flux Stefan number
T = $(\bar{T}-T_o)/(qaXt/k)$, dimensionless temperature
V = F^2-1, dimensionless melt volume
X = $(R-a)/at$, nonsingular form of the dimensionless gap function
α = $k/\rho c$, thermal diffusivity of the fluid (α = 8.79 × 10^{-8} m²/s for $C_{18}H_{36}$ at 33°C)
β = coefficient of thermal expansion (β = 9.01 × 10^{-4}/°C for $C_{18}H_{36}$ at 33°C)
μ = $1 + B_{00}$
ν = kinematic viscosity (ν = 4.76 × 10^{-6} m²/s for $C_{18}H_{36}$ at 33°C)
ρ = density (ρ_l = 777 kg/m³ for $C_{18}H_{36}$ at 33°C)
ψ = $\bar{\psi}$, dimensionless angular coordinate
ω = $\bar{\omega}/(\alpha/a^2)$, dimensionless vorticity

Superscripts

• = $\frac{\partial}{\partial t}$ or $\frac{\partial}{\partial \bar{t}}$, time derivative
′ = $\frac{\partial}{\partial \psi}$ or $\frac{\partial}{\partial \bar{\psi}}$, first angular derivative
″ = $\frac{\partial}{\partial \psi^2}$ or $\frac{\partial^2}{\partial \bar{\psi}^2}$, second angular derivative

Subscripts

i = inner boundary
l = liquid phase
o = outer boundary
s = solid phase
00 = term of zero order in perturbation method
01 = term of order St_q in perturbation method
10 = term of order Ra in perturbation method

dimensional variables are vorticity, $\bar{\omega}$, stream function, $\bar{f}$, and temperature, $\bar{T}$. The independent variables are radius, $\bar{r}$, angular coordinate, $\bar{\psi}$, and time, $\bar{t}$. The radius of the outer boundary, R, is the fourth dependent variable in the phase-change problem. The equation for R is found by considering the energy balance in a control system at the interface. The conservation of vorticity, thermal energy, stream function, and the governing equation for R provide four equations for the four dependent variables.

Initially, at time $\bar{t} = 0^-$ (solid phase only), $\bar{T} = T_o$ for all $\bar{r} \geq a$ (there is no subcooling effect, all of the solid is at the melting temperature). At time $\bar{t} = 0^+$, the heating of the solid phase begins. Instantaneously, a concentric annular melt region of infinitesimal thickness appears around the heated cylinder. This sudden appearance of liquid phase where none existed the moment before corresponds to a singularity in the governing equations at time zero. Thus at $\bar{t} = 0^+$ (infinitesimal melt region exists)

$$-k\frac{\partial \bar{T}}{\partial \bar{r}} = q_i \text{ at } \bar{r} = a \text{ and } \bar{T} = T_o \text{ for } \bar{r} > a \tag{1a}$$

$$\bar{\omega} \equiv \bar{f} \equiv 0, R \equiv a. \tag{1b,c}$$

As time advances from $\bar{t} = 0^+$, the size of the melt region grows and R increases beyond a for all values of $\bar{\psi}$. The following boundary conditions then become necessary

$$-k\frac{\partial \bar{T}}{\partial \bar{r}} = q_i, \bar{f} = 0, \bar{\omega} = -\frac{\partial^2 \bar{f}}{\partial \bar{r}^2} \text{ at } \bar{r} = a \tag{2a}$$

$$\bar{T} = T_o, \bar{f} = 0, \bar{\omega} = -\frac{\partial^2 f}{\partial \bar{r}^2} - \frac{1}{R^2}\frac{\partial^2 \bar{f}}{\partial \psi^2} \text{ at } \bar{r} = R \tag{2b}$$

Since R varies with ψ, the $\partial^2 \bar{f}/\partial \bar{\psi}^2$ term in the vorticity boundary condition at the interface ($\bar{r} = R$) must be retained. The shape of the interface is determined by the local rate of heat transfer, which occurs in two modes. Conduction tends to produce a liquid-solid interface that is circular and concentric with respect to the inner cylinder. Natural convection tends to produce an interface that is symmetric with respect to the direction of gravity (provided the flow is steady). The superposition of these two effects produces an interface that is symmetric with respect to the vertical [15–17]. The following final boundary conditions then result

$$\frac{\partial \bar{T}}{\partial \bar{\psi}} = 0, \bar{f} = \bar{\omega} = 0 \text{ at } \bar{\psi} = 0, 180 \text{ deg} \tag{2c}$$

The radial coordinate is nondimensionalized so that the outer boundary formed by the liquid-solid interface, at $\bar{r} = R$, is transformed into the unit circle, $r = 1$. The inner boundary, $\bar{r} = a$, is transformed into the pole, $r = 0$. This constitutes the radial transformation. In dimensionless form, the radial distance from the inner cylinder to the interface is measured by the gap function.

Numerical Method. When the cylinder is heated so as to maintain a constant surface heat flux, the singularity in the governing equations at time zero is of order t [9–11]. This requires that t be factored out of the gap function in order to remove the singularity. The coordinate transformation then takes on the following form

$$r = \frac{\bar{r} - a}{aXt}, \quad \psi = \bar{\psi}, \quad t = \bar{t}/(a^2/\alpha) \qquad \text{(coordinates)} \tag{3a}$$

$$X = (R - a)/at \qquad \text{(gap function)} \tag{3b}$$

The governing equations are nondimensionalized using (3). After simplification, the following dimensionless governing equations result

$$\frac{1}{\text{Pr}}\left\{t^2X^2\frac{\partial \omega}{\partial t} - rt(X^2 + tX\dot{X})\frac{\partial \omega}{\partial r} + \frac{1}{r + 1/tX}\frac{\partial(f,\omega)}{\partial(r,\psi)}\right\} = (\nabla^2_2 - N_2)\omega$$
$$- X^2t^2\text{Ra}\left\{\frac{\cos\psi}{r + 1/tX}\left(\frac{\partial T}{\partial \psi} + \frac{X'}{X}\left(T - r\frac{\partial T}{\partial r}\right)\right) + \sin\psi\frac{\partial T}{\partial r}\right\} \tag{4a}$$

$$t^2X^2\frac{\partial T}{\partial t} + t(X^2 + tX\dot{X})\left(T - R\frac{\partial T}{\partial r}\right) + \frac{1}{r + 1/tX}\frac{\partial(f,t)}{\partial(r,\psi)} + \frac{X'}{X}\frac{1}{r + 1/tX}\frac{\partial f}{\partial r} \cdot T = (\nabla^2_2 - N_2^*)T \tag{4b}$$

$$(\nabla^2_2 - N_2)f = -t^2X^2\omega \tag{4c}$$

$$t\dot{X} + X = -\text{St}_q\left\{1 + \frac{t^2X'^2}{(1 + tX)^2}\right\}\frac{\partial T}{\partial r}\bigg|_{r=1} \tag{4d}$$

where

$$\nabla^2_2 = \frac{\partial^2}{\partial r^2} + \frac{1}{r + 1/tX}\frac{\partial}{\partial r} + \frac{1}{(r + 1/tX)^2}\frac{\partial^2}{\partial \psi^2}$$

$$N_2 = \frac{1}{(r + 1/tX)^2}\left[\frac{2rX'}{X}\frac{\partial^2}{\partial r \partial \psi} + \left(\frac{X''}{X} - \frac{2X'^2}{X^2}\right)r\frac{\partial}{\partial r} - \frac{r^2X'^2}{X^2}\frac{\partial^2}{\partial r^2}\right]$$

$$N_2^* = \frac{1}{(r + 1/tX)^2}\left[\frac{2rX'}{X}\frac{\partial^2}{\partial r \partial \psi} + \frac{rX''}{X}\frac{\partial}{\partial r} - \frac{r^2X'^2}{X^2}\frac{\partial^2}{\partial r^2} - \frac{2X'}{X}\frac{\partial}{\partial \psi} - \frac{Z''}{Z}\right]$$

$$\frac{\partial(P,Q)}{\partial(x,y)} = \frac{\partial P}{\partial x}\frac{\partial Q}{\partial y} - \frac{\partial P}{\partial y}\frac{\partial Q}{\partial x}$$

and

$$X' = \frac{\partial X}{\partial \psi}, \quad X'' = \frac{\partial^2 X}{\partial \psi^2}, \quad \dot{X} = \frac{\partial X}{\partial t}$$

The differential operators N_2 and N_2^* represent the effects of the irregular curvature of the interface. They vanish if the interface is a circle centered on the pole. The implicit partial differentiation of the transformation also causes a $r\partial/\partial r$ term to appear on the left-hand sides of (*4a, b*). This term introduces the effects of the movement of the interface into the dimensionless governing equations.

The dimensionless initial conditions are found by letting $t = 0$ in the governing equations (4), and then solving for each of the four dependent variables. The results are

at $t = 0^+$ (infinitesimal melt region exists)

$$T = 1 - r, \quad \omega \equiv f \equiv 0, \quad X = \text{St}_q \tag{5}$$

The dimensionless boundary conditions are

$$\frac{\partial T}{\partial r} = -1, \quad f = 0, \quad \omega = -\frac{1}{t^2X^2}\frac{\partial^2 f}{\partial r^2} \text{ at } r = 0 \tag{6a}$$

$$T = f = 0, \quad \omega = -\frac{1}{t^2X^2}\left[1 + \frac{t^2X'^2}{(1 + tX)^2}\right]\frac{\partial^2 f}{\partial r^2} \text{ at } r = 1 \tag{6b}$$

$$\frac{\partial T}{\partial \psi} = 0, \quad f = \omega = 0 \text{ at } \psi = 0 \text{ deg}, 180 \text{ deg} \tag{6c}$$

The method of approximating equations (4) and (6) with finite difference equations follows that used in [21] and is explained in detail in [9]. Details of the computational procedure can also be found in [9]. In order to compare the numerical results with [15], computations were performed over the interval of time, $0 \leq t \leq 7$ for $\text{St}_q = 0.374$, Ra = 5000, and Pr = 54.

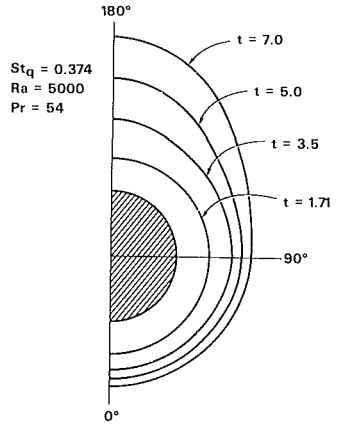

Fig. 1 Interface growth

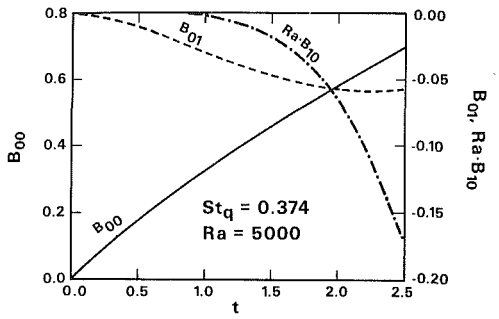

Fig. 2 Perturbation solution for gap function

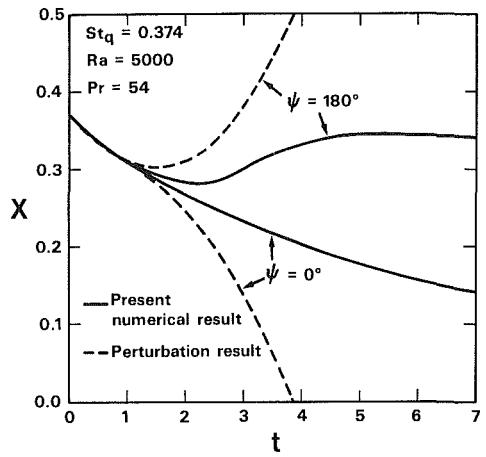

Fig. 3 Comparison of numerical and perturbation solutions for gap function

Results and Discussion

Figure 1 shows the growth of the melt region as determined in the numerical solution: St_q = 0.374, Ra = 5000, and Pr = 54. The position of the solid-liquid interface, R/a, is shown at four different times. The growth is quite similar to the isothermal boundary condition case [22]. Although the interface is nearly a concentric circle at t = 1.71, the melting process is actually in the transition stage of the melting process. By t = 3.5, the melting process has moved into the convection stage. The rate of melting above the cylinder is enhanced, due to the formation of a thermal plume. Below the cylinder, melting is decreased due to the motion of the fluid away from the interface there. Melting below the cylinder

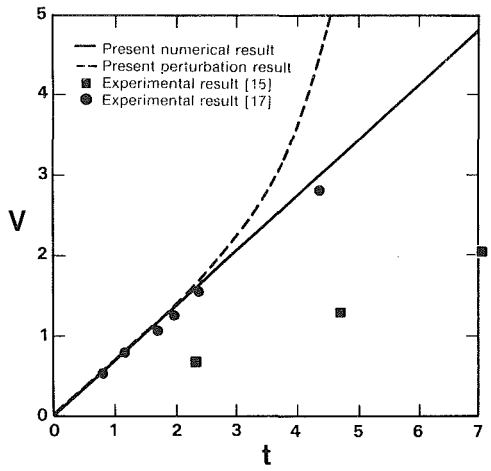

Fig. 4 Melt volume: comparison of present numerical and perturbation results (St_q = 0.374) with experimental results

does not decrease as sharply as in the case with an isothermal boundary condition. This is the result of the difference in the order of the initial singularity in the governing equations.

Figure 2 shows the first three contributions to the gap functions, as determined by the perturbation solution. The zero-order solution B_{00} makes the dominant contribution to the gap function for early values of time. It gives the interface growth which results from quasi-steady conduction heat transfer. B_{00} increases with St_q and t. B_{01} is the first-order unsteady effect. B_{10} gives the first correction for the effects of natural convection. Since $B_{10} < 0$, this correction will cause the interface to grow more rapidly at the top and more slowly at the bottom of the melt region.

The limitations of the perturbation solution are readily observed in a comparison with the numerical solution. In Fig. 3, a comparison is made using the gap function X. The perturbation solution accurately predicts the gap function during the conduction stage of melting. It predicts the correct trends during the transition stage, but begins to diverge from the numerical solution. At t = 2.0, the perturbation solution departs from the numerical solution by 10 percent. Once the convection stage is reached, around t = 2.5, the divergence is very rapid. The numerical results extend well into the convection stage and indicate that the interface continues to grow more rapidly above the cylinder than below it.

The variation of dimensionless melt volume V, with time is shown in Fig. 4. V is determined by the volume integration

$$V = \frac{1}{\pi}\int_0^{\pi}(1+Xt)^2 d\psi - 1 \qquad (7)$$

Here the numerical solution for St_q = 0.374, Ra = 5000, and Pr = 54 is compared with the result from the perturbation solution. The numerical results are also compared with two sets of experimental data. The outstanding characteristic which emerges from this comparison is a (nearly) linear increase of melt volume with time. This occurs because at the value of St_q used, liquid superheating (sensible heat gain) is unimportant. Almost all of the incoming thermal energy is being used to melt solid material. The effect of superheating is that it will cause the melting rate to be less than a linear variation with time; at the scale of Fig. 4 this is not perceptible for $St_q < 1$.

The perturbation solution remains within 5 percent of the numerical solution up to t = 2.7, and is 10 percent off at t = 3.2. It appears that the perturbation solution can correctly predict V up to the beginning of the convection stage. Also of interest is the zero-order solution $V_{00} = 2t \cdot St_q$, which gives

the asymptotic linear volume growth rate for the limits of zero superheating and natural convection effects.

The numerical value of Ra does not match the experimental values, but this in not important in Fig. 4 for two reasons. First, the value of Ra is irrelevant when conduction is the dominant mode of heat transfer (up to $t \sim 2$ in the present case). Note that a significant comparison can already be made in this interval of time. Second, since the heat flux is specified, natural convection has little effect on the melting rate, even when it is the dominant mode of heat transfer. The slight effect of fluid motion is due to its influence on reducing the degree of liquid superheating.

In the experimental results of [15] – which use the paraffin n-octadecane, C_{18} H_{36} – a surface heat flux of $q_i = 656$ W/m^2 was used (private communication with R. Viskanta). Using the thermophysical properties of C_{18} H_{36} given in [23] (listed in nomenclature), a constant flux Stefan number of $St_q = 0.374$ and Pr = 54 can be determined for the experimental data. The thermophysical properties were evaluated at an average temperature of 33°C (5° above the melting temperature), which was estimated from the data in [15]. These values of St_q and Pr were matched in the present numerical computation. Unfortunately, the experimental results [15] and present numerical results do not agree very well. Although the same qualitative trends are observed, the numerical results in Fig. 4 predict an increase in volume 100 percent greater than the experimental results.

There are several possible sources of error which may contribute towards the discrepancy. First, the thermophysical properties of C_{18} H_{36} are not precisely known. References which list properties of paraffins deviate from each other by as much as 25 percent (see [9]). Also, the constant property assumptions in the present model may introduce some error. Second, the physical model in the present analysis is two dimensional. There are no thermal or viscous end effects. In practical experiments, thermal and viscous end effects exist. Such effects can be minimized by making the length of the heated cylinder long compared to the diameter. In [15], this ratio is approximately 2:1. This is rather small and may lead to large end effects, especially once a large melt region has formed. A third and final effect is the presence of subcooling in the experiment. It is estimated in [15] that no more than a couple of degrees of subcooling exist. From this, a subcooling parameter $S_b = (k_s/k_l) \cdot (T_o - T_{solid})/(T_i - T_o) \sim 0.3$ can be computed for the experiment ($k_s/k_l \sim 1.7$ for C_{18} H_{36}). This may decrease the rate of melting significantly [8], since thermal energy is required to raise the solid's temperature to T_o, making less energy available for melting. This subcooling effect is enhanced if the ratio of solid to liquid thermal diffusivities is greater than unity [8]. This occurs because thermal energy is more rapidly diffused throughout the solid. Since $c_l/c_s \sim 1.2$ for C_{18} H_{36} [23], $\alpha_{sl} = \alpha_s/\alpha_l \sim 2$ can be computed for the experimental results [15]. Consequently, the decrease in melting rate which occurs due to subcooling is enhanced.

The second set of experimental data [17] compare much more favorably with the numerical result in Fig. 4. In this experiment, naphthalene is now the PCM. Corresponding to the surface heat flux and thermophysical properties given in [17], $St_q = 0.465$ can be determined, along with Pr = 10.2. Since the Stefan number for [17] is 25 percent larger than the value in the numerical result, the rate of melting measured in [17] should be somewhat higher than the numerical result for $St_q = 0.374$. Instead, the data appear to closely match the numerical result. This means that the experimental results are about 25 percent lower than would be predicted by the present numerical method. The same three sources of error are again involved. Only now the diameter-to-length ratio of the heated cylinder is ~ 3.7. Consequently, end effects are reduced when compared to [15]. Also the temperature of solid naphthalene

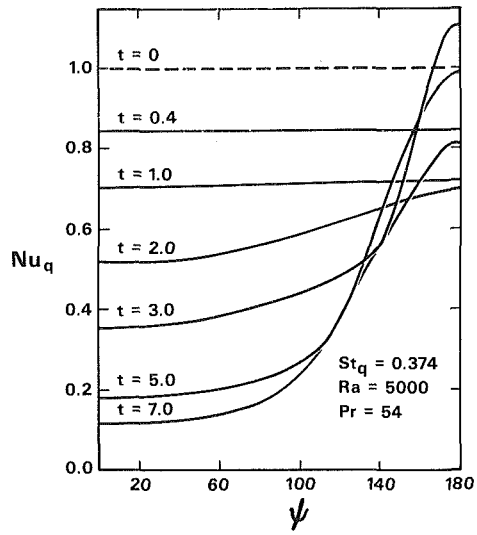

Fig. 5 Variation of local heat transfer rates along interface with time

was kept within 0.2°C of the melting temperature. This represents an order of magnitude reduction in subcooling effects when compared to [15].

The local heat transfer rate along the solid-liquid interface as determined in the numerical solution is shown in Fig. 5. The dimensionless heat transfer rate is

$$Nu_q = \frac{q_o}{q_i} = -\left\{1 + \frac{X'^2}{X^2(1+1/tX)^2}\right\} \frac{\partial T}{\partial r}\bigg|_{r=1} \tag{8}$$

At the initial time of zero, the melt region is only infinitesimal in extent. As a result, the rate of heat transfer at the interface is exactly equal to the rate of heat transfer at the cylinder. In dimensionless form, $Nu_q \equiv 1$. The conduction stage, characterized by flat Nu_q profiles, appears to extend to $t = 1$. Note that since the heat flux at the cylinder is specified, energy balance requires that $\overline{Nu}_q \cdot F \leq 1$. From this, it follows that the average value of Nu_q must decrease monotonically from 1. The profile at $t = 2$ indicates the melting process is in the transition stage. By $t = 3$, the convection stage has been reached. The thermal plume above the cylinder increases Nu_q greatly near $\psi = 180$ deg. Motion of the fluid away from the interface near $\psi = 0$ deg causes Nu_q to decrease rapidly to small values.

The variations of average dimensionless heat transfer rate along the interface $\overline{Nu}_q$ with time, is shown in Fig. 6. $\overline{Nu}_q$ is determined from

$$\overline{Nu}_q = \frac{1}{\pi F}\int_0^\pi Nu_q(1+tX)d\psi \tag{9}$$

The numerical solution shows the steady monotonic decrease for $\overline{Nu}_q$ deduced from the energy balance argument. Also of interest is the variation of $\overline{Nu}_q \cdot F$ with t. If all of the thermal energy from the heated cylinder is used to melt the solid, then $\overline{Nu}_q \cdot F = 1$. Since the numerical result indicates $\overline{Nu}_q \cdot F < 1$, some thermal energy is used to superheat the liquid. This sensible heat gain is proportional to the area between the $\overline{Nu}_q \cdot F$ contour and the horizontal line, $\overline{Nu}_q = 1$. In Fig. 6, this area corresponds to a sensible heat gain of 8.2 percent for $0 \leq t \leq 7$. The perturbation result for $\overline{Nu}_q$ remains within 5 percent of the numerical solution up to $t = 2.5$, the end of the transition stage. The result for $\overline{Nu}_q \cdot F$ diverges much sooner, however, due to the multiplication of the separate errors in the perturbation predictions for $\overline{Nu}_q$ and F.

Since it is the heat flux which is specified along the heated

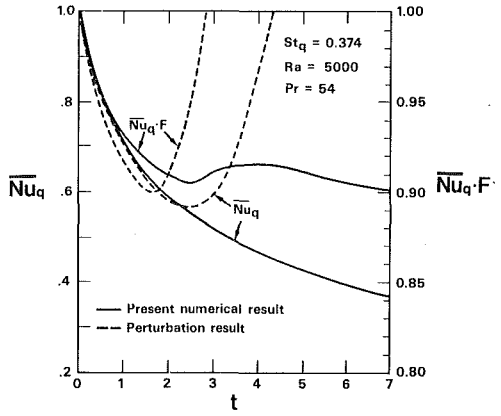

Fig. 6 Average heat transfer rate along interface

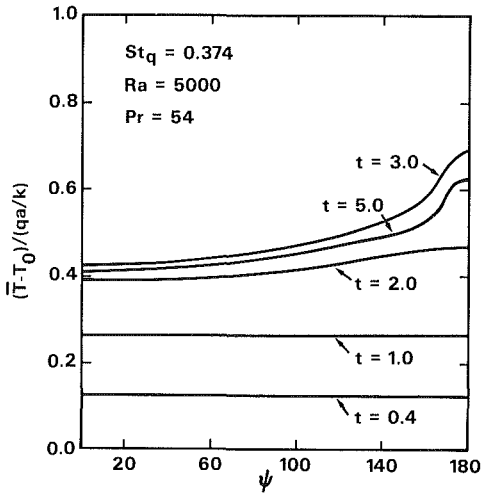

Fig. 7 Variation of cylinder temperature with time

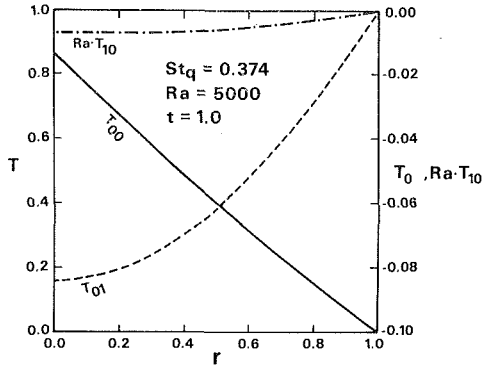

Fig. 8 Perturbation solution for temperature

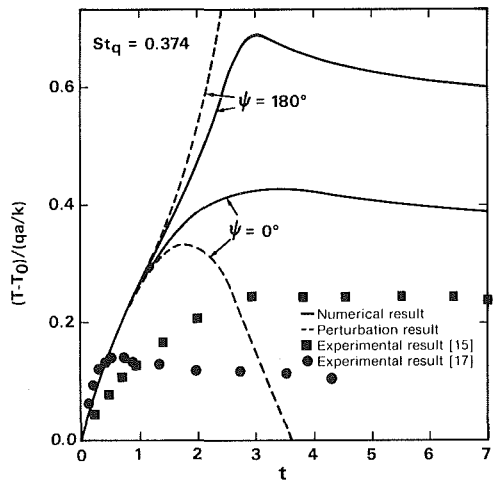

Fig. 9 Extrema in cylinder temperature: comparison of present numerical and perturbation results with experimental results

cylinder, the cylinder surface temperature is unknown. The temperature profile along the cylinder is shown in several different times in Fig. 7. The temperature is presented in the dimensionless form

$$(\bar{T}-T_o)/(qa/k)=T\cdot Xt \tag{10}$$

which has a more direct physical significance than T. The initial temperature profile at $t = 0$ is identically zero. The temperature profiles in the conduction stages ($t = 0.4$ and $t = 1$) are horizontal. The cylinder is isothermal. As the melting process advances into the transition stage ($t = 2$), the temperature profile along the cylinder becomes skewed, with the temperature being hottest on the top of the cylinder. Throughout the conduction and transition stages, the temperature on the cylinder increases with time. By $t = 3$, the convection stage has been reached. The profile now has a very pronounced peak at $\psi = 180$ deg, due to natural convection. A lot of hot fluid is located here near the cylinder. It is this hot fluid that forms the thermal plume. In order for the thermal boundary condition of constant flux to be satisfied in this area, the cylinder must locally become hotter than the fluid at the base of the plume. Once the convection stage is reached, the shape of the temperature profile matures and changes little as t increases. As a whole, the profile decreases in magnitude asymptotically towards the steady profile for natural convection heat transfer from a heated horizontal cylinder in an infinite fluid. This predicted asymptotic behavior qualitatively matches the numerical results of Kuehn and Balvanz [24] for a heated horizontal cylinder in an infinite fluid.

The perturbation solution for temperature is shown in Fig. 8 for $St_q = 0.374$, Ra = 5000, and $t = 1.0$. The perturbation results for T and B can then be substituted into equation (10) and compared with the numerical results. Figure 9 shows such a comparison at two points in the temperature field, at the top ($r = 0$, $\psi = 180$ deg) and bottom of the heated cylinder ($r = 0$, $\psi = 0$ deg. The perturbation result follows the numerical result to within 5 percent up to $t = 1.5$, or into the transition stage of melting. It then quickly diverges from the numerical result. The numerical solution is also compared with the experimental results of [15] and [17]. The data points are for the temperature at the top of the heated cylinder.

The numerical and experimental results show the same qualitative behavior. The temperature at the top of the cylinder increases rapidly during the conduction-dominated start of melting to a maximum or overshoot temperature which occurs at the end of the transition stage. At this point, natural convection becomes the dominant heat transfer mechanism, and the temperature drops off slowly in an asymptotic decay towards the limiting case of a heated cylinder in an infinite fluid. The overshoot results because the convection process requires less temperature difference for a given heat transfer rate. Note in Fig. 9 that earlier overshoots will occur for larger values of Ra, given a specified value of St_q (hence melting rate). This occurs because natural convection becomes the dominant heat transfer process sooner for larger values of Ra. Convection becomes important only when $Ra \cdot B^3$ (see the Appendix) passes a certain critical value. Since B will be the same for all values of Ra in the initially conduction dominated process, larger values of Ra cause the critical value of $Ra \cdot B^3$ to be reached sooner. Consequently, the value of Ra is very important in the comparison of local temperatures (unlike the comparison of melt volume in Fig. 4).

In Fig. 9, the data of [17] follows the numerical result closely up to a dimensionless time of 0.7. At this point, a clear temperature overshoot is reached. This occurs because Ra $\sim$ 4.4×10^6 for [17]. Hence convection dominated heat transfer is reached sooner and requires less temperature difference than in the numerical result. The temperature for [15] reaches a limiting value which is closer to the numerical result than [17]. In this case, Ra $\sim 7.6 \times 10^5$ for [15] is still larger than 5000, but not so large as in [17]. It can be seen that [15] initially increases more slowly than the numerical result – unlike [17]. This is likely due to the subcooling, end effects, and unknown variations in thermophysical properties mentioned in the discussion of Fig. 4. Note that Fig. 9 gives information in terms of the dimensionless temperature. The actual temperature differences $\bar{T} - T_o$ for large times are about 10.7°C for [15] and 5.1°C for [17] (the heat transfer rates for [15] and [17] are within 15 percent of each other). Consequently, we observe the interesting result that for specified heat transfer rate, larger values of Ra result in smaller values of $\bar{T} - T_o$.

The entire temperature field can be gauged from Fig. 10. Here the variation of temperature along lines of constant ψ are plotted at two different times. The numerical solution at $t = 2$ is located in the transition stage. The temperature profile at $\psi = 180$ deg is slightly higher than the other profiles. This is the result of a very weak thermal plume. Along $\psi = 0$ deg, the profile is slightly lower than the other profiles. This is due to a weak flow separation away from the interface in the bottom of the melt region. At $t = 7$, the melting process is now well advanced into the convection stage. The hot thermal plume keeps the profile along $\psi = 180$ deg high. A temperature inversion appears at intermediate values of ψ [9]. In the bottom of the melt region, the motion of fluid away from the interface keeps the $\psi = 0$ deg profile low.

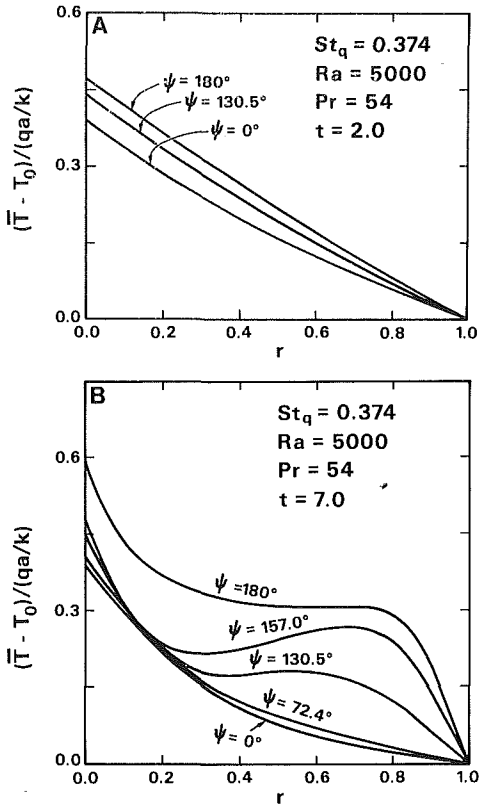

Fig. 10 Variation of temperature along lines of constant ψ

Conclusion

A coordinate transformation method is used to immobilize the moving boundary formed by the liquid-solid interface in a melting problem. The transformation has the additional advantage of transforming the melt region – which is very irregularly shaped due to the effects of natural convection – into a very simple shape. Use of the transformation results in a negligible increase in computing time for numerical method. Futhermore, it is so simple that is can even be used in a perturbation method.

The numerical solution indicates that three distinct stages appear in the melting process – as occurs in the isothermal boundary condition case [22]. In the first stage, heat transfer is dominated by conduction. The melt region appears annular, and all characteristics of the melting process are dominated by St_q. As time advances, the melting process passes into a transition stage. Natural convection heat transfer becomes much more important. Finally a convection stage is reached where natural convection is the dominant mode of heat transfer. Although natural convection is more efficient than conduction as a mode of heat transfer (Pr >> 1), the average heat transfer rates will not be increased as natural convection develops because the influx of thermal energy is specified. Consequently, the rate of melting is only slightly influenced by Ra. This is in direct contrast to the isothermal case where the advent of fluid motion results in increased heat transfer rates [22]. The shape of the melt region, local heat transfer rates, and the temperature field will be strongly influenced by Ra, however. The perturbation solution, which is accurate throughout the conduction stage and often well into the transition stage for small values of St_q and Ra, indicates that the Pr effect is minor. The zero-order term of the perturbation solution gives a linear melt volume growth rate. The numerical solution provides information on the melting process into the convection stage, well beyond the region where the perturbation solution remains valid.

Acknowledgments

The authors would like to thank Professor R. Viskanta for his generous help in sending additional information on the results of [15] and also for his help in intepreting the physical meaning of the results. Our appreciation and gratitude is further extended to Professor R. J. Goldstein for providing us with a copy of [17].

References

1 Thompson, J. F., Thames, F. C., and Mastin, C. W., "Automatic Numerical Generation of Body-Fitted Curvilinear Coordinate System for Field Containing Any Number of Arbitrary Two-Dimensional Bodies," *Journal of Computational Physics*, Vol. 15, 1974, pp. 299-319.

2 Thames, F. C., Thompson, J. F., Mastin, C. W., and Walker, R. L., "Numerical Solutions for Viscous and Potential Flow About Arbitrary Two-Dimensional Bodies Using Body-Fitted Coordinate Systems," JOURNAL OF COMPUTATIONAL PHYSICS, Vol. 24, 1977, pp. 245-273.

3 Thompson, J. F., Thames, F. C., and Mastin, C. W., "TOMCAT—A Code for Numerical Generation of Boundary-Fitted Curvilinear Coordinate Systems on Fields Containing Any Number of Arbitrary Two-Dimensional Bodies," *Journal of Computational Physics*, Vol. 24, 1977, pp. 274-302.

4 Sparrow, E. M., Patankar, S. V., and Ramadhyani, A., "Analysis of Melting in the Presence of Natural Convection in the Melt Region," ASME JOURNAL OF HEAT TRANSFER, Vol. 99, 1977, pp. 520-526.

5 Solomon, J. M., Climent, M., and Ferguson, R. E., "Inviscid Flowfield Calculations for Re-Entry Vehicles With Control Surfaces," *AIAA Journal*, Vol. 15, 1977, pp. 1742-1749.

6 Yao, L. S., "Analysis of Heat Transfer in Slightly Eccentric Annuli," ASME JOURNAL OF HEAT TRANSFER, Vol. 102, 1980, pp. 279-284.

7 Yao, L. S., and Chen, F. F., "Effects of Natural Convection in the Melted Region Around a Heated Horizontal Cylinder," ASME JOURNAL OF HEAT TRANSFER, Vol. 102, 1980, pp. 667-672.

8 Yao, L. S., and Cherney, W., "Transient Phase-Change Around a Horizontal Cylinder," *International Journal of Heat and Mass Transfer*, Vol. 24, 1981, pp. 1971-1981.

9 Prusa, J., "A Spatial Stefan Problem Modified by Natural Convection: Melting Around a Horizontal Cylinder," Ph.D. dissertation, University of Illinois at Urbana-Champaign, 1983.

10 Carslaw, H. S., and Jaeger, J. C., *Conduction of Heat in Solids*, 2d ed., Oxford University Press, London, 1962, pp. 282–296.
11 Rubenstein, L. I., "The Stefan Problem," *Translations of Mathematical Monographs*, Vol. 27, 1971, pp. 1–15.
12 Murray, W. D., and Landis, F., "Numerical and Machine Solutions of Transient Heat-Conduction Problems Involving Melting or Freezing: Part 1—Method of Analysis and Sample Solutions," ASME *Transactions*, Vol. 81, 1959, pp. 106–112.
13 Boger, D. V., and Westwater, J. W., "Effect of Buoyancy on the Melting and Freezing Process," ASME JOURNAL OF HEAT TRANSFER, Vol. 89, 1967, pp. 81–89.
14 Heitz, W. L., and Westwater, J. W., "Extension of the Numerical Method for Melting and Freezing Problems," *International Journal of Heat and Mass Transfer*, Vol. 13, 1970, pp. 1371–1375.
15 Bathelt, A. G., Viskanta, R., and Leidenfrost, W., "An Experimental Investigation of Natural Convection in the Melted Region Around a Heated Horizontal Cylinder," *Journal of Fluid Mechanics*, Vol. 90, 1979, pp. 227–229.
16 Sparrow, E. M., Schmidt, R. R., and Ramsey, J. W., "Experiments on the Role of Natural Convection in the Melting of Solids," ASME JOURNAL OF HEAT TRANSFER, Vol. 100, 1978, pp. 11–16.
17 Goldstein, R. J., and Ramsey, J. W., "Heat Transfer in a Melting Solid With Applications to Thermal Energy Storage Systems," *Heat Transfer Studies: Festschrift for E.R.G. Eckert*, Hemisphere, 1979, pp. 199–208.
18 Ramachandran, N., Gupta, J. P., and Jaluria, Y., "Thermal and Fluid Flow Effects During Solidification in a Rectangular Enclosure," *International Journal of Heat and Mass Transfer*, Vol. 25, 1982, pp. 187–193.
19 Saitoh, T., and Hirose, K., "High Rayleigh Number Solutions to Problems of Latent Heat Thermal Energy Storage in a Horizontal Cylinder Capsule," ASME JOURNAL OF HEAT TRANSFER, Vol. 104, 1982, pp. 545–553.
20 Rieger, H., Projahn, U., and Beer, H., "Analysis of the Heat Transport Mechanisms During Melting Around a Horizontal Circular Cylinder," *International Journal of Heat and Mass Transfer*, Vol. 25, 1982, pp. 137–147.
21 Prusa, J., and Yao, L. S., "Heat Transfer of Fully Developed Flow in Curved Tubes," *Journal of Fluid Mechanics*, Vol. 123, 1982, pp. 503–522.
22 Prusa, J., and Yao, L. S., 'Melting Around a Horizontal Heated Cylinder: Part I—Numerical Solution for Isothermal Boundary Condition," Proceedings of the ASME-JSME Thermal Engineering Joint Conference, Mar. 20–24, 1983, Honolulu, Hawaii.
23 Humphries, W. I., and Griggs, E. I., "Design Handbook for Phase-Change Thermal Control," NASA Technical Paper 1074, 1977.
24 Kuehn, T. H., and Balvanz, J. L., "Conjugate Heat Transfer by Natural Convection From a Horizontal Heat Exchanger Tube," *Proceedings of the 7th International Heat Transfer Conference*, Vol. 2, Sept. 1982, Munich, Germany, pp. 317–322.

APPENDIX

Perturbation Method and Solution

The perturbation solution is based upon dual assumptions: (*i*) the melting process is conduction dominated; and (*ii*) the melting process is quasi-steady.

Consequently, the effects of natural convection and unsteady heat transfer can be treated as perturbations on a conduction dominated, quasi-steady process [7, 8]. The perturbation parameter for the convection effect is Ra. For the unsteady effect, the proper perturbation parameter is St_q, since this measures the ratio of available thermal energy in the melt to the latent heat of fusion – hence the speed of melting.

The solution which follows can only be expected to be valid as long as conditions (*i*) and (*ii*) *are both independently satisfied.* This requires that the time t, St_q, and Rayleigh number *all independently be sufficiently small.* From the comparison with the numerical solution, t is small enough if the melting process is no further along than the transition stage (note from Figs. 3, 6, and 9 that the perturbation solution will give unmistakable signs that the transition stage has been reached). Also the good agreement indicates that $St_q \leq 0.3$ is sufficiently small.

Since our Ra is based upon the cylinder radius, it is really not an appropriate measure of the convection effect (it is actually a dimensionless heat transfer rate!). An appropriate Rayleigh number is $Ra \cdot B^3$ [7], where B is the dimensionless gap function, equation (A2). The appropriate Rayleigh number must take into account the size of the melt region, and B is our dimensionless measure of the width of the melt region. If B is small (beginning of melting process), then condition (*i*) can be satisfied even for moderately large values of Ra. Consequently, Ra = 5000 is also small enough for the perturbation solution. In summary, the solution is valid if t, $Ra \cdot B^3$, and St_q are all small, independently of each other.

As a first step, the radial transformation is cast into a dimensionless form appropriate for the perturbation method

$$r = \frac{\bar{r}-a}{aB}, \quad \psi = \bar{\psi}, \quad t^* = St_q \cdot \bar{t}/(a^2/\alpha) \qquad \text{(coordinates)} \tag{A1}$$

$$B = (R-a)/a. \qquad \text{(gap function)} \tag{A2}$$

For the regular perturbation method, it is not necessary to extract the initial singularity out of the gap function. The dimensionless time is also slightly modified when compared to the version used in the numerical method, equation (3*a*). It differs by a factor of St_q. For small values of Stefan number, this decreases the effects of St_q on the solution and increases the convergence and accuracy of the solution. This dimensional similitude was observed in [4].

Next the dependent variables are expanded into the following two parameter series

$$B = (B_{00} + St_q \cdot B_{01} + \ldots) + Ra\,(B_{10} \cdot \cos\psi + \ldots) + \ldots \tag{A3}$$

$$T = (T_{00} + St_q \cdot T_{01} + \ldots) + Ra(T_{10} \cdot \cos\psi + \ldots) + \ldots \tag{A4}$$

$$\omega = Ra(\omega_{10} \cdot \sin\psi + \ldots) + \ldots \tag{A5}$$

$$f = Ra(f_{10} \cdot \sin\psi + \ldots) + \ldots \tag{A6}$$

where $B_{ij} = B_{ij}(t^*)$ and $\phi_{ij} = \phi_{ij}(r,t^*)$ for $\phi = T$, ω, and f.

The series (A3–A6) are substituted into the governing equations, and when terms of like order are collected, systems of partial differential equations result. The complexity of systems of higher order increases very rapidly. The first three systems are sufficient for determining a short time solution for low values of St_q and $Ra \cdot B^3$. Most of the equations occurring in these three systems can be recast into linear form and be solved exactly using standard techniques for linear differential equations. The gap function equations remain difficult to solve, however. Only the zero-order gap function equation is simple enough to allow an exact solution for $B_{00}(t)$ to be readily found. In order to determine the higher-order gap functions B_{01} and B_{10}, the quasi-steady assumption is again used. T_{01} and T_{10} are considered functions of radial coordinate only. This assumption is valid as long as Ra and St_q are small. The solutions are

$$Ra^0 \cdot St_q^0: \quad T_{00}(s,t) = \ln(\mu/s)^{B_{00}} \tag{A7}$$

$$B_{00}(t) = (2St_q \cdot t + 1)^{1/2} - 1 \tag{A8}$$

$$Ra^0 \cdot St_q^1: \quad T_{01}(s,t) = c_1 \ln s + c_2 + \frac{B_{01}}{B_{00}^2}\frac{1}{s} - \frac{B_{00}-1}{B_{00}^2}s + \frac{B_{00}-1}{4B_{00}^2}(2+\ln\mu)s^2 - \frac{B_{00}-1}{4B_{00}^2}s^2 \ln s \tag{A9}$$

$$B_{01}(t) = \frac{3\mu^2 - 2\mu^3 - 1}{6}\left[\frac{c_1}{\mu} - \frac{B_{01}}{\mu^2 B_{00}^2} - \left(\frac{B_{00}-1}{4B_{00}^2}\right)\{1 - 2(1-\mu)\ln\mu\}\right] \tag{A10}$$

$$Ra^1 \cdot St_q^0: \quad f_{10}(s,t) = \frac{c_3}{s} + c_4 s + c_5 s \ln s + c_6 s^3 + \frac{1}{16}s^3 \ln s \tag{A11}$$

$$\omega_{10}(s,t) = -\frac{2c_3}{s} - \left(8c_4 + \frac{3}{8}\right)s - \frac{1}{2}\ s\ln s \qquad \text{(A12)}$$

$$T_{10}(s,t) = \frac{c_7}{s} - d_6 + c_8 s + \frac{1}{32B_{00}}\left(4c_6 - \frac{3}{16}\right)s^3 - \left(\frac{c_3}{2B_{00}}\right)\frac{\ln s}{s} + \frac{B_{10}}{B_{00}^2}\ \ln s + \frac{1}{4B_{00}}(2c_4 - c_5)\ s\ln s + \frac{c_5}{4B_{00}}\ s\ln^2 s + \frac{1}{128B_{00}}s^3\ln s \qquad \text{(A13)}$$

$$B_{10}(t) = \frac{3\mu^2 - 2\mu^3 - 1}{6}\left[-\left(c_7 + \frac{c_3}{2B_{00}}\right)\frac{1}{\mu^2} + \frac{B_{10}}{B_{00}^2}\ \frac{1}{\mu} + \frac{1}{4B_{00}}(2c_4 - c_5 + 4c_8 B_{00}) + \frac{3}{32B_{00}}\left(4c_6 - \frac{5}{48}\right)\mu^2 + \frac{1}{4B_{00}}(2c_4 + c_5)\ln\mu + \frac{c_5}{4B_{00}}\ln^2\mu + \frac{3}{128B_{00}}\mu^2\ln\mu\right] \qquad \text{(A14)}$$

where

$$c_1 = \frac{B_{01}}{B_{00}^2} + \frac{B_{00} - 1}{4B_{00}^2}(1 - 2\cdot\ln\mu)$$

$$c_2 = -\frac{B_{01}}{\mu B_{00}^2} + \frac{B_{00} - 1}{B_{00}^2}\left[1 - \frac{\mu}{2}(1 + \ln\mu)\right]\mu - c_1\ln\mu$$

$$c_3 = \frac{1}{16}d_3 - \frac{1}{64}d_4 d_5\mu^2$$

$$c_4 = -\frac{1}{32}(4d_3 - 1) - \frac{1}{64}d_1 d_4 d_5$$

$$c_5 = -\frac{1}{32}d_2 d_4 d_5$$

$$c_6 = \frac{1}{32}(2d_3 - 1) + \frac{1}{64}d_4 d_5$$

$$c_7 = \frac{\mu(d_7\mu + d_8)}{1 + \mu^2}$$

$$c_8 = -\frac{d_8\mu + d_7}{1 + \mu^2}$$

and

$$d_1 = 1 - \mu^2,\ d_2 = 1 + \mu^2$$

$$d_3 = (\mu^4\ln\mu)/d_1 d_2,\ \ d_4 = \mu^2/(d_1 + d_2\ln\mu)$$

$$d_5 = (4\cdot\ln\mu)/d_2 + d_1/\mu^2,\ d_6 = B_{10}(1 + \ln\mu)/B_{00}^2$$

$$d_7 = \left[\frac{B_{10}}{B_{00}} - \frac{1}{2}(c_3 - c_4) - \frac{c_5}{4} + \frac{3c_6}{8} - \frac{5}{512}\right]/B_{00}$$

$$d_8 = -d_6 + 4c_6 - \frac{3}{16}\mu^3/32B_{00} - (c_3\ln\mu)/2\mu B_{00} + (B_{10}\ln\mu)/B_{00}^2 + (2c_4 - c_5)(\mu\ln\mu)/4B_{00} + (c_5\mu\ln^2\mu)/4B_{00} + (\mu^3\ln\mu)/128B_{00}$$

The solutions (A7–A14) give the first three terms of the perturbation series (A3–A6). They provide the basis for generating the perturbation results, which are compared with the numerical results in the Results and Discussion. Further details of the perturbation analysis can be found in [9].

Note that the remaining dimensionless group, Pr, is nowhere to be seen in the perturbation solution. This is because Pr first appears in the second-order systems of equations of order $\mathrm{Ra}\cdot\mathrm{St}_q$ and Ra^2. Consequently, it can be deduced that the Pr effect is insignificant. This is typical for convection phase-change problems for $7 \le \mathrm{Pr} \le 50$ [4].

L. J. Fang

F. B. Cheung[2]
Mem. ASME

J. H. Linehan[3]
Mem. ASME

D. R. Pedersen

Reactor Analysis and Safety Division,
Argonne National Laboratory,
Argonne, Ill. 60439

Selective Freezing of a Dilute Salt Solution on a Cold Ice Surface[1]

The growth of a solid–liquid, two-phase region during selective freezing of a dilute, eutectic-forming, salt solution over a subcooled ice slab is investigated experimentally and theoretically. The morphology of the two-phase region and the kinetics of the solid–liquid interface observed for a NaCl-H_2O system are described photographically. The motion of the two-phase, liquidus front, recorded by a telescopic device that amplifies the local phenomena of the two-phase region, is presented along with the measured transient temperature distribution of the system. Based on the assumption that the solution element of the two-phase region is in local thermodynamic equilibrium with the solid phase, a similarity model is developed to predict the dependence of the freezing rate on various controlling parameters of the system. Transient heat conduction in the ice slab is also included in the model to study the effect of the wall. Comparison is made between the analytical and the experimental results and found to be good.

1 Introduction

The solidification of a binary, eutectic-forming solution has recently received considerable attention because of its relevance to metal processing [1], preservation of biomaterials [2], desalination of sea water [3], and nuclear reactor safety studies involving the interaction between a molten UO_2 pool and a refractory material such as MgO [4, 5]. Our primary interest here is in reactor safety studies concerning the accommodation of core debris in a MgO-lined reactor cavity following a postulated core-meltdown accident. One of the current design concepts is to use a MgO delay bed as a sacrificial material to retain the molten fuel within the ex-vessel cavity. Melting of the MgO bed not only serves as an effective means of decay heat removal but also dilutes the heat sources of the pool. This, together with the fact that the decay power of the fuel is dropping with time, would eventually lead to freezing of the pool. To ensure the long-term coolability of the fuel, however, it is necessary to understand the mechanism and the rate of freezing of the MgO-UO_2 solution mixture.

Unlike the freezing of a pure material in which the process takes place isothermally at a sharp solid-liquid moving boundary [6–9], the solidification of a binary, eutectic-forming solution occurs over a temperature range within which a solid–liquid, two-phase region exists. Typically, a single component is frozen in the early stage of solidification until the concentration of the remaining solution reaches the eutectic composition. Only after this stage would freezing of both components proceed as a solid eutectic [10–14]. Tien and Geiger [10] and Cho and Sunderland [11] solved the eutectic freezing problem by treating the latent heat of fusion over a range of temperature as internal heat generation. Muehlbauer et al. [12] considered the heat of fusion as a pseudo-specific heat and obtained an approximate solution for the freezing of a binary, eutectic-forming solution using a heat-balance integral method. Hayashi and Komori [13] also used the pseudo-heat-capacity approach to derive an approximate solution for the freezing of saline solutions. Recently, O'Callaghan et al. [14] developed a "two-zone" model to analyze the heat and mass transfer during dendritic solidification of an aqueous binary solution. In all of these studies, the wall temperature was lower than the eutectic temperature in question. As a result, two solidification fronts, one for the liquidus and the other for the solidus, were propagating simultaneously with time.

For the case when the wall temperature is lower than the liquidus temperature but higher than the solidus temperature of the binary system, a selective freezing process will occur without the formation of a solid eutectic. There is only one moving boundary in the system, i.e., the liquidus front, behind which a solid–liquid, two-phase region grows continuously with time. This fundamentally interesting and technically important case has not been investigated previously. The solidification of a molten MgO-UO_2 pool in a reactor cavity, for example, is likely to take place in this manner. This is because by the time pool freezing occurs, the solution mixture would be very rich in MgO and the pool boundary would be at or above the eutectic temperature. In metallurgy industry, as another example, one may control the wall temperature such that selective freezing of one component in a molten alloy would take place before the formation of a solid eutectic so as to refine the surface properties during the casting process. The objective of this work is to explore experimentally and theoretically the mechanism of selective freezing of a binary eutectic system.

2 Experimental Method

To simulate the phenomena of pool freezing in a MgO-lined cavity, water and sodium chloride, which possess a binary eutectic phase diagram, are chosen as the working materials. A selective freezing process may be initiated by placing a pool fo dilute sodium chloride solution on top of a subcooled air-bubble-free ice slab.[4] This pair of simulant materials not only has known properties but also has a temperature range suitable for visual observation. In addition, the thermal diffusivity of the salt solution, which is of the order of 10^{-7} m^2/s, is much larger than the mass diffusivity of sodium chloride in water, which is of the order of 10^{-9} m^2/s. Thus the choice of this system also minimizes the effect of mass transfer on the selective freezing process, which greatly simplifies the analysis. In addition, the use of a subcooled ice slab provides a uniform nucleation surface for the selective freezing process enabling us to investigate the effect of boundary conditions.

[1] Based in part on a dissertation performed at Argonne to be submitted to the faculty of Marquette University by L. J. Fang in partial fulfillment of the degree of Doctor of Philosophy

[2] To whom correspondence concerning this paper should be addressed

[3] Present address: Mechanical Engineering Department, Marquette University, Milwaukee, Wisconsin 53233

Contributed by the Heat Transfer Division for publication in the JOURNAL OF HEAT TRANSFER. Manuscript received by the Heat Transfer Division June 1, 1983.

[4] The use of air-bubble-free ice instead of ordinary ice is to eliminate the possible effects of air bubbles on the heat transfer process.

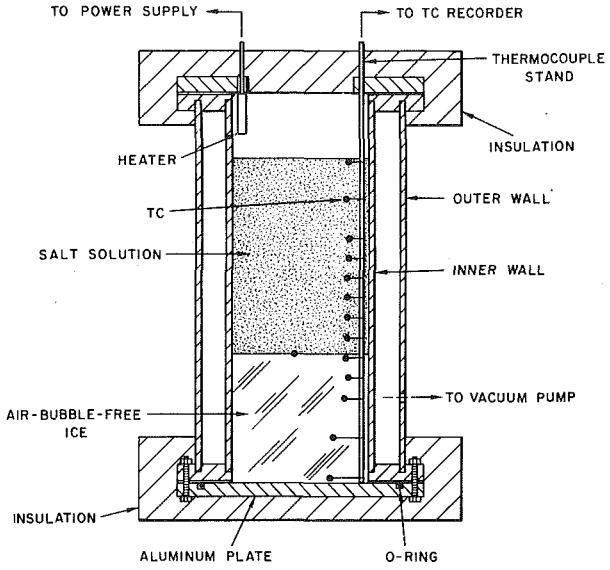

Fig. 1 Schematic of experimental apparatus

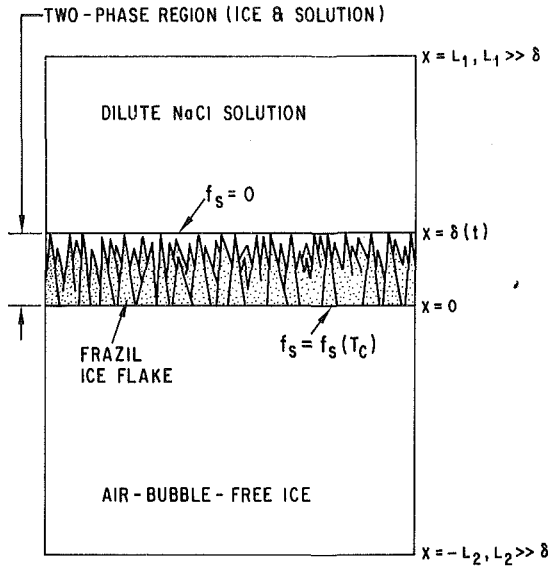

Fig. 2 Schematic of the two-phase region, showing the individual ice flakes

Figure 1 shows a schematic diagram of the experimental apparatus. The test chamber was a double-walled lucite cylinder with wall diameters of 127 mm and 178 mm, respectively, fitted at the bottom with an aluminum plate. The space between the two cylindrical walls was evacuated to reduce heat transfer in the radial direction. Before each run, air-bubble-free ice was prepared on top of the aluminum plate inside the test chamber. To do this, a mechanical stirrer and an electrical space heater (25 W) were placed through the cylinder at the top. Distilled water was then introduced into the cylinder and the entire system was placed in a freezer held at a desired subzero temperature for about 48 hours. With the space between the double side walls put under vacuum, the water layer was cooled from below by the cold aluminum plate and heated from above by the electrical heater. In this way, the ice was able to grow upward from the bottom of the water layer. Meanwhile, water motion created by the stirrer swept away air bubbles that formed at the ice-water interface. After the "clear" ice grew to a thickness of about 150 mm during a two-day period, the remaining water on top of the clear ice was removed. The surface of the ice was made smooth and flat by melting the top portion of the ice slab.

The temperature of the ice slab was determined by embedding a set of thermocouples (K type, 30-gauge chromel-alumel) at different vertical locations of the ice. To avoide any problems with the thermocouple junctions due to the stirring motion of the mechanical stirrer during the formation of the clear ice, the junctions were positioned 20 mm to 50 mm away from the center of the test cylinder. These thermocouples, as well as those located in the salt solutoin above the ice slab, were used to measure the temperature transients of the system

Nomenclature

A = internal heat generation, equation (4)
C = solution concentration
C^* = dimensionless concentration, C/C_{eut}
C_o = initial solution concentration
C_o^* = dimensionless initial concentration, C_o/C_{eut}
C_{eut} = eutectic concentration
C_p = specific heat
D = mass diffusion coefficient in the solution
E_m = error due to neglecting mass diffusion
E_v = error due to neglecting volumetric change upon freezing
f_s = solid fraction in the two-phase region
k = thermal conductivity
R_l = dimensionless initial solution temperature, equation (19)
R_s = dimensionless initial solid temperature, equation (19)
S = Stefan number, equation (19)
t = time
T^* = temperature in the two-phase region
T_o = liquidus temperature at C_o
T_c = contact or surface temperature
T_{eut} = eutectic temperature
T_l = liquid temperature
T_{lo} = initial solution temperature
T_m = normal melting point of pure solid
T_s = solid temperature
T_{so} = initial solid temperature
V = vertical velocity induced by volumetric change upon freezing
x = vertical coordinate measured from the surface of the solid

Greek Symbols

δ = thickness of the two-phase region
ρ = density
α = thermal diffusivity
λ = latent heat of fusion
σ = solidification constant, equation (13)
η = similarity coordinate, equation (13)
θ^* = dimensionless temperature in the two-phase region, equation (10)
θ_o = dimensionless liquidus temperature at C_o^*
θ_l = dimensionless liquid temperature, equation (14)
θ_s = dimensionless solid temperature, equation (14)
θ_c = dimensionless surface temperature

Subscripts

o = initial or liquidus conditions
eut = eutectic point
l = liquid region
m = normal melting point
s = solid region

Superscripts

$'$ = derivative with respect to η
$*$ = two-phase region or dimensionless quantities normalized by the eutectic properties

Fig. 3 A close-up of the frazil ice flakes in the two-phase region for a 10 percent NaCl solution at 1°C on top of ice at −25°C: (*a*) sideview, (*b*) top-view

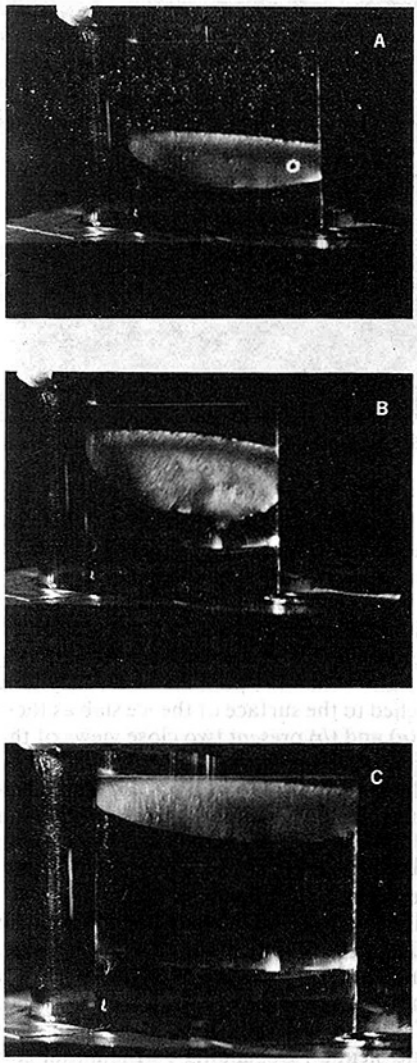

Fig. 4 Departure of the lumped ice-flakes material: (*a*) leaving the surface of the original ice slab, (*b*) moving upward through the salt solution, (*c*) floating on top of the solution pool

during each run. In addition, a thermocouple was placed at the center of the test chamber with the bead attached to the exposed surface of the ice slab to determine the temperature response at the ice surface. The recorded temperatures from this center thermocouple and from two off-center thermocouples showed very little temperature variation in the radial direction during the process of selective freezing. Hence heat transfer in the system may be regarded as one-dimensional.

During each run, a premixed sodium chloride solution with a bulk concentration that was less than the eutectic concentration (~23.3 percent by weight) was introduced on top of the ice slab. The depth of the solution pool was about 100 mm. The initial temperatures of the ice and the solution were chosen such that the contact temperature, i.e., the temperature at the original ice-salt solution interface, would fall into the temperature range between the liquidus and the eutectic point. When this was done, selective freezing of the dilute salt solution was found to occur near the bottom of the pool. Ice crystals were observed to form over the surface of the original ice slab as a result of solvent rejection. The structure of the solid–liquid, two-phase region and the form of the ice crystals were studied photographically. A cathetometer with 0.01-mm resolution, which amplifies the two-phase region, was used to measure the time variation of the moving front. The outputs of the various thermocouples were recorded by a multichannel recorder.

3 Observations of the Two-Phase Region

A typical configuration of the system during the growth of the two-phase region is shown schematically in Fig. 2. Small ice flakes were found uniformly distributed over the surface of the cold ice slab at the very beginning of each run. The ice flakes were apparently isolated from each other and remained so as they grew gradually and vertically toward the interior of the solution pool.[5] It also appeared that the total number of ice flakes was fixed at the beginning of the selective freezing process. There were no new ice flakes formed on the surface of the ice slab during the growth of the two-phase region. The total number of the ice flakes was found to depend on the initial ice and solution conditions. If the initial conditions

[5] An ice flake might grow slightly wider in the horizontal direction. However, the most rapid growth always occurred in the vertical direction. This will be further discussed in later sections.

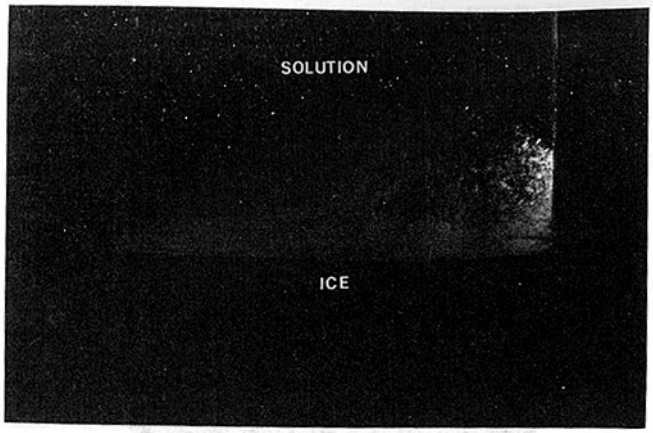

Fig. 5 Bottom-view of the departed ice-flakes material

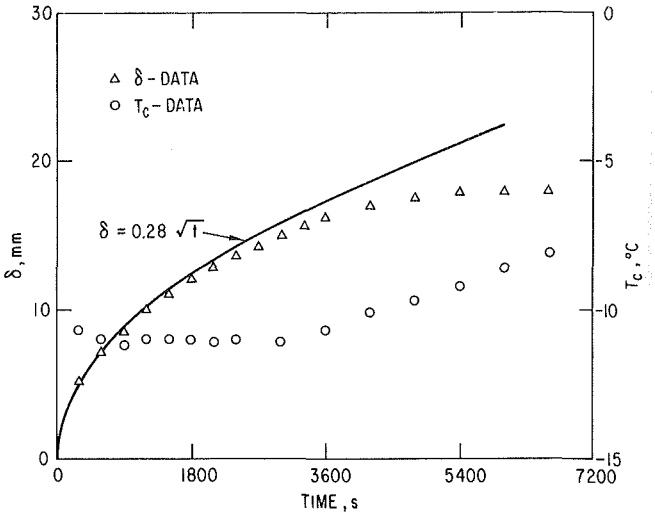

Fig. 6 Transient thickness of the two-phase region and the surface temperature of the ice slab during selective freezing of 10 percent NaCl solution initially at −1°C. Initial temperature of ice = −25°C

were such that the contact temperature[6] fell only slightly below the liquidus curve, a small number of ice flakes would form on the cold ice slab. On the other hand, if the initial conditions were such that the contact temperature fell far below the liquidus curve, a very high population of ice flakes would be observed on the cold ice slab. Although the ice flakes were lighter than the pool material, they were found to remain attached to the surface of the ice slab as they grew.

Figures 3(*a*) and (*b*) present two close views of the ice flakes formed during selective freezing of a dilute, sodium chloride solution. The picture shown in Fig. 3(*a*) was taken from the side of the test chamber with an angle of inclination pointed downward from above the two-phase region, whereas the picture shown in Fig. 3(*b*) was taken directly from top of the system. The average size of the ice flakes could be estimated by comparison with the diameter of the thermocouple wires shown in the picture, which was about 0.4 mm. Our observations indicate that the form of the ice crystals was neither needlelike nor cylindrical, as proposed by O'Callaghan [14]. Rather, a fully grown ice flake looked similar to a bamboo leaf, thin and slender. Depending on the initial conditions of freezing, an ice flake could be 10–20 mm tall but only 1–4 mm wide. Its thickness was probably much less than 0.4 mm. The property of the ice flakes appeared to be quite similar to the frazil ice occurring in rivers and oceans as described by Martin [15]. In fact, the average width of the ice flakes was the same size as the frazil ocean ice disks. In our case, however, the frazil ice flakes were pointed upward and were submerged in the salt solution as opposed to those observed in rives and oceans, which were normally laying flat and floating on top of the water. Like the ocean ice disks, our ice flakes also had the tendency to aggregate together and adhere to almost any foreign materials.[7] This may explain why the ice flakes, although much lighter than the salt solution, remained attached to the surface of the original ice slab as they grew. Owing to the fact that the salt solution was completely stagnant[8] and that there was a strong buoyancy force acting on each ice flake, the ice flakes remained isolated from each other as they grew vertically upward.

A rather interesting phenomenon was observed in the later stage of the selective freezing process. After the frazil ice flakes grew to a certain height, which was about 10–20 mm in our case, they started to depart from the surface of the ice slab. Typically, this occurred during the second hour of the growing period. If the population of the two-phase region was very small and the ice flakes were far apart, they would tend to leave the surface and float to the top of the solution pool individually. However, if the population was sufficiently large, the ice flakes would join together at the bottom and float to the top of the pool as a whole. This situation is shown in Fig. 4. The entire event from (A) to (C) took place in only a few seconds. This lumped ice-flake material looked like a piece of sod, rooted together at the base, thinner in the upper portion and thicker in the lower portion. Although the ice flakes traveled through the solution pool as an entity, the body of the lumped material was highly porous, as shown in Fig. 5. The solid fraction was apparently less than unity. The morphology of the two-phase region will be further discussed in later sections.

To understand the cause of the ice-flakes departure, the measured surface temperature of the ice slab and the thickness of the two-phase region during selective freezing of a 10 percent NaCl solution initially at −1°C on top of an air-bubble-free ice slab initially at −25°C are shown in Fig. 6. The surface temperature of the ice slab was practically constant during the first hour of the growing period having a value of ~ −11°C. The two-phase material at the surface was in thermodynamic equilibrium at this temperature. In the second hour of the growing period, however, the surface temperature began to rise, owing to the finite thickness of the ice slab.[9] This resulted in partial melting of the lower part of the ice flakes[10] which eventually triggered the event of ice-flake departure. During the time interval in which the surface temperature was virtually constant, the rate of growth of the two-phase region, $\delta(t)$, was proportional to the square root of time, as shown by the solid line in the figure. The solid line

[6] The contact temperature, which was the temperature at the surface of the ice slab upon contact with the salt solution, was measured by the thermocouple located at the center of the test chamber.

[7] This property of frazil ice had caused serious problems with hydroelectric facilities [15].

[8] As a result of solvent rejection during selective freezing, the solution was more dense at the bottom. The liquid system was hydrodynamically stable. No convection was observed in the solution pool.

[9] The test chamber was insulated at the bottom during the experiment. Thus freezing would proceed only at the expense of the sensible heat of the ice slab. As the *entire* ice slab was heated up, the initial contact condition could no longer prevail in the system.

[10] As the surface temperature rose, the local solid (ice) element could not be in phase equilibrium with the dense solution. Consequently, a fraction of the solid began to dissolve into the solution. It should be noted that the two-phase region was still growing during this time, though very slowly. This is quite similar to the phenomenon associated with the growth of dendrites in solutions known as "dendritic coarsening" [16]. Due to local variations in the supersaturation, the base of a dendrite may be dissolving away at the same time the tip was still growing.

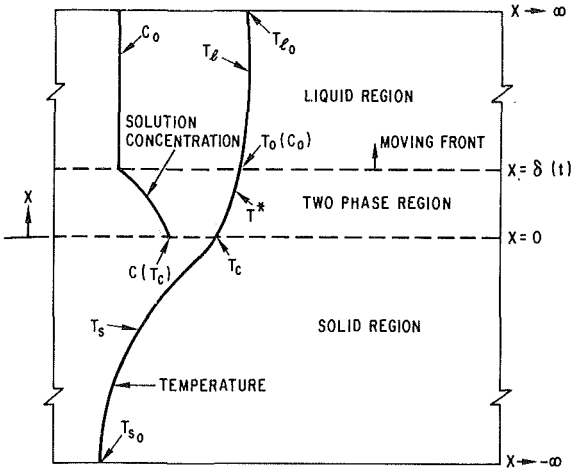

Fig. 7 Schematic of the selective freezing system, indicating nomenclature

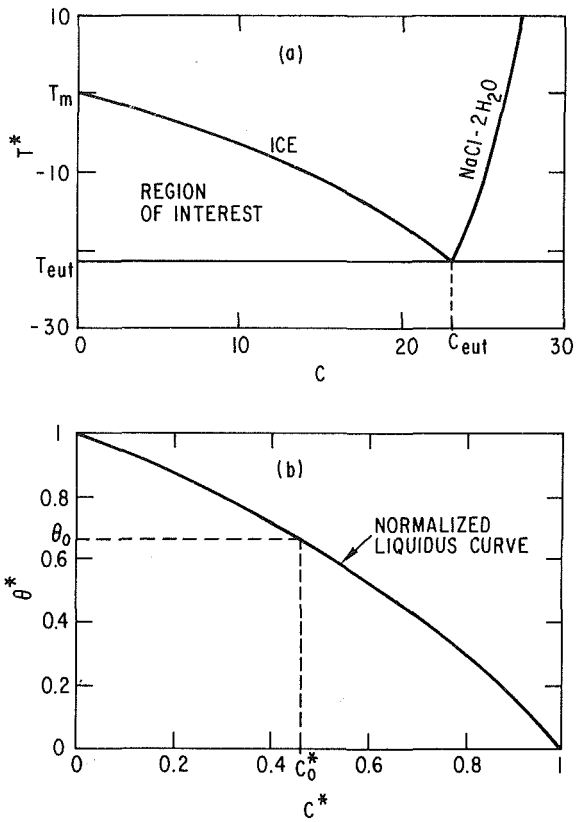

Fig. 8 Treatment of the local phase equilibrium condition: (*a*) a binary eutectic phase diagram, (*b*) the transformed liquidus curve

was obtained by linear regression analysis of data for times < 3000 s. This familiar behavior indicates that the system may be described by a similarity model in this period of growth.

4 Analytical Model

To seek a similarity solution describing the behavior of the two-phase region for the period in which the surface temperature remains constant, we assume both the solid (wall) region and the liquid (solution) region to be semi-infinite (see Fig. 7). The moving liquidus or two-phase front, defined as the location at which the solid fraction is identically zero, is the principal unknown quantity to be determined. The temperature T_o at the moving front is equal to the liquidus temperature which is a function of the local solution concentration. During the selective freezing process, the solution near the surface of the cold ice slab rejects the solvent in a solid form, leaving more dense solution in the two-phase region. The liquid phase is therefore hydrodynamically stable, and there is no convection in the liquid pool. With negligible diffusion mass transfer, the concentration of the solution above the two-phase region remains uniform, having a value of C_o. As the two-phase region grows into the solution, the temperature as well as the solid fraction distribution in the two-phase region will change with time. To investigate the transient behavior of the system, the following simplifying assumptions are made:

(*i*) The volume change during the solidification process is negligible.

(*ii*) The horizontal extent is large enough so that heat transfer is virtually one-dimensional.

(*iii*) The physical properties within the liquid and the solid regions are constant but different from each other.

(*iv*) In the heterogeneous, two-phase region, the physical properties are assumed to be the horizontally averaged values of the two different phases, weighted according to the local solid fraction, f_s.

(*v*) Local thermodynamic equilibrium exists such that the solute concentration and the temperature of the two-phase region follows the liquidus curve of the binary eutectic phase diagram. Thus the temperature distribution can be used to determine the local solid fraction, f_s, distribution directly from the phase diagram. Accordingly, the local rate of change of the solid fraction, which is proportional to the rate at which the latent heat of fusion is liberated within the two-phase region, is a function of the temperature only.

(*vi*) The average thermal diffusivity of the two-phase material is much larger than the mass diffusivity of the solution such that the growth of the two-phase region is controlled mainly by heat conduction.

(*vii*) Both the liquid region and the solid region are semi-infinite in the vertical (or growth) direction.

(*viii*) The material in the solid region is the same as the solid crystals in the two-phase region.[11]

With the foregoing assumptions, the governing equations describing the temperatures of the system are as follows

$$\rho_l C_{pl} \frac{\partial T_l}{\partial t} = k_l \frac{\partial^2 T_l}{\partial x^2}, \; x \geq \delta \tag{1}$$

$$\rho^* C_p^* \frac{\partial T^*}{\partial t} = \frac{\partial}{\partial x}\left(k^* \frac{\partial T^*}{\partial x}\right) + A, \; 0 \leq x \leq \delta \tag{2}$$

$$\rho_s C_{ps} \frac{\partial T_s}{\partial t} = k_s \frac{\partial^2 T_s}{\partial x^2}, \; x \leq 0 \tag{3}$$

where, according to assumption (*v*), the local heat generation A is given by

$$A = \rho_s \lambda \frac{df_s}{dT^*} \frac{\partial T^*}{\partial t} \tag{4}$$

The initial and boundary conditions are

$$t = 0: \; T_l = T_{lo}, \; T_s = T_{so}, \; \delta = 0 \tag{5a}$$

$$x \to \infty: \; T_l = T_{lo} \tag{5b}$$

$$x = \delta: \; T_l = T^* = T_o(C_o) \tag{5c}$$

$$k_l \frac{\partial T_l}{\partial x} = k^* \frac{\partial T^*}{\partial x} \tag{5d}$$

[11] This is merely to minimize the number of the property parameters and is not a limitation of the present model.

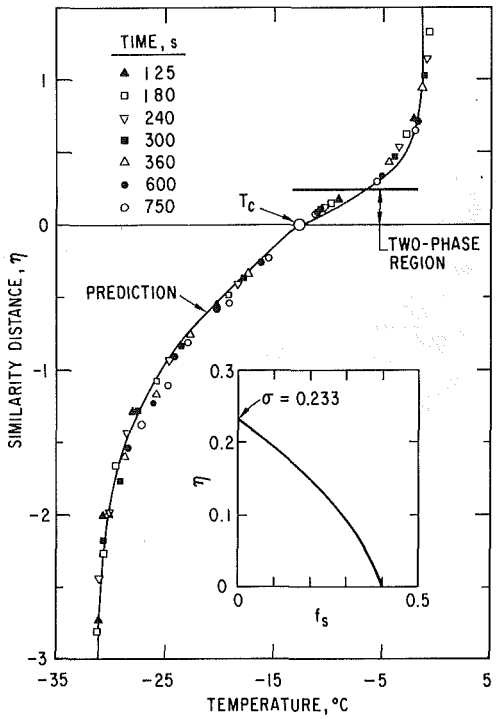

Fig. 9 Comparison of the predicted temperature profiles with experiment for the case of 10 percent NaCl solution initially at −1.5°C on top of ice at −31°C

$$x=0:\ T^*=T_s=T_c \tag{5e}$$

$$k^*\frac{\partial T^*}{\partial x}=k_s\frac{\partial T_s}{\partial x} \tag{5f}$$

$$x\to-\infty:\ T_s=T_{so} \tag{5g}$$

where T_c is the temperature at the surface of the solid region, an unknown to be determined during the course of analysis.[12] We shall assume the values of T_{so}, T_{lo}, and C_o to be such that $T_{\text{eut}} < T_c < T_m$. The two-phase properties are related to f_s according to assumption (*iv*) as follows

$$\rho^*=\left[\frac{1}{\rho_l}+\left(\frac{1}{\rho_s}-\frac{1}{\rho_l}\right)f_s\right]^{-1}\simeq\rho_s\simeq\rho_l \tag{6}$$

$$k^*=\left(\frac{\rho^*}{\rho_l}\right)(1-f_s)k_l+\left(\frac{\rho^*}{\rho_s}\right)f_sk_s\simeq(1-f_s)k_l+f_sk_s \tag{7}$$

$$C_p^*=(1-f_s)C_{pl}+f_sC_{ps} \tag{8}$$

In writing equations (6) and (7), the condition given by assumption (*i*) has been employed. The error introduced by this assumption as well as the error involved in assumption (*vi*), will be examined at the end of the paper.

Assuming local thermodynamic equilibrium to exist, the solid fraction may be related to the temperature of the two-phase region by

$$f_s=\frac{C(T^*)-C_o}{C(T^*)} \tag{9}$$

where $C(T^*)$ is determined by the liquidus curve of the binary eutectic phase diagram[13] as shown in Fig. 8(*a*). A generalized expression can be obtained by invoking the following transformation

$$C^*=C/C_{\text{eut}},\ \theta^*=(T^*-T_{\text{eut}})/(T_m-T_{\text{eut}}) \tag{10}$$

[12] T_c is not determined solely by conduction heat transfer as in the case of two semi-infinite bodies being placed in contact, its value is also dependent on the phase diagram.

[13] The phase diagram of H_2O-NaCl can be found in [17].

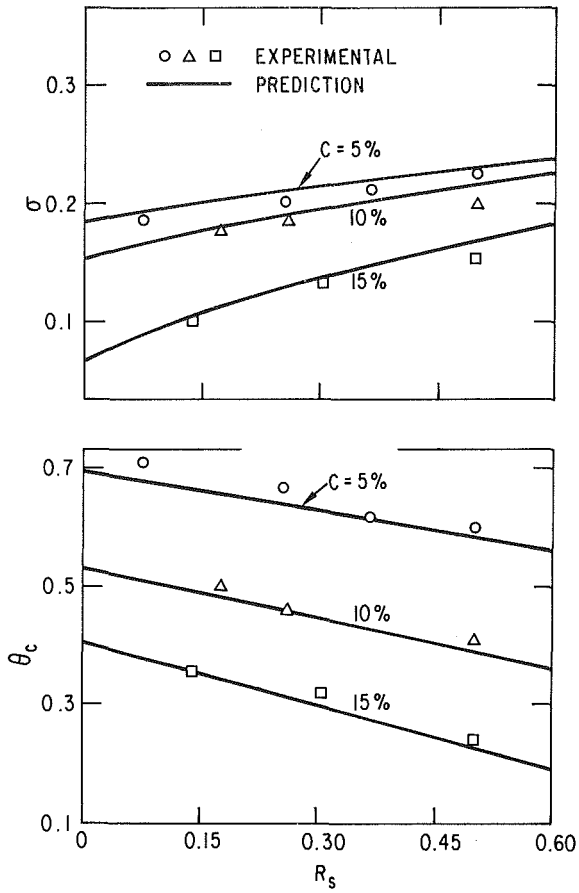

Fig. 10 Effects of the initial ice temperature and solution concentration on the growth of the two-phase region (R_l = 1.0)

where T_m is the melting point of the solid phase. This gives

$$f_s=1-C_o^*C^{*-1} \tag{11}$$

and

$$A=\left(\frac{\rho_s\lambda}{T_m-T_{\text{eut}}}\right)C_o^*C^{*-2}\frac{dC^*}{d\theta^*}\frac{\partial T^*}{\partial t} \tag{12}$$

where $C_o^*=C_o/C_{\text{eut}}$ and $dC^*/d\theta^*$ is a property of the phase diagram (see Fig. 8(*b*) for illustration). Consistent with (10), the following similarity variables are introduced

$$\eta=x/\sqrt{2\alpha_s t},\ \delta=\sigma\sqrt{2\alpha_s t} \tag{13}$$

$$\theta_l=(T_l-T_{\text{eut}})/(T_{lo}-T_{\text{eut}}),\ \theta_s=(T_s-T_{so})/(T_{\text{eut}}-T_{so}) \tag{14}$$

The governing system of differential equations becomes

$$\left(\frac{k_l}{k_s}\right)\left(\frac{C_{ps}}{C_{pl}}\right)\theta_l''+\eta\theta_l'=0,\ \eta\geq\sigma \tag{15}$$

$$[1-(1-k_l/k_s)C_o^*C^{*-1}]\theta^{*\prime\prime}$$

$$+(1-k_l/k_s)C_o^*C^{*-2}\frac{dC^*}{d\theta^*}\theta^{*\prime 2} \tag{16}$$

$$+\left[1-(1-C_{pl}/C_{ps})C_o^*C^{*-1}\right.$$

$$\left.-S\,C_o^*C^{*-2}\frac{dC^*}{d\theta^*}\right]\eta\,\theta^{*\prime}=0,\ 0\leq\eta\leq\sigma$$

$$\theta_s''+\eta\theta_s'=0,\ \eta\leq0 \tag{17}$$

The transformed initial and boundary conditions are

$$\eta\to\infty:\ \sigma_l=1 \tag{18a}$$

$$\eta=\sigma:\ R_l\theta_l=\theta^*=\theta_o(C_o^*) \tag{18b}$$

$$R_l\theta_l' = \theta^{*\prime} \tag{18c}$$

$$\eta = 0:\ \theta^* = R_s(\theta_s - 1) = \theta_c \tag{18d}$$

$$[1-(1-k_l/k_s)C_o^*C^{*-1}]\theta^{*\prime} = R_s\theta_s' \tag{18e}$$

$$\eta \to -\infty:\ \theta_s = 0 \tag{18f}$$

where the superscript prime denotes the total derivative of the dimensionless temperatures with respect to η. The solidification constant σ and the dimensionless surface temperature θ_c defined by $\theta_c = (T_c - T_{\text{eut}})/(T_m - T_{\text{eut}})$, are functions of six dimensionless parameters, namely, k_l/k_s, C_{pl}/C_{ps}, C_o^*, S, R_l, and R_s, where

$$S = \frac{\lambda}{C_{ps}(T_m - T_{\text{eut}})},\ R_l = \frac{T_{lo} - T_{\text{eut}}}{T_m - T_{\text{eut}}},\ R_s = \frac{T_{\text{eut}} - T_{so}}{T_m - T_{\text{eut}}} \tag{19}$$

In terms of σ and θ_c, closed-form solutions can be obtained for equations (15) and (17). These are

$$\theta_l = 1 + \frac{\theta_o/R_l - 1}{\operatorname{erfc}\left[\sigma\sqrt{\frac{1}{2}(k_s/k_l)(C_{pl}/C_{ps})}\right]} \operatorname{erfc}\left[\eta\sqrt{\frac{1}{2}(k_s/k_l)(C_{pl}/C_{ps})}\right]$$

$$\text{for } \eta \geq \sigma \tag{20}$$

$$\theta_s = (1+\theta_c/R_s)[1-\operatorname{erf}(-\eta/\sqrt{2})]$$

$$\text{for } \eta \leq 0 \tag{21}$$

Using equations (20) and (21) in equations (18*b*–18*c*) the boundary conditions for the differential equation governing the temperature of the two-phase region may now be written as

$$\eta = 0:\ \theta^* = \theta_c \tag{22a}$$

$$\theta^{*\prime} = \frac{\sqrt{2}}{\sqrt{\pi}}[1-(1-k_l/k_s)C_o^*C^{*-1}]^{-1}(R_s+\theta_s) \tag{22b}$$

$$\eta = \sigma:\ \theta^* = \theta_o(C_o^*) \tag{22c}$$

$$\theta^{*\prime} = \left[\frac{2}{\pi}\left(\frac{k_s}{k_l}\right)\left(\frac{C_{pl}}{C_{ps}}\right)\right]^{1/2} \frac{(R_l-\theta_o)\exp\left[-\frac{1}{2}\sigma^2(k_s/k_l)(C_{pl}/C_{ps})\right]}{\operatorname{erfc}\left[\sigma\sqrt{\frac{1}{2}(k_s/k_l)(C_{pl}/C_{ps})}\right]} \tag{22d}$$

Equation (16) is solved using the Runge-Kutta method. During the numerical integration, a natural cubic spline function interpolation scheme [18] is employed to evaluate the values of C^* and $dC^*/d\theta^*$ from the phase diagram. The two extra constraints given by equation (22) determine the actual values of σ and θ_c.

5 Analytical Results – Comparison With Experiment

Comparison of the measured and predicted temperature distribution of the system for the case of a 10 percent by weight of NaCl solution initially at $-1.5°C$ on top of an air-bubble-free ice slab initially at $-31°C$ is shown in Fig. 9. Also shown in the figure is the calculated distribution of the solid fraction in the two-phase region. In η-coordinates, the similarity curve is in good agreement with the data obtained at times ranging from 125 to 750 s, indicating that similarity was prevailing in the system during this growing period. The ice slab may be regarded as semi-infinite in extent within this time interval. One important result of the present model is that the measured surface contact temperature T_c is constant during the selective freezing process, and in close agreement with the predicted value of the contact temperature. This result is a direct consequence of the semi-infinite and local-thermodynamic-equilibrium assumptions. Deviations from the similarity solution resulting from the semi-infinite assumption are expected when the thermal wave has penetrated through the finite thickness of the ice slab. The deviations begin first at large negative values of η and, over the time interval from 750 to 2000 s, are manifest at successive, smaller negative values of η. In fact, Fig. 6 shows that T_c remains constant over this time interval. Since these data are beyond the scope of the present analysis, they are not included in Fig. 9.

Although the present model has identified six controlling dimensionless parameters, only three of them are dependent on the initial conditions of the binary eutectic system. These are the dimensionless initial solution concentration, C_o^*, the dimensionless initial solid temperature, R_s, and the dimensionless initial liquid temperature, R_l. The effects of these parameters[14] on the growth of the two-phase region in the H_2O-NaCl system are presented graphically in Figs. 10 and 11. In these figures, the predicted results are represented by the solid lines, whereas the measured results are given by the data points. As expected, a lower contact temperature can be obtained either by increasing the value of R_s, corresponding to a lower initial ice temperature, or by decreasing the value of R_l, corresponding to a lower initial solution temperature. For a given initial solution concentration, this leads to a larger value for the solidification constant, which indicates a faster rate of growth of the two-phase region. Note that the contact temperature is not completely determined by the initial ice and solution temperatures, as would be in the case of sudden contact between a solid and a single-component liquid. By increasing the initial solution concentration, a significantly lower contact temperature can be obtained at fixed values of R_s and R_l.[15] However, an increase in the solution concentration actually results in a decrease in the value of σ, or a decrease in the freezing rate, as shown in Figs. 10 and 11. Physically, this is because the growth of the two-phase region is driven by the temperature difference between the liquidus point and the surface (or contact) temperature. Although an increase in C_o leads to a decrease in θ_c, the corresponding liquidus temperature θ_o is dropping even faster due to freezing-point depression. The net result is a decrease in the driving temperature $(\theta_o - \theta_c)$, which in turn leads to a smaller rate of growth. In general, the model is in good agreement with the experimental data.

A physical explanation of the observed morphology of the two-phase region may now be given. We have shown that the temperature of the two-phase region at the surface of the ice slab is constant and equal to the initial contact temperature as long as the ice slab is effectively semi-infinite. This is valid up to the time when the temperature at the bottom-end of the ice slab begins to rise. During this period, the local solid fraction of the two-phase material at the surface of the ice slab remains constant as required by the thermodynamic equilibrium condition.[16] Therefore, the total number of frazil ice flakes is determined at the outset of selective freezing process by the contact condition. The population of the two-phase region does not increase as the region grows. A schematic representation of the structure of the base of the two-phase region is shown in Fig. 12(*a*). This structure may also be

[14] Due to space limitation, the effects of the other three parameters, i.e., k_l/k_s, C_{pl}/C_{ps}, and S, which have been studied quite extensively in the case of freezing of a pure material [6–9], will not be discussed here.

[15] It should be pointed out that in Fig. 11, the value of $R_l = 0.86$ corresponds to the liquidus point for the 5 percent NaCl solution. Therefore, the solid lines are terminated at this particular location.

[16] This is true provided that the effect of mass transfer is negligible (see the Final Remarks section).

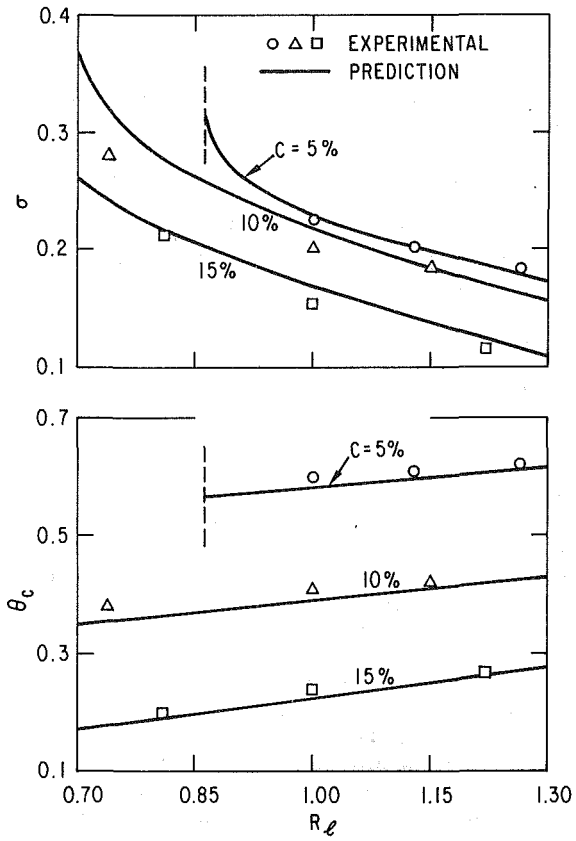

Fig. 11 Effects of the initial solution temperature and solution concentration on the growth of the two-phase region (R_S = 0.5)

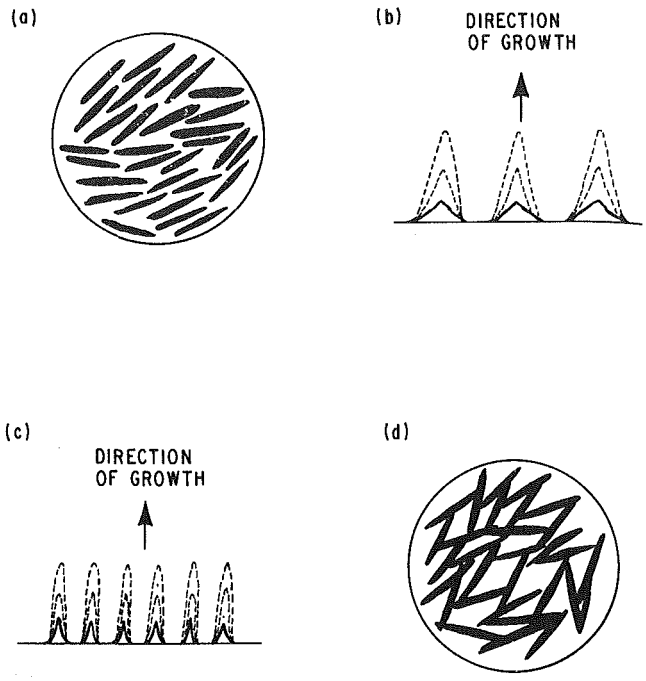

Fig. 12 Illustrative diagrams of the individual ice flake and the morphology of the two-phase region: (a) the base of the two-phase region, (b) growth of the frazil ice flake (front-view), (c) growth of the frazil ice flake (side-view), (d) joining of the ice flakes upon departure from the surface of the original ice slab (top-view)

regarded as a schematic of the nucleation sites for the growth of frazil ice over the surface of the cold ice slab. The individual site is very slender in shape, about 1–4 mm in length and much less than 0.4 mm in width. Since the solid fraction is constant at the surface of the ice slab, the total number, as well as the size of the ice flakes, is fixed at the base. Hence the ice flakes can only grow vertically in the manner illustrated in Fig. 12(*b*) and (*c*). Owing to the adhesive property of frazil ice [15], the ice flakes, once formed, remain strongly attached to the cold ice slab. With the salt solution being much more dense than ice, the most stable configuration of the two-phase region is such that all the ice flakes point up, vertical and parallel to the direction of the gravitational force. In this way, each ice flake remains isolated as it grows. A departure takes place due to the rise of the surface temperature and subsequently melting of the base, the frazil ice flakes quickly reorient themselves and attach to each other as shown in Fig. 12(*d*). The "lumped" ice flake material then floats to the top of the solution pool as an entity. Of course, this is not the case if the population of the two-phase region is very small, since the two adjacent ice flakes are too far apart for them to join together and they simply float up individually.

6 Final Remarks

We have assumed that there is no volume change on freezing and that the effect of mass diffusion is negligible on the selective freezing system. It is desirable to examine these two assumptions based on the results we have obtained.

It is well-known that there is a volumetric expansion during ice formation. The density of water is about 1000 Kg/m^3, whereas the density of ice is only 910 Kg/m^3. Therefore, the velocity induced by the selective freezing process is

$$V=\left(\frac{1}{\rho_s}-\frac{1}{\rho_l}\right)\int_0^x \rho^*\frac{\partial f_s}{\partial t}dx \tag{23}$$

where $(1/\rho_s - 1/\rho_l) \sim 0.1$ and $\rho^* \sim 1.0$ will be assumed. The error introduced to the solution by neglecting this convection effect is

$$E_v=\frac{V\partial T^*/\partial x}{\partial T^*/\partial t}=\frac{V}{\eta}\sqrt{\frac{2t}{\alpha_s}} \tag{24}$$

As an order of magnitude estimate, we have

$$O(V)=0.1\int_0^\delta \frac{\partial f_s}{\partial t}dx=0.1\sqrt{\frac{\alpha_s}{2t}}\int_0^\sigma f_s d\eta \tag{25}$$

Taking $O(\eta)\sim\sigma$ in equation (24) and $f_s \sim 0.5\ (1-\eta/\sigma)$ in equation (25) as indicated by our results, we obtain $O(E_v)\sim 0.025$, which is indeed negligible.

To estimate the error introduced by omitting the mass diffusion effect, we have to determine the magnitude of the ratio

$$E_m=\frac{D\partial^2 C/\partial x^2}{(dC/dT^*)(\partial T^*/\partial t)} \tag{26}$$

In terms of the similarity variables, we obtain

$$E_m=\left(\frac{D}{\alpha_s}\right)\frac{d^2C^*/d\eta^2}{\eta dC^*/d\eta} \tag{27}$$

Hence

$$O(E_m)\sim\frac{D}{\alpha_s}\frac{\Delta C^*/\sigma^2}{\sigma\Delta C^*/\sigma}=\frac{1}{\sigma^2}\left(\frac{D}{\alpha_s}\right) \tag{28}$$

where $\Delta C^* = C_o^* - C^*(\theta_c)$ is the concentration difference across the two-phase region. In our case, we have $\sigma \sim 0.2$ and $D/\alpha_s \sim 0.001$ for the NaCl-H_2O system. Thus $O(E_m)\sim 0.025$ which is again negligible. The mass diffusion effect is important only if the freezing rate is very small (i.e., $\sigma << 1$) or the mass diffusivity is about the same order as the thermal

diffusivity. This restriction on the material properties can be regarded as a limitation of the model.

Acknowledgments

The authors wish to thank Karen Jenicek for typing the manuscript. This work was performed at Argonne National Laboratory under the auspices of the U.S. Department of Energy.

References

1 Elliot, R., "Eutectic Solidification," *Int. Metals Reviews*, Vol. 219, 1977, pp. 161–186.

2 O'Callaghan, M. G., "An Analysis of the Heat and Mass Transport During the Freezing of Biomaterials," Ph.D. thesis, Massachusetts Institute of Technology, Cambridge, Mass., 1978.

3 Weiss, P. A., "Desalination by Freezing," *Practice of Desalination*, edited by R. Bakish, Noyes Data Corp., N.J., 1973, pp. 260–270.

4 Cheung, F. B., "Eutectic Penetration Model," *U.S. Fast Reactor Safety Program Report*, ANL/TMC 82-1, 1982, pp. 184–185.

5 Fang, L. J., Cheung, F. B., Linehan, J. H., and Pedersen, D. R., "An Experimental Study of the Mechanisms of Melt Penetration of Materials With a Binary Eutectic Phase Diagram," *Trans. Am. Nucl. Soc.*, Vol. 43, 1982, pp. 518–519.

6 Bankoff, S. G., "Heat Conduction or Diffusion with Change of Phase," *Adv. Chem. Eng.*, Vol. 5, 1964, pp. 75–150.

7 Muehlbauer, J. C., and Sunderland, J. E., "Heat Conduction with Freezing or Melting," *Appl. Mech. Rev.*, Vol. 18, 1965, pp. 951–959.

8 Wilson, D. G., Solomon, A. D., and Boggs, P. T., *Moving Boundary Problems*, Academic Press, New York, 1978.

9 Cheung, F. B., and Epstein, M., "Solidification and Melting in Fluid Flow," *Adv. Transport Process*, Vol. III, Wiley Eastern, New York, 1984, pp. 35–118.

10 Tien, R. H., and Geiger, G. E., "A Heat Transfer Analysis of the Solidification of a Binary Eutectic System," ASME JOURNAL OF HEAT TRANSFER, Vol. 89, 1967, pp. 230–234.

11 Cho, S. H., and Sunderland, J. E., "Heat Conduction Problems With Melting or Freezing," ASME JOURNAL OF HEAT TRANSFER, Vol. 91, 1969, pp. 421–426.

12 Muehlbauer, J. C., Hatcher, J. D., Lyons, D. W., and Sunderland, J. E., "Transient Heat Transfer Analysis of Alloy Solidification," ASME JOURNAL OF HEAT TRANSFER, Vol. 95, 1973, pp. 324–331.

13 Hayashi, Y., and Komori, T., "Investigation of Freezing of Salt Solutions in Cells," JOURNAL OF HEAT TRANSFER, Vol. 101, 1979, pp. 459–464.

14 O'Callaghan, M. G., Cravalho, E. G., and Huggins, C. E., "An Analysis of the Heat and Solute Transport During Solidification of an Aqueous Binary Solution," *Int. J. Heat Mass Transfer*, Vol. 25, 1982, pp. 553–573.

15 Martin, S., "Frazil Ice in Rivers and Oceans," *Ann. Review Fluid Mech.*, Vol. 13, 1981, pp. 379–398.

16 Denk, E. G., Jr., and Botsaris, G. D., "Fundamental Studies in Secondary Nucleation from Solution," *J. Crystal Growth*, Vol. 13/14, 1972, pp. 493–499.

17 Rose, J., "Phase Equilibria," *Dynamic Physical Chemistry*, John Wiley & Sons, New York, 1961, pp. 406–410.

18 Ahlberg, J. H., Nilson, E. N., and Walsh, J. L., "Best Approximation and Convergence Properties of Higher-order Spline Approximations," *J. Math. Mech.*, Vol. 14, 1965, pp. 231–244.

Effect of Inclination on Freezing in a Sealed Cylindrical Capsule

E. D. Larson

E. M. Sparrow
Fellow ASME

Department of Mechanical Engineering,
University of Minnesota,
Minneapolis, Minn. 55455

Experiments were performed to study the heat transfer processes that occur during freezing inside of a sealed cylindrical capsule when the inclination of the capsule is varied parametrically from vertical to horizontal. The phase-change medium was 99 percent pure n-eicosane paraffin. It was found that the amount of mass that solidified during a given freezing period was insensitive to the inclination of the capsule, as was the amount of energy extracted from the capsule. Only highly localized quantities such as the local frozen layer thickness reflected the inclination of the cylinder. Parametric variations were also performed for the degree of subcooling of the capsule wall below the fusion temperature and for the degree of superheating of the liquid phase at the onset of freezing. These variations facilitated the identification of the relative importance of the latent and sensible energies to the total extracted energy.

Introduction

This paper describes experiments undertaken to study the fundamental heat transfer processes that occur during freezing of a phase-change material contained in an externally cooled cylindrical capsule. The special feature of the work was to investigate the effect of capsule inclination. Since natural convection in the liquid phase is the only inclination-sensitive mode of heat transfer that participates in the freezing process, natural convection will be of special concern throughout this presentation.

In recent years, under the impetus of the energy storage application, many aspects of melting and freezing have been investigated both experimentally and computationally. Two recent publications [1, 2] survey much of such work that has been done in relation to thermal energy storage systems, while [3, 4] review much of the freezing work performed in the field of metallurgy. Several other literature review articles are identified in the thesis [5] from which this paper is taken.

Although an extensive literature exists on the subject of phase-change energy storage, experimental investigations of encapsulated freezing are rather spare. Freezing in vertical and horizontal tubes, respectively, has been investigated through experimentation in [6] and [7, 8]. Owing to differences in the phase-change media and in the experimental conditions, no conclusions can be drawn about the effect of orientation from these experiments.

The present paper constitutes a systematic study of fully encapsulated freezing in which parametric variations are made of the capsule inclination, the initial superheating of the liquid phase, and the degree of subcooling of the capsule wall relative to the fusion temperature. The experiments were performed using 99 percent pure n-eicosane paraffin (with a fusion temperature of 36.3°C) as the phase-change material. Freezing of the paraffin was initiated and maintained by a step-change decrease in the capsule wall temperature.

Three values of each of the two thermal parameters (liquid superheating and wall subcooling) were used, resulting in nine different thermal conditions under which the effects of inclination were studied. For the condition of zero initial liquid superheating, no natural convection exists during freezing. Because of this, the results for no initial superheating serve as a baseline against which the with-superheating results are compared.

Data collected during the experiments included the instantaneous frozen mass, local solid-layer thickness distributions, and the liquid-phase bulk temperature, all as functions of time and of the three aforementioned parameters. In addition, all of the components of the total energy extracted during freezing (i.e., latent and sensible) are evaluated.

A supplementary, simplified numerical model was developed for purposes of comparison to the experiments. In the model, conduction constitutes the sole liquid-phase heat transfer mechanism, thereby providing for an interesting and enlightening comparison of results.

Experimental Apparatus

The main components of the experimental apparatus included the cylindrical capsule within which the freezing occurred, a constant-temperature water bath in which the capsule was situated during the freezing experiments, and a second constant-temperature water bath used to establish the thermal state of the capsule and its contents (i.e., the liquid phase of the phase-change medium) prior to the initiation of a freezing experiment.

The paraffin-containment capsule was designed to facilitate the intact removal of the frozen specimen at the conclusion of a data run. To this end, the capsule was made of two identical troughlike sections. The respective troughs were semicylinders which, when mated, formed a cylinder in which the paraffin was contained. In the practical realization of this design concept, it was convenient to fabricate each section from a rectangular bar into which a semicylindrical trough was machined with a ball end mill. The ends of the trough were closed by solder-attached blocks. When assembled, the two sections created a right cylindrical cavity 18.73 cm in length and 3.81 cm in diameter (approximately a 5:1 aspect ratio). Because the capsule was a cylinder within a rectangular bar, its wall thickness varied from 0.58 to 1.69 cm.

Brass was chosen as the capsule material because of its good machinability and its high thermal diffusivity, which was required to attain the desired rapid temperature response at the inner wall of the capsule. The rapidity and uniformity of this response was found to be satisfactory by monitoring the outputs of six thermocouples situated at the inner wall.

Two apertures were provided at one end of the capsule to allow the introduction of liquid paraffin prior to the data run or the vacuum extraction of unfrozen liquid at the end of the run. The apertures were sealed during the freezing period of a data run.

To establish a uniform initial temperature ($= T_o$) of the liquid paraffin at or above the fusion value, the fully charged capsule was left to equilibrate in a temperature-controlled,

Contributed by the Heat Transfer Division for publication in the JOURNAL OF HEAT TRANSFER. Manuscript received by the Heat Transfer Division August 25, 1983.

agitated hot water bath. Once equilibrated, the capsule was transferred to a large, highly agitated water bath maintained at a temperature T_w below the fusion value. This bath was continuously supplied with water at a temperature slightly below T_w by a separate 2.3 kW capacity chilling unit. A heater-equipped controller was used to maintain the bath temperature at T_w. Vigorous agitation was used to obtain as high a heat transfer coefficient as possible over the outside surface of the capsule.

To support the capsule in the cold water bath, a variable-inclination stand was employed. The stand was designed to securely hold the capsule, not to interfere with the water flow, and to have minimal thermal contact with the capsule. With appropriate adjustments of the stand, the capsule could be positioned with its axis at any angle from the horizontal to the vertical.

A vacuuming device was used to extract the residual liquid paraffin from inside the capsule at the end of a data run. Access to the inside of the capsule was gained through one of the apertures described earlier. Special care was taken during the extraction procedure to avoid damaging the surface of the frozen specimen.

All thermocouple emfs were read and recorded by a Fluke model 2240B digital data logger with a resolution of 1 μV. The readings included water bath temperatures, inner and outer wall temperatures of the capsule, and liquid-phase bulk temperatures. Mass measurements were made with a triple-beam balance which had a resolution of 0.1 g (smallest mass measurement ~ 35 g). A dial-gage-equipped caliper with a resolution of 0.001 in. was used for the measurement of the thickness of the frozen layer (smallest thickness measurement ~ 0.1 in.).

Experimental Procedure

A data run was started by submerging the empty capsule in the hot water bath and then introducing the liquid paraffin via an extension tube connected to one of the apertures. A similar tube connected to the other aperture allowed the displaced air to escape. Once the capsule was completely filled, a minimum period of 30 min was allowed for the paraffin to come to thermal equilibrium with the water bath. After that, the capsule was then briefly removed from the hot bath, the apertures capped, and the capsule returned to the bath for about 10 min for final equilibration. Then, the capsule was transferred from the hot water bath to the cold water bath and placed securely on the variable-inclination support stand. This transfer, which was accomplished in 5 s, marked the initiation of the freezing process, which was allowed to continue for a preselected time.

Two alternative run-termination procedures were used, depending on the data desired. The first involved rapid removal of the capsule from the cold bath, opening one of the apertures, and entering the inner liquid core of the capsule with the vacuuming device to withdraw the residual liquid. The capsule was then opened, the solid paraffin sample carefully removed, and its mass measured. The sample was then sectioned perpendicular to its axis at nine equally spaced axial locations. At each axial station, measurements of the solid-layer thickness were made at eight uniformly spaced circumferential locations using the aforementioned caliper. Thickness measurements for data runs corresponding to the same thermal conditions but having different durations provided a picture of the timewise movement of the solid-liquid interface.

The other end-of-run measurement sequence was used to obtain the bulk temperature of the residual liquid. The initial steps of this run-ending procedure were identical to the foregoing, but instead of extracting the liquid paraffin with the vacuuming device, a thin, stiff nylon rod fitted with two thermocouples was used first to thoroughly mix the residual liquid and then to record its bulk temperature.

Each of these two types of data runs were performed for all combinations of the inclination angle and the thermal parameters. In supplementary data runs, solidification was allowed to go to completion. By weighing the sample obtained in this manner, the total possible frozen mass M_T could be ascertained. In the presentation of results, M_T will serve as a reference mass.

Data Reduction

In the presentation of results, several dimensionless quantities are used. Two Stefan numbers, the solid-phase Stefan number Ste_S and the liquid-phase Stefan number Ste_L, are evaluated as

$$\mathrm{Ste}_S = c_S(T^* - T_w)/\lambda, \mathrm{Ste}_L = c_L(T_o - T^*)/\lambda \quad (1)$$

Note that Ste_L is based on the temperature T_o of the liquid phase at the beginning of the freezing period. When the liquid is initially at the fusion temperature T^*, then $\mathrm{Ste}_L = 0$. Thus Ste_L serves as a dimensionless measure of the initial liquid superheat. Also Ste_S is a measure of the temperature difference across the frozen layer. The duration t of the freezing period is expressed in dimensionless terms by means of the Fourier number Fo

$$\mathrm{Fo} = \alpha_S t/r_w^2 \quad (2)$$

The local solid layer thicknesses δ will be presented as such and are also employed to calculate two other quantities: δ and

Nomenclature

c_L = liquid-phase specific heat
c_S = solid-phase specific heat
E_{S1} = sensible energy release from subcooled solid
E_{S2} = sensible energy release from frozen liquid
E_{S3} = sensible energy release from unfrozen liquid
E_λ = latent energy release
$E_{\lambda,\max}$ = maximum possible latent energy release
Fo = Fourier number, $\alpha_S t/r_w^2$
k = thermal conductivity
L = cylinder length
M_S = mass solidified during period from $t = 0$ to $t = t$
M_T = total possible solidified mass
M' = circumferentially integrated frozen mass per unit length
r = radial coordinate
r_w = radius of cylinder wall
r_δ = local radial distance to solid-liquid interface
Ste_L = initial liquid-phase Stefan number, $c_L(T_0 - T^*)/\lambda$
Ste_S = solid-phase Stefan number, $c_S(T^* - T_w)/\lambda$
T = temperature
$T_{b,L}$ = bulk temperature of liquid
$T_{b,S}$ = bulk temperature of solid
T_o = initial temperature of liquid
T_w = cylinder wall temperature
T^* = fusion temperature
t = time
X = axial coordinate measured from lower end of cylinder
α_S = thermal diffusivity of solid
δ = local frozen layer thickness
$\bar{\delta}$ = spatial-average frozen layer thickness
θ = angular coordinate
λ = latent heat of fusion
ρ_S = density of solid

M'. For any time t, the δ values at all circumferential and axial measurement points were averaged to yield $\bar{\delta}$. The quantity M' is the circumferentially integrated frozen mass per unit axial length. At any given axial station where eight uniformly spaced measurements of the solid-layer thickness were made, M' was determined from

$$M' = \int_0^{2\pi} \int_{r_\delta}^{r_w} \rho_S r dr d\theta \tag{3}$$

where r_w is the cylinder radius and r_δ, which varies around the circumference, is the distance from the cylinder axis to the solid-liquid interface. The quantity ρ_S is the density of the solid phase. After integration over r and nondimensionalization

$$M'/\rho_S \pi r_w^2 = (1/2\pi)\int_0^{2\pi} [1-(r_\delta/r_w)^2]d\theta \tag{4}$$

Simpson's rule integration was used to obtain numerical results.

The total energy released during freezing was calculated as the sum of four individual components, one of which was a latent energy and three of which were sensible components.

The latent component is designated E_λ. From the mass measurement, the amount of mass M_S solidified from $t = 0$ to $t = t$ was known, so that

$$E_\lambda = \lambda M_S \tag{5}$$

where λ is the latent heat of fusion of the paraffin.

The second energy component, designated E_{S1}, was that associated with the subcooling of the solidified paraffin. The specific heat of the solid is taken as constant, since no information is available regarding its temperature dependence, so that

$$E_{S1} = M_S c_S (T^* - T_{b,S}) \tag{6}$$

where c_S is the specific heat of the solid, and $T_{b,S}$ is the bulk temperature of the solid given by

$$T_{b,S} = \int_{r_\delta}^{r_w} T(r)\rho_S 2\pi r dr / \int_{r_\delta}^{r_w} \rho_S 2\pi r dr \tag{7}$$

The temperature distribution $T(r)$ was regarded as depending only on the radius r (end effects are considered negligible) and was obtained by assuming the existence of an instantaneous steady state in the solid, with account being taken of the temperature dependence of the thermal conductivity [9]. Details relating to the determination of $T_{b,S}$ are available in [5].

Two components of sensible energy released from the liquid were calculated. E_{S2} is the energy release associated with the liquid which solidified during the data run, while E_{S3} is the energy released by liquid which did not freeze during the run. The first of these components is given by

$$E_{S2} = M_S \int_{T^*}^{T_o} c_L dT \tag{8}$$

where c_L is the liquid specific heat. A linear fit of the specific heat data given in [10] was used in equation (8). The component E_{S3} is

$$E_{S3} = (M_T - M_S)\int_{T_{b,L}}^{T_o} c_L dT \tag{9}$$

where M_T is the reference mass, and $T_{b,L}$ is the measured bulk temperature of the liquid at the end of the data run.

To allow easy comparison of the four energy components, they were normalized by a constant – the maximum possible latent energy release $E_{\lambda,\max}$, which is given by

$$E_{\lambda,\max} = \lambda M_T \tag{10}$$

Results and Discussion

Effects of Cylinder Inclination Angle. In the initial experiments, consideration was given to cylinder inclination angles of 0 (horizontal), 45, 60, and 90 deg. However, during the course of the experiments, it was found that three angles, 0, 45, and 90 deg, were sufficient to characterize the effects of inclination. Therefore, very little 60 deg data were collected, and this will be reflected in the presentation of results.

Three values each of the initial liquid superheat ($T_o - T^*$) and the subcooling imposed on the capsule wall ($T^* - T_w$) were used. In the presentation, these thermal parameters are expressed in terms of Stefan numbers. Table 1 gives the values of the Stefan numbers and their associated temperature differences.

Figure 1 shows the effect of the cylinder inclination angle on the amount of mass M_S solidified between $t = 0$ and $t = t$, where the ratio M_S/M_T is plotted as a function of the dimensionless freezing time FoSte_S for four different thermal

Table 1 Temperature differences and associated Stefan numbers

$(T^* - T_w)$	Ste_S	$(T_o - T^*)$	Ste_L
6.0°C	0.047	0°C	0
20.0	0.155	22.2	0.202
30.3	0.235	44.4	0.413

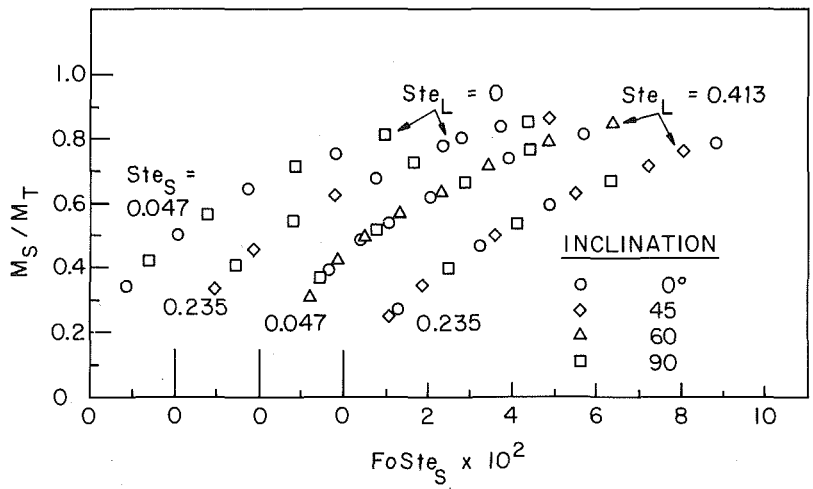

Fig. 1 Effect of cylinder inclination on the frozen mass

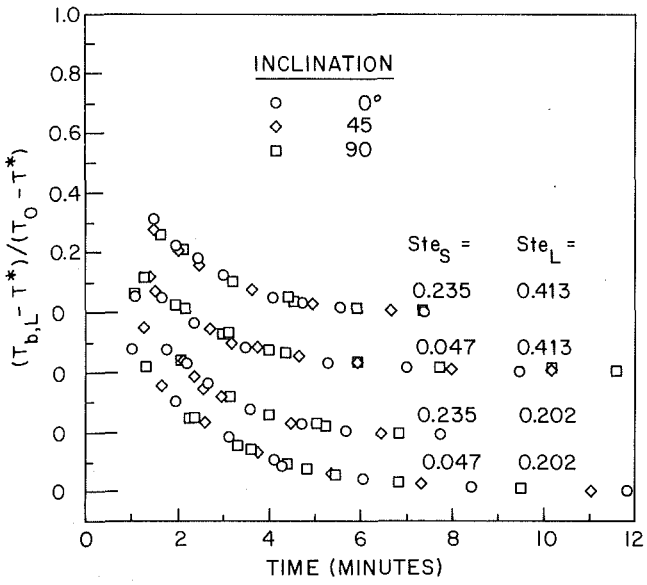

Fig. 2 Effect of cylinder inclination on the decay of the liquid superheat

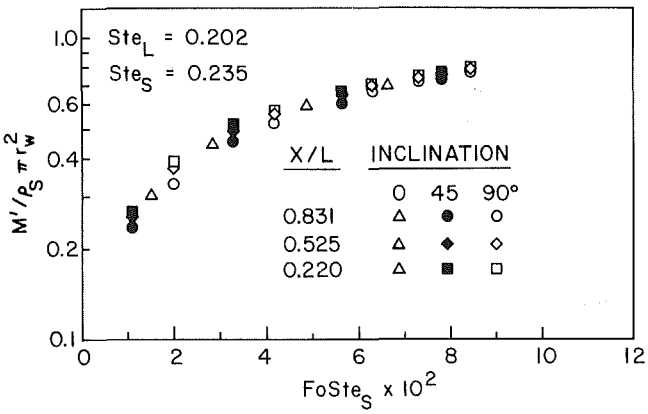

Fig. 3 Effect of cylinder inclination on the circumferentially integrated frozen mass per unit length

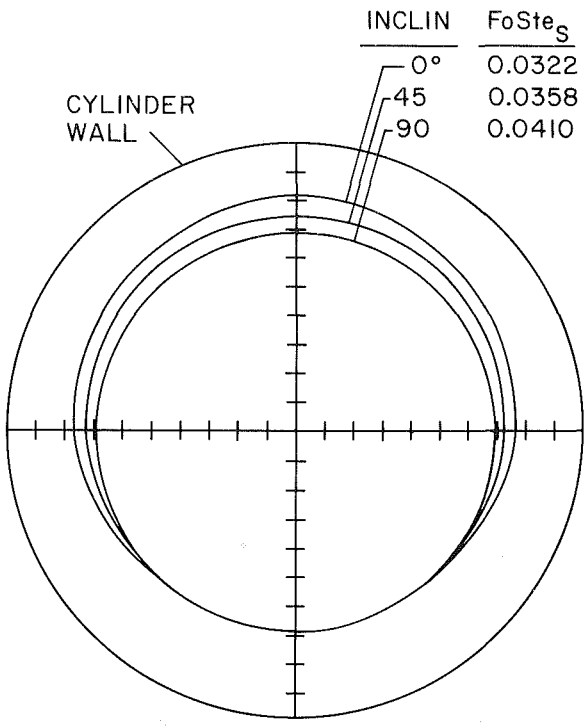

Fig. 4 Effect of cylinder inclination on the local solid-layer thickness (X/L = 0.525, Ste_S = 0.235, Ste_L = 0.413)

conditions. The choice of $FoSte_S$ as the time variable was based on its effectiveness as a correlating group in the theory of heat conduction with change of phase. The property values in $FoSte_S$ were evaluated at the fusion temperature of solid n-eicosane. It was found tht this choice of reference temperature gave the tightest grouping of the data for the baseline cases ($Ste_L = 0$).

Attention is first directed to the two sets of data for Ste_L = 0. For this case, there is no initial superheating of the liquid paraffin, and no natural convection exists in the liquid phase during freezing. Consequently, no effect of cylinder inclination is expected, and the data for both Ste_S cases confirm this expectation.

The other two sets of data in the figure are for Ste_L = 0.413 (the largest Ste_L investigated here). Since $T_o > T^*$, natural convection occurs in the liquid phase during some part of the freezing period. Since inclination is expected to affect the natural convection, it might also be expected that the freezing process would be affected. However, the two sets of data in Fig. 1 for Ste_L = 0.413 show no dependence on inclination angle. An explanation of this unexpected behavior will emerge as additional data are presented.

Figure 2 was prepared to show the dependence of liquid bulk temperature on cylinder inclination angle. The instantaneous bulk-to-fusion temperature difference in the liquid, normalized by the initial superheat, is plotted against dimensional time. $FoSte_S$, which pertains to heat conduction in a freezing solid, is not an appropriate time variable here, since the data of Fig. 2 relate to convection/conduction processes in the liquid. The figure contains four sets of data encompassing the two levels of superheating and the smallest and largest subcoolings of the capsule wall. As in Fig. 1, a somewhat surprising result is displayed: for all of the four thermal conditions, the instantaneous liquid superheat is independent of inclination.

The frozen mass (Fig. 1) and the instantaneous liquid superheat (Fig. 2) are both global quantities in that they represent averages over the entire capsule. Consequently, they mask possible local variations which might occur with changes of inclination. Attention is now turned to quantities with more local content.

Consider first the circumferentially integrated frozen mass per unit length M'. This is a quasi-local quantity which depends on the axial coordinate X measured along the axis of the cylinder from the lower end. Representative results for M' are presented in Fig. 3 at three axial stations, X/L = 0.220, 0.525, and 0.831, where end effects are not present (L = axial length of cylinder). The results correspond to the maximum initial superheat.

It is useful to examine the M' results for a fixed inclination at any given $FoSte_S$ and to note any variations with X/L. As can be seen, for example, in the 45 deg case, M' decreases with increasing X/L, indicating a solid-layer thickness decrease with X/L. A similar trend is observed for the 90 deg inclination angle (vertical case). The existence of these axial thickness variations clearly indicates the presence of liquid-phase natural convection during freezing. For the horizontal orientation (0 deg), M' is independent of X, since the natural convection gives rise to circumferential thickness variations but not to axial variations.

It may also be noted in Fig. 3 that with increasing time ($FoSte_S$), the variation of M' with X/L decreases. This is because in the period after natural convection has ceased, the

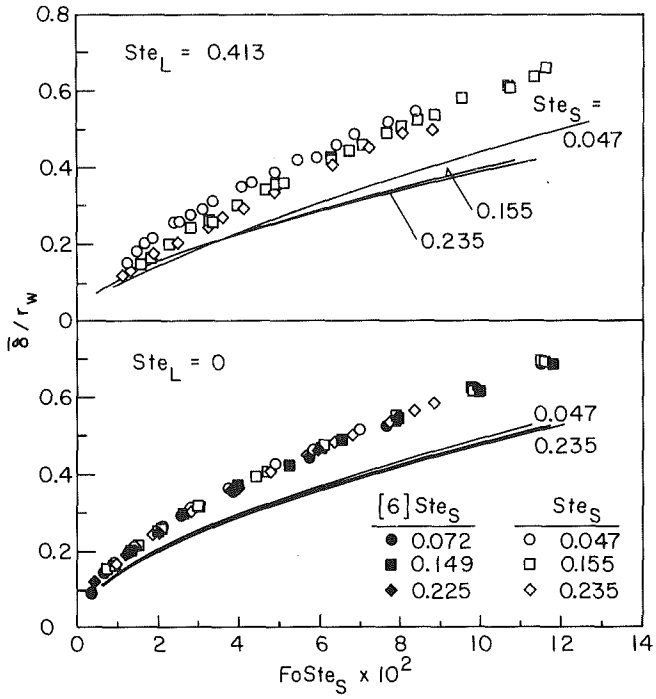

Fig. 5 Comparison of experimental and numerical results for the frozen layer thickness

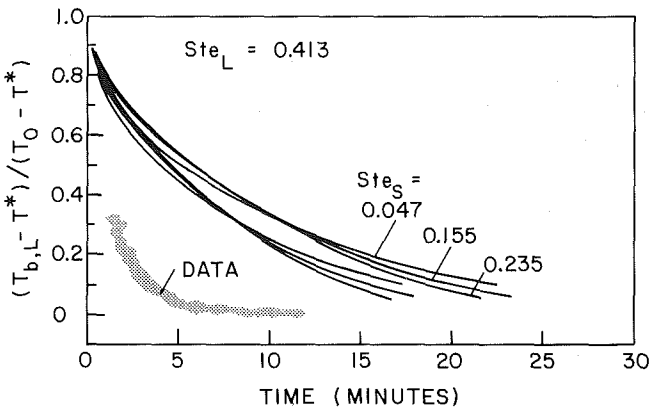

Fig. 6 Comparison of experimental and numerical results for the decay of the liquid superheat

thinner portions of the solid layer grow more rapidly than the thicker portions since they offer less resistance to heat flow.

Although natural convection has been shown to be present, the M' data for a fixed X/L in Fig. 3, e.g., $X/L = 0.525$, indicate little variation with inclination. There does appear to be a distinct variation between the 0 deg case and either of the other two, but no consistent pattern among all three cases emerges. The absence of strong inclination-related effects in Fig. 3 may be due, in part, to the circumferential averaging that occurs in the evaluation of M'.

The most localized data available are the local solid-layer thicknesses, a sampling of which is presented in Fig. 4. The figure is a polar plot showing the circumferential distribution of the solid-layer thickness for three different inclinations at fixed Ste_S, Ste_L, X/L, and for as nearly the same FoSte_S values as were available.

Figure 4 shows that the most localized data do reflect the effects of inclination, thereby confirming that such effects exist. However, as already established, these effects are washed out for spatial-averaged quantities.

A Comparison With Computation. To help assess the role of natural convection in the freezing process, a one-dimensional (i.e., radial) constant-properties, conduction-based (i.e., no convection) numerical model was developed to provide predictions for comparison with the experimental data. The key feature of the numerical solution method was the immobilization of the moving boundary between the solid and liquid regions. The finite difference equations expressing energy conservation in the solid and liquid regions were formulated implicitly, while the interface energy balance was treated explicitly. Details are available in [5] and [11].

In Fig. 5, numerical and experimental results for the growth of the solid layer thickness are compared. Each data point represents the average of the locally measured thicknesses corresponding to a given freezing time (i.e., given FoSte_S). The average does not include any points in the end-affected regions of the frozen sample.

The figure consists of two graphs, the lower of which is for zero superheat ($\mathrm{Ste}_L = 0$). In this graph, there are two groups of experimental data. The open symbols represent data from the present study, while the blackened symbols are from [6] and correspond to freezing in an open-top vertical cylinder. The agreement between the two sets of experimental data is excellent. For $\mathrm{Ste}_L = 0$, no natural convection is present, and it might be expected that the numerical results would predict the experimental values fairly accurately. However, the numerical results consistently fall about 25 percent below the measured values at any FoSte_S value. The most likely cause of the discrepancy is the uncertainty in the available values of the thermal conductivity used to evaluate FoSte_S for the experimental data. Reference [9] suggests a 20–30 percent uncertainty in the conductivity values. Although the numerical and experimental results are not in quantitative agreement, they are in excellent trendwise agreement.

In support of the contention that the aforementioned discrepancy is not due to errors in the numerical work, it may be noted that the same computed predictions have been obtained independently by three different investigators (present, [6], and [12]) using different schemes.

In the upper portion of Fig. 5, with $\mathrm{Ste}_L = 0.413$, somewhat greater deviations between the computed and measured results appear, although the trends are still similar. The lower predicted solid layer thicknesses and smaller growth rates indicate that in the conduction-controlled numerical model the liquid is maintaining a role in the energy release for a longer period of time than occurs in reality.

This is more clearly seen in Fig. 6, which shows a comparison of the calculated and measured timewise decay of the liquid superheat. Two sets of numerical results are shown. For the upper set, values of dimensional time were obtained from the dimensionless numerical results by using the thermophysical property values used in the evaluation of FoSte_S for the experimental data. For the lower set, the thermal conductivity value was increased by 30 percent. This increase, which is within the accuracy range specified in [9], was selected because it forces a near fit of the computational and experimental results in the lower graph of Fig. 5. Even with the increased thermal conductivity, the predicted decay rate is much slower than the measured rate, indicating that pure condition in the liquid is playing a minor role in comparison to natural convection.

Effects of the Thermal Parameters. Attention is now directed to a discussion of the effects of the two thermal parameters Ste_S and Ste_L. Since cylinder inclination was found to have a negligible effect on the global frozen mass and the liquid bulk temperature, the following presentation is simplified by eliminating the identification of data according to inclination. Figure 7 shows the effect of Ste_S on the frozen

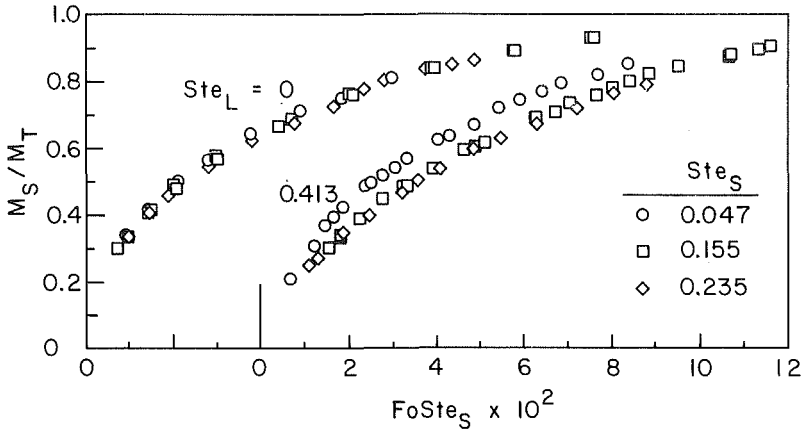

Fig. 7 Effect of Ste_S on the frozen mass

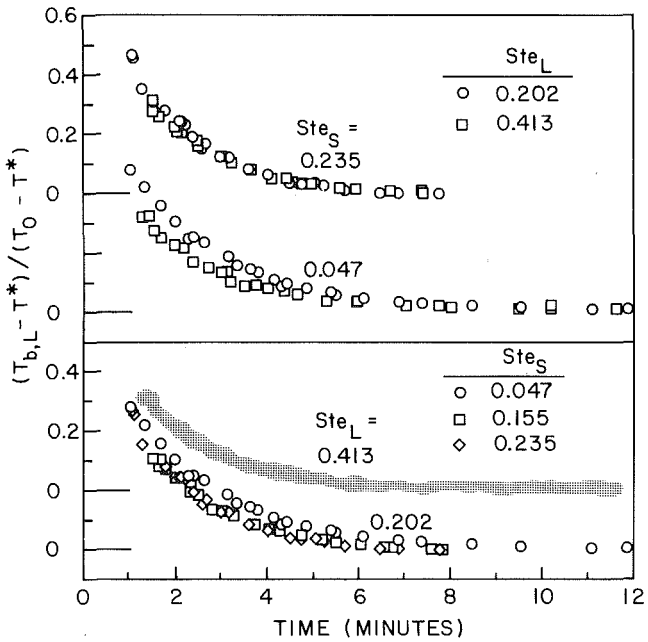

Fig. 8 Effect of Ste_S and Ste_L on the decay of the liquid superheat

mass, both in the absence and in the presence of liquid superheating. For the former (i.e., $Ste_L = 0$), there is only a slight dependence of M_S/M_T on Ste_S, with M_S/M_T increasing with decreasing values of Ste_S as predicted by the theory of conduction phase change. When there is superheating (e.g., $Ste_L = 0.413$), the natural convection which occurs during freezing causes the M_S/M_T data for different Ste_S to separate.

With regard to the spreading of the data in the $Ste_L = 0.413$ case, it is well established that the existence of liquid superheat will retard the growth of the frozen layer. In particular, the larger the value of $FoSte_S$ to which liquid superheat persists, the smaller will be the frozen mass (at a given value of $FoSte_S$). This reasoning can be quantified with the aid of Fig. 8, which presents results for the timewise decay of the liquid superheat. Note in Fig. 8 that for the $Ste_L = 0.413$ case, the superheat persists to about the same time for all three Ste_S values, which means that the superheat persists to larger values of $FoSte_S$ at larger Ste_S. According to Fig. 7, larger Ste_S corresponds to smaller M_S/M_T at a given $FoSte_S$, thereby verifying the foregoing assertion.

The variation of frozen mass with Ste_L is examined with the aid of Fig. 9. Data for the three Ste_L cases are plotted there for fixed values of $Ste_S = 0.047$ and 0.235. For both Ste_S, a characteristic trend is noted: at small values of $FoSte_S$, the data for the various Ste_L are fairly well separated, but at larger values, the data begin to converge. This behavior is more apparent in the $Ste_S = 0.047$ case than in the 0.235 case.

For the $Ste_L = 0$ case, no liquid superheating exists, resulting in the largest frozen mass production, particularly at small values of $FoSte_S$. In the cases for which $Ste_L > 0$, the frozen mass decreases in the order of increasing Ste_L. This is most apparent at smaller values of $FoSte_S$, where the liquid sensible energy contribution is greatest. After the superheating decays, the rate of freezing will be greater for the solid with the thinnest frozen layer, which, as noted in the foregoing, is characterized by the largest Ste_L. The upper portion of Fig. 8 shows that the dissipation of the superheat is completed at about the same time for a fixed value of Ste_S, i.e., at the same $FoSte_S$.

Energy Accounting. The final two figures show the results of an energy accounting analysis made for four representative thermal conditions. As discussed in detail in the Data Reduction section, the total energy extracted consists of a single latent and three sensible components. These components and their sum are presented in Figs. 10 and 11. In these figures, E_λ represents the latent energy released, E_{S1} is the energy released from subcooling of the solid, E_{S2} accounts for sensible energy released by liquid which has solidified, and E_{S3} represents sensible energy that has been released by the remaining (i.e., unfrozen) liquid. In the cases for which $Ste_L = 0$, no liquid sensible energy is available for release, so that E_{S2} and E_{S3} are both zero.

Figure 10 shows the results for $Ste_S = 0.047$. For both Ste_L cases shown there, the sensible subcooling of the solid E_{S1} is very small compared to the latent energy released, as is consistent with the small value of Ste_S.

For significant initial liquid superheating ($Ste_L = 0.413$), the total liquid sensible energy release ($E_{S2} + E_{S3}$) provides over half the energy released at small $FoSte_S$ values and remains an important contributor over the entire range of $FoSte_S$. As freezing progresses, E_{S2} increases due to the increasing amount of solid, while, correspondingly, E_{S3} decreases. The sum of E_{S2} and E_{S3}, however, becomes a constant when the initial liquid superheat has been completely dissipated. This regime is initiated in Fig. 10 at the point at which triangles and diamonds begin to follow parallel paths.

The total energy extracted is represented in Fig. 10 by the uppermost set of data for each of the two cases shown there. Considerably greater total energy release occurs when initial superheating is present.

Figure 11 conveys results for cases for which $Ste_S = 0.235$.

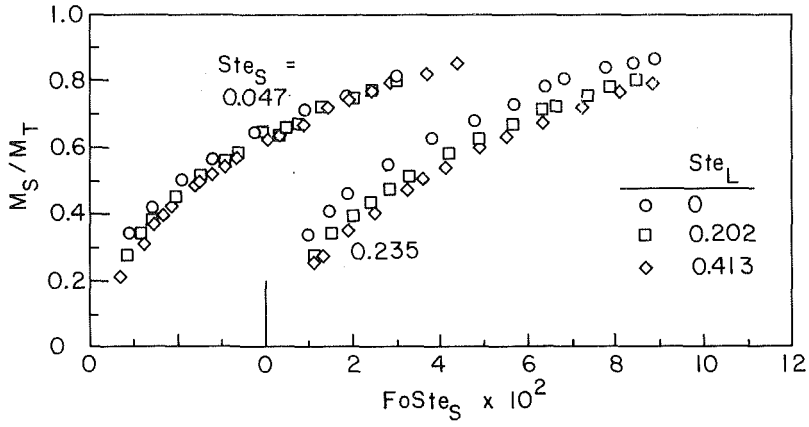

Fig. 9 Effect of Ste_L on the frozen mass

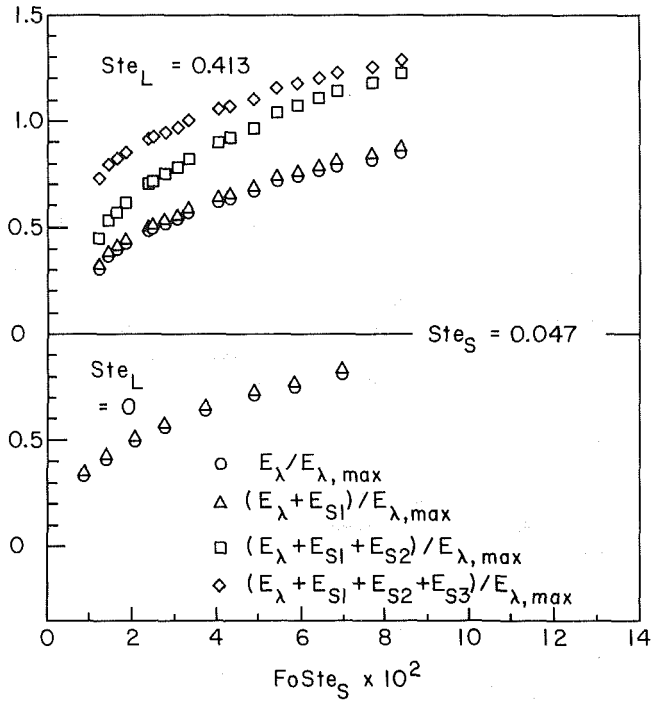

Fig. 10 Energy accounting for Ste_S = 0.047

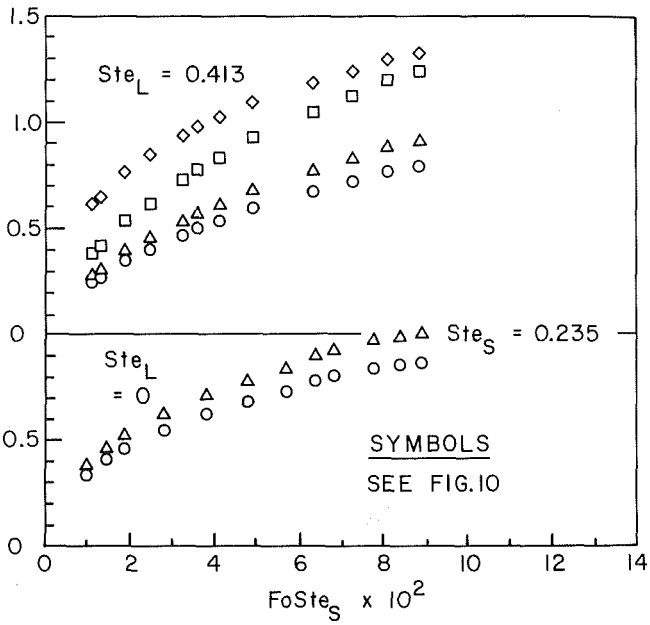

Fig. 11 Energy accounting for Ste_S = 0.235

The trends observed here are similar to those in the previous figure. In accordance with the larger value of Ste_S, the magnitude of E_{S1} has increased but still remains a relatively small portion of the total. In the presence of significant initial liquid superheating, the liquid sensible energy release continues to play a major role in the total release, but the constancy of $(E_{S2} + E_{S3})$ is initiated at a larger value of $FoSte_S$. A comparison of the total energy release for the Ste_L = 0.413 cases in Figs. 10 and 11 shows that this quantity is relatively independent of the value of Ste_S.

Conclusion

It was found that cylinder inclination played a negligible role in determining the amount of energy released during freezing under any of the investigated conditions of initial liquid superheat or cylinder wall subcooling. Only for more local quantities such as the local frozen-layer thickness was it possible to detect inclination-related variations, but even these were moderate. Whatever inclination effects did occur resulted from changes in the pattern of the natural convection in the superheated liquid. For freezing which is initiated without liquid superheat, there is no natural convection and there can be no effects of inclination.

Although the energy release was insensitive to the inclination-related aspects of natural convection, there is evidence that the natural convection did play an important role in the freezing process in the presence of large liquid-phase initial superheat. Comparisons of the experimental results with numerical solutions which ignored the natural convection suggested that the convection significantly increased the rate at which the sensible energy of the superheated liquid was delivered to the solid-liquid interface. These effects were strongest during the initial portion of the freezing period and waned as the superheat was dissipated.

Acknowledgment

This research was performed under the auspices of the U.S. Department of Energy.

References

1 Viskanta, R., "Phase-Change Heat Transfer," *Solar Heat Storage:*

Latent Heat Materials, edited by G. A. Lane, CRC Press, Boca Raton, Fla., 1983.

2 Viskanta, R., Bathelt, A. G., and Hale, N. W., Jr., "Latent Heat-of-Fusion Energy Storage: Experiments on Heat Transfer During Solid-Liquid Phase Change," *Alternative Energy Sources III. Solar Energy 1*, Vol. 1, edited by T. N. Veziroglu, Hemisphere Publishing, Washington, D.C., 1983, pp. 279-304.

3 Ruddle, R. W., *The Solidification of Castings*, Institute of Metals, London, 1967.

4 Cole, G. S., "Transport Processes and Fluid Flow in Solidification," *Solidification*, American Society for Metals, Metals Park, Ohio, 1969.

5 Larson, E. D., "Freezing Inside a Circular Cylindrical Capsule at Various Angular Inclinations, Initial Liquid Superheats, and Cylinder Wall Subcoolings," Ph.D. thesis, Department of Mechanical Engineering, University of Minnesota, Minneapolis, Minn., 1983.

6 Sparrow, E. M., and Broadbent, J. A., "Freezing in a Vertical Tube," ASME JOURNAL OF HEAT TRANSFER, Vol. 105, 1983, pp. 217-225.

7 Viskanta, R., and Gau, C., "Inward Solidification of a Superheated Liquid in a Cooled Horizontal Tube," *Wärme-und Stoffübertragung*, Vol. 17, 1982, pp. 39-46.

8 Katayama, K., Saito, A., Utaka, Y., Saito, A., Matsui, H., Maekawa, H., and Saifullah, A. Z. A., "Heat Transfer Characteristics of the Latent Heat Thermal Energy Storage Capsule," *Solar Energy*, Vol. 27, 1981, pp. 91-97.

9 Griggs, E. I., and Yarbrough, D. W., "Thermal Conductivity of Solid Unbranched Alkanes from n-Hexadecane to n-Eicosane," *Proceedings, 14th Southeastern Seminar on Thermal Sciences*, 1978.

10 Humphries, W. R., and Griggs, E. I., "A Design Handbook for Phase Change Thermal Control and Energy Storage Devices," NASA Technical Paper 1074, 1977.

11 Sparrow, E. M., and Chuck, W., "An Implicit/Explicit Numerical Solution Scheme for Phase-Change Problems," *Numerical Heat Transfer*, Vol. 7, 1984, pp. 1-15.

12 Ohkubo, Y., personal communication, University of Minnesota, Oct. 1983.

A Photographic Investigation of the Stability of a Vapor Nucleus in a Glass Cavity

T. W. Forest
Associate Professor,
Department of Mechanical Engineering,
University of Alberta,
Edmonton, Alberta,
T6G 2G8
Canada

A set of experiments was conducted to observe the stability of a vapor nucleus trapped inside a small glass capillary for water at a uniform superheat. The glass cavity was of a shape that allowed the incipient growth and collapse of the nucleus to be clearly distinguished. Photographs showing the nucleus instabilities are presented at one of three different system pressures used in the experiments. The observed stability of the nucleus and the measured superheats corresponding to the incipient instabilities agree with predictions based on a previous thermodynamic analysis.

Introduction

The thermodynamic stability of a vapor nucleus, trapped in a surface cavity is essential to the study of boiling from surfaces. Preexisting nuclei on a solid surface are thought to act as nucleation sites. At a particular site, the sequence of events leading to fully active boiling is as follows. An initial superheat is applied to the liquid in order to activate the vapor nucleus, i.e., force the liquid-vapor interface up to the mouth of the cavity. A bubble now forms at the mouth of the cavity and grows until bouyancy forces lift the bubble from the surface. As a bubble departs, a residual vapor pocket is left in the cavity, which acts as the source for the next bubble. This cycle is repeated, causing a stream of bubbles from the site. The superheat in this latter stage is usually less than the initial superheat required to activate the site. As the superheat decreases, the bubble frequency decreases until boiling stops; the liquid-vapor interface moves back inside the cavity and the site becomes deactivated. Several experimental studies by Griffith and Wallis [1] and Cole [2, 3] concentrated on verifying the thermodynamic analysis for predicting the superheat at which the initial activation of the nucleus occurs. In each of these studies, a conical or cylindrical cavity was exposed to a uniformly superheated liquid and the temperature at which the cavity was activated (or deactivated) was measured. For the types of cavities studied, the activation and deactivation superheats were essentially the same. In each study, it was concluded that the superheat at which activation occurred could be predicted reasonably well from the thermodynamic analysis. However, for these relatively simple cavity geometries, the instability (i.e., unstable growth or collapse) of the nucleus occurred when the liquid-vapor interface reached the mouth of the cavity and the difference between the activation and deactivation superheats was small. It is interesting to note that the enhanced boiling surfaces currently being developed utilized a more complicated cavity geometry in which there may be large differences between the superheat required to activate and deactivate the nucleation sites. Recent tests of these surfaces [4, 5] have shown that a wall superheat on the order of 5 to 10°C is required to activate these surfaces while deactivation of the nucleation sites occurs at about 1/10 this value.

Other studies by Wei and Preckshot [6], Kosky [7], and Marto and Sowersby [8] concentrated on the dynamic behavior of the nucleus during fully active boiling. Using high-speed photography, these authors observed the motion of the liquid-vapor interface in small glass capillaries. They noted that following the departure of a bubble from the cavity, the liquid-vapor interface penetrated inside the cavity, the depth of penetration being influenced by varoius factors such as cavity geometry and surface tension. Their photographs illustrate the dynamic nature of the bubble growth-departure cycle.

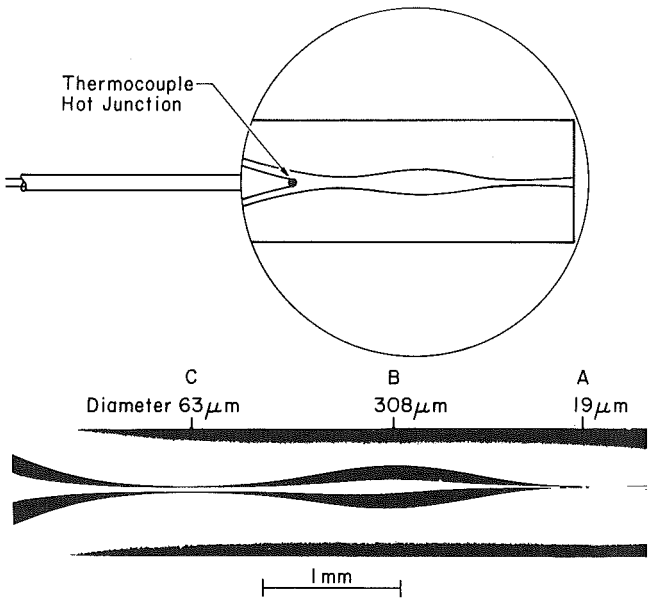

Fig. 1 Schematic and photomicrograph of the glass cavity

In this paper, a photographic investigation was undertaken to observe the initial activation and deactivation of a vapor nucleus in a small glass cavity and as such differs from the photographic investigations of active boiling from cavities. The shape of the cavity was designed so that there is a clear difference in the position of the liquid-vapor interface at each of several, separate instabilities that are observed. Furthermore, the superheats, required to activate and deactivate the nucleus differ by an order of magnitude, thus allowing a clear test of the theoretical predictions. Recently, in a thermodynamic analysis [9] of vapor nuclei trapped in cavities, it was shown that the stability of a nucleus can be predicted directly from a curve showing the variation in the radius of a curvature with position of the liquid-vapor interface. It was predicted that a nucleus will be stable at positions within the cavity where the slope of this curve is negative and unstable at positions where the slope is positive. Furthermore, a local minimum in this curve corresponds to the point at which the nucleus begins to grow (activation) while a local maximum corresponds to the point at which the nucleus begins to collapse or dissolve (deactivation). This curve is essentially

Contributed by the Heat Transfer Division for publication in the JOURNAL OF HEAT TRANSFER. Manuscript received by the Heat Transfer Division April 13, 1983.

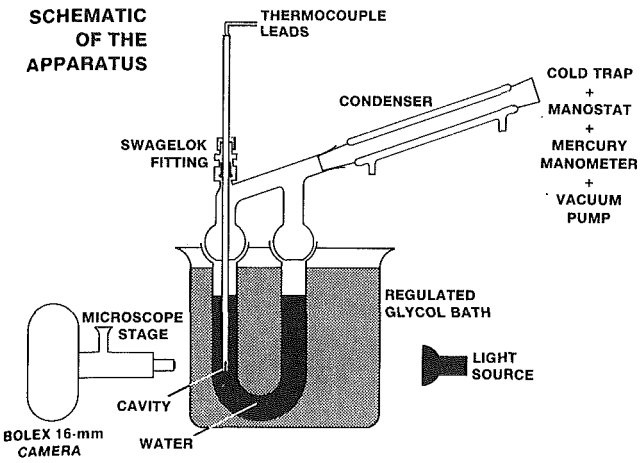

Fig. 2 Schematic of the test apparatus

identical to the curve of radius versus nucleus volume shown by Griffith and Wallis [1].

Test Apparatus

Boiling Cavity. In order to observe the activation and deactivation of the vapor nucleus, the cavity shape adopted was a double hourglass shape. A schematic and a photograph of the test cavity are shown in Fig. 1, together with the internal diameters of the cavity at points A, B, and C. The reason for adopting this particular caity profile will be discussed in the section, "Cavity Characteristic."

The cavity was formed by gently heating a 3-mm-o.d. Pyrex glass tube with a micro-flame torch. As the glass softened, surface tension forces caused the glass tube to contract until the desired internal dimensions were obtained. Finally, the bottom end of the cavity was sealed off by allowing the glass to completely contract when heated. The temperature inside the cavity was measured with a calibrated chromel-alumel thermocouple.

Apparatus. The experimental apparatus is shown in Fig. 2. The apparatus used was similar to that used by others [1, 3] to subject the artificial cavity to conditions of uniform superheat. The glass cavity was immersed in water, which was held in a U-shaped test tube. The temperature of the water in the U-tube was maintained at a uniform level by immersion in a large regulated heat bath. The system pressure inside the test tube was regulated by connecting the test tube to a vacuum pump through a Cartesian manostat. To prevent large amounts of water evaporating from the U-tube, an inclined, water-cooled condenser was placed between the system and the cold trap; this allowed the condensate to run back into the U-tube on the side opposite to the cavity. This prevented large temperature fluctuations near the cavity. The cavity itself was inserted into the system and held in place by a standard Swagelok fitting, with Viton O-rings. This allowed the glass rod holding the cavity to be slid up or down while the system was at the desired temperature and pressure.

The motion of the liquid–vapor interface within the cavity

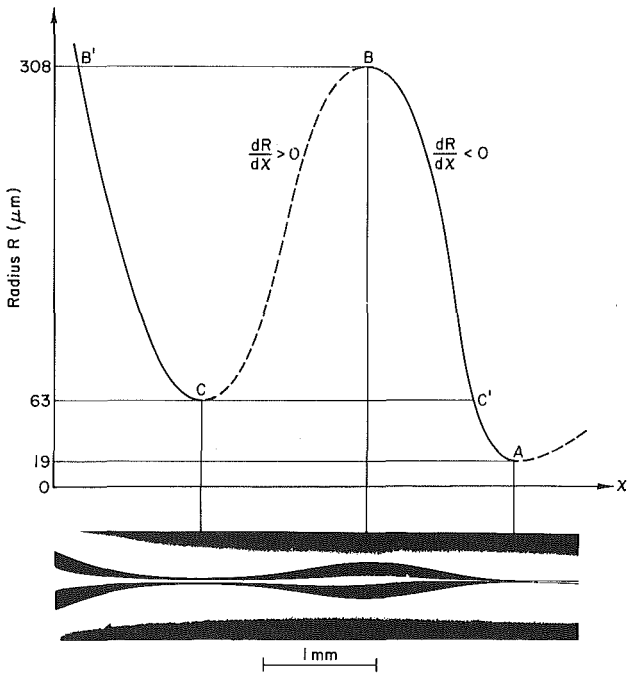

Fig. 3 The cavity characteristic corresponding to the test cavity. Solid line portions of the characteristic refer to stable positions; dashed line portions refer to unstable portions.

was observed and recorded using a Bolex 16-mm movie camera. The camera was adapted to attach to the end of a standard microscope, mounted horizontally. The objective used for filming was 4x, with a long working distance since the cavity was located at least 1 to 2 cm inside the heat bath.

Procedure. The U-tube was filled with distilled water prior to assembly of the system. At this point, the glass tube holding the thermocouple and cavity was attached to the system with the cavity held above the liquid surface. The manostat was adjusted to obtain the desired pressure in the system. The temperature of the bath was slowly increased and reached a value corresponding to several degrees of superheat in the liquid. Some dissolved gas was liberated during this warm-up. The cavity was lowered into the superheated water where virorous boiling occurred at the mouth opening of the cavity. The boiling was maintained for approximately 1 hr, in order to expel air from inside the cavity.

The test commenced by slowly lowering the temperature of the bath (0.3–0.4°C/minute) while observing the liquid–vapor interface through the microscope-camera. The first instability observed corresponded to the interface moving past the maximum in the cavity profile at point B. The minimum temperature at which this instability occurred was recorded on a strip chart recorder which monitored the thermocouple output. In practice, the point at which the instability occurred was easily detected because the interface, having slowly reached point B in response to the slow temperature decrease would move suddenly to a new position on the other side of

Nomenclature

k = Boltzmann's constant
P' = pressure in the liquid phase
P_{vap} = vapor pressure of the liquid
R = radius of the liquid–vapor interface
R_C = critical radius
T = temperature
v' = molecular volume of the liquid
x = axial position of the three phase line of contact within the cavity
W = cross-sectional radius of the cavity
α = angle defined by equation (1*a*)
γ = surface tension of the liquid–vapor interface
θ = contact angle

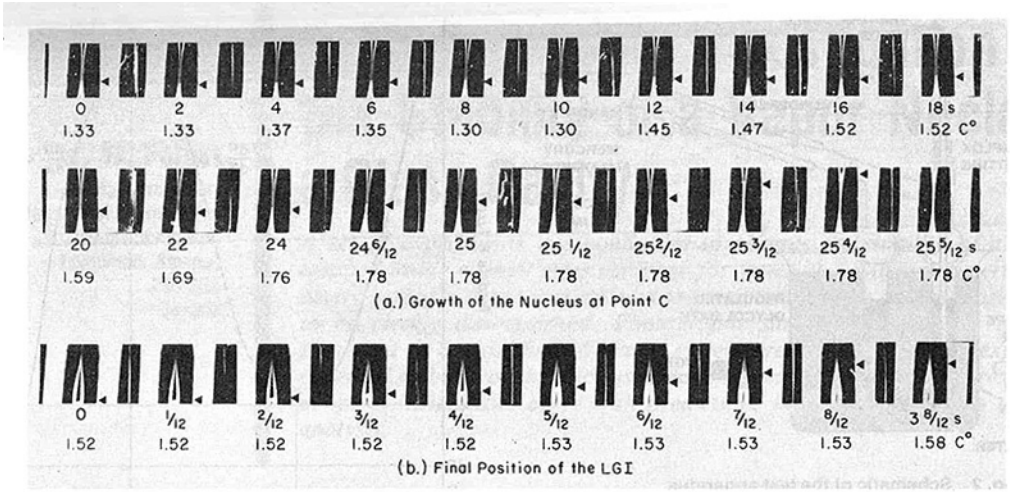

Fig. 4 Sequence of photographs showing the nucleus instability at point C (filmed at 12 fps). The dark portion within the cavity outline corresponds to the liquid phase and the arrowheads show the position of the liquid-vapor interface. System pressure is 74.1 kPa.

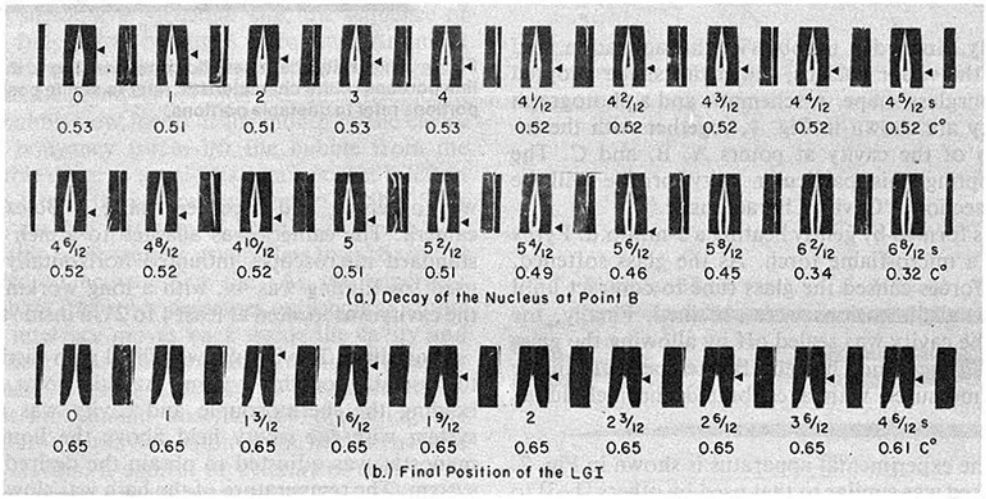

Fig.5 Sequence of photos showing the nucleus instability at point B (filmed at 12 fps). System pressure is 74.1 kPa.

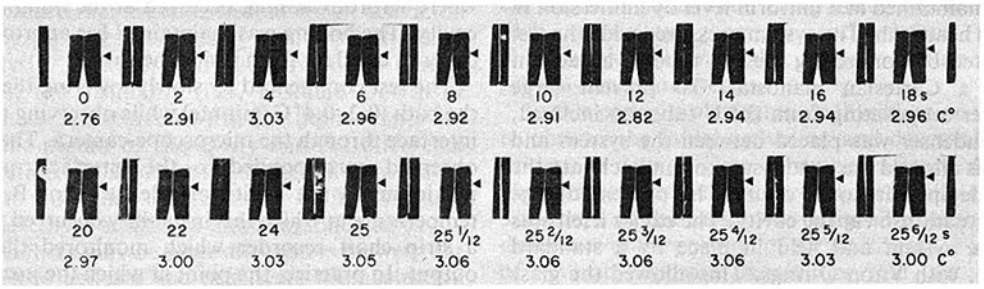

Fig. 6 Sequence of photos showing the nucleus instability at point A (filmed at 12 fps). System pressure is 74.1 kPa.

point C. Next the temperature of the bath was slowly increased to observe the second instability at point C. Since the diameter of the cavity at point C was smaller than at B, a higher temperature was required to force the interface past point C. Again, the instability was easily detected because the interface, having slowly reached C, would move rapidly to a new position between points A and B. The temperature at which this instability occurred was recorded. The bath temperature was allowed to slowly decrease to allow the interface to penetrate past B and then raised to bring the interface past C. This cycle was repeated a minimum of six times in order to obtain a reasonable average for the temperatures of the instabilities. The temperatures corresponding to the instabilities were quite reproducible. After this set of tests, the bath temperature was raised to measure the superheat required to force the interface past point A. Since the diameter of the cavity at A was less than at C, this required a higher temperature than at point C. Again the temperature at which the nucleus became unstable was easily detected since the interface moved rapidly to the mouth of the

cavity where a stream of bubbles emerged. This was also noted by a relatively large drop in temperature on the strip chart recorder. This measurement was repeated several times to obtain a reasonable average.

This set of measurements of the superheat corresponding to each of the instabilities was repeated at three different system pressures: 44.3, 74.1, and 93.4 kPa. A 16-mm movie was taken at 12 fps with an overall magnification of approximately 15x of the instabilities at a pressure of 74.1 kPa.

Cavity Characteristic

For a given pressure, the temperatures at which the three instabilities occur can be predicted from a plot of radius of curvature (for the liquid-vapor interface) versus axial position of the interface. Such a curve, called the "cavity characteristic" is shown in Fig. 3 for the cavity used in this study. It should be noted that the shape of the cavity characteristics depends on the contact angle of the liquid on the solid. The contact angle is a function of the particular liquid-solid combination being considered. In the present case, water is in contact with clean glass giving a contact angle of zero (complete wetting); furthermore, the advancing and receding contact angles are both zero. For this case (zero contact angle), the minima and maxima in the cavity characteristic correspond to the minima and maxima in the cavity profile. This can be seen from the geometric relation between the radius of curvature R and the cavity profile $W(x)$

$$R = \frac{W(x)}{\cos[\theta - \alpha(x)]} \tag{1a}$$

where

$$\alpha(x) = \tan^{-1}\left(\frac{dW}{dx}\right) \tag{1b}$$

With θ equal to zero and α equal to zero at the minima and maxima of the cavity profile, R is equal to W at these points. At any other position, R is not equal to W, since α is not zero. If the contact angle is not zero, then the shape of the cavity characteristic will be different from that shown in Fig. 3, with minima and maxima in this curve occurring at different positions.

In [9], it was theoretically shown that the vapor nucleus is stable at all positions where the cavity characteristic has a negative slope and unstable at positions where the slope is positive. For the stable nucleus positions, the radius of the liquid-vapor interface is equal to the thermodynamic critical radius [1]

$$R = R_C = \frac{2\gamma}{\eta P_{\text{vap}} - P'} \tag{2}$$

where $\eta = \exp\{v'(P' - P_{\text{vap}})/kT\}$. The thermodynamic critical radius is a property of the liquid phase and depends on temperature and pressure. In the present experimental study the factor η is very close to unity.

In [9], it was also shown that the extrema in the cavity characteristic correspond to instabilities of the nucleus. At a maximum in the cavity characteristic, e.g., point B in Fig. 3, the nucleus becomes unstable and will dissolve until the liquid-vapor interface reaches B′, on the stable portion of the characteristic. Conversely, at a minimum, e.g., point C in Fig. 3, the nucleus becomes unstable and will grow until the liquid-vapor interface reaches C′. The superheat at which these instabilities occur can be calculated by equating the critical radius, R_C with the radius at the extremum in the characteristic. Thus the cavity characteristic provides all the information required to predict the stability of the nucleus.

From the foregoing discussion it can be seen that the particular shape of cavity used in this investigation was chosen to illustrate both types of instabilities. This means that the cavity radius beyond point C has to be larger than the radius at B in order for the interface to reach a stable position at B′; otherwise, the nucleus would completely dissolve away and the cavity would be deactivated. For similar reasons, the radius at C was made larger than at A in order that the interface reach a stable position at C′.

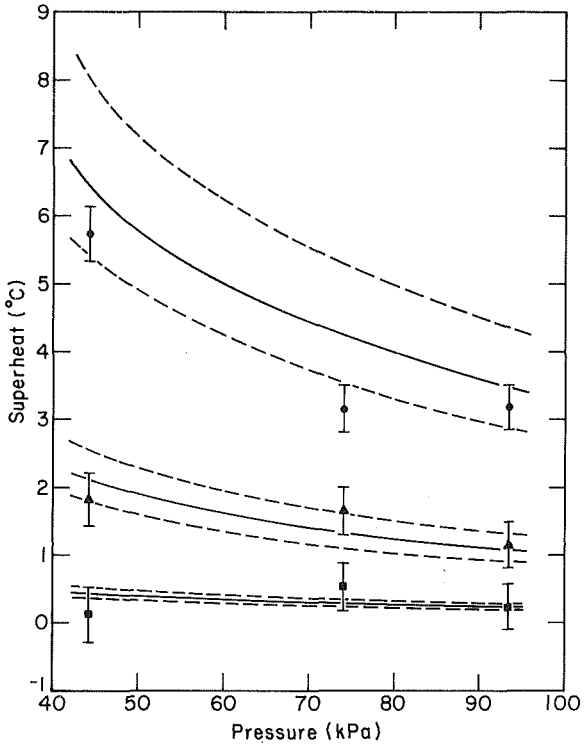

Fig. 7 Comparisons of predicted and measured superheats for the three instabilities: —— predicted results; • Measured superheat for the instability at A; ■ Measured superheat for the instability at B; ▲ Measured superheat for the instability at C

Results and Discussion

The results of the photographic investigation of the stability of the vapor nucleus are summarized in Figs. 4-6. All these sequences were filmed at a system pressure of 74.1 kPa. Figure 4(*a*) shows a sequence of frames of the liquid-vapor interface slowly moving toward the first cavity profile minimum at C. The time (relative to the first frame) and the corresponding superheat are listed below each frame. From this sequence we can see that the interface slowly advances toward the minimum in response to a gradual increase in superheat. At 25 1/12 s from the start, the interface reaches the minimum at C. The subsequent frames show a rapid movement of the interface away from C (growth of the nucleus), even though the superheat remains constant. From this sequence, the instability of the vapor nculeus at point C can clearly be seen; the superheat corresponding to this instability is 1.78°C. This visual observation agrees with the prediction made in the previous section that the nucleus becomes unstable and begins to grow spontaneously when the interface reaches C. Furthermore, it was predicted that the interface would reach a stable position between B and A, after the instability. Figure 4(*b*) shows a sequence of frames of the interface arriving at a new position between B and A after undergoing the instability at C. The superheat is slightly different from the superheat in Fig. 4(*a*), because this sequence was taken from a different experimental run and indicates a variation in the measured superheat. During this sequence, the superheat is virtually constant. The last frame in

the sequence was taken 3 s after the previous frame and shows that the position of the interface has not changed appreciably; this implies that the interface is stable at the new position, in agreement with the predictions.

Figure 5(*a*) shows a sequence of frames of the instability at B (maximum in the cavity profile). In this case, it is predicted that the nucleus will spontaneously dissolve when the interface reaches B. The sequence shows the interface receding past the maximum at B. It is not clear that the instability occurs exactly at B. However, it was observed during other runs that when the interface was between A and B, it would move back and forth in direct response to temperature changes. Once the interface reached B, it would always recede towards C, despite any temperature variations. When the interface began to recede, it would always come to a stable position beyond C. This is illustrated in Fig. 5(*b*), which shows the interface at a stable position. Again the superheat for this sequence is slightly different from that in Fig. 5(*a*), because it was taken from a different run. Taken together, these observations agree qualitatively with the prediction that the nucleus becomes unstable at B and dissolves until the interface reaches a new position beyond C.

Finally, the instability at A is shown in the sequence of frames in Fig. 6. The position of the liquid–vapor interface is shown in each frame by the arrowhead. Again, the interface slowly advances out of the cavity in response to an increase in temperature. The instability occurs 25 1/4 s from the start of the sequence; the last three frames show the interface rapidly moving towards the mouth of cavity. It can be seen that the position of the interface just prior to the instability is not exactly at the minimum in the cavity profile but displaced toward the mouth of the cavity. This observation disagrees with the prediction made in the previous section. This discrepancy is most likely due to the effect of contamination on the cavity wall. This series of photographs was the last experimental run and contamination of the cavity was highly likely. The effect of contamination is to increase the contact angle slightly from zero; the glass surface becomes slightly nonwetting. For a small contact angle, the minimum in the cavity characteristic is positioned between A and the cavity mouth. The nucleus does not become unstable at A but rather at the position of the minimum in the cavity characteristic.

A comparison of the measured superheat and the pedicted superheat is presented in Fig. 7. The predicted superheats are calculated by setting R_C equal to the maximum or minimum in the cavity profile. The resulting equation must be iterated to solve for the temperatures at which the instabilities occur since temperature enters equation (1) implicitly through the dependence of γ and P_{vap} on temeprature. The solid curves in Fig. 7 represent the predicted superheats with the dashed lines giving the uncertainty in the predictions due to errors in measurement of the cavity profile. Figure 7 shows a reasonably good comparison between the measured and predicted superheats for each of the three instabilities. The only exception to this occurs for the instability at A at 74.1 kPa. This was the last instability observed, an example of which is shown in Fig. 6. For the reason previously noted, (effect of contamination), the minimum in the cavity characteristic occurs at a position displaced from A, with a corresponding interfacial radius which is larger than the radius of the profile at A. Thus the predicted superheat based on the cavity radius at A will be higher than the measured superheat, as is the case.

Conclusions

The stability of a vapor nucleus in a surface cavity was observed for conditions of uniform superheat. It was shown that the behavior of the nucleus in response to changes in superheat agreed with the predictions based on the cavity characteristic. The measured and predicted superheats at which the nucleus becomes unstable (for both activation and deactivation) also agreed. These direct experimental observations have shown that the thermodynamic analysis is correct for liquids which wet the cavity. Further experiments are underway, to test the analysis in situations where the liquid exhibits a nonzero contact angle with the cavity.

The results of these tests may eventually lead to the design of surface cavities that have small activation superheats and which are resistant to deactivation. Undoubtedly, this will involve the cavity geometry and control of the wettability of the cavities. For example, if the liquid–vapor interface can be made concave to the liquid (i.e., negative radius of curvature) on a portion of the cavity then a vapor nucleus will be present even when the liquid is subcooled. Such a cavity would be activated at a relatively small superheat (2–3°C versus the 5–10°C observed with boiling surfaces). Such developments will ultimately depend on finding suitable materials for the boiling surface.

Acknowledgment

The author wishes to acknowledge the support given by the National Science and Engineering Research Council of Canada through grant No. A4201.

References

1 Griffith, P., and Wallis, J. D., "The Role of Surface Conditions in Nucleate Boiling," *Chemical Engineering Progress Symposium Series*, Vol. 56, No. 30, 1960, pp. 49–63.

2 Schultz, R. R., Kasturirangan, S., and Cole, R., "Experimental Studies of Incipient Vapor Nucleation," *The Canadian Journal of Chemical Engineering*, Vol. 53, 1975, pp. 408–413.

3 Jemison, T. R., Rivers, R. J., and Cole, R., "Incipient Vapor Nucleation of Methanol from an Artificial Site-Uniform Superheat," ASME, JOURNAL OF HEAT TRANSFER, Vol. 104, 1982, pp. 567–596.

4 Bergles, A. E., and Chyu, M. C., "Characteristics of Nucleate Pool Boiling From Porous Metallic Coatings," ASME, JOURNAL OF HEAT TRANSFER, Vol. 104, 1982, pp. 279–285.

5 Marto, P. J., and Lepere, V. J., "Pool Boiling Heat Transfer From Enhanced Surfaces to Dielectric Fluids," ASME, JOURNAL OF HEAT TRANSFER, Vol. 104, 1982, pp. 292–299.

6 Wei, C. C., and Preckshot, G. W., "Photographic Evidence of Bubble Departure from Capillaries During Boiling," *Chemical Engineering Science*, Vol 19, 1964, pp. 838–839.

7 Kosky, P. G., "Nucleation Site Instability in Nucleate Boiling," *International Journal of Heat and Mass Transfer*, Vol. 11, 1968, pp. 929–932.

8 Marto, P. F., and Sowersby, R. L., "A Photographic Investigation of Bubble Nucleation from Glass Cavities," Paper 70-HT-16, ASME Fluids Engineering, Heat Transfer and Lubrication Conference, Detroit, Mich., May 24–27, 1970.

9 Forest, T. W., "The Stability of Gaseous Nuclei at Liquid-Solid Interfaces," *Journal of Applied Physics*, Vol. 53, No. 9, 1982, pp. 6191–6201.

Flash Evaporation From Turbulent Water Jets

D. Bharathan
Mem. ASME

T. Penney
Mem. ASME
Solar Energy Research Institute,
Thermal Research Branch,
Golden, Colo. 80401

Results of an experimental investigation of flash evaporation from turbulent planar and axisymmetric water jets are reported. In the range of jet thicknesses tested, for planar jets, due to shattering, evaporation is found to be nearly independent of the jet thickness. Evaporation from the planar jets was found to be dependent on the initial level of turbulence in the water supply manifold. An approximate analysis to model the evaporation process based on the physical phenomena and experimental observations is outlined. Comparisons between the experimental data and analytical predictions of the liquid temperature variation along the jet are included. Use of screens in the water jet are shown to be effective for enhancing evaporation.

Introduction

Direct-contact heat transfer is an area of current research interest for several reasons. First, there are many applications in which the heat exchange surfaces constitute a major portion of the expense of the total system and are subject to problems such as corrosion, fouling, and maintenance. Further, whenever a solid surface separates two fluids between which heat is exchanged, a significant temperature difference is required to transfer the heat, which results in a loss of overall system efficiency. Examples of such situations can be found in geothermal systems, in ocean thermal energy conversion systems, in bottoming cycles for power plants situated near low-temperature sinks, solar ponds, and energy systems in which the available temperature difference is small. As high-quality energy becomes more expensive and less available, techniques which enhance the heat transfer efficiency and reduce the deterioration in the energy quality available for doing productive work are increasingly more important. The work reported in this paper deals with one aspect of direct-contact heat transfer problems, namely the heat and mass transfer between two streams of the same fluid in which a liquid jet undergoes a phase change by flash evaporation in direct contact with its own vapor. This report presents the results of an experimental investigation of evaporation from planar and axisymmetric turbulent water jets and an analysis to model the evaporation from the jets. Comparisons between the experimental data and analytical predictions of the liquid temperature variation along the jet are also provided.

Background

Experiments. Early definitive experimental studies of flash evaporation were conducted by Maa [1], using laminar jets of various liquids. Using an ingenious method not requiring a probe to measure surface temperature, Maa concluded that there is no resistance to molecules crossing the vapor-liquid interface in addition to the natural resistance imposed by gas laws; i.e., when any vapor molecule strikes the interface, the chance of failing to cross it is small. Under this condition, for evaporation of liquids such as water, the vapor-side resistance to mass transfer is nonnegligible but extremely low in comparison with the resistance to heat transfer on the liquid side. The evaporation rate is thus controlled by the heat transport within the liquid.

For laminar jets, heat transport on the liquid side is governed by molecular diffusion. For turbulent jets, enhanced heat transport may be expected due to increased mixing caused by eddies in addition to the molecular diffusion. However, definitive data on the enhancement due to turbulence are scarce. Mills et al. [2] present data for evaporation from 4-mm-dia circular turbulent water jets of 95, 133, and 171 mm in length. In their experiments, they took precautions to maintain a coherent jet and prevent jet shattering due to cavitation. For a jet Reynolds number in the range of 3000 to 25,000, an average Stanton number for these jets was found to be 3 to 11 times larger than predictions based on laminar flow, suggesting a major role played by turbulent transport. However, for similar jets and Reynolds numbers, they argue that the turbulent mixing for mass transfer is probably dominant in a central core region of the jet and is not likely to enhance transport mechanisms at the thin outer boundary layers adjacent to the interface. Thus turbulent transport plays a minor role in this case. Adequate explanation for the discrepancy between heat and mass transport was not offered.

Other reported works on experimental investigation of flash evaporation from turbulent jets are few and in most cases, the jets were reported to be "shattered." Explosive growth of vapor bubbles from within the jets results in shattering the jet into discontinuous fragments and droplets. Brown and York [3] studied flash evaporation as a means of producing a fine spray of liquid droplets for aerosol applications.

Balitskiy and Shurchkova [4] report experimental studies of flash evaporation from 15-cm-long water jets of 1, 3, and 5 mm in diameters. For liquid superheat of over 7°C, the emerging jets shattered into a spray of droplets.

Miyatake et al. [5] studied flash evaporation from cylindrical water jets of 3.5, 5.0, and 8.2 mm in diameter and of 12, 25, and 25 cm in length, respectively. The water exit Reynolds number ranged from 66,000 to 155,000. Photographs of increased jet shattering with increasing superheat were presented, along with measurements of temperature profiles of the falling jet. They attempted to correlate their data based on qualitative arguments of the shape of the jet temperature profile. While their data and correlations match reasonably well, these correlations may not be extended to other laboratory tests because of a lack of physical reasoning underlying the correlation.

Analysis. Analytical modeling of heat transport in coherent unshattered turbulent jets is complicated by the effect of turbulent mixing, the distribution of the effective eddy mixing across the jet, and the decay of turbulence downstream. Theofanous et al. [6] present the only reported attempt to model turbulent transport in jets to include all these effects; the variation of eddy mixing across the jet is assumed to follow the Levich model [7], and the decay of

Contributed by the Heat Transfer Division and presented at the ASME-JSME Joint Thermal Engineering Conference, Honolulu, Hawaii, March 1983. Manuscript received by the Heat Transfer Division May 2, 1983.

turbulence downstream is assumed to follow the decay of homogeneous turbulence behind a grid. However, the heat and mass transport is assumed to occur in a fully developed situation. Mills et al. [2] reviewed this approach to indicate that the transport process cannot be treated in a fully developed sense and must be treated as an entrance region problem. Further, they indicate that available experimental data for mass transfer into turbulent coherent jets do not support the Levich theory or the approach of Theofanus et al.

Modeling of evaporation from turbulent jets that are shattered by the vapor escape is further complicated by the associated exposure of new surfaces and the resulting increases in the interfacial area due to a spectrum of droplets. Heertjes and deNie [8] report on experimental and analytical efforts to quantify the mechanism of mass transfer to drops during formation, release, and coalescence. Mass and heat transfer during the period of formation can be substantial. Once formed, the droplets undergo internal circulation and vibrations during free fall. The ratio of an effective diffusion rate to the molecular diffusion rate may lie in the range of 1 to 4 for circulating drops but may be 10 or more for oscillating drops [9].

It is clear that for accurate predictions of flash evaporation from turbulent jets, an adequate data base on variations of effective thermal diffusivity in the regions of major temperature gradients within the jet and effective exposed interfacial area with downstream distance are required, and such a data base is not available.

In this paper, we present our initial attempts at modeling evaporation from falling turbulent water sheets and experimental results on evaporation from turbulent planar and axisymmetric sheets. Comparisons between the model and experimental data are also included.

For the analyses,we made certain simplifying assumptions. The effect of turbulent mixing within the jet is modeled by a constant multiplier for the effective turbulent thermal conductivity. For shattering jets, the increased interfacial area is taken to be the resulting surface area, assuming that the jets were distributed in the form of uniform size droplets. Effect of remixing due to screens at any downstream distance in the jet is modeled by reimposing the initial conditions at the corresponding bulk liquid temperature.

Evaporation data from 0.8-m-long planar water sheets of initial uniform thicknesses of 6.35, 19.05, and 25.4 mm are presented. We found that for the jets tested, evaporation was essentially independent of the jet thickness because of jet shattering. Jet temperature profiles with downstream distance are included. Screens located strategically below the falling jet are shown to sustain a high evaporation rate over the entire jet length. We also present evaporation data from an innovative vertical spout evaporator where major mixing occurs at the liquid exit due to fall back.

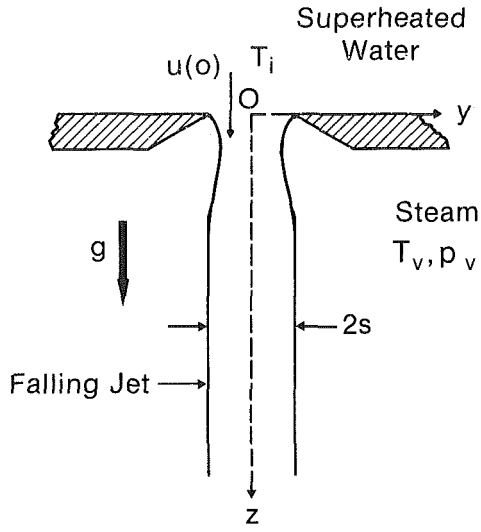

Fig. 1 Cross-sectional view of a falling planar water jet

Modeling of Evaporation from Turbulent Water Sheets

Evaporation from turbulent jets is complicated by turbulent mixing, decay, and jet shattering. In the following section, we present a simplified model to illustrate the nature of the heat transport in turbulent jets and to provide insight for increasing the evaporation rates. However, adequate means for accurate prediction of evaporation from turbulent jets are considerably complicated by uncertainty in the details of the internal structure of the jets and by the effective interfacial areas available for evaporation.

The analytical model presented here follows the method proposed by Maa [1] for evaporation from laminar jets. Analytical results in the form of variations in average bulk liquid temperature with downstream distance are presented for five cases, namely, (*a*) laminar unbroken jet, (*b*) turbulent unbroken jet, (*c*) laminar broken jet, (*d*) turbulent broken jet, and (*e*) turbulent broken jet with surface renewals. The words "broken" and "shattered" are used interchangeably throughout this report.

Problem Statement. Consider a water jet of thickness 2*s*

Nomenclature

C = horizontal coverage for the spout evaporator (m)
c_p = specific heat of water (kJ/kg•K)
D = pipe diameter (m)
d = droplet diameter (mm)
g = acceleration due to gravity (m/s^2)
H = pipe length above water pool (m)
h_o = overall heat transfer coefficient (kW/m^2•K)
h_G = gas-side heat transfer coefficient (kW/m^2•K)
$\bar{h}_G$ = time-averaged gas-side heat transfer coefficient (kW/m^2•K)
h_{fg} = latent heat of evaporation (kJ/kg)
k = thermal conductivity of water (W/m•K)
k_T = multiplier for effective turbulent conductivity
M = molecular weight of water
p = vapor pressure (Pa)
R = universal gas constant (kJ/kg mol•K)
s = one-half of initial jet thickness (mm)
T = temperature (K)
t = time (s)
u = water jet velocity (m/s)
u_o = inlet water velocity (m/s)
V = horizontal component of water velocity over spout (m/s)
V_v = vapor velocity (m/s)
$\dot{w}$ = vapor mass flux (kg/m^2•s)
y = horizontal coordinate (m)
z = vertical coordinate (m)

Greek

α = thermal diffusivity of water (m^2/s)
ϵ = effectiveness
ρ = density of water (kg/m^3)

Subscripts

b = bulk
i = inlet
o = outlet
s = surface (interface)
v = vapor

exiting at an initial temperature, T_i, into a chamber held at a vapor pressure, p_v, corresponding to a saturation temperature, T_v, as shown in Fig. 1. For an unbroken jet under steady state, heat transport in the liquid jet can be represented by

$$u\frac{\partial T}{\partial z}=\alpha\frac{\partial^2 T}{\partial y^2} \tag{1}$$

where

z = the vertical coordinate directed downward
y = the horizontal coordinate with the origin at the center of the jet at the exit plane
T = the local liquid temperature which is a function of y and z
u = the vertical downward jet velocity assumed invariant with y
α = the effective thermal diffusivity, $k/\rho c_p$
k = the effective thermal conductivity of the liquid
ρ = density
c_p = specific heat

The associated boundary conditions for the geometry shown in Fig. 1 are

$$\text{at } z=0,\ T=T_i \text{ for all } y \tag{2a}$$

and

$$\text{at } y=\pm s,\quad T=T_s(z) \tag{2b}$$

Here T_i is the inlet water temperature, and T_s is the interfacial surface temperature.

Further, the heat flux at the interface is matched by

$$k\frac{\partial T}{\partial y}\bigg|_{y=\pm s}=h_{fg}\mathring{w} \tag{3}$$

where $\mathring{w}$ is the mass flux of the interfacial evaporative steam and h_{fg} is the latent heat of vaporization.

In equation (3), the steam flux can be related to the surface and the surrounding steam temperatures, based on kinetic theory for the differential rate collisions of molecules at the interface, as

$$\mathring{w}=\sqrt{\frac{M}{2\pi R}}\left(\frac{p_s}{\sqrt{T_s}}-\frac{p_v}{\sqrt{T_v}}\right) \tag{4}$$

Here p_s is the vapor pressure at T_s, M is the molecular weight of water, and R is the universal gas constant.

Gas-side and overall heat transfer coefficients h_G and h_o can now be defined as

$$h_G=h_{fg}\mathring{w}/(T_s-T_v) \tag{5}$$

and

$$h_o=h_{fg}\mathring{w}/(T_b-T_v) \tag{6}$$

Here T_b represents the average bulk liquid temperature at any z defined as:

$$T_b(z)=\frac{1}{2s}\int_{-s}^{s}T(z,y)dy \tag{7}$$

Further, if the jet is assumed to fall freely with negligible interfacial drag, $u(z)$, can be expressed as

$$u(z)=\sqrt{u(0)^2+2gz} \tag{8}$$

and the Taylor's hypothesis

$$\frac{\partial}{\partial t}\equiv u\frac{\partial}{\partial z} \tag{9}$$

can be used to relate time and space derivatives.

Assuming that the jet remains a flat sheet with insignificant changes in thickness due to gravitational acceleration and evaporation, equations (1-9) can be integrated numerically.

In cases where the thermal boundary layer thickness is small compared to the jet thickness (i.e., $\sqrt{\alpha t}<<s$), one may assume the liquid is semi-infinite.[1] In this case, Carslaw and Jaeger [12] show that the surface temperature may be related to the bulk and vapor temperatures as

$$T_s=T_v+(T_b-T_v)\exp\left\{\frac{h_G^2\alpha t}{k^2}\right\}\operatorname{erfc}\left\{\frac{h_G}{k}\sqrt{\alpha t}\right\} \tag{10}$$

In this equation, since h_G is not a constant, a time-averaged value for h_G

$$\bar{h}_G=\frac{1}{t}\int_0^t h_G dt \tag{11}$$

may be used with equation (10). Using equations (10) and (11), Maa [1] demonstrates excellent agreement between the numerically integrated set of exact equations and the semianalytical method presented earlier. Thus the semianalytical method has been used for the rest of this report.

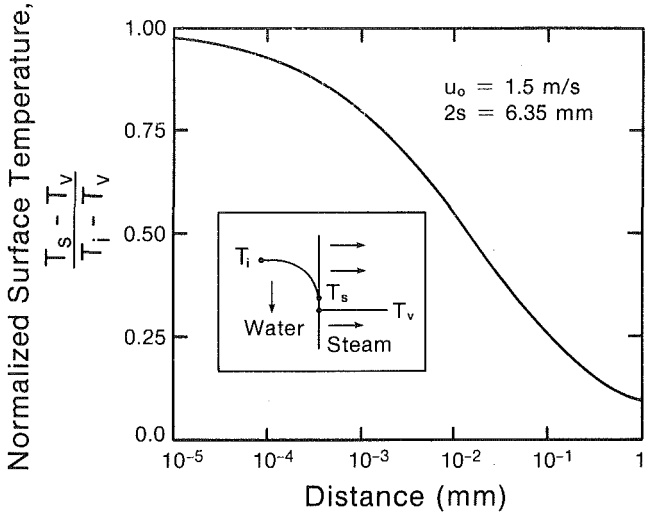

Fig. 2 Predicted variation of liquid jet surface temperature with downstream distance for a laminar, unbroken jet

Analytical Results

Laminar, Unbroken Jet. For the present case, and all other cases for which analytical results are reported, the following conditions have been assumed: $T_i=25°C$, $T_v=20°C$, $p_v=2337$ Pa, $\rho=1000$ kg/m^3, $c_p=4.186$ kJ/kg•K, $h_{fg}=2450$ kJ/kg, and a jet length of 0.8 m. The jet thickness $2s$ was 6.35 mm, and the jet inlet velocity was 1.5 m/s, unless otherwise noted. For a laminar jet at the foregoing temperatures, the thermal conductivity of water, k, is 0.618 W/m•K.

The variation of normalized jet surface temperature with downstream distance is shown in Fig. 2. The surface temperature decreases monotonically with distance and reaches a value of less than 0.1 within a jet travel distance of 1 mm. Correspondingly, the evaporation rate, which is related to the surface and vapor temperature by equation (4), decreases monotonically and reaches a value of less than 0.1 of the initial rate within this distance. Thickness of a thermal boundary layer at this time is only about 10 μm. Further evaporation from this surface is severely impeded by the growing thermal boundary layer in the liquid. A freshly

[1] For a large t, closed-form series solutions are available for internal conduction and external convection from simple body geometries such as slabs [10] and spheres [11]. However, for a small t, these solutions require evaluation of many terms when the temperature gradients in the thermal boundary layer are steep.

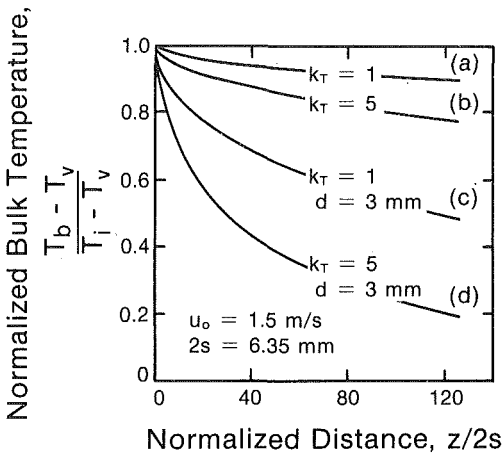

Fig. 3 Predicted variation of normalized bulk liquid temperature versus jet length for four cases: (*a*) laminar unbroken jet; (*b*) turbulent unbroken jet; (*c*) laminar broken jet; (*d*) turbulent broken jet

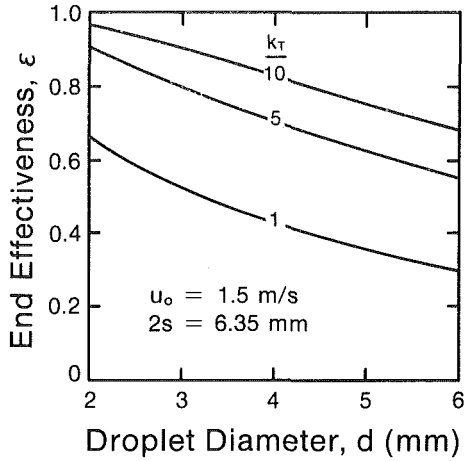

Fig. 5 Effect of increased interfacial area due to jet shattering into uniform size droplets of various diameters on end effectiveness for a 6.35-mm jet

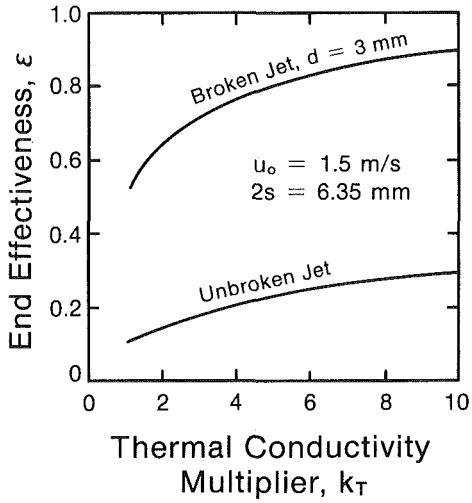

Fig. 4 Effect of increased effective thermal conductivity due to turbulence on end effectiveness for a broken and an unbroken jet

exposed interface loses its potential for high evaporation within the short distance and can be said to "age" within a millisecond.

For longer exposure distances, the variation of normalized bulk liquid temperature with distance for a laminar unbroken jet is shown as case (*a*) in Fig. 3. The bulk temperature decreases monotonically but gradually, and reaches a value of nearly 0.9 at $z/2s$ of 120.

The effectiveness ϵ is defined as

$$\epsilon = \frac{T_i - T_o}{T_i - T_v} = 1 - \frac{T_o - T_v}{T_i - T_v}\bigg|_{z=0.8\text{ m}} \tag{12}$$

where T_o is the bulk water temperature at the outlet $z = 0.8$ m, or $z/2s = 126$ reaches a value of only 0.1 for this case.

The slope of the curve at any location is an indicator of the local rate of evaporation. Note that the slope at any z for the laminar, unbroken jet is the lowest of the following cases.

Turbulent, Unbroken Jet. The effective thermal conductivity for the turbulent case is enhanced by turbulent mixing. However, there are unanswered questions regarding the intensity of turbulence near the interface and its decay downstream. Because of lack of sufficient information at present, turbulent effects are modeled by a simple approach through the use of a turbulent multiplying factor k_T for the effective thermal conductivity. Boyadzhiev et al. [13] indicate that the values for k_T can range from 2 to 10. For illustrative purposes, a midrange value for k_T of 5 has been used. The variation of normalized bulk temperature with distance for the turbulent jet with $k_T = 5$ is shown as curve (*b*) in Fig. 3. The evaporation rate for this case is generally higher than for the laminar case, as expected. The effectiveness ϵ increases only by about 0.1 from the previous case.

Laminar, Broken Jet. When the jet shatters, a spectrum of droplets is likely. However, again because of a lack of adequate information on such sprays, the broken jet is modeled by assuming that the liquid in the planar sheet is redistributed in the form of droplets of certain uniform diameter d. The interfacial area increases by a factor of $6s/d$ due to the droplets. Since the present method assumes that the liquid jet is infinitely thick for the calculation of the processes at the interface, evaluation of evaporation from droplets is essentially similar to that of planar jets, except for the increased interfacial area.

In Fig. 3, curve (*c*) is generated for a laminar jet with $k_T = 1$ and an assumed droplet diameter of 3 mm. The evaporation rate in this case is over five times the rate for the laminar unbroken jet, giving an end effectiveness of nearly 0.5. The increased interfacial area results in greater rates of evaporation for this case than when the jet is unbroken, but enhances mixing due to turbulence as shown in curve (*b*).

The effect of varied k_T (in the practical range of 1 to 10) on effectiveness ϵ for a 6.35-mm-thick, 0.8-m-long jet is shown in Fig. 4. Shown are cases for an unbroken jet and a broken jet with an assumed droplet diameter of 3 mm. Of course, here $k_T = 1$ represents a laminar jet. For the unbroken jet, ϵ increases monotonically with increasing k_T, attaining a value of 0.3 for $k_T = 10$. For the broken jet, the effect of increasing k_T is more pronounced, with ϵ increasing from about 0.5 for $k_T = 1$ to about 0.9 for $k_T = 10$.

For the broken jet, the foregoing analytical results are plotted as a function of droplet diameter d in Fig. 5. Again, for an expected range of d from 2 to 6 mm, the variation of ϵ for three different assumed k_T values of 1, 5, and 10 are shown. For each case, ϵ increases monotonically with decreasing d. As expected, the smaller droplets yield higher interfacial area for enhanced evaporation.

Turbulent, Broken Jet. This case is essentially the same as the previous case, except a value of 5 has been used for k_T to account for turbulent mixing. The drop diameter d is 3 mm. A combined effect of increased turbulence and increased interfacial area results in an end effectiveness of nearly 0.8.

Even though our models are simplistic, we note that the evaporation rate from a jet that is broken into droplets can be

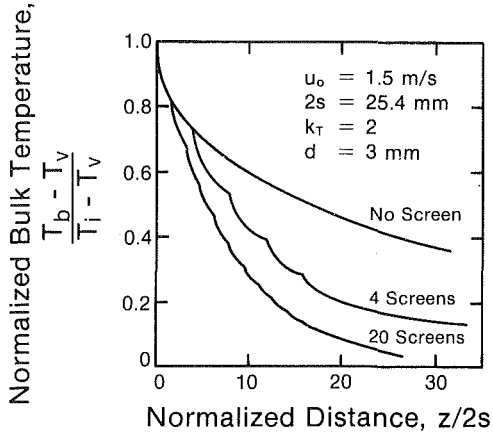

Fig. 6 Predicted variation of bulk liquid temperature with downstream distance for three cases

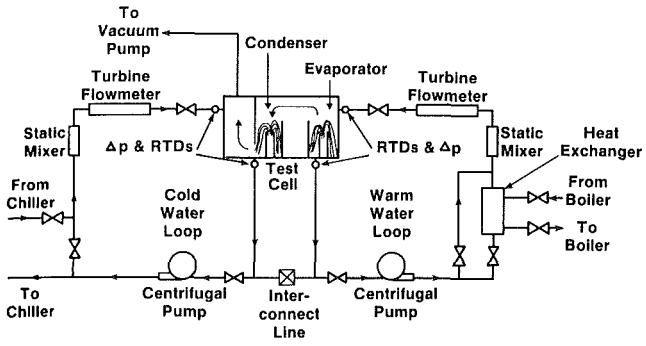

Fig. 7 Schematic diagram of the experimental apparatus

significantly higher than when the jet remains a coherent sheet but undergoes tubulent mixing.

Turbulent Broken Jet With Surface Renewals. Because an exposed interface ages extremely rapidly and the liquid at the interface attains the vapor temperature in a short distance (see Fig. 2), one may visualize a surface renewal process to enhance flash evaporation where the liquid is collected and mixed to achieve a uniform bulk temperature and is then reexposed to the vapor. Thus, once again, the initial high rate of heat transfer may be established, and the jet length required to achieve a given temperature drop in the jet can be reduced.

For a 25.4-mm-thick, 0.8-m-long jet, the effects of such renewal on the bulk temperature variation with jet length is illustrated in Fig. 6. For this case, $k_T = 2$ and $d = 3$ mm have been used. The renewal process is modeled by reimposing the initial conditions corresponding to the bulk liquid temperature at any specified downstream location. Liquid temperature variations for three cases are included: with no surface renewal, with four renewals (assumed to take place instantaneously), at nominally 10 cm intervals starting from the jet exit and with 20 renewals assumed to occur at 4 cm intervals over the entire jet length.

The discontinuities in the curves of temperature variation with renewals represent the locations where mixing takes place. The increased rate of evaporation following each renewal is evident. A larger number of renewals yields higher evaporation rates. For example, to achieve an effectiveness of 0.6 (i.e., normalized bulk liquid temperature of 0.4), the required normalized vertical distances $z/2s$ for the three cases mentioned earlier are nearly 25, 12, and 7, respectively. Since the vertical jet fall is directly related to the liquid pumping power, effective surface renewals will result in significant reductions in the parasitic power.

In practice, effective surface renewal can be accomplished in many ways, including the use of catch buckets, packings, and screens. Screens, while being the least expensive and requiring minimum volume, are likely to yield higher entrainment levels. However, due to the jet break-up into droplets, screens probably yield higher interfacial area per unit volume than other choices. Screens were thus chosen for use in the experiments reported later.

While the analyses indicate that screens may be placed as close as one millimeter apart, in practice the requirements for minimizing vapor side pressure losses would limit the screen separation.

Experimental Apparatus

The heat and mass transfer laboratory of the Solar Energy Research Institute (SERI) is designed to study and improve methods of transferring heat and mass under the small driving forces that often exist when the sun is the energy source for the process. The near-term objective of the laboratory research is to investigate the heat and mass transfer phenomena relevant to various open-cycle ocean thermal energy conversion (OTEC) systems.

The experimental apparatus, shown in Fig. 7, consists of a test cell that houses the evaporator and the condenser and warm and cold water loops that supply heat to and from the water jets. The warm water loop consists of a pump with a bypass, a heat exchanger with a bypass, a static mixer, a turbine flowmeter, and the falling jet in the evaporator. A valve upstream of the heat exchanger regulates the warm water flow rate from 7 to 40 kg/s. The heat exchanger is supplied with hot water from a boiler with a variable heating capacity of 50 to 300 kW. The cold water loop is similar to the warm loop, except that the water is piped directly to a chiller. Falling jets of cold water condense the vapor generated during evaporation. Since both loops are closed, an interconnecting line between the loops replenishes the amount of water lost during evaporation from cold to warm loop.

The test cell is a horizontal, 1.5-m-dia, 1.8-m-long cylinder. Reservoirs underneath the evaporator and the condenser sections allow separate collection of warm and cold water. Glass ports on the top and side provide for lighting, viewing, and photography. The cell is evacuated by a two-stage water ring vacuum pump with an air ejector. A threshold pressure of 700 Pa can be attained in the cell. At the operating conditions, the air leakage into the cell is nominally less than 1 mg/s. Additional details of the apparatus may be found in Green et al. [14].

Results from tests of two different evaporator geometries – falling turbulent planar shattered jets and a vertical spout evaporator (resembling a fountain) – are reported in this paper. Figure 8 shows an artist's rendering of the evaporator section of the test cell with a falling turbulent planar jet. The test cell (A) and its end cap (B) enclose the water jet (F). Water from a 13-cm-dia pipe (E) enters a $0.4 \times 0.4 \times 0.5$ m rectangular upper plenum (G). The floor of the plenum is made of two sections that can be separated to yield varied jet exit thicknesses. Plexiglass windows on the front and back of the plenum allow viewing of the water pool within the plenum. The water level in the plenum is monitored using a meter scale mounted on the front of the plenum.

The falling jet (F) is collected in a bottom pool (C) and drained through a collection tank (D). Typical locations of temperature sensors (T) are also shown in this figure. Evaporated steam escapes towards the condenser section of the test cell.

A vertical spout where natural mixing due to gravity occurs at the liquid exit was also tested as a viable configuration for evaporation. An artist's sketch of the spout evaporator is shown in Fig. 9. Warm water is introduced into the

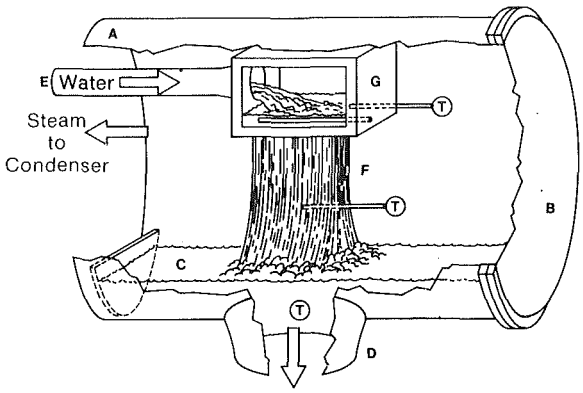

Fig. 8 Artist's sketch of the turbulent planar water jet, showing (A) vacuum tank, (B) tank end cap, (C) bottom liquid pool, (D) drain, (E) water supply line, (F) falling jet, and (G) upper plenum. T indicates temperature sensors.

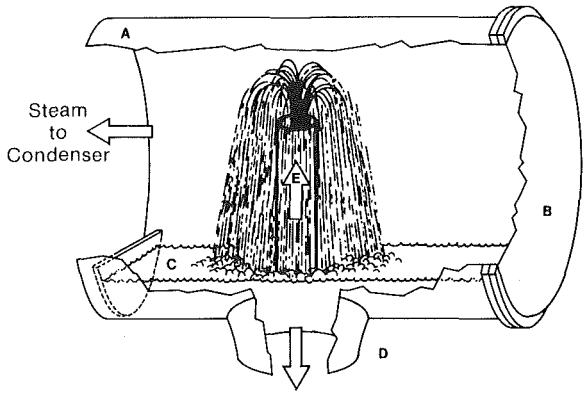

Fig. 9 Artist's sketch of the spout evaporator, showing (A) vacuum tank, (B) tank end cap, (C) bottom liquid pool, (D) drain, and (E), vertical water inlet pipe

evaporator through a vertical 12.7-cm i.d. polyvinyl chloride (PVC) pipe (E). For the tests, the pipe extended nominally 0.5 m above the lower collection water pool (C). The cooled water is drained through the lower collection tank (D).

Instrumentation and Accuracies. The warm and cold water flow rates are measured using two turbine flowmeters, each connected to a flow rate indicator and a frequency counter. The pressure loss in each liquid stream across the test cell is measured using a variable reluctance pressure transducer. Temperatures in the liquid streams are measured with platinum resistance temperature detectors (RTD). The RTD for measuring the inlet water temperature in the evaporator was submerged in the pool within the upper plenum for the turbulent jets and was placed in the inlet manifold for the spout. Outlet water temperature was measured nearly 3 m downstream in the drain pipe to ensure uniformity in the bulk temperature distribution.

To obtain the variation of bulk liquid temperature in the jet, an RTD was mounted on a vertical traverse located directly below the jet exit. The probe can be positioned at any vertical location by a remotely controlled stepping motor drive. Since the liquid is distributed discontinuously in a spray of droplets and the temperature distribution within the droplets is highly nonuniforrm, accurate measurement of bulk liquid temperature within the falling jet is difficult. To suppress intermittent fluctuations in the reading and to ensure measurement of an average bulk liquid temperature, a coarse plastic wire mesh pad of nominally 1 cm thickness was wrapped around the 0.6 cm diameter sensing RTD.

Wet-bulb vapor temperatures were measured by three RTDs above the evaporator and condenser sections of the test

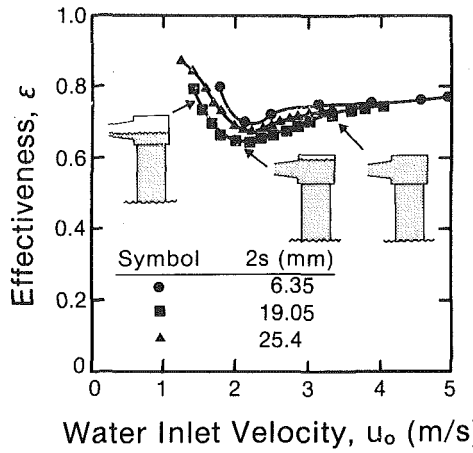

Fig. 10 Measured variation of effectiveness ϵ with water inlet velocity u_o for planar turbulent water jets of three thicknesses

cell. For these measurements, the vapor RTDs are blanketed with cotton wicks wetted from a water reservoir.

A meter stick mounted within the cell permits visual checking of the jet length. Another meter stick mounted on the upper plenum was used for monitoring the liquid level in the plenum.

RTD resistances and pressure transducer voltages are scanned through a data acquisition and control unit and are digitized with a digital voltmeter. All data are collected at a sampling rate of 2 to 3 per s through a desktop computer and stored on magnetic tape. At each test condition, 10 samples were collected and averaged to yield a data point.

Uncertainties in liquid and vapor temperatures arise from calibration errors in the RTD probe, self-heating of the probe, stem conduction through the support elements, background radiation, and random errors in reading. The 1σ uncertainties in the inlet and outlet liquid temperatures are estimated to be ± 0.015°C. Uncertainties in liquid jet temperature measured with the traversing probe are generally higher and are difficult to estimate. Random fluctuations in the experimental measurements indicate an uncertainty level of ± 0.2°C. Uncertainty in the vapor temperature measurements are estimated to be ± 0.02°C.

Uncertainties in flow rate measurements arising from calibration errors in the flow meter and from random errors in reading are estimated to be ± 0.14 kg/s. Uncertainties in the jet length are estimated to be ± 5 cm. With steady-state, heat balance in the test cell can be accurate to ± 2 percent.

Based on random error propagation analysis for a nominal experimental condition (200 kW heat flux; 10 kg/s warm water flow rate: 0.8 m jet length; 25°C inlet temperature), uncertainties in the reported flash effectiveness ϵ (see equation (12)) and the liquid inlet velocity u_o are estimated to be ± 0.005, and ± 0.012 m/s, respectively. Systematic error in ϵ arises from the following conditions in decreasing order of importance: temperature drifts, heat transferred to and from the surroundings, and liquid entrainment in the vapor. This error is estimated to be ± 0.002.

Discussion of Experimental Results

Planar Jets. Experimental results for evaporation from water jets of three different initial thicknesses – 6.35, 19.05, and 25.4 mm – are shown in Fig. 10 as a plot of effectiveness ϵ as a function of the liquid inlet velocity u_o. Uncertainties in ϵ and u_o are approximately within the size of the symbols. Faired lines through the data points are also included. It should be noted that ϵ is an indicator of the total evaporation from both the jet and pool below. For the data in this figure,

T_i was approximately 28°C, and the heat transferred was nearly 230 kW. Since the heat transferred was held constant, the ratio of the vapor to liquid flow rates and the liquid superheat decreases with increasing thickness at any given u_o and with increasing u_o at any given jet thickness. For all jets, ϵ is observed to decrease initially with increasing u_o, attain a minimum, and then increase gradually at higher velocities. Note that the variation of ϵ with u_o is almost independent of the jet thickness and, thus, the initial superheat. However, the minimum of ϵ with u_o can be explained based on visual observations of the water level in the upper plenum and the general structure of the jet and is discussed in the following paragraphs.

For all jet thicknesses tested, at low values of u_o near 1.5 m/s, the water level in the upper plenum was nearly 11 cm (see sketches shown with the data in Fig. 10). Water from the inlet pipe poured on the pool within the upper plenum causing violent mixing in the plenum and resulting in the jet exiting in a spray of droplets right from the plenum. Measured variation of downstream temperature for a 25.4 mm jet, corresponding to this condition at $u_o = 1.41$ m/s, is shown in Fig. 11 as case 1. This figure includes a representative uncertainty level in the jet temperature measurement. For this case, a high rate of heat transfer is seen from the jet exit to a nondimensional downstream distance of about 10. At higher downstream distances, based on the slope of the temperature variation with distance, a decrease in the evaporation rate by a factor of more than 18 can be seen.

The water level in the upper plenum increases with increasing u_o (see Fig. 10). Mixing caused by the incoming water is suppressed by the larger pool water in the upper plenum. The jet exits more and more as a sheet rather than a spray and the effectiveness decreases. At u_o of nearly 2.2 m/s, the upper plenum is filled completely. The jet exits as a sheet extending approximately 10 cm below the plenum, before breaking into droplets. At this point a minimum in ϵ versus u_o is observed for all jet thicknesses tested. A corresponding jet temperature profile for a 25.4 mm jet at $u_o = 2.1$ m/s, shown as case 2 in Fig. 11, exhibits nearly 3 times as low an evaporation rate as does case 1. The associated decrease in the evaporation rate with increasing distance for this case is minimal, up to a $z/2s$ of 20.

Increasing u_o beyond 2.2 m/s up to 5 m/s (Fig. 10) results in an increase in ϵ from nearly 0.65 to 0.75. The jet temperature profile corresponding to a point in this range of u_o is shown in Fig. 11 as case 3 for a 25.4 mm jet at $u_o = 3.25$ m/s. Here the initial evaporation rate is similar to case 2, indicating that the jet exits from the plenum as a solid, coherent unbroken sheet, which is confirmed by visual observations. However, for this case, at $z/2s > 10$, the evaporation rate increases to a rate nearly equal to that for early evaporation for case 1, indicating a dropwise evaporation. Visual observations of the jet at these distances confirm shattering of the sheet into droplets. The evaporation rate decreases with increasing distance, with the rate at $z/2s$ of 30 nearly three times smaller than a maximum observed at a $z/2s$ of nearly 13. The smaller changes in the evaporation rate observed for this case probably result from decreased residence times for the droplets due to increased jet velocity.

A comparison of a measured variation of the bulk liquid temperature with a corresponding analytical predictions is shown in Fig. 12. The experimental data are for the 25.4 mm jet at $u_o = 1.41$ m/s. A faired broken line through the experimental data is included. For the analytical prediction, a droplet diameter of 3 mm was assumed; the value for $k_T = 1.6$ was chosen to match the analytical and measured bulk liquid temperature at $z/2s = 32$. The slope of the bulk temperature variation is an indicator of the local evaporation rate. The evaporation rate for the analytical prediction decreases monotonically with downstream distance. For the experimental data, the initial evaporation rate for $z/2s$ of up to 2.5 is lower than that for the analytical prediction, the difference resulting from the assumed dropwise evaporation for the analytical model as opposed to a probable combination of sheet and spray geometry for the jet.

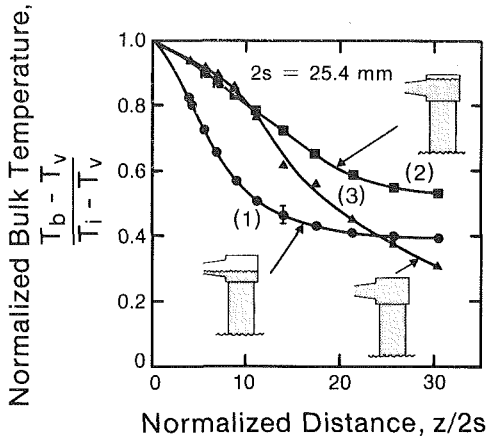

Fig. 11 Measured variation of normalized liquid jet temperature with downstream distance for a 25.4-mm-jet at three water inlet velocities: 1, $u_o = 1.41$; 2, $u_o = 2.1$; and 3, $u_o = 3.25$ m/s

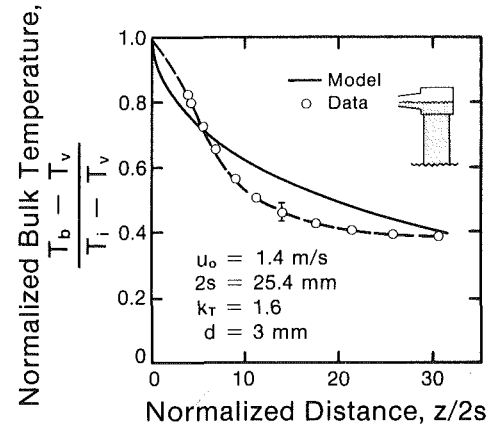

Fig. 12 Comparison of the analytical and measured variations of bulk liquid temperature

For $2.5 < z/2s < 4$, the evaporation rate for the analytical model and the experimental data are comparable. For $4 < z/2s < 14$, the evaporation rate from the jet is larger than predicted. The discrepancy here arises from shattering of the jet, associated increase in turbulent mixing, and exposure of additional fresh surfaces.

Once again for $14 < z/2s < 17$, the evaporation rates for the analyses and the experimental data agree fairly well. For $z/2s > 17$, the measured data indicate a lower evaporation rate than predicted, probably due to a smaller effective exposed interfacial area and a laminar conduction within the droplets. For the analysis, both the interfacial exposed area and the effective turbulence multiplier do not vary throughout the jet.

While evaporation from simple geometries such as films, coherent sheets, and droplets can be modeled with a certain degree of empiricism in estimating an effective thermal conductivity and its decay, the comparison of the jet temperature profiles discussed earlier illustrates the complex nature of shattering jets and the associated difficulties in modeling the evaporation process.

Effect of Screens. For flash evaporation, screens act as efficient mixers that expose a considerable number of fresh surfaces. Effects of placing single and multiple screens

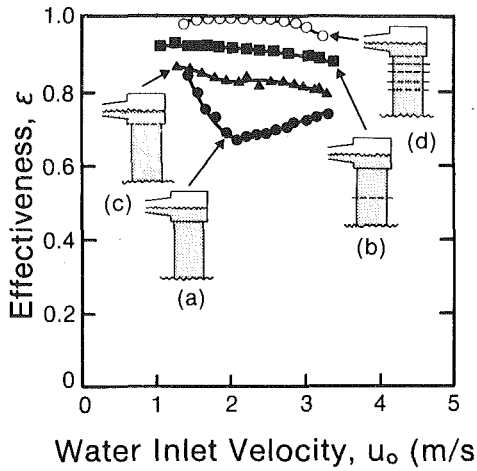

Fig. 13 Effects of single and multiple screens – variation of effectiveness ϵ with jet inlet velocity u_o for a 25.4-mm jet for (*a*) no screen, (*b*) single screen, 40 cm below, (*c*) single screen at inlet, and (*d*) one screen at inlet and four others 10 cm apart

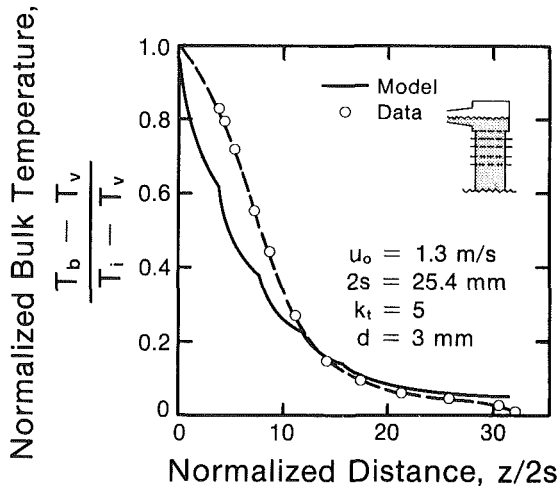

Fig. 14 Comparison of the analytical and measured variations of bulk liquid temperature with downstream distance with one screen at inlet and four others 10 cm apart

beneath a 2.54-cm jet are shown in Fig. 13. For comparison, evaporator data for the case without screens shown as curve (*a*) are also repeated (from Fig. 10) in this figure.

A single screen (6×25 mm diamond grid, 1 mm thick) placed nominally at midlength (40 cm downstream from the jet exit) yields an effectiveness as high as 0.92, as shown by curve (*b*). At $u_o = 2$ m/s, an increase in ϵ of up to 35 percent can be seen. With increasing u_o, ϵ now decreases more gradually almost to an extent of being insensitive to u_o and the upper plenum water pool level.

Data for curve (*c*) corresponds to a condition where a screen was placed right at the bottom of the upper plenum. Since this screen (2 mm thick, with 4.8-mm-dia holes at 6.4 mm centers) had a blockage of nearly 50 percent, the width of the opening at the plenum floor was correspondingly increased to yield, at any water flow rate, jet exit velocities nearly the same as the 2.54-mm-wide jet. Note that ϵ for case (*c*) falls in between the data for cases (*a*) and (*b*). Thus, a screen placed at the liquid exit is not as effective as a screen placed in the liquid free-fall region due to the increased splashing above and below the screen for the latter case. ϵ decreases slightly with increasing u_o for case (*c*). A small but finite local minima corresponding to a full upper plenum can be seen in curve (*c*). Also note that

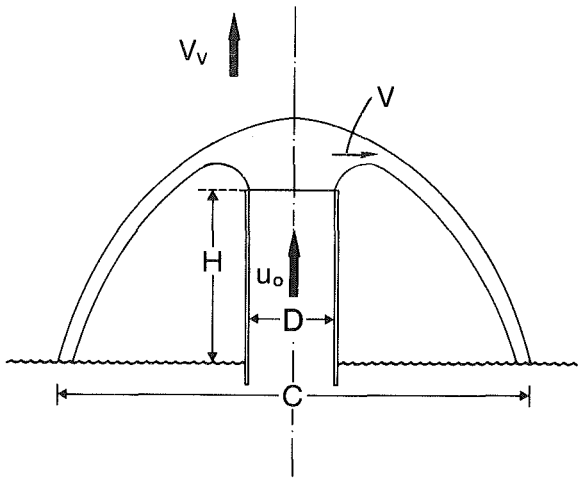

Fig. 15 Cross-sectional view of the vertical spout evaporator

curves (*a*) and (*c*) merge at low velocities, because at these low velocities a spray of droplets emerges from the plenum right from the beginning for case (*a*); similar jet breakup was observed again for case (*c*).

Curve (*d*) shows data for the case where a stack of four screens (6 mm × 25 mm diamond grid, 1 mm thick) was placed in the jet. These screens were located approximately 10 cm apart vertically, starting from the jet exit. At all jet velocities, a dense spray of water droplets developed. Within the uncertainty of the data, an effectiveness of unity is observed for u_o in the range 1.5 to 2.5 m/s. At higher velocities ($u_o > 3$ m/s), a slight decrease in ϵ due to decreased residence times may be seen.

Figure 14 shows a measured jet temperature profile for case (*d*) at $u_o = 1.34$ m/s. Cutouts in the screens were made to allow free passage for the remote traversing temperature probe. The initial evaporation rate is nearly the same as in case 1 in Fig. 11. However, the initial evaporation rate with the screens is maintained for lengths up to nearly $z/2s = 15$. An effectiveness of 0.9 is achieved within a nondimensional length of 17. From the figure, we can infer that the evaporation from the bottom pool is now limited to less than 2-3 percent as evident from the jet temperature datum at $z/2s$ of 30.

For comparison, analytical prediction of the bulk liquid temperature variation with distance for a 25.4 mm jet with four renewals (occurring in the locations of the screens) is also shown in this figure as a solid line. Values for k_T and d here are 5 and 3 mm, respectively, chosen to match the experimental temperature profile for $z/2s$ in the range 20 to 30. The initial evaporation rate of $0 < z/2s < 4$ for the prediction is high (by nearly a factor of 4) compared to the measurements. This difference, of course, results from the assumed dropwise evaporation for the analysis, as opposed to a probable sheet geometry for the jet with lesser exposed interfacial area. For $4 < z/2s < 15$, the analysis predicts lower evaporation rates than those for the measurements. Where $z/2s$ is greater than 20, the evaporation rates for the two cases are comparable.

Vertical Spout Evaporator. Since mixing of the liquid jet by screens in the vapor region to generate fresh surfaces proved effective in enhancing evaporation, evaporation from a vertical spout, shown in Fig. 15, was considered an attractive alternate means for liquid injection. Due to liquid fallback on the incoming liquid, a naturally well-mixed region persists at the liquid entry. Further, a liquid spray forms and distributes itself uniformly over an axisymmetric region around the inlet pipe. With this arrangement, a natural separation with the vapor above and the liquid below occurs

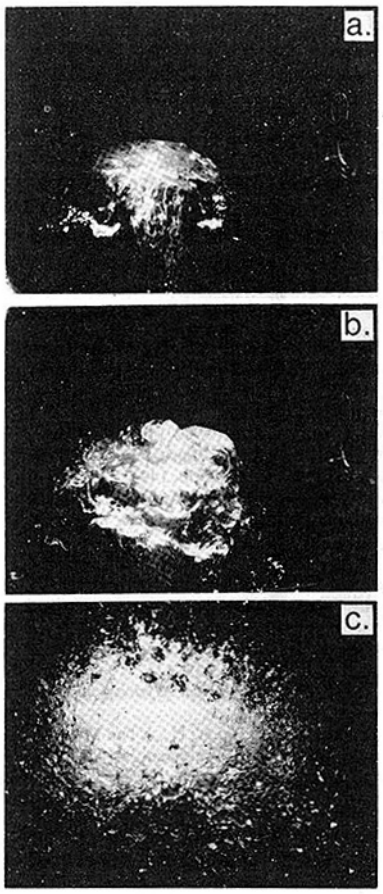

Fig. 16 Photographs of the spout evaporator: (*a*) without heat transfer; (*b*) with 100 kW of heat flux; (*c*) with 250 kW of heat flux

with no obstructions in the vapor path due to liquid distribution pipes as in the previous configuration.

Since the liquid exits vertically upwards, the spout configuration must be selected suitably for each specific application. Choices of liquid velocity u_o, vapor exit velocity V_v, and the spout height H readily allow proper selection of pipe diameter D, and the horizontal coverage C (see Fig. 15). For minimal liquid side pressure losses, the spout height must be kept as low as possible. For evaporation with screens, the required height is less than 30 cm, however, and other considerations (such as sea states and plant motion for a floating OTEC plant) may limit a practical minimum height.

For the present experiments, the physical size of the test cell and its plumbing layout limited the maximum diameter of the spout to 12.7 cm. A second constraint on the facility is the maximum heat transfer rate of 300 kW. Correspondingly, a water inlet velocity u_o of 1.5 m/s, and a spout height of 0.5 m were chosen as representative values for a spout in OTEC applications. At the design water flow rate, a temperature drop of 3.8°C, again typical of OTEC application, could be achieved with the present choices of the spout parameters.

A series of three photographs of the spout evaporator with and without flashing is shown in Fig. 16. Case (*a*) without evaporation shows that the water jet exits smoothly and distributes itself as an axisymmetric sheet. Upon increasing evaporation (i.e., lowering the condenser inlet water temperature), bubbles begin to emerge from the spout and grow on the falling liquid sheet. Bubbles on the order of 10 cm diameter can be seen at heat fluxes of 100 kW [case (b)]. As the evaporation rate is further increased, the jet exit becomes more violent, with the vapor escaping from bursting bubbles. Explosive growth of the vapor shatters the jet into fragments and droplets. Most of the liquid escaping upward falls back

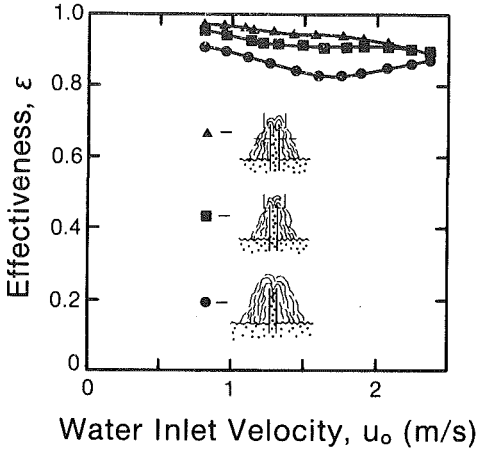

Fig. 17 Measured variations of effectiveness ϵ with inlet velocity u_o for the spout evaporator for three cases: no screens, a cylindrical enclosure and one screen, and a cylindrical enclosure and two screens

on the incoming liquid. The coherent liquid sheet is totally destroyed, becoming a spray of droplets [case (c)].

Plots of the effectiveness ϵ versus the liquid inlet velocity u_o for the spout evaporator with and without screens are shown in Fig. 17. For these data, the heat flux from the jet was held constant at nearly 210 kW. For a spout with no screens, the effectiveness ranges from 0.85 to 0.92. ϵ is seen to decrease slightly with increasing u_o up to 1.7 m/s and then increase once again. The initial decrease is a result of decreasing superheat of the inlet water with increasing flow rate. The latter increases result from increased vertical throw or stagnation heights of the jet due to larger u_o and the resulting extended horizontal coverage of the shattering jet.

For other data shown in this figure, a cylindrical enclosure, 36 cm in diameter and 30.5 cm long, with a screen (2 mm thick, with 4.8-dia holes at 6.4-mm centers) at the bottom, was placed around the spout, with the screen 10 cm below the liquid exit level. The purpose of the enclosure was to restrict the horizontal spread of the liquid and to allow further mixing below. The shattering jet collects, remixes, and then exits as droplets through the screen. For this case, the effectiveness is seen to range from 0.9 to 0.95. For u_o greater than 2 m/s, a considerable amount of liquid spilled over the enclosure and showed a marked decrease in performance.

An additional and similar screen, 40 cm in dia, placed nominally 10 cm below the bottom screen of the enclosure, yielded slightly increased ϵ up to 0.97 in the range $0.7 < u_o < 2$ m/s. For u_o over 2 m/s, due to spilled liquid, the data for the case with and without this second screen do not show any significant difference.

The spout geometry yields effectiveness in the range of 0.9 to 0.97, with a liquid side pressure loss of nearly 0.7 m (the spout height plus the exit kinetic energy losses). The corresponding pressure loss for the planar jets in the reported experiments ranges from 0.8 to 1.0 m.

Although effectiveness is an indicator of the evaporator preformance, for an effective design, many system considerations must be carefully weighed in each application. For example, in design of an open-cycle OTEC plant, considerations that will impact the design include pressure losses on the liquid and vapor paths, simplicity of liquid inlet and exhaust manifolds, evaporator volume, entrainment of droplets, mist elimination needs and losses, immunity to sea states and plant motion for a floating platform, gas desorption, and fabrication costs.

Conclusions

The results of our investigation of flash evaporation from

turbulent jets can be summarized as follows:

- A semianalytical model for evaporation shows that surface evaporation is the dominant mechanism of heat transfer, confined to short times and distances, compared to the conventional gross jet parameters such as jet residence time and thickness. For shattered jets, residence time and jet thickness are not the relevant correlating parameters.
- The analytical model has been extended for analyzing shattered turbulent jets through use of "gross" parameters representing the effective turbulent thermal diffusivity and the increased interfacial area due to the spray of droplets. Due to lack of other reliable accurate means of representing these effects, the current modeling approach offers a most practical means for modeling.
- Surface renewals that result in destroying growing thermal boundary layers on the liquid side by mixing the bulk liquid and reexposing fresh surfaces at the bulk liquid temperature have been shown both analytically and experimentally to be effective for enhancing evaporation.
- The present analytical model can be readily extended for analyzing other evaporator geometries such as open channels and falling films with suitable parameters to represent the effective turbulent mixing and exposed interfacial areas.
- In the experimental investigation of evaporation from falling jets of initial thicknesses of 6 to 25 mm, all jets were observed to shatter into a spray of droplets with their effectiveness nearly independent of the initial thickness. For shattered jets, analytical results yield a similar independence of evaporation effectiveness on the initial jet thickness.
- Measured temperature variations with the jet distance of fall illustrate the complex nature of the heat transport, shown to be dependent upon both the initial level of jet turbulence and the subsequent shattering.
- Screens placed directly below the jet result in further break-up of the jet into droplets and exposing fresh surfaces for enhanced evaporation. Four screens placed one below the other under a 25-mm jet yielded an evaporator effectiveness of nearly unity.
- For shattered jets, the independence of evaporator effectiveness on the jet thickness leads to a liquid inlet geometry, namely the vertical spout, with a simple means for liquid distribution and minimal liquid side pressure losses. Experiments with the spout evaporator indicate that an effectiveness of over 0.95 can be achieved with this configuration in realistic applications.

Acknowledgment

The authors would like to express their gratitude to the U.S. Department of Energy, Ocean Energy Technology Division, for funding this research.

References

1 Maa, J. R., "Evaporation Coefficient of Liquids," *Industrial and Engineering Chemistry Fundamentals*, Vol. 6, No. 4, 1967, pp. 504–518.

2 Mills, A. F., Kim, S., Leininger, T., Ofer, S., and Pearson, A., "Heat and Mass Transport in Turbulent Liquid Jets," *International Journal of Heat and Mass Transfer*, Vol. 25, No. 6, 1982, pp. 889–897.

3 Brown, R., and York, J. L., "Sprays Formed by Flashing Liquid Jets," *AIChE Journal*, Vol. 8, No. 2, 1962, pp. 149–153.

4 Balitskiy, S. A., and Shurchkova, Y. A., "Flashing of a Superheated Liquid Under Vacuum," *Heat Transfer-Soviet Research*, Vol. 1, No. 3, 1969, pp. 106–109.

5 Miyatake, O., Tomimura, T., Ide, Y., and Fumii, T., "An Experimental Study of Spray Flash Evaporation," *Desalination*, Vol. 36, 1981, pp. 113–128.

6 Theofanous, T. G., House, R. N., and Brumfield, L. K., "Turbulent Mass Transfer at Free, Gas-Liquid Interfaces, With Applications to Open-Channel, Bubble, and Jet Flows," *International Journal of Heat and Mass Transfer*, Vol. 19, No. 6, 1976, pp. 613–624.

7 Levich, V. G., *Physicochemical Hydrodynamics*, Prentice-Hall, N.J., 1962, pp. 689–699.

8 Heertjes, P. M., and deNie, L. H., "The Mechanism of Mass Transfer During Formation, Release, and Coalescence of Drops. Part I—Mass Transfer to Drops Formed at a Moderate Speed," *Chemical Engineering Science*, Vol. 21, 1966, pp. 755–768.

9 Sherwood, T. K., Pigford, R. L., and Wilke, C. R., *Mass Transfer*, McGraw-Hill, New York, 1975, p. 228.

10 Hasson, D., Luss, D., and Peck, R., "Theoretical Analyses of Vapour Condensation on Laminar Liquid Jets," *International Journal of Heat and Mass Transfer*, Vol. 7, 1964, pp. 969–981.

11 Butkov, E., *Mathematical Physics*, Addison-Wesley, Reading, Mass., 1968, pp. 385–388.

12 Carlslaw, H. S., and Jaeger, J. C., *Conduction of Heat in Solids*, Oxford University Press, New York, 1947.

13 Boyadzhiev, L., Elenkov, D., and Kyuchukov, G., "On Liquid-liquid Mass Transfer Inside Drops in a Turbulent Flow Field," *The Canadian Journal of Chemical Engineering*, Vol. 47, 1969, pp. 42–44.

14 Green, H. J., Olson, D. A., Bharathan, D., and Johnson, D. H., *Measured Performance of Falling Jet Flash Evaporators*, SERI/TP-631-1270, Solar Energy Research Institute, Golden, Colo., June 1981.

A Mathematical Model of Condensation Heat and Mass Transfer to a Moving Droplet in its Own Vapor

J. N. Chung

Tae-Ho Chang

Department of Mechanical Engineering,
Washington State University,
Pullman, Wash. 99164

A mathematical model appropriate for predicting condensation heat and mass transfer rates along the surface of a droplet moving in pure vapor is developed. A Karman-Pohlhansen type of integral approach was adopted for the solution of vapor-phase boundary layer equations. The diffusion-dominated internal core was solved using a finite difference numerical scheme. The rate-controlling mechanism of pure vapor condensing on a droplet was found in the thermal core region of the liquid phase where the streamlines correspond to the isotherms and diffusion is the primary transport mechanism. The total rate of heat transfer is found to be inversely proportional to the droplet radius. The condensation velocity at the vapor-liquid interface reduces the boundary layer thickness and moves the separation point toward the rear stagnation point. The internal motion also helps increase the transport rates by reducing both the boundary layer thickness and thermal resistance in the liquid phase. The results predicted by this model compare favorably with available experimental values.

Introduction

An understanding of the condensation heat and mass transfer mechanisms associated with a droplet translating in a vapor is necessary in a variety of industrial processes and applications and also in atmospheric science. Several authors [1-8] have investigated a variety of situations involving the heat and mass transfer of spherical droplets at various values of the Reynolds and the Peclet numbers. Ford and Lekic [9] experimentally studied the condensation of pure steam on a cold droplet through a photographic measurement of the droplet size. A correlation based only on conduction inside the droplet predicts their experimental results reasonably well in the early part of the process. This is as expected because the droplets were generated in such a way that the internal circulation was absent. Chung and Ayyaswamy [10-12] investigated analytically the condensation heat and mass transfer to a moving droplet with internal circulation. The effects of noncondensibles, internal circulation, and other system parameters on condensation rates were reported through a stagnation point approach which reduced the complication of the solution procedures.

In this paper, we extended the previous stagnation point analyses to cover the entire development of momentum and thermal boundary layers along the droplet surface through a Karman-Pohlhausen type of integral approach [13]. The Karman-Pohlhausen integral method has become a standard technique for both fluid mechanics and heat transfer in boundary layer problems. This technique was also used in [7] for the analysis of an evaporating hydrocarbon droplet. In [7], the investigation was mainly concerned with the overall evaporation rates and size changes. Also the momentum, thermal, and concentration boundary layers were assumed all equal and all species were assumed to have equal specific heats and to behave like ideal gases. In this paper, all the foregoing assumptions used in [7] have been relaxed and in general the heat sink capacity, i.e., the heat transfer inside the droplet, dominates the condensation rates, while the rates of supply of latent heat from the gas stream dominate the evaporation rates. This study, including the entire droplet surface, presents specifically the local condensation heat and mass transfer rates, the separation point, and the effects of condensation interfacial velocity on the developments of both momentum and thermal boundary layers and on the separation point. This boundary-layer-type analysis is considered to be valid only for large droplet Reynolds number ($\mathrm{Re} = U_\infty R/\nu_\infty$), i.e., of 0(100), where laminar boundary layers are believed to form near the droplet surface [13]. In many practical industrial systems where the droplet is introduced through a spray nozzle and rain drops of medium to large sizes in atmospheric study, the internal motion is fully developed and the droplet Reynolds numbers are usually greater than 100.

The theoretical prediction of the condensation rates, including the liquid-phase convective motion, involves the solution of the coupled equations of motion and energy in both the vapor and the liquid phases. The coupling between the conservation equations occurs at the vapor-liquid interface.

Analysis

Consider a spherical water droplet of uniform temperature T_o, with steady internal motion, that is moving at U_∞ relative to the ambient pure steam at T_∞ and under atmospheric pressure. A schematic representation of the physical model and coordinate system are shown in Fig. 1. For most liquid droplets translating in a gas environment, the internal motion is one order of magnitude for droplets with uncontaminated surface [7] to two orders of magnitude slower than the droplet velocity for droplets contaminated with surfactants [14]. Taking account of the differences in thermal properties between common vapor and liquid phases and the velocity variations, the Peclet numbers for both the vapor and the liquid phases are assumed of 0(100) in this analysis. A Peclet number of 0(100) for the liquid phase represents the aforementioned range of internal motion.

Contributed by the Heat Transfer Division for publication in the JOURNAL OF HEAT TRANSFER. Manuscript received by the Heat Transfer Division January 3, 1983.

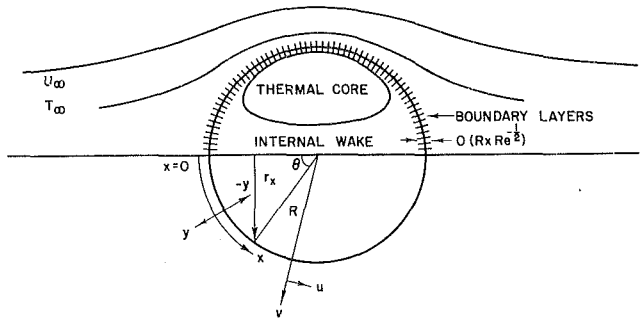

Fig. 1 Schematic and coordinate system

Vapor-Phase Analysis.

(*a*) In view of the high Reynolds number and the high Peclet number assumption, the flow field and the heat transfer will be taken to correspond to laminar boundary layers.

(*b*) Since the flow velocity range considered is moderate, viscous dissipation and expansion work will be neglected.

(*c*) The vapor momentum and heat transfer processes are assumed quasi-steady due to a short boundary layer residence time compared to the droplet lifetime [7].

(*d*) For the range of Reynolds numbers, there is a recirculating wake near the rear stagnation point. Boundary layer assumptions are no longer valid, but the shear stress and the heat flux in the wake region are negligible for the Reynolds number of interest [13]. Hence this region will be ignored in estimating the overall condensation rates.

(*e*) The ambient gas is composed of only pure steam and there are no noncondensibles and surfactants.

The conservation equations with axisymmetry in orthogonal boundary layer coordinates (see Fig. 1) for compressible flow over a sphere is given as follows

$$\frac{\partial}{\partial x}(\rho u r_x) + \frac{\partial}{\partial y}(\rho v r_x) = 0 \quad \text{conservation of mass} \tag{1}$$

$$\rho u \frac{\partial u}{\partial x} + \rho v \frac{\partial u}{\partial y} = \frac{\partial}{\partial y}\left(\mu \frac{\partial u}{\partial y}\right) + \rho_e u_e \frac{du_e}{dx} - g(\rho - \rho_\infty)\sin(x/R) \quad \text{conservation of momentum} \tag{2}$$

$$\rho u \frac{\partial T}{\partial x} + \rho v \frac{\partial T}{\partial y} = \frac{1}{C_p}\frac{\partial}{\partial y}\left(K \frac{\partial T}{\partial y}\right) \quad \text{conservation of energy} \tag{3}$$

where

$$r_x = R \sin(x/R)$$

The last term on the right-hand side of equation (2) represents the buoyancy contribution, which is small in this analysis but is included for completeness. The corresponding boundary conditions are

$$\begin{aligned} u &= u_e(x), \quad T = T_\infty \quad \text{as } y \to \infty \\ u &= u_i(x), \quad T = T_i \quad \text{at } y = 0 \end{aligned} \tag{4}$$

where $u_e = (3/2)U_\infty \sin(x/R)$, T_∞ is the temperature of the superheated steam, and T_i is assumed as the saturation

Nomenclature

a_n = coefficients defined in equation (16)
b_n = coefficients defined in equation (17)
c_p = specific heat at constant pressure
Fr = Froude number $= (gR/u_\infty{}^2)$
g = acceleration due to gravity
$g_1(\phi)$ = dimensionless function as defined in [8]
$g_2(\phi)$ = dimensionless function as defined in [8]
K = thermal conductivity
$\dot{m}$ = mass flux
p = pressure
Pe_∞ = vapor phase Peclet number $= (U_\infty R/\alpha_\infty)$
Pe_l = liquid phase Peclet number $= (U_{im} R/\alpha_l)$
Pr = Prandtl number $= (\nu/\alpha)$
Q = rate of heat flow
Re_∞ = Reynolds number $= (U_\infty R/\nu_\infty)$
q = heat flux
R = droplet radius
r = r-direction in spherical coordinate
r_x = normal distance of the interface from the axis of symmetry
T = temperature
t = time
U_∞ = free stream velocity
u = velocity component in x-direction
v = velocity component in y-direction
x = vapor-phase tangential boundary layer coordinate
y = vapor-phase boundary layer coordinate normal to interface

Greek Symbols

α = thermal diffusivity $= (K/\rho c_p)$
β = coefficient of thermal expansion
δ_1 = displacement thickness
δ_2 = momentum thickness
δ_3 = energy thickness
δ_m' = dimensionless momentum boundary layer thickness as defined in equation (12)
δ_T' = dimensionless thermal boundary layer thickness as defined in equation (12)
η = similarity variable as defined in equation (31)
η_m = dimensionless y in momentum equation as defined in equation (12)
η_T = dimensionless y in energy equation as defined in equation (12)
η_δ = value of η at edge of liquid-phase thermal boundary layer
θ = dimensionless temperature
θ_η = dimensionless temperature at η
$\bar{\theta}$ = average temperature on a closed stream surface in Hill's vortex
θ = angle in spherical coordinate
λ = latent heat of vaporization
μ = dynamic viscosity
ν = kinematic viscosity
ρ = density
τ = dimensionless time
ϕ = dimensionless stream function defined in [8]
ϕ_o = value ϕ at the outer boundary of thermal core
ϕ_ρ = ratio (ρ/ρ_∞)
ϕ_μ = ratio (μ/μ_∞)
ϕ_{cp} = ratio $(c_p/c_{p\infty})$
ϕ_K = ratio (K/K_∞)

Subscripts

CD = condensation
CV = convection
e = outer edge of vapor-phase boundary layer
en = normalized value at the outer edge of vapor boundary layer
i = vapor–liquid interface
in = normalized value at the vapor–liquid interface
l = liquid phase
n = normalized value
δ = at the outer boundary of liquid thermal boundary layer
∞ = in the bulk phase, far away from droplet surface

temperature corresponding to the system pressure. U_i is the surface velocity of the droplet, and it can be written as the following if only dominant terms are kept for the liquid boundary layer [4]

$$U_i(x) = (3/2)U_{im}\sin(x/R) \tag{5}$$

This maximum surface velocity, $(3/2)U_{im}$, located at the droplet equator can be calculated based on the assumption stated before that

$$\mathrm{Pe}_l = 100, \left(\mathrm{Pe}_l = \frac{U_{im}R}{\alpha_l}\right) \tag{6}$$

This results in a surface velocity which is one to two orders of magnitude smaller than the free-stream velocity U_∞ based on common Prandtl numbers of both phases.

The compatibility condition at the interface which couples the vapor phase and the liquid phase, $y=0$, is the continuity of heat flux

$$K_l \frac{\partial T}{\partial y}\bigg|_l = \dot{m}\lambda + K\frac{\partial T}{\partial y}\bigg|_v \tag{7}$$

$$\dot{m} = \text{mass condensation flux} \tag{8}$$

The governing equations are then integrated over the boundary layer from $y = 0$ to $y = \delta$ (where δ is the thickness of the boundary layer which is different for momentum and energy boundary layers). Let us define the following

$$\delta_1 = \int_0^{\delta_M}\left(1-\frac{\rho u}{\rho_e u_e}\right)dy \tag{9}$$

$$\delta_2 = \int_0^{\delta_M}\frac{\rho u}{\rho_e u_e}\left(1-\frac{u}{u_e}\right)dy \tag{10}$$

$$\delta_3 = \int_0^{\delta_T}\frac{\rho u}{\rho_e u_e}\left(1-\frac{T}{T_e}\right)dy \tag{11}$$

$$x_n = x/R,\ \eta_M = y/\delta_M,\ \eta_T = y/\delta_T,\ \bar{u}_n = u/U_\infty,$$
$$v_n = (v/U_\infty)\mathrm{Re}_\infty^{1/2},\ \delta_{1n} = (\delta_1/R)\mathrm{Re}_\infty^{1/2},\ \delta_{2n} = (\delta_2/R)\mathrm{Re}_\infty^{1/2},$$
$$\delta_{3n} = (\delta_3/R)\mathrm{Re}_\infty^{1/2},\ \delta'_M = (\delta_M/R)\mathrm{Re}_\infty^{1/2},\ \delta'_T = (\delta_T/R)\mathrm{Pe}_\infty^{1/2}$$

and

$$\theta = T/T_e \tag{12}$$

also

$$\mathrm{Pe}_\infty = (U_\infty R/\alpha_\infty) \text{ and } \mathrm{Fr} = (gR/U_\infty^2) \tag{13}$$

where the subscript i represents the value at the interface, and e represents the value at the outer edge of the boundary layer. The variables δ_1, δ_2, and δ_3 correspond to displacement, momentum, and energy thicknesses, respectively. δ_M and δ_T are momentum and energy boundary layer thicknesses, respectively.

Then the dimensionless integrated form of the momentum and energy equations become

$$\frac{d\delta_{2n}}{dx_n} + \cot(x_n)\left(3+\frac{\delta_{1n}}{\delta_{2n}}\right)\delta_{2n} - \phi_{\rho i}\left(\frac{v_{in}}{u_{en}}\right)\left(1-\frac{u_{in}}{u_{en}}\right) = \left.\frac{(\phi_{\mu i}/\delta'_M)\left(\frac{\partial u_n}{\partial \eta_M}\right)}{U_{en}^2}\right|_i + \frac{\mathrm{Fr}\,\beta T_e \sin x_n}{\mathrm{Pr}_\infty^{1/2}u_{en}^2}\int_0^1 \phi_\rho\beta(1-\theta)\,d\eta_T \tag{14}$$

$$\frac{d\delta_{3n}}{dx_n} + 2\cot(x_n)(\delta_{3n}) - \frac{\mathrm{Pr}_\infty^{1/2}v_{in}}{u_{en}}(1-\theta_i) = (\phi_K/\phi_{c_p})\frac{1}{\delta'_T u_{en}}\left(\frac{\partial\theta}{\partial\eta_T}\right)\bigg|_i - \frac{1}{u_{en}\delta'_T}\int_0^1\frac{\phi_K}{\phi_{C_p}}\left(\frac{\partial\theta}{\partial\eta_T}\right)\frac{\partial \ln c_p}{\partial\eta_T}\,d\eta_T \tag{15}$$

The velocity and temperature profiles are assumed to be fourth-order polynomials in η.

$$\frac{u_n}{u_{en}} = \sum_{n=0}^{4} a_n \eta_M^n \tag{16}$$

$$\theta = \sum_{n=0}^{4} b_n \eta_T^n \tag{17}$$

Based on boundary conditions (4), the compatibility condition (7) and the following extra conditions

$$\frac{\partial^2 u}{\partial y^2} = \frac{\partial^2 T}{\partial y^2} = 0$$
$$\frac{\partial u}{\partial y} = \frac{\partial T}{\partial y} = 0 \qquad \text{as } y\to\infty \tag{18}$$

and

$$\rho_i u_i\left(\frac{\partial u}{\partial x}\right)\bigg|_{y=0} + \rho_i v_i\left(\frac{\partial u}{\partial y}\right)\bigg|_{y=0} = \left[\frac{\partial}{\partial y}\left(\mu\frac{\partial u}{\partial y}\right)\right]\bigg|_{y=0} + \rho_e u_e\frac{du_e}{dx} \tag{19}$$

$$\rho_i u_i\left(\frac{\partial T}{\partial x}\right)\bigg|_{y=0} + \rho_i v_i\left(\frac{\partial T}{\partial y}\right)\bigg|_{y=0} = \left[\frac{1}{C_p}\frac{\partial}{\partial y}\left(K\frac{\partial T}{\partial y}\right)\right]\bigg|_{y=0} \tag{20}$$

The differential momentum and energy equation are satisfied at $y=0$. The coefficients are determined and they are given below

$$\begin{aligned}
a_0 &= \frac{u_i}{u_e}\\
a_1 &= 2-2a_0-(1/3)a_2\\
a_2 &= \left[9/2\left[(\phi_{\rho i}a_0^2-1)\cos x_n + \phi_{\rho i}a_0\frac{da_0}{dx}\sin x_n\right]\delta_M'^2 - \left(\phi_{\rho i}v_{in} - \frac{d\phi_{\mu i}}{dx_\eta}/\delta'_M\right)(6-6a_0)\delta'_M - 2\mathrm{Fr}(1-\phi_{\rho i})\delta_M'^2\right]\Big/\left(6\phi_{\mu i} + \phi_{\rho i}\delta'_M v_{in} - \frac{d\phi_{\mu i}}{dx_n}\right)\\
a_3 &= -2+2a_0-a_2\\
a_4 &= 1-a_0+(1/3)a_2
\end{aligned} \tag{21}$$

and

$$\begin{aligned}
b_0 &= T_i/T_e\\
b_1 &= 2-2b_0-(1/3)b_2\\
b_2 &= \left(a_0\frac{3}{2}(\sin x_n)\frac{db_0}{dx_n} + \frac{\mathrm{Pr}_\infty^{1/2}\frac{dv_{in}}{dx_n}b_1}{\delta'_T}\right)\left(\frac{\delta_T'^2}{2}\right)\left(\frac{\mathrm{Pe}_i}{\mathrm{Pe}_\infty}\right) - \frac{b_i}{2\phi_{Ki}}\left(\frac{d\phi_{Ki}}{dx_n}\right)\\
b_3 &= 4-4b_0-3b_1-2b_2\\
b_4 &= -3+3b_0+2b_1+b_2
\end{aligned} \tag{22}$$

The compatibility equation (5) becomes

$$b_1 = \frac{-R\delta_T'}{K_i T_e \mathrm{Pe}_\infty^{1/2}} q(x_n) + \frac{\mu_e \phi_{\rho i} \delta_T' v_{in} \lambda}{\mathrm{Pr}_\infty^{1/2} T_e K_i} \tag{23}$$

where

$q(x)$ = heat flux entering the droplet

$$= -K_l \frac{\partial T_l}{\partial y}\bigg|_{y=0} \tag{24}$$

These coefficients a_n and b_n are functions of x only after using the polynomial profiles, equations (14) and (15) become the following

$$\frac{d\delta_{2n}}{dx_n} + \frac{1}{\sin x_n}\left[\left(3+\frac{\delta_{1n}}{\delta_{2n}}\right)\delta_{2n}\cos x_n - \frac{2}{3}\phi_{\rho i} v_{in}(1-a_0)\right.$$

$$\left. - \frac{2}{3}\frac{\phi_\mu a_1}{\delta_M'}\right] - \frac{\mathrm{Fr}}{\mathrm{Pr}_\infty^{1/2}} \frac{\delta_T' T_e \phi_\rho \sin x_n}{\left(\frac{3}{2}\sin x_n\right)^2} \int_0^1 \beta(1-\theta)\, d\eta_T = 0 \tag{25}$$

$$\frac{d\delta_{3n}}{dx_n} + \frac{1}{\sin x_n}\left[2\delta_{3n}\cos x_n - \frac{2}{3}\phi_{\rho i} v_{in}(1-b_0)\right.$$

$$\left. - \frac{2}{3}\frac{b_1}{\delta_T'} + \frac{2}{3}\frac{1}{\delta_T'}\int_0^1 \left(\frac{\partial \phi}{\partial \eta_T}\right)\left(\frac{\partial \ln c_p}{\partial \eta_T}\right) d\eta_T\right] = 0 \tag{26}$$

Liquid-Phase Analysis.

(*a*) Since both the Reynolds number and the Peclet number for the liquid phase are of 0(100), three separate regions of flow can, in general, be discerned [6]; i.e., a boundary-layer-type flow near the surface of the droplet, an internal wake that follows the boundary layer, and an internal core of Hill's vortex that is surrounded by the boundary layer and the internal wake (see Fig. 1) corresponding to the flow structure, thermal boundary layer, thermal internal wake, and thermal core are present and responsible for heat transfer inside the droplet [15]. It was shown in [11] that the thermal boundary layer may be assumed quasi-steady if the Peclet number is large, but the thermal core heat transfer is a transient process because its characteristic time of transport is comparable to the droplet lifetime.

(*b*) The increase in droplet size is neglected. For the cases investigated, the radius of the droplet only increases around 1 percent. The droplet is also assumed to remain spherical.

(*c*) The effect of condensate on the fluid motion is also neglected due to negligible mass addition from condensation.

(*d*) The liquid properties are assumed constant. A simple 1/3 rule [16] is adopted for establishing the reference temperature at which the properties are evaluated.

(*e*) The low heat transfer rates in the region after flow separation is assumed to have negligible effect on the heat transfer structure, already mentioned.

(*i*) *Thermal Boundary Layer.* The quasi-steady energy equation for the thin thermal boundary can be written as follows

$$u_l \frac{\partial T_l}{\partial x} + v_l \frac{\partial T_l}{\partial y} = \alpha_l \frac{\partial^2 T_l}{\partial y^2} \tag{27}$$

where $y = r - R$ boundary conditions are,

$$\begin{aligned} T_l &= T_i \qquad y = 0 \\ T_l &= T_\delta(t) \qquad y = y_\delta \end{aligned} \tag{28}$$

where y_δ is the thickness of the thermal boundary layer, and $T_\delta(t)$ is the transient temperature of the thermal core at the core-boundary layer interface.

Since the boundary layer is thin, we can approximate the velocity field as given below [5]

$$\begin{aligned} u_l &= \frac{3}{2} U_{im} \sin\theta \\ v_l &= 3U_{im}\left(\frac{-y}{R}\right)\cos\theta \end{aligned} \tag{29}$$

The energy equation then becomes

$$\frac{3}{2}\mathrm{Pe}_l\left(-2y\cos\theta\frac{\partial T_l}{\partial y} + \sin\theta\frac{\partial T_l}{\partial \theta}\right) = \frac{\partial^2 T_l}{\partial y^2} \tag{30}$$

This equation can be transformed into an ordinary differential by defining a new independent variable η.

$$\eta = \frac{(3/2)^{1/2}\mathrm{Pe}_l^{1/2} y_n \sin^2\theta}{[8/3\text{-}4(\cos\theta - (1/3)\cos^3\theta)]^{1/2}}, \quad y_n = y/R \tag{31}$$

The energy equation now is

$$-2\eta\frac{\partial \theta_l}{\partial \eta} = \frac{\partial^2 \theta_l}{\partial \eta^2} \quad \text{and} \quad \theta_l = \frac{T_l - T_o}{T_i - T_o} \tag{32}$$

The corresponding boundary conditions are transformed as

$$\begin{aligned} \theta_l &= 1 \qquad , \quad \eta = 0 \\ \theta_l &= \frac{T_\delta - T_0}{T_i - T_o} \\ &= \theta_\delta(t) \qquad , \quad \eta = \frac{1.22\mathrm{Pe}_l^{1/2} y_{\delta n} \sin^2\theta}{[8/3\text{-}4(\cos\theta - (1/3)\cos^3\theta]^{1/2}} \\ &= \eta_\delta \end{aligned} \tag{33}$$

The solution to equation (32), subject to boundary condition (33) is given as follows

$$\theta_l = \frac{(\theta_\delta(t) - 1)}{\mathrm{erf}(\eta_\delta)}\mathrm{erf}(\eta) + 1 \tag{34}$$

(*ii*) *Thermal Core.* As mentioned previously, the thermal core heat-up should be treated as an unsteady process. Furthermore, Brignell [15] has shown that the transfer mechanism in the core, where Hill's vortex streamlines are all isotherms, is essentially a diffusion process. That is, there is no temperature gradient in the direction of fluid motion. The heat transfer is only taking place perpendicular to those streamlines. In this case, orthogonal streamline coordinates are more appropriate than spherical coordinates. The governing equation for the core in general orthogonal coordinate symbols is

$$\frac{\partial T_l}{\partial t} + \mathbf{v}_l \cdot \nabla T_l = \alpha_l \nabla^2 T_l \tag{35}$$

where $\mathbf{v}_l$ is the velocity vector representing Hill's vortex.

Following [8], the energy equation (35) can be written in terms of the streamline orthogonal coordinates as follows

$$\frac{\partial \bar{\theta}_l}{\partial \tau} = \frac{g_2(\phi)}{g_1(\phi)}\frac{\partial^2 \bar{\theta}_l}{\partial \phi^2} + \frac{dg_2(\phi)}{d\phi}\frac{1}{g_1(\phi)}\frac{\partial \bar{\theta}_l}{\partial \phi} \tag{36}$$

where $\bar{\theta}_l = (\bar{T}_l - T_o)/(T_i - T_o)$, $\bar{T}_l$ is the average temperature on a streamline.

$\tau = \alpha_l t / R^2$

ϕ is the dimensionless stream function and is equal to

$$\phi = 1 - 4\left(\frac{r}{R}\right)^2\left(1 - \left(\frac{r}{R}\right)^2\right)\sin^2\theta$$

$g_1(\phi)$ and $g_2(\phi)$ are also given in [8]. The corresponding initial and boundary conditions to equation (36) are

$$\bar{\phi}_l = 0, \quad \tau = 0 \tag{37}$$

$$\frac{\partial \bar{\theta}_l}{\partial \tau} = \frac{dg_2(\phi)}{d\phi}\frac{1}{g_1(\phi)}\frac{\partial \bar{\theta}_l}{\partial \phi}, \phi = 0 \quad \text{(the vortex center)} \tag{38}$$

This implies that temperature is a regular function of ϕ at vortex center.

$$\frac{\partial \bar{\theta}_l}{\partial \phi} = Q_1(t), \ \phi = \phi_o \quad \text{(thermal core and thermal boundary layer interface)} \tag{39}$$

The foregoing condition is written based on the continuity of heat flux. That is, the rate of heat transfer through the droplet surface is equal to the rate of heat transfer through the outer boundary of the thermal core at any moment.

The rate of heat transfer through the droplet surface can be calculated as follows

$$Q_2(t) = \int_0^{\pi} -K_l \frac{\partial T_l}{\partial y}\bigg|_{y=0} 2\pi R(\sin\theta) R d\theta$$

$$= \frac{6.1 K_l \Delta T R \, \mathrm{Pe}_l^{1/2}(1-\theta_\delta(t))}{\mathrm{erf}(\eta_\delta)} \int_0^{\pi} \frac{\sin\theta(1+\cos\theta)}{(2+\cos\theta)^{1/2}} d\theta \tag{40}$$

But $Q_1(t)$ is not equal to $Q_2(t)$ because of the difference in coordinate systems and their relationship is given as follows. It is noted that

$$\frac{\partial T_l}{\partial y}\bigg|_{y=\delta} = \frac{8\sin^2\theta}{R}\left(\frac{\partial \bar{T}_l}{\partial \phi}\right)\bigg|_{\phi=\phi_o} \tag{41}$$

Therefore,

$$Q_2(t) = \frac{64}{3} K_l \pi R \Delta T \left(\frac{\partial \bar{\theta}_l}{\partial \phi}\right)\bigg|_{\phi=\phi_0} \left(1 - \frac{y_\delta}{R}\right)^2 \tag{42}$$

$$\left(\frac{\partial \bar{\theta}_l}{\partial \phi}\right)\bigg|_{\phi=\phi_0} = Q_1(t)$$

combining (41) and (42), we obtain

$$\frac{\partial \bar{\theta}_l}{\partial \phi}\bigg|_{\phi=\phi_0} = \frac{0.122 \mathrm{Pe}_l^{1/2}(1-\theta_\delta(t))}{(1-y_\delta/R)^2 \mathrm{erf}(\eta_\delta)} \tag{43}$$

In the condensation of pure steam on a water droplet, the condensation heat and mass transfer rates are completely dominated by the liquid phase transport mechanism. First, the droplet surface temperature is known and stays constant during the transient process. Therefore, the liquid phase heat transfer is independent of the vapor phase if the characteristic time of transport of the vapor phase is much smaller than that of the liquid phase. As mentioned previously, the characteristic time of transport for both boundary layers are much smaller than that of the thermal core because conduction is the primary heat transfer mechanism in the core, while forced convection is the dominant mechanism in the boundary layers. Hence the conduction heat transfer in the core is the rate controlling process for the overall condensation heat transfer of pure steam on a droplet.

As required by the matching condition at the interface between the thermal boundary layer and the thermal core, the temperature at the interface is unique, i.e.,

$$\theta_\delta(t) = \bar{\theta}_\delta(t)_{\phi=\phi_o}$$

and the heat flux is continuous at the interface. If the interface temperature, $\theta_\delta(t)$, is known, the heat flux input to the thermal core can be calculated from equation (43). Then one can solve the transient energy equation (36) to obtain the new interface temperature. The time-dependent heat flux transferred to the droplet can also be calculated by equation (34)

$$-K_l \frac{\partial T_l}{\partial y}\bigg|_{y=0} = 0.98 \frac{K_l \Delta T}{R} \frac{\mathrm{Pe}_l^{1/2}(1-\theta_\delta(t))}{\mathrm{erf}(\eta_\delta)} \frac{1+\cos\theta}{(2+\cos\theta)^{1/2}} \tag{44}$$

This is the flux, $q(x)$, required in equation (23) for vapor-phase calculation.

Solution Procedure

A computer program was developed to solve the governing equation for both phases. Because of the transient process, a marching procedure in time is required for the liquid thermal core calculation. At the beginning of each time step, the heat-up in the thermal core is computed first by solving equation (36) with boundary conditions (37) and (43). The Crack-Nicholson scheme was adopted for writing the finite difference form of equation (36). The functions $g_1(\phi)$ and $g_2(\phi)$ are defined as constant integral, and they have to be numerically integrated. The solutions of the thermal core are used to update the temperature at the interface of core and thermal boundary layer. With this new interface temperature, $\theta_\delta(t)$, the heat flux entering the droplet from its surface can thus be calculated from equation (44). Based on this new heat flux $q(x)$, equation (23) is updated, and we may proceed to solve the quasi-steady vapor phase equations. Before discussing the vapor-phase equations, a discussion is needed of how to determine the thermal boundary-layer thickness or the location of the interface between the thermal boundary layer and the thermal core. According to Brignell [15], the dimensionless thermal boundary thickness, y_δ/R, is of 0 ($\mathrm{Pe}_l^{-1/2}$) for high Peclet number condition inside droplet. In this analysis, y_δ is assumed to be equal to $2R\mathrm{Pe}_l^{-1/2}$, based on an analysis that the temperature at this point has reached more than 99 percent of the thermal core boundary temperature.

For vapor-phase solutions, equations (25) and (26) are solved in connection with those coefficients of a_n and b_n given in equations (21) and (22). In order to satisfy the compatibility condition, equation (23), an iterative procedure is required. First, an initial guess is provided for v_{in}, the condensation velocity at the interface. The term b_1 is then calculated, based on equation (23). Next, the vapor-phase equations (25) and (26), including (21) and (22), are solved. From equation (22), a new b_1 results from the solutions. If this new b_1 is close enough to the b_1 evaluated from equation (23), convergence is reached. Otherwise, the process is repeated until convergence is obtained. Since the vapor phase is an initial value problem, this iteration procedure is required at each tangential marching step. Also a starting solution at the stagnation point is needed to begin the marching technique for equations (25) and (26). Procedures similar to those in [10] were followed for obtaining the stagnation point solutions, where a set of similar ordinary differential equations were solved using quasi-linearization methods. With the starting solutions, equations (25) and (26) are integrated numerically moving forward in the x-direction. The integration is performed until the zero-shear-stress point is reached. Beyond this point, the boundary layer becomes very thick, invalidating the usual boundary layer assumptions, and the heat and mass transfer rates are relatively small in the separated region for large Reynolds number. The numerical integration was performed, using the fourth-order Runge-Kutta method. A supplementary subroutine was developed and was incorporated with the main program to optimize the step-size, and also to keep track of the single step and accumulated errors to maintain a desired accuracy.

Results and Discussion

Numerical calculations for condensation heat transfer to a translating droplet with steady internal circulation were performed for droplet sizes ranging in radius from 0.25 to 0.75 mm. The system was under atmospheric pressure and steam superheated at 150°C. Water droplets were introduced into the superheated steam environment with an initial temperature of 75°C and a Peclet number of 100. It is understood that the total heat flux $q(x_n, \tau)$, at local point X_n and

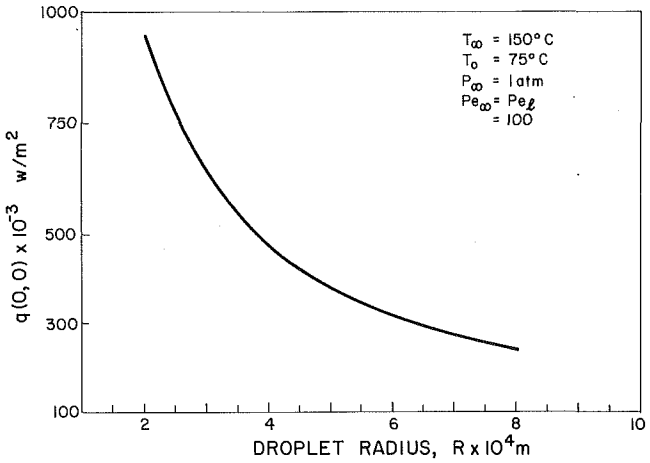

Fig. 2 Total initial heat flux at forward stagnation point versus droplet radius

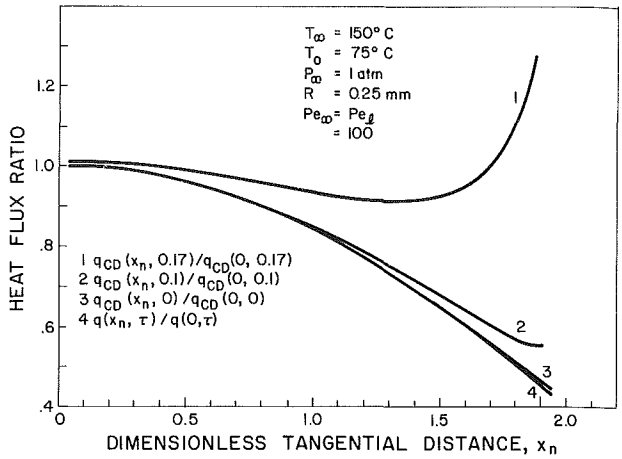

Fig. 4 Variation of condensation heat flux along the droplet surface

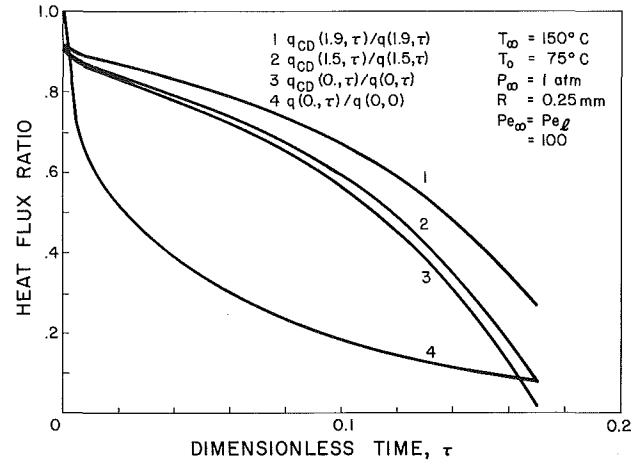

Fig. 3 Fraction of condensation heat flux to total heat flux

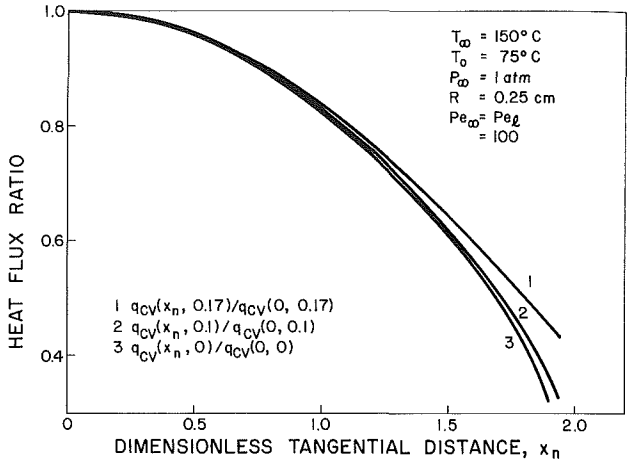

Fig. 5 Variation of convection heat flux along the droplet surface

time τ, entering the liquid side is composed of both the latent heat condensation heat flux $q_{CD}(x_n,\tau)$ and the sensible forced convection heat flux $q_{CV}(x_n,\tau)$.

Figure 2 shows the effects of droplet radius on the condensation rates, where the total heat flux of condensation and convection entering the liquid phase at the forward stagnation point, $x_n = 0$, and in the beginning of the condensation process, $\tau = 0$ is plotted for different droplet radii. Clearly this total heat flux is inversely proportional to the radius of the droplet, and it is indicated by equation (41). In Figs. 3–7, the droplet radius is fixed at 0.25 mm. In Fig. 3, the concave curve presents the total heat flux entering the liquid side at the forward stagnation point as a function of time. The flux is nondimensionalized by the beginning total stagnation point heat flux. The reduction in heat flux is due to the heat-up of the core that decreases the heat transfer potential. The other three curves demonstrate the ratio of local latent heat flux, $q_{CD}(x_n,\tau)$ to total local heat flux, $q(x_n,\tau)$ as a function of time at $x_n = 0$, 1.5, and 1.9. These ratios are decreasing with time due to the fact that the total heat flux, $q(x_n,\tau)$ is decreasing with time at a slower rate than q_{CD} due to the fact that the sensible forced convection heat flux, $q_{CV}(x_n,\tau)$ stays almost constant in the transient because of the surface temperature being constant. The sensible heat flux will decrease only slightly with time due to a weakening of the condensation interface velocity, which has an equivalent effect of suction at the interface that reduces the thermal boundary thickness as shown in Fig. 7. Figure 4 shows the variation of condensation heat flux $q_{CD}(x_n,\tau)$ along the boundary layer. It is nondimensionalized by its own value at the stagnation point. This normalized condensation heat flux is shown for three different dimensionless times, τ = 0, 0.1, and 0.17.

To explain Fig. 4, one has to use the information of Fig. 5 also. First it is found from equation (44) that

$$\frac{q(x_n,\tau)}{q(0,\tau)} = \frac{1+\cos\theta}{(2+\cos\theta)^{1/2}} \times (\sqrt{3}/2) \tag{45}$$

This relationship is independent of time and is plotted as curve 4 in Fig. 4. It is helpful to keep in mind that the total heat flux entering the liquid phase is completely determined by the liquid-phase transport mechanisms, and the vapor phase only responds to the liquid-phase instantaneously due to the quasi-steady state assumption. Figure 5 shows the variations of the convective heat flux along the boundary layer. The normalized convective heat flux does not show a strong dependence on time. This is as expected, because the surface temperature is constant and is unchanged with time. The slight deviations of those curves in Fig. 5 from each other at large x_n are explained from curves in Fig. 4 where the local normalized condensation heat flux increases with increasing time. It is this higher condensation heat flux for larger x_n that thins the thermal boundary thickness and therefore induces slightly higher convective heat flux as shown by curve 1, 2, and 3 in Fig. 5. Now, one can explain curves 1, 2, and 3 in Fig. 4 by noting that both the total heat flux and the convective heat flux decrease with increasing x_n, but they decrease at different rates for larger x_n, basically due to the separation phenomenon of the external boundary layer. The faster decrease in convection heat flux than in the total heat flux

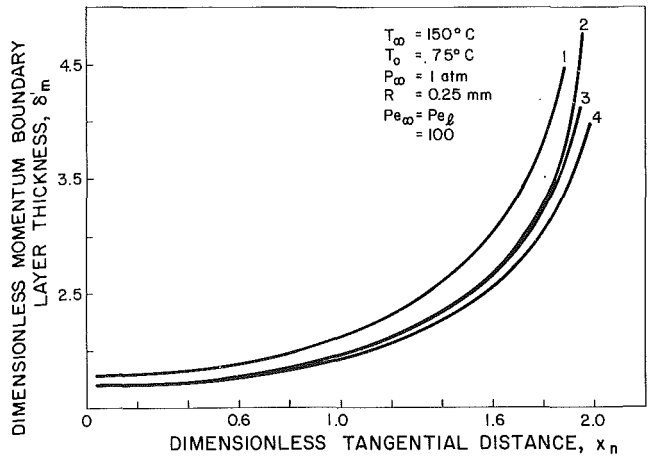

Fig. 6 The effects of condensation and surface motion on boundary-layer thickness. Curve 1: no condensation; Curve 2: condensation with no surface motion; Curve 3: condensation with surface motion two orders of magnitude smaller than U_∞; and Curve 4: condensation with surface motion one order of magnitude smaller than U_∞.

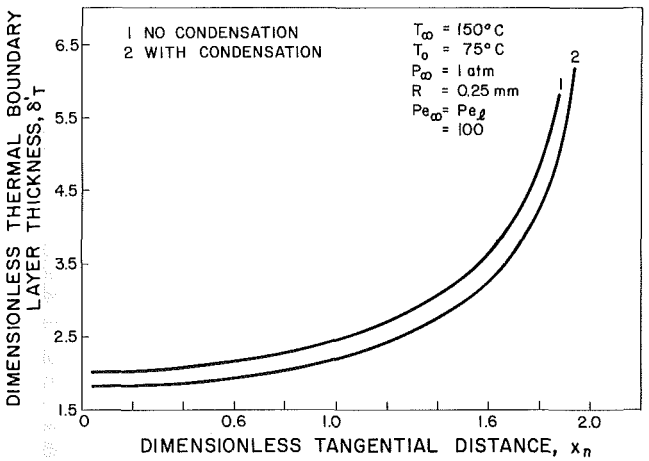

Fig. 7 The effects of condensation of thermal boundary-layer thickness

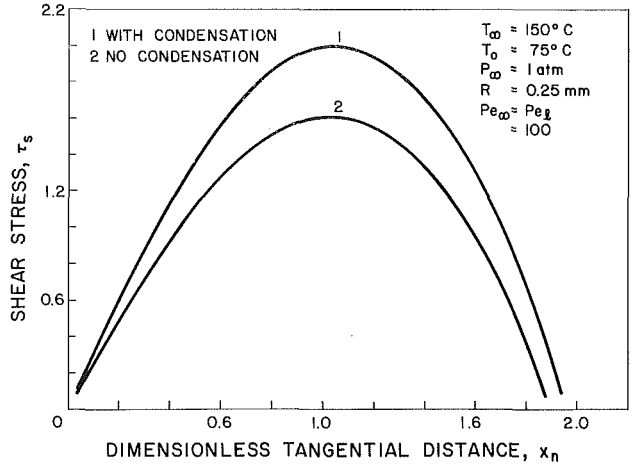

Fig. 8 The effects of condensation on shear stress

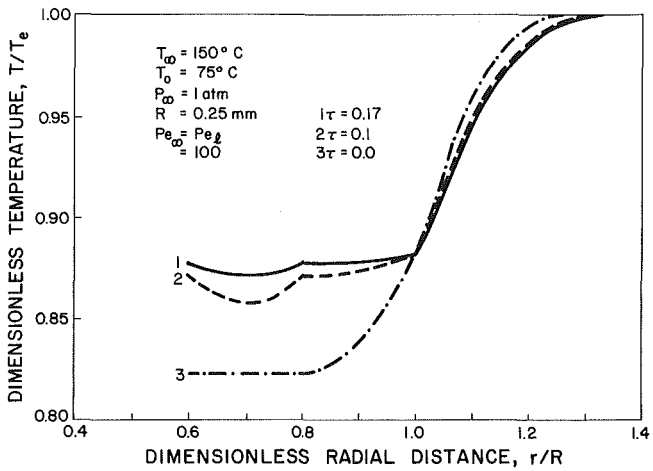

Fig. 9 Temperature distributions on equatorial plane

explains the rises of curves 1 and 2 in Fig. 4 for larger x_n, because the condensation heat flux makes up the difference between the total heat flux and the convective heat flux. For small times, the convective heat flux only amounts to less than 10 percent of the total heat flux; therefore, the normalized condensation heat flux following the same trend as the total heat flux (curve 3 and 4 in Fig. 4). At $\tau = 0.17$, the convective heat flux is even larger than the condensation heat flux, the faster rate of decrease in convective heat flux than the total heat flux makes the condensation heat flux increase when x_n is larger than unity. The effects of condensation and surface motion on the momentum boundary thickness are demonstrated in Fig. 6. Curve 3 is the standard case, which includes condensation and a surface velocity that is two orders of magnitude smaller than the free-stream velocity. Curve 1 is a pseudo-physical situation, where every system parameter is identical with curve 1, except that the condensation is turned off. This comparison between curve 3 and curve 1 shows the effect of condensation on the thinning of the boundary thickness explicitly. Curves 2 and 4 were plotted to demonstrate the effects of surface mobility on the boundary layer structure. Curve 2 corresponds to no surface motion. For curve 4, the surface velocity is only one order of magnitude smaller than the free-stream velocity. Hence the droplet internal motion on surface movement decreases the momentum boundary-layer thickness. Figure 7 examines the effects of condensation-induced interfacial velocity being equivalent to the situation where suction is applied at the interface. This interface velocity will decrease the momentum boundary thickness and hence also decrease the thermal boundary thickness as shown in Fig. 7. In Fig. 7, curve 1 includes condensation while condensation is turned off for curve 2. The relocation of the separation point toward the rear stagnation point due to condensation interfacial velocity is shown in Fig. 8, through the shear stress calculated at the interface. Separation occurs at $x_n = 1.96$, with condensation comparing with $x_n = 1.87$ without condensation. The maximum shear stress is increased substantially by the condensation velocity. For all cases analyzed here, the increase in droplet radius due to condensate accumulation is around 1 percent.

Temperature distributions on the equatorial plane ($\theta = 90$ deg) in both phases are plotted in Fig. 9 for three different dimensionless times, $\tau = 0$, 0.1, and 0.17. The temperature is normalized by free-stream temperatures, T_e. At $\tau = 0$, typical boundary layer profiles in both phases are present, and there is no temperature variation in the thermal core. As time increases, the thermal core gets heated up with lowest temperature located at the Hill's vortex center ($y/R = 0.707$). Also noted that the vapor-phase boundary layer grows thicker with time due to the weakening of condensation velocity as discussed in Fig. 7.

Figure 10 shows the comparison between the current model and the only available experimental results of Ford and Lekic [9]. The initial droplet temperature, saturated steam tem-

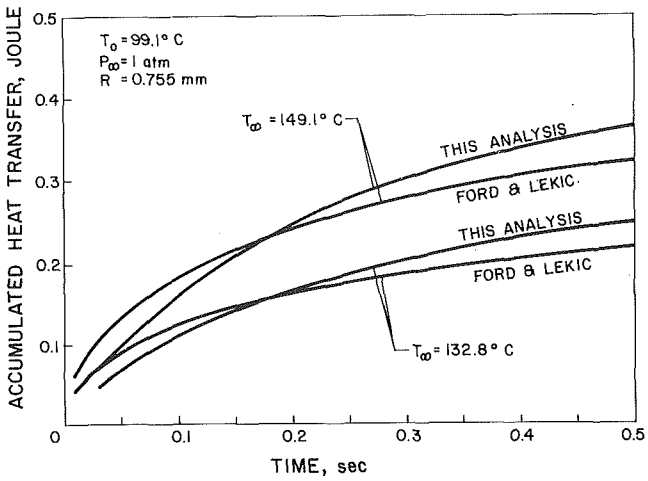

Fig. 10 The comparison of numerical results with experiments

perature, and droplet size used in the numerical model are identical with those of the experiment. There are two major differences between the model and the experiment. First, the numerical model assumes that both the hydrodynamic and the thermal boundary layers are fully developed at the very beginning of the process, while the experimental droplet starts from a uniform temperature in the droplet. This accounts for the difference in the comparison where the experimental results show higher heat transfer rates in the beginning. Second, the experimental droplet does not have any internal motion, while the numerical model assumes fully developed internal circulation. This explains the higher heat transfer rates predicted by the numerical model from about 0.19 s after the starting of the process.

Conclusions

A mathematical model appropriate for predicting condensation heat and mass transfer to a droplet translating in its own pure vapor is developed based on laminar boundary layer theory and inviscid vortex flow inside the droplet to account for the effect of internal circulation. An integral method similar to that of Karman-Pohlhausen was adopted for the solutions of boundary layer equations. The diffusion equation governing the thermal core was solved using a Crank-Nicholson type of finite difference numerical scheme.

The rate-controlling mechanism is found to be the diffusion process in the thermal core region of the droplet. The total rate of heat transfer is inversely proportional to the droplet radius. The condensation velocity at the vapor-liquid interface reduces the boundary layer thickness and moves the separation point toward the rear stagnation point. The internal motion also helps increase the transport rates by reducing both the boundary layer thickness and the inside resistance. The mathematical model compares favorably with experimental measurement.

Acknowledgment

This research work was supported through a National Science Foundation grant, CME-8006762.

References

1 Acrivos, A., and Taylor, T. D., "Heat and Mass Transfer From Single Sphere in Stokes Flow," *Physics of Fluids*, Vol. 5, 1962, pp. 387-394.

2 Ranz, W., and Marshall, W., "Evaporation From Drops," *Chem. Engrg. Prog.*, Vol. 48, 1952, pp. 141-146; 173-180.

3 Kronig, R., and Brink, J. C., "On the Theory of Extraction From Falling Droplets," *Appl. Scient. Res.*, Vol. A2, 1951, pp. 142-154.

4 Chao, B. T., "Motion of Spherical Gas Bubbles in a Viscous Liquid at Large Reynolds Numbers," *Physics of Fluids*, Vol. 5, 1962, pp. 69-79.

5 Chao, B. T., "Transient Heat and Mass Transfer to a Translating Droplet," ASME JOURNAL OF HEAT TRANSFER, Vol. 91, 1969, pp. 273-281.

6 Harper, J. F., and Moore, D. W., "The Motion of a Spherical Liquid Drop at High Reynolds Number," *J. of Fluid Mechanics*, Vol. 32, 1968, pp. 367-391.

7 Prakash, S., and Sirignano, W. A., "Theory of Convective Droplet Vaporization with Unsteady Heat Transfer in the Circulating Liquid Phase," *International Journal of Heat and Mass Transfer*, Vol. 23, 1980, pp. 253-268.

8 Tong, A. Y., and Sirignano, W. A., "Analytical Solution for Diffusion in the Case of a Droplet with Internal Circulation," *AICHE Symposium Series*, No. 208, Vol. 77, 1981, pp. 400-407.

9 Ford, J. D., and Lekic, A., "Rate of Growth of Drops During Condensation," *International Journal of Heat and Mass Transfer*, Vol. 16, 1973, pp. 61-64.

10 Chung, J. N., and Ayyaswamy, P. S., "Laminar Condensation Heat and Mass Transfer in the Vicinity of the Forward Stagnation Point of a Spherical Droplet Translating in a Ternary Mixture: Numerical and Asymptotic Solutions," *International Journal of Heat and Mass Transfer*, Vol. 21, 1978, pp. 1307-1324.

11 Chung, J. N., and Ayyaswamy, P. S., "Laminar Condensation Heat and Mass Transfer to a Moving Drop," *AIChE Journal*, Vol. 27, 1981, pp. 372-377.

12 Chung, J. N., and Ayyaswamy, P. S., "Material Removal Associated With Condensation on a Droplet in Motion," *International Journal of Multiphase Flow*, Vol. 7, 1981, pp. 329-342.

13 Schlichting, H., *Boundary Layer Theory*, McGraw-Hill, New York, 1968.

14 Chang, T. H., and Chung, J. N., "The Effects of Surfactant on the Motion and Transport Mechanisms of a Condensing Droplet," presented at the 1983 AIChE-ASME National Heat Transfer Conference; also published in *Interfacial Transport Phenomena*, edited by J. C. Chen and S. G. Bankoff.

15 Brignell, A. S., "Solute Extraction From an Internally Circulating Spherical Liquid Drop," *International Journal of Heat and Mass Transfer*, Vol. 18, 1975, pp. 61-68.

16 Hubbard, G. L., Denny, V. E., and Mills, A. F., "Droplet Evaporation: Effects of Transients and Variable Properties," *International Journal of Heat and Mass Transfer*, Vol. 18, 1975, pp. 1003-1008.

I. S. Lim

R. S. Tankin
Mem. ASME

M. C. Yuen
Mem. ASME

Department of Mechanical and Nuclear Engineering, Northwestern University, Evanston, Ill. 60201

Condensation Measurement of Horizontal Cocurrent Steam/Water Flow

Condensation of steam on a subcooled water layer was studied in a cocurrent horizontal channel at atmospheric pressure. The heat transfer coefficients were found to vary from 1.3 kW/m²°C to 20 kW/m²°C, depending on whether the liquid interface was smooth or wavy, increased with increasing steam flow rates and water flow rates. For all cases, 50 to 90 percent of the steam condensed within 1.2 m from the entrance. The average Nusselt numbers were correlated with average steam and water Reynolds numbers and average liquid Prandtl numbers, for both smooth and wavy interface flows. Finally, a correlation of the average heat transfer coefficient and condensation rate for wavy interface flow was obtained as a function of inlet conditions and distance downstream.

1 Introduction

There have been extensive studies dealing with heat and mass transfer in two-phase, stratified flow. Most of these studies have involved either gas absorption at a gas-liquid interface or condensation on a thin liquid film which is only slightly subcooled. In these experiments, measurements are generally made at a sufficient distance from the entrance where the velocity profiles and wave patterns have reached fully developed shapes. Theoretical models have been proposed to account for these transfer rates. For condensation studies, several good reviews are available [1, 2].

More recently, there has been considerable interest in studies of rapid condensation of vapor on a fairly thick layer of subcooled liquid. This problem is of particular relevance to nuclear reactor safety analysis, where in the hypothetical LOCA (loss of coolant accident) sequence, steam comes into contact with cold water at several locations. Quantitative prediction of these events require knowledge of the local condensation rates.

A literature search shows that this problem has not been studied extensively. Related works include the measurements of Linehan, Petrick, and El-Wakil [3], which were limited to a subcooled thin liquid film, and measurements by Thomas [4] of condensation on a turbulent liquid from quiescent steam. The measured heat transfer coefficients were of the order of 10 kW/m²°C. Measurement of condensation of a high-speed steam jet was reported by Young, Yang, and Novotny [5]. The measured heat transfer coefficients were of the order of 6×10^3 kW/m²°C. The difference in the heat transfer coefficients of [4] and [5] was due to the difference in turbulent intensity and the effect of entrainment.

The present experiment was undertaken to provide a carefully measured set of data on the condensation of steam on subcooled water layer in a simple, well-defined system. The system chosen was a horizontally stratified, cocurrent channel flow. The resultant data set provides a firm base for comparison with other data as well as with the various models for condensation. The present work is a continuation of earlier work by Lee et al. [6] and Lim et al. [7].

In the present study, a new test section and entrance section was used. The test section was made of single plates (sides, top, and bottom) of stainless steel that were welded together to form a channel rather than the segmented test section of the earlier studies. The new test section has no protuberances to disturb the water flow. With the new entrance section the steam flow is two-dimensional; three-dimensional flow may have existed in the earlier work. Also in the present study, measurements are made at smaller spatial intervals (axially and vertically) resulting in a better definition of the experimental curves—especially important where slopes are needed to obtain the local heat transfer coefficients. In addition, the range of the steam and water flows was extended, making it possible to distinguish the two regimes of heat transfer: where the interface is smooth or wavy.

2 Experiment

A test facility was designed and constructed in which condensation rates of steam along the channel could be measured. A schematic diagram of the system is shown in Fig. 1. In this horizontal channel, which has a rectangular cross section (6.35 cm high, 30.48 cm wide, and 160.1 cm long), steam and water flow cocurrently. The channel is made of stainless steel with windows on all sides and is insulated with a 5-cm-thick layer of fiberglass. The steam and water inlet plenums were designed to provide uniform flow at the channel entrance. Typical steam velocity profiles across the width of the channel at $x=0$ (entrance) are shown in Fig. 2. The velocity profiles of the water layer at $x=15.7$ cm in the absence of steam flow were measured at two different locations across the width of the channel; centerline and 1.9 cm from side wall. The results are shown in Fig. 3. The data indicate that the water velocity profile was also uniform across the width of the channel.

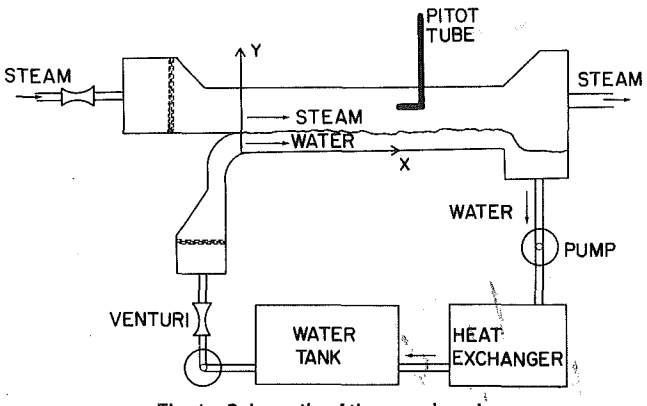

Fig. 1 Schematic of the experiment

Contributed by the Heat Transfer Division for publication in the JOURNAL OF HEAT TRANSFER. Manuscript received by the Heat Transfer Division July 26, 1983.

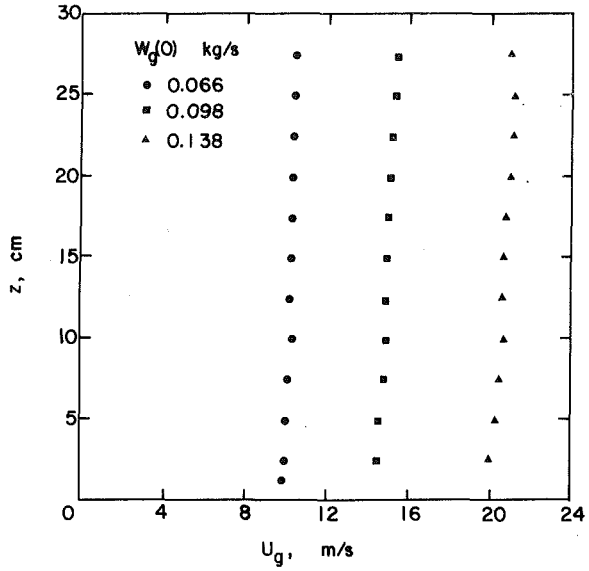

Fig. 2 Steam velocity profile across the width of channel at entrance ($x = 0$)

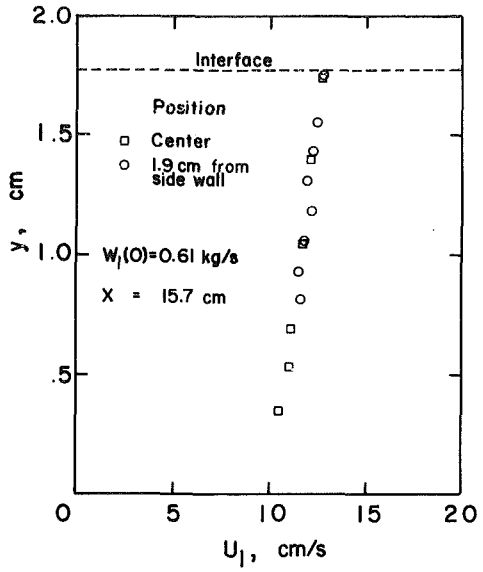

Fig. 3 Axial water velocity profile at x = 15.7 cm with no steam flow

The entrance length (plenum exit to entrance of test section) on the steam side is only 0.1 m and for the liquid side is 0.85 m. The flow of the steam at the entrance to the test section is never fully developed. For the liquid side, the ratio of entrance length to entrance height is 55; thus the liquid flow is partially developed. The liquid Reynolds number based on entrance height varies from 660 to 5000. Therefore, at low flow rates, the liquid flow at entrance to test section is laminar and at high flow rates it is turbulent.

Five pitot tubes (3.1-mm o.d.) are inserted at ports along the top of the channel as well as electrical conductivity probes (3.1-mm o.d. with sharp tip) and thermocouples (0.5-mm o.d.). The tips of the pitot tubes are located at $x = 15.7$ cm, 30.6 cm, 58.6 cm, 86.6 cm and 123.3 cm, respectively. The pitot tubes are used to measure the local mean steam velocity, and the conductivity probes to measure the water height. The conductivity probes and pitot tubes are attached to a traversing table.

Steam is obtained from the building supply line which has a line pressure of 1.0 MPa. The steam was measured to contain about 3 ppm of air and 20 ppm of diethylaminoethanol, an anticorrosion agent. A centrifugal separator is used to separate the water droplets from the steam. After passing through a throttling valve, a venturi meter, and the settling plenum, the steam flows through the test channel and ultimately discharges to the atmosphere. Water, which is pumped from a storage tank to the test section, is also monitored with a venturi meter. The water and condensate, which leave the channel through an exit plenum, are pumped through a heat exchanger to the storage tank. Thus the water line is a closed loop, whereas the steam line is an open loop.

Local steam velocity profiles were obtained by traversing the pitot tubes from the water-steam interface to the top of the channel. The local steam flow rate was obtained at each station by integrating the velocity profile at that station. To overcome the problem of steam condensing in the pitot tubes, the pitot tubes were thermally insulated, electrically heated, and purged with air, if necessary. During start-up, air was slowly purged through the pitot tubes to ensure no condensate collected in the pitot tubes. When the system was at a desired steady-state condition, the air was turned off and data were taken. Air was used again only if a pitot tube was plugged by condensate; then the air to that pitot tube was turned on at a fairly high flow rate to expel the condensate. When the air supply was turned off, data taking was resumed. In practice, the pitot tubes provided consistent readings even after hours of operation.

The normal operating procedure was to accurately position the conductivity probes and pitot tubes with respect to the bottom of the test section before tests were begun (the test section was empty and at room temperature). Thermal deformation of the test section (due to different temperatures of the steam and water during the experiment) was accounted for in the water depth measurements by measuring the shifts in the reference positions (bottom of channel) for each steam and water flow rates.

The accuracy of the inlet steam mass flow measurement

Nomenclature

b = channel width
C_p = heat capacity
F = term defined in equation (15)
G = mass velocity
h = heat transfer coefficient
H = specific enthalpy
H_{fg} = latent heat of evaporation
k = thermal conductivity
K = $C_{p,l}[T_s - T_l(0)]/H_{fg}$, degree of subcooling
Nu = Nusselt number
p = pressure
Pr = Prandtl number
Q = heat transfer
Re = Reynolds number
T = temperature
t = thickness
u = velocity
V = superficial velocity
W = mass flow rate
x = axial coordinate
y = vertical coordinate
z = cross-sectional coordinate, perpendicular to x- and y-coordinates
α = $[C_{p,l}T_l(0) - H_g]$
β = $C_{p,l}T_s - H_g$
μ = viscosity coefficient

Subscript

c = condensate
g = gas
l = liquid
s = saturation
t = channel thickness
x = axial distance

Superscript

— = average

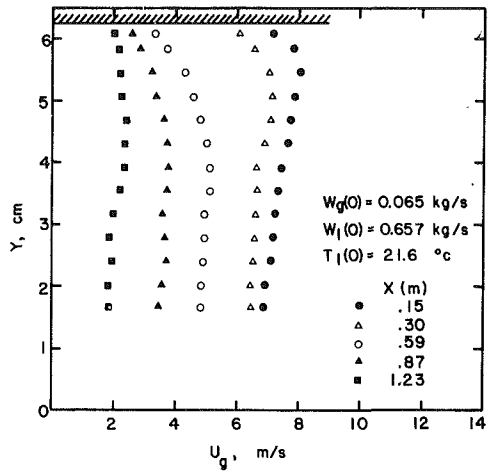

Fig. 4 Typical steam velocity profiles

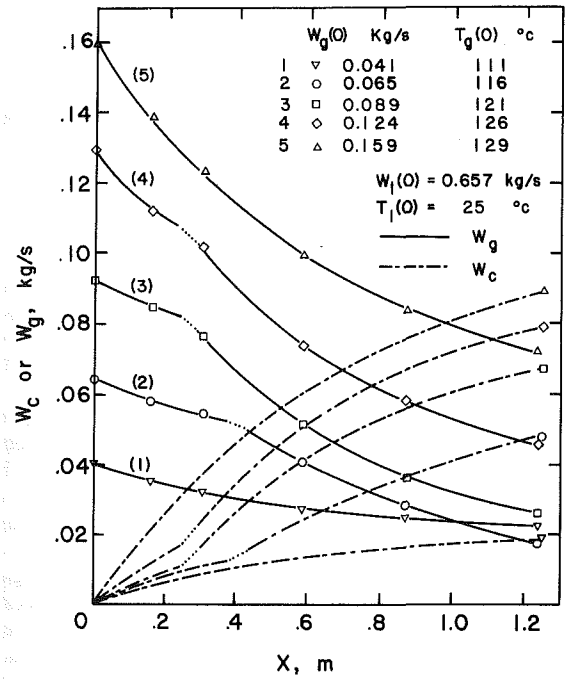

Fig. 5 Axial steam and condensation rate profiles as a function of inlet steam flow rate

(venturi) and each pitot tube measurement was checked by two methods: (*i*) energy balance, and (*ii*) comparison between the venturi reading and the integrated pitot tube measurements. In the energy balance method, the inlet and outlet temperature of the water along with its flow rate were measured when all the steam was condensed in the channel. The enthalpy change in the water was then compared with the steam venturi measurement. In the second method, a comparison beween the venturi measurement and the integrated pitot tube measurements was made without condensation in the test section. In these tests, steam flowed through the test section with either no water present in the test section, or saturated water present in the test section. The results agreed within ±3 percent of each other.

When desired steam and water flow rates have reached steady conditions, the flow data together with the water layer thickness data were stored in the minicomputer. The pitot tubes were then positioned close to the water interface and the velocity traverses were begun. At each elevation, the computer sampled the pitot tube output at a rate of 240 readings per s for a 30-s interval. The computed average velocities of

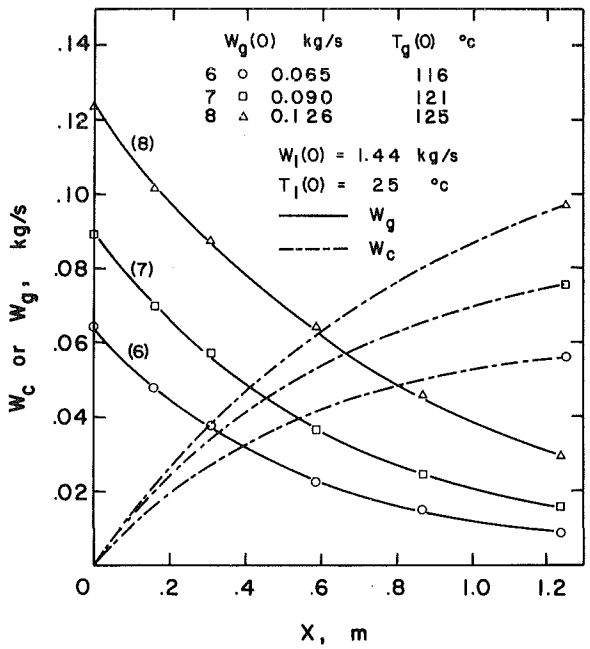

Fig. 6 Axial steam and condensation rate profiles as a function of inlet steam flow rate

each of the pitot tubes were displayed on the CRT screen and briefly examined. Should condensation plug a pitot tube, the reading would be in error by orders of magnitude; then the air purging system was used to eliminate the condensate. Measurements at that level would be repeated and examined before moving to the next elevation. Typical velocity profiles are shown in Fig. 4. The decrease in velocity in the downstream direction is a direct result of condensation. Typical results of steam mass flow rate as a function of channel length are shown in Figs. 5 and 6.

For further interpretation of experimental data, the local heat transfer coefficient is defined as

$$h = \frac{dW_c}{dx}\,\frac{[H_g - C_{p,l}T_s]}{b(T_s - T_l)} \tag{1}$$

where h is the heat transfer coefficient, W_c is the mass flow rate of condensate, H_g is the gas enthalpy, $C_{p,l}$ is the heat capacity of liquid, b is the width of channel, T_s is the saturation liquid temperature, and T_l is the bulk liquid temperature. Although equation (1) assumes that all the heat transfer is due to condensation; the effect of superheat is taken into account by evaluating H_g at steam temperature T_g. For the present experiment, T_g is typically about 120°C, and the liquid surface temperature is the same as the steam saturation temperature, which is 100°C.

From mass and energy balance, T_l can be shown (see [7]) to be

$$T_l = \frac{1}{C_{p,l}}\left\{\frac{W_l(0)[C_{p,l}T_l(0) - H_g]}{W_l(x)} + H_g\right\} \tag{2}$$

where W_l is the liquid mass flow rate. The average heat transfer coefficient can then be shown to be equal to

$$\bar{h} = \frac{1}{x}\int_0^x h\,dx$$

$$= \frac{C_{p,l}[H_g - C_{p,l}T_s]}{b\beta x}\left\{W_l(x) - W_l(0) + \frac{W_l(0)\alpha}{\beta}\ln\left[\frac{W_l(x)\beta - W_l(0)\alpha}{C_{p,l}W_l(0)[T_s - T_l(0)]}\right]\right\} \tag{3}$$

where $\alpha = [C_{p,l}T_l(0) - H_g]$

$$\beta = C_{p,l} T_s - H_g$$

The following definitions are used in determining the average Reynolds numbers:

Average steam mass velocity ($\bar{G}_g$) is

$$\bar{G}_g = \frac{1}{2}[G_g(0) + G_g(x)] = \frac{1}{2b}\left[\frac{W_g(0)}{t - t_l(0)} + \frac{W_g(x)}{t - t_l(x)}\right] \quad (4)$$

where t is the channel height and t_l is the liquid layer thickness.

Average water mass velocity ($\bar{G}_l$) is

$$\bar{G}_l = \frac{1}{2}[G_l(0) + G_l(x)] = \frac{1}{2b}\left[\frac{W_l(0)}{t_l(0)} + \frac{W_l(x)}{t_l(x)}\right] \quad (5)$$

Thus, the average steam Reynolds number is

$$\overline{\mathrm{Re}_g} = \frac{x\,\bar{G}_g}{\mu_g} \quad (6)$$

and, the average water Reynolds number is

$$\overline{\mathrm{Re}_l} = \frac{2x\,\bar{G}_l}{[\mu_l(0) + \mu_l(x)]} \quad (7)$$

The average liquid Prandtl number is

$$\overline{\mathrm{Pr}_l} = [\mathrm{Pr}_l(0) + \mathrm{Pr}_l(x)]/2 \quad (8)$$

3 Results

A total of seventy experiments have been performed by varying the following initial conditions: (*i*) inlet steam flow rate, (*ii*) inlet water flow rate, (*iii*) initial water layer thickness and (*iv*) degree of water subcooling. The steam flow rate varied from 0.04 kg/s to 0.16 kg/s and the water flow rate varied from 0.2 kg/s to 1.45 kg/s. The maximum ranges of water and steam flow rates were limited by bridging, hydraulic jump, or entrainment. Three initial water layer heights, 0.95, 1.59, and 2.22 cm were used. The effect of water subcooling was studied by operating at two initial (inlet) water temperatures: 25°C and 50°C. All experiments were performed with exit of the test channel opened to atmosphere. The steam pressure at entrance ($x = 0$) was about 0.3 kPa to 0.4 kPa above ambient pressure, depending on flow rate; and the steam temperature varied from 105°C to 140°C. Even though there was a variation of 35°C in steam temperature, the effect of superheat is small because latent heat of vaporization is large. For example, in the case of maximum steam temperature of 140°C, the steam enthalpy is only 3 percent higher than the saturation steam enthalpy at 100°C. It was found that the free-stream steam temperature remained constant in the test channel.

Figures 5 and 6 show the effects of steam flow rate on condensation for two different liquid flow rates. Both figures show that the steam mass flow rates (W_g) decrease rapidly in the axial direction. In a length of 1.2 m, from 50 percent to as high as 90 percent of the steam was condensed. This rapid change of steam flow rate proved that the flow was never fully developed. Both Figs. 5 and 6 show that the condensate flow rate (W_c) increases markedly with steam flow rate. By comparing the condensate flow rate curves for the same initial steam flow rate in Figs. 5 and 6, one sees that the condensation rate also increases with water flow rate, but the effect is not as pronounced.

In the present experiment, the thermal resistance in the gas side is negligible compared to the thermal resistance in the liquid side. The condensation rate therefore depends on the ability of the liquid motion to transport thermal energy away from the interface into the liquid mainstream. In this case, it is the interfacial shear which enhances the convection (turbulent or otherwise). This explains the increase of condensation rates with higher steam flow rates. On the other hand, the increase in condensation rate with water flow rate

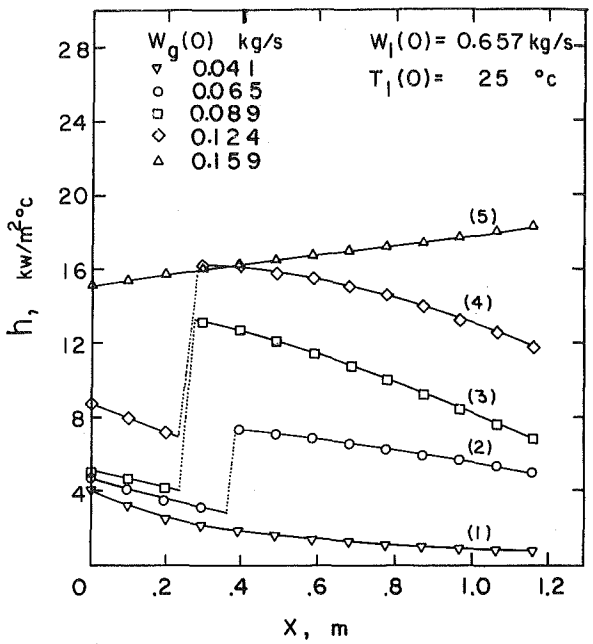

Fig. 7 Axial local heat transfer coefficient profiles as a function of inlet steam flow rate (corresponding to data in Fig. 5)

can be explained as follows: at the higher water flow rates, T_l increases, but only slowly (see equation (2)), and therefore the temperature difference remains relatively larger. Because the steam velocity is much greater than water velocity (under normal operating conditions), an increase in water velocity does not change the interfacial shear significantly. However, an increase in water flow rate may increase the initial turbulence in the water and therefore increase h.

During the experiment, it was observed that the interface was either smooth (glossy looking interface) or wavy (pebble like interface), depending on both the steam and water flow rates. For certain experimental conditions, the interface was smooth at the entrance and became wavy some distance downstream. The introduction of a fine filament of color dye near the interface revealed that in the smooth interface region, the dye persisted as a filament. Where the interface became wavy, the dye would quickly disperse into the main stream exhibiting a turbulent behavior. The wavy interfaces included roll waves near entrance. Mostly they were three-dimensional, cross-hatched waves with wave lengths of about 1 cm and wave heights of less than 2 mm.

Based on laminar theory of condensation on a flat plate, it was decided to fit the smooth interface experimental data with the following curve

$$W_g = A(x + B)^{-0.5} \quad (9)$$

where x is the axial distance from entrance, A and B are arbitrary constants determined by best fit of experimental data. For the case of wavy interface, the following empirical curve was used

$$W_g = C \exp[-D(x - x_0)] \quad (10)$$

where x is the axial distance from entrance, x_0 is the axial distance where rough interface starts, C and D are arbitrary constants determined by best fit of experimental data. For further analysis of data, readings would be taken directly from these curves.

In Fig. 5, the interface of curve 1 was smooth throughout; thus, equation (9) was fitted to these data. For curves 5 to 8 in Figs. 5 and 6, the interfaces were wavy throughout and equation (10) was fitted to these data. For curves 2 to 4 in Fig. 5, the interfaces were observed to be smooth in the beginning and wavy further downstream. Therefore, the initial part of

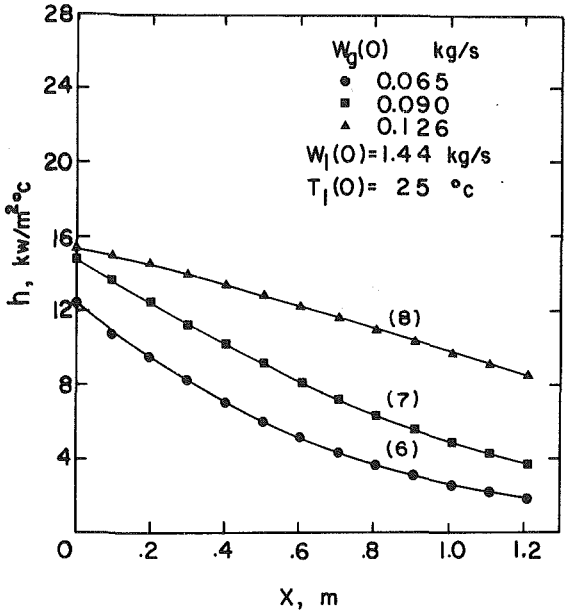

Fig. 8 Axial local heat transfer coefficient profiles as a function of inlet steam flow rate (corresponding to data in Fig. 6)

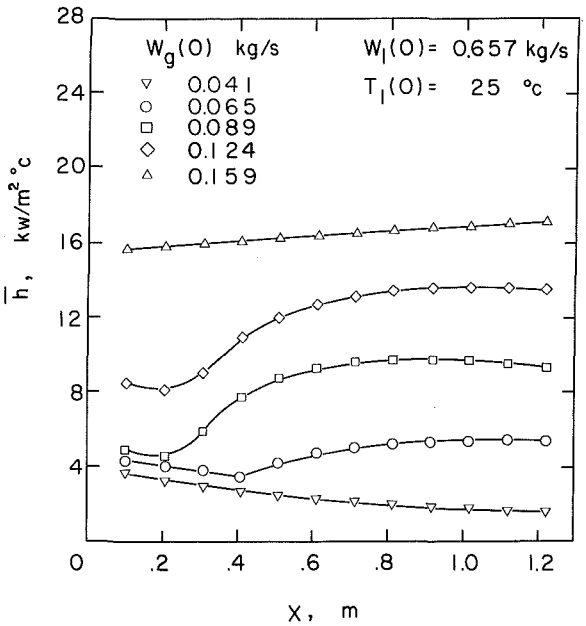

Fig. 9 Axial average heat transfer coefficient profiles as a function of inlet steam flow rate (corresponding to data in Fig. 5)

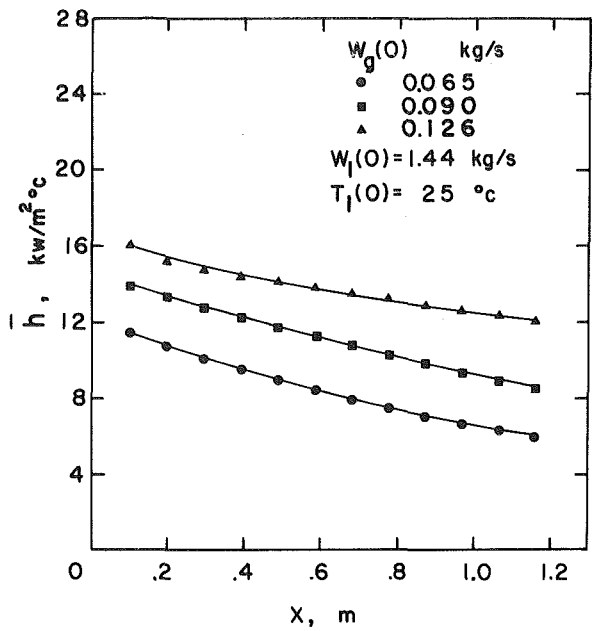

Fig. 10 Axial average heat transfer coefficient profiles as a function of inlet steam flow rate (corresponding to data in Fig. 6)

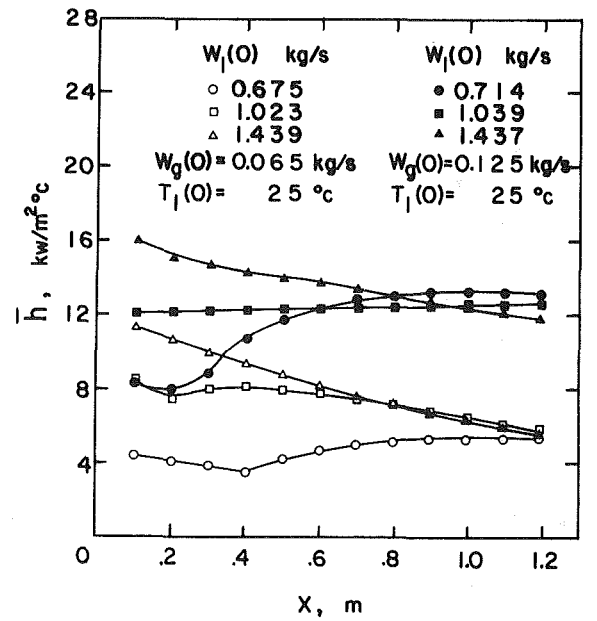

Fig. 11 Axial average heat transfer coefficient profiles as a function of water flow rate

these data (smooth interface) was fitted with equation (9) and the latter part (wavy interface) with equation (10). The transition from smooth to wavy interface was observed to occur quite abruptly and in some cases the transition oscillated back and forth. Therefore, in curves 2 to 4 in Fig. 5, the transition regions are denoted by dotted lines. The discontinuity in the slope at the transition region results in a discontinuity of the local heat transfer coefficient as shown in Fig. 7.

As seen in equation (2), T_l increases with x; whereas T_s, the liquid surface temperature, remains at the vapor saturation temperature, which in the present experiment is 100°C. Thus, although dW_c/dx generally decreases with x, $T_s - T_l$ also decreases with x. Depending on the rate of decrease of these terms, h (see equation (1)) can increase, decrease, or stay constant. In most entry flows, h usually decreases with x or stays constant. Figures 7 and 8 show that generally if the interface is either smooth or wavy throughout the channel, the heat transfer coefficients do decrease with x. Therefore, the sudden jump in h in curves 2 to 4 can be attributed to the change in interfacial conditions resulting in enhanced convection. An estimate of the increase in surface area due to wavy interface is no more than 20 percent, which cannot, in the present case, account for the 100 percent increase in the values of h. The exception to the above observations is curve 5. In this experiment the water flow rate was low and the steam flow rate was high. Under these conditions, T_l increased rapidly so that ΔT decreased more rapidly than dW_c/dx, resulting in an increase in h. For example in this case at $x = 1.2$ m, $T_l = 89.3$°C and $\Delta T = 10.7$°C, whereas for the same location in curve 4, $T_l = 85.3$°C and $\Delta T = 14.7$°C. The averaged heat transfer coefficients, as defined by equation (3), for the data of Figs. 5 and 6 are shown in Figs. 9 and 10. Although the average quantities tend to smooth out the rapid variations in the local quantities, they still retain all the important features. For the same initial steam flow rate but

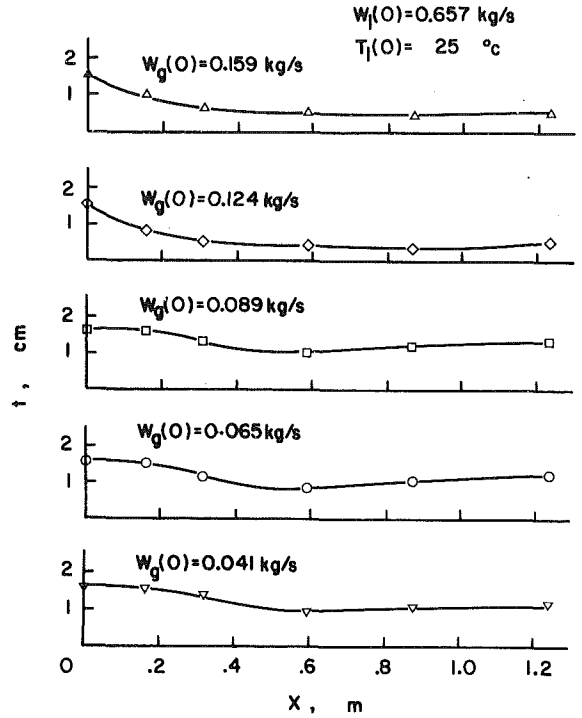

Fig. 12 Typical axial water layer thickness profiles as a function of inlet steam flow rate

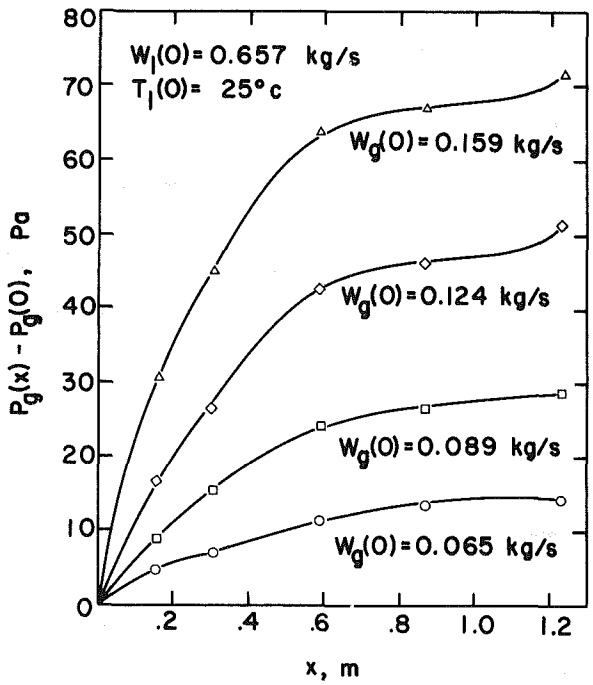

Fig. 13 Typical axial steam pressure profiles as a function of inlet steam flow rate. $P_g(0)$ is between 0.3 kPa to 0.4 kPa above atmospheric pressure depending on steam flow rates.

different water flow rates, the data in Fig. 11 show that initially the average heat transfer coefficients are higher for the higher water flow rates. Further downstream, the average heat transfer coefficients have practically the same value. This does not mean that the heat transfer is the same because T_l are different for each of these cases.

Figure 12 shows typical water layer thicknesses along the channel. For the first half of the channel, the thicknesses decreased due to high interfacial shear stress by the steam. As condensation continued along the channel, the steam velocity decreased and the water thicknesses began to increase. Figure

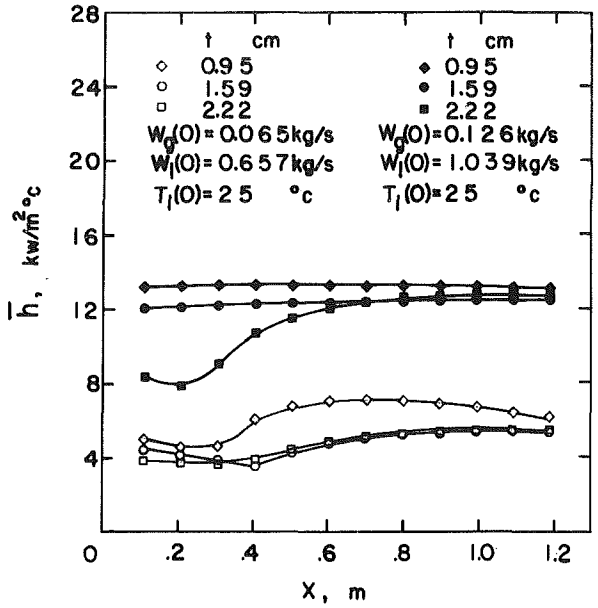

Fig. 14 Typical average heat transfer coefficients as a function of inlet water layer thickness

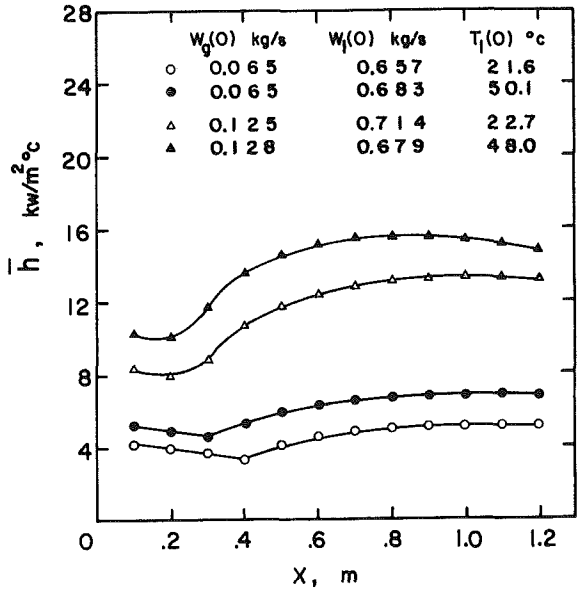

Fig. 15 Typical axial average heat transfer coefficient profiles as a function of inlet water temperature

13 shows a typical change in static pressure along the channel. The increase in static pressure was due to the Bernoulli effect which was a direct result of the decrease in steam velocity.

All the data discussed so far is for a constant liquid entrance height. Therefore, constant liquid flow rate is synonymous to constant velocity. A series of experiments was performed in which the inlet steam, and the water flow rates were kept constant but the inlet velocities (particularly water) were changed by varying the initial water layer thicknesses. Figure 14 shows the typical results of the variations of average heat transfer coefficients with initial liquid heights. For the two cases shown, the liquid and steam flow rates were kept constant. The effect of changing the liquid velocity on condensation was confined to the entrance region. This was probably related to the occurrence of roll waves and initial bulging of the liquid surface due to the mismatch of the liquid pressure with respect to the vapor pressure at the entrance. These phenomena, in turn, affected the transition from smooth to wavy interface.

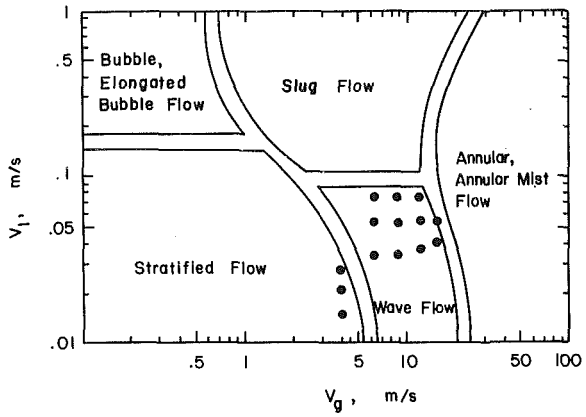

Fig. 16 Flow pattern map of [8] with present data

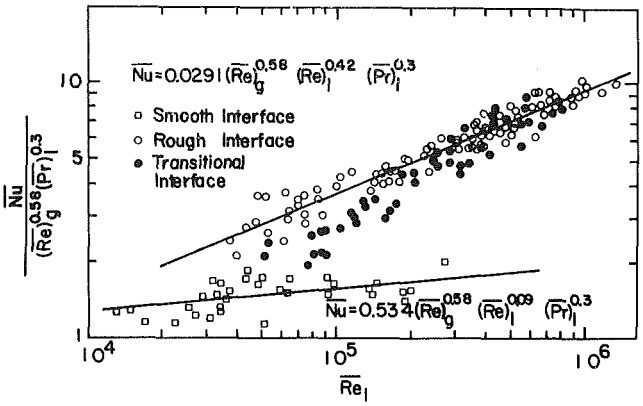

Fig. 17 Correlation of Nusselt number as a function of steam and water Reynolds numbers, and water Prandtl number

The effect of subcooling on the average heat transfer coefficients is shown in Fig. 15. For the same inlet steam and water flow rates, the heat transfer coefficients are lower for the case of higher subcooling. However, the heat transfer for the higher subcooling is higher; because the temperature difference, $(T_s - T_l)$, is larger.

The present measured h is in the neighborhood of 10 kW/m^2°C, which is closer to the measured values of [4] than that of [5]. The reason is that in [5] both the steam velocity (300 m/s) and the water velocity (3 m/s) are an order of magnitude higher than the present experiment. In their experiment, liquid entrainment contributes significantly to the condensation rate. In [4], condensation rates are shown to be dependent on turbulence in the liquid layer, which was generated by a grid at the channel entrance. For both [4] and the present experiments, thermal resistance in the liquid layer dominates. The primary transport mechanism in [4] was artificially generated turbulence in the liquid, and in the present experiment it was interfacial shear. In both of these experiments there was no entrainment. It is therefore reasonable to expect that the heat transfer coefficients of these two experiments are of the same order of magnitude.

The flow pattern map of [8] is shown in Fig. 16 together with the present experiment based on entrance conditions. The present experimental conditions lie in the wavy flow and stratified flow regimes. This shows that the flow pattern map of [8] can be used as a guide even for highly condensing flow as long as the superficial velocities are based on entrance conditions.

An attempt is made to correlate the complete set of data of seventy experiments. Following the normal practice in convective heat transfer, the Nusselt numbers as a function of the gas and liquid Reynolds numbers and liquid Prandtl numbers were sought. That is

$$\overline{\mathrm{Nu}} = c\,\overline{\mathrm{Re}}_g^{\,p}\,\overline{\mathrm{Re}}_l^{\,q}\,\overline{\mathrm{Pr}}_l^{\,r} \tag{11}$$

where

$$\overline{\mathrm{Nu}} = \frac{\bar{h}\,x}{\bar{k}_l}$$

and

$$\bar{k}_l = \frac{1}{2}\,[k_l(0) + k_l(x)]$$

and $\overline{\mathrm{Re}}_g$, $\overline{\mathrm{Re}}_l$, $\overline{\mathrm{Pr}}_l$ are defined in equations (6), (7), and (8), respectively.

A least-square fit method was used to find the optimum coefficients c, p, q, and r in equation (11). The results are presented in Fig. 17. There are three types of data. One type is where the interface was smooth throughout the channel; the second type is where the interface was wavy throughout the channel; the third type is where the interface was smooth at entrance and became wavy somewhere downstream. The third type of data are labeled as transitional data points. There are two different correlations for the first two types of data, they are

for smooth interface

$$\overline{\mathrm{Nu}} = 0.534\,\overline{\mathrm{Re}}_g^{0.58}\,\overline{\mathrm{Re}}_l^{0.09}\,\overline{\mathrm{Pr}}_l^{0.3} \tag{12}$$

for wavy interface

$$\overline{\mathrm{Nu}} = 0.0291\,\overline{\mathrm{Re}}_g^{0.58}\,\overline{\mathrm{Re}}_l^{0.42}\,\overline{\mathrm{Pr}}_l^{0.3} \tag{13}$$

For those data points where the interface is wavy throughout, the data closely follow equation (13). For the data where the interface is smooth throughout, the data points follow equation (12). In the case of transitional flow (x_0 is the transition point) where $x < x_0$, the data should follow equation (12). Where $x > x_0$, the data points will deviate from equation (12) and gradually approach equation (13) as x increases. For the case where x_0 is small, the transitional data for large x will lie on the curve described by equation (13) as shown in Fig. 17.

The correlation for condensation as represented by equation (13) has the same slope but is about 30 percent higher than earlier data [6]. In the earlier experiments, the mass flow measured by the pitot tubes and steam venturi were not in agreement. Calibration constants were determined for the pitot tubes based on the venturi readings. Later, it was found that this discrepancy was probably due to wet steam flowing past the venturi. A separator was subsequently installed which ensured dry steam in the flow. Also additional screens were installed in the settling chamber—ensuring uniform steam flow. With these improvements, good agreement in mass flow readings between the venturi and pitot tubes was obtained. Finally, there were more pitot tube stations in the present set-up, which resulted in more accurate determination of the mass flux curves. Thus we believe the present data are superior.

4 Engineering Application

The correlation as shown in Fig. 17 cannot be easily applied in practice where only the entrance conditions are known. For the case where the interface is wavy throughout, the present experimental data indicate the condensate flow profiles are similar (Fig. 6). For this particular case, an attempt was made to correlate the condensate flow rate as a function of x and entrance conditions.

It seems reasonable that the entrance conditions can be characterized by the following dimensionless parameters

$$\mathrm{Re}_{l,t} = \frac{W_l(0)t}{b\,t_l(0)\mu_l(0)}$$

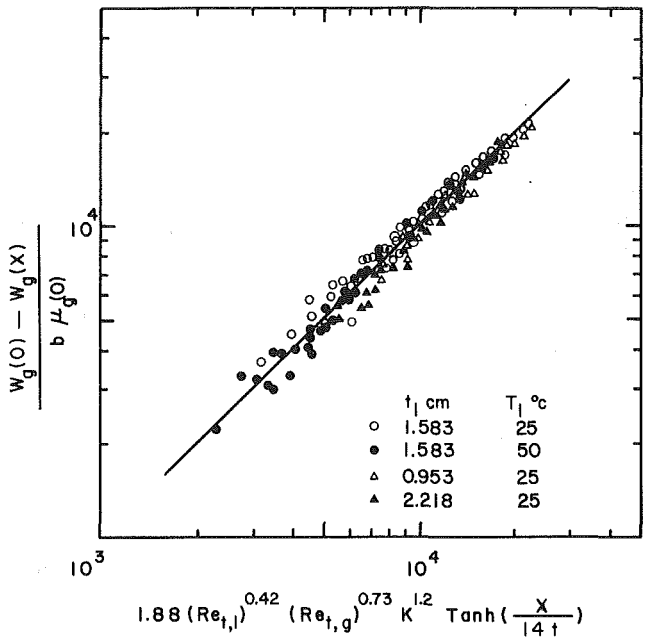

Fig. 18 Correlation of condensate flow rate as a function of inlet steam and water Reynolds numbers, distance downstream, and degree of subcooling

$$\mathrm{Re}_{g,t} = \frac{W_g(0)t}{b\ t_g(0)\mu_g(0)}$$

and

$$K = C_{p,l}[T_s - T_l(0)]/H_{fg}$$

We therefore seek a dimensionless correlation so that

$$\frac{W_g(0) - W_g(x)}{b\ \mu_g(0)} = F[\mathrm{Re}_{l,t}\mathrm{Re}_{g,t}, K, x/t] \tag{14}$$

The dimensionless variable $W_g(0)/b\ \mu_g(0)$ can be interpreted as a Reynolds number based on superficial gas phase velocity and channel height.

For the wavy interface data, the best experimental correlation is

$$\frac{W_g(0) - W_g(x)}{b\ \mu_g(0)} = F$$

$$= 1.88[\mathrm{Re}_{l,t}]^{.42}[\mathrm{Re}_{g,t}]^{.73}K^{1.2}\tanh\left[\frac{x}{14t}\right] \tag{15}$$

The correlation of experimental data with equation (15) is shown in Fig. 18. The agreement is satisfactory. Equation (15) shows that the condensate flow rate approaches a constant value for x/t equal to 30. It also shows that the steam flow rate has a much greater influence than water flow rate as exemplified by the exponents of the respective Reynolds numbers.

Since $W_l(x) - W_l(0) = W_g(0) - W_g(x)$, equation (15) can be substituted into equation (3) to obtain $\bar{h}$ as a function of x and entrance conditions

$$\bar{h} = \frac{C_{p,l}H_g}{x\ \beta} F\ \mu_g(0)$$

$$+ \frac{C_{p,l}H_g}{bx\beta^2}\alpha W_l(0)\ \ln\left\{\frac{Fb\ \mu_g(0)\beta - W_l(0)[\beta - \alpha]}{C_{p,l}W_l(0)[T_s - T_l(0)]}\right\} \tag{16}$$

Given the initial conditions, equations (15), (16), and (2) can predict the condensation rate, the heat transfer coefficient, and the rise in water temperature for a cocurrent, stratified, two-phase flow where the interface is wavy throughout as in most practical cases.

5 Conclusion

Condensation rates of atmospheric steam on subcooled water in a cocurrent horizontal channel were measured and heat transfer coefficients were deduced. The experiments were performed at atmospheric pressure with slightly superheated steam. The effects of steam flow rates (0.4–0.16 kg/s), water flow rates (0.2–1.45 kg/s), inlet water temperatures (25°C and 50°C), inlet water layer thickness (0.95 cm, 1.59 cm, 2.22 cm) on condensation rates were examined. The heat transfer coefficients were found to vary from 1.3 kW/m²°C to 20 kW/m²°C, depending on whether the interfaces were smooth or wavy; increasing with steam and water flow rates. For all experiments, 50 percent to as high as 90 percent of the steam condensed within 1.2 m from the entrance. The steam pressure gradients were found to be positive due to the condensation effect.

The average Nusselt numbers were correlated with the average steam and water Reynolds numbers, and the water Prandtl numbers. Two correlations were obtained, one for smooth and the other for wavy interfaces. Finally, a correlation of heat transfer coefficients and condensation rates for wavy interface flow were obtained as a function of inlet conditions and the distance downstream.

Acknowledgment

This research was partially supported by the U.S. Nuclear Regulatory Commission and National Science Foundation.

References

1 Collier, J. G., *Convective Boiling and Condensation*, McGraw-Hill, New York, 1972.

2 Merte, Herman, Jr., "Condenstaion Heat Transfer," *Advances in Heat Transfer*, Vol. 9, 1973, pp. 181–272.

3 Linehan, J. H., Petrick, M., and El-Wakil, M., "The Condensation of a Saturated Vapor on a Subcooled Film During Stratified Flow," *Chem. Eng. Progress Symposium Series*, No. 102, Vol. 66, 1970, pp. 11–20.

4 Thomas, R. M., "Condensation of Steam on Water in Turbulent Motion," *Int. J. Multiphase Flow*, Vol. 5, 1979, pp. 1–15.

5 Young, R. J., Yang, K. T., and Novotny, J. L., "Vapor-Liquid Interaction in a High Velocity Vapor Jet Condensing in a Coaxial Water Flow," *Proc. 5th Int. Heat Transfer Conf.*, Tokyo, Japan, Vol. 3, 1974, pp. 226–230.

6 Lee, L, Bankoff, S. G., Yuen, M. C., Jensen, R., and Tankin, R. S., "Local Condensation Rates in Horizontal Cocurrent Steam-Water Flow," *Symposium in Nonequilibrium Interfacial Transport Processes*, edited by J. C. Chen and S. G. Bankoff, ASME, New York, 1979, pp. 79–83.

7 Lim, I. S., Bankoff, S. G., Tankin, R. S., and Yuen, M. C., "Cocurrent Steam/Water Flow in a Horizontal Channel," NUREG/CR-2289, 1981.

8 Mandhane, J. M., Gregory, G. A., and Aziz, K., "A Flow Pattern Map for Gas-Liquid Flow in Horizontal Pipes," *Int. J. Multiphase Flow*, Vol. 1, 1974, pp. 537–553.

Analysis of Radiative Equilibrium in a Rectangular Enclosure With Gray Medium

W. W. Yuen

L. W. Wong[1]

Department of Mechanical and Environmental Engineering, University of California, Santa Barbara, Calif. 93106

Radiative heat transfer and temperature profile in a two-dimensional rectangular enclosure with gray medium are calculated. Successive approximate solutions are generated by a point allocation method in which the temperature profile is expressed as polynomials of successively higher order. The technique is shown to converge rapidly with the third-order results already comparing favorably with available numerical solution. It is also demonstrated to be computationally efficient. Comparing with a solution with the same number of unknowns generated by the Hottel zonal method, the present approach represents a reduction in computational time by at least one order of magnitude. Based on the mathematical behavior of the numerical results, simple empirical closed-form approximate expressions for both the heat transfer and temperature profile in general multidimensional systems at radiative equilibrium are proposed. For a rectangular enclosure, these expressions are demonstrated to be quite accurate over all optical thickness.

1 Introduction

Radiative heat transfer in an absorbing and emitting medium constitutes an important element in many engineering disciplines. A great deal of work has been reported in this area. Most, however, has been confined to one-dimensional systems, largely due to the complexity of the problem. Over the past decade, there has been a considerable increase in the interest of multidimensional radiative transfer. Different numerical techniques [1,2] and approximation methods [3–5] have been developed for some selected cases. But the success of these works, in terms of their applicability to radiative transfer in general multidimensional systems, is still quite limited.

Numerically, both the Monte Carlo method [1] and the Hottel zonal method [2] have been widely used for multidimensional computations. But results of the computation generally show that these methods can be quite time consuming and inaccurate under certain conditions. Without significant improvements, it appears unlikely that these two methods can be effectively applied for predicting radiative heat transfer in practical engineering systems.

For approximate analysis, the most successful technique for multidimensional radiative transfer appears to be the modified differential approximation. Based on this method, Glatt and Olfe [3] calculated the temperature distribution in a gray medium bounded by a black rectangular enclosure. Utilizing essentially the same technique and aided by the introduction of a number of geometric parameters, Modest [4, 5] obtained solutions not only for a rectangular enclosure with gray walls, but also for a two-dimensional problem with cylindrical symmetry. But both of these approaches require extensive numerical computation for their prediction of temperature distribution and heat flux. It also appears difficult, if not impossible, to apply these methods for systems with arbitrary geometry. The value of any approximation method depends on its simplicity, accuracy, and applicability to general systems. None of the existing approximation methods appears to have all of these qualities.

The objective of the present work is twofold. First, the point allocation method, which was successful in generating accurate solutions to one-dimensional radiative transfer problems even including the effect of conduction and anisotropic scattering [6, 7], will be demonstrated to be applicable for two-dimensional problems. A gray medium bounded by a rectangular enclosure at radiative equilibrium is analyzed as an illustration. By expanding the unknown temperature distribution as a polynomial, the governing integral equation is reduced to a set of algebraic equations in terms of the expansion coefficients. Successive solutions with increasing degree of accuracy can be readily generated. Comparing with the Hottel zonal method, the present approach is both accurate and efficient. The third-order solution, which involves 28 unknown expansion coefficients, already compares favorably with the available numerical results. This rapid rate of convergence appears to hold for all optical thicknesses and aspect ratios of the rectangular enclosure. By expressing elements of the resulting matrix equation in terms of a class of generalized exponential integral functions which was studied extensively in a recent work [8], the present solution method is extremely efficient numerically. All solutions are generated by evaluating a finite number of single integrations and a matrix inversion. The number of single integrals required is approximately the same as the number of double integrals required for a Hottel zonal calculation with the same number of unknowns.

The second objective of the present work is to develop simple closed-form approximate expressions for the prediction of radiative heat transfer and temperature profile in a gray medium at radiative equilibrium within a general multidimensional enclosure. By requiring that the approximation yield the correct result both in the optically thick and thin limits, a generalized diffusion approximation is proposed. For the present rectangular enclosure, the accuracy of the approximation is shown to be quite good.

2 Mathematical Formulation

The physical model and its associated coordinate system is shown in Fig. 1. For simplicity, the four boundaries are assumed to be black isothermal surface with normalized

[1] Now with The Xerox Corporation, Redondo Beach, Calif.

Contributed by the Heat Transfer Division for publication in the JOURNAL OF HEAT TRANSFER. Manuscript received by the Heat Transfer Division September 16, 1982.

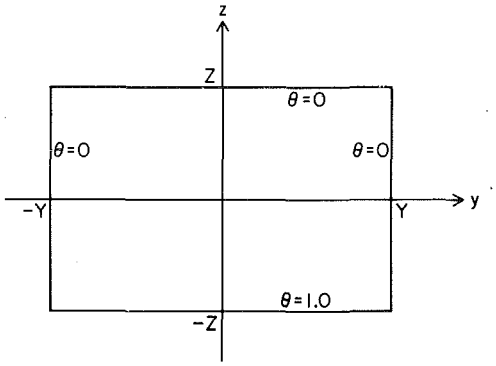

Fig. 1 Geometry and coordinate system for the two-dimensional rectangular enclosure

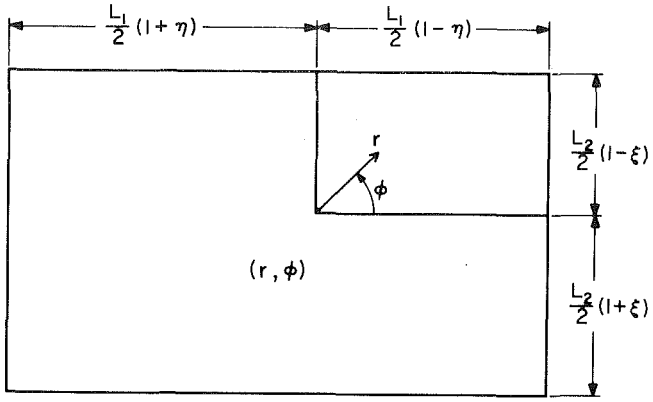

Fig. 2 Domain of integration used in equations (13-15)

emissive powers of 1, 0, 0, and 0, respectively. From standard reference [9], the energy equation for the medium at radiative equilibrium is given by

$$4\vartheta(\mathbf{r}) = \int_{\partial V} \frac{\mathbf{n}(\mathbf{r}')(\mathbf{r}-\mathbf{r}')}{\pi|\mathbf{r}-\mathbf{r}'|^3} C(\mathbf{r}-\mathbf{r}')dS + \int_V \vartheta(\mathbf{r}'') \frac{e^{-a|\mathbf{r}-\mathbf{r}'|}}{\pi|\mathbf{r}-\mathbf{r}''|^2} adV \tag{1}$$

where $\vartheta(\mathbf{r}) = \sigma T^4(\mathbf{r})$ is the blackbody emissive power; $\mathbf{r}'$, a point located at the boundary and $\mathbf{n}(\mathbf{r}')$ the corresponding unit normal vector; a, the absorption coefficient which for the present work is assumed to be constant; and $C(\mathbf{r}-\mathbf{r}')$, a function given by

$$C(\mathbf{r}-\mathbf{r}') = \begin{cases} e^{-a|\mathbf{r}-\mathbf{r}'|} & z' = -Z \\ 0 & \text{otherwise} \end{cases} \tag{2}$$

The medium's temperature is determined by solution to equation (1). Once the temperature distribution is determined, the radiative heat flux is given by

$$\mathbf{Q}(\mathbf{r}) = \int_{\partial V} \frac{\mathbf{n}(\mathbf{r}')(\mathbf{r}-\mathbf{r}')}{\pi|\mathbf{r}-\mathbf{r}'|^4} C(\mathbf{r}-\mathbf{r}')(\mathbf{r}-\mathbf{r}')dS + \int_V \vartheta(\mathbf{r}'') \frac{e^{-a|\mathbf{r}-\mathbf{r}''|}}{\pi|\mathbf{r}-\mathbf{r}''|^3} a(\mathbf{r}-\mathbf{r}'')dV \tag{3}$$

For the present two-dimensional problem, all integrals in the x-direction can be integrated. Introducing the following dimensionless variables

$$\eta = \frac{y}{Y} \tag{4}$$

$$\zeta = \frac{z}{Z}$$

$$L_1 = 2aY$$

$$L_2 = 2aZ,$$

equations (1) and (3) can be simplified to yield

$$\vartheta(\eta,\zeta) = \frac{L_1L_2}{16}\int_{-1}^{1}\int_{-1}^{1} \vartheta(\eta',\zeta')\frac{S_1(d_1)}{d_1}d\eta'd\zeta' + \frac{L_1L_2}{16}(1+\zeta)\int_{-1}^{1}\frac{S_2(d_2)}{d_2^2}d\eta' \tag{5}$$

$$Q_\eta(\eta,\zeta) = \frac{L_1^2L_2}{8}\int_{-1}^{1}\int_{-1}^{1} \vartheta(\eta',\zeta')\frac{S_2(d_1)(\eta-\eta')}{d_1^2}d\eta'd\zeta' + \frac{L_1^2L_2}{8}(1+\zeta)\int_{-1}^{1}\frac{S_3(d_2)(\eta-\eta')}{d_2^3}d\eta' \tag{6}$$

$$Q_\zeta(\eta,\zeta) = \frac{L_1L_2^2}{8}\int_{-1}^{1}\int_{-1}^{1} \vartheta(\eta',\zeta')\frac{S_2(d_1)(\zeta-\zeta')}{d_1^2}d\eta'd\zeta' + \frac{L_1L_2^2}{8}(1+\zeta)^2\int_{-1}^{1}\frac{S_3(d_2)}{d_2^3}d\eta' \tag{7}$$

Nomenclature

a = absorption coefficient
$C(\mathbf{r}-\mathbf{r}')$ = function defined by equation (2)
$d_1(\eta,\eta',\zeta,\zeta',)$ = function defined by equation (8)
$d_2(\eta,\eta',\zeta,)$ = function defined by equation (9)
$G_{m,n,k}(x,y)$ = function defined by equation (22)
$H_{m,n,k,s}(\eta,\zeta)$ = function defined by equations (A3) and (A4)
L_1 = optical thickness of the enclosure in the y-direction
L_2 = optical thickness of the enclosure in the z-direction
$M_{i,j}$ = function defined by equation (20)
$\mathbf{n}$ = unit normal vector
$NY_{i,j}$ = function defined by equation (27)
$NZ_{i,j}$ = function defined by equation (28)
$P_{i,j}$ = coefficients of assumed polynomial defined by equation (18)
Q_i = heat flux in the i-direction
$\mathbf{Q}$ = heat flux vector
r = "polar" coordinate defined by equations (11) and (12)
$\mathbf{r}$ = position vector
$S_n(x)$ = exponential integral function
T = temperature
$W_{m,n,k}(\eta,\zeta)$ = functions defined by equations (21)
x = coordinate
y = coordinate
z = coordinate
$\Gamma(n)$ = gamma function
ζ = optical thickness variable in the z-direction
η = optical thickness variable in the y-direction
ϑ = dimensionless emissive power
φ = angular coordinate defined by equations (11) and (12)
φ_1 = angle defined by equation (16)
φ_2 = angle defined by equation (17)
σ = Stefan-Boltzmann constant

Subscripts

0 = optically thin limit
c = optically thick (conduction) limit

where

$$d_1(\eta,\eta',\zeta,\zeta') = \tfrac{1}{2}[L_1^2(\eta-\eta')^2 + L_2^2(\zeta-\zeta')^2]^{1/2} \quad (8)$$

$$d_2(\eta,\eta',\zeta) = d_1(\eta,\eta',\zeta,-1) \quad (9)$$

In equations (5), (6), and (7), $S_n(x)$ is a generalized exponential integral function defined by

$$S_n(x) = \frac{2}{\pi}\int_1^\infty \frac{e^{-xt}dt}{t^n(t^2-1)^{1/2}} \quad (10)$$

Analytical and numerical properties of $S_n(x)$ are presented in [8].

Since $S_n(x)$ is a smooth function for all values of x, evaluation of the integrals appearing in equations (5), (6), and (7) is quite straightforward for any assumed temperature distribution. Note that even at regions with $d_1 = 0$ or $d_2 = 0$, these integrals remain finite because the product of the integrand with the respective volume element and surface element remains finite. To illustrate this mathematical behavior more clearly and also for the convenience of numerical computation, equations (5-7) are now rewritten in terms of a "polar" coordinate. Introducing two new variables, r and φ, such that

$$\eta' = \eta + \frac{2r}{L_1}\cos\varphi \quad (11)$$

$$\zeta' = \zeta + \frac{2r}{L_2}\sin\varphi \quad (12)$$

equations (5), (6), and (7) can be rewritten as

$$4\vartheta(\eta,\zeta) = \int\int_{(r,\varphi)} \vartheta\left(\eta + \frac{2r}{L_1}\cos\varphi, \zeta + \frac{2r}{L_2}\sin\varphi\right) \quad (13)$$

$$S_1(r)drd\varphi + \int_{\varphi_1}^{\varphi_2} S_2\left[\frac{L_2}{2}(1+\zeta)\sec\varphi\right]d\varphi$$

$$Q_\eta(\eta,\zeta) = -\int\int_{(r,\varphi)} \vartheta\left(\eta + \frac{2r}{L_1}\cos\varphi, \zeta + \frac{2r}{L_2}\sin\varphi\right) \quad (14)$$

$$S_2(r)\cos\varphi drd\varphi - \int_{\varphi_1}^{\varphi_2} S_3\left[\frac{L_2}{2}(1+\zeta)\sec\varphi\right]\sin\varphi d\varphi$$

$$Q_\zeta(\eta,\zeta) = -\int\int_{(r,\varphi)} \vartheta\left((\eta + \frac{2r}{L_1}\cos\varphi, \zeta + \frac{2r}{L_2}\sin\varphi\right) \quad (15)$$

$$S_2(r)\sin\varphi drd\varphi + \int_{\varphi_1}^{\varphi_2} S_3\left[\frac{L_2}{2}(1+\zeta)\sec\varphi\right]\cos\varphi d\varphi$$

with

$$\varphi_1 = -\tan^{-1}\frac{L_1(1+\eta)}{L_2(1+\zeta)} \quad (16)$$

$$\varphi_2 = \tan^{-1}\frac{L_1(1-\eta)}{L_2(1+\zeta)} \quad (17)$$

The region of integration (r,φ) for the above double integration at a given (η,ζ) is illustrated by Fig. 2. Note that equations (13-15) are indeed free of any apparent singularites.

3 Method of Solution

The method of point allocation is now applied to develop solutions to the present problem. Specifically in the nth approximation, the unknown temperature distribution is assumed to be a polynomial as follows

$$\vartheta(\eta,\zeta) = \sum_{i=0}^{i=n}\sum_{j=0}^{j=2n} P_{2i,j}\eta^{2i}\zeta^j \quad (18)$$

Substituting equation (18) into equation (13), the following equation results

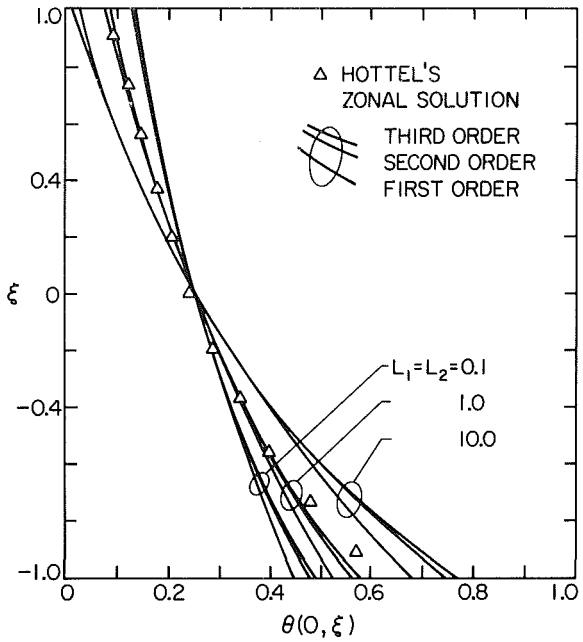

Fig. 3 Comparison between the first three order approximate temperature solutions with results generated by the Hottel's zonal method

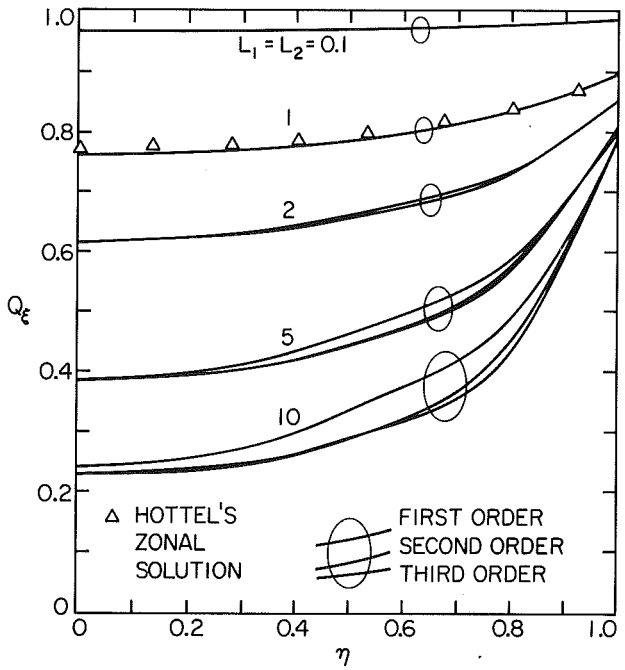

Fig. 4 Comparison between the first three order approximate heat flux solutions with results generated by the Hottel's zonal method

$$\sum_{i=0}^{i=n}\sum_{j=0}^{j=2n} P_{2i,j}[4\eta^{2i}\zeta^j - M_{2i,j}(\eta,\zeta,L_1,L_2)]$$

$$= G_{0,0,0}(\zeta^+,\eta^+) + G_{0,0,0}(\zeta^+,\eta^-) \quad (19)$$

where

$$M_{2i,j} = \sum_{mi=0}^{mi=2i}\sum_{ni=0}^{ni=j}\binom{2i}{mi}\binom{j}{ni}\left(\frac{2}{L_1}\right)^{mi}\left(\frac{2}{L_2}\right)^{ni}$$

$$\eta^{2i-mi}\zeta^{j-ni}W_{mi,ni,1}(\eta,\zeta) \quad (20)$$

with

$$W_{m,n,k}(\eta,\zeta) = \int\int_{(r,\varphi)} \cos^m\varphi\sin^n\varphi r^{m+n}S_k(r)drd\varphi \quad (21)$$

Table 1(*a*) Expansion coefficient $P_{i,j}$ and the corresponding temperature profile generated by a third-order solution with $L_1 = L_2 = 1.0$

$P_{00} =$ 2.5000e-01	$P_{01} = -$2.2896e-01	$P_{02} =$ 1.0359e-01	$P_{03} = -$3.4222e-02
$P_{04} =$ 8.516e-03	$P_{05} = -$8.7643e-03	$P_{06} = -$4.3067e-03	$P_{20} = -$1.0359e-01
$P_{21} =$ 9.6454e-02	$P_{22} = -$5.8112e-16	$P_{23} = -$8.0216e-02	$P_{24} = -$3.0798e-02
$P_{25} = -$3.6243e-03	$P_{26} =$ 3.3752e-02	$P_{40} = -$8.5162e-02	$P_{41} =$ 5.3491e-02
$P_{42} = -$3.0798e-02	$P_{43} =$ 6.4432e-02	$P_{44} = -$5.9828e-16	$P_{45} = -$1.6837e-01
$P_{46} =$ 1.0463e-01	$P_{60} =$ 4.3067e-03	$P_{61} = -$3.7104e-02	$P_{62} = -$3.3752e-02
$P_{63} =$ 1.3701e-01	$P_{64} = -$1.0463e-01		

ζ \ η	0	0.2	0.4	0.6	0.8	1.0
1.0000	0.0859	0.0848	0.0819	0.0767	0.0661	0.0401
0.8000	0.1151	0.1132	0.1080	0.0997	0.0878	0.0680
0.6000	0.1427	0.1405	0.1339	0.1237	0.1095	0.0891
0.4000	0.1729	0.1702	0.1621	0.1489	0.1304	0.1046
0.2000	0.2081	0.2047	0.1945	0.1775	0.1534	0.1211
0.0000	0.2500	0.2458	0.2332	0.2118	0.1813	0.1422
0.2000	0.3002	0.2953	0.2802	0.2540	0.2159	0.1663
−0.4000	0.3606	0.3551	0.3379	0.3070	0.2591	0.1901
−0.6000	0.4336	0.4280	0.4102	0.3763	0.3181	0.2190
−0.8000	0.5222	0.5175	0.5025	0.4726	0.4122	0.2832
−1.0000	0.6297	0.6278	0.6235	0.6152	0.5828	0.4599

Table 1(*b*) $Q_\eta[\eta,\xi)$ generated from a third-order solution with $L_1 = L_2 = 1.0$

ζ \ η	0	0.1667	0.3333	0.5000	0.6667	0.8333	1.0000
1.0000	0.0000	0.0184	0.0362	0.0528	0.0671	0.0795	0.0894
0.8333	0.0000	0.0229	0.0442	0.0653	0.0845	0.1025	0.1158
0.6667	0.0000	0.0274	0.0539	0.0784	0.1002	0.1234	0.1385
0.5000	0.0000	0.0275	0.0641	0.0961	0.1234	0.1474	0.1651
0.3333	0.0000	0.0371	0.0766	0.1124	0.1433	0.1714	0.1929
0.1667	0.0000	0.0455	0.0905	0.1329	0.1695	0.1996	0.2215
0.0000	0.0000	0.0534	0.1029	0.1527	0.1961	0.2333	0.2588
−0.1667	0.0000	0.0577	0.1163	0.1732	0.2255	0.2687	0.2970
−0.3333	0.0000	0.0593	0.1243	0.1897	0.2496	0.3102	0.3459
−0.5000	0.0000	0.0560	0.1256	0.1996	0.2784	0.3535	0.3984
−0.6667	0.0000	0.0550	0.1152	0.1868	0.2570	0.3889	0.4594
−0.8333	0.0000	0.0417	0.0867	0.1437	0.2271	0.3721	0.5375
−1.0000	0.0000	0.0225	0.0451	0.0686	0.0925	0.1179	0.6436

Table 1(*c*) $Q_\xi(\eta,\xi)$ generated from a third-order solution with $L_1 = L_2 = 1.0$

ζ \ η	0	0.1667	0.3333	0.5000	0.6667	0.8333	1.0000
1.0000	0.2439	0.2435	0.2331	0.2213	0.2055	0.1830	0.1594
0.8333	0.2645	0.2632	0.2533	0.2386	0.2205	0.1974	0.1735
0.6667	0.2907	0.2868	0.2807	0.2613	0.2537	0.2167	0.1873
0.5000	0.3200	0.3163	0.3071	0.2877	0.2659	0.2358	0.2023
0.3333	0.3572	0.3523	0.3408	0.3215	0.2924	0.2582	0.2192
0.1667	0.3992	0.3945	0.3827	0.3625	0.3239	0.2836	0.2378
0.0000	0.4484	0.4443	0.4272	0.3999	0.3614	0.3130	0.2578
−0.1667	0.5059	0.4977	0.4791	0.4459	0.4063	0.3482	0.2787
−0.3333	0.5630	0.5590	0.5416	0.5112	0.4614	0.3892	0.3005
−0.5000	0.6253	0.6225	0.6091	0.5834	0.5311	0.4448	0.3237
−0.6667	0.6828	0.6817	0.6735	0.6631	0.6109	0.5283	0.3469
−0.8333	0.7310	0.7315	0.7349	0.7395	0.7328	0.6719	0.3710
−1.0000	0.7615	0.7621	0.7719	0.7848	0.8034	0.8362	0.8922

$$G_{m,n,k}(x,y) = x^k \int_0^{\tan^{-1}\frac{y}{x}} S_{2+m+n-k}(x\sec\varphi)\tan^m\varphi\cos^{m+n-k}\varphi\, d\varphi \tag{22}$$

and

$$\eta^+ = \frac{L_1}{2}(1+\eta) \tag{23}$$

$$\eta^- = \frac{L_1}{2}(1-\eta)$$

$$\zeta^+ = \frac{L_2}{2}(1+\zeta) \tag{24}$$

$$\zeta^- = \frac{L_2}{2}(1-\zeta)$$

Evaluating equation (19) at $(n+1)(2n+1)$ discrete locations ($\eta = i/n$, $i = 0, \ldots n$; $\zeta = j/n$, $j = -n, \ldots, 0, \ldots n$), a matrix equation is generated for the determination of $P_{2i,j}$.

Once the coefficients $P_{2i,j}$ are determined, the corresponding heat fluxes can be written as

$$Q_\eta(\eta,\zeta) = -\sum_{i=0}^{i=n}\sum_{j=0}^{j=2n} P_{2i,j} NY_{2i,j}(\eta,\zeta,L_1,L_2) + G_{1,0,0}(\zeta^+,\eta^+) - G_{1,0,0}(\zeta^+,\eta^-) \tag{25}$$

Table 2 Third-order results for the radiative heat flux at the lower wall, $Q_\xi(\eta, -1)$

L_1	L_2	$\eta=0$	0.1667	0.0500	0.8333
0.1	0.1	0.9687	0.9689	0.9712	0.9769
	0.5	0.9624	0.9627	0.9647	0.9697
	1.0	0.9579	0.9582	0.9603	0.9658
	2.0	0.9485	0.9488	0.9514	0.9578
	5.0	0.9310	0.9313	0.9345	0.9421
1.0	0.1	0.9210	0.9213	0.9241	0.9402
	0.5	0.7954	0.7973	0.8137	0.8606
	1.0	0.7615	0.7621	0.7848	0.8362
	2.0	0.7514	0.7537	0.7730	0.8183
	5.0	0.7376	0.7395	0.7561	0.8003
5.0	0.1	0.9158	0.9159	0.9159	0.9273
	0.5	0.7074	0.7081	0.7152	0.7760
	1.0	0.5686	0.5708	0.5924	0.6963
	2.0	0.4476	0.4521	0.4919	0.6350
	5.0	0.3802	0.3859	0.4362	0.5854

Table 3 Third-order results for the radiative heat flux at the upper wall, $Q_\xi[\eta,1)$

L_1	L_2	$\eta=0$	0.1667	0.5000	0.8333
0.1	0.1	0.4153	0.4124	0.3899	0.3484
	0.5	0.0612	0.0611	0.0607	0.0599
	1.0	0.0172	0.0172	0.0171	0.0171
	2.0	0.0021	0.0021	0.0021	0.0021
	5.0	0.0000	0.0000	0.0000	0.0000
1.0	0.1	0.9029	0.9016	0.8849	0.7521
	0.5	0.5178	0.5117	0.4616	0.3585
	1.0	0.2439	0.2435	0.2213	0.1830
	2.0	0.0638	0.0633	0.0596	0.0523
	5.0	0.0000	0.0000	0.0000	0.0000
5.0	0.1	0.9156	0.9155	0.9155	0.8981
	0.5	0.7003	0.6994	0.6877	0.5753
	1.0	0.5356	0.5328	0.5012	0.3657
	2.0	0.3276	0.3230	0.2825	0.1864
	5.0	0.0750	0.0734	0.0614	0.0357

Table 4 Third-order results for the radiative heat flux at the side wall, $Q_\eta(1,\xi)$

L_1	L_2	$\xi=-018333$	-0.3333	0	0.3333	0.8333
0.1	0.1	0.4719	0.3452	0.2767	0.2208	0.1565
	0.5	0.3142	0.0717	0.0356	0.0206	0.0101
	1.0	0.1866	0.0207	0.0090	0.0048	0.0015
	2.0	0.0828	0.0048	0.0018	0.0008	0.0000
	5.0	0.0308	0.0000	0.0000	0.0000	0.0000
1.0	0.1	0.5409	0.4964	0.4704	0.4454	0.4078
	0.5	0.5601	0.4359	0.3694	0.3202	0.2286
	1.0	0.5375	0.3459	0.2588	0.1929	0.1158
	2.0	0.4732	0.2076	0.1233	0.0740	0.0313
	5.0	0.3319	0.0491	0.0165	0.0058	0.0000
5.0	0.1	0.5350	0.4909	0.4660	0.4426	0.4081
	0.5	0.5815	0.4711	0.4136	0.3607	0.2829
	1.0	0.5928	0.4435	0.3689	0.3021	0.2076
	2.0	0.5789	0.3847	0.2959	0.2224	0.1266
	5.0	0.5168	0.2401	0.1526	0.0948	0.0328

Table 5 Third-order results for the centerline temperature $\theta(0,\xi)$

L_1	L_2	$\xi=-1.0$	-0.4	0	0.4	1.0
0.1	0.1	0.5179	0.3329	0.2500	0.1935	0.1373
	0.5	0.5206	0.0959	0.0533	0.0345	0.0189
	1.0	0.5226	0.0405	0.0203	0.0123	0.0050
	2.0	0.5264	0.0125	0.0058	0.0039	0.0005
	5.0	0.5330	0.0000	0.0000	0.0000	0.0000
1.0	0.1	0.5596	0.5093	0.4797	0.4503	0.4016
	0.5	0.6171	0.4544	0.3697	0.2959	0.1927
	1.0	0.6297	0.4336	0.2500	0.1729	0.0859
	2.0	0.6345	0.2205	0.1178	0.0653	0.0219
	5.0	0.6415	0.0601	0.0170	0.0054	0.0000
5.0	0.1	0.5706	0.5257	0.4995	0.4733	0.4284
	0.5	0.6839	0.5636	0.4953	0.4272	0.3083
	1.0	0.7474	0.5782	0.4830	0.3892	0.2292
	2.0	0.7990	0.5626	0.4355	0.3180	0.1363
	5.0	0.8276	0.4134	0.2500	0.1419	0.0306

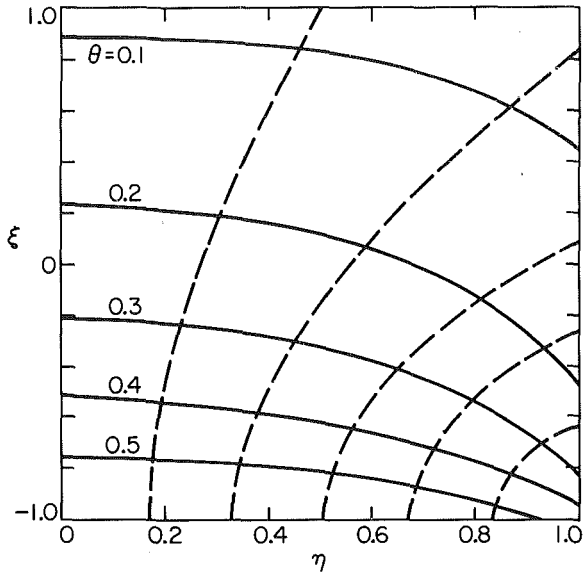

Fig. 5 Isotherms (——) and flux lines (---) for the case with $L_1 = L_2 = 1.0$

$$Q_\zeta(\eta,\zeta) = -\sum_{i=0}^{i=n}\sum_{j=0}^{j=2n} P_{2i,j} NZ_{2i,j}(\eta,\zeta,L_1,L_2) + G_{0,1,0}(\zeta^+,\eta^+) + G_{0,1,0}(\zeta^+,\eta^-) \tag{26}$$

where

$$NY_{2i,j} = \sum_{mi=0}^{mi=2i}\sum_{ni=0}^{ni=j}\binom{2i}{mi}\binom{j}{ni}\left(\frac{2}{L_1}\right)^{mi}\left(\frac{2}{L_2}\right)^{ni} \eta^{2i-mi}\zeta^{j-ni} W_{mi+1,ni,2}(\eta,\zeta) \tag{27}$$

and

$$NZ_{2i,j} = \sum_{mi=0}^{mi=2i}\sum_{ni=0}^{ni=j}\binom{2i}{mi}\binom{j}{ni}\left(\frac{2}{L_1}\right)^{mi}\left(\frac{2}{L_2}\right)^{ni} \eta^{2i-mi}\zeta^{j-ni} W_{mi,ni+1,2}(\eta,\zeta) \tag{28}$$

It is important to note that based on the mathematical properties of $S_n(x)$ developed in [8], a set of recursive relations for $G_{m,n,k}(\eta,\zeta)$ and $W_{m,n,k}(\eta,\zeta)$ can be readily generated. They are listed in Appendix A. Based on these relations, $M_{2i,j}$, $NY_{2i,j}$ and $NZ_{2i,j}$ in the above equations can be readily evaluated. Indeed, the analysis in Appendix A shows that the present technique requires only the numerical evaluation of a finite number of single integrals for a complete solution to the problem.

4 Results and Discussion

(a) Numerical Accuracy and Efficiency. The major advantage of the present solution method is that extremely accurate solutions for both the temperature and heat flux distribution can be readily obtained with little effort. Predictions of the centerline temperature and heat flux distribution at the bottom walls generated by the first three approximation ($n = 1,2,3$) of the present approach and those obtained by the Hottel zonal method as reported in [4] are compared in Figs. 3 and 4. The rapid rate of convergence shown in those figures holds in general for all optical thicknesses L_1 and L_2.

Direct comparison between different numerical procedures based on computer time is difficult and often misleading because computer time depends not only on the complexity of the calculation, but also on the size of a computer and the efficiency of the programmer. A more accurate comparison of the relative efficiency between the present technique and the Hottel zonal method is the number of numerical integrals required by the two methods and the relative complexity of the required integrations. Based on results presented in Appendix A, the number of single integration required by the present technique is approximately the same as the number of double integrals required by the Hottel zonal method with the same number of unknowns. Since numerical evaluation of a double integration is at least one order of magnitude more

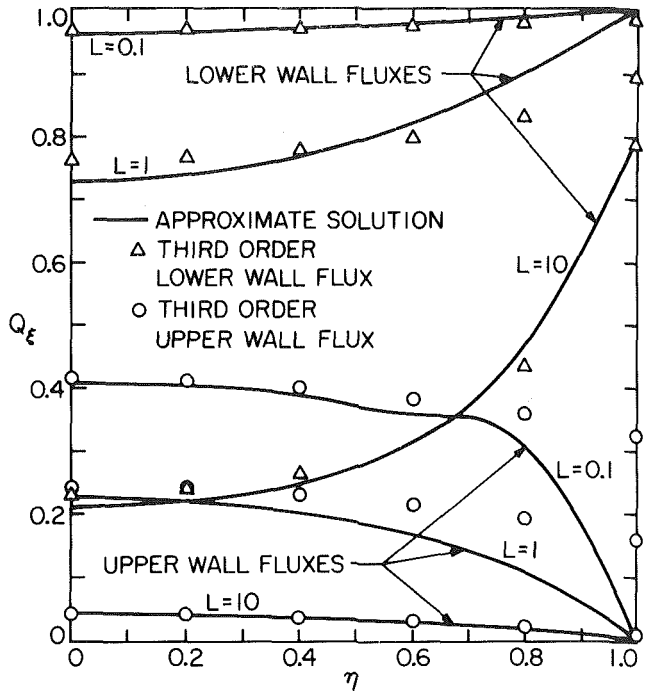

Fig. 6 Comparison between equation (30) and the third-order result at the upper and lower wall for enclosures with $L_1 = L_2 = L$

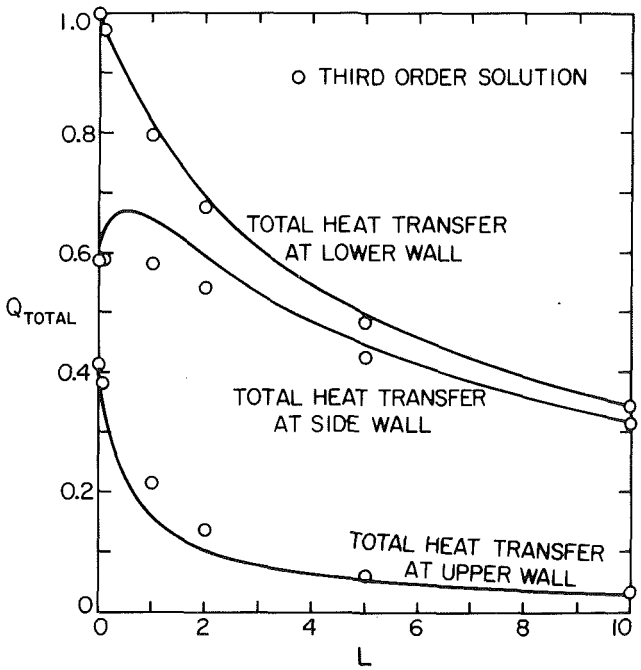

Fig. 7 Comparison between total heat transfer results generated from equation (30) and the corresponding third-order results for enclosures with $L_1 = L_2 = L$

complex than that of a single integration, the present technique is clearly numerically more efficient than the Hottel zonal method.

Another advantage of the present technique is that in addition to temperature distribution, detailed information concerning heat flux distribution is also generated by the computation with no additional effort. The third-order results of $P_{2i,j}$, $\vartheta(\eta,\zeta)$, $Q_\eta(\eta,\zeta)$ and $Q_\zeta(\eta,\zeta)$ for the case with $L_1=L_2=1$ are presented in Tables 1(*a*), 1(*b*), and 1(*c*). Results in these tables can be combined to yield the isotherm and flux line plot shown in Fig. 5. Similar results for other typical cases (L_1, $L_2=0.1$, 0.5, 1.0, 2.0, 5.0, 10.0) are presented in [10]. Centerline temperature and heat flux distribution at the three boundaries for some typical cases (which might be of interest to researchers for comparison with other techniques) are presented in Tables 2–5. It is interesting to note that to generate the same information based on the Hottel zonal method would require a tripling of the number of double integrations. A direct comparison of numerical results also shows that a 28-zones Hottel zonal calculation is generally less accurate than the present third order solution. To the best of the present authors' knowlege, no other solution methods (approximate or exact) for radiative transfer can generate as much information with such numerical efficiency as the present technique.

(*b*) **Important Physical Results.** The qualitative behavior of the heat flux and temperature distribution of the present two-dimensional problem is well known from previous studies [1–5]. Results presented in Tables 2–5 demonstrate the expected behavior more quantitatively over a wide range of system parameters.

Over the years, numerous analysis of different engineering systems have been presented in which the radiative heat flux is approximated as a simple diffusion process with $\mathbf{Q}=-4/3\nabla\vartheta$. Until now, quantitative evaluation of the accuracy of this assumption has never been made, except for one-dimensional systems. The isothermal and flux line plot generated by the present work as shown in Fig. 5 offers an interesting possibility for such evaluation. Note that for $L_2=L_1=1$ (which is optically thick compared to most combustion systems), the isothermal line is in not perpendicular to the flux line. The diffusion approximation is thus in general not accurate for such systems, both in predicting the magnitude and the direction of the radiative heat flux vector. The validity of many previous analysis which utilized this approximation is thus needed to be reevaluated. It is also interesting to observe that because of the temperature slip, the isotherms shown in Fig. 5 are not parallel to the isothermal wall.

(*c*) **Approximate Solutions.** For practical engineering application, the development of accurate and simple-to-use expressions for the prediction of heat transfer and temperature profile within a multidimensional systems at radiative equilibrium is important. Until now, development of such expressions, even empirically, is difficult due to the lack of reliable numerical data. The present results, which include detail information concerning both temperature and heat flux distribution, serve ideally as basis for such development.

In one-dimensional analysis, it is well known [9] that the traditional diffusion approximation is quite accurate and yields the following expression for the radiative heat flux,

$$Q=\frac{1}{1+3L/4} \tag{29}$$

Using the fact that $1/L$ and 1 can be interpreted as the optically thick and thin limits of the radiative heat flux, the present work proposes to generalize the above expression for multidimensional application to become

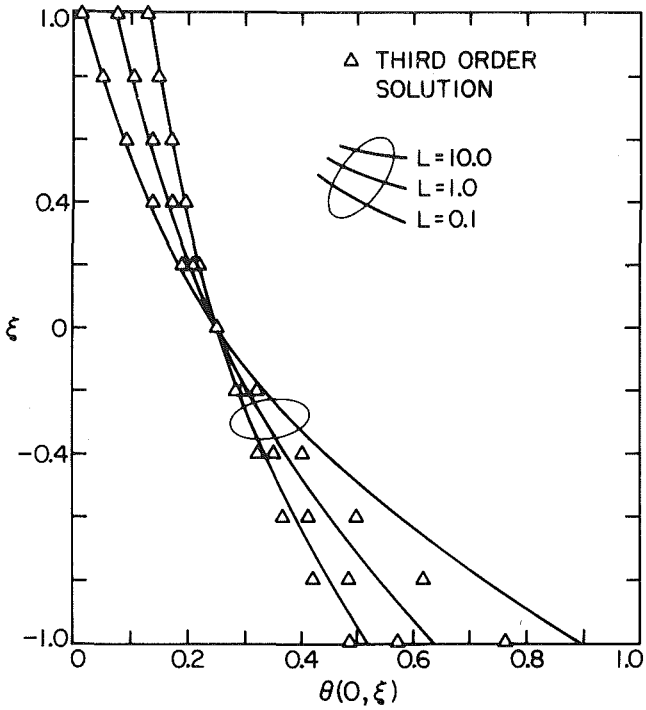

Fig. 8 Comparison between equation (31) and the corresponding third-order solution of the centerline temperature $\theta[0,\xi)$ with $L_1=L_2=L$

$$Q_i=\frac{1}{\dfrac{1}{Q_{0,i}}+\dfrac{3}{4Q_{c,i}}} \qquad i=x,y,z \tag{30}$$

In the above expression, $Q_{0,i}$ stands for the optically thin limiting expression of the radiative heat flux which is a function only of geometry, and $Q_{c,i}$ stands for the corresponding optically thick limit which can be readily generated by solving an equivalent conduction problem with identical boundary conditions. Since solutions to conduction problems (by both analytical and numerical method) are well known, equation (28) clearly represents an exceedingly simplified approach in evaluating approximately radiative heat flux in a multidimensional system.

It is important to note that equation (30) is developed entirely empirically from physical reasoning. It is intended only to be a tool for practicing engineer to generate first-order estimate of the radiative heat flux. For the present rectangular enclosure, however, the accuracy of the expression is surprisingly good. Heat flux distributions and average heat flux at the three boundaries predicted by equation (30) and the corresponding third-order results for different system parameters are compared in Figs. 6 and 7.

Utilizing a similar argument, the present work proposes the following empirical expression for the temperature distribution

$$\vartheta=\left(1-\frac{|\mathbf{Q}|}{|\mathbf{Q}_0|}\right)\vartheta_c+\frac{|\mathbf{Q}|}{|\mathbf{Q}_0|}\vartheta_0 \tag{31}$$

In the above expression, ϑ_c and ϑ_0 stand of the optically thick and thin limiting expression of the medium's temperature, respectively. For a general enclosure, ϑ_0 can be generated by solving an energy equation such as equation (13) in the optically thin limit. For the rectangular enclosure, for example, it can be readily shown that ϑ_0 is given by

$$\vartheta_0(\eta,\zeta)=\frac{1}{4\pi}(\varphi_2-\varphi_1) \tag{32}$$

Similar to $\mathbf{Q}_c(\eta,\zeta)$, $\vartheta_c(\eta,\zeta)$ can be generated from an analytical or numerical solution to a corresponding con-

duction problem. The accuracy of equation (31) is again quite good for the rectangular enclosure. Centerline temperature profiles generated by equation (31) and the corresponding third-order results for some typical cases are shown in Fig. 8.

5 Conclusion

Radiative heat transfer in a rectangular enclosure with gray medium at equilibrium is considered. The method of point allocation is demonstrated to be effective in generating accurate solutions to the problem. Utilizing properties of $S_n(x)$, a class of generalized exponential integral functions studied extensively in a previous reference [8], the present solution technique is shown to be extremely efficient compared to the Hottel zonal method. Detailed temperature and heat flux distribution both within the medium and at the different boundaries are readily generated from the present approach. Based on the present results, the physics of multidimensional radiative heat transfer is illustrated and discussed.

Simple closed-form expressions are proposed for the estimate of heat transfer and temperature profile in a multidimensional system at radiative equilibrium. These expressions are generated empirically by requiring that they have the correct behavior in both the optically thick and thin limits and are intended only for practical engineering application. For the rectangular enclosure, the accuracy of these expressions over all optical thicknesses is demonstrated to be good.

6 Acknowledgment

This work is based upon work supported by the National Science Foundation Grants No. ENG 78-05587 and MEA 80-24824.

References

1 Taniguchi, H., "The Radiative Heat Transfer of Gas in a Three-Dimensional System Calculated by Monte Carlo Method," *Bulletin JSME*, Vol. 12, 1969, pp. 67–78.

2 Hottel, H. C., and Cohen, E. S., "Radiant Heat Exchange in a Gas-Filled Enclosure: Allowance for Non-Uniformity of Gas Temperature," *AIChE Journal*, Vol. 4, No. 1, 1958, pp. 3–14.

3 Glatt, L., and Olfe, D. B., "Radiative Equilibrium of a Gray Medium in a Rectangular Enclosure," *Journal of Quantitative Spectroscopy and Radiative Transfer*, Vol. 13, 1973, pp. 881–895.

4 Modest, M. F., "Radiative Equilibrium of a Gray Medium in a Rectangular Enclosure," *Journal of Quantitative Spectroscopy and Radiative Transfer*, Vol. 15, 1975, pp. 445–461.

5 Modest, M. F., "Two-Dimensional Radiative Equilibrium of a Gray Medium Between Concentric Cylinders," *Journal of Quantitative Spectroscopy and Radiative Transfer*, Vol. 19, 1978, pp. 353–365.

6 Yuen, W. W., and Tien, C. L., "A Successive Approximation Approach to Problems in Radiative Transfer with a Differential Formulation," ASME JOURNAL OF HEAT TRANSFER, Vol. 102, No. 1, 1980, pp. 86–91.

7 Yuen, W. W., and Wong, L. W., "Heat Transfer by Conduction and Radiation in a One-Dimensional Absorbing, Emitting and Anisotropically Scattering Medium," ASME JOURNAL OF HEAT TRANSFER, Vol. 102, 1980, pp. 303–307.

8 Yuen, W. W., and Wong, L. W., "Numerical Computation of an Important Integral Function in Two-Dimensional Radiative Transfer," *Journal of Quantitative Spectroscopy and Radiative Transfer*, Vol. 29, No. 2, 1983, pp. 145–149.

9 Siegel, R., and Howell, J. R., *Thermal Radiation Heat Transfer*, McGraw-Hill, N.Y., 1972.

10 Yuen, W. W., "Numerical Results of Radiative Heat Transfer in a Rectangular Enclosure With Gray Medium at Radiative Equilibrium," UCSB Report No. ME-83-1, 1983.

APPENDIX A

Properties of $W_{m,n,k}[\eta,\varphi)$ and $G_{m,n,k}(x,y)$

Using the recursive relation of $S_n(x)$ as illustrated in [8], it can be readily shown that

$$\int_0^r S_k(x)x^{m+n}dx=(m+n)!\left[S_{m+n+k+1}(0)-\sum_{s=0}^{s=m+n}S_{m+n+k+1-s}(r)\frac{r^s}{s!}\right] \tag{A1}$$

Based on the above equation, equation (21) is reduced to

$$W_{m,n,k}(\eta,\varphi)=-(m+n)!\left[\sum_{s=0}^{s=m+n}\frac{H_{m,n,k,s}(\eta,\varphi)}{s!}-\frac{[1+(-1)^m][1+(-1)^n]}{2}\left[\frac{\Gamma\left(\frac{m+1}{2}\right)\Gamma\left(\frac{n+1}{2}\right)}{\Gamma\left(\frac{m+n+2}{2}\right)}\right]S_{m+n+k+1}(0)\right] \tag{A2}$$

where

$$H_{m,n,k,s}(\eta,\varphi)=\int_0^{2\pi}[r(\varphi)]^s S_{m+n+k+1-s}[r(\varphi)]\cos^m\varphi\sin^n\varphi d\varphi \tag{A3}$$

Values for $r(\varphi)$ can be readily deduced from Fig. 2. Indeed, $H_{m,n,1,s}(\eta,\varphi)$, which is required for the solution to equation (19), can be expressed as

$$\begin{aligned}H_{m,n,1,s}(\eta,\varphi)=&G_{n,m,s}(\eta^-,\zeta^-)+G_{m,n,s}(\zeta^-,\eta^-)\\&(-1)^m[G_{n,m,s}(\eta^+,\zeta^-)+G_{m,n,s}(\zeta^-,\eta^+)]\\&(-1)^n[G_{n,m,s}(\eta^-,\zeta^+)+G_{m,n,s}(\zeta^+,\eta^-)]\\&(-1)^{m+n}[G_{n,m,s}(\eta^+,\zeta^+)+G_{m,n,s}(\zeta^+,\eta^+)]\end{aligned} \tag{A4}$$

where η^+, η^-, ζ^+, and ζ^- are as defined by equations (23) and (24). Similar expressions can also be generated for $H_{m,n,2,s}(\eta,\zeta)$, which is required for the evaluation of heat fluxes.

The foregoing development proves that the evaluation of $W_{m,n,1}(\eta,\varphi)$ and $W_{m,n,2}(\eta,\varphi)$ requires only the evaluation of $G_{m,n,k}(x,y)$. Based on equation (22) and properties of $S_n(x)$, it can be readily shown that $G_{m,n,k}(x,y)$ satisfies

$$G_{m,n,k}(x,y)=\begin{cases}x^kG_{m,n-k,0}(x,y) & k<n\\ x^nG_{m,0,k-n}(x,Y) & n<k<m+n\end{cases} \tag{A5}$$

and

$$G_{m,n,0}(x,y)=-\frac{S_{2+m+n}[(x^2+y^2)^{1/2}]y^{m-1}x^{n+1}}{(1+n)[(x^2+y^2)^{1/2}]^{m+n}}+\frac{(m-1)G_{m-2,n+2,0}(x,y)-xG_{m,n-1,0}(x,y)}{1+n} \tag{A6}$$

when $m>1$ and $n>1$ and

$$G_{m,0,k}(x,y)=-\frac{S_{3+m-k}[(x^2+y^2)^{1/2}]xy^{m-1}}{[(x^2+y^2)^{1/2}]^{m-k+1}}+(k-2)G_{m,0,k-1}(x,y)+(m-1)x^2G_{m-2,0,k-3}(x,y) \tag{A7}$$

when $k>2$.

Based on the foregoing relations, it is apparent that the determination of $G_{m,n,k}(x,y)$ requires only the numerical evaluation of $G_{m,0,0}(x,y)$, $G_{0,n,0}(x,y)$, $G_{m,0,1}(x,y)$ and $G_{m,0,2}(x,y)$. In the Nth approximation, the value of m and n required for the evaluation of various coefficients in equations (19), (25), and (26) ranges between 0 and $2N+1$. At each allocation point, each integral is required to be evaluated 4 times (for both η^+, η^-, and ζ^+, ζ^-). For $(2N+1)(N+1)$ allocation points, a total of $16(2N+2)(2N+1)(N+1)$ single integrations are thus required for the Nth order solution. A Hottel zonal calculation utilizing $(2N+1)(N+1)$ zones, on the other hand, would require a total of $(2N+1)(N+1)[(2N+1)(N+1)+1]/2$ double integrations.

A Limiting Approach for the Evaluation of Geometric Mean Transmittance in a Multidimensional Absorbing and Isotropically Scattering Medium

W. W. Yuen
Associate Professor,
Department of Mechanical and Environmental Engineering,
University of California,
Santa Barbara, Calif. 93106
Assoc. Mem. ASME

The calculation of the geometric-mean transmittance factor between areas with an intervening absorbing and isotropically scattering medium is considered. While an exact expression for the factor is shown to be quite complicated, the upper and lower limits of the factor can be readily generated from physical consideration. Integral expressions for successively increasing (decreasing) values of the lower (upper) limits are obtained. For two-dimensional systems, these expressions are reduced to integrals involving $S_n(x)$, a class of exponential integral function that has been tabulated in a previous work. Utilizing the kernel substitution technique, these integrals are evaluated analytically in closed form for some selected geometries. For cases with small optical thickness and large scattering albedo, both limits are shown to converge relatively slowly to the actual transmittance factor. But the decreasing difference between the two limits provides accurate estimate of the geometric-mean transmittance factor. Based on these results, some interesting conclusions concerning the effect of scattering on multidimensional radiative transmission are established.

1 Introduction

The importance of scattering in the analysis of radiative heat transfer in many practical combustion systems is well known [1]. In recent years, significant work has been reported in determining the scattering effect on various radiating systems with simple geometries [2-5].

For practical application, one of the important radiation parameters is the geometric-mean transmittance factor between two arbitrary surfaces. For an intervening medium that is nonparticipating or purely absorbing, the mathematical formulation and method of evaluation for such factors are well known [6, 7]. For an intervening absorbing and scattering medium, however, the amount of reported work is scarce. In their book [6], Hottel and Sarofim estimated the upper and lower limits of the transmisivity and reflectivity of a one-dimensional isotropically scattering slab. In a recent work [8], the present author developed simple analytical expressions for the first approximation of the upper and lower limits of the geometrical-mean transmittance for three selected geometries. These two works, to the best of the present author's knowledge, appear to be the only reported efforts attempting to deal with this difficult problems.

The objective of the present work is to show that by utilizing some simple physical reasoning, the mathematical development presented in [8] can be generalized to yield successively improved estimates of the upper and lower limits of the geometric-mean transmittance factor. Rates of convergence of the two limiting expressions toward the exact value of the transmittance factor are shown to be quite slow for cases with small optical thickness and large scattering albedo. If considered separately, each limiting expression thus has uncertain accuracy in determining the exact transmittance factor. But considered together, the decreasing difference between the two expressions can be used to yield successively improved approximate values for the transmittance factor and the associated uncertainty. These results are used to assess the effect of scattering on radiative transmission in simple systems. At certain optical thicknesses and scattering albedos, the scattering contribution to the total geometric-mean transmittance factor is shown to be very significant.

2 Analysis

(a) General Formulation. For two arbitary infinitesimal area dA_0 and dA, the energy transfer by radiation from dA_0 to dA can be written as

$$dQ_{d0-dA} = q_{o,0} dA_0 dF_{d0-dA} (\tau_{d0-dA} + \tau^s_{d0-dA}) \tag{1}$$

where $q_{o,0}$ is the radiative heat flux leaving surface dA_0, dF_{d0-dA} is the shape factor between dA_0 and dA, τ_{d0-dA} is the geometric-mean transmittance between dA_0 and dA calculated only along the line of sight between the two areas, and τ^s_{d0-dA} is the added fraction of energy transfer due to the effect of scattering from elements away from the line of sight. The expression of τ_{d0-dA} can be readily obtained from standard reference [6].

In reference [8], first-order approximation for the upper and lower limits of τ^s_{d0-da} were generated by considering radiative transfer between dA_0 and dA via scattering from a single volume element. Indeed, utilizing a coordinate system as shown in Fig. 1, these limiting expressions are shown to be

$$dF_{d0-dA}[\tau^s_{d0-dA}]^1_u = \frac{\sigma}{\pi} \int\int\int \frac{z_1 e^{-EL_1}}{L_1^3} dx_1 dy_1 dz_1 \tag{2}$$

$$dF_{d0-dA}[\tau^s_{d0-dA}]^1_l = \frac{\sigma}{4\pi^2} dA \int\int\int \frac{z_1 (\mathbf{n}\cdot\mathbf{r}_{1A}) e^{-EL_1 - Er_{1A}}}{L_1 r_{1A}^3} dx_1 dy_1 dz_1 \tag{3}$$

Contributed by the Heat Transfer Division and presented at the ASME-JSME Joint Thermal Engineering Conference, Honolulu, Hawaii, March 1983. Manuscript received by the Heat Transfer Division January 28, 1983.

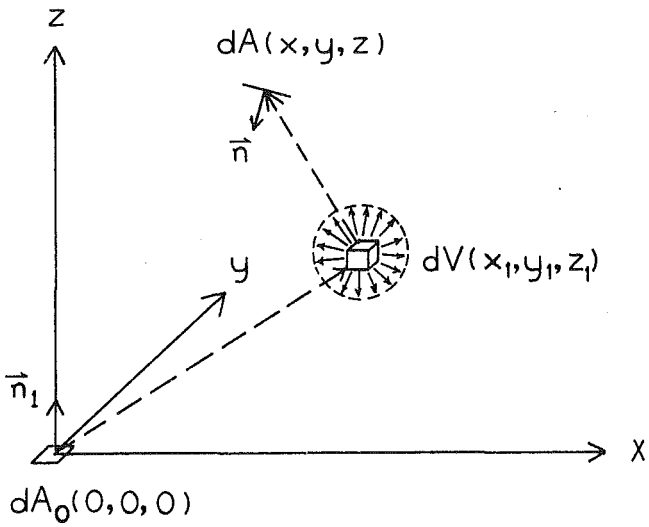

Fig. 1 Coordinate system and geometry for the calculation of the first-order approximation of the geometric-mean transmittance

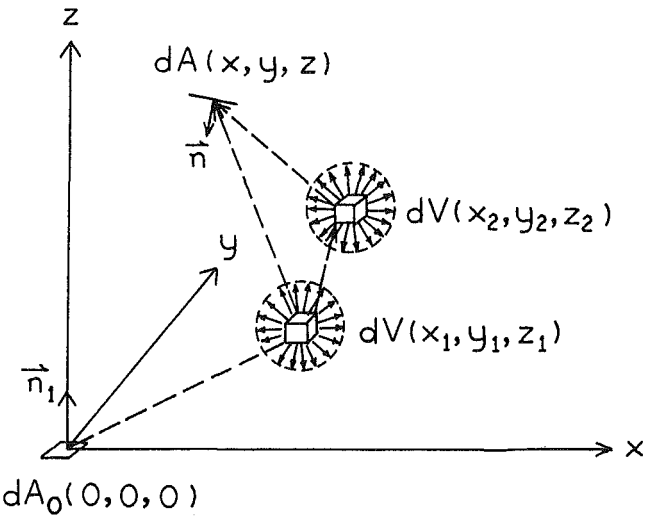

Fig. 2 Coordinate system and geometry for the calculation of the second-order approximation of the geometric-mean transmittance

where

$$E = a + \sigma \tag{4}$$

$$L_1 = (x_1^2 + y_1^2 + z_1^2)^{1/2} \tag{5}$$

and

$$\mathbf{r}_{1A} = (x_1 - x)\hat{i} + (y_1 - y)\hat{j} + (z_1 - z)\hat{k} \tag{6}$$

In the foregoing expressions, dA_0 is assumed to be a diffuse surface; a and σ are the absorption and scattering coefficients of the medium; $\hat{i}$, $\hat{j}$, and $\hat{k}$, unit vectors in the x- y- and z-direction; $\mathbf{n}$, the unit normal to the surface dA; and r_{1A}, the magnetude of the vector $\mathbf{r}_{1A}$. Physically, equation (2) is generated by assuming that all energy scattered by the volume $dx_1 dy_1 dz_1$ will be absorbed by dA. It is clearly the upper limit of τ^s_{d0-dA}. Equation (3), on the other hand, assumes that only the energy scattered from the volume $dx_1 dy_1 dz_1$ in the direction of dA will be absorbed by dA. Since there are always secondary scatterings, equation (3) clearly gives the lower limit of τ^s_{d0-dA}. The limits of integration for equations (2) and (3) generally remain unspecified until the geometry of the scattering medium surrounding dA_0 and dA is defined.

Improved estimates for the upper and lower limits of τ^s_{d0-dA} can be generated by considering physically the added energy transfer between dA_0 and dA due to scattering by multiple volume elements. For example, consider the effect of scattering from two volume elements as shown in Fig. 2. The second-order approximations of the lower and upper limits of τ^s_{d0-dA} can be readily written as

$$dF_{d0-dA}[\tau^s_{d0-dA}]^2_u = dF_{d0-dA}[\tau^s_{d0-dA}]^1_l + G^2_u \tag{7}$$

$$dF_{d0-dA}[\tau^s_{d0-dA}]^2_l = dF_{d0-dA}[\tau^s_{d0-dA}]^1_l + G^2_l \tag{8}$$

where

$$G^2_u = \frac{\sigma^2}{4\pi^2}$$

$$\int \cdots \int \frac{z_1 e^{-E(L_1 + r_{12})}}{L_1^3 r_{12}^2}\, dx_1 dy_1 dz_1 dx_2 dy_2 dz_2 \tag{9}$$

and

$$G^2_l = \frac{\sigma^2}{16\pi^3}\, dA$$

$$\int \cdots \int \frac{z_1(\mathbf{n}\cdot\mathbf{r}_{2A})\, e^{-E(L_1 + r_{12} + r_{2A})}}{L_1^3 r^2_{12} r^3_{2A}}\, dx_1 dy_1 dz_1 dx_2 dy_2 dz_2 \tag{10}$$

Nomenclature

a = absorption coefficient
A = area
dF = shape factor between differential areas
E = extinction coefficient
F = shape factor
G = functions defined by equations (15), (16), (24) and (25)
$\hat{i}$ = unit vector in x-direction
$\hat{j}$ = unit vector in y-direction
$\hat{k}$ = unit vector in z-direction
l = component of normal vector $\mathbf{n}$ in the x-direction
L_1 = length defined by equation (5)
L_i = length defined by equation (17)
M_1 = length defined by equation (22)
M_i = length defined by equation (26)
M_{1A} = length defined by equation (23)
M_{nA} = length defined by equation (27)
n = component of normal vector $\mathbf{n}$ in the z-direction
$\mathbf{n}$ = unit normal to area A
q_o = outgoing radiosity
Q = energy transfer, equation (1)
$\mathbf{r}_{nA}$ = vector directed from element dA_n to dA
$S_n(x)$ = experimental integral function
U_n = functions defined by equations (32) and (52)
V_n = functions defined by equations (33) and (53)
W^m_n = functions defined by equations (36), (43) and (56)
x = coordinate
y = coordinate
z = coordinate
σ = scattering coefficent
τ = geometric transmittance factor

Subscripts

0 = parameter associated with area $\mathbf{dA}_0$
$d0-dA$ = between area dA_0 and dA
i = coordinates of the ith scattering element
l = lower limit
u = upper limit

Superscripts

n = order of approximation
s = scattering contribution

In the above equations, r_{12} and the vector $\mathbf{r}_{2A}$ are given by

$$r_{12} = [(x_1 - x_2)^2 + (y_1 - y_2)^2 + (z_1 - z_2)^2]^{1/2} \quad (11)$$

$$\mathbf{r}_{2A} = (x_2 - x)\hat{i} + (y_2 - y)\hat{j} + (z_2 - z)\hat{k} \quad (12)$$

Physically, G_u^2 represents the radiative energy that is scattered in all direction after scattering by two arbitrary volume elements. It is clearly the maximum amount of energy which can be scattered twice and intercepted by dA. G_l^2, on the other hand, represents the radiative energy that is scattered in the direction of and intercepted by dA after two scatterings. It is a minimum since energies that are scattered more than twice and intercepted by dA are not included in the consideration.

The foregoing mathematical consideration can be readily generalized to yield successively higher-order approximations of the two limits. Using the same physical arugment, it can be readily shown that the nth approximations for the two limits can be written in terms of the (n-1)th approximation by

$$dF_{d0-dA}[\tau^s_{d0-dA}]^n_u = dF_{d0-dA}[\tau^s_{d0-dA}]^{n-1}_l + G^n_u \quad (13)$$

$$dF_{d0-dA}[\tau^s_{d0-dA}]^n_l = dF_{d0-dA}[\tau^s_{d0-dA}]^{n-1}_l + G^n_l \quad (14)$$

where

$$G^n_u = \left(\frac{\sigma}{\pi}\right)\left(\frac{\sigma}{4\pi}\right)^{n-1} \int \cdots \int \left(\frac{z_1 e^{-EL_1}}{L_1^3}\right)\left(\prod_{i=2}^{i=n} \frac{e^{-EL_i}}{L_i^2} dx_i dy_i dz_i\right) dx_1 dy_1 dz_1 \quad (15)$$

and

$$G^n_l = \left(\frac{\sigma}{4\pi}\right)^n \frac{dA}{\pi} \int \cdots \int \frac{z_1(\mathbf{n}\cdot\mathbf{r}_{nA})e^{-E(L_1 + r_{nA})}}{L_1^3 r_{nA}^3} \left(\prod_{i=2}^{i=n} \frac{e^{-EL_i} dx_i dy_i dz_i}{L_i^2}\right) dx_1 dy_1 dz_1 \quad (16)$$

In the above expressions, (x_i, y_i, x_i) is the coordinate of the ith scattering volume elements; L_i and $\mathbf{r}_{nA}$ 2are given by

$$L_i = [(x_i - x_{i-1})^2 + (y_i - y_{i-1})^2 + (z_i - z_{i-1})^2]^{1/2} \quad (17)$$

$$\mathbf{r}_{nA} = (x_n - x)\hat{i} + (y_n - y)\hat{j} + (z_n - z)\hat{k} \quad (18)$$

Physically, it is reasonable to expect that in the limit of $n \to \infty$, the upper (lower) limit of the scattering contribution to the geometric mean transmittance decreases (increases) monotonically toward the exact value. Mathematically, however, it can be readily shown that the rate of convergence is quite slow. A single limiting expression is thus ineffective in approximating the exact value. Considering both limiting expressions simultaneously, on the other hand, relatively narrow bound of the exact value can be readily generated even with small values of n.

(*b*) Two-Dimensional Systems. For systems with two-dimensional geometry, the foregoing equations can be simplified. Specifically, consider dA to be an infinite strip of width dS with the unit normal $\mathbf{n}$ given by

$$\mathbf{n} = l\hat{i} + n\hat{k} \quad (19)$$

equations (1), (13), and (14) still remain valid provided dA_0 and dA are interpreted as infinite stripes. Integrals in the y-direction in equations (2), (3), (9), (10), (15), and (16) can be readily evaluated. As shown in [8], the first-order approximation of the upper and lower limits become

$$dF_{d0-dA}(\tau^s_{d0-da})^1_u = \sigma \int \int \frac{z_1 S_2(EM_1)}{M_1^2} dx_1 dz_1 \quad (20)$$

$$dF_{d0-dA}(\tau^s_{d0-dA})^1_l = \frac{\sigma dS}{4} \int \int \frac{z_1[(x_1 - x)l + (z_1 - z)n]S_2(EM_1)S_2(EM_{1A})}{M_1^2 M_{1A}^2} dz_1 dz_1 \quad (21)$$

where

$$M_1 = (x_1^2 + z_1^2)^{1/2} \quad (22)$$

and

$$M_{1A} = [(x_1 - x)^2 + (z_1 - z)^2]^{1/2} \quad (23)$$

Equations (15) and (16) become

$$G^n_u = 4\left(\frac{\sigma}{4}\right)^n \int \cdots \int \frac{z_1 S_2(EM_1)}{M_1^2}\left(\sum_{i=2}^{i=n} \frac{S_1(EM_i)\,dx_1 dz_i}{M_i}\right) dx_1 dz_1 \quad (24)$$

$$G^n_l = \left(\frac{\sigma}{4}\right)^n dS \int \cdots \int \frac{z_1[(x_n - x)l + (z_n - z)n]S_2(EM_1)S_2(EM_{nA})}{M_1^2 M_{nA}^2} \left(\sum_{i=2}^{i=n} \frac{S_1(EM_i)}{M_i} dx_i dz_i\right) dx_1 dz_1 \quad (25)$$

where

$$M_i = [(x_i - x_{i-1})^2 + (z_i - z_{i-1})^2]^{1/2} \quad (26)$$

and

$$M_{nA} = [(x_n - x)^2 + (z_n - z)^2]^{1/2} \quad (27)$$

In the foregoing equations, $S_n(x)$ is the exponential integral function, which has been defined and studied extensively in [8] and [9]. Equations (20), (21), (24), (24), together with equations (13) and (14), thus constitute a complete set of methematical relations, from which the upper and lower limits of τ^s_{d0-dA} can be estimated to an arbitrary order degree of accuracy.

3 Application

In this section, the general mathematical expressions developed in the previous section are applied to three selected geometries to illustrate quantitatively the effect of scattering on the geometric-mean transmittance. The effectiveness of the present approach is also demonstrated. The three cases considered are identical to those studied in [8].

Case 1. In this case, the scattering contribution to the geometric-mean transmittance between dA_0 at the origin and an infinite parallel plane A facing downward toward dA_0 at a given vertical height z is considered. The geometry is shown in Fig. 3(*a*). The scattering medium is the semi-infinite region below the horizontal plane at z. As in [8], all required integrations are simplified by the introduction of the following kernel substitution

$$S_1(x) = e^{-\frac{\pi x}{2}} \quad (28)$$

$$S_2(x) = \left(\frac{2}{\pi}\right)e^{-\frac{4x}{\pi}} \quad (29)$$

The accuracy of equations (28) and (29) is illustrated in the same reference.

Substituting equations (28) and (29) into equations (24) and (25) and integrating over the following limits

$$-\infty < x_i < \infty, \quad i = 1,n$$
$$-\infty < x < \infty$$
$$-\infty < z_i < z, \quad i = 2,n$$
$$0 < z_1 < z$$

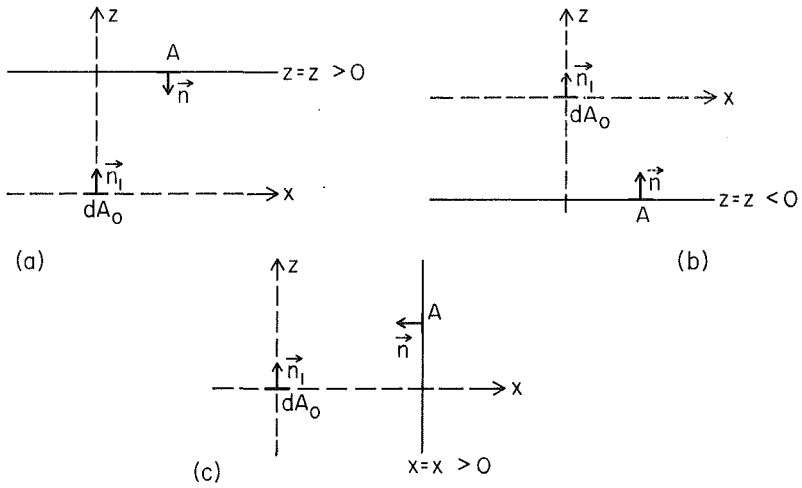

Fig. 3 Geometries of the three specific cases for dA_0 and A considered in the present work

it can be readily shown that G_u^n and G_l^n are readily reduced to

$$G_u^n = 2\sigma\left(\frac{\sigma\pi^2}{8}\right)^{n-1} V_n \tag{30}$$

$$G_l^n = \sigma\left(\frac{\sigma\pi^2}{8}\right)^{n-1} e^{-2Ez} U_n \tag{31}$$

The functions U_n and V_n in the above equations satisfy the following recursive relations

$$U_n = \left[\frac{16}{E(\pi^4-64)}\right]\left[\frac{\pi^2}{2}U_{n-1} - \left(\frac{\pi^2+8}{4}\right)e^{\left(2-\frac{n^2}{4}\right)Ez} W_n^0\right] \tag{32}$$

$$V_n = \left(\frac{4}{\pi^2 E}\right)\left(2V_{n-1} - e^{-\frac{\pi^2}{4}Ez} W_n^0\right) \tag{33}$$

with

$$U_1 = z \tag{34}$$

and

$$V_1 = \left(\frac{1}{2E}\right)(1-e^{-2Ez}) \tag{35}$$

The function W_n^m in the above equations is defined by

$$W_n^m = \int \cdots \int z_{n-1}^m e^{-E\left(2z_1 - \frac{\pi^2}{4}z_{n-1}\right)} \left(\prod_{i=2}^{i=n-1} e^{-\frac{\pi^2}{4}E|z_i - z_{i-1}|} dz_i\right) dz_1 \tag{36}$$

For $n = 2$, the above integral can be readily evaluated to yield

$$W_2^m = e^{\left(\frac{\pi^2}{4}-2\right)Ez} \sum_{r=0}^{r=m} (-1)^r \frac{m! z^{m-r}}{(m-r)!\left[\left(\frac{\pi^2}{4}-2\right)E\right]^{r+1}} - \frac{(-1)^m m!}{\left[\left(\frac{\pi^2}{4}-2\right)E\right]^{m+1}} \tag{37}$$

For $n > 2$, W_n^m can be obtained from the following recursive relation

$$W_n^m = \sum_{r=0}^{r=m} \frac{2(-2)^r m! W_{n-1}^{m-r}}{(m-r)!(\pi^2 E)^{r+1}} + \frac{z^{m+1} W_{n-1}^0 - W_{n-1}^{m+1}}{m+1} \tag{38}$$

From [8], the first-order approximation of the two limits of τ_{d0-A}^s are

$$F_{d0-A}(\tau_{d0-A}^s)\}_u^l = \omega(1-e^{-2Ez}) \tag{39}$$

$$F_{d0-A}(\tau_{d0-A}^s)\}_l^l = \omega Ez e^{-2Ez} \tag{40}$$

with $\omega = \sigma/E$ being the familiar scattering albedo. Based on equations (39) and (40), and the recursive relations defined by equations (13) and (14), and the expressions for G_u^n and G_l^n as expressed in equations (30–38), the upper and lower limits of the scattering contribution to the geometric-mean transmittance can be readily determined for arbitrary values of n.

Case 2. In this case, A is an infinite parallel plane facing upward at a given location $-z$ as shown in Fig. 3(*b*). The scattering medium is the semi-infinite region above the horizontal plane at $-z$. Limits of integration become

$$\begin{aligned} -\infty < x_i < \infty, &\qquad i = 1,n \\ -\infty < x < \infty & \\ -z < z_i < \infty, &\qquad i = 2,n \\ 0 < z_1 < \infty & \end{aligned}$$

Direct integration of equations (24) and (25) shows that the generalized relations represented by equations (30–33) remain valid for this geometry. Equations (34–38), however, are replaced by

$$U_1 = \frac{1}{4E} \tag{41}$$

$$V_1 = \frac{1}{2E} \tag{42}$$

$$W_n^m = \int \cdots \int z_{n-1}^m e^{-E\left(2z_1 + \frac{\pi^2}{4}z_{n-1}\right)} \left(\prod_{i=2}^{i=n-1} e^{-\frac{\pi^2}{4}E|z_i - z_{i-1}|} dz_i\right) dz_1 \tag{43}$$

$$W_2^m = \frac{m!}{\left[E\left(\frac{\pi^2}{4}+2\right)\right]^{m+1}} \tag{44}$$

$$W_n^m = \sum_{r=0}^{r=m} \frac{2^{r+1} m! W_{n-1}^{m-r}}{(m-r)!(\pi^2 E)^{r+1}} + \frac{z^{m+1} W_{n-1}^0 + W_{n-1}^{m+1}}{m+1} \tag{45}$$

Results in reference [8] yield the following expressions for the lower and upper limits of τ_{d0-A}^s

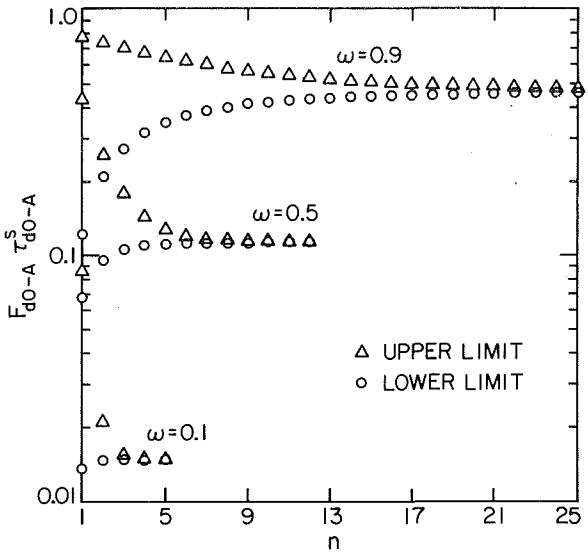

Fig. 4 The convergence behavior of $F_{d0-A}\ \tau^s_{d0-A}$ for case 1 with $Ez = 1.0$

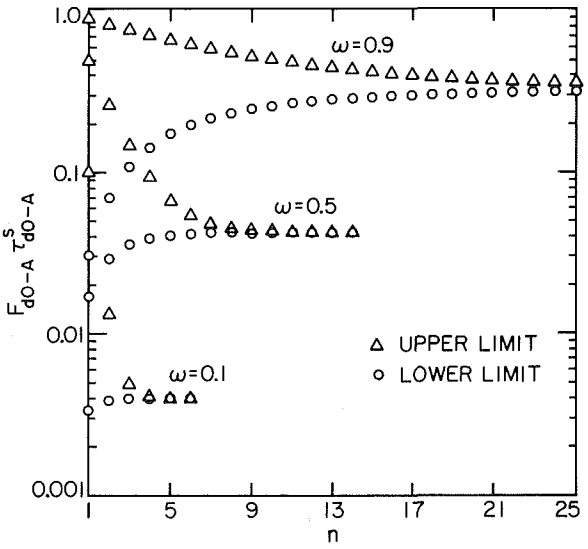

Fig. 5 The convergence behavior of $F_{d0-A}\ \tau^s_{d0-A}$ for case 2 with $Ez = 1.0$

$$F_{d0-A}\,(\tau^s_{d0-A})^1_u = \omega \tag{46}$$

$$F_{d0-A}\,(\tau^s_{d0-A})^1_l = \left(\frac{\omega}{4}\right) e^{-2Ez} \tag{47}$$

Equations (30–33), (41–47), together with equations (13) and (14) can now be used to generate successive approximations for the upper and lower limits of τ^s_{d0-A} for this case.

Case 3. In this case, A is an infinite vertical plane facing the origin at a given location z as shown in Fig. 3(*c*). The scattering medium is the semi-infinite region to the left of the vertical plane at x. Limits of integration for this case become

$$\begin{aligned} &-\infty < x_i < x, \qquad i = 1, n \\ &-\infty < z < \infty \\ &-\infty < z_i < \infty, \qquad i = 2, n \\ &0 < z_1 < \infty \end{aligned}$$

As shown in [8], additional kernel substitutions for the regular exponential functions $E_1(x)$ and $E_2(x)$ are required before integrals as represented by equations (24) and (25) can be evaluated in closed form. These substitutions are

$$E_1(x) = 2e^{-2x} \tag{48}$$

$$E_2(x) = e^{-2x} \tag{49}$$

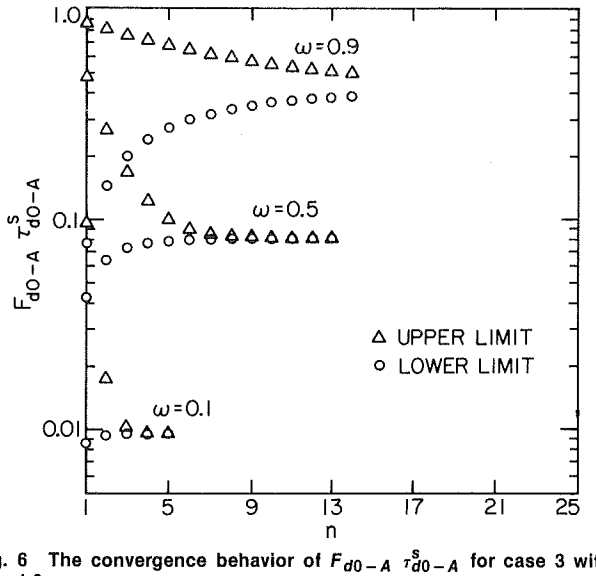

Fig. 6 The convergence behavior of $F_{d0-A}\ \tau^s_{d0-A}$ for case 3 with $Ex = 1.0$

After integrations, a set of equation analogous to equations (30–40) are generated. They are

$$G^n_l = \frac{4\sigma}{\pi}\left(\frac{\sigma\pi^2}{8}\right)^{n-1} V_n \tag{50}$$

$$G^n_l = \frac{2\sigma}{\pi}\left(\frac{\sigma\pi^2}{8}\right)^{n-1} e^{-2Ex} U_n \tag{51}$$

$$U_n = \left[\frac{16}{E(\pi^4 - 64)}\right]\left[\frac{\pi^2}{2} U_{n-1} - \left(\frac{\pi^2+8}{4}\right) e^{\left(2-\frac{\pi^2}{4}\right)Ex} W^0_n\right] \tag{52}$$

$$V_n = \left(\frac{4}{\pi^2 E}\right)\left(2V_{n-1} - e^{-\frac{\pi^2}{4}Ex} W^0_n\right) \tag{53}$$

$$U_1 = \left[\frac{\pi}{2E(\pi-4)}\right]\left(e^{\left(2-\frac{8}{\pi}\right)Ex} - \frac{8}{4+\pi}\right) \tag{54}$$

$$V_1 = \left(\frac{\pi}{4E}\right)\left(1 - \frac{e^{-\frac{8}{\pi}Ex}}{2}\right) \tag{55}$$

$$W^m_n = \int \cdots \int x_1^m e^{\frac{\pi^2}{4}Ex_{n-1}} e^{-\frac{8}{\pi}E|x_1|}\left(\sum_{i=2}^{i=n-1} e^{-\frac{\pi^2}{4}E|x_i - x_{i-1}|} dx_i\right) dx_1 \tag{56}$$

$$W^m_2 = e^{\left(\frac{\pi^2}{4}-\frac{8}{\pi}\right)Ex} \sum_{r=0}^{r=m} (-1)^r \frac{m!\,x^{m-r}}{(m-r)!\left[\left(\frac{\pi^2}{4}-\frac{8}{\pi}\right)E\right]^{r+1}} - (-1)^m m!\left[\frac{1}{\left[\left(\frac{\pi^2}{4}-\frac{8}{\pi}\right)E\right]^{m+1}} - \frac{1}{\left[\left(\frac{\pi^2}{4}+\frac{8}{\pi}\right)E\right]^{m+1}}\right] \tag{57}$$

$$M^m_n = \sum_{r=0}^{r=m} \frac{2(-2)^r m!\, W^{m-r}_{n-1}}{(m-r)!(\pi^2 E)^{r+1}} + \frac{x^{m+1} W^0_{n-1} - W^{m+1}_{n-1}}{m+1} \tag{58}$$

Table 1 Values of the upper and lower limits of $F_{d0-A}\tau^s_{d0-A}$ for case 1 (n is the order of approximation used in generating the presented values)

$Ez(F_{d0-A}\tau_{d0-A})$	ω	n	$F_{d0-A}(\tau^s_{d0-A})_l$	$F_{d0-A}(\tau^s_{d0-A})_u$
0.1(0.8326)	0.1	5	0.8479e-2	0.8479e-2
	0.5	12	0.5062e-1	0.5062e-1
	0.9	25	0.1285	0.1302
0.5(0.4432)	0.1	5	0.1950e-1	0.1950e-1
	0.5	13	0.1304	0.1304
	0.9	25	0.4035	0.4122
1.0(0.2194)	0.1	5	0.1472e-1	0.1472e-1
	0.5	12	0.1125	0.1126
	0.9	25	0.4518	0.4696
2.0(0.0602)	0.1	5	0.4155e-2	0.4156e-2
	0.5	9	0.4071e-1	0.4075e-1
	0.9	25	0.2890	0.0329

Table 2 Values of the upper and lower limits of $F_{d0-A}\tau^s_{d0-A}$ for case 2 (n is the order of approximation used in generating the presented values: note that $F_{d0-A}\tau_{d0-PA}$ is zero for this case)

Ez	ω	n	$F_{d0-A}(\tau^s_{d0-A})_l$	$F_{d0-A}(\tau^s_{d0-A})_u$
0	0.1	5	0.2648e-1	0.2648e-1
	0.5	11	0.1779	0.1781
	0.9	25	0.5782	0.5955
0.1	0.1	5	0.2192e-1	0.2193e-1
	0.5	12	0.1552	0.1553
	0.9	25	0.5490	0.5682
0.5	0.1	5	0.1025e-1	0.1026e-1
	0.5	13	0.8803e-1	0.8809e-1
	0.9	25	0.4320	0.4585
1.0	0.1	6	0.3928e-2	0.3929e-2
	0.5	14	0.4182e-1	0.4186e-1
	0.9	25	0.3059	0.3407
2.0	0.1	7	0.5647e-3	0.5648e-3
	0.5	17	0.8761e-2	0.8767e-2
	0.9	25	0.1424	0.1911

Table 3 Values of the upper and lower limits of $F_{d0-A}\tau^s_{d0-A}$ for case 1 (n is the order of approximation used in generating the presented values)

$Ex(F_{d0-A}\tau_{d0-A})$	ω	n	$F_{d0-A}(\tau^s_{d0-A})_l$	$F_{d0-A}(\tau^s_{d0-A})_u$
0(0.5000)	0.1	5	0.1478e-1	0.1479e-1
	0.5	11	0.9759e-1	0.9766e-1
	0.9	13	0.2963	0.3333
0.1(0.3480)	0.1	5	0.1749e-1	0.1749e-1
	0.5	11	0.1166	0.1167
	0.9	13	0.3600	0.4059
0.5(0.1409)	0.1	5	0.1660e-1	0.1661e-1
	0.5	12	0.1216	0.1217
	0.9	13	0.4408	0.5231
1.0(0.5822e-1)	0.1	5	0.9447e-2	0.9454e-2
	0.5	13	0.7974e-1	0.7980e-1
	0.9	14	0.3771	0.4558
2.0(0.1203e-1)	0.1	6	0.1948e-2	0.1949e-2
	0.5	15	0.2204e-1	0.2206e-1
	0.9	15	0.1920	0.3368

$$F_{d0-A}(\tau^s_{d0-A})^l_u = \frac{\omega}{2}\left(2 - e^{-\frac{8}{\pi}Ex}\right) \tag{59}$$

$$F_{d0-A}(\tau^s_{d0-A})^l_l = \left(\frac{\omega}{4-\pi}\right)\left(\frac{8e^{-2Ex}}{4+\pi} - e^{-\frac{8}{\pi}}\right) \tag{60}$$

4 Results and Discussion

The rate of convergence of the present approach in determining the actual scattering contribution of the geometric-mean transmittance is illustrated for the three cases in Figs. 4, 5, and 6. Since G^n_u and G^n_l are both proportional to σ^n (and consequently to ω^n) as shown in equations (50) and (51), the upper and lower limits of the geometric mean transmittance is a polynominal in ω of order n at the nth approximation. Cases with small scattering albedo thus converge relatively quickly. The general behavior of the numerical results for different optical thickness is similar to those presented in these figures. The rate of convergence general decreases with increasing optical thickness. For cases 1 and 2, evaluations of the two limits are carried out only up to $n = 25$. At $n > 25$, numerical results show that the difference between successive approximations is smaller than the accuracy of the computer. The higher-order results for these two cases are thus meaningless. For case 3, the two limiting solutions begin to oscillate as n becomes large. This behavior

is probably due to the error of the kernel substitution. The computation is thus stopped at the lowest value of n beyond which this oscillation occurs.

In spite of the foregoing limitations, the present results show clearly that the effect of scattering is extremely important and cannot be ignored in any realistic engineering calculation involving radiative transfer. The best estimates of the two limits of the scattering contribution to the geometric mean transmittance for the three cases are presented in Tables 1, 2, and 3. Geometric mean transmittances without the scattering contribution are presented in these same Tables for comparison. In all three cases, it can be readily observed that for cases with intermediate or large scattering albedo ($\omega > 0.5$), scattering is the major contribution to the geometric transmittance. Neglecting scattering in these cases can lead to errors ranging from 6 percent ($\omega = 0.5$, $Ez = 0.1$ in case 1) to 1000 percent ($\omega = 0.9$, $Ex = 2.0$ in case 3). In case 2, in fact, scattering represents the only contribution to the geometric transmittance function. The effect of scattering also appears to be most dominant for cases withn intermediate optical thickness.

Finally, it is interesting to observe that the geometry in case 2, with $Ez = 0$, can be considered as an approximation of a burning fuel bed. Results in Table 2 show that the amount of radiation reabsorbed by a fuel bed enclosed by a scattering medium (such as the flame) can be as high as 60 percent. Because of the presence of soot and other products of incomplete combustion, the scattering albedo for most combusting media is not small. The present results clearly demonstrate that any energy balance calculations for such fuel beds without including the effect of scattering can be in substantial error.

5 Conclusion

An approach is developed to evaluate the upper and lower limits of the geometric mean transmittance between surfaces with an intervening absorbing and scattering medium. Explicit analytical expressions are generated for three systems with two-dimensional geometry. Results show that for such systems, the effect of scattering is extremely important and in some cases constitutes the dominant effect in radiative transfer. An interesting result concerning the reabsorption by a burning fuel bed is also generated.

Acknowledgment

This paper is based upon work supported by the National Science Foundation, Grant No. MEA80-24824.

References

1 de Ris, J., "Fire Radiation, A Review," *The Seventeen Symposium (International) on Cumbustion*, The Combustion Institute, 1978, pp. 1003-1016.

2 Crosbie, A. L., and Linsenbardt, T. L., "Two-Dimensional Isotropic Scattering in a Semi-Infinite Medium," *Journal of Quantitative Spectroscopy and Radiative Transfer*, Vol. 19, 1978, pp. 257-284.

3 Dolin, L. S., "Propagation of a Narrow Beam of Light in a Medium With Strongly Anisotropic Scattering," *Soviet Radiophysics*, Vol. 9, 1966, pp. 40-47.

4 Lee, H., and Buckius, R. O., "Scaling Anisotropic Scattering in Radiation Heat Transfer for a Planar Medium," ASME JOURAL OF HEAT TRANSFER, Vol. 104, 1982, pp. 68-75.

5 Goswami, D. Y., and Vachou, R. I., "Radiative Heat Transfer Analysis Using an Effective Absorptivity for Absorption, Emission, and Scattering," *International Journal of Heat and Mass Transfer*, Vol. 20, 1977, pp. 1233-1239.

6 Hottel, H. C., and Sarofim, A., F., *Radiative Transfer*, McGraw Hill, New York, 1967.

7 Yuen, W. W., "A Simplified Approach to the Evaluation of Geometric-Mean Transmittance and Absorption for Gas Enclosure," ASME JOURNAL OF HEAT TRANSFER, Vol. 102, 1981, pp. 88-813.

8 Yuen, W. W., "Evalaution of Geometric-Mean Transmittance Factor in Multidimensional Absorbing and Isotropically-Scattering Media," *Proceeding of The 1983 ASME/JSME Thermal Engineering Joint Conference*, Vol. 4, 1983, pp. 27-32.

9 Yuen, W. W., and Wong, L. W., "Numerical Computation of an Important Integral Function in Two-Dimensional Radiative Transfer," *The Journal of Quantitative Spectroscopy and Radiative Transfer*, Vol. 29, No. 2, 1983, pp. 145-149.

Two-Dimensional, Combined-Mode Heat Transfer by Conduction, Convection, and Radiation in Emitting, Absorbing, and Scattering Media-Solution by Finite Elements

T. J. Chung
Professor.
Mem. ASME

J. Y. Kim
Graduate Research Assistant.

Department of Mechanical Engineering,
The University of Alabama in Huntsville
Huntsville, Ala. 35899

This paper is concerned with a two-dimensional analysis of combined mode heat transfer using finite elements. Conduction, convection, and radiation are coupled in the emitting, absorbing, and scattering medium. The standard Galerkin finite elements can be used if the product of Reynolds number and Prandtl number is equal to or less than 1000. It is shown that the two-dimensional heat flux integration can be efficiently performed via Gaussian quadrature applied to isoparametric finite elements where no limitations to optical thicknesses are imposed. Numerical results are demonstrated for a diverging or converging channel. It is observed that the radiation effect on the temperature profile is more significant in the diverging than in the converging channel. Effects of Reynolds number, Prandtl number, albedo, and optical thickness upon temperature distributions are also investigated.

1 Introduction

Energy transfer in absorbing, emitting, and scattering media is an important consideration in rocket propulsion, plasma generators for nuclear fusion, ablating systems, hypersonic shock layers, nuclear explosions, etc. Equations governing such energy transfer may represent a combining mode heat transfer by conduction, convection, and radiation.

The radiative heat transfer problems with one-dimensional radiative heat flux have been solved and well documented in the literature [1, 2]. In recent years, solutions by finite elements have also been reported [3-5]. The purpose of the present paper is to compute the radiation function in terms of surface and volume integrals through arbitrary optical coordinates. In this approach, no limitations on optical thickness are imposed. Numerical solutions of the governing equations are implemented through the Galerkin finite elements. It is shown that use of isoparametric elements facilitate numerical integration via Gaussian quadrature, unlimited by optical depths of the participating media.

Example problems to demonstrate efficiency of the solution procedure include two-dimensional diverging and converging channels. Effects of combined mode (conduction-convection-radiation), albedo, optical thicknesses, etc., are investigated.

In the present investigation, relatively small Reynolds numbers are used ($RePr \leq 1000$). For high Reynolds numbers, however, accuracy may deteriorate due to ill-conditioning of convective terms, and a special technique such as optimal control penalty finite elements would be required. Discussion of such cases will be the subject of the subsequent paper.

2 Governing Equations

In general, it is convenient to have the energy equation in terms of the fluid temperature and heat capacity rather than internal energy. It is also assumed that the radiant energy and the radiation stresses are much smaller than the corresponding molecular quantities and can therefore be neglected even at very high temperatures. Thus, if the radiating fluid is an ideal gas, we have, for a steady state

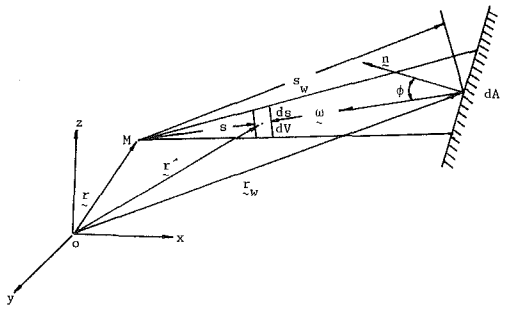

Fig. 1 Radiation contribution of a surface element, *dA*, and a volume element, dV, to a point M in a direction ω

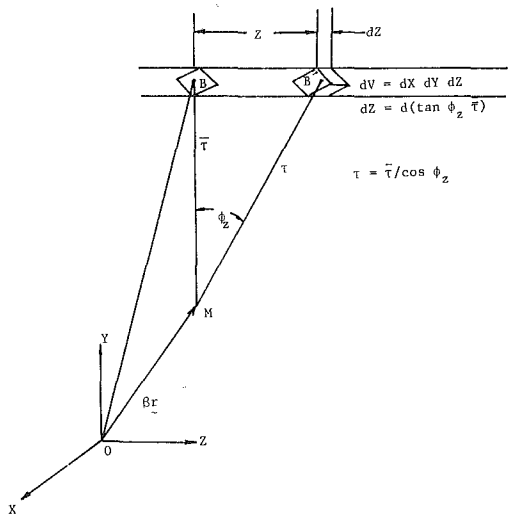

Fig. 2 Geometry for volume integral

Contributed by the Heat Transfer Division for publication in the JOURNAL OF HEAT TRANSFER. Manuscript received by the Heat Transfer Division January 13, 1983.

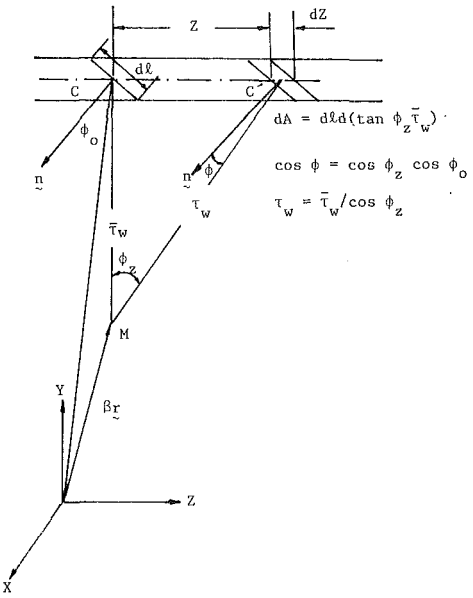

Fig. 3 Geometry for surface integral

$$\rho c_p \frac{\partial T}{\partial x_i} u_i - k \frac{\partial^2 T}{\partial x_i \partial x_i} + \frac{\partial q_i^R}{\partial x_i} = 0 \tag{1}$$

Consider a spectral optical volume, V_λ, and a spectral surface area, A_λ, as defined in [6]

$$dV_\lambda = \tau_\lambda^2 d\tau_\lambda d\omega \tag{2a}$$

$$dA_\lambda = \tau_\lambda^2 d\omega / \cos\phi \tag{2b}$$

where ϕ is the angle between the normal vector to the surface and the direction ω as shown in Fig. 1. Note that V_λ and A_λ are the functions of the spectral optical length, τ_λ measured from the point M at $\mathbf{r}$ in the direction ω. Expressing the spectral optical space defined in equations (2*a*,*b*) we have

$$q_{\lambda i}^R(\mathbf{r}) = \int_{A_\lambda} I_\lambda(\mathbf{r}_w) \frac{e^{-\tau_{\lambda w}}}{\tau_{\lambda w}'^2} l_i \cos\phi dA_\lambda + \int_{V_\lambda} S_\lambda(\mathbf{r}') \frac{e^{-\tau_\lambda'}}{\tau_\lambda'^2} l_i dV_\lambda \tag{3}$$

$$q_{\lambda i,i}^R(\mathbf{r}) = 4\eta a_\lambda(\mathbf{r}) B_\lambda(r)$$

$$- a_\lambda(\mathbf{r}) \int_{A_\lambda} I_\lambda(\mathbf{r}_w) \frac{c^{-\tau_{\lambda w}}}{\tau_{\lambda w}^2} \cos\phi dA_\lambda - a_\lambda \int_{V_\lambda} S_\lambda(\mathbf{r}') \frac{e^{-\tau_\lambda'}}{\tau_\lambda'^2} dV_\lambda \tag{4}$$

For a gray medium with gray bounding surfaces, it can be shown that

$$q_i^R(\mathbf{r}) = \int_A \frac{\sigma T_w^4}{\pi} \frac{e^{-\tau_w}}{\tau^2} l_i \cos\phi dA + \int_V S(\mathbf{r}') \frac{e^{-\tau'}}{\tau'^2} l_i dV \tag{5}$$

and

$$\frac{\partial q^R(r)}{\partial x_i} = 4\beta\left(1 - \frac{\gamma}{\beta}\right)\left(\sigma T^4(\mathbf{r}) - \frac{1}{4}\bar{H}\right) \tag{6}$$

where T_w represents the surface temperature and $\bar{H}$ is an integral defined by

$$\bar{H} = \int_A \frac{\sigma T_w^4}{\pi} \frac{e^{-\tau_w}}{\tau_w^2} \cos\phi dA + \int_V S(r') \frac{e^{-\tau'}}{\tau'^2} dV \tag{7}$$

with

$$S(\mathbf{r}') = \left(1 - \frac{\gamma}{\beta}\right) \frac{\sigma T^4}{\pi} + \frac{\omega_0}{4\pi} \bar{H} \tag{8}$$

Assume that all the radiative physical properties (i.e., β, a, and γ) are constant throughout the flow domain and define dimensionless quantities

$$V_i = u_i / U_o \ , \ \theta = T/T_o$$

$$X_i = \beta x_i \ , \ \tau_0 = \beta L$$

where U_o, T_o, and L are, respectively, the reference velocity, temperature, and length. Then the energy equation can be written in dimensionless forms as

$$\frac{\partial^2 \theta}{\partial X_i \partial X_i} - \frac{\mathrm{RePr}}{\tau_o} V_i \frac{\partial \theta}{\partial X_i} - \frac{1 - \omega_o}{N}\left(\theta^4 - \frac{1}{4\pi} H\right) = 0 \tag{9}$$

Here H is the radiation function given by

$$H = \int_V \eta_s \frac{e^{-\tau}}{\tau^2} dV + \int_A \theta_w^4 \frac{e^{-\tau_w}}{\tau_w^2} \cos\phi dA \tag{10}$$

where η_s is the dimensionless source function defined by $\eta_s = \pi S / \sigma T_o^4$. that is

$$\eta_s(\mathbf{r}) = (1 - \omega_o)\theta^4 + \frac{\omega_o}{4\pi} H \tag{11}$$

To determine H, let us now consider an optical volume element, dV, centered at B', as shown in Fig. 2, in which all distances are measured by the optical coordinates X, Y, and Z. Let ϕ_z be the angle at which the point, M, sees the volume element, dV, with respect to a point B at $Z = 0$, and let $\bar{\tau}$ and τ be the optical distances of $\overline{\mathrm{MB}}$ and $\overline{\mathrm{MB}}'$, respectively. The volume integral of H is then evaluated as follows

$$\begin{aligned} \int_V \eta_s \frac{e^{-\tau}}{\tau^2} dV &= \iiint_{-\infty}^{\infty} \eta_s(B) \frac{e^{-\tau}}{\tau^2} dZ\, dXdY \\ &= \iiint_{-\pi/2}^{\pi/2} \eta_s(B) \frac{e^{-\tau/\cos\phi_z}}{(\bar{\tau}/\cos\phi_z)^2} d(\tan\phi_z \bar{\tau}) dXdY \\ &= \iint \eta_s F_v(\bar{\tau}) dXdY \end{aligned} \tag{12}$$

Nomenclature

A_λ = spectral surface
a = absorption coefficient
B = radiosity
c_p = specific heat at constant pressure
H = radiation function
I_λ = intensity of radiation
k = thermal conductivity
N = dimensionless parameter, $a\beta/4\sigma T^3$
Pr = Prandtl number, $c_p \mu / k$
Re = $\rho U_o L/\mu$ = Reynolds number
q_R = radiation heat flux
S = source function
T = absolute temperature
u = velocity in x-direction
u_m = mean or bulk velocity in x-direction
V_λ = spectral volume
β = extinction coefficient
γ = scattering coefficient
ϵ = emissivity of a surface
ϕ_α = finite element interpolation function
ρ = density
λ = wavelength, or penalty constant
σ = Stefan-Boltzmann constant
τ = optical depth
θ = dimensionless temperature
ω = solid angle
ω_o = γ/β, albedo for single scattering
η = dimensionless source function

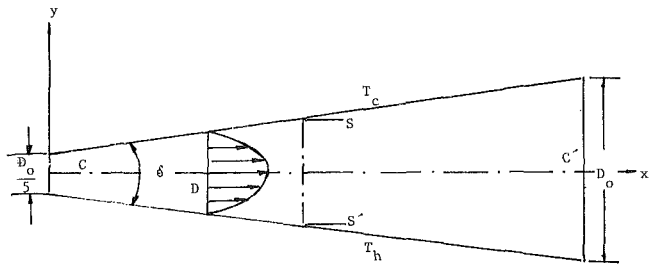

Fig. 4 Geometry of two-dimensional radiation problem

where B is a point in the two-dimensional domain of the X- and Y-coordinates, and $F_v(\bar{\tau})$ is a geometric function of the optical distance, $\bar{\tau}$, measured from the point, M, involved in the volume integral,

$$F_v(\bar{\tau}) = 2\int_0^{\pi/2} \frac{e^{-\bar{\tau}/\cos\phi_z}}{\bar{\tau}}\, d\phi_z \tag{13}$$

To determine the surface integral of H, we consider a surface element $dA = dldZ$, in which dl is a boundary segment of the two-dimensional domain (Fig. 3). Let ϕ be the angle between the normal vectors to the surface element centered at C' and the line $\overline{MC}'$. Also let ϕ_o be the angle at $Z=0$.

Noting $\cos\phi = \cos\phi_z \cos\phi_o$ where ϕ_z is the angle between $\overline{MC}$ and $\overline{MC}'$, it follows that

$$\int_A^{\theta_w^4} \frac{e^{-\tau_w}}{\tau_w^2}\cos\phi dA$$

$$= \int\int_{\frac{\pi}{2}}^{\frac{\pi}{2}} \theta_w^4 \frac{e^{-\bar{\tau}_w/\cos\phi_z}}{(\bar{\tau}_w/\cos\phi_z)}\cos\phi_z\, \cos\phi_o d(\tan\phi_z \bar{\tau}_w) dl \tag{14}$$

Thus, the integral, H, at the point, M, at $\mathbf{r}$ in the domain can be evaluated with η_s solved simultaneously by means of equation (11).

3 Galerkin Finite Elements

Using Galerkin finite elements to solve problems such as equation (9, 10) are well known [7]. We consider that the temperature, θ, and radiation function, H, are approximated as

$$\theta = \Phi_\alpha \theta_\alpha \tag{15a}$$

$$H = \Phi_\alpha H_\alpha \tag{15b}$$

where Ψ_α denotes the four-node isoparametric interpolation function, with α representing the global nodes. Substituting equation (15) into equation (9) and equation (10), we arrive at the Galerkin finite element equations in the form

$$A_{\alpha\beta}\theta_\beta + B_{\alpha\beta}\theta_\beta + C_{\alpha\beta}H_\beta = F_\alpha + G_\alpha \tag{16a}$$

$$D_{\alpha\beta}H_\beta = L_\alpha + M_\alpha \tag{16b}$$

where

$$A_{\alpha\beta} = \int_\Omega \frac{\partial\Phi_\alpha}{\partial X_i}\frac{\partial\Phi_\beta}{\partial X_i} d\Omega$$

$$B_{\alpha\beta} = \frac{\mathrm{RePr}}{\tau_o}\int_\Omega V_i \Phi_\alpha \frac{\partial\Phi_\beta}{\partial X_i} d\Omega$$

$$C_{\alpha\beta} = \frac{1-\omega_o}{4\pi N}\int_\Omega \Phi_\alpha\Phi_\beta d\Omega$$

$$F_\alpha = \int_\Gamma \frac{\partial\theta}{\partial X_i} n_i \overset{*}{\Phi}_\alpha d\Gamma$$

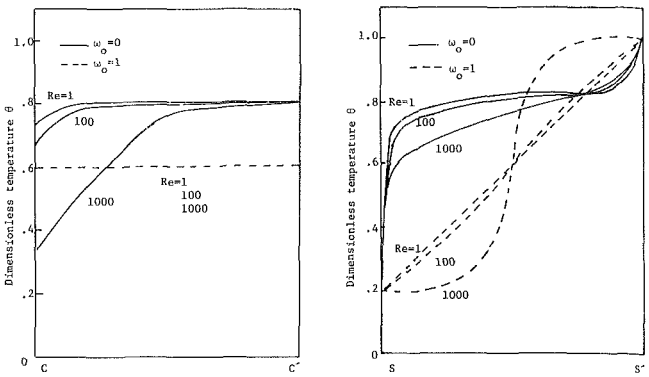

Fig. 5 Effects of Reynolds number on the temperature profiles along $\overline{CC}'$ and $\overline{SS}'$, $\tau_o = 1.0$, $N = 0.001$, Pr = 1.0

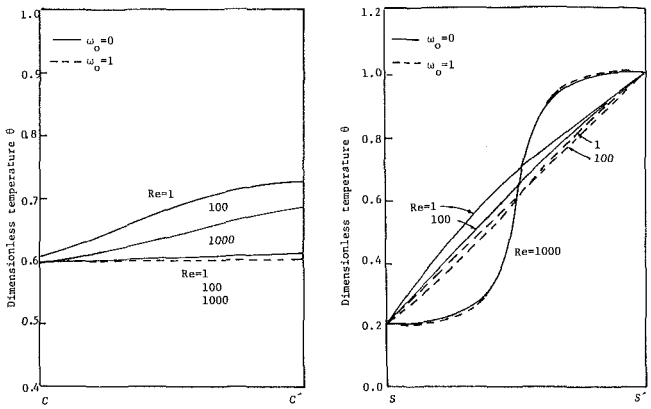

Fig. 6 Effects of Reynolds number on the temperature profiles along $\overline{CC}'$ and $\overline{SS}'$, $\tau_o = 0.1$, $N = 0.001$, Pr = 1

$$G_\alpha = \frac{1-\omega_o}{N}\left[\int_\Omega \Phi_\alpha\Phi_\beta d\Omega\right]\theta_\beta^4$$

$$D_{\alpha\beta} = \int_\Omega \Phi_\alpha\Phi_\beta d\Omega$$

$$L_\alpha = -\int_\Omega\left[\int_V \eta_s \frac{e^{-\tau}}{\tau^2} dV\right]\Phi_\alpha d\Omega$$

$$M = -\int_\Gamma\left[\int_A \theta_w^4 \frac{e^{-\tau_w}}{\tau_w^2}\cos\phi dA\right]\overset{*}{\Phi}_\alpha d\Gamma$$

Here $\overset{*}{\Phi}_\alpha$ represents boundary interpolation functions.

Combining equations (16*a*) and (16*b*), we write the resulting equations in the form

$$K_{ij}X_j = f_i \tag{17}$$

with

$$X_j = \begin{bmatrix} \theta_\alpha \\ H_\alpha \end{bmatrix}$$

The solution of nonlinear equations (17) may best be carried out by the Newton-Raphson technique in the form

$$J_{ij}\Delta X_j^{(n+1)} = -f_i^{(n)} \tag{18}$$

where

$$J_{ij} = \frac{\partial f_i^{(n)}}{\partial X_j}$$

$$\Delta X_j^{(n+1)} = X_j^{(n+1)} - X_j^{(n)} \tag{19}$$

with $f_i^{(n)}$ denoting the ith finite element equation in (17). Note that, in equation (17), an inversion of the Jacobian matrix is

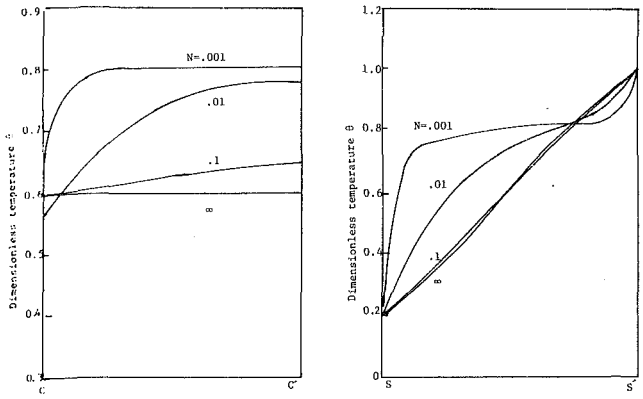

Fig. 7 Effects of N on the temperature profiles along $\overline{CC'}$ and $\overline{SS'}$, $\tau_o = 1.0$, $\omega_o = 0$, RePr = 100

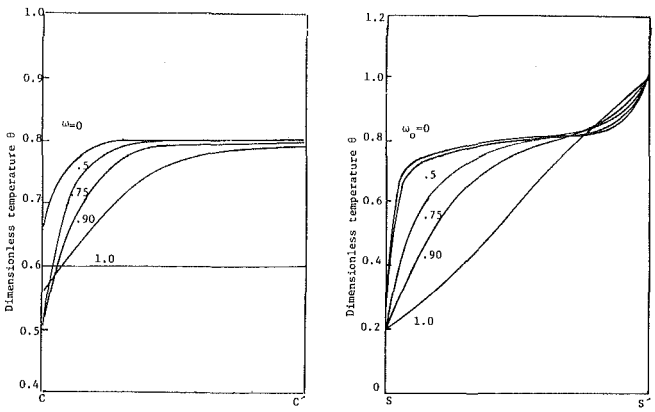

Fig. 9 Effects of albedo, ω_o, on the temperature profiles along $\overline{CC'}$ and $\overline{SS'}$, $\tau_0 = 1.0$, $N = 0.001$, RePr = 100

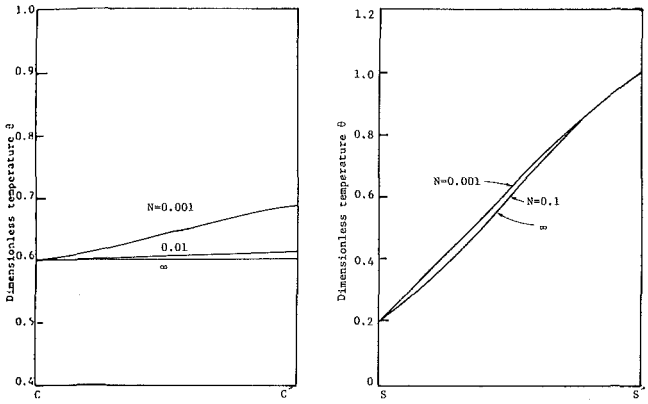

Fig. 8 Effects of N on the temperature profiles along $\overline{CC'}$ and $\overline{SS'}$, $\tau_o = 0.1$, $\omega_o = 0$, RePr = 100

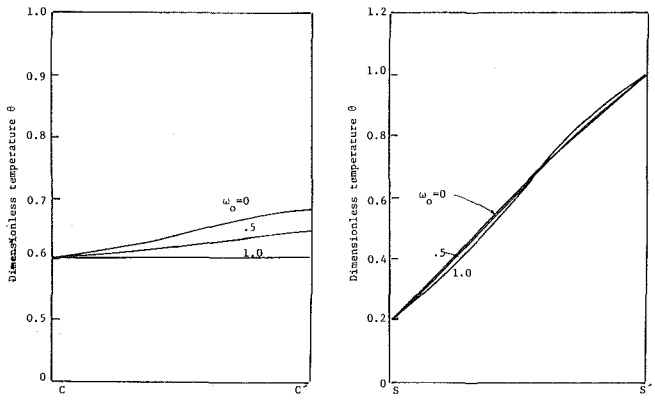

Fig. 10 Effects of albedo, ω_o, on the temperature profiles along $\overline{CC'}$ and $\overline{SS'}$, $\tau_0 = 0.1$, $N = 0.001$, RePr = 100

avoided. The solution involves calculation of $\Delta X_j^{(n+1)}$, and the unknowns $X_j^{(n+1)}$ are then determined from equation (19).

4 Example Problems

Consider a divergent or convergent channel flow through two infinitely wide plates with an angle, δ, having different wall temperatures, as shown in Fig. 4. It is assumed that the velocity profile of the channel flow is fully developed, laminar, and approximately given by

$$u(x,y) = \frac{3}{2} u_m(x)\left[1 - 4\left(\frac{y}{D(x)}\right)^2\right], \quad u_m(x) = \frac{D_o}{D(x)} u_m(x = L)$$

where $u_m(x)$ and $D(x)$ are, respectively, the mean flow velocity and the channel width at a section, and D_o denotes the width at the channel exit. The upper and lower surfaces are also assumed to have uniform temperature T_c and T_h, respectively, and they are assumed to be black for simplicity. Furthermore, the inlet and outlet sections of the channel are assumed to be imaginary porous black surfaces, through which the flowing medium passes without any restrictions. The outlet mean velocity and channel width, D_o, are used as reference velocity and length, respectively, and the lower plate temperature, T_h, is assumed to be the reference temperature.

With the foregoing assumptions, the energy equation (9) and the equation (10) are solved simultaneously using the Galerkin finite elements. The boundary conditions are

$$\theta = \theta_h \text{ on lower surface}$$

$$\theta = \theta_c \text{ on upper surface}$$

where $\theta_h = T_h/T_o$ and $\theta_c = T_c/T_o$. Note also that normal

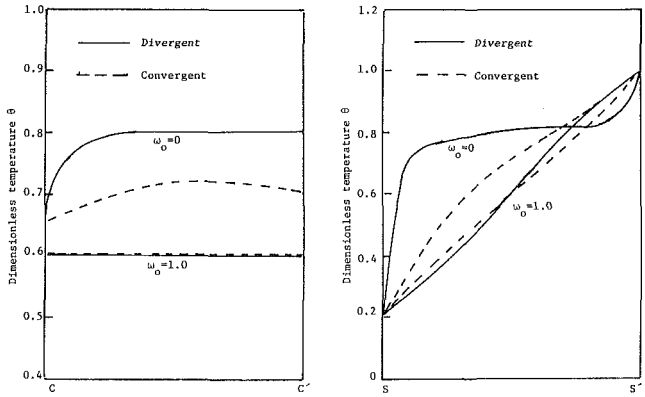

Fig. 11 Comparison of the temperature profiles in divergent and convergent channels, $N = 0.001$, $\tau_0 = 1.0$, RePr = 100

temperature gradients at the entrance and exit boundaries are set equal to zero.

In this example, it is assumed that $\theta_h = 1.0$, $\theta_c = 0.2$, and $\delta = 15$ deg. For given Reynolds and Prandtl numbers, the temperature distributions along the center line $\overline{CC'}$ and the middle section $\overline{SS'}$, are investigated for selected values of conduction-radiation ratio, N, optical thickness, τ_o, and albedo, ω_o.

A total of 72 linear two-dimensional isoparametric elements with 91 nodes are used in this example. An average of 6 iterations for the Newton-Raphson process was required for convergence with 0.1 percent in error.

For the Prandtl number of unity, Figs. 5 and 6 show the

effects of the Reynolds number, Re, and the optical thickness, τ_o, on the temperature profiles for a small $N=0.001$. It is noted that for pure scattering ($\omega_o = 1$), the temperature profile at the center line $\overline{CC'}$ is independent of Re and τ_o, while the profile at the middle section $\overline{SS'}$ is strongly dependent on the Reynolds number but not the optical thickness. If the medium does not scatter but only absorbs radiation ($\omega_o = 0$), the center line temperatures become close to $\theta = 0.8$ for a lower Reynolds number when it is optically thick ($\tau_o = 1.0$). However, they become close to $\theta = 0.6$ for a higher Re when optically thin ($\tau_0 = 0.1$). It is also indicated that the middle section temperature profile becomes closer to a straight line as Re increases for $\tau_0 = 1.0$ (optically thick) and $\omega_o = 0$, whereas the opposite is true in the case of $\omega_o = 1.0$.

On the other hand, if conduction energy transfer dominates over radiation (large N), there are very little effects of τ_o on the temperature profiles for $\omega_o = 0$, as noted in Figs. 7 and 8. Also, the figures indicate that the profiles strongly depend on N if it is optically thick, but the dependence on N is moderate for a small optical depth ($\tau_o = 0.1$). The same trend also appears in Figs. 9 and 10, which show the dependence of the temperature distributions on albedo, ω_o, for a low N. However, for a higher N the profiles converge to those for pure scattering.

It should also be noticed that, for pure scattering the temperature profile at the middle section $\overline{SS'}$ is strongly dependent on the Reynolds number, but along the centerline CC' it remains independent of Reynolds numbers since the temperatures for upper and lower boundaries are kept constant.

The results we have discussed so far are for the case of a divergent channel flow. If the flow is reversed (that is, if it is convergent channel flow), the radiation effect on the temperature profiles is not strong, as indicated in Fig. 11, compared with that in the divergent flow even for a very small N.

6 Conclusions

The finite element solution for the two-dimensional radiation flux combined with convection and conduction has been obtained. The following conclusions are reached:

1 Isoparametric finite elements offer advantage of easy intergration for the two-dimensional radiation function involving the specular volume and specular surface elements through Gaussian quadrature.

2 For the diverging channel, for pure scattering, the temperature profile at the center line is independent of Reynolds number and optical thickness. In the absence of scattering, however, the middle section temperature profile becomes linear as Reynolds number increases for large optical thickness.

3 If conduction energy transfer dominates over radiation, there are very little effects of optical thickness on the temperature profile in the absence of scattering.

4 For the converging channel, the radiation effect on the temperature profiles is small even when conduction and convection are small.

5 Standard Galerkin finite elements may be used if the convection domination is relatively small ($\mathrm{RePr} \leq 1000$). However, for large Reynolds numbers ($\mathrm{RePr} > 1000$), it is concluded that the nonsymmetric form and ill-conditioning of the matrix from the convective terms would cause the solution to deteriorate. In this case optimal control penalty finite elements can be used to overcome such difficulties. Discussions of this subject is the subject of the forthcoming paper.

References

1 Viskanta, R., "Heat Transfer by Conduction and Radiation in Absorbing and Scattering Materials," ASME JOURNAL OF HEAT TRANSFER, Vol. 87, No. 1, 1965, pp. 143-150.

2 Viskanta, R., and Grosh, R. J., "Heat Transfer by Simultaneous Conduction and Radiation in an Absorbind Medium," ASME JOURNAL OF HEAT TRANSFER, Vol. 84, 1962, pp. 63-72.

3 Fernandes, R., Francis, J., and Reddy, J. N., "A Finite Element Approach to Combined Conductive and Radiative Heat Transfer in a Planar Medium," AIAA 15th Thermophysics Conference, July 14-16, Snowmass, Colo. 1980.

4 Chung, T. J., and Kim, J. Y., "Numerical Solutions of Radiative Heat Transfer with Convection," AIAA Paper 82-HT-45, AIAA/ASME 3rd Joint Thermophysics, Fluids, Plasma and Heat Transfer Conf., St. Louis, June 7-11, 1982.

5 Razzaque, M. M., Klein, D. E., and Howell, J. R., "Finite Element Solution of Radiative Heat Transfer in a Two-Dimensional Rectangular Enclosure With Gray Participating Media," ASME Paper 82-WA/HT-51, Nov. 1982.

6 Goulard, R., "Gundamental Equations of Radiation Gas Dynamics," Purdue University School of Aero. and Eng. Sci. Report 62-4, 1962.

7 Chung, T. J., *Finite Element Analysis in Fluid Dynamics*, McGraw-Hill, 1979.

Thermal Insulation in Flow Systems: Combined Radiation and Convection Through a Porous Segment

K. Y. Wang
Solar Energy
Research Institute
Golden, Colo. 80401
Assoc. Mem. ASME

C. L. Tien
Fellow ASME

Department of Mechanical Engineering,
University of California,
Berkeley, Calif. 94720

The present work reports analytical findings on a new concept for thermal insulation in flow systems. The basic operating principles are illustrated by a duct flow system with a nonradiating gas passing through a porous segment, where convection and radiation take place. The radiative properties of the porous segment are computed from electromagnetic theory assuming that the porous medium is of homogeneous composition. The coupled energy and radiative transfer equations are solved numerically by iterative method in conjunction with over-relaxation. For the limiting case of no scattering, the present results based on the two-flux radiation model agree well with the exact calculations reported recently. It is found that in order to have higher recaptured radiation and temperature drop, a porous medium with large optical thickness and low scattering albedo is preferred. Two illustrative examples indicate that the pressure drop which resulted from installation of the porous segment is of little concern, especially in view of the resulting huge energy savings.

Introduction

For high-temperature systems such as heat exchangers, exhaust-chimneys, furnaces and combustion chambers, it is often desirable to recover as much as possible of the residual energy from exhaust or wasted gas. In order to achieve this goal, many methods have been suggested or employed in the past. One of the promising methods is the installation of radiation-shield-like porous media placed normal to the flow direction so as to recapture some of the fluid energy. The porous material may be composed of packed spheres, foam-metals, fibers, or screens which, in addition to exchanging heat convectively with the gas, can absorb, emit, and scatter thermal radiation. Due to the solid matrix, part of the fluid energy and the incoming radiative energy is absorbed and converted to raise the temperature of the solid matrix, which, in turn, emits and scatters radiation in both upstream and downstream directions. The gas temperature downstream of the segment is thus much lower than that upstream. It is desired to have a large amount of radiation scattered in the upstream direction so as to minimize the energy which may otherwise be wasted. A recent study by Echigo [1] shows that with an appropriate choice of the optical thickness of the permeable media, up to 60 percent of the nonradiating gas energy can be saved due to the converted radiation. However, one of the important radiative characteristics, scattering from the solid matrix, was not considered in that study. The present study concerns a similar flow system, with particular emphasis on the influence of scattering on the effectiveness of this energy conversion.

The physical model is complicated by the directional characteristics of scattering, and exact analytical expressions for radiative heat flux and solid-matrix temperature, like those for nonscattering cases, cannot be achieved. The analysis here employs the two-flux gray radiation model for heat flux because it remains simple in expressions but retains important physical insights. The radiative properties of the porous medium are evaluated directly through the application of electromagnetic scattering theory.

Contributed by the Heat Transfer Division and presented at the ASME Winter Annual Meeting, Boston, Massachusetts, November 13-18, 1983. Manuscript received by the Heat Transfer Division August 9, 1983. Paper No. 83-WA/HT-81.

Theoretical Analysis

The high-temperature fluid passing through the duct is shown schematically in Fig. 1. Fluid initially at temperature T_{go} enters the duct at $x = 0$. The duct's width is much longer than its height $2y_o$ to assure the validity of one-dimensional approximation. The fluid velocity u_g is constant everywhere and temperature distribution T_g is assumed uniform over every cross section. The porous segment is located between x_1 and x_2 where $x_2 - x_1 << y_o$. The fluid is assumed transparent to thermal radiation. Thus, radiation is considered only between the particles which comprise the porous segment. The conductive resistance through the fluid or solid matrix is assumed negligible. The only external radiation sources are from either upstream or downstream directions. The effective heat transfer coefficient across the duct wall is h_w, i.e., heat exchange with the surrounding environment at T_∞ is $h_w(T_g - T_\infty)$ per unit area. Thus, the energy equation for fluid upstream or downstream of the porous segment is

$$\rho_g c_g u_g (2y_o)\, dT_g/dx + 2h_w (T_g - T_\infty) = 0 \qquad (1)$$

with boundary conditions

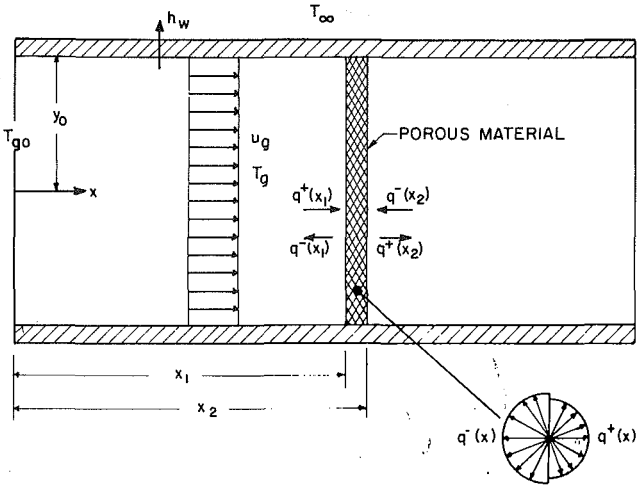

Fig. 1 Schematic of thermal insulation in flow systems

$$T_g = T_{go} \text{ at } x=0, \text{ for } 0<x<x_1 \tag{2a}$$

or

$$T_g = T_g(x=x_2) \text{ at } x=x_2, \text{ for } x>x_2 \tag{2b}$$

where T_g $(x=x_2)$ is obtained from the solution of the governing equations in the porous segment given below.

Inside the porous segment, the fluid and the solid matrix have different temperatures, T_g and T_s, respectively. Since the sizes of the solid particles are much smaller than the other dimensions of the whole segment, the system can be considered as of homogeneous composition. The energy equation for the fluid is

$$\rho_g c_g u_g (2y_o)\, dT_g/dx + 2h_w (T_g - T_\infty) + h_s N_s A_s (2y_o)(T_g - T_s) = 0 \tag{3}$$

where h_s is the heat transfer coefficient between the fluid and the solid matrix, N_s is the number density of particles, and A_s is the surface area of an individual particle. The fluid temperature T_g at $x = x_1$ calculated from equation (1) is a boundary condition for equation (3).

For the solid matrix, equilibrium between convection and radiation yields

$$h_s N_s A_s (T_s - T_g) + dq_r/dx = 0 \tag{4}$$

The quantity q_r is the diffusive heat flux and can be expressed in terms of the heat flux q^+ and q^- in the forward and backward directions, respectively, as

$$q_r = q^+ - q^- \tag{5}$$

By using the two-flux gray radiation model [2], the governing equations for q^+ and q^- are expressed as

$$dq^+/qx = -2\sigma_a q^+ - 2b\sigma_s q^+ + 2\sigma_a \sigma T_s^4 + 2b\sigma_s q^- \tag{6}$$

and

$$-dq^-/dx = -2\sigma_a q^- - 2b\sigma_s q^- + 2\sigma_a \sigma T_s^4 + 2b\sigma_s q^+ \tag{7}$$

where σ_a, σ_s, and b represent the absorbing coefficient, the scattering coefficient, and the back-scattered fraction factor, respectively. Such radiative properties can be calculated theoretically by using electromagnetic scattering theory for spherical or cylindrical particles [2, 3, 4]. The boundary conditions for q^+ and q^- are

$$q^+(x_1) = B_1 \text{ and } q^-(x_2) = B_2 \tag{8}$$

Adding equation (7) to (6), one obtains

$$dq_r/dx = 4\sigma_a \sigma T_s^4 - 2\sigma_a (q^+ + q^-) \tag{9}$$

The combination of equations (4) and (9) gives another relation between temperatures and radiative heat flux inside the porous medium.

For parametric studies, the governing equations and boundary conditions are nondimensionalized by introducing the following dimensionless groups:

$$P = h_w/(\rho_g c_g u_g)$$
$$Q = h_s N_s A_s y_o/(\rho_g c_g u_g) \tag{10}$$
$$R = h_s N_s A_s/(2\sigma_e \sigma T_{go}^3)$$

where P, Q, and R represent ratios of heat loss through the duct wall to fluid energy, solid-fluid convective heat transfer to fluid energy, and solid-fluid convective heat transfer to radiative heat transfer, respectively.

The new variables are defined as

$$X = x/y_o$$
$$\tilde{q} = q/\sigma T_{go}^4$$
$$\theta_{g,s} = T_{g,s}/T_{go} \tag{11}$$
$$\tau = \sigma_e (x - x_1)$$
$$\omega = \sigma_s/\sigma_e$$

where σ_e $(= \sigma_a + \sigma_s)$ is the extinction coefficient, τ is the optical thickness, and ω is the scatteriong albedo of the homogeneous porous medium. The optical thickness of the porous medium is simply defined as $\tau_o = \sigma_e (x_2 - x_1)$.

Equation (1) then reduces to

$$d\theta_g/dX + P(\theta_g - \theta_\infty) = 0 \text{ for } 0<X<X_1 \text{ or } X>X_2 \tag{12}$$

In the domain $X_1 < X < X_2$, or equivalently $0 < \tau < \tau_o$, equations (3), (4), (6), and (7) reduce to

$$d\theta_g/dX + P(\theta_g - \theta_\infty) + Q(\theta_g - \theta_s) = 0 \tag{13}$$

$$R(\theta_g - \theta_s) = 2(1-\omega)\theta_s^4 - (1-\omega)(\tilde{q}^+ + \tilde{q}^-) \tag{14}$$

$$d\tilde{q}^+/d\tau = -2(1-\omega)\tilde{q}^+ - 2b\omega\tilde{q}^+ + 2(1-\omega)\theta_s^4 + 2b\omega\tilde{q}^- \tag{15}$$

$$-d\tilde{q}^-/d\tau = -2(1-\omega)\tilde{q}^- - 2b\omega\tilde{q}^- + 2(1-\omega)\theta_s^4 + 2b\omega\tilde{q}^+ \tag{16}$$

respectively, with boundary conditions

$$\tilde{q}^+(\tau=0) = \tilde{B}_1 \text{ and } \tilde{q}^-(\tau=\tau_o) = \tilde{B}_2 \tag{17}$$

By combining equations (3) to (5), and integrating from $x = x_1$ to x_2, one obtains the following dimensionless overall energy balance [1]:

$$H_1 = H_2 + H_3 + H_4 + H_5 \tag{18}$$

where

$$H_1 = \rho_g c_g u_g \theta_{g1}/4\sigma T_{go}^3 + (1/4)\tilde{B}_1 + (1/4)\tilde{B}_2$$
$$H_2 = \rho_g c_g u_g \theta_{g2}/4\sigma T_{go}^3$$
$$H_3 = (1/4)\tilde{q}^-(\tau=0)$$

Nomenclature

A = surface area
b = back-scattered fraction factor
B = incoming radiation
c = specific heat
d = particle diameter
f_v = solid volume fraction
h = heat transfer coefficient
k = thermal conductivity
N = number density of solid particles
P = dimensionless group defined in equation (10)
q = heat flux
$q^-(0)$ = recaptured radiation
Q = dimensionless group defined in equation (10)
R = dimensionless group defined in equation (10)
T = temperature
u = velocity
x = coordinate along flow direction
y = coordinate normal to flow direction
y_o = half-height of duct
δ = thickness of the porous medium
θ = dimensionless temperature
ρ_g = fluid density
σ = Stefan-Boltzmann constant
σ_e = extinction coefficient
τ, τ_o = optical depth and optical thickness, respectively
ω = scattering albedo

Superscripts

$+, -$ = forward and backward directions, respectively
$-$ = (overbar) nondimensionalized quantity

Subscripts

g = fluid
r = radiation
s = solid phase
w = wall
1,2 = inlet and exit of porous segment, respectively

$$H_4 = (1/4)\tilde{q}^+(\tau=\tau_o)$$

$$H_5 = h_w\int_{x_1}^{x_2}(T_g - T_\infty)\,dx/4y_o\sigma T_{go}^4$$

In the expression, H_1 is the total incoming energy on both surfaces of the porous segment, which includes fluid enthalpy and incoming radiation from either upstream or downstream direction. H_2 can be considered as energy carried away by the fluid at $X = X_2$. H_3 represents the diffusive thermal radiation directed upstream from $X = X_1$, H_4 represents a similar quantity directed downstream from $X = X_2$, and H_5 is considered as the energy exchange with the surrounding environment through the duct walls. In the present case $P << Q$, and therefore H_5 is negligible compared to other terms. Equation (18) implies that part of the incoming energy is converted to radiative energy through scattering and absorbing (H_3 and H_4), and what remains is either carried away by the fluid (H_2) or is lost to the surrounding environment (H_5). A high value of H_3/H_1 then indicates higher converted radiative energy into the upstream direction and is highly desirable.

Exact Limiting Solutions

Exact expressions under limiting cases for radiative flux or temperatures in the region $X_1 < X < X_2$ are available and given below. Such expressions will be useful in understanding the controlling parameters, and in checking the numerical calculations.

(*a*) $\omega = 1$. This corresponds to the nonabsorbing case. It follows from the governing equations that radiation and convection are uncoupled. The temperature of the solid matrix rises only due to convective heat exchange with fluid, and thus $\theta_s = \theta_g$ in equilibrium. The radiative heat flux is determined separately, and therefore has no dependence on convective parameters. The solutions to the simplified equations are

$$\begin{aligned}\theta_s &= \theta_g = \theta_\infty + (\theta_{g1} - \theta_\infty)\exp(-PX)\\ \tilde{q}^+ &= \bar{B}_1 - (\bar{B}_1 - \bar{B}_2)(2b\tau)/(1+2b\tau_o)\\ \tilde{q}^+ &= \bar{B}_1 - (\bar{B}_1 - \bar{B}_2)(1+2b\tau)/(1+2b\tau_o)\end{aligned} \tag{19}$$

(*b*) $R << 1$. With low overall convective heat transfer inside the porous segment, the solid matrix receives little influence from the fluid. The temperature of the solid matrix is thus determined from radiative equilibrium alone. This results in

$$\begin{aligned}\tilde{q}^+ &= \bar{B}_1 - (\bar{B}_1 - \bar{B}_2)(1-\omega+2b\omega)\tau/(1+(1-\omega+2b\omega)\tau_o)\\ \tilde{q}^- &= \bar{B}_1 - (\bar{B}_1 - \bar{B}_2)(1+(1-\omega+2b\omega)\tau)/(1+(1-\omega\\ &\quad +2b\omega)\tau_o)\\ \theta_s &= (1/2(\tilde{q}^+ + \tilde{q}^-))^{1/4}\end{aligned} \tag{20}$$

$$\theta_g = \frac{P\theta_\infty}{P+Q} + \left(\theta_{g1} - \frac{P\theta_\infty}{P+Q}\right)e^{-\frac{P+Q}{\sigma_e y_o}\tau}$$

$$+ \frac{Q}{\sigma_e y_o}\int_o^\tau e^{-\frac{P+Q}{\sigma_e y_o}(\tau-\tau')}\left\{\bar{B}_1 - \frac{\bar{B}_1 - \bar{B}_2}{2}\cdot \frac{1+2(1-\omega+2b\omega)\tau'}{1+(1-\omega+2b\omega)\tau_o}\right\}^{1/4} d\tau'$$

(*c*) $R >> 1$, $Q >> P$. When convection is the dominant mode of heat transfer, the thermal insulation effect due to radiation becomes relatively less significant. The temperature of solid matrix is raised to that of the fluid. The mathematical manipulation is straightforward but tedious, and only $\tilde{q}^-$ ($\tau = 0$) is given below [5].

$$\tilde{q}^-(0) = \frac{M}{b\omega}\left[\frac{-2b\omega\theta_{g1}^4 - (N-M)(\bar{B}_1 - \theta_{g1}^4)\exp(-M\tau_o)}{(N+M)\exp(M\tau_o) - (N-M)\exp(-M\tau_o)}\right]$$

$$+ \frac{N-M}{2b\omega}(\bar{B}_1 - \theta_{g1}^4) + \theta_{g1}^4 \tag{21}$$

where $M = 2((1-\omega)(1-\omega+2b\omega))^{1/2}$ and $N = 2(1-\omega+b\omega)$.

Such expressions clearly indicate that b, which characterizes the anisotropy of the scattering, has a pronounced effect in the highly scattering ($\omega \to 1$) regime, and has a relatively less important effect in the absorbing-emitting ($\omega \to 0$) regime.

Method of Calculations

The solutions to equation (12) are

$$\theta_g = \theta_\infty + (1-\theta_\infty)\exp(-PX) \text{ for } 0 < X < X_1 \tag{22a}$$

and

$$\theta_g = \theta_\infty + (\theta_{g2} - \theta_\infty)\exp(-P(X-X_2)) \text{ for } X > X_2 \tag{22b}$$

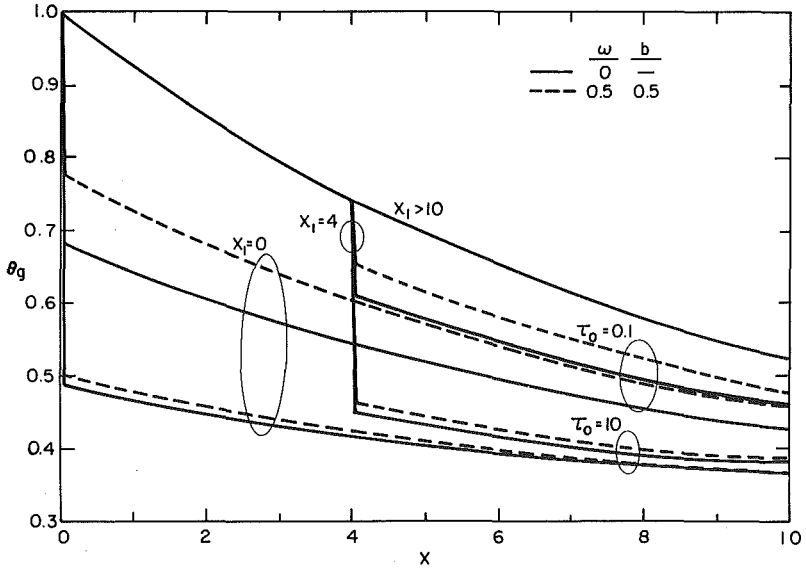

Fig. 2 Fluid temperature along flow direction; $\theta_\infty = 0.3$, $\delta/y_o = 0.05$, $P = 0.114$, $Q = 952.4$, $B_1 = B_2 = 0$, $h_s N_s A_s y_o/2\sigma T_{go}^3 = 250$

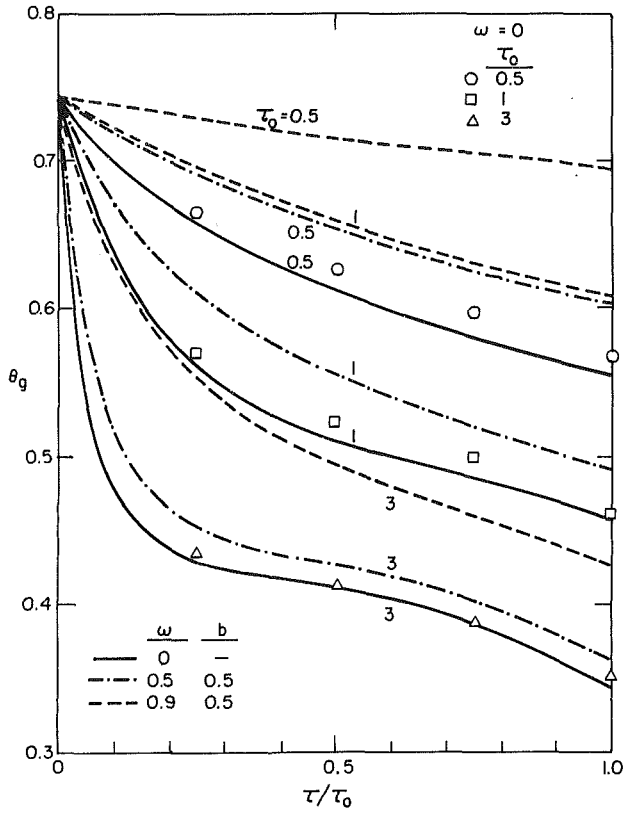

Fig. 3(*a*) Fluid temperature inside porous segment: $X_1 = 4$, $\theta_\infty = 0.3$, $\delta/y_o = 0.05$, $P = 0.114$, $Q = 952.4$, $B_1 = B_2 = 0$, and $\sigma_e k_g / 4\sigma T_{go}^3 = 0.05$

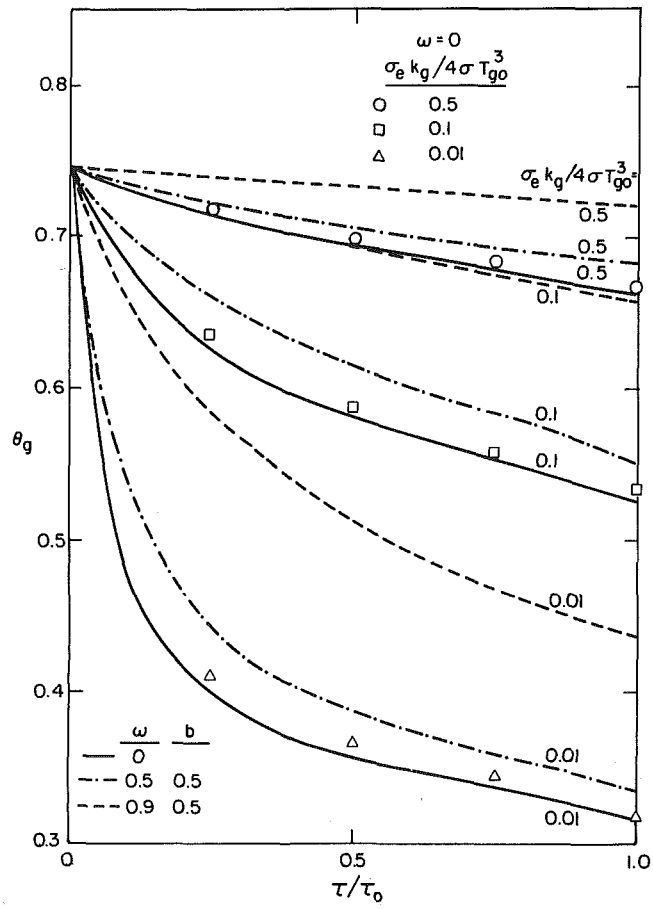

Fig. 3(*b*) Fluid temperature inside porous segment: $X_1 = 4$; $\theta_\infty = 0.3$, $\delta/y_o = 0.05$, $P = 0.114$, $Q = 952.4$, $B_1 = B_2 = 0$, and $\tau_o = 1$

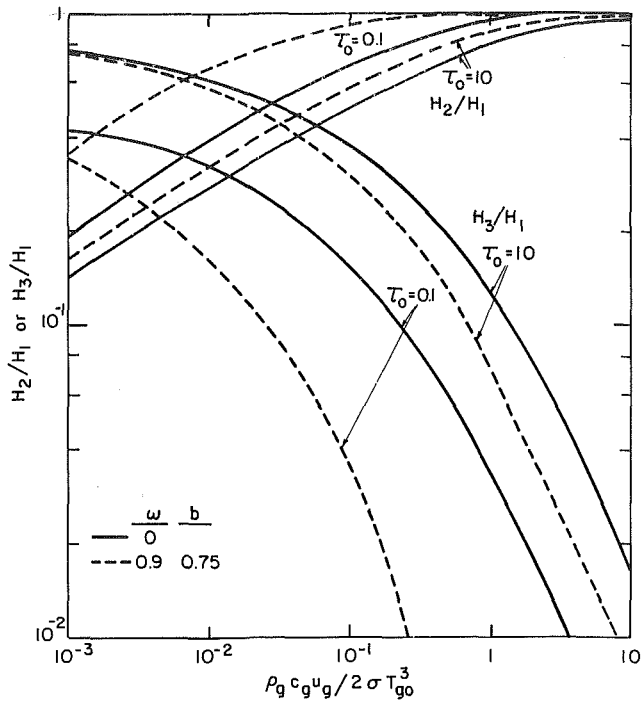

Fig. 4 Ratio of recaptured radiation and outgoing fluid enthalpy to incoming energy: $X_1 = 4$, $\theta_\infty = 0.3$, $\delta/y_o = 0.05$, $P = 0.114$; $Q = 500$, $B_1 = B_2 = 0$

For the solutions to equations (13) to (16), an iterative method is utilized. The values of $\bar{q}^+$ and $\bar{q}^-$ are first solved from equations (15) and (16) by substituting assumed values of $\bar{q}^+$, $\bar{q}^-$ and θ_s into the right-hand side of the equations. The first order differentiation is approximated by finite difference expressions. The temperature difference $(\theta_g - \theta_s)$ is then calculated from equation (14). Thus, the fluid temperature θ_g can be determined from equation (13), and the solid matrix temperature θ_s is obtained by subtracting the previously calculated $(\theta_g - \theta_s)$ from θ_g. Repeated computations are performed until all the calculated variables satisfy certain imposed convergence criteria. An over-relaxation factor is found necessary for fast convergence. The fluid temperature at $X = X_2$ obtained from the aforementioned procedure is also a boundary condition for equation (13) in the region $X > X_2$.

Results and Discussion

The fluid temperature as a function of X is shown in Fig. 2. The effect of the porous segment is clearly observed from the sharp temperature drops. The curve corresponding to $X_1 > 10$ represents the fluid temperature distribution inside a duct with no porous segment in the region $X < 10$, and reveals no sharp temperature drop. The temperature decreases smoothly along the flow direction because of heat exchange with the environment through the walls. The parameters P, Q, and so on are chosen based on the ones reported by Echigo [1] to make the comparisons in Fig. 3(*a*) and Fig. 3(*b*) possible. The variable X_1 indicates the position of the porous segment. It is found that smaller ω or larger τ_o cause larger temperature drop.

The fluid temperature inside a porous segment with no incoming radiation is presented in detail in Fig. 3(*a*) and Fig. 3(*b*). For the limiting case of no scattering ($\omega = 0$), the results are compared to Echigo's calculations [1] which appear as symbols. It is found that the two-flux radiation approximation is generally good, and the maximum difference between the two methods is less than 5 percent. The two-flux model is more accurate for higher $\sigma_e k_g / 4\sigma T_{go}^3$ and τ_o values

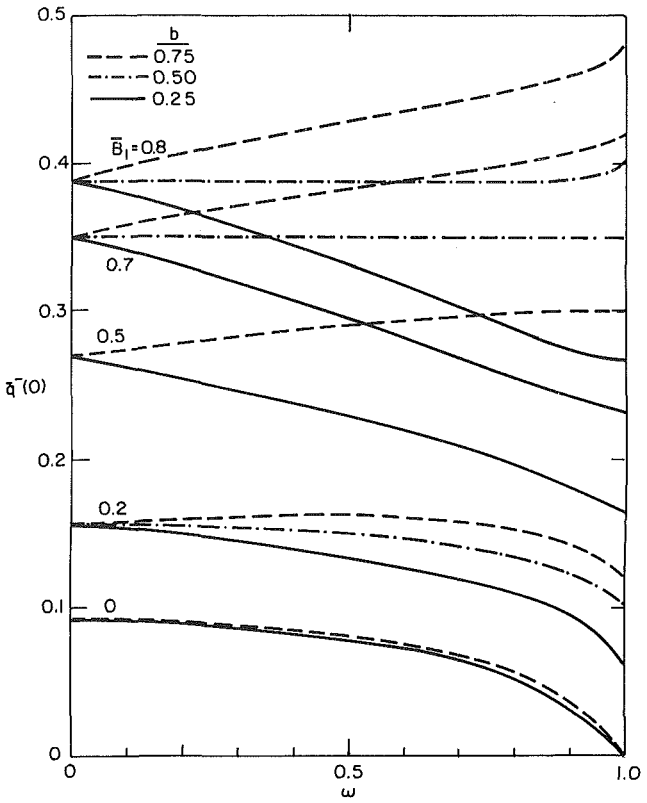

Fig. 5 Dependence of recaptured radiation on ω for different incoming radiation and b values: $X_1 = 4$, $\theta_\infty = 0.3$, $\delta/y_o = 0.05$, $P = 0.114$, $Q = 1000$, $R = 12.5$, $\tau_o = 1$

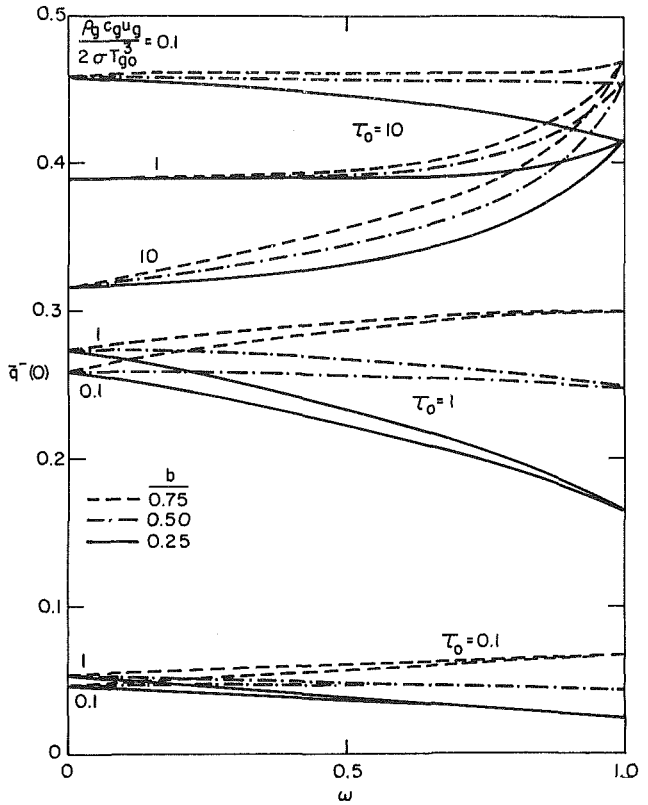

Fig. 6(a) Dependence of $\bar{q}^-(0)$ on ω for different values of $\rho_g c_g u_g / 2\sigma T_{go}^3$ and τ_o: $X_1 = 4$, $\theta_\infty = 0.3$, $\delta/y_o = 0.05$, $P = 0.114$, $\bar{B}_1 = 0.5$, $\bar{B}_2 = 0$, and $Q = 100$

since under such conditions the radiative heat transfer is attenuated more and thus plays a less important role. Hence, the difference between the approximate two-flux model and the exact radiation expressions diminishes accordingly. The solid phase temperature θ_s is very close to the fluid temperature θ_g, except near the entrance of the porous segment and is not shown in either figure.

Since the primary goals of this study are focused on the recaptured radiation in the upstream direction and the temperature drop across the porous segment, only H_2/H_1 and H_3/H_1 in equation (18) are shown in Fig. 4. As convective heat transfer increases, the solid matrix temperature tends to rise too close to the fluid temperature, which results in higher H_2/H_1 and lower H_3/H_1 values. The effect of optical thickness is also presented. Scattering from the solid matrix reduces $\bar{q}^-(0)$ in this case.

The influence of scattering albedo to the recaptured radiation $\bar{q}^-(0)$ can further be explained from Fig. 5. Without incoming radiation $\bar{B}_1$, $\bar{q}^-(0)$ is mainly attributed to emission from the solid particles near $X = X_1$, while the contribution from reflection is little. Since the increase of albedo means less absorption and emission, the recaptured radiation $\bar{q}^-(0)$ is thus depressed. On the other hand, the contribution from scattering becomes more significant as $\bar{B}_1$ increases, and particles with higher b values can scatter more radiative energy into the upstream direction. When $\bar{B}_1$ is high enough, such as the curves correspond to $\bar{B}_1 > 0.5$, it is possible to have $\bar{q}^-(0)$) increase with ω. However, practically speaking, since small particles are mostly forward-scattering rather than backward-scattering, i.e., $b < 0.5$ in general, it is desirable to choose porous materials with low albedo values. On the other hand, high back scattering pattern is observed for diffusive reflecting spheres which are large compared with wavelength of incident radiation [6]. If this is the case, high ω particles will be desirable for large incoming radiation.

The recaptured radiation $\bar{q}^-(0)$ as a function of albedo is

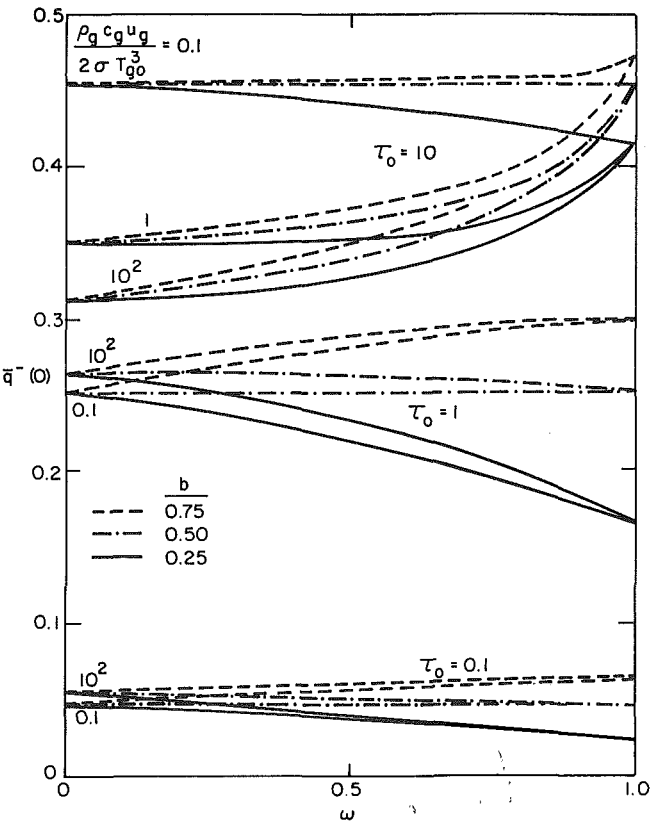

Fig. 6(b) Dependence of $\bar{q}^-(0)$ on ω for different values of $\rho_g c_g u_g / 2\sigma T_{go}^3$ and τ_o: $X_1 = 4$, $\theta_\infty = 0.3$, $\delta/y_o = 0.05$, $P = 0.114$, $\bar{B}_1 = 0.5$, $\bar{B}_2 = 0$, and $Q = 1000$

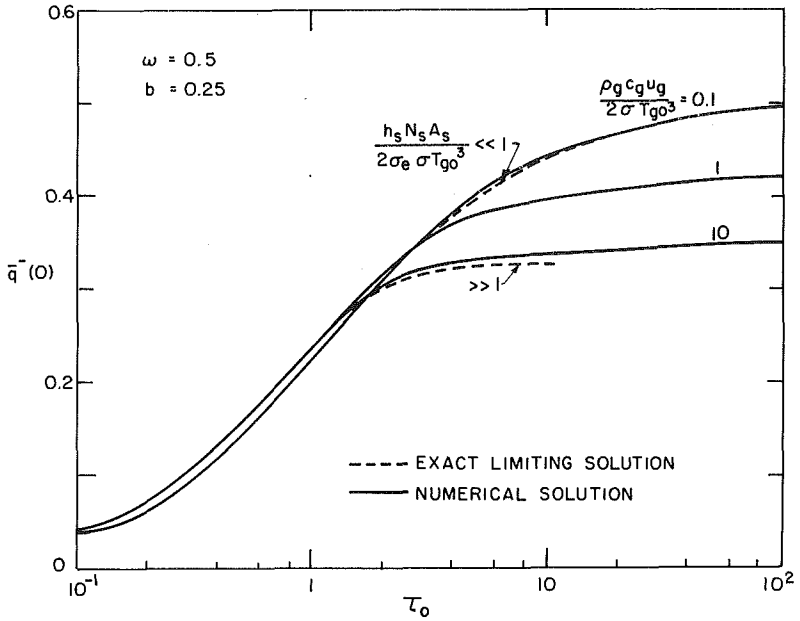

Fig. 7 Dependence of $\bar{q}^-(0)$ on τ_o for different values of $\rho_g c_g u_g / 2\sigma T_{go}^3$: $X_1 = 4, \theta_\infty = 0.3, \bar{B}_1 = 0.5, \bar{B}_2 = 0, P = 0.114, Q = 500$

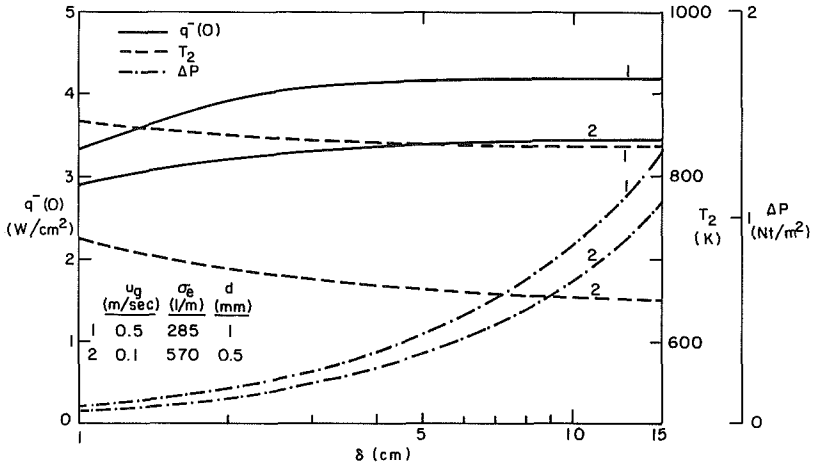

Fig. 8 Thermal performance of and pressure drop across the porous segment for varous thicknesses

shown in Fig. 6(*a*) and Fig. 6(*b*) for different parameters. It is preferable to choose porous materials with high ω for large τ_o since in these circumstances the porous segment is effective for shielding the incoming radiation rather than converting radiation from the flowing gas enthalpy. The comparison between the two figures shows that the effects of Q on $\bar{q}^-(0)$ are small. Although Q increases tenfold from Fig. 6(*a*) to Fig. 6(*b*), it turns out that $\bar{q}^-(0)$ varies by less than 10 percent. This conclusion makes the calculations less dependent on the validity of the heat transfer coefficient h_s.

The exact limiting solutions from equations (20) and (21) are shown in Fig. 7, together with several representative numerical calculations. The results imply that for small τ_o equation (21) is a very good approximation especially if $R >> 1$; while for large τ_o, equation (20) is good only if R is small. Since the present study concerns flow insulation problems, only large τ_o will be of interest. The effect of τ_o on $\bar{q}^-(0)$ remains almost unchanged in the optically thick regime. In other words, a porous medium with high extinction coefficients need not be thick itself to achieve high insulation ability in flow systems.

Illustrated Examples

Air flowing through various layers of aluminum screens is taken as an example. Assume in Fig. 1 that $y_o = 15$ cm, $T_{go} = 1000$ K, $u_g = 0.5$ m/s (Case 1) or 0.1 m/s (Case 2) and the duct walls are insulated. Incoming radiation from upstream direction is $B_1 = 5.729$ W/cm^2. There is no radiation source from the downstream direction. The metal screens consist of thin wires 1 mm (Case 1) or 0.5 mm (Case 2) in diameter. These layers of screens are considered as a homogeneous porous medium which have a solid volume fraction $f_v = 0.18$. The radiative properties are $\omega = 0.9$, $b = 0.3$, $\sigma_e = 285$ 1/m (Case 1) and $\sigma_e = 570$ 1/m (Case 2) based on the methods described in [3]. The fluid temperature at x_2, the recaptured radiation, and the pressure drop across the porous medium are presented in Fig. 8 as functions of the porous segment thickness δ. The temperature drop is larger in case (2) because the parameter $\rho_g c_g u_g / \sigma T_{g0}^3$ is smaller. It is noted that due to the high extinction coefficients, the recaptured radiation reaches asymptotic value even for small δ. The pressure drop is calculated by using Darcy's law [7], which varies linearly

with δ. The numerical values of pressure drop Δp reveal that the high porosity medium does not cause significant pressure loss. However, in order to have best performance as far as energy conservation and pumping power are concerned, an optimal value for δ should be established.

Concluding Remarks

A numerical study has been made on the potential recovery of energy through thermal radiation in high-temperature flow systems by installing a porous segment normal to the flow direction. The two-flux model is used to describe the radiative flux which scatters anisotropically from the solid matrix. The results indicate that both the scattering albedo ω and the back-scattered fraction factor b are important factors. For maximization of the recaptured energy, an optically thick medium should be considered. However, the dependence on ω and b are more complicated: for a lower intensity of external radiative source, the increase of ω leads to the decrease of the recaptured radiation, while for higher values of incoming radiation, the increase of ω may enhance or reduce the recaptured radiation depending on the b value. If particles are strongly forward scattering, low ω materials will be preferred. But for particles with strong backward scattering pattern, like large diffuse spheres, the contrary will be true. The results also reveal that the anisotropic scattering effect is more pronounced in the optically thick regime than in the optically thin regime. Also interesting to note is that the convective heat transfer coefficient between the solid matrix and the fluid is not a very sensitive factor in this particular study. The numerical calculations are found to agree well with the exact expressions in several limiting cases. The illustrative numerical examples show that the pressure loss across the porous segment is not of major concern.

References

1 Echigo, R., "Effective Energy Conversion Method Between Gas Enthalpy and Thermal Radiation and Application to Industrial Furnaces," *7th Int. Heat Transfer Conf.*, Munchen, Vol. 6, 1982, pp. 361-366.

2 Tong, T. W., and Tien, C. L., "Radiative Heat Transfer in Fibrous Insulations—Part I: Analytical Study," ASME JOURNAL OF HEAT TRANSFER, Vol. 105, No. 1, Feb. 1983, pp. 70-75.

3 Wang, K. Y., and Tien, C. L., "Radiative Heat Transfer through Opacified Fibers and Powders," *J. Quant. Spectrosc. Radiat. Transfer*. Vol. 30, 1983, pp. 213-223.

4 Van de Hulst, H. C., *Light Scattering by Small Particles*, New York, Wiley, 1957.

5 Tong, T. W., and Tien, C. L., "Resistance-Network Representation of Radiative Heat Transfer with Particulate Scattering," *J. Quant. Spectrosc. Radiant Transfer*, Vol. 24, 1980, pp. 491-503.

6 Siegel, R., and Howell, J. R., *Thermal Radiation Heat Transfer*, 2nd Ed., New York, McGraw-Hill, 1981.

7 Scheidegger, A. E., *The Physics of Flow Through Porous Media*, 3rd Ed., Toronto, University of Toronto Press, 1974.

Design Considerations for Aerodynamically Quenching Gas Sampling Probes

L. Chiappetta

M. B. Colket, III

United Technologies Research Center,
United Technologies Corporation,
East Hartford, Conn. 06108

An aerodynamic quench is the most rapid method for quenching temperature and pressure-dependent chemical reactions. Attempts have been made to quench gas samples aerodynamically, but many of these attempts have been unsuccessful because of a lack of understanding of the internal aerodynamics of sampling probes. A one-dimensional model developed previously by the authors has been used for the design and analysis of aerodynamically quenching probes. This paper presents in detail the important aerodynamic and heat transfer equations used in the model, a description of the method of solution, and the results of a sensitivity study. These calculations demonstrate the limitations and important trade-offs in design and operating conditions of probes using an aerodynamic quench.

Introduction

When gas samples are extracted from combustion gases by means of gas sampling probes, chemical reactions occurring within the probe or transfer lines may alter significantly species concentrations prior to analysis. Many of these reactions depend strongly on gas temperature and/or pressure. Several methods exist to quench chemical reactions by reducing the temperature of the gas sample. These techniques include: (*i*) dilution of the sample with a cold, inert gas; (*ii*) convective heat transfer from the sample to a coolant; and (*iii*) rapid expansion of the sample to supersonic speeds, followed by convective cooling of the sample [1]. The third method is known as aerodynamic quenching and is generally most desirable due to the exceptionally high quenching rates [2]. An aerodynamic quench also provides a rapid reduction in static pressure and thereby enhances quenching rates for many two- and three-body chemical reactions. Recently, it has been demonstrated that NO/NO_2 interconversion occurring within sample probes can be minimized by reducing sample pressure to a low value [3–5].

An aerodynamic quench in a gas sampling probe is defined as a rapid reduction in static temperature and static pressure achieved by rapidly accelerating the flow to supersonic speeds. Supersonic flow is maintained until the stagnation temperature of the sample is reduced to a low value by convective heat transfer from the sample to the coolant such that, upon return to subsonic conditions through a shock system, the static temperature and pressure are sufficiently low to minimize chemical reactions. The temperature and pressure below which chemical reactions are no longer important for the gas being sampled are dependent upon the appropriate chemical kinetics.

In a previous paper [6], many of the limitations and difficulties of achieving an aerodynamic quench within a gas sampling probe were discussed and a one-dimensional model was briefly described. This paper presents the mathematical details of this model for the design and analysis of aerodynamically quenching gas sampling probes and the results of a sensitivity study. It is shown that the performance of aerodynamically quenching probes is a strong function of probe geometry and operating conditions and that no single probe design is capable of providing an aerodynamic quench for all sampling conditions.

Description of the Probe

The principal features of a probe capable of quenching a gas sample aerodynamically are depicted in Fig. 1, which shows the probe geometry and representative axial profiles of Mach number and both static and stagnation temperature. In order for such a probe to produce an aerodynamic quench when operated in a subsonic stream, the flow must be choked at the probe orifice and then accelerated to a high supersonic Mach number (Fig. 1(*b*)) and low static temperature (Fig. 1(*c*)) via the area expansion of the probe tip (Fig. 1(*a*)). This flow expansion must be large enough to achieve a rapid reduction in static temperature ($\sim 10^8$ K/s), yet not so large that subsequent friction and shock system losses are excessive. The transition between the tip region and constant area section must be smooth enough to avoid coalescence of compression waves into a shock system. In the constant area section located immediately downstream of the probe tip, the stagnation temperature of the supersonic flow (Fig. 1(*c*)) is reduced by convective heat transfer to the coolant. Cooling tends to increase the Mach number and stagnation pressure while friction tends to reduce these properties. If, in the trade-off between these competing effects of cooling and friction, the Mach number is reduced to unity in the constant area

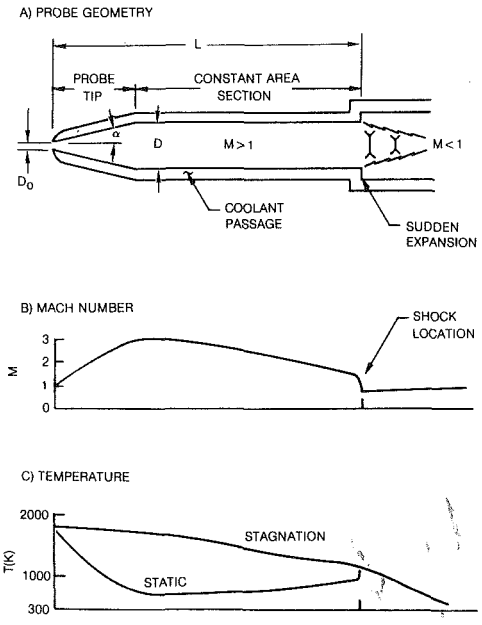

Fig. 1 Features of a typical aerodynamically quenching probe

Contributed by the Heat Transfer Division for publication in the JOURNAL OF HEAT TRANSFER. Manuscript received by the Heat Transfer Division June 2, 1982, Paper No. 82-HT-39.

section, then either a shock system will occur at some upstream location or the probe orifice will unchoke; in either case, the static temperature will be approximately equal to the local stagnation temperature and no aerodynamic quench will occur. The constant area section is terminated by a sudden expansion in flow area that is used to stabilize the shock system that reduces the Mach number to a subsonic value. This return to subsonic conditions must occur only after the stagnation temperature has been reduced to a level where the static temperature downstream of the shock system (Fig. 1(*c*)) will be sufficiently low such that the sample remains quenched. This expansion must be large enough to result in a relatively low Mach number downstream of the shock system so that additional stagnation pressure losses due to friction are small; otherwise, the flow will choke in the subsonic portion of the probe with the attendant risk of unchoking the sampling orifice. The probe, of course, must not contain a sharp bend prior to the desired location of the shock system.

Description of the Model

A one-dimensional, gas-dynamic model is used to describe the flow phenomena important to the aerodynamic quench process in a probe having a configuration like that shown in Fig. 1(*a*)). This model is based on a differential equation which relates the change in local Mach number to the effects of heat transfer, skin friction, flow area variations, and thermal property changes for a steady, one-dimensional flow. Using the influence coefficient approach by Shapiro [7], the Mach number variation is given by

$$\frac{dM^2}{M^2}(1-M^2) = -2\left(1+\frac{\gamma-1}{2}M^2\right)\frac{dA}{A} + (1+\gamma M^2)\frac{dQ}{\dot{w}_s c_{p_s} T_s} \tag{1}$$

$$+\gamma M^2\left(1+\frac{\gamma-1}{2}M^2\right)4f\frac{dx}{D} - (1+\gamma M^2)\frac{dW}{W} - (1-M^2)\frac{d\gamma}{\gamma}$$

The determination of each of the terms used in equation (1) is discussed in the following subsections.

Area Variation. For probes with circular passages, the flow area is given by

$$A = \Pi D^2/4 \tag{2}$$

and the fractional change in flow area is calculated from

$$dA/A = 2dD/D \tag{3}$$

Heat Transfer. For that portion of the probe in good thermal contact with the coolant, the heat transfer rate is calculated by the expression

$$dQ = -\bar{h}(T_{r_s} - T_c)\Pi D dx \tag{4}$$

with the recovery temperature of the sample determined from

$$T_{r_s} = T_s\left(1+\frac{\gamma-1}{2}M^2\mathrm{Pr}^n\right) \tag{5}$$

and $n = 0.5$ (laminar flow) or $n = 0.33$ (turbulent flow).

The overall heat transfer coefficient, $\bar{h}$, is calculated for cylindrical sample and coolant passages as follows

$$\bar{h} = \left[\frac{1}{h_s} + \frac{D_w}{2K_w}\ln\frac{D_{w'}}{D_w} + \frac{1}{h_c(D_{w'}/D_w)}\right]^{-1} \tag{6}$$

where $D_{w'}/D_w$ is the ratio of outside to inside sample tube diameters. The sample heat transfer coefficient is determined from Nusselt number correlations for both laminar and turbulent flow. For laminar flow ($\mathrm{Re}_D < 2300$)

$$\mathrm{Nu} = h_s D/K_s = \mathfrak{F}\left[\mathrm{Re}_D\mathrm{Pr}/(x/D)\right] \tag{7}$$

where $\mathfrak{F}\,[\mathrm{Re}_D\mathrm{Pr}/(x/D)]$ is a correction factor for entrance length [8]. For fully developed turbulent flow ($\mathrm{Re}_D > 2300$), the McAdams equation [9] is used

$$\mathrm{Nu} = h_s D/K_s = 0.023\,\mathrm{Re}_D^{0.8}\mathrm{Pr}^{0.4} \tag{8}$$

For convenience, it is assumed that thermal properties used in the heat transfer coefficient correlations can be evaluated at the bulk temperature.

The heat transfer between the gas sample and the relatively massive probe tip is more difficult to estimate because the two-dimensional temperature distribution within the tip is a function of both the gas sample and external environment conditions. If the wall temperature distribution is known, then

$$dQ = -h_s(T_{r_s} - T_w)\Pi D dx \tag{9}$$

However, for the calculations reported in this paper, a conservative estimate of probe performance was made by assuming dQ equals zero in the tip region.

If chemical reactions are occurring within the flow passage, then an amount ΔH_R of energy per unit time liberated by chemical reaction must be added to dQ.

Skin Friction. The friction factor, f, is estimated from correlations for flow in smooth tubes [10]:

$$f = 16\,\mathrm{Re}_D \qquad \mathrm{Re}_D < 2300 \tag{10}$$

$$f = 0.079/\mathrm{Re}_D^{0.25} \qquad 2300 < \mathrm{Re}_D < 10^5 \tag{11}$$

$$(4f)^{-0.5} = 2.0\log_{10}[\mathrm{Re}_D(4f)^{0.5}] - 0.8 \qquad \mathrm{Re}_D > 10^5 \tag{12}$$

Thermal Property Variations. The ratio of specific heats is a function of both temperature and composition and the molecular weight is a function of composition. For the present analysis, it is assumed that the gas composition is

Nomenclature

A = flow area
A/A_o = tip region area ratio
c_p = heat capacity
D = diameter
f = friction factor
h = heat transfer coefficient
K = thermal conductivity
L = distance from probe orifice to end of constant area (supersonic flow) section
M = Mach number
n = exponent
Nu = Nusselt number
Pr = Prandtl number, $\mu c_p/K$
Q = heat transfer rate
Re = Reynolds number, $\rho u D/\mu$
R_o = universal gas constant
T = temperature
u = velocity
$\dot{w}$ = flow rate
W = molecular weight
X = axial distance
α = tip region divergence half-angle
ΔH_R = heat released by chemical reaction per unit time
γ = ratio of specific heats
μ = molecular viscosity
ρ = density

Subscripts

c = coolant
D = diameter
IDL = ideal value
O = orifice station
r = recovery condition
S = static condition
s = sample
T = stagnation (total) condition
w = wall (gas sample side)
w' = wall (coolant side)

Superscripts

$(\bar{\ })$ = overall value

invariant (dW/W is equal to zero) and the quantity $d\gamma/\gamma$ is evaluated from input thermal property data tables.

Coolant Conditions. The coolant is assumed to be an incompressible fluid whose properties are evaluated from tables of molecular viscosity, thermal conductivity, heat capacity, and density as a function of temperature. The coolant is assumed to flow in the same direction as the gas sample within an annular passage surrounding the sample passage. The dimensions of the coolant passage can vary in the axial direction. The coolant heat transfer coefficient and friction factor are estimated from equations (7) and (8) and (10), (11) or (12), respectively, using a Reynolds number defined in terms of the local coolant passage hydraulic diameter.

In typical probe operations, the coolant flows in the direction opposite to that of the gas sample. The coolant is turned at the probe tip (to provide impingement cooling for the tip) and then returns to the probe exit via an outer annular passage to provide coolant to the probe shroud (not shown in Fig. 1(*a*)). The heat extracted by the coolant from the sample gas is small relative to the heat absorbed by the coolant in cooling the probe shroud. Coolant flow rates are typically determined by probe thermal protection requirements rather than gas sample cooling requirements. Consequently, relatively little temperature rise due to heat extracted from the sample gas is experienced by the coolant, and therefore, the use in the model of coflowing gas sample and coolant streams is justifiable and eliminates the need for solving the coupled gas sample-coolant heat transfer problem iteratively.

Shock Systems. As noted earlier, the supersonic flow portion of the probe is terminated by an abrupt change in flow area that stabilizes a shock system. The flow is subsonic downstream of this system. The simplest shock system may consist of a shock train, a system of oblique shocks occurring over a finite length of probe passage. The stagnation pressure ratio across a shock train is less than that across a normal shock. Correlations for the length of shock trains as a function of upstream Mach number are available [11]. In either case, the flow is determined by integrating equation (1) to a point just upstream of the shock system; the Rankine-Hugoniot equations are used to determine properties just downstream of the shock and these properties are used as initial conditions for the continued integration of equation (1).

Estimate of Off-Design Performance. The model may also be used to estimate the performance (*i*) for probes that are designed to achieve an aerodynamic quench but are operated under off-design conditions or (*ii*) for probes in which it is not necessary to achieve an aerodynamic quench. For a probe designed to provide an aerodynamic quench, the expansion angle of the tip region is relatively large. If the orifice of such a probe is unchoked, or if the orifice is choked but subsonic flow occurs within the tip region (downstream of a shock system located in the tip), then separated flow is likely to occur in the tip region and the flow will sustain an additional stagnation pressure loss. A method to estimate this loss as applied to the design of gas sample probes is discussed by Colket et al. [2].

Method of Solution

Integration of equation (1) is performed using a simple, forward-marching procedure. Specifically, the right-hand side of equation (1) is evaluated at each axial location x so that

$$M^2(x+\Delta x) = M^2(x) + dM^2(x) \tag{13}$$

where $dM^2(x)$ is determined using equation (1) with all parameters evaluated at x. Shapiro [7] has presented equations having the form of equation (1) for the other flow variables of interest. However, the evaluation of these parameters is accomplished in the present model using standard one-dimensional flow equations once $M^2(x+\Delta x)$ is determined. For example, the stagnation temperature is calculated from

$$T_T(x+\Delta x) = T_T(x) + dQ/\dot{w}_s c_{p_s} \tag{14}$$

The static temperature is determined from the adiabatic relationship

$$T_s(x+\Delta x) = T_T(x+\Delta x)/\left[1+\frac{\gamma-1}{2}M^2(x+\Delta x)\right] \tag{15}$$

while the static pressure is determined from the mass continuity equation:

$$P_s(x+\Delta x) = \dot{w}_s/A(x+\Delta x)[R_o T_T(x+\Delta x)/(\gamma W)]^{0.5} \tag{16}$$
$$[M(x+\Delta x)]^{-1}\left[1+\frac{(\gamma-1)}{2}M^2(x+\Delta x)\right]^{-0.5}$$

Other flow variables may be calculated using similar techniques.

Since the probe orifice is presumed to be choked, and since equation (1) is singular at a Mach number of unity, it is necessary to assume a low supersonic Mach number (~ 1.05) to initiate the integration of this equation. This singularity also requires that a small step-size (Δx) be used initially to perform the integration. However, as the Mach number departs from unity, a larger step-size may be used. The computer program incorporating the model alters step-size by examining the magnitude of dM^2/M^2 throughout the calculation. Good results are obtained using a step-size equal to approximately one-tenth of the local passage diameter.

The model has been programmed for use on a UNIVAC 1100/81A computer. Approximately 20 s of machine time are required to estimate the performance of a given probe operating at a specified ambient condition.

Model Validation

The one-dimensional model was used to design an aerodynamically quenching gas sampling probe. An instrumented probe was fabricated in accordance with this design and used to extract gas samples from a simulated gas turbine engine exhaust at a pressure of 0.1 MPa and temperatures of 1000 K. In addition, axial static pressure profiles calculated using the model were shown to be in excellent agreement with the experimental results. Details of this probe design and the comparisons between calculated and experimental results have been reported elsewhere [6, 12].

The model has also been used to analyze the performance of microprobes (orifice diameters $\sim 100\ \mu$m) and predicts that such probes are generally not capable of providing an aerodynamic quench. Experimental mass flow measurements for microprobes show that the mass flow rate varies with back pressure even for back pressures as low as 1/10 of the ambient pressure. Thus the flow cannot be choked at the orifice of the microprobe and no aerodynamic quench is possible; these experimental results are in agreement with the predictions of the model. The experimental results and model predictions are discussed in detail by Colket et al. [6, 12].

Two-Dimensional Effects

It has been assumed in the model that the flow within the probe can be treated as one-dimensional. The good agreement between calculated and measured axial static pressure profiles, cited previously, indicates that the one-dimensional flow assumption is reasonable for treating the hydrodynamics of the flow. Chemical reaction rates depend exponentially on local static temperature; thus, small changes in static tem-

perature in the radial direction can produce large variations in reaction rates. However, it can be argued that the one-dimensional flow assumption is still reasonable. While the local static temperature approaches the local stagnation temperature near the wall, the local stagnation temperature is generally much lower than the bulk value because the sample passage is cooled; hence radial static temperature variations are less in the nonadiabatic case than in the adiabatic case. To determine the importance of radial variations in static temperature on species concentrations, a two-dimensional flow model must be used in conjunction with a detailed chemical kinetics analysis. However, a one-dimensional model produces reasonable initial estimates of probe performance and is more economical to use than a two-dimensional model.

Sensitivity Study

In this section, calculations made using the model are presented to demonstrate the trade-offs in probe geometric factors that can be made to design a probe capable of providing an aerodynamic quench over a range of operating conditions. The geometric factors include: orifice diameter, D_o; the area ratio between the first (supersonic) constant area section and the orifice, $A/A_o = (D/D_o)^2$; the average divergence half-angle in the tip regon, α; and the distance from the orifice to the end of the first constant area section, L. Calculated results are presented for assumed values of stagnation pressure of 0.1 and 1.0 MPa and stagnation temperature of 2000 and 3000 K. For all cases, the sample gas was assumed to be air with temperature-dependent thermal and transport properties. Heat transfer in the tip region was assumed to be negligible in these calculations. It was assumed that the coolant was water with an initial temperature of 298 K and flowrate of 63 gm/s; the hydraulic diameter of the coolant passage was calculated from the outside diameter of the sample tube (as determined from the orifice diameter, the tip region area ratio, and the wall thickness of the sample tube, 0.07 cm) and the inside diameter of the coolant tube (2.0 cm for all calculations described below). Since no desired quenching rate has been specified in performing these calculations, the model was used to predict the maximum value for L for each flow condition and configuration; the maximum value of L is defined as the length required for the Mach number to be reduced to unity by frictional forces. The minimum back pressure is the stagnation pressure at this position in the probe and is the minimum pressure that must be provided by the pumping system to maintain supersonic flow up to the end of the constant area section. (Obviously, the minimum back pressure must be reduced by shock losses and friction losses in the subsonic flow downstream of the shock system to determine the minimum pressure required of the pumping system.) A summary of the assumed ambient gas conditions and probe geometric factors is presented in Table 1. The results presented in graphic form are also labeled in accordance with Table 1. As indicated in Table 1 and in the appropriate graphs, the area ratio for the tip region is also characterized by an ideal Mach number, M_{IDL}. The ideal Mach number is the supersonic Mach number at the exit of the probe tip region in the absence of friction and heat transfer (i.e., for isentropic flow in the tip region).

Effect of Orifice Diameter. Calculated values of the distance, L, from the probe orifice to the end of the first constant area (supersonic flow) section are plotted as a function of local stagnation temperature in Figs. 2 and 3 for two ambient stagnation pressures, two ambient stagnation temperatures, and three probe orifice diameters. Calculations such as those shown here can be used to determine the length of the constant area section for given ambient stagnation conditions, for a required reduction in sample stagnation

Table 1 Summary of model inputs and calculated results

Case	$P_{o-\mathrm{MPa}}$	$T_{o-\mathrm{K}}$	$D_{o-\mathrm{cm}}$	A/A_o	M_{IDL}	α deg	$L_{\max}$ cm[a]	P_o/P_o[b]	$T_{T_{\min}}$K[c]
1	0.1	2000	0.2	9.1	3.5	4	18.8	0.085	1229
2	0.1	3000	0.2	9.1	3.5	4	11.0	0.090	2038
3	1.0	2000	0.2	9.1	3.5	4	24.6	0.091	1386
4	1.0	3000	0.2	9.1	3.5	4	23.6	0.088	1975
5	0.1	2000	0.1	9.1	3.5	4	4.0	0.095	1514
6	0.1	3000	0.1	9.1	3.5	4	2.4	0.099	2462
7	1.0	2000	0.1	9.1	3.5	4	10.0	0.093	1437
8	1.0	3000	0.1	9.1	3.5	4	9.5	0.091	2067
9	0.1	2000	0.5	9.1	3.5	4	47.3	0.088	1301
10	0.1	3000	0.5	9.1	3.5	4	51.8	0.082	1720
11	1.0	2000	0.5	9.1	3.5	4	60.0	0.103	1445
12	1.0	2000	0.5	9.1	3.5	4	60.0	0.100	2039
13	0.1	2000	0.2	9.1	3.5	4	20.0	0.083	1164
14	0.1	2000	0.2	9.1	3.5	4	20.6	0.082	1131
15	0.1	2000	0.2	5.2	3.5	4	23.9	0.130	912
16	0.1	2000	0.2	15.9	4.0	4	17.2	0.053	1441
17	0.1	2000	0.2	1.2	1.5	4	1.6	0.797	1810
18	0.1	2000	0.2	1.8	2.0	4	4.0	0.505	1623
19	0.1	2000	0.2	3.0	2.5	4	8.5	0.280	1396
20	0.1	2000	0.2	6.9	3.27	4	20.6	0.106	1091
21	0.1	2000	0.5	3.9	2.75	4	15.2	0.191	1134
22	0.1	3000	0.2	5.2	3.0	4	10.1	0.157	1992
23	0.1	3000	0.2	3.0	2.5	4	8.7	0.273	1986
24	1.0	2000	0.2	5.2	3.0	4	16.7	0.167	1504
25	1.0	2000	0.2	3.0	2.5	4	10.4	0.305	1645
26	0.1	3000	0.2	15.9	4.0	4	11.6	0.052	2120
27	0.1	3000	0.2	1.2	1.5	4	4.6	0.706	2139
28	0.1	3000	0.2	1.8	2.0	4	6.9	0.460	2023
29	1.0	2000	0.2	15.9	4.0	4	34.1	0.050	1301
30	1.0	2000	0.2	16.6	4.5	4	34.8	0.048	1296
31	1.0	3000	0.2	1.8	2.0	4	5.2	0.528	2645
32	1.0	3000	0.2	5.2	3.0	4	15.9	0.164	2171
33	1.0	3000	0.2	16.6	4.5	4	33.7	0.047	1824

[a] Distance from probe orifice to end of constant area section; calculation terminated if L attained a value of 60.0 cm.
[b] Ratio of back pressure to ambient stagnation pressure
[c] Sample gas stagnation temperature at L

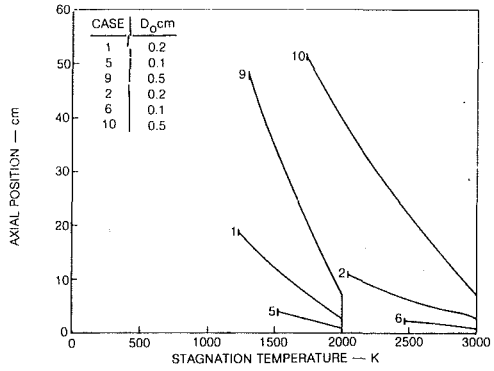

Fig. 2 Effect of probe orifice diameter on length of supersonic section of probe—P_T = 0.1 MPa

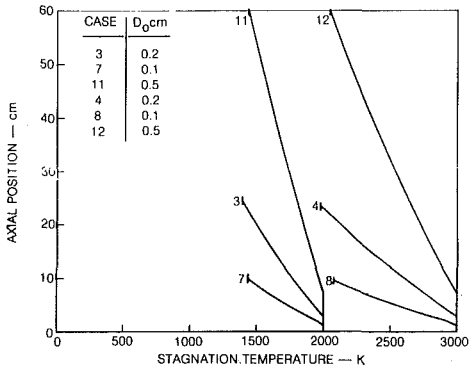

Fig. 3 Effect of probe orifice diameter on length of supersonic section of probe—P_T = 1.0 MPa

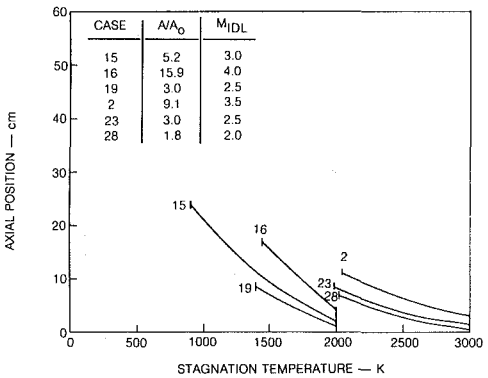

Fig. 4 Effect on tip region area ratio on length of supersonic section of probe

temperature prior to the occurrence of the shock system, and for a required sample flow rate.

For a given reduction in stagnation temperature, the calculated results shown in Figs. 2 and 3 indicate that the required length of the supersonic flow section of the probe increases with increasing ambient stagnation pressure and orifice diameter. The effect of ambient stagnation temperature on length is not clear. As the ambient stagnation temperature increases, the mass flow rate of the sample decreases and the amount of energy that must be extracted from the sample to achieve a specified reduction in stagnation temperature increases. At the same time, the ability of the coolant to extract heat from the sample (*i*) may increase due to the larger difference between the recovery temperature of the sample and the coolant or (*ii*) may decrease due to the reduction in sample heat transfer coefficient due to a reduction in sample Reynolds number. Assuming that the sample heat transfer coefficient is representative of the overall heat transfer coefficient and that the flow within the probe is turbulent (the latter is true for all calculations described in this section), then it can be shown that L increases as the ambient stagnation temperature increases. For the flow conditions assumed here, a probe designed to reduce the sample stagnation temperature from 2000 K to a specified value may be incapable of reducing the sample stagnation temperature from 3000 K to the same specified value. The calculated results for an ambient stagnation temperature of 3000 K indicate that the minimum stagnation temperature that can be achieved prior to the end of the supersonic flow section is (approximately) 1900 K. For a kinetic process with an apparent activation energy of 30 Kcal/mole, this temperature decrease reduces reaction rates by a factor of 20. While this reduction in reaction rates is substantial, the static temperatures of the flow may still be high enough for reactions to occur in the subsonic section of the probe or in the sample transfer line. Whether reactions occurring in the subsonic region are important can only be determined by combining the results of the appropriate aerodynamic model with a detailed kinetics analysis.

As the ambient stagnation pressure or the probe orifice diameter increases, the sample mass flow rate increases so that more heat must be extracted from the sample to achieve the desired reduction in stagnation temperature; therefore, L increases.

Effect of Tip Area Ratio. The calculated distance (L) from the probe orifice to the end of the constant area (supersonic flow) section of the probe is plotted as a function of stagnation temperature in Fig. 4 for a fixed ambient stagnation pressure and orifice diameter, but for various tip geometric area ratios (or, equivalently, ideal Mach numbers); calculations are presented for values of ambient stagnation temperature of 2000 K and 3000 K. For a specified ambient stagnation temperature, the greatest reduction in sample stagnation temperature is achieved at an intermediate area ratio of approximately 5 for an ambient stagnation temperature of 2000 K and approximately 3 for an ambient stagnation temperature of 3000 K. As the area ratio decreases (relative to these extrema), the length required to achieve a given reduction in sample stagnation temperature decreases whereas the minimum achievable stagnation temperature increases. As the area ratio increases beyond the optimal value, both the distance required to achieve a given reduction in stagnation temperature and the minimum achievable stagnation temperature increases. For a fixed mass flow rate, the heat transfer *rate* decreases as the local diameter of the probe increases. Since sample passage diameter increases with increasing tip region area ratio, the length required to achieve a given reduction in sample stagnation temperature (to extract a given amount of heat from the sample) increases with increasing tip region area ratio as shown in Fig. 4. The Mach number at the entrance of the first constant area section increases with increasing tip region area ratio. While friction forces (which are proportional to M^2) are larger in higher Mach number flows, a larger reduction of Mach number is required to choke such flows. Friction forces reduce the local stagnation pressure thereby decreasing the local supersonic Mach number; for a given mass flow rate, a larger value of sample stagnation pressure is associated with a larger value of supersonic Mach number.

Calculations were also performed for an ambient stagnation pressure of 1.0 MPA and ambient stagnation temperature of 2000 K over the same range of tip region area ratio as summarized in Fig. 4 (see Cases 3, 24, 25, 29, and 30 in Table 1). No extremum in geometric parameter L or required back pressure was determined by the model for the assumed ambient conditions throughout this range of area ratios. The value of L for a required change in stagnation temperature decreases with increasing tip region area ratio. Examination of the calculated results presented in Table 1

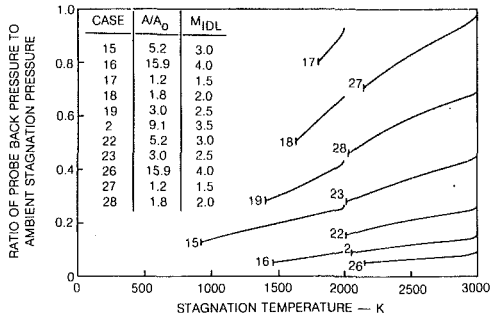

Fig. 5 Effect of tip region area ratio on minimum probe back pressure

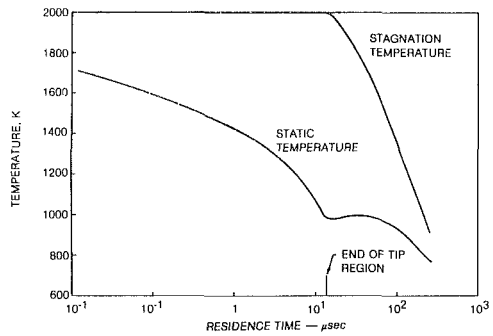

Fig. 6 Sample gas temperatures—time variation for Case 15

indicates that an area ratio of (approximately) 16 may be near optimum.

In order to maintain the supersonic flow thoughout the required length of the first constant area section (as determined, for example, from Fig. 4), it is necessary to maintain the back pressure on the sample below some minimum value. Calculated back pressures corresponding to the cases shown in Fig. 4 are depicted in Fig. 5. In these calculations, it has been assumed that the back pressure is the stagnation pressure behind a normal shock located at the end of the required constant area section. Stagnation pressure losses due to the sudden expansion of the resulting subsonic flow at the end of the constant area section or due to friction in the subsonic section of the probe and transfer line have been neglected; in any case, these losses generally are only a few percent of the overall stagnation pressure loss. For a practical gas sampling system, variations in pumping system capability must be considered; that is, it should be assumed for design purposes that the shock occurs at some low value of supersonic Mach number ($\sim$ 1.2). As an example of the variation in required back pressure, assume that a reduction is desirable in the stagnation temperature at the end of the supersonic flow section to (say) 1450 K. From Fig. 5, it can be determined that the required back pressure ratio is between 0.05 and 0.28, depending on the value of tip region area ratio for an ambient stagnation temperature of 2000 K. Furthermore, there is no back pressure which will permit a calculated reduction of sample stagnation temperature from 3000 to 1450 K.

The required back pressure to obtain a specified stagnation temperature is essentially invariant with changes in orifice diameter for a fixed tip region area ratio, divergence half-angle and stagnation conditions. For example, the calculated back pressures for a given stagnation temperature are similar for Cases 1, 5, and 9 (Table 1). Generalization of this result for conditions other than those examined in this paper is not possible. For example, if the orifice diameter is sufficiently small, the flow within the probe will be laminar; the flow within the probe is turbulent for all conditions considered in this study. Skin friction and heat transfer coefficients have substantially different values in laminar and turbulent flows.

Effect of Tip Divergence Half-Angle. Examination of Table 1 for Cases 1, 13, and 14 indicates that the effect of tip divergence half-angle is relatively small on both the maximum achievable reduction in sample stagnation temperature and the corresponding minimum back pressure. Since heat transfer within the tip region was assumed to be negligible for these calculations, the differences in calculated results may be due simply to variations in the length of the adiabatic probe section. Consequently, if the flow within the tip region does not separate, changes in tip divergence half-angle result in negligible changes in overall probe performance. Whether the flow separates in the tip region can best be determined using the calculated flow profiles together with an appropriate viscous flow (e.g., boundary layer) analysis.

Calculated Quenching Rates. Static and stagnation temperature quenching rates can be determined from calculated profiles of static and stagnation temperature with sample gas residence time such as those presented in Fig. 6. The gas static temperature is reduced to a relatively low value ($<$ 1000 K from 2000 K) within a few microseconds as the flow is accelerated supersonically. The stagnation temperature is reduced at a slower rate by heat transfer to the coolant. For the cases considered here, no reduction in stagnation temperature occurs within the adiabatic tip region. Assume that the chemical reactions of interest are quenched below a static temperature of 1200 K. Thus, for the flow conditions depicted in Fig. 6, an aerodynamic quench is achieved with 6 μs. Supersonic flow must be maintained until the stagnation temperature is reduced to 1200 K; e.g., until 140 μs. From Fig. 4 (Case 15), it can be determined that the constant area section can therefore be terminated 16 cm from the probe orifice.

Summary

A one-dimensional model has been described and used to predict the performance of probes designed to achieve an aerodynamic quench. The calculated probe performance (maximum achievable reduction in sample stagnation temperature within the length of the supersonic flow section of the probe) is a strong function of ambient stagnation conditions, probe orifice diameter, and tip region area ratio, but is only a weak function of probe tip divergence half-angle. The minimum back pressure required to sustain supersonic flow is a strong function of the tip region area ratio but appears to be insensitive to variations in orifice diameter for otherwise fixed geometric and ambient conditions for the range of parameters examined in this study.

Experimental results [6, 12] and the model indicate that aerodynamically quenching gas sampling probes can be designed, constructed, and operated successfully but the complexities of probe design construction and operation are more severe than indicated previously [13, 14]. Probes designed to achieve an aerodynamic quench must contain a divergent tip that makes a smooth transition to the first constant area section which is terminated by a sudden enlargement in flow area. The sudden expansion provides a means of stabilizing a shock system and minimizing additional pressure losses in the subsonic section of the probe. Construction of such probes is somewhat complicated by the geometric requirements of the tip region and by the desirability to install sufficient instrumentation to assure that an aerodynamic quench has been achieved. The calculated results indicate that the probe may be incapable of achieving an aerodynamic quench for all ambient conditions of interest; in any case, the required back pressure is quite low and may be lower than the pressure achievable by the pumping system.

References

1 Tine, G., *Gas Sampling and Chemical Analyses in Combustion Processes*, Pergamon Press, Oxford, 1961.

2 Fristrom, R. M., Prescott, R., and Grunfelder, C., *Combustion and Flame*, Vol. 1, 1957, pp. 102–113.

3 Kramlich, J. C., and Malte, P. C., *Combustion Science and Technology*, Vol. 18, 1978, pp. 91–104.

4 Hori, M., *Combustion Science and Technology*, Vol. 23, 1980, p. 131.

5 Hargreaves, K. J. A., Harvey, R., Roper, F. G., and Smith, D. B., *Eighteenth Symposium (International) on Combustion*, The Combustion Institute, Pittsburgh, 1981.

6 Colket, M. B., Chiappetta, L., Guile, R. N., Zabielski, M. F., and Seery, D. J., "Internal Aerodynamics of Gas Sampling Probes," *Combustion and Flame*, Vol. 44, 1982, pp. 3–14.

7 Shapiro, A. H., *The Dynamics and Thermodynamics of Compressible Fluid Flow*, Vol. I, Ronald Press, 1953.

8 Kays, W. M., "Numerical Solutions for Laminar-Flow Heat Transfer in Circular Tubes," ASME *Transactions*, Vol. 77, 1965, pp. 1265–1274.

9 Rohsenow, W. M., and Choi, H. Y., *Heat, Mass, and Momentum Transfer*, Prentice-Hall, Englewood Cliffs, N.J., 1961, p. 192.

10 Eckert, E. R. G., and Drake, R. M., *Heat and Mass Transfer*, McGraw-Hill, New York, 1959.

11 "Ducts, Nozzles and Diffusers," Section 17, *Handbook of Supersonic Aerodynamics*, Bureau of Naval Weapons, NAVWEPS Report 1488, Vol. 6, Jan. 1964.

12 Colket, M. B., Zabielski, M. F., Chiappetta, L., Dodge, L. G., Guile, R. N., and Seery, D. J., "Nitric Oxide Measurement Study: Probe Methods," Task II Report, DOT-FAA Report for Contract FA77WA-4081, Nov. 1979.

13 Fristrom, R. M., and Westenberg, A. A., *Flame Structure*, McGraw-Hill, New York, 1965.

14 Lengelle, G., and Verdier, C., "Gas Sampling and Analysis in Combustion Phenomena," AGARD-AC-168, July 1973.

ERRATA

Corrections to "A Correlation Theory for Steady Natural Convective Heat Transport in Horizontal Annuli," by R. D. Boyd, published in the February 1983 issue of the ASME JOURNAL OF HEAT TRANSFER, pp. 144–150.

$$\overline{\mathrm{Nu}}_{\Delta} \equiv \left.\frac{\overline{\partial T_i}}{\partial y_n}\right|_{y=0} \frac{\Delta'}{(T_i' - T_o')}$$

$$= \sum_{j=1}^{\infty} \lambda_j \gamma^{(j-1)} \mathrm{Ra}_{T_i}^{(2-j)/4}, \tag{15}$$

where

$$\mathrm{Ra}_{R_i} = \beta g T_i^* R_i^3 \alpha^{-1} \nu^{-1}, T_i^* = (T_i' - T_o')(1+\xi^{-1})^{-1}$$

$$R_i^3 = (1+\xi^{-1})^{-4} (r_i')^{-1} (\Delta')^4, \xi = C^{*-1} \left(\frac{r_o'}{r_i'}\right)^{-1/5} = C^{*-1}\xi^*$$

$$\lambda_j =$$

$$\mathrm{Pr}^{-(2-j)/4} \left[\int_o^{\pi} f_i d\phi\right]^{-1} \left[\int_o^{\pi} \theta_{j_i}'(o) \left(\int_o^{\phi_i} f_i d\phi_i\right)^{3(2-j)/4-1} d\phi_i\right]$$

$$\gamma = (1+\xi^{-1})^{-1} \Delta'/r_i'$$

Journal of Heat Transfer

Technical Notes

This section contains shorter technical papers. These shorter papers will be subjected to the same review process as that for full papers.

Fully Developed Laminar Heat Transfer in Circular Sector Ducts With Isothermal Walls

A. C. Trupp[1] and A. C. Y. Lau[1]

Nomenclature

A_f = cross-sectional area of circular sector duct, ϕr_0^2
c_p = specific heat at constant pressure
D_h = equivalent hydraulic diameter, $2\phi r_0/(1+\phi)$
f = Fanning friction factor, $D_h(-dP/dx)/(2\rho u_b^2)$
f^* = $(\pi^2 \rho r_0^5/\dot{m}^2)(-dP/dx)$
$\bar{h}$ = average heat transfer coefficient at solid-fluid interface, $\bar{q}/(t_w - t_b)$
h^* = $\bar{q}_w/(t_w - t_b)$
H = dimensionless fin height, l/r_0
k = thermal conductivity of fluid
l = fin height
$\dot{m}$ = total mass flow rate through entire (partitioned/finned) tube
M = number of equispaced fins
Nu = average Nusselt number, $\bar{h}D_h/k$
Nu* = $h^*(2r_0)/k$
P = pressure
P_w = wetted perimeter of circular sector duct, $2r_0(1+\phi)$
$\bar{q}$ = overall average heat flux, $Q/(MP_w)$
$\bar{q}_w$ = $Q/(2\pi r_0)$
Q = total heat transfer rate for entire (partitioned/finned) tube
r = radial coordinate
r_0 = radius of tube
R = dimensionless radial coordinate, r/r_0
Re = Reynolds number, $\rho u_b D_h/\mu$
Re* = $2\dot{m}/(\pi r_0 \mu)$
t = temperature
T = dimensionless temperature, $(t - t_w)/(\bar{q}_w r_0/k)$
u = axial velocity
U = dimensionless axial velocity, $u/[(r_0^2/\mu)(-dP/dx)]$
x = axial coordinate
β = half the angle subtended by one fin
θ = angular coordinate
μ = dynamic viscosity
ρ = density
ϕ = half the apex angle of a circular sector duct

Subscripts

b = bulk
w = wall
$H1$ = uniform heat input axially, uniform temperature peripherally
T = uniform temperature axially and peripherally

Introduction

The circular sector duct (see inset to Fig. 1 for cross section) has received renewed attention in recent years, since it forms a limiting case for internally finned tubes (full tapered fins) and is expected to be a common element in multipassage tubes. Certain characteristics of fully developed laminar flow of a constant properties fluid through straight circular sector ducts have been known for some time. Values for fRe for $0 \le \phi \le \pi/2$ have been documented by Shah and London [1]. Furthermore, Soliman and Feingold [2] have provided analytical solutions for axial velocity distribution, bulk velocity, and f^*Re*. Regarding heat transfer, results are available for average Nusselt number for $0 \le \phi \le \pi/2$ for the case of uniform heat input axially and uniform temperature at any cross section (Nu_{H1}). These results have been documented in [1] and are shown in Fig. 1 for later comparison. These results have also been confirmed (for various ϕ) by both Masliyah and Nandakumar [3] and by Soliman and Feingold [4] in connection with their work on internally finned tubes. Apart from these results, it appears that there are no published solutions for other thermal boundary conditions, except for the case of uniform heat flux in both the axial and peripheral directions, for which the results are also provided in [1]. Recently, in our work on internally finned tubes, results were obtained [5] for the case of constant temperature in both the axial and peripheral directions (Nu_T). Following essentially the same finite difference procedure, results for this boundary condition were obtained for circular sector ducts for 4 deg $\le \phi \le$ 90 deg. The purpose of this technical note is simply to communicate our results for average Nusselt number.

Analysis

For fully developed laminar flow of a constant properties fluid subject to negligible body forces, the governing momentum equation is

[1]Department of Mechanical Engineering, University of Manitoba, Winnipeg, Manitoba, Canada R3T 2N2

Contributed by the Heat Transfer Division for publication in the JOURNAL OF HEAT TRANSFER. Manuscript received by the Heat Transfer Division May 22, 1983.

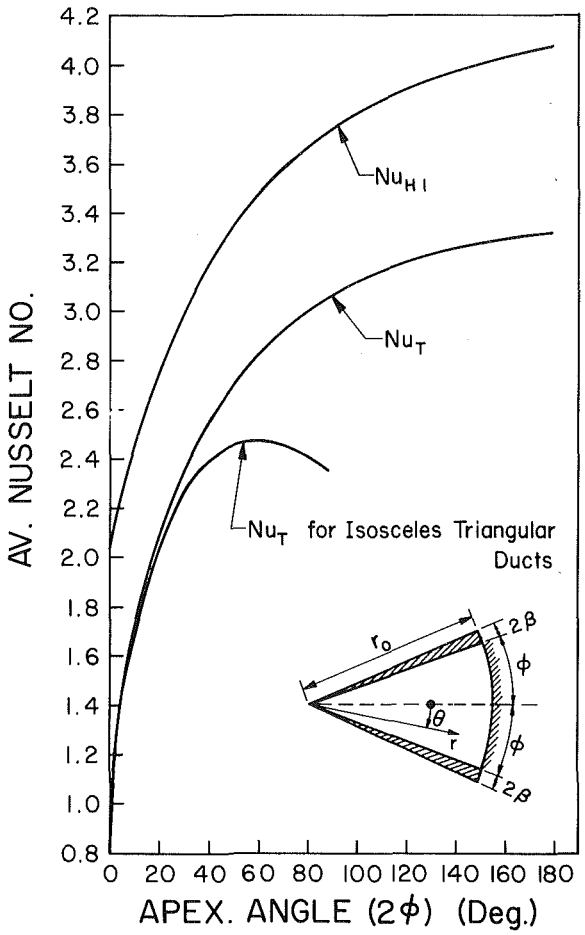

Fig. 1 Circular sector ducts – fully developed laminar heat transfer

$$\frac{1}{r}\frac{\partial}{\partial r}\left(r\frac{\partial u}{\partial r}\right)+\frac{1}{r^2}\frac{\partial^2 u}{\partial\theta^2}=\frac{1}{\mu}\frac{dP}{dx} \tag{1}$$

Nondimensionalizing, using quantities defined in the Nomenclature, results in

$$\frac{1}{R}\frac{\partial}{\partial R}\left(R\frac{\partial U}{\partial R}\right)+\frac{1}{R^2}\frac{\partial^2 U}{\partial\theta^2}=-1 \tag{2}$$

Using tapered fins as in [2], identical circular sector ducts can be obtained by partitioning a circular tube (of radius r_0) by M equispaced full fins ($H=1$) of thickness 2β. In this context, both f^* and Re* are meaningful [2], and the product f^* Re* is a "tube" property and a function of M and β. On the other hand, the product fRe for a circular sector duct is a function only of ϕ. It can be easily shown that fRe and f^*Re* are related by:

$$\frac{f\mathrm{Re}}{f^*\mathrm{Re}^*}=\frac{D_h^2 M A_f}{4\pi r_0^4}=\frac{(\pi-M\beta)^3}{\pi(\pi+M-M\beta)^2}=\frac{\phi^3}{(\phi+\beta)(1+\phi)^2} \tag{3}$$

For the heat transfer, as already mentioned, Nu_T values were sought for circular sector ducts. For fully developed flow of a constant properties fluid with axial conduction and viscous dissipation both negligible, the governing energy equation is

$$\frac{1}{r}\frac{\partial}{\partial r}\left(r\frac{\partial t}{\partial r}\right)+\frac{1}{r^2}\frac{\partial^2 t}{\partial\theta^2}=\frac{\rho c_p}{k}u\frac{\partial t}{\partial x} \tag{4}$$

Again nondimensionalizing, for a fully developed temperature profile ($\partial T/\partial x=0$), equation (4) becomes:

$$\frac{1}{R}\frac{\partial}{\partial R}\left(R\frac{\partial T}{\partial R}\right)+\frac{1}{R^2}\frac{\partial^2 T}{\partial\theta^2}=f^*\mathrm{Re}^* UT/T_b \tag{5}$$

It can be shown that $\mathrm{Nu}^*_T=-2/T_b$, but (again) whereas Nu^*_T is a "tube" property and a function of M and β, Nu_T for a circular sector duct is a function of ϕ alone. The relationship between Nu_T and Nu^*_T is given by

$$\frac{\mathrm{Nu}_T}{\mathrm{Nu}^*_T}=\frac{\pi D_h}{MP_w}=\frac{\pi(\pi-M\beta)}{(\pi+M-M\beta)^2}=\frac{\phi(\phi+\beta)}{(1+\phi)^2} \tag{6}$$

It follows from (3) and (6), for $\beta=0$, that

$$\frac{f\mathrm{Re}}{f^*\mathrm{Re}^*}=\frac{\mathrm{Nu}_T}{\mathrm{Nu}^*_T}=\left[\frac{\phi}{1+\phi}\right]^2 \tag{7}$$

For the circular sector duct, geometric symmetry reduces the solution domain to $0\le\theta\le\phi$. This region was fitted with a uniform 20 × 20 grid. The adequacy of this mesh size for fluid flow was tested by solving (2) (recast in finite difference form) subject to $U=0$ at the solid walls and $\partial U/\partial\theta=0$ on the symmetry line ($\theta=0$). The results for local velocity and f^*Re* for the six ducts tested (ϕ from 4 deg to 90 deg) were in good agreement with the analytical results of [2]. However, in order to maximize accuracy, it was decided to employ the analytical results [2] (for f^*Re* and U) directly in (5). Before proceeding with the solution to (5), the adequacy of the mesh for heat transfer was tested by solving for the case of uniform heat input axially and uniform temperature at any cross section. The governing equation (no net axial conduction now) is identical to (5) except that the right-hand-side product consists only of f^*Re*U. The results for Nu_{H1} were within 0.4 percent of the values tabulated in [1] for the ten cases of ϕ between 4 deg and 90 deg. Finally, equation (5) was solved subject to $T=0$ at the walls and $\partial T/\partial\theta=0$ at $\theta=0$. Using an iterative procedure, the temperature field was taken to be converged when changes in T between successive iterations (ΔT) achieved values of $\Delta T<0.0001T$ for all nodes.

Results and Discussion

The results for Nu_T for fifteen cases are listed in Table 1 and plotted in Fig. 1. As expected, $\mathrm{Nu}_T<\mathrm{Nu}_{H1}$ for a given circular sector duct. In fact, with increasing ϕ, the ratio $\mathrm{Nu}_{H1}/\mathrm{Nu}_T$ (see Table 1) first decreases monotonically from a value of 1.50 at $\phi=4$ deg to 1.23 at $\phi=30$ deg, and then remains almost constant at about 1.23. The latter is close to the value 1.19, which is the corresponding ratio for circular tubes ($\phi=180$ deg).

For a circular sector duct, as $\phi\to 0$, it is logical to expect the heat transfer to be the same as for an isosceles triangular duct. Hence the Nu_T curve in Fig. 1 has been extended from $\phi=4$ deg to the value $\mathrm{Nu}_T=0.943$ at $\phi=0$ [1]. Furthermore, using data reported in [1], the curve for Nu_T for isosceles triangular ducts has been included in Fig. 1 for comparison. For the same ϕ and r_0, an isosceles triangular duct differs from a circular sector duct only in that the circular arc side is replaced by its chord. As can be seen in Fig. 1, for small ϕ, the Nusselt numbers differ only slightly, as would be expected. But as ϕ increases, Nu_T for the circular sector duct continues to progressively exceed that for the isosceles triangular duct. This behavior is probably due mainly to increased heat transfer in the base corners. For circular sector ducts, these corner angles remain at 90 deg but equal $(90-\phi)$ for isosceles triangular ducts.

The present Nu_T results for circular sector ducts can be described by

$$\begin{aligned}\mathrm{Nu}_T&=0.943+2.714[1-\exp\{-1.89(\phi)^{0.729}\}],0\le\phi\le 0.655\\&=0.943+2.714[1-\exp\{1.68(\phi)^{0.453}\}],0.655\le\phi\le\pi/2\end{aligned} \tag{8}$$

Equation (8) reproduces the Nu_T values listed in Table 1 to within 0.75 percent. It is also of interest to note for circular sector ducts that fRe is given by

$$f\mathrm{Re}=12+4[1-\exp\{-1.50(\phi)\}] \tag{9}$$

Table 1 Circular sector ducts – average Nusselt numbers (Nu_T)

2ϕ	Nu_T	Nu_{H1}/Nu_T
8	1.586	1.50
10	1.686	1.45
15	1.898	1.38
20	2.072	1.33
30	2.342	1.28
36	2.469	1.26
40	2.543	1.25
45	2.625	1.24
60	2.819	1.23
72	2.932	1.22
80	2.993	1.22
100	3.108	1.22
120	3.188	1.22
160	3.285	1.23
180	3.316	1.23

to well within 1 percent for $0 \leq \phi \leq \pi/2$, whereas for the same range, Nu_{H1} is given (within about 3 percent) by

$$Nu_{H1} = 2.059 + 2.305[1 - \exp\{-1.74(\phi)] \quad (10)$$

Note: ϕ is in radians for equations (8-10).

Acknowledgment

This research was supported by the Natural Sciences and Engineering Research Council of Canada.

References

1 Shah, R. K., and London, A. L., "Laminar Flow Forced Convection in Ducts," *Advances in Heat Transfer*, Supplement 1, Academic Press, 1978.

2 Soliman, H. M., and Feingold, A., "Analysis of Fully Developed Laminar Flow in Longitudinal Internally Finned Tubes," *The Chemical Engineering Journal*, Vol. 14, 1977, pp. 119-128.

3 Masliyah, J. H., and Nandakumar, K., "Heat Transfer in Internally Finned Tubes," ASME JOURNAL OF HEAT TRANSFER, Vol. 96, 1976, pp. 257-261.

4 Soliman, H. M., and Feingold, A., "Analysis of Heat Transfer in Internally Finned Tubes Under Laminar Flow Conditions," *Proc. 6th Int. Heat Transfer Conf.*, Vol. 2, 1978, pp. 571-576.

5 Soliman, H. M., Chau, T. S., and Trupp, A. C., "Analysis of Laminar Heat Transfer in Internally Finned Tubes With Uniform Outside Wall Temperature," ASME JOURNAL OF HEAT TRANSFER, Vol. 102, 1980, pp. 598-604.

Melting Around a Horizontal Heated Cylinder: Part II – Numerical Solution for Isothermal Boundary Condition

J. Prusa[1] and L. S. Yao[2]

Introduction

Many important problems in engineering science, when formulated in mathematical terms, involve very irregularly shaped boundaries which move with time. Such problems require that the position of the boundaries be determined as part of the solution. Obvious examples can be found in the growth of crystals, in phase-change, bubble dynamics, cavitation, surface waves, combustion, and in compressible flow problems. Irregular, moving boundaries cause enormous complications by adding extra dependent variables to a given analysis and by making it more difficult to apply boundary conditions. This study solves a typical engineering problem that involves an irregular moving boundary – the melting of a solid about an isothermally heated horizontal cylinder. The complications introduced by irregular moving boundaries are handled by using a transformation method. The boundaries in the physical plane are mapped into simple fixed geometric shapes in a transformed plane. Analysis is done in the simple fixed geometry of the transformed plane using an orthogonal coordinate system such as polar or Cartesian coordinates. In the physical plane, the elementary Cartesian or polar coordinates of the transformed plane form a curvilinear coordinate (generally nonorthogonal) system which grows with and precisely matches the irregular moving shapes of the boundaries. The curvilinear coordinates are called "natural coordinates" [1]. The net effect of these transformations is to reduce problems with complicated transient geometries to problems with simple and fixed geometries.

In the present study, the coordinate transformation used to determine the natural coordinates has the following form [2-7]:

$$r = \frac{\bar{r} - R_i}{R_o - R_i} + c \quad \text{and} \psi = \bar{\psi}$$

R_i and R_o are the radii of the inner and outer boundaries. In general, $R_i = R_i(\bar{\psi}, \bar{t})$ and $R_o = R_0(\bar{\psi}, \bar{t})$. In two dimensions, the transformation works by mapping the irregular moving physical domain into concentric circles in the transformed plane; c is a constant which determines the radii of the circular boundaries in the transformed plane. The natural coordinate system which is generated by the coordinate transformation is equivalent to the system generated by the body-fitted coordinate method [1]. However, since the present transformation is so simple, its use is not limited to numerical methods. It can be useful even in analytical methods (see [4, 5, 8]. This simplicity also means that in a numerical method, the exact calculation of the coordinate system requires an insignificant amount of computer time. This is in direct contrast to the body-fitted coordinate method. Finally, if R_i or R_o have fixed circular or spherical shapes, fewer extra terms are added to the transformed governing equations. Clearly, for enclosed geometries the radial transformation can exhibit greater efficiency than the method of body-fitted coordinates.

This work is primarily motivated by interest in demonstrating the use of a coordinate transformation method in engineering problems characterized by doubly connected regions. The transformation is very simple and can be used to generate natural coordinates for analytical methods. In the present melting problem, the transformation is used to generate natural coordinates for a numerical method. This requires a negligible increase in computer time. All of the terms generated by the transformation are kept in the governing equations, and as a result, the numerical method is not limited to small variations in the shape of the melt region (consequently, to small values of buoyancy force or heat transfer rates). Significant information on the melting process is generated for intervals of time far beyond the initial period that is conduction dominated. The solution is restricted to the case of an isothermally heated cylinder. The solution for the constant heat flux cylinder is given in [8]. The governing equations in the present work are also recast into forms which remove the initial singularity in the solution. This allows the numerical solution to begin immediately at the start of melting. A direct comparison is then made with solutions using an ad hoc starting method in order to demonstrate the errors which such methods introduce.

[1] Department of Mechanical Engineering, Iowa State University, Ames, Iowa 50011 Assoc. Mem. ASME

[2] Department of Mechanical and Aerospace Engineering, Arizona State University, Tempe, Ariz. 85203 Mem. ASME

Contributed by the Heat Transfer Division for publication in the JOURNAL OF HEAT TRANSFER. Manuscript received by the Heat Transfer Division January 13, 1983.

Table 1 Circular sector ducts – average Nusselt numbers (Nu_T)

2ϕ	Nu_T	Nu_{H1}/Nu_T
8	1.586	1.50
10	1.686	1.45
15	1.898	1.38
20	2.072	1.33
30	2.342	1.28
36	2.469	1.26
40	2.543	1.25
45	2.625	1.24
60	2.819	1.23
72	2.932	1.22
80	2.993	1.22
100	3.108	1.22
120	3.188	1.22
160	3.285	1.23
180	3.316	1.23

to well within 1 percent for $0 \leq \phi \leq \pi/2$, whereas for the same range, Nu_{H1} is given (within about 3 percent) by

$$Nu_{H1} = 2.059 + 2.305[1 - \exp\{-1.74(\phi)] \quad (10)$$

Note: ϕ is in radians for equations (8-10).

Acknowledgment

This research was supported by the Natural Sciences and Engineering Research Council of Canada.

References

1 Shah, R. K., and London, A. L., "Laminar Flow Forced Convection in Ducts," *Advances in Heat Transfer*, Supplement 1, Academic Press, 1978.

2 Soliman, H. M., and Feingold, A., "Analysis of Fully Developed Laminar Flow in Longitudinal Internally Finned Tubes," *The Chemical Engineering Journal*, Vol. 14, 1977, pp. 119-128.

3 Masliyah, J. H., and Nandakumar, K., "Heat Transfer in Internally Finned Tubes," ASME JOURNAL OF HEAT TRANSFER, Vol. 96, 1976, pp. 257-261.

4 Soliman, H. M., and Feingold, A., "Analysis of Heat Transfer in Internally Finned Tubes Under Laminar Flow Conditions," *Proc. 6th Int. Heat Transfer Conf.*, Vol. 2, 1978, pp. 571-576.

5 Soliman, H. M., Chau, T. S., and Trupp, A. C., "Analysis of Laminar Heat Transfer in Internally Finned Tubes With Uniform Outside Wall Temperature," ASME JOURNAL OF HEAT TRANSFER, Vol. 102, 1980, pp. 598-604.

Melting Around a Horizontal Heated Cylinder: Part II – Numerical Solution for Isothermal Boundary Condition

J. Prusa[1] and L. S. Yao[2]

Introduction

Many important problems in engineering science, when formulated in mathematical terms, involve very irregularly shaped boundaries which move with time. Such problems require that the position of the boundaries be determined as part of the solution. Obvious examples can be found in the growth of crystals, in phase-change, bubble dynamics, cavitation, surface waves, combustion, and in compressible flow problems. Irregular, moving boundaries cause enormous complications by adding extra dependent variables to a given analysis and by making it more difficult to apply boundary conditions. This study solves a typical engineering problem that involves an irregular moving boundary – the melting of a solid about an isothermally heated horizontal cylinder. The complications introduced by irregular moving boundaries are handled by using a transformation method. The boundaries in the physical plane are mapped into simple fixed geometric shapes in a transformed plane. Analysis is done in the simple fixed geometry of the transformed plane using an orthogonal coordinate system such as polar or Cartesian coordinates. In the physical plane, the elementary Cartesian or polar coordinates of the transformed plane form a curvilinear coordinate (generally nonorthogonal) system which grows with and precisely matches the irregular moving shapes of the boundaries. The curvilinear coordinates are called "natural coordinates" [1]. The net effect of these transformations is to reduce problems with complicated transient geometries to problems with simple and fixed geometries.

In the present study, the coordinate transformation used to determine the natural coordinates has the following form [2-7]:

$$r = \frac{\bar{r} - R_i}{R_o - R_i} + c \quad \text{and} \psi = \bar{\psi}$$

R_i and R_o are the radii of the inner and outer boundaries. In general, $R_i = R_i(\bar{\psi}, \bar{t})$ and $R_o = R_0(\bar{\psi}, \bar{t})$. In two dimensions, the transformation works by mapping the irregular moving physical domain into concentric circles in the transformed plane; c is a constant which determines the radii of the circular boundaries in the transformed plane. The natural coordinate system which is generated by the coordinate transformation is equivalent to the system generated by the body-fitted coordinate method [1]. However, since the present transformation is so simple, its use is not limited to numerical methods. It can be useful even in analytical methods (see [4, 5, 8]. This simplicity also means that in a numerical method, the exact calculation of the coordinate system requires an insignificant amount of computer time. This is in direct contrast to the body-fitted coordinate method. Finally, if R_i or R_o have fixed circular or spherical shapes, fewer extra terms are added to the transformed governing equations. Clearly, for enclosed geometries the radial transformation can exhibit greater efficiency than the method of body-fitted coordinates.

This work is primarily motivated by interest in demonstrating the use of a coordinate transformation method in engineering problems characterized by doubly connected regions. The transformation is very simple and can be used to generate natural coordinates for analytical methods. In the present melting problem, the transformation is used to generate natural coordinates for a numerical method. This requires a negligible increase in computer time. All of the terms generated by the transformation are kept in the governing equations, and as a result, the numerical method is not limited to small variations in the shape of the melt region (consequently, to small values of buoyancy force or heat transfer rates). Significant information on the melting process is generated for intervals of time far beyond the initial period that is conduction dominated. The solution is restricted to the case of an isothermally heated cylinder. The solution for the constant heat flux cylinder is given in [8]. The governing equations in the present work are also recast into forms which remove the initial singularity in the solution. This allows the numerical solution to begin immediately at the start of melting. A direct comparison is then made with solutions using an ad hoc starting method in order to demonstrate the errors which such methods introduce.

[1] Department of Mechanical Engineering, Iowa State University, Ames, Iowa 50011 Assoc. Mem. ASME

[2] Department of Mechanical and Aerospace Engineering, Arizona State University, Tempe, Ariz. 85203 Mem. ASME

Contributed by the Heat Transfer Division for publication in the JOURNAL OF HEAT TRANSFER. Manuscript received by the Heat Transfer Division January 13, 1983.

Analysis

The analysis begins by considering the equations for unsteady laminar flow in polar coordinates. The dependent variables are vorticity, streamfunction, and temperature. The independent variables are radius, angular coordinate, and time. The radius of the liquid-solid boundary, R, is a fourth dependent variable in the phase-change problem. A fourth governing equation must be determined for R – it is found by considering the energy balance in a control system at the interface. The complete mathematical description also requires initial and boundary conditions. At time zero the heating of the solid phase begins. Instantaneously, a concentric annular melt region of infinitesimal thickness appears around the heated cylinder. The sudden appearance of liquid phase corresponds to a singularity in the governing equations at time zero.

Nonsingular Nondimensionalization. The radial coordinate is nondimensionalized so that the outer boundary formed by the liquid-solid interface, at $\bar{r}=R$, is transformed into the unit circle, $r=1$. The inner boundary, $\bar{r}=a$, is transformed into the pole, $r=0$. This constitutes the coordinate transformation. In dimensionless form, the radial distance from the inner cylinder to the interface is measured by the gap function, Z. When the cylinder is heated so as to maintain a constant surface temperature, the singularity in the governing equations at time zero is of order $t^{1/2}$ [9]. Consequently, in order to remove the singularity from the governing equations, $t^{1/2}$ is factored out of the gap function. The coordinate transformation then takes on the following form

$$r = \frac{\bar{r}-a}{aZ(2t)^{1/2}}, \psi=\bar{\psi}, t=\bar{t}/(a^2/\alpha) \qquad \text{(coordinates)} \qquad (1a)$$

$$Z = (R-a)/a(2t)^{1/2} \qquad \text{(gap function)} \qquad (1b)$$

The governing equations and boundary conditions are nondimensionalized using equation (1). The dimensionless initial conditions are found by letting $t=0$ in the governing equations and then solving for each of the four dependent variables. Details of the governing equations, initial conditions, and boundary conditions can be found in [7] and [10].

The method of approximating the dimensionless governing equations with finite difference equations follows that used in [11] and is explained in detail in [7]. Details of the computational procedure can also be found in [7]. Computations were performed with three values of the Stefan number: St = 0.02, 0.10, and 1.0.

Singular Nondimensionalization. Since the present numerical method makes accurate predictions beginning at time zero, it can be used to estimate the errors that result when false-starting techniques are used. Such techniques are required when the square root singularity is not removed from the governing equations. By using the coordinate transformation

$$r = \frac{\bar{r}-a}{aB}, \psi=\bar{\psi}, t=\bar{t}/(a^2/\alpha) \qquad \text{(coordinates)} \qquad (2a)$$

$$B = \frac{R-a}{a} \qquad \text{(gap function)} \qquad (2b)$$

in lieu of equation (1), the dimensionless governing equations can be cast into a singular dimensionless form. Note that early periods of time are of greatest interest for this comparison because the error that results from false-starting techniques decays with time [12]. At early times in the melting process, conduction is the dominant mode of heat transfer [5, 6]. As a result, flow variables need not be considered in examining the error introduced by false-starting techniques. The singular dimensionless equations (energy and gap function equations) are solved using an integral method. A parabolic profile is chosen to represent the temperature. Two of the coefficients in this profile are determined so that the isothermal boundary conditions are satisfied. The third coefficient, which is the temperature gradient along the heated cylinder, is an unknown function Γ, which must be determined by the integral method. Using this temperature profile, the singular equations are then integrated over the melt volume to produce ordinary differential equations for $\Gamma(t)$ and $B(t)$. Since $B=0$ when $t=0$, these two equations are singular at time zero ($1/B$ is a common term in the integrated equations). Accurate initial conditions at times greater than zero can be obtained from the results of the numerical method. When accurate initial conditions are supplied, the integral method duplicates the numerical predictions for Γ and B within 3 percent. Details of the integral method can be found in [10].

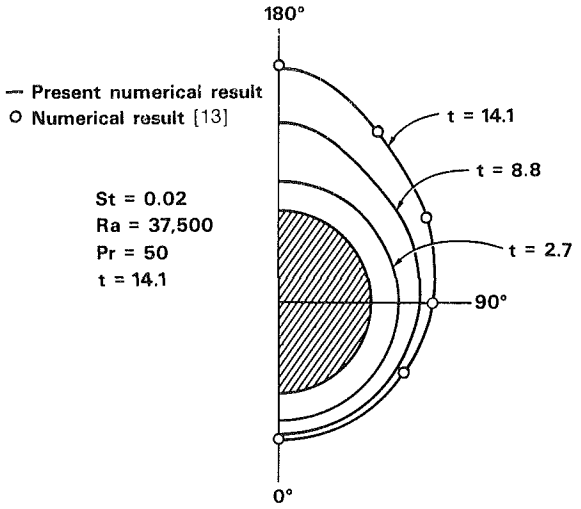

Fig. 1 Interface growth

Results and Discussion

The rate of growth of the melt region, its shape, and the heat transfer rates all depend upon the values of St, Ra, and Pr. The dependence upon Pr is the weakest. It has been found to be insignificant for natural convection phase-change problems for $7 \leq \text{Pr} \leq 50$ [2]. The influence which St or Ra have on the melting problem varies with time. Three distinct stages appear to occur in the melting process. In the first stage, heat transfer is dominated by conduction. As time advances, the melting process passes into a transition stage. Natural convection heat transfer becomes much more important. Finally a convection stage is reached, where natural convection is the dominant mode of heat transfer.

Growth of the Melt Region. The growth of the interface is illustrated in Fig. 1. In this figure, St = 0.02, Ra = 37,500, and Pr = 50. The position of the interface is shown at three different times. Although the interface is nearly a concentric circle at $t=2.7$, the melting process is actually in the transition stage between conduction and convection dominated modes of heat transfer. By $t=8.8$, an irregularly shaped interface now growing more rapidly above the heated cylinder than elsewhere indicates that the melting process is well into the natural convection stage. This localized rapid growth is due to the thermal plume formed by hot fluid separating away from the top of the heated cylinder. By $t=14.1$, the interface has become even more irregular in shape. Note that melting below the heated cylinder has slowed greatly compared to its earlier rate. The fluid motion is now rapidly convecting thermal energy away from this lower region. Comparison is made with

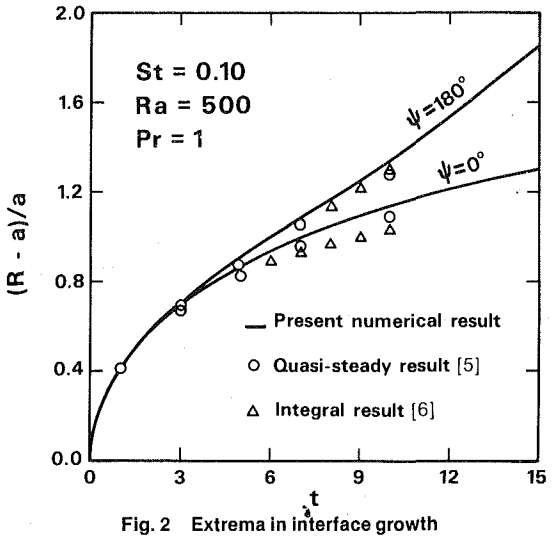

Fig. 2 Extrema in interface growth

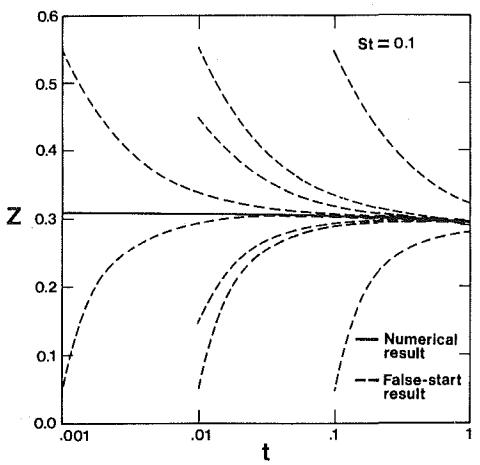

Fig. 3 Gap function errors resulting from incorrect initial conditions for the gap function

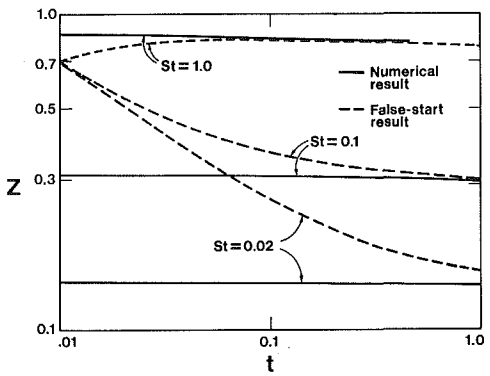

Fig. 4 Gap function errors resulting from false-starting technique using a linear temperature profile

the numerical results of [13]. The agreement appears to be very good.

The rate of melting depends most strongly upon the St. Larger values of St result in faster rates of melting. The shape of the melt region is determined largerly by Ra. The larger the Ra, the more irregular the interface. At a local level, the thermal plume above the cylinder is strengthened with Ra, while thermal energy is more readily convected away from the bottom of the cylinder. A greater amount of thermal energy is delivered to the top of the interface, while less is delivered to the bottom.

The present numerical results are also compared with the quasi-steady and integral solutions [5] and [6] in Fig. 2. Here the dimensionless radial length scale $(R-a)/a$ is compared at $\psi=0$ deg and 180 deg for $\mathrm{St}=0.10$, $\mathrm{Ra}=500$, and $\mathrm{Pr}=1$. This can be computed from the gap function according to: $(R-a)/a=Z(2t)^{1/2}$. This dimensionless length scale provides another measure of the interface position. $(R-a)/a$ grows most rapidly at $\psi=180$ deg, due to the thermal plume located at the top of the melt region. The numerical results provide a measure of the range of validity of the solutions [5, 6], which are based on the premise that natural convection effects are only a perturbation on a conduction dominated process. The integral method determines the interface position more accurately at $\psi=180$ deg, while the quasi-steady result is better at $\psi=0$ deg. On average, the quasi-steady result is slightly better. It has a maximum error of 5 percent at $t=10$. The integral solution has a maximum error of 5 percent at $t=5$. Overall, from Fig. 2, it can be observed that these short time solutions are very reasonable over the interval of time shown. This is because at these values of moderate St and low Ra, the melting process has advanced only to the intermediate stage of melting. Even at $t=15$, convection is still relatively weak. The short time solutions will diverge from the numerical result considerably once the final convection dominated stage has been reached.

Additional details of the numerical solution giving melt volume, average and local heat transfer rates, temperature distributions, and flow fields can be found in [7 and 10].

Comparison With False-Starting Results. The numerical result for the case $\mathrm{St}=0.1$ is compared with several false-starting solutions in Fig. 3. Correct initial conditions for the cylinder surface heat flux, Γ (based upon the numerical solution), have been used for the integral solution. However, the initial condition for the gap function, $Z=B/(2t)^{1/2}$, was systematically chosen to be higher or lower than the values specified by the numerical solution. Apparently the error introduced by the incorrect initial condition for Z decays very rapidly. By noting the four false-starting solutions which begin at $t=0.01$, one can observe that the rate of error decay increases with the magnitude of the error in the initial condition. Comparison of the false-starting solutions which begin with erroneous initial conditions of similar magnitude, but at different times, indicates that the rate of error decay depends only very weakly upon the temporal position of the initial condition.

In general, the correct initial condition for the surface heat flux, Γ, will not be known. As a result, the false-starting technique must also supply this initial condition. Figure 4 illustrates this more realistic case. Here, the integral solution is started when the melt region is 10 percent of the cylinder diameter, $B=0.1$. The time is set to $t=0.01$. In order to generate an initial condition for Γ, a linear temperature profile is assumed (a logarithmic profile produces almost identical results). In this case, the error in the gap function does not decay as rapidly as in Fig. 3. This is because the initial conditions for both Γ and B are now in error. Figure 4 indicates that errors due to false-starting techniques can be significant through a large portion of the conduction stage of the melting process.

Note that if the overheating degree is so large that the false-starting solution begins in the transition or convection dominated stage of melting, the error introduced by false-starting methods may be much more serious than what is demonstrated in Figs. 3 and 4. The asymptotic decay shown in these figures is based upon the assumption that convection has not yet become important.

Conclusion

This study presents a coordinate transformation method

which maps irregular moving boundaries into simple immobilized boundaries. The transformation is similar in spirit to the method of body-fitted coordinates, but is far simpler in practice. The utility of the transformation is demonstrated by using a numerical method to determine the solution to the melting problem about an isothermally heated horizontal cylinder. This problem is characterized by a singularity in the governing equations at time zero, due to sudden appearance of liquid phase when none existed the moment before. This singularity is extracted from the governing equations, allowing the numerical method to actually begin with the exact initial conditions at time zero. The numerical method is then used to illuminate the error resulting from a false-starting method that fails to properly consider the initial singularity. The present results indicate that false-starting errors can be significant.

References

1 Thompson, J. F., Thames, F. C., and Mastin, C. W., "Automatic Numerical Generation of Body-Fitted Curvilinear Coordinate System for Field Containing Any Number of Arbitrary Two-Dimensional Bodies," *Journal of Computational Physics*, Vol. 15, 1974, pp. 299-319.

2 Sparrow, E. M., Patankar, S. V., and Ramadhyani, S., "Analysis of Melting in the Presence of Natural Convection in the Melt Region," ASME JOURNAL OF HEAT TRANSFER, Vol. 99, 1977, pp. 520-526.

3 Solomon, J. M., Climent, M., and Ferguson, R. E., "Inviscid Flowfield Calculations for Re-Entry Vehicles With Control Surfaces," *AIAA Journal*, Vol. 15, 1977, pp. 1742-1749.

4 Yao, L. S., "Analysis of Heat Transfer in Slightly Eccentric Annuli," ASME JOURNAL OF HEAT TRANSFER, Vol. 102, 1980, pp. 279-284.

5 Yao, L. S., and Chen, F. F., "Effects of Natural Convection in the Melted Region Around a Heated Horizontal Cylinder," ASME JOURNAL OF HEAT TRANSFER, Vol. 102, 1980, pp. 667-672.

6 Yao, L. S., and Cherney, W., "Transient Phase-Change Around a Horizontal Cylinder," *International Journal of Heat and Mass Transfer*, Vol. 24, 1981, pp. 1971-1981.

7 Prusa, J., "A Spatial Stefan Problem Modified by Natural Convection: Melting Around a Horizontal Cylinder," Ph.D. dissertation, University of Illinois at Urbana-Champaign, 1983.

8 Prusa, J., and Yao, L. S., "Melting Around a Horizontal Heated Cylinder: Part II - Perturbation and Numerical Solutions For Constant Heat Flux Boundary Condition," Paper No. 83-HT-18, AIChE/ASME 21st National Heat Transfer Conference, Seattle, Wash., July 24-27, 1983.

9 Rubenstein, L. I., "The Stefan Problem," *Translations of Mathematical Monographs*, Vol. 27, 1971, pp. 1-15.

10 Prusa, J., and Yao, L. S., "Melting Around a Horizontal Heated Cylinder: Part I - Numerical Solution for Isothermal Boundary Condition," *Proceedings of the ASME-JSME Thermal Engineering Joint Conference*, March 20-24, 1983, Honolulu, Hawaii.

11 Prusa, J., and Yao, L. S., "Heat Transfer of Fully Developed Flow in Curved Tubes," *Journal of Fluid Mechanics*, Vol. 123, 1982, pp. 503-522.

12 Heitz, W. L., and Westwater, J. W., "Extension of the Numerical Method for Melting and Freezing Problems," *International Journal of Heat and Mass Transfer*, Vol. 13, 1970, pp. 1371-1375.

13 Rieger, H., Projahn, U., and Beer, H., "Analysis of the Heat Transport Mechanisms During Melting Around a Horizontal Circular Cylinder," *International Journal of Heat and Mass Transfer*, Vol. 25, 1982, pp. 137-147.

Eigenvalues Basic to Diffusion in the Part of a Sphere Cut Out by a Cone

M. N. Özişik[1,2], M. A. Boles[1,2], and R. M. Cotta[2]

Introduction

Transient heat diffusion in solids having a shape in the form of part of a sphere cut out by the cone $\theta = \theta_0$, has been the subject of numerous investigations, and formal analytic solutions have been presented in various texts [1, 2]. To utilize such analytic solutions, one needs appropriate eigenvalues for the problem. However, the eigenvalues associated with such problems are very difficult to compute numerically. It appears that only a limited number of approximate eigenvalues has been obtained [3, 4] by utilizing asymptotic expressions for the $P_n^m(\mu)$ functions; but in such results some of the most important first roots have been missed and miscalculated.

The objective of this work is to present an accurate evaluation of the roots of some of the transcendental equations associated with the analytic solution of transient heat diffusion in a part of sphere cut off by the cone $\theta = \theta_0$. To achieve this objective, we have chosen to use the recently advanced Sign-count method [5-7] to determine the roots, since with this approach, one can calculate accurately as many roots as desired without missing any of them.

Analysis

Consider the part of the sphere cut out by the cone $\theta = \theta_0$, confined to the region $\mu_0 \le \mu \le 1$ and $0 \le \phi \le 2\pi$, where $\mu = \cos\theta$ and $\mu_0 = \cos\theta_0$ as illustrated in Fig. 1. In the analytic solution of heat or mass diffusion in such a domain, the separation of variables in the spherical coordinate system leads to the differential equation [2]

$$\frac{d}{d\mu}\left[(1-\mu^2)\frac{dM(\mu,n)}{d\mu}\right]+\left[n(n+1)-\frac{m^2}{1-\mu^2}\right]M(\mu,n)=0, \quad \text{in } \mu_0 \le \mu \le 1 \tag{1}$$

which is Legendre's associated differential equation. The solutions of this equation are the associated Legendre functions of degree n and order m. If the region contains $\mu = 1$ (i.e., $\theta = 0$), as is the case specified above, only the $P_n^m(\mu)$ functions are required, since $Q_n^m(\mu)$ functions have singularity at $\mu = 1$, hence should be excluded from the solution.

Here we focus our attention to the case involving integer values of m, that is, in the ϕ variable, the region is confined to $0 \le \phi \le 2\pi$. Furthermore, we consider the case $\mu_0 > -1$ (i.e., $\theta_0 < \pi$). Then the type of boundary condition at the conical surface $\mu = \mu_0$ establishes the transcendental equation for the determination of the permissible values of n.

When the boundary condition for the surface at $\mu = \mu_0$ is a prescribed temperature, the values of n are the roots of the following transcendental equation, which is regarded as an equation in n

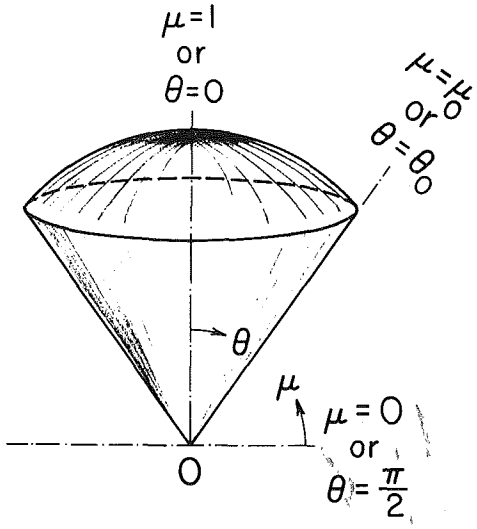

Fig. 1 Geometry and coordinate for the sphere cut out by cone $\theta = \theta_0$

[1] Mem. ASME

[2] Department of Mechanical and Aerospace Engineering, North Carolina State University, Raleigh, N.C. 27650

Contributed by the Heat Transfer Division for publication in the JOURNAL OF HEAT TRANSFER. Manuscript received by the Heat Transfer Division June 6, 1983.

which maps irregular moving boundaries into simple immobilized boundaries. The transformation is similar in spirit to the method of body-fitted coordinates, but is far simpler in practice. The utility of the transformation is demonstrated by using a numerical method to determine the solution to the melting problem about an isothermally heated horizontal cylinder. This problem is characterized by a singularity in the governing equations at time zero, due to sudden appearance of liquid phase when none existed the moment before. This singularity is extracted from the governing equations, allowing the numerical method to actually begin with the exact initial conditions at time zero. The numerical method is then used to illuminate the error resulting from a false-starting method that fails to properly consider the initial singularity. The present results indicate that false-starting errors can be significant.

References

1 Thompson, J. F., Thames, F. C., and Mastin, C. W., "Automatic Numerical Generation of Body-Fitted Curvilinear Coordinate System for Field Containing Any Number of Arbitrary Two-Dimensional Bodies," *Journal of Computational Physics*, Vol. 15, 1974, pp. 299-319.

2 Sparrow, E. M., Patankar, S. V., and Ramadhyani, S., "Analysis of Melting in the Presence of Natural Convection in the Melt Region," ASME JOURNAL OF HEAT TRANSFER, Vol. 99, 1977, pp. 520-526.

3 Solomon, J. M., Climent, M., and Ferguson, R. E., "Inviscid Flowfield Calculations for Re-Entry Vehicles With Control Surfaces," *AIAA Journal*, Vol. 15, 1977, pp. 1742-1749.

4 Yao, L. S., "Analysis of Heat Transfer in Slightly Eccentric Annuli," ASME JOURNAL OF HEAT TRANSFER, Vol. 102, 1980, pp. 279-284.

5 Yao, L. S., and Chen, F. F., "Effects of Natural Convection in the Melted Region Around a Heated Horizontal Cylinder," ASME JOURNAL OF HEAT TRANSFER, Vol. 102, 1980, pp. 667-672.

6 Yao, L. S., and Cherney, W., "Transient Phase-Change Around a Horizontal Cylinder," *International Journal of Heat and Mass Transfer*, Vol. 24, 1981, pp. 1971-1981.

7 Prusa, J., "A Spatial Stefan Problem Modified by Natural Convection: Melting Around a Horizontal Cylinder," Ph.D. dissertation, University of Illinois at Urbana-Champaign, 1983.

8 Prusa, J., and Yao, L. S., "Melting Around a Horizontal Heated Cylinder: Part II - Perturbation and Numerical Solutions For Constant Heat Flux Boundary Condition," Paper No. 83-HT-18, AIChE/ASME 21st National Heat Transfer Conference, Seattle, Wash., July 24-27, 1983.

9 Rubenstein, L. I., "The Stefan Problem," *Translations of Mathematical Monographs*, Vol. 27, 1971, pp. 1-15.

10 Prusa, J., and Yao, L. S., "Melting Around a Horizontal Heated Cylinder: Part I - Numerical Solution for Isothermal Boundary Condition," *Proceedings of the ASME-JSME Thermal Engineering Joint Conference*, March 20-24, 1983, Honolulu, Hawaii.

11 Prusa, J., and Yao, L. S., "Heat Transfer of Fully Developed Flow in Curved Tubes," *Journal of Fluid Mechanics*, Vol. 123, 1982, pp. 503-522.

12 Heitz, W. L., and Westwater, J. W., "Extension of the Numerical Method for Melting and Freezing Problems," *International Journal of Heat and Mass Transfer*, Vol. 13, 1970, pp. 1371-1375.

13 Rieger, H., Projahn, U., and Beer, H., "Analysis of the Heat Transport Mechanisms During Melting Around a Horizontal Circular Cylinder," *International Journal of Heat and Mass Transfer*, Vol. 25, 1982, pp. 137-147.

Eigenvalues Basic to Diffusion in the Part of a Sphere Cut Out by a Cone

M. N. Özişik[1,2], M. A. Boles[1,2], and R. M. Cotta[2]

Introduction

Transient heat diffusion in solids having a shape in the form of part of a sphere cut out by the cone $\theta = \theta_0$, has been the subject of numerous investigations, and formal analytic solutions have been presented in various texts [1, 2]. To utilize such analytic solutions, one needs appropriate eigenvalues for the problem. However, the eigenvalues associated with such problems are very difficult to compute numerically. It appears that only a limited number of approximate eigenvalues has been obtained [3, 4] by utilizing asymptotic expressions for the $P_n^m(\mu)$ functions; but in such results some of the most important first roots have been missed and miscalculated.

The objective of this work is to present an accurate evaluation of the roots of some of the transcendental equations associated with the analytic solution of transient heat diffusion in a part of sphere cut off by the cone $\theta = \theta_0$. To achieve this objective, we have chosen to use the recently advanced Sign-count method [5-7] to determine the roots, since with this approach, one can calculate accurately as many roots as desired without missing any of them.

Analysis

Consider the part of the sphere cut out by the cone $\theta = \theta_0$, confined to the region $\mu_0 \le \mu \le 1$ and $0 \le \phi \le 2\pi$, where $\mu = \cos\theta$ and $\mu_0 = \cos\theta_0$ as illustrated in Fig. 1. In the analytic solution of heat or mass diffusion in such a domain, the separation of variables in the spherical coordinate system leads to the differential equation [2]

$$\frac{d}{d\mu}\left[(1-\mu^2)\frac{dM(\mu,n)}{d\mu}\right]+\left[n(n+1)-\frac{m^2}{1-\mu^2}\right]M(\mu,n)=0, \quad \text{in } \mu_0 \le \mu \le 1 \tag{1}$$

which is Legendre's associated differential equation. The solutions of this equation are the associated Legendre functions of degree n and order m. If the region contains $\mu = 1$ (i.e., $\theta = 0$), as is the case specified above, only the $P_n^m(\mu)$ functions are required, since $Q_n^m(\mu)$ functions have singularity at $\mu = 1$, hence should be excluded from the solution.

Here we focus our attention to the case involving integer values of m, that is, in the ϕ variable, the region is confined to $0 \le \phi \le 2\pi$. Furthermore, we consider the case $\mu_0 > -1$ (i.e., $\theta_0 < \pi$). Then the type of boundary condition at the conical surface $\mu = \mu_0$ establishes the transcendental equation for the determination of the permissible values of n.

When the boundary condition for the surface at $\mu = \mu_0$ is a prescribed temperature, the values of n are the roots of the following transcendental equation, which is regarded as an equation in n

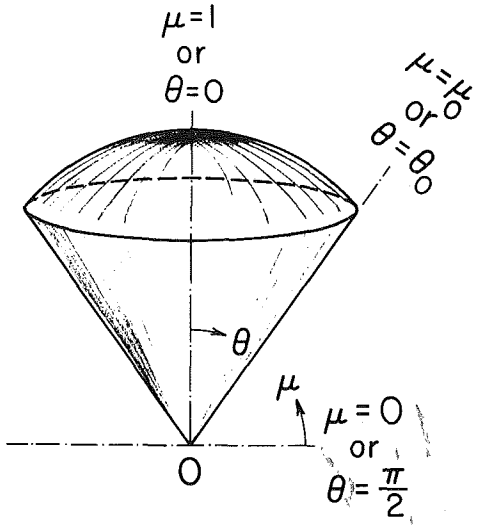

Fig. 1 Geometry and coordinate for the sphere cut out by cone $\theta = \theta_0$

[1] Mem. ASME

[2] Department of Mechanical and Aerospace Engineering, North Carolina State University, Raleigh, N.C. 27650

Contributed by the Heat Transfer Division for publication in the JOURNAL OF HEAT TRANSFER. Manuscript received by the Heat Transfer Division June 6, 1983.

$$P_n^m(\mu)\Big|_{\mu=\mu_0}=0 \tag{2}$$

When the boundary condition at the surface $\mu = \mu_0$ is a prescribed heat flux, then the values of n are the roots of the following transcendental equation which is regarded as an equation in n

$$\frac{dP_n^m(\mu)}{d\mu}\Big|_{\mu=\mu_0}=0 \tag{3}$$

The eigenvalues n_k of the differential equation (1) subject to the boundary condition given by equation (2) or (3) can be determined directly by the Sign-count method described in [5, 6], instead of trying to solve the transcendental equation (2) or (3) as an equation in n. By following the formalism discussed in these references, we consider the Sturm-Liouville problem given in the form

$$\frac{d}{d\mu}\left[k(\mu)\frac{dM(\mu,\lambda)}{d\mu}\right]+\left[\lambda^2 w(\mu)-d(\mu)\right]M(\mu,\lambda)=0, \quad \text{in } \mu_0<\mu<1 \tag{4a}$$

$$\alpha_0 M(\mu,\lambda)-\beta_0 k(\mu)\frac{dM(\mu,\lambda)}{d\mu}=0, \quad \text{at } \mu=\mu_0 \tag{4b}$$

$$\alpha_1 M(\mu,\lambda)+\beta_1 k(\mu)\frac{dM(\mu,\lambda)}{d\mu}=0, \quad \text{at } \mu=1 \tag{4c}$$

Clearly the eigenvalue problem associated with equation (1) subject to the boundary condition given by equation (2) or (3), and the implicitly stated requirement at $\mu = 1$, is a special case of this Sturm-Liouville problem. By direct comparison of equations (1) and (4a) we write

$$k(\mu)=1-\mu^2, \qquad w(\mu)=1 \tag{5a,b}$$

$$d(\mu)=\frac{m^2}{1-\mu^2}, \qquad \lambda^2=n(n+1) \tag{5c,d}$$

The general boundary conditions (4b,c) of this Sturm-Liouville problem can be readily simplified to obtain the boundary conditions for the original specific problem as special cases. For example, the implicit requirement of the boundary condition at $\mu = 1$ is obtained by setting $\alpha_1 = 0$, $\beta_1 = 1$ in equation (4c). The boundary condition (2) is obtained by setting $\alpha_0 = 1$, $\beta_0 = 0$; or the boundary condition (3) is obtained by setting $\alpha_0 = 0$, $\beta_0 = 1$ in equation (4b).

By following the formalism in the application of the Sign-count method, we let the coefficients $k(\mu)$, $w(\mu)$ and $d(\mu)$ of equation (4a) be approximated by stepwise functions as

$$k(\mu)=k_k, \quad w(\mu)=w_k \quad \text{and} \quad d(\mu)=d_k \tag{6}$$

$$\text{for } \mu_k<\mu<\mu_{k+1}, \quad k=0,1,\ldots,N-1 \tag{7}$$

where N is the number of subdivisions in the spacial domain $\mu_0 \le \mu \le 1$, considered for the problem (4). The values of the constants k_k, w_k, and d_k can be estimated by some weighted

Table 1 First ten roots of $P_n^m(\mu)\big|_{\mu=\mu_0}=0$ regarded as an equation in n

θ_0	μ_0	m	Roots n_k									
			n_1	n_2	n_3	n_4	n_5	n_6	n_7	n_8	n_9	n_{10}
π/3	0.5000	0	1.7773	4.7628	7.7583	10.7561	13.7548	16.7540	19.7534	22.7530	25.7527	28.7524
		1	3.1957	6.2195	9.2289	12.2338	15.2369	18.2390	21.2405	24.2417	27.2426	30.2434
		2	4.5422	7.6220	10.6571	13.6770	16.6898	19.6988	22.7054	25.7105	28.7146	31.7178
		3	5.8532	8.9908	12.0557	15.0942	18.1198	21.1381	24.1519	27.1626	30.1712	33.1783
		4	7.1423	10.3361	13.4322	16.4911	19.5312	22.5604	25.5827	28.6002	31.6144	34.6261
π/4	0.7071	0	2.5479	6.5222	10.5143	14.5106	18.5084	22.5069	26.5060	30.5052	34.5046	38.5041
		1	4.4053	8.4471	12.4633	16.4720	20.4773	24.4809	28.4836	32.4856	36.4872	40.4885
		2	6.1388	10.2781	14.3390	18.3734	22.3957	26.4113	30.4228	34.4316	38.4386	42.4443
		3	7.8117	12.0508	16.1634	20.2301	24.2745	28.3062	32.3301	36.3487	40.3636	44.3757
		4	9.4472	13.7831	17.9497	22.0516	26.1211	30.1716	34.2101	38.2405	42.2651	46.2853
π/6	0.8660	0	4.0837	10.0385	16.0248	22.0183	28.0145	34.0120	40.0103	46.0090	52.0080	58.0071
		1	6.8354	12.9083	18.9365	24.9514	30.9607	36.9669	42.9715	48.9750	54.9778	60.9801
		2	9.3733	15.6154	21.7210	27.7808	33.8193	39.8463	45.8662	51.8816	57.8937	63.9036
		3	11.8074	18.2220	24.4170	30.5325	36.6094	42.6644	48.7057	54.7379	60.7637	66.7848
		4	14.1778	20.7588	27.0470	33.2236	39.3438	45.4313	51.4980	57.5506	63.5931	69.6282
π/12	0.9659	0	8.6812	20.5832	32.5535	44.5394	56.5312	68.5259	80.5222	92.5194	104.5172	116.5154
		1	14.1446	26.3023	38.3631	50.3953	62.4152	74.4287	86.4386	98.4461	110.4521	122.4570
		2	19.1487	31.6711	43.8987	56.0275	68.1107	80.1688	92.2118	104.2448	116.2709	128.2922
		3	23.9306	36.8237	49.2439	61.4928	73.6584	85.7768	97.8658	109.9352	121.9907	134.0363
		4	28.5764	41.8265	54.4471	66.8273	79.0862	91.2747	103.4184	115.5316	127.6232	139.6989

Table 2 First ten roots of $|dP_n^m(\mu)/d\mu|_{\mu=\mu_0}=0$ regarded as an equation in n

θ_0	μ_0	m	Roots n_k									
			n_1	n_2	n_3	n_4	n_5	n_6	n_7	n_8	n_9	n_{10}
π/3	0.5000	0	0.0000	3.1957	6.2195	9.2288	12.2338	15.2369	18.2390	21.2406	24.2417	27.2426
		1	1.4680	4.6542	7.6906	10.7068	13.7160	16.7219	19.7261	22.7292	25.7316	28.7336
		2	2.7526	6.0404	9.1109	12.1452	15.1658	18.1795	21.1894	24.1968	27.2026	30.2072
		3	4.0000	7.3884	10.4984	13.5554	16.5909	19.6153	22.6331	25.6467	28.6575	31.6662
		4	5.2295	8.7117	11.8623	14.9439	17.9963	21.0330	24.0603	27.0814	30.0983	33.1120
π/4	0.7071	0	0.0000	4.4053	8.4471	12.4633	16.4719	20.4773	24.4810	28.4836	32.4856	36.4872
		1	2.0000	6.3339	10.3970	14.4251	18.4410	22.4514	26.4586	30.4640	34.4682	38.4715
		2	3.6332	8.1373	12.2592	16.3186	20.3542	24.3780	28.3950	32.4079	36.4179	40.4259
		3	5.2014	9.8747	14.0645	18.1631	22.2245	26.2667	30.2976	34.3211	38.3398	42.3548
		4	6.7388	11.5696	15.8291	19.9703	24.0608	28.1243	32.1715	36.2081	40.2372	44.2610
π/6	0.8660	0	0.0000	6.8354	12.9083	18.9364	24.9514	30.9607	36.9670	42.9716	48.9751	54.9778
		1	3.1196	9.7121	15.8216	21.8702	27.8979	33.9158	39.9283	45.9377	51.9449	57.9506
		2	5.4928	12.3720	18.5830	24.6858	30.7474	36.7886	42.8182	48.8404	54.8578	60.8717
		3	7.7524	14.9180	21.2462	27.4167	33.5229	39.5960	45.6494	51.6902	57.7225	63.7486
		4	9.9589	17.3910	23.8390	30.0829	36.2396	42.3495	48.4312	54.4944	60.5449	66.5861
π/12	0.9659	0	0.0000	14.1446	26.3022	38.3630	50.3952	62.4152	74.4289	86.4388	98.4463	110.4520
		1	6.5842	19.8793	32.1154	44.2203	56.2799	68.3185	80.3456	92.3656	104.3812	116.3936
		2	11.2452	25.1472	37.6017	49.8231	61.9558	74.0446	86.1083	98.1562	110.1936	122.2236
		3	15.6600	30.1702	42.8762	55.2433	67.4722	79.6295	91.7446	103.8325	115.9020	127.9582
		4	19.9605	35.0364	47.9996	60.5246	72.8618	85.0986	97.2745	109.4108	121.5194	133.6082

average of the values of these coefficients at the subintervals. Here, we have chosen this averaging process as

$$f_k = \frac{1}{\mu_{k+1} - \mu_k} \int_{\mu_k}^{\mu_{k+1}} f(\mu')\, d\mu', \quad \text{for } \mu_k < \mu < \mu_{k+1} \tag{8}$$

where $f_k \equiv k_k$, w_k or d_k.

With this consideration we write

$$k_k = \frac{1}{\mu_{k+1} - \mu_k} \left[\mu_{k+1} \left(1 - \frac{\mu_{k+1}^2}{3} \right) - \mu_k \left(1 - \frac{\mu_k^2}{3} \right) \right], \quad w_k = 1 \tag{9a,b}$$

$$d_k = \frac{m^2}{2(\mu_{k+1} - \mu_k)} \ln \left[\frac{(1+\mu_{k+1})(1-\mu_k)}{(1-\mu_{k+1})(1+\mu_k)} \right] \tag{9c}$$

We also make use of the asymptotic formula for μ_i in order to estimate the spacing between the eigenvalues as

$$\delta = \frac{\pi}{\int_{\mu_0}^{1} \sqrt{\frac{w(\mu)}{k(\mu)}}\, d\mu} \tag{10}$$

or for the specific problem considered here we find $\delta = \pi/\theta_0$. In view of the foregoing assumptions, equation (4*a*), in any of the subintervals $\mu_{k+1} - \mu_k$, $k = 0,1, \ldots, N-1$, is replaced by

$$\frac{d^2 M_k(\mu,\lambda)}{d\mu^2} + \omega_k^2 M_k(\mu,\lambda) = 0, \quad \text{in} \quad \mu_k < \mu < \mu_{k+1} \tag{11a}$$

where

$$\omega_k^2 = (\lambda^2 w_k - d_k)/k_k. \tag{11b}$$

Since the original function $M(\mu,\lambda)$ defined by equation (4*a*) has a continuous first derivative in the interior of the entire domain, then the functions $M_k(\mu,\lambda)$ and its first derivatives at the end points of the corresponding intervals should satisfy the following continuity requirements

$$M_k(\mu,\lambda) = M_{k+1}(\mu,\lambda), \quad \text{at} \quad \mu = \mu_k, \quad k = 1,2, \ldots, N-1 \tag{12a}$$

$$k_k \frac{dM_k(\mu,\lambda)}{d\mu} = k_{k+1} \frac{dM_{k+1}(\mu,\lambda)}{d\mu}, \quad \text{at} \quad \mu = \mu_k, \quad k = 1,2, \ldots, N-1 \tag{12b}$$

The boundary conditions (4*b*) and (4*c*) take the form

$$\alpha_0 M_1(\mu,\lambda) - \beta_0 k_1 \frac{dM_1(\mu,\lambda)}{d\mu} = 0, \quad \text{at} \quad \mu = \mu_0 \tag{12c}$$

$$\alpha_N M_N(\mu,\lambda) + \beta_N k_N \frac{dM_N(\mu,\lambda)}{d\mu} = 0, \quad \text{at} \quad \mu = \mu_N \tag{12d}$$

where in the last equation α_1 and β_1 are replaced, respectively, by α_N and β_N, since the boundary condition now belongs to the end point of the last subregion.

Thus the eigenvalue problem (4) is now replaced by the problem defined by equations (11) and (12), hence the computed eigenvalues of the latter problem represent the eigenvalues of the problem (2), if sufficiently small subintervals are chosen for computations.

Once λ's are available, the values of n are determined from its definition given by equation (5*d*). Only the values of n greater than $-1/2$ are of interest [2]; therefore, from equation (5*d*), we write

$$n_i = \frac{(1+4\lambda_i^2)^{1/2} - 1}{2} \tag{13}$$

We also note that the parameter ω_k^2, defined by equation (11*b*), can be both positive or negative, as a result ω_k can be both real or imaginary.

By utilizing the sign-count method [5, 6], we calculate the eigenvalues λ_i of the eigenvalue problem defined by equations (11) and (12). Knowing the λ_i, the roots n_i are determined from equation (13).

Results

We present in Tables 1 and 2, the first ten roots n_i of the transcendental equations (2) and (3), respectively, for the values of m from 0 to 4, and for $\theta_0 = \pi/3$, $\pi/4$, $\pi/6$ and $\pi/12$. The calculations are performed by using subdivisions up to $N \leq 10{,}000$. Because of the behaviour of the coefficient $d(\mu)$ close to $\mu = 1$, more subdivisions were used in the region near $\mu = 1$. The results given in these tables are considered to be correct to within ± 1 in the last digit given. These results are also checked by using Hobson's asymptotic expressions to calculate the roots. The roots computed by both methods showed excellent agreement for $\theta_0 = \pi/3$ and $\pi/4$; the agreement was still good for the limit of application of Hobson's formula at $\theta_0 = \pi/6$. However, for $\theta_0 = \pi/12$, the generalization of Laplace's formula obtained by Hobson did not produce good results. For this particular case, the formula obtained by Macdonald [8] should be preferred. Here we wish to point out that if the asymptotic expressions for the Legendre functions are used for the calculation of the roots, as it has been done in [3, 4], the roots can easily be missed or miscalculated.

Acknowledgment

One of the authors (R. M. C.) wishes to acknowledge the financial support of Comissão Nacional de Energia Nuclear of Brazil. This work was partially supported by the National Science Foundation grant No. MEA 81-10705.

References

1 Carslaw, H. S., and Jaeger, J. C., *Conduction of Heat in Solids*, Oxford University Press, 1959.

2 Ozisik, M. N., *Heat Conduction*, John Wiley & Sons, New York, 1980.

3 Pal, B., "On the Numerical Calculation of the Roots of the Equation $p_n{}^m(\mu) = 0$ and $d/d\mu\, P_n{}^m$ Regarded as Equation in n," *Bul. Calcutta Math. Soc.*, Vol. 9, 1917, pp. 85-95.

4 Pal, B., "On the Numerical Calculation of the Roots of the Equation $p_n{}^m(\mu) = 0$ and $d/d\mu p_n{}^m(\mu)$ Regarded as Equation in n," *Bul. Calcutta Math. Soc.*, Vol. 10, 1918, pp. 187-194.

5 Mikhailov, M. D., Ozisik, M. N., and Vulchanov, N. L., "Transient Heat Diffusion in One-Dimensional Composite Media and Automatic Solution of the Eigenvalue Problem," *Int. J. Heat Mass Transfer*, Vol. 26, 1983, pp. 1131-1141.

6 Mikhailov, M. D., and Ozisik, M. N., *Unified Analysis and Solutions of Heat and Mass Diffusion*, John Wiley and Sons, New York, 1984.

7 Mikhailov, M. D., and Vulchanov, N. L., "A Computational Procedure for Sturm-Liouville Problems," *J. Comp. Phys.*, Vol. 50, 1983, pp. 323-336.

8 Hobson, E. W., *The Theory of Spherical and Ellipsoidal Harmonics*, Cambridge University Press, 1932.

An Approximating Temperature Profile of an Instantaneous Heat Source

M. Slonim[1] and A. Tslaf[1]

Nomenclature

x = coordinate, m
t, τ = time, s
γ = density, kg/m^3
c = specific heat, J/kgK
λ = thermal conductivity, W/mK

[1] Ben Gurion University of the Negev, Beer-Sheva, Israel 84120

Contributed by the Heat Transfer Division for publication in the JOURNAL OF HEAT TRANSFER. Manuscript received by the Heat Transfer Division March 1, 1982.

average of the values of these coefficients at the subintervals. Here, we have chosen this averaging process as

$$f_k = \frac{1}{\mu_{k+1}-\mu_k}\int_{\mu_k}^{\mu_{k+1}} f(\mu')\,d\mu', \quad \text{for } \mu_k < \mu < \mu_{k+1} \tag{8}$$

where $f_k \equiv k_k$, w_k or d_k.

With this consideration we write

$$k_k = \frac{1}{\mu_{k+1}-\mu_k}\left[\mu_{k+1}\left(1-\frac{\mu_{k+1}^2}{3}\right)-\mu_k\left(1-\frac{\mu_k^2}{3}\right)\right], \quad w_k = 1 \tag{9a,b}$$

$$d_k = \frac{m^2}{2(\mu_{k+1}-\mu_k)}\ln\left[\frac{(1+\mu_{k+1})(1-\mu_k)}{(1-\mu_{k+1})(1+\mu_k)}\right] \tag{9c}$$

We also make use of the asymptotic formula for μ_i in order to estimate the spacing between the eigenvalues as

$$\delta = \frac{\pi}{\int_{\mu_0}^{1}\sqrt{\dfrac{w(\mu)}{k(\mu)}}\,d\mu} \tag{10}$$

or for the specific problem considered here we find $\delta = \pi/\theta_0$. In view of the foregoing assumptions, equation (4*a*), in any of the subintervals $\mu_{k+1}-\mu_k$, $k = 0,1,\ldots,N-1$, is replaced by

$$\frac{d^2M_k(\mu,\lambda)}{d\mu^2} + \omega_k^2 M_k(\mu,\lambda) = 0, \quad \text{in} \quad \mu_k < \mu < \mu_{k+1} \tag{11a}$$

where

$$\omega_k^2 = (\lambda^2 w_k - d_k)/k_k. \tag{11b}$$

Since the original function $M(\mu,\lambda)$ defined by equation (4*a*) has a continuous first derivative in the interior of the entire domain, then the functions $M_k(\mu,\lambda)$ and its first derivatives at the end points of the corresponding intervals should satisfy the following continuity requirements

$$M_k(\mu,\lambda) = M_{k+1}(\mu,\lambda), \quad \text{at} \quad \mu=\mu_k, \quad k=1,2,\ldots,N-1 \tag{12a}$$

$$k_k\frac{dM_k(\mu,\lambda)}{d\mu} = k_{k+1}\frac{dM_{k+1}(\mu,\lambda)}{d\mu}, \quad \text{at} \quad \mu=\mu_k, \quad k=1,2,\ldots,N-1 \tag{12b}$$

The boundary conditions (4*b*) and (4*c*) take the form

$$\alpha_0 M_1(\mu,\lambda) - \beta_0 k_1\frac{dM_1(\mu,\lambda)}{d\mu} = 0, \quad \text{at} \quad \mu=\mu_0 \tag{12c}$$

$$\alpha_N M_N(\mu,\lambda) + \beta_N k_N\frac{dM_N(\mu,\lambda)}{d\mu} = 0, \quad \text{at} \quad \mu=\mu_N \tag{12d}$$

where in the last equation α_1 and β_1 are replaced, respectively, by α_N and β_N, since the boundary condition now belongs to the end point of the last subregion.

Thus the eigenvalue problem (4) is now replaced by the problem defined by equations (11) and (12), hence the computed eigenvalues of the latter problem represent the eigenvalues of the problem (2), if sufficiently small subintervals are chosen for computations.

Once λ's are available, the values of n are determined from its definition given by equation (5*d*). Only the values of n greater than $-1/2$ are of interest [2]; therefore, from equation (5*d*), we write

$$n_i = \frac{(1+4\lambda_i^2)^{1/2}-1}{2} \tag{13}$$

We also note that the parameter ω_k^2, defined by equation (11*b*), can be both positive or negative, as a result ω_k can be both real or imaginary.

By utilizing the sign-count method [5, 6], we calculate the eigenvalues λ_i of the eigenvalue problem defined by equations (11) and (12). Knowing the λ_i, the roots n_i are determined from equation (13).

Results

We present in Tables 1 and 2, the first ten roots n_i of the transcendental equations (2) and (3), respectively, for the values of m from 0 to 4, and for $\theta_0 = \pi/3$, $\pi/4$, $\pi/6$ and $\pi/12$. The calculations are performed by using subdivisions up to $N \leq 10{,}000$. Because of the behaviour of the coefficient $d(\mu)$ close to $\mu = 1$, more subdivisions were used in the region near $\mu = 1$. The results given in these tables are considered to be correct to within ± 1 in the last digit given. These results are also checked by using Hobson's asymptotic expressions to calculate the roots. The roots computed by both methods showed excellent agreement for $\theta_0 = \pi/3$ and $\pi/4$; the agreement was still good for the limit of application of Hobson's formula at $\theta_0 = \pi/6$. However, for $\theta_0 = \pi/12$, the generalization of Laplace's formula obtained by Hobson did not produce good results. For this particular case, the formula obtained by Macdonald [8] should be preferred. Here we wish to point out that if the asymptotic expressions for the Legendre functions are used for the calculation of the roots, as it has been done in [3, 4], the roots can easily be missed or miscalculated.

Acknowledgment

One of the authors (R. M. C.) wishes to acknowledge the financial support of Comissão Nacional de Energia Nuclear of Brazil. This work was partially supported by the National Science Foundation grant No. MEA 81-10705.

References

1 Carslaw, H. S., and Jaeger, J. C., *Conduction of Heat in Solids*, Oxford University Press, 1959.

2 Ozisik, M. N., *Heat Conduction*, John Wiley & Sons, New York, 1980.

3 Pal, B., "On the Numerical Calculation of the Roots of the Equation $p_n{}^m(\mu)=0$ and $d/d\mu\, P_n{}^m$ Regarded as Equation in n," *Bul. Calcutta Math. Soc.*, Vol. 9, 1917, pp. 85-95.

4 Pal, B., "On the Numerical Calculation of the Roots of the Equation $p_n{}^m(\mu)=0$ and $d/d\mu p_n{}^m(\mu)$ Regarded as Equation in n," *Bul. Calcutta Math. Soc.*, Vol. 10, 1918, pp. 187-194.

5 Mikhailov, M. D., Ozisik, M. N., and Vulchanov, N. L., "Transient Heat Diffusion in One-Dimensional Composite Media and Automatic Solution of the Eigenvalue Problem," *Int. J. Heat Mass Transfer*, Vol. 26, 1983, pp. 1131-1141.

6 Mikhailov, M. D., and Ozisik, M. N., *Unified Analysis and Solutions of Heat and Mass Diffusion*, John Wiley and Sons, New York, 1984.

7 Mikhailov, M. D., and Vulchanov, N. L., "A Computational Procedure for Sturm-Liouville Problems," *J. Comp. Phys.*, Vol. 50, 1983, pp. 323-336.

8 Hobson, E. W., *The Theory of Spherical and Ellipsoidal Harmonics*, Cambridge University Press, 1932.

An Approximating Temperature Profile of an Instantaneous Heat Source

M. Slonim[1] and A. Tslaf[1]

Nomenclature

x = coordinate, m
t, τ = time, s
γ = density, kg/m^3
c = specific heat, J/kgK
λ = thermal conductivity, W/mK

[1] Ben Gurion University of the Negev, Beer-Sheva, Israel 84120

Contributed by the Heat Transfer Division for publication in the JOURNAL OF HEAT TRANSFER. Manuscript received by the Heat Transfer Division March 1, 1982.

$a = \dfrac{\lambda}{\gamma c}$, thermal diffusivity, m^2/s

T = temperature rise, K
Q_s = heat flux, W/m^2
A_s = heat flow, J/m^2

1 Introduction

The heat transfer problem that arises in the high-current pulse discharge on the gas-solid interface of a solid dielectric body as a result of a flashover [1] can be formulated as follows: a semi-infinite body has a one-dimensional temperature distribution $T(x,0)$ and insulated boundary surface; at the instant $\tau=0$, the temperature diffusion process starts. We seek the temperature profile $T(x,\tau)$ as a function of time τ.

Approaching linear conditions, the sought temperature distribution can be written in the form [2]

$$T(x,\tau)=\frac{1}{2\sqrt{\pi a\tau}}\int_0^\infty T(x',0)\left\{\exp\left[-\frac{(x-x')^2}{4a\tau}\right]+\exp\left[-\frac{(x+x')^2}{4a\tau}\right]\right\}dx' \tag{1}$$

This integration can be realized numerically or analytically, depending on the initial temperature distribution $T(x,0)$. However, even if an integration in a closed form is possible, it can appear as an inconvenient expression when used as a component in a further more sophisticated analysis.

Therefore, an approximation of equation (1) by an elementary function which still describes the main features of an actual thermal problem seems to be desirable.

A temperature distribution can be proposed in the form

$$T_a=\frac{A_{s0}}{\sqrt{\pi\gamma c\lambda(\tau_0+\tau)}}\times\exp\left[-\frac{(x-x_0)^2}{4a(\tau_0+\tau)}\right] \tag{2}$$

where the fictitious surface heat A_{s0} relates to the actual heat A_s liberated on the surface as

$$\frac{A_{s0}}{A_s}=\exp(x_0{}^2/4a\tau_0) \tag{3}$$

τ_0 and x_0 are parameters that have to be derived in accordance with the approximation limits.

Physically, equation (2) can be interpreted as a temperature field created by a fictitious heat source A_{s0} instantaneously liberated on the surface shifted in space ($x=x_0$) and time ($\tau=\tau_0$) relative to the position $x=0$ and release time $\tau=0$ of a real heat source A_s.

The advantages of the temperature distribution (2) are:

(*i*) The simplicity of an exponential function

(*ii*) It satisfies the heat equation for a one-dimensional case

$$\frac{\partial T}{\partial t}=a\nabla^2 T=a\frac{\partial^2 T}{\partial x^2} \tag{4}$$

(*iii*) In contrast to the well-known [2] case of an ordinary instantaneous source ($\tau_0=0$), the temperature at $\tau=0$ is finite.

The question regarding equation (2) is how well it can approximate to the result of integration of equation (1).

2 The Procedure of Approximation

The further analysis is intended to illustrate the procedure of approximation for the practically important following case:

A semi-infinite solid is initially at zero temperature. A constant heat flux, Q_s, is supplied at the boundary surface of the solid ($x=0$) during the time t. At this time, which is the end of the "heating" period and start ($\tau=0$) of the "cooling" period, the heat flux Q_s ceases, the boundary surface $x=0$ becomes insulated, and the temperature profile tends toward zero by the diffusion of heat away from the surface. We seek an approximate description of the temperature profile by an elementary function (2) requiring:

(*i*) Equality of the surface temperature at $\tau=0$ given by an accurate (1) and approximate (2) temperature distributions

$$T(0,0)=T_a(0,0) \tag{5}$$

(*ii*) Admissible relative deviation of the surface temperature $[\Delta T/T]$ at $\tau>0$

$$\frac{T_a(0,0)}{T(0,0)}-1=\frac{\Delta T}{T}\le\left[\frac{\Delta T}{T}\right] \tag{6}$$

(It has to be noted that the positive $\Delta T/T$ is the most interesting case, since it means that $T_a>T$ and ensures a more secure approximation when used for problems mentioned in the Introduction).

The final temperature distribution of the "heating" period, which is the initial distribution $T(x,0)$ of the "cooling" period, is well known [2]

$$T(x,0)=T(x,t)=2Q_s\sqrt{\frac{t}{\gamma c\lambda}}\,\mathrm{ierfc}\,\frac{x}{2\sqrt{at}} \tag{7}$$

When (1) is integrated in a closed form for the particular case (7) under discussion, it becomes

$$T=T(x,\tau)=\frac{2Q_s}{\sqrt{\gamma c\lambda}}\left[\sqrt{t+\tau}\,\mathrm{ierfc}\,\frac{x}{2\sqrt{a(t+\tau)}}-\sqrt{\tau}\,\mathrm{ierfc}\,\frac{x}{2\sqrt{a\tau}}\right] \tag{8}$$

Actually, equation (8) represents a sum of two temperature distributions: the first one from a source Q_s as a function of total time $(t+\tau)$ and a second from a sink of the same value as a shifted function of time τ over the temperature diffusion period.

When the only purpose is to find the final temperature distribution, then equation (8) is the easiest solution, since tabulated values of *ierfc* can be used. However, when the foregoing use of temperature distribution $T(x,\tau)$ for further more sophisticated general analysis is required, an elementary function (2) can be more convenient.

The time shift τ_0 in equation (2) can be immediately estimated from (2), (3), and (5) as

$$\tau_0=\frac{A_s^2}{4Q_s^2 t}=0.25t \tag{9}$$

since the liberated energy in equation (2) is suggested to be the integral of the heat flux Q_s in equation (5) over the time t of the "heating" period

$$A_s=\int_0^t Q_s dt=Q_s t \tag{10}$$

The required space shift x_0 in equation (2) can be estimated using (6). After substitution of equations (2), (3), and (10) at $x=0$ into equation (6), the relative deviation of the temperature can be written in the form

$$\frac{\Delta T}{T}=\frac{\exp[-(x_0/\sqrt{at})^2(1+0.25t/\tau)^{-1}]}{2\sqrt{0.25+(\tau/t)}[\sqrt{1+(\tau/t)}-\sqrt{\tau/t}]}-1 \tag{11}$$

To be compared with the permissible temperature deviation according to (6), equation (11) has to be searched for the maximum of $\Delta T/T$ over the time $\tau>0$ of the whole "cooling" period. Thus the time τ_m as a function of $x_0/\sqrt{at}$ will be estimated in conditions when $\Delta T/T$ reaches its maximum value. Then, substituting τ_m into equation (11), the admissible nondimensional space shift $[x_0/\sqrt{at}]$ can be calculated versus

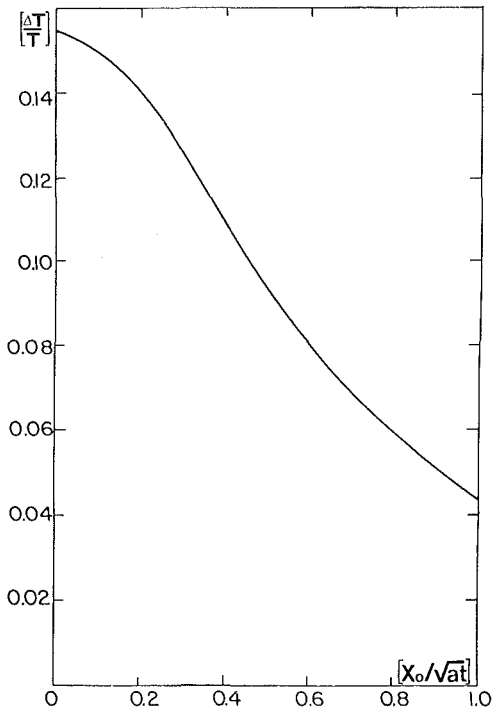

Fig. 1 Admissible relative deviation of temperature $[\Delta T/T]$ versus the nondimensional space shift $[x_0/\sqrt{at}]$

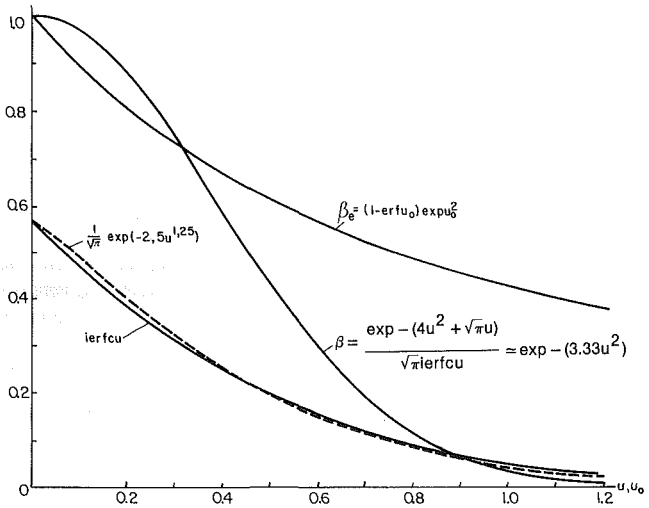

Fig. 2 Functions of nondimensional parameters $u_0 = x_0/2\sqrt{at}$ and $u = x/2\sqrt{at}$

the admissible temperature deviation $[\Delta T/T]$. The result of this estimation is plotted on Fig. 1.

The evaluation of the space shift in terms of a "best" value depends on the chosen criteria for such an evaluation at the given limits of approximation. An energetic criteria is discussed below (equation (12), Fig. 2).

Thus the procedure of approximation that matches the conditions (5) and (6) is simple

(*i*) Estimation of time shift τ_0 from equation (9)

(*ii*) Estimation of the admissible space shift $[x_0]$ versus the admissible temperature deviation $[\Delta T/T]$ from Fig. 1

(*iii*) Use of τ_0 and $x_0 \le [x_0]$ in equation (2)

3 Conditions of Approximation Different From (5) and (6)

Generally, the procedure of time and space shift estimation for equation (2) remains the same. However, some of the numbers or (and) relationships will be different.

A useful quantitative indication of the approximation by equation (2) at different conditions can be the criterion

$$\beta_e = A_\tau / A_t \tag{12}$$

where A_τ is the energy associated with the temperature distribution (2)

$$A_\tau = \gamma c \int_0^x T(x,0)dx = A_s \left(\exp \frac{x_0^2}{4a\tau_0}\right)\left(\operatorname{erf} \frac{x - x_0}{2\sqrt{a\tau_0}} + \operatorname{erf} \frac{x_0}{2\sqrt{a\tau_0}}\right)$$

A_t is the energy associated with the temperature distribution (7)

$$A_t = \gamma c \int_0^x T_t dx = 4Q_s t \left(0.25 - i^2 \operatorname{erfc} \frac{x}{2\sqrt{at}}\right) \tag{13}$$

and

$$i^2 \operatorname{erf} cu = \int_u^\infty \operatorname{ierf} cu du = 0.25[(1 - \operatorname{er} fu) - 2u \operatorname{ierfc} u] \tag{14}$$

Thus when A_τ and A_t are integrated over the whole semi-infinite body $(0 \le x \le \infty)$, the criterion (18) can be written as

$$\beta_e \le (1 + \operatorname{erf} u_0) \exp u_0^2 \tag{15}$$

where

$$u_0 = x_0/2\sqrt{a\tau_0} = x_0/\sqrt{at} \tag{16}$$

Thus the "best" value of space shift from the energetic point of view ($\beta_e = 1$) is $x_0 = 0$. However, conditions of a specific problem (for example, temperature distribution in the depth of the body) can dictate a use of $[x_0] > x_0 \ne 0$. Then it can be evaluated according to the criteria β_e.

Figure 2 shows the plot of (15) at negative values of x_0 and u_0 which are of interest in equation (2). It illustrates a decrease of energy absorbed by the body with the increasing x_0 and u_0 due to the approximate temperature profile. It means, for example, with regard to Fig. 1, that the decrease of the temperature deviation with increasing space shift within certain time limits of (16) is achieved at the price of a worse approximation outside these limits.

A brief description of some different conditions for approximation is given below.

1 Equality of the temperature and heat flux given by equations (2) and (7) at $\tau = 0$ and $x = 0$. Then the time shift is estimated by (9). The space shift can be derived from (2), (7), (10), and

$$Q_s(x,t) = -\lambda \frac{\partial T(x,t)}{\partial x}\bigg|_t = Q_s(x,0) = -\lambda \frac{\partial T(x,\tau)}{\partial x}\bigg|_{\tau=0} \tag{17}$$

Then

$$x_0 = -\frac{1}{4}\sqrt{\pi at} \tag{18}$$

With these conditions, the relative deviation of temperature at $\tau = 0$ as a function of nondimensional depth is plotted on Fig. 2, according to

$$\beta = \frac{T_a(x,0)}{T(x,t)} = \frac{\exp[-(4u^2 + \sqrt{\pi}u)]}{\sqrt{\pi}\operatorname{ierfc} u} \le 1 \tag{19}$$

where the nondimensional depth is

$$u = x/2\sqrt{at} \tag{20}$$

The function $\beta = \beta(u)$ can be well approximated as

$$\beta = \exp(-3.33u^2) \tag{21}$$

The depth x_* of the relative deviation β prescribed by equation (21) can be estimated as

$$x_* \simeq 1.1\sqrt{-at \ln \beta} \tag{22}$$

2 Equality of the temperatures on the surface $x = 0$ and in

a depth x_1 at $\tau=0$ given by equations (2) and (7). Then the time shift τ_0 can still be estimated from equation (9).
The second condition

$$T(x_1,t)=T_a(x_1,0) \tag{23}$$

can be used to estimate the space shift

$$x_0=\frac{1}{2}x_1\left[1+\frac{1}{4}\left(\frac{2\sqrt{at}}{x_1}\right)^2\ln\left(\sqrt{\pi}\,\mathrm{ierfc}\,\frac{x_1}{2\sqrt{at}}\right)\right] \tag{24}$$

The appropriate depth x_1 has to be estimated from equation (7) using the prescribed value of temperature $T=T_1$. It can be done directly using an approximation (see Fig. 2)

$$\mathrm{ierfc}\,u\simeq\frac{1}{\sqrt{\pi}}\exp(-2.5u^{1.25}) \tag{25}$$

Then from (7), (20), and (25), we have

$$x_1=2\sqrt{at}\left[\ln\left(\frac{Q_s}{\lambda T_1}\times\frac{2\sqrt{at}}{\sqrt{\pi}}\right)^{0.4}\right]^{0.8} \tag{26}$$

and

$$x_0=0.5x_1[1-1.05(\sqrt{at}/x_1)^{0.75}] \tag{27}$$

The acceptability of certain values of x_0 can be estimated according to the appropriate value of β_e (Fig. 2).

3 In some problems the requirement (5) at $\tau=0$ can be reduced up to

$$\left|\frac{T_a(0,0)}{T(0,0)}-1\right|\le\left[\frac{\Delta T}{T}\right]_1 \tag{28}$$

or included in (6) at $\tau\le 0$ as

$$\left|\frac{T_a(0,0)}{T(0,0)}-1\right|\le\left[\frac{\Delta T}{T}\right] \tag{29}$$

Such a reduction of requirement (5) leads to the change of the number 0.25 in equations (9), (11), and (18) in accordance with equations (28) and (29). It can be used to reduce the maximum of relative deviation or (and) extend the limits of approximation. Of course, under the conditions described in paragraph 2, other curves similar to those presented in Fig. 1 have to be plotted.

Concluding, it has to be noted that the proposed temperature distribution (2) is both a mathematical and physical approximation. It is based on the well-known and distinct physical idea of an instantaneous energy source and extends the use of that concept in the range of a short time. As a combination of two elementary functions, it can be convenient for the description of an actual temperature profile, especially when used as a component in a further analysis.

References

1 Tslaf, A., "Calculation of the Temperature in a Conductive Track of an Arc on the Surface of a Magnet-Blast Chute," *Tr. IEEE on Plasma Science*, Vol. PS-8, No. 4, 1980, pp. 455–460.

2 Carslaw, H. S., and Jaeger, J. C., *Conduction of Heat in Solids*, Oxford at the Clarendon Press, 1959.

Enhancement of the Critical Heat Flux in Pool Boiling of Refrigerant-Oil Mixtures

M. K. Jensen[1]

Introduction

The fluid being circulated in refrigeration systems quite often is not a pure refrigerant but is a mixture of the oil used to lubricate the compressors and the refrigerant itself. The oil concentration in the system may approach 2 percent [1]. Various studies [2–4] using miscible oils in various refrigerants have shown that, with increasing oil concentration, the nucleate boiling heat transfer coefficient decreases compared to that in a pure refrigerant at the same wall superheat. In addition, at a given oil concentration there is a larger decrease in the heat transfer coefficient at high wall superheats than at lower superheats [2]. (The literature on the heat transfer coefficients in refrigerant–oil mixtures has been reviewed in detail in various papers, e.g., [1–4].) These studies have been performed generally at heat fluxes well below the critical heat flux (CHF) of the pure refrigerant. No CHF data for refrigerant–oil mixtures have been presented in the literature. Thus the effect of the dissolved oil on the CHF in pool boiling is unknown. The purpose of this paper is to report some data on the effect of the concentration of three different viscosity oils on the CHF in R113 and R11 in a saturated pool at one atmosphere.

Experimental Apparatus and Procedure

The test apparatus used in this study was basically the same as that reported in [2], except that a smaller diameter test section was used. CHF data were obtained by boiling R11, R113, and refrigerant–oil mixtures on the outside of an electrically (d-c) heated tube that was immersed in a saturated pool of the fluids at one atmosphere. The vessel was closed and incorporated a water-cooled condenser to maintain a known amount of refrigerant in the system. Thus the oil concentration for any run remained constant. An auxiliary heater in addition to the test section was used to preheat the fluid. The rising vapor bubbles from both heaters thoroughly mixed the refrigerant and oil. The pool was heavily insulated so that it remained at the saturation condition during the tests. The test section was constructed from seamless 304 stainless steel tubing 6.4 mm in dia with a wall thickness of 0.79 mm. The heated length was 102 mm. Power was conducted to the test section through 76-mm-long brass end plugs. The distance between a bus bar and the end of the test section was about 65 mm; thus the bus bars did not interfere with vapor removal.

One thermocouple was used to measure the inside wall temperature of the test section. The outside wall temperature was calculated using the one-dimensional conduction equation in cylindrical coordinates, assuming constant thermophysical properties, the measured power dissipation, and the measured inside wall temperature. One thermocouple was used to measure the pool temperature. This temperature agreed well with the saturation temperatures measured in [2]. Because of the patchiness of the boiling of refrigerant–oil mixtures on the test section, e.g., [2, 3], uncertainty in the wall superheat measurements for the refrigerant–oil mixtures is estimated to be ± 5°K at the higher heat fluxes.

The oils used in this study were the same as used in [2] and [3]. A table of the experimentally measured thermophysical properties (density, viscosity, specific heat, thermal conductivity, and surface tension) of the oils and of refrigerant–oil mixtures is given in [2]; interpolating equations are also presented which predict the mixture properties. The oils are identified in the same manner in this paper and in [2]. For identification purposes, the oil viscosities at 47°C of Oil No. 1, no. 2, and no. 3 are 22.5×10^{-3} Ns/m^2, 36.5×10^{-3} Ns/m^2, and 71.0×10^{-3} Ns/m^2, respectively.

Before testing began, the test section was thoroughly cleaned with pure refrigerant to remove any oil residue which might be present on the surface. No polishing, sanding, etc., was done on the test section. The pool was filled with approximately 6 L of pure refrigerant and heated to saturation.

[1] Department of Mechanical Engineering, University of Wisconsin—Milwaukee, Milwaukee, Wis. 53201 Mem. ASME

Contributed by the Heat Transfer Division for publication in the JOURNAL OF HEAT TRANSFER. Manuscript received by the Heat Transfer Division April 22, 1983.

a depth x_1 at $\tau=0$ given by equations (2) and (7). Then the time shift τ_0 can still be estimated from equation (9).
The second condition

$$T(x_1,t)=T_a(x_1,0) \tag{23}$$

can be used to estimate the space shift

$$x_0=\frac{1}{2}x_1\left[1+\frac{1}{4}\left(\frac{2\sqrt{at}}{x_1}\right)^2\ln\left(\sqrt{\pi}\,\mathrm{ierfc}\,\frac{x_1}{2\sqrt{at}}\right)\right] \tag{24}$$

The appropriate depth x_1 has to be estimated from equation (7) using the prescribed value of temperature $T=T_1$. It can be done directly using an approximation (see Fig. 2)

$$\mathrm{ierfc}\,u\simeq\frac{1}{\sqrt{\pi}}\exp(-2.5u^{1.25}) \tag{25}$$

Then from (7), (20), and (25), we have

$$x_1=2\sqrt{at}\left[\ln\left(\frac{Q_s}{\lambda T_1}\times\frac{2\sqrt{at}}{\sqrt{\pi}}\right)^{0.4}\right]^{0.8} \tag{26}$$

and

$$x_0=0.5x_1[1-1.05(\sqrt{at}/x_1)^{0.75}] \tag{27}$$

The acceptability of certain values of x_0 can be estimated according to the appropriate value of β_e (Fig. 2).

3 In some problems the requirement (5) at $\tau=0$ can be reduced up to

$$\left|\frac{T_a(0,0)}{T(0,0)}-1\right|\le\left[\frac{\Delta T}{T}\right]_1 \tag{28}$$

or included in (6) at $\tau\le 0$ as

$$\left|\frac{T_a(0,0)}{T(0,0)}-1\right|\le\left[\frac{\Delta T}{T}\right] \tag{29}$$

Such a reduction of requirement (5) leads to the change of the number 0.25 in equations (9), (11), and (18) in accordance with equations (28) and (29). It can be used to reduce the maximum of relative deviation or (and) extend the limits of approximation. Of course, under the conditions described in paragraph 2, other curves similar to those presented in Fig. 1 have to be plotted.

Concluding, it has to be noted that the proposed temperature distribution (2) is both a mathematical and physical approximation. It is based on the well-known and distinct physical idea of an instantaneous energy source and extends the use of that concept in the range of a short time. As a combination of two elementary functions, it can be convenient for the description of an actual temperature profile, especially when used as a component in a further analysis.

References

1 Tslaf, A., "Calculation of the Temperature in a Conductive Track of an Arc on the Surface of a Magnet-Blast Chute," *Tr. IEEE on Plasma Science*, Vol. PS-8, No. 4, 1980, pp. 455–460.

2 Carslaw, H. S., and Jaeger, J. C., *Conduction of Heat in Solids*, Oxford at the Clarendon Press, 1959.

Enhancement of the Critical Heat Flux in Pool Boiling of Refrigerant-Oil Mixtures

M. K. Jensen[1]

Introduction

The fluid being circulated in refrigeration systems quite often is not a pure refrigerant but is a mixture of the oil used to lubricate the compressors and the refrigerant itself. The oil concentration in the system may approach 2 percent [1]. Various studies [2–4] using miscible oils in various refrigerants have shown that, with increasing oil concentration, the nucleate boiling heat transfer coefficient decreases compared to that in a pure refrigerant at the same wall superheat. In addition, at a given oil concentration there is a larger decrease in the heat transfer coefficient at high wall superheats than at lower superheats [2]. (The literature on the heat transfer coefficients in refrigerant–oil mixtures has been reviewed in detail in various papers, e.g., [1–4].) These studies have been performed generally at heat fluxes well below the critical heat flux (CHF) of the pure refrigerant. No CHF data for refrigerant–oil mixtures have been presented in the literature. Thus the effect of the dissolved oil on the CHF in pool boiling is unknown. The purpose of this paper is to report some data on the effect of the concentration of three different viscosity oils on the CHF in R113 and R11 in a saturated pool at one atmosphere.

Experimental Apparatus and Procedure

The test apparatus used in this study was basically the same as that reported in [2], except that a smaller diameter test section was used. CHF data were obtained by boiling R11, R113, and refrigerant–oil mixtures on the outside of an electrically (d-c) heated tube that was immersed in a saturated pool of the fluids at one atmosphere. The vessel was closed and incorporated a water-cooled condenser to maintain a known amount of refrigerant in the system. Thus the oil concentration for any run remained constant. An auxiliary heater in addition to the test section was used to preheat the fluid. The rising vapor bubbles from both heaters thoroughly mixed the refrigerant and oil. The pool was heavily insulated so that it remained at the saturation condition during the tests. The test section was constructed from seamless 304 stainless steel tubing 6.4 mm in dia with a wall thickness of 0.79 mm. The heated length was 102 mm. Power was conducted to the test section through 76-mm-long brass end plugs. The distance between a bus bar and the end of the test section was about 65 mm; thus the bus bars did not interfere with vapor removal.

One thermocouple was used to measure the inside wall temperature of the test section. The outside wall temperature was calculated using the one-dimensional conduction equation in cylindrical coordinates, assuming constant thermophysical properties, the measured power dissipation, and the measured inside wall temperature. One thermocouple was used to measure the pool temperature. This temperature agreed well with the saturation temperatures measured in [2]. Because of the patchiness of the boiling of refrigerant–oil mixtures on the test section, e.g., [2, 3], uncertainty in the wall superheat measurements for the refrigerant–oil mixtures is estimated to be ± 5°K at the higher heat fluxes.

The oils used in this study were the same as used in [2] and [3]. A table of the experimentally measured thermophysical properties (density, viscosity, specific heat, thermal conductivity, and surface tension) of the oils and of refrigerant–oil mixtures is given in [2]; interpolating equations are also presented which predict the mixture properties. The oils are identified in the same manner in this paper and in [2]. For identification purposes, the oil viscosities at 47°C of Oil No. 1, no. 2, and no. 3 are 22.5×10^{-3} Ns/m^2, 36.5×10^{-3} Ns/m^2, and 71.0×10^{-3} Ns/m^2, respectively.

Before testing began, the test section was thoroughly cleaned with pure refrigerant to remove any oil residue which might be present on the surface. No polishing, sanding, etc., was done on the test section. The pool was filled with approximately 6 L of pure refrigerant and heated to saturation.

[1] Department of Mechanical Engineering, University of Wisconsin—Milwaukee, Milwaukee, Wis. 53201 Mem. ASME

Contributed by the Heat Transfer Division for publication in the JOURNAL OF HEAT TRANSFER. Manuscript received by the Heat Transfer Division April 22, 1983.

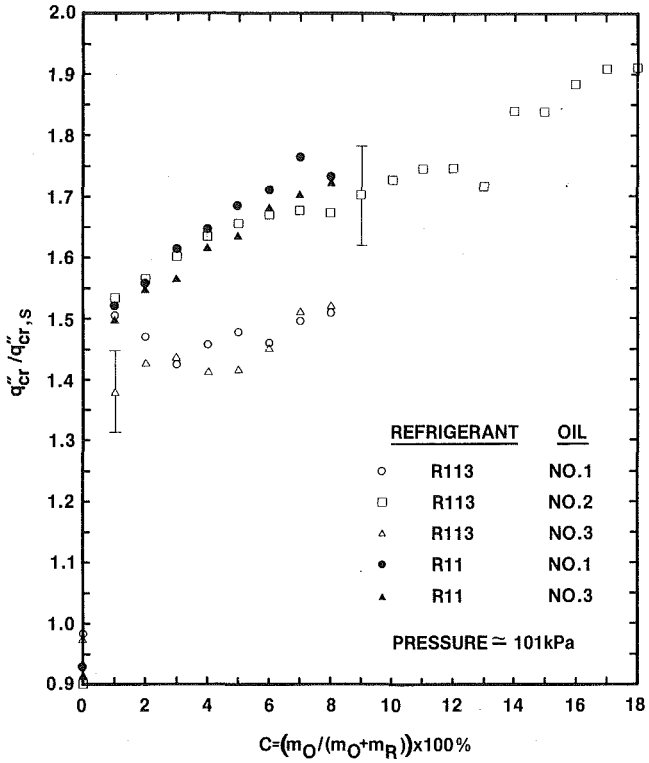

Fig. 1 Variation in the critical heat flux in refrigerant-oil mixtures

The auxiliary heater was shut off and the test section power was increased in steps until the CHF condition was indicated; power was then rapidily reduced to prevent destruction of the test section. The heat flux was raised in increments in the range of 6000–12,000 W/m^2. After the power was raised, the new level was maintained from 30 to 45 s or until the initiation of the CHF condition was observed. Oil was then added to raise the concentration of the oil in the mixture to the desired level, the auxiliary heater turned on to mix and heat the mixture, and test-section power set to about 50,000 W/m^2. After about 15 min, the auxiliary heater was shut off and testing began for a new oil concentration.

The initiation of the CHF condition was indicated by a rapid decrease in the electric current flowing through the test section. The resistance of the test section metal increases with increasing temperature. When the CHF condition is initiated, the wall temperature increases sharply. Since the voltage across the test section is the adjustable output from the power supply, the increasing test-section resistance caused by the increasing temperature causes the electrical current through the test section to fall sharply. The CHF condition initiated at localized areas. When this area was near the wall thermocouple, the wall temperature was shown to increase rapidly.

Oil concentrations up to 8 percent by weight were tested for oils no. 1 and no. 3. For each concentration of these two oils, two values of the CHF were obtained. The two values of the CHF varied less than 3 percent. The reported data are the average of the two CHF values. Likewise, the wall superheats reported are the average of the two readings. There was a variation in the wall superheats but the variations were usually less than about 5 percent. For the R113 oil no. 2 mixture, only one test was run at each oil concentration, since such consistent results were obtained during the preceding tests with the other oils. In addition, an oil concentration up to 18 percent was tested. This was done after the other oils were tested in order to determine at what oil concentration the CHF will begin to decrease. The uncertainty in the reported CHF values are estimated to be ±5 percent. The CHF condition was initiated at random axial locations along the test section.

Results

Figure 1 shows the CHF for refrigerant-oil mixtures as a function of the oil concentration. The experimental CHF, q''_{cr}, is nondimensionalized by dividing by the value of the pure refrigerant CHF, $q''_{cr,s}$ as determined by using Sun's [5] correlation as modified by Lienhard and Dhir [6]. The oil concentration is calculated by $C = m_0/(m_0 + m_R)$, where m_0 is the mass of oil and m_R is the mass of refrigerant. Figure 2 shows the wall superheat, ΔT, at the CHF, nondimensionalized by the wall superheat of the pure refrigerant, ΔT_p, which was found experimentally.

Good agreement was found between the experimental CHF's and those calculated by the modified Sun correlation for the pure refrigerant data. The R113 data fell between 0.90 and 0.98 of the modified Sun value and the R11 fell between 0.91 and 0.93. As can be seen in Fig. 1, the addition of 1 percent oil to the pure refrigerants resulted in an increase in q''_{cr} by 38 to 53 percent. Higher concentrations of oil resulted in an even higher CHF.

The behavior of a rapidly increasing q''_{cr} with a small addition of another miscible liquid on small diameter wires and on test sections with diameters comparable to the one used in this study has been discussed in detail by Van Stralen [7]. He explains this behavior as follows: In binary mixtures, because of diffusion of one component through the other, the bubble growth rate slows down. In addition, the bubble departure diameter in the binary mixture is smaller than that in a pure liquid. Both of these points have been determined experimentally [7]. Various studies have shown that bubble departure diameter and bubble frequency have an inverse relationship. Thus the smaller bubbles formed in the binary mixture are generated at higher frequencies. The higher-frequency bubbles disrupt the transient thermal boundary layer more often than in a pure liquid, stripping away the heated liquid layer more frequently. These bubbles tend not to coalesce, because of the Marangoni effect, until there is a dense bubble population on the surface. The result of this combination of increased bubble frequency and bubble population density is an increased peak CHF in the binary mixture compared to the pure liquid. Depending upon the two fluids being mixed, (e.g., water - 1 - butanol, water - ethanol, water - 1 - propanol), the CHF increases rapidly, reaches a peak, and decreases just as rapidly with increasing concentration of the more volatile component. This peak occurs at concentrations ranging from about 2 to 30 percent.

The present data are consistent with these previous findings even though the fluids being mixed have considerably different properties than the water-organic mixtures previously tested. In particular, it is the less volative liquid (oil) which is being added to the more volatile liquid (refrigerants). While there may be other possible mechanisms that could explain the CHF behavior in binary mixtures, it seems reasonable to assume that Van Stralen's basic explanation for the CHF enhancement in binary mixtures is a credible model to describe the CHF behavior for the present combination of fluids.

As can be seen in Fig. 2, there is a large increase in the peak wall superheat at the CHF for refrigerant-oil mixtures compared to the peak wall superheat at the CHF for the pure refrigerants. The increase in the peak ΔT increases with increasing oil concentration. Since the nucleate boiling curves for refrigerant-oil mixtures generally are shifted toward higher ΔT's (e.g., [2, 3]) and since the slope of the nucleate boiling curve decreases with increasing oil concentration [2, 4], the higher peak wall superheat at the CHF is to be expected. Nevertheless, the peak ΔT's obtained here are much greater than anticipated.

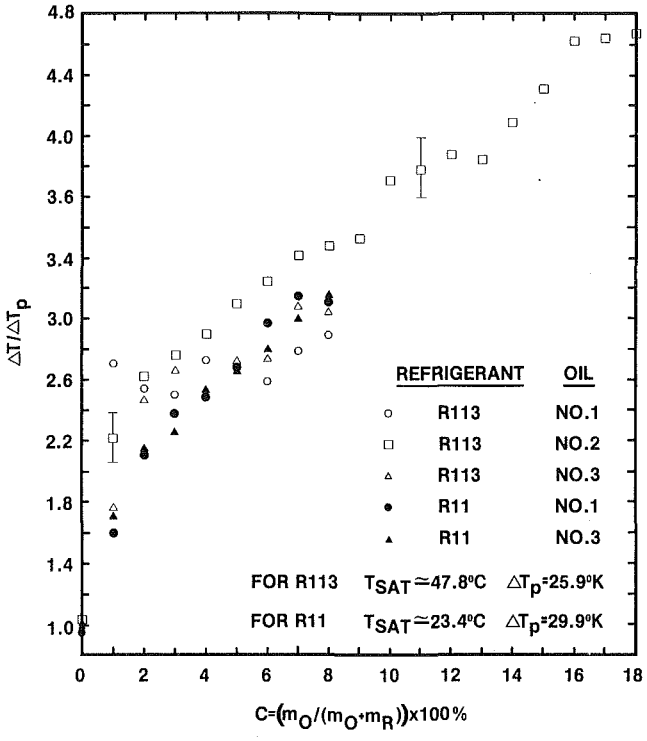

Fig. 2 Variation in wall superheat at the critical heat flux in refrigerant-oil mixtures

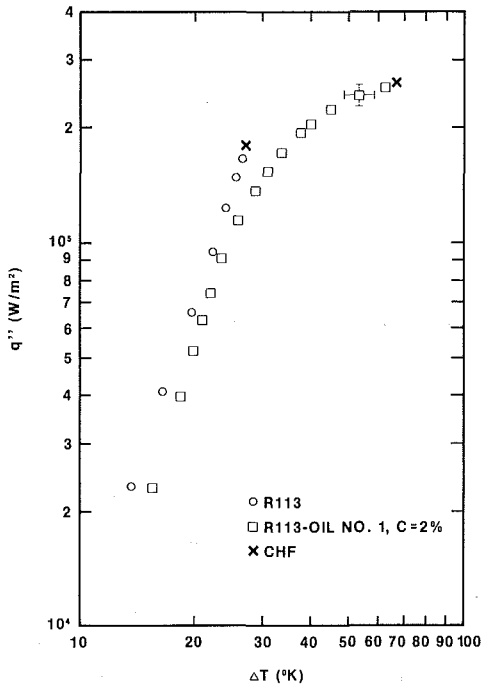

Fig. 3 Typical boiling curves for pure R-113 and R-113-oil no. 1 mixture

The shape of the boiling curves shown in Fig. 3 can be used to help explain the large increases in the peak ΔT at the CHF. These curves are consistent with previous investigations [2-4]. On this log-log plot the slope of the pure refrigerant nucleate boiling curve is linear up to the CHF; the slope of the curve for the refrigerant-oil mixture is linear up to about 60-70 percent of the pure refrigerant CHF. Then the slope of the curve for the refrigerant-oil mixture begins to decrease and becomes quite low as the CHF is approached. Jensen and Jackman [2] have shown a decreasing slope for the nucleate boiling curve with increasing oil concentration. This was attributed to an enriched-oil layer forming at the interface between the vapor bubble and the bulk liquid, with the enriched-oil layer thickness increasing with increasing wall superheat. However, in that study the maximum wall heat fluxes tested were kept to values in the range of 75 percent of the pure refrigerant CHF; thus whether or not the mechanism remains the same or changes as the CHF is approached is unknown. Perhaps as the critical heat flux is approached this enrichment mechanism is accentuated. This would cause a much shallower slope and would lead to the much larger increase in the wall superheat compared to the increase in the CHF as indicated by the present data.

The effect of the different viscosity oils is hard to assess. While the general trend in the data is consistent for all of the combinations of refrigerants and oils, there is no consistent pattern to the data with respect to the oil viscosity. For nucleate pool boiling, the viscosity of the oil has been shown to have a significant effect on the location of the boiling curve [2, 3]. However, as far as the effect of viscosity on the CHF, it is uncertain what effect, if any, it has on the CHF. More testing is required to determine just what effect the oil viscosity does have on the CHF in nucleate pool boiling.

Conclusions

An experimental investigation has been performed to determine the CHF in refrigerant-oil mixtures. A large range of concentrations of oil in R113 and R11 was tested for three different viscosity oils. The data show large increases in the CHF and much larger increases in the wall superheat at the CHF with a small addition of oil when compared to pure refrigerant data. Increasing the oil concentration results in further increases in the CHF and the wall superheat. While the data from the different viscosity oils in the two refrigerants did show some variations, no quantitative conclusions can be drawn about the effect of viscosity on the CHF condition.

References

1 Chaddock, J. B., "Influence of Oil on Refrigerant Evaporation Performance," *ASHRAE Transactions*, Vol. 82, Pt. 1, 1976, pp. 474-486.

2 Jensen, M. K., and Jackman, D. L., "Prediction of Nucleate Pool Boiling Heat Transfer Coefficients of Refrigerant-Oil Mixtures," ASME JOURNAL OF HEAT TRANSFER, Vol. 106, 1984, pp. 184-190.

3 Sauer, H. J., and Chongrungreong, S., "Nucleate Boiling Performance of Refrigerants and Refrigerant-Oil Mixtures," ASME JOURNAL OF HEAT TRANSFER, Vol. 102, 1980, pp. 701-705.

4 Stephan, K., and Mitrovic, J., "Heat Transfer in Natural Convective Boiling of Refrigerant-Oil Mixtures," *Proceedings of the 7th International Heat Transfer Conference*, Vol. 4, Munich 1982, Hemisphere Publishing, Washington, D. C., pp. 73-87.

5 Sun, K. H., and Lienhard, J. H., "The Peak Pool Boiling Heat Flux on Horizontal Cylinders," *International Journal of Heat and Mass Transfer*, Vol. 13, 1970, pp. 1425-1439.

6 Lienhard, J. H., and Dhir, V. K., "Hydrodynamic Prediction of Peak Pool Boiling Heat Fluxes from Finite Bodies," ASME JOURNAL OF HEAT TRANSFER, Vol. 95, 1973, pp. 152-158.

7 Van Stralen, S., and Cole, R., *Boiling Phenomena*, Vol. 1, ch. 9, Hemisphere Publishing, Washington, D. C., 1979, pp. 61, 219, 41-45, 219-224.

Journal of Heat Transfer

Discussion

Steady Laminar Flow Through Twisted Pipes: Fluid Flow in Square Tubes[1]

Steady Laminar Flow Through Twisted Pipes: Heat Transfer in Square Tubes[2]

Z. G. Xu[3] and D. N. Fan[4]. We would like to make two comments on the papers by Masliyah et al. The first comment is on the correct form of the viscous dissipation function, which they used to check the closure errors of their numerical results.[1] The second comment is to show their numerical solutions of cases 2, 3, and 4 are dependent.[2]

As shown by the authors [1] using a generalized matrix procedure based upon tensor analysis, the correct form of the viscous dissipation function Φ in the helical-Cartesian coordinate system is

$$\Phi=\mu\Big[2\Big(\frac{\partial V_x}{\partial x}-\frac{1}{3}\nabla\cdot\mathbf{V}\Big)^2+2\Big(\frac{\partial V_y}{\partial y}-\frac{1}{3}\nabla\cdot\mathbf{V}\Big)^2+2\Big(\frac{\delta V_z}{\delta z}-\frac{1}{3}\nabla\cdot\mathbf{V}\Big)^2+\Big(\frac{\partial V_x}{\partial y}+\frac{\partial V_y}{\partial x}\Big)^2+\Big(\frac{\delta V_y}{\delta z}+\frac{\partial V_z}{\partial y}+\theta' V_x\Big)^2+\Big(\frac{\delta V_x}{\delta z}+\frac{\partial V_z}{\partial x}-\theta' V_y\Big)^2\Big]+\eta(\nabla\cdot\mathbf{V})^2 \tag{1}$$

where μ and η are coefficients of viscosity; $\theta'(z)$ denotes the derivative of pitch angle $\theta(z)$ with respect to z; the differential operator $\delta/\delta z$ stands for $\theta'(y\,(\partial/\partial x)-x\,(\partial/\partial y))+\partial/\partial z$ and the divergence of $\mathbf{V}$ is $\partial V_x/\partial x+\partial V_y/\partial y+\delta V_z/\delta z$. The incompressible viscous dissipation function given by equation (30)[1] failed to include the $\theta' V_x$ and $\theta' V_y$ terms.

In the associated heat transfer study, it will be shown below that the temperature fields and Nusselt numbers for cases 2 and 3 can be deduced from those of case 4 by applying symmetry and the principle of superposition. The temperature fields of case 2 and case 3 are related, respectively, to that of case 4 by

$$T_2(x,y)=T_4(-x,-y)+T_4(-y,x)$$
$$T_3(x,y)=T_4(x,y)+T_4(-x,-y) \tag{2}$$

Thus it is to be expected that the respective fluid bulk temperatures satisfy the relations

$$T_{b2}=T_{b3}=2T_{b4}$$

A local Nusselt number based on the temperature difference between the local wall temperature and the fluid bulk temperature is

$$\mathrm{Nu}\,(\xi)=\frac{2a}{|T_w(\xi)-T_b|}\left.\frac{\partial T}{\partial n}\right|_\xi \tag{3}$$

where $\xi=x$ if $y=\pm a$ or $\xi=y$ if $x=\pm a$; and $T_w(\xi)$ is either a finite constant, T_0 or zero. The unit normal $\mathbf{n}$ at the wall points away from the fluid (or into the wall). The average Nusselt number for a wall is defined by

$$\overline{\mathrm{Nu}}=\frac{\int_{-a}^{a}\mathrm{Nu}\,(\xi)(1+\theta'^2\xi^2)^{1/2}d\xi}{\int_{-a}^{a}(1+\theta'^2\xi^2)^{1/2}d\xi} \tag{4}$$

The $\overline{\mathrm{Nu}}$ for a wall in case 2 and case 3 can also be obtained by superimposing $\overline{\mathrm{Nu}}$'s for case 4. It can be derived, for example, that

$$\overline{\mathrm{Nu}}_2(y=-a)=\frac{1}{T_0-T_{b2}}[T_{b4}\overline{\mathrm{Nu}}_4(y=a)+(T_0-T_{b4})\overline{\mathrm{Nu}}_4(x=a)] \tag{5}$$

$$\overline{\mathrm{Nu}}_3(x=a)=\frac{1}{T_0-T_{b3}}[(T_0-T_{b4})\overline{\mathrm{Nu}}_4(x=a)+T_{b4}\overline{\mathrm{Nu}}_4(x=-a)] \tag{6}$$

Other average Nusselt numbers can analogously be deduced.

Using the numerical values of $\overline{\mathrm{Nu}}$ for case 4 presented in Table 3[2], the calculated value of $\overline{\mathrm{Nu}}_2$ $(y=-a)$ is 11.45 compared with 11.42 as given in the table. Similarly, the calculated value of $\overline{\mathrm{Nu}}_3$ $(x=a)$ is 21.55 compared with 21.54 as deduced from tabulated values of $\overline{\mathrm{Nu}}$'s for a half of a wall. In general, the agreement between values of $\overline{\mathrm{Nu}}$ deduced from case 4 and those tabulated (presumably by direct numerical integration) is to the third significant digit inclusive.

References

1 Fan, D. N., and Xu, Z. G., *Tensorial Fluid Mechanics—a Work Book*, Space Graphic, Inc., Washington, D.C., 1983; also Chinese edition to be published by the Water Resources and Electric Power Press, Beijing, the People's Republic of China.

[1] By J. H. Masliyah and K. Nandakumar, published in the November 1981 issue of the ASME JOURNAL OF HEAT TRANSFER, Vol. 103, No. 4, pp. 785–790.

[2] Ibid, pp. 791–796.

[3] Visiting Scholar, Department of Mechanical Engineering, Howard University, Washington, D.C. 20059; also instructor, Department of Mechanical Engineering, Hangzhou Institute of Electronic Engineering, Hangzhou, Zhejiang Province, People's Republic of China.

[4] Professor, Department of Mechanical Engineering, Howard University, Washington, D.C. 20059.

Transient Heat Flux Measurement in the Combustion Chamber of a Spark Ignition Engine[1]

A. H. George[2]. Alkidas and Myers reported significant cycle-to-cycle variations in the local surface temperature and local heat flux within the combustion chamber of a spark-ignition engine.

The steady periodic solution of the one-dimensional heat conduction equation [1] was used to compute the local heat flux from measurements of the local surface temperature taken during a particular engine cycle. Unfortunately, this solution to the one-dimensional heat conduction equation is valid only if the local surface temperature time history is a periodic function of time, i.e., only if no cycle-to-cycle variations exist.

The cycle-to-cycle variations in local heat flux reported by Alkidas and Myers may not be meaningful since they are apparently based on an incorrect solution of the one-dimensional heat conduction equation.

Reference

1 Alkidas, A. C., "Heat Transfer Characteristics of a Spark-Ignition Engine," ASME JOURNAL OF HEAT TRANSFER, Vol. 102, No. 1, 1980, pp. 189–193.

Authors' Closure

Professor George's comments on the method used to evaluate cycle-to-cycle variation of local heat flux are valid. The authors are well aware that the technique used is approximate because it assumes that the local surface temperature history is a periodic function of time.

However, the authors are not aware of an "exact" technique that may be used to evaluate heat flux at each cycle. It is also important to note that the cycle-to-cycle variations in heat flux appear to be caused by cycle-to-cycle variations in flame propagation, which are random.

[1] By A. C. Alkidas and J. P. Myers, published in the February 1982 ASME JOURNAL OF HEAT TRANSFER, Vol. 104, No. 1, pp. 62–67.

[2] Division of Engineering, California State University, Chico, Calif. 95929, Assoc. Mem. ASME